

Carlos Murilo Romero Rocha

POTENTIAL ENERGY SURFACES OF ELEMENTAL CARBON CLUSTERS

Tese de doutoramento em Química, Ramo de Especialização em Química Teórica e Computacional,
orientada por António Joaquim de Campos Varandas e apresentada ao Departamento de Química
da Universidade de Coimbra

Novembro de 2017



UNIVERSIDADE DE COIMBRA



UNIVERSIDADE DE COIMBRA
Faculdade de Ciências e Tecnologia
Departamento de Química

POTENTIAL ENERGY SURFACES OF ELEMENTAL CARBON CLUSTERS

Carlos Murilo Romero Rocha

Tese de doutoramento em Química, Ramo de Especialização em Química Teórica e Computacional, orientada por António Joaquim de Campos Varandas e apresentada ao Departamento de Química da Universidade de Coimbra

Coimbra
2017

à minha família

Agradecimentos

Não seria possível aqui expressar com a devida intensidade toda a minha gratidão e apreço àqueles que contribuíram para realização deste objetivo. Primeiramente, agradeço ao meu orientador, Professor Doutor António Joaquim de Campos Varandas, pelos ensinamentos e entusiasmo que me transmitiu e pelo apoio na realização dos trabalhos aqui apresentados. Agradeço também ao meu orientador do mestrado, Professor Doutor Rogério Custodio, pelo aprendizado, companheirismo e pela fundamental ajuda em me encaminhar para o presente doutoramento.

À todos os amigos do grupo QT&C pela ajuda, paciência demonstrada e amizade. Em especial, ao Professor Sérgio, ao Caridade e ao Viegas pelo companheirismo e por compartilharem sempre seus conhecimentos e experiências.

Ao Departamento de Química da Universidade de Coimbra, pelas condições de investigação disponibilizadas, sem as quais não seria possível a realização de tais atividades.

Agradeço também à fundação de Coordenação de Aperfeiçoamento de Pessoal de Nível Superior (CAPES) pela bolsa de doutoramento Ciências sem Fronteiras (CsF - processo BEX 0417/13-0) que me foi concedida.

Um agradecimento muito especial vai à minha família, em particular, meus pais, Clezia e Antonio, e meu irmão, Eduardo, pelo amor, carinho e apoio nas horas mais difíceis. Agradeço, por fim, à Simone, pelo carinho, compreensão, apoio, e, cuja presença trará sempre luz e paz de espírito à minha vida.

Abstract

In this thesis, the structure and properties of elemental carbon clusters, notably C_2 , C_3 and C_4 , are analyzed afresh from a purely theoretical perspective and using high-level *ab initio* techniques. Special efforts are put into the characterization and computation of their potential energy surfaces (PESs) by making use of state-of-the-art electronic structure calculations followed by analytic modeling using the double many-body expansion method. Particular emphasis will be paid on C_3 whose potential energy landscape shows quite peculiar topographical attributes. For this system, rovibrational energy calculations have also been performed.

The first part of this thesis addresses the theoretical background on which the current research was based, namely the concept, the computation and the modeling of global PESs, together with their use in the calculations of spectroscopic properties. The second part though gathers the main scientific contributes of the present work. Thus, an accurate PES for ground-state C_3 will be initially obtained that obviously employs the diatomic curve of C_2 as two-body terms. Subsequently, a detailed study on the vibronic coupling effects in carbon trimer will be further presented and a Jahn-Teller plus *pseudo*-Jahn-Teller potential matrix proposed that is capable of modeling locally the 4 conical intersections (Cis) of D_{3h} and C_{2v} symmetries characteristic to the title species. Novel approaches for the analytic representation of global PESs based on the accurate description of multiple Cis as well as for obtaining spectroscopically accurate global forms will also be developed and illustrated for C_3 . Finally, a survey on the most relevant isomeric forms for the PES of C_4 will be additionally performed and a fully six-dimensional global surface is reported that reproduces all known topographical aspects of its ground triplet state.

Resumo

Nesta dissertação foram abordados os principais aspectos estruturais e eletrônicos intrínsecos à agregados de carbono elementares, nomeadamente C_2 , C_3 e C_4 , por meio de uma perspectiva teórica e baseada exclusivamente em metodologias *ab initio*. Tal estudo envolveu sobretudo a investigação e a obtenção das correspondentes superfícies de energia potencial (SEPs) empregando-se cálculos de estrutura eletrônica de alto nível e posterior representação analítica através do método da dupla expansão de multicorpos. Especial ênfase será dada ao C_3 cuja SEP apresenta características topográficas peculiares. Para tal sistema foram ainda realizados cálculos de seu espectro rotational-vibracional.

Na primeira parte, resumem-se os aspectos teóricos fundamentais para o estudo em questão, em particular, o conceito, o cálculo e a modelação de superfícies globais, bem como a utilização destas últimas no estudo de propriedades espectroscópicas. Na segunda parte, apresentam-se os principais contributos da presente investigação. Inicialmente será obtida a SEP global para o estado fundamental do C_3 , obviamente empregando-se como termo de 2 corpos a curva diatômica do C_2 . Um estudo sistemático dos efeitos vibrônicos no referido trímero será, posteriormente, efetuado e uma matriz de potencial Jahn-Teller+*pseudo*-Jahn-Teller será proposta visando à adequada descrição local de suas 4 intersecções cônicas características. Métodos de modelação de SEPs globais baseados na correta representação de múltiplos cúspides, bem como na obtenção de potenciais com qualidade (quasi-) espectroscópica serão subsequentemente desenvolvidos e aplicados ao C_3 . Por fim, serão ainda efetuados estudos de pontos estacionários relevantes para a SEP do radical C_4 e uma superfície global será obtida de forma a reproduzir os principais aspectos topográficos do estado fundamental tripleto do referido sistema.

Contents

Acronyms	5
Introductory remarks	9
Bibliography	13
I Theoretical Background	21
1 The concept of potential energy surface	23
1.1 The Schrödinger equation	24
1.2 Transformation of the Hamiltonian	26
1.2.1 Removal of translational motion	26
1.2.2 The body-fixed Hamiltonian	28
1.3 Adiabatic approximation	30
Bibliography	34
2 Conical intersections and their topological implications	37
2.1 Classification of conical intersections	38
2.2 The non-crossing rule	38
2.3 The Jahn-Teller vibronic coupling theory	42
2.4 Geometric phase effect	53
Bibliography	60

3	Calculation of potential energy surfaces	65
3.1	The Hartree-Fock self-consistent field theory	66
3.2	Electron correlation methods	74
3.2.1	CI method	76
3.2.2	Multi-configurational SCF theory	78
3.2.3	Multi-reference CI	79
3.2.4	Møller-Plesset perturbation theory	81
3.2.5	Coupled cluster methods	87
3.3	One-electron basis sets	89
3.4	Extrapolations to the complete basis set limit	93
3.5	Semiempirical corrections to <i>ab initio</i> energies	98
3.5.1	Size-consistency and size-extensivity errors	98
3.5.2	Scaling of the correlation energy	99
	Bibliography	101
4	Analytical modeling of <i>ab initio</i> energies	109
4.1	General rules and strategies	110
4.2	The MBE method	113
4.3	The DMBE method	114
4.4	Modeling of multi-sheeted potentials	116
4.5	Modeling cusps in adiabatic potentials	118
4.6	The energy-switching approach	119
	Bibliography	120
5	Exploring potential energy surfaces via rovibrational calculations	127
5.1	Coordinate systems and embedding schemes	128
5.2	Hamiltonians	130
5.3	Solutions to the bound-state problem	133
5.3.1	The variational method	134
5.3.2	Discrete variable representation	136
	Bibliography	140

II	Case Studies	145
6	Accurate <i>ab initio</i> -based double many-body expansion potential energy surface for the adiabatic ground-state of the C ₃ radical including combined Jahn-Teller plus pseudo-Jahn-Teller interactions [<i>J. Chem. Phys.</i> 143 , 074302 (2015)]	147
7	The Jahn-Teller plus pseudo-Jahn-Teller vibronic problem in the C ₃ radical and its topological implications [<i>J. Chem. Phys.</i> 144 , 064309 (2016)]	165
8	Multiple conical intersections in small linear parameter Jahn-Teller systems: the DMBE potential energy surface of ground-state C ₃ revisited (submitted)	181
9	Energy-switching potential energy surfaces for ground-state C ₃ (submitted)	195
10	C _n (n=2-4): current status [<i>Phil. Trans. R. Soc. A</i> (in Press)]	205
III	Conclusions and Outlook	251
IV	Appendices	257
A	Atomic units and conversion factors	259
	Bibliography	260
B	Derivation of the vibronic coupling constants	263
	B.1 The linear plus quadratic $E \otimes e$ problem	263
	B.2 The $(E + A_1) \otimes e$ problem	272
	Bibliography	275
C	General linear least squares method	279
	Bibliography	280
D	Parameters for the ground-state PESs of C₃	283
	D.1 DMBE I PES	283

D.2	DMBE II PES	289
D.3	ABW local PES	294
D.4	SS local PES	295
E	Rovibrational energy levels for the ground-state PESs of C₃	297
	Bibliography	305
F	Parameters for the ground-state triplet PES of C₄	307

Acronyms

ATD	adiabatic-to-diabatic.
au	atomic units.
BF	body-fixed.
BH	Born and Huang.
BO	Born and Oppenheimer.
BSSE	basis set superposition error.
CASSCF	complete active space self-consistent field.
CBS	complete basis set.
CC	coupled cluster.
cc	correlation consistent.
CGTO	contracted Gaussian-type orbital.
CI	configuration interaction.
Gi	conical intersection.
COM	center-of-mass.
CP	conterpoise.
CSF	configuration state function.
DBOC	diagonal Born-Oppenheimer correction.
DC	Davidson correction.
dc	dynamical correlation.

DGB	distributed Gaussian basis.
DIM	diatomics-in-molecules.
DMBE	double many-body expansion.
DVR	discrete variable representation.
EHF	extended Hartree-Fock.
ES	energy-switching.
FBR	finite basis representation.
FCI	full configuration interaction.
FVCAS	full valence complete active space self-consistent field.
GBO	generalized Born-Oppenheimer.
GP	geometric phase.
GTO	Gaussian-type orbital.
HF	Hartree-Fock.
irrep	irreducible representation.
JT	Jahn and Teller.
LF	laboratory-fixed.
MBE	many-body expansion.
MCSCF	multi-configurational self-consistent field.
MES	multiple energy-switching.
MO	molecular orbital.
MPn	Møller-Plesset perturbation theory.
MRCI	multi-reference CI.

NACT	non-adiabatic coupling term.
ndc	non-dynamical correlation.
PES	potential energy surface.
PJT	pseudo-Jahn-Teller.
PJTE	pseudo-Jahn-Teller effect.
RHF	restricted Hartree-Fock.
RHS	right-hand side.
rmsd	root-mean-square deviation.
ROHF	restricted open-shell Hartree-Fock.
RSPT	Rayleigh-Schrödinger perturbation theory.
RT	Renner-Teller.
RTE	Renner-Teller effect.
SCF	self-consistent field.
SD	Slater determinant.
SEC	scaled external correlation.
SF	space-fixed.
SI	international system of units.
SLP	small linear parameter.
STO	Slater-type orbital.
TDSE	time-dependent Schrödinger equation.
TIESE	time-independent electronic Schrödinger equation.
TISE	time-independent Schrödinger equation.
UHF	unrestricted Hartree-Fock.
USTE	uniform singlet- and triplet-pair extrapolation.

VBR variational basis representation.

VCC vibronic coupling constant.

Introductory remarks

Carbon is one of the most abundant element in the Universe and is of paramount importance to all living organisms on Earth. It provides the backbone of structural and functional compounds necessary for life like DNA, proteins, fats, and carbohydrates [1]. Undoubtedly, the raw material for these complex biological molecules is primarily atmospheric carbon dioxide (CO_2) which is incorporated in terrestrial ecosystems via photosynthetic organisms. In the course of such well-known carbon cycle, carbon (again, in the form of CO_2) is released back into atmosphere through respiration and other oxidative processes (such as decomposition or combustion of organic materials) [2].

Besides being crucial to life, carbon-bearing molecules are also key for a wide range of technology fields ranging from material chemistry to pharmaceuticals [3, 4]. Clearly, what brings all such vast branches of science together is the uniqueness of carbon chemistry itself. Carbon is capable of forming strong covalent bonds with almost all elements (and with itself) in diverse hybridization states (sp , sp^2 and sp^3), yielding a myriad of possible structures with outstanding chemical and physical properties [5, 6].

Elemental carbon exists in nature as two common allotropes, diamond and graphite. They differ in the way that C atoms are attached together to form extended crystalline networks. Diamond is made up of sp^3 -hybridized (tetrahedral) carbon atoms, while graphite comprises of stacked sp^2 carbon sheets (or graphene layers) arranged in a hexagonal manner [7–9]. As expected from these distinct bonding patterns, such allotropic forms exhibit quite remarkable differences in their observable properties. Diamond is a transparent insulator material which is widely appreciated as being the hardest natural substance known. On the other hand, graphite is an opaque, fragile dark material that shows

exceptional conductivity properties due to its delocalized π electrons [6, 10].

New avenues on the field of carbon chemistry have been traced after the isolation and structural characterization of the soccer-ball-shaped C_{60} molecule [11, 12]. Such carbon allotrope consists of 60 sp^2 -hybridized C atoms which are arranged in 12 pentagons and 20 hexagons to form an I_h -symmetrical structure [11]. Indeed, several other fullerene structures such as C_{70} , C_{76} , C_{78} , C_{84} and C_{90} have soon been recognized [10, 13]. The astonishing properties and diverse potential applications of fullerenes motivated intense research toward the identification of new possible stable allotropic forms. This led to the discovery of the single- and multi-walled carbon nanotubes [14, 15], the preparation of single-layer graphene sheets [16] and the introduction of various elusive synthetic allotropes [6, 17], all of them with remarkable electrical, mechanical, chemical and optical properties.

Undoubtedly, a detailed knowledge of the fascinating (and often unexpected) complexities of these large carbon aggregates is only attainable once the chemical properties of their involved precursors, *i.e.*, the smallest pure carbon molecules, have been fully clarified. Indeed, small C_n clusters have been the subject of an intense research effort and continue to be target prototypes for understanding a large variety of complex chemical environments [18, 19]. Molecules of this kind are known to appear in a myriad of astrophysical objects, particularly in the atmospheres of carbon stars [20–24] and in the sun [25] as well as in comets [26–28] and interstellar clouds [29–32].

Carbon is formed by nuclear fusions in the cores of stars (a phenomenon often referred to as 3α process [33]) which, in the late stages of stellar evolution, is ejected into their outer layers and subsequently to the interstellar medium. In these latter environments, chemical reactions are prone to occur that transform atomic C gas into complex organic molecules and dust grains [34, 35]. In this context, small carbon aggregates are thought to be fundamental building blocks for the formation of such involved interstellar C-rich compounds like $HC_{2n+1}N$, C_nH , C_nH_2 , C_nN , C_nO , C_nS , polycyclic aromatic hydrocarbons and fullerenes (C_{60} and C_{70}) [35–38]. Apart from their astrochemical ubiquity, carbon clusters are also prominent species in equilibrium hot carbon vapors and plasmas generated through energetic processing of C-containing materials [39], hydrocarbon

flames [40] and in other soot-forming terrestrial environments [41].

Clearly, the elucidation of the structural, spectroscopic, and energetic properties of such species could provide valuable tools for unraveling their underlying chemistry and also for clarifying the unknown growth processes leading to the formation of larger aggregates. Yet, small C_n clusters are highly reactive (short-lived) molecules under most laboratory conditions which makes their experimental characterization extremely involved [18, 19]. Moreover, the existence of numerous close-in-energy isomeric forms (ranging from linear chains to monocyclic/polycyclic rings), high-density of low-lying singlet/triplet electronic states, pronounced biradical character and (pseudo-) Jahn-Teller effects all complicate their theoretical description too [42–50]. Definitely, a detailed study of these molecules requires a fruitful interplay of state-of-the-art experimental techniques and high-level *ab initio* approaches.

What bridges the gap between these latter two is unavoidably the very notion of potential energy surfaces (PESs). Within the adiabatic approximation [51–53], PESs describe the potential energy of a system in terms of the relative positions of the atoms that make up this system. Inevitably, such potentials carry precise information about the underlying species, and are therefore conceptually important tools for the analysis of structural isomers, spectroscopy and chemical reaction dynamics [54]. From the theoretical perspective, PESs are obtained by solving the electronic Schrödinger equation at sufficiently many (fixed) nuclear configurations whose energies are subsequently modeled by some physically motivated analytic function. In so doing, one therefore is faced with the usefulness of such functional representations of PESs which can then be subjected to the nuclear motion problem, yielding dynamical observables in which to compare and corroborate with experiment. At present, robust theoretical framework and computational resources make thus possible to extensively explore the nuclear configuration space of small polyatomics with the aim of constructing accurate and global *ab initio*-based PESs.

The main goal of the present doctoral thesis is to provide such PESs for the smallest pure carbon chains, namely C_2 , C_3 and C_4 , using high-level *ab initio* calculations and the double many-body expansion (DMBE) method [55–57] for the modeling. Besides shedding light on some fundamental issues of such species, it is also expected that,

by making full use of the many-body expansion methodology [54], the potentials so obtained should offer the fundamental building blocks for constructing PESs of more involved carbon aggregates, an assumption already demonstrated here for C_4 .

This thesis is divided into three parts. The first concerns with the theoretical framework supporting the current research, while the second part gathers the results so obtained. The major scientific achievements and outlook are briefly summarized in the last part of this work. The first five chapters are entirely theoretical in character and are intended to cover only the fundamental aspects on each topic discussed. The subsequent chapters, which cover the results obtained by our research, are presented as manuscripts published in peer-reviewed journals. They can all be outlined as follows.

Chapter 1 presents the concept of PESs. Chapter 2 gives insights into the main aspects of conical intersections and their implications on molecular systems. The general vibronic coupling theory as typified by the so-called Jahn-Teller effect is also summarized. Chapter 3 gives a survey onto the electronic structure methods currently available for calculating PESs, while in chapter 4 the formalism used to construct analytic representation of global potentials are discussed. Chapter 5 deals with the methods here employed for the calculation of rovibrational energy levels using the present DMBE forms.

In chapter 6, an accurate global DMBE PES for ground-state C_3 is presented [58] that utilizes the potential energy curve of $C_2(a^3\Pi_u)$ as two-body terms and describes the main topographical features of the title system. In a subsequent chapter, the Jahn-Teller plus *pseudo*-Jahn-Teller vibronic problem characteristic to the carbon trimer is further exploited [45] in order to rationalize its interesting topographical attributes (4 conical intersections) near the region defined by equilateral triangular geometries.

Based on the results so obtained, in chapter 8, a revisited form for the previously obtained potential for $C_3(1^1A')$ is proposed [59] by developing a novel approach for the modeling of multiple conical intersections [60, 61] on the title and related systems. Additionally, in chapter 9, (near) spectroscopic accuracy is also conveyed [62] to this latter global form by applying a simplified version of the multiple energy switching scheme [63, 64] and the best currently available local (spectroscopic) potentials for C_3 [65, 66].

Finally, in chapter 10, the most relevant isomeric forms on both singlet and triplet

PESs of C_4 radical are surveyed using full-valence multi-configurational approaches and extrapolations to the complete basis set limit [67]. Starting from an approximate cluster expansion of the molecular potential that utilizes the latest reported function for C_3 radical, an approximate four-body term has also been proposed and calibrated using accurate *ab initio* energies. The resulting fully six-dimensional global DMBE form reproduces all known topographical aspects of the ground triplet state of the title system as well as its linear-rhombic isomerization path [67].

Bibliography

- [1] K. West, *Carbon Chemistry*, 1st ed. (Chelsea House, New York, 2008).
- [2] M. Heimann, *Ambio* **26**, 17 (1997).
- [3] T. D. Burchell, *Carbon Materials for Advanced Technologies*, 1st ed. (Pergamon, Oxford, 1999).
- [4] A. Demming, *Nanotechnology* **21**, 300201 (2010).
- [5] A. Hirsch, *Nat. Mater.* **9**, 868 (2010).
- [6] V. Georgakilas, J. A. Perman, J. Tucek, and R. Zboril, *Chem. Rev.* **115**, 4744 (2015).
- [7] W. H. Bragg and W. L. Bragg, *Nature* **91**, 557 (1913).
- [8] W. H. Bragg and W. L. Bragg, *Proc. R. Soc. Lond. A* **89**, 277 (1913).
- [9] A. W. Hull, *Phys. Rev.* **10**, 661 (1917).
- [10] P. W. Atkins, T. L. Overton, J. P. Rourke, W. T. Weller, and F. A. Armstrong, *Shriver and Atkins' Inorganic Chemistry*, 5th ed. (Oxford University Press, New York, 2010).
- [11] H. W. Kroto, J. R. Heath, S. C. O'Brien, R. F. Curl, and R. E. Smalley, *Nature* **318**, 162 (1985).
- [12] W. Krätschmer, L. D. Lamb, K. Fostiropoulos, and D. R. Huffman, *Nature* **347**, 354 (1990).

-
- [13] H. Yang, C. Beavers, Z. Wang, A. Jiang, Z. Liu, H. Jin, B. Mercado, M. Olmstead, and A. Balch, *Angew. Chem. Int. Ed.* **49**, 886 (2010).
- [14] S. Iijima, *Nature* **354**, 56 (1991).
- [15] S. Iijima and T. Ichihashi, *Nature* **363**, 603 (1993).
- [16] K. S. Novoselov, A. K. Geim, S. V. Morozov, D. Jiang, Y. Zhang, S. V. Dubonos, I. V. Grigorieva, and A. A. Firsov, *Science* **306**, 666 (2004).
- [17] F. Diederich and M. Kivala, *Adv. Mat.* **22**, 803 (2010).
- [18] W. Weltner and R. J. Van Zee, *Chem. Rev.* **89**, 1713 (1989).
- [19] A. Van Orden and R. J. Saykally, *Chem. Rev.* **98**, 2313 (1998).
- [20] A. McKellar, *J. R. Astron. Soc. Can.* **54**, 97 (1960).
- [21] D. Crampton, A. P. Cowley, and R. M. Humphreys, *Astrophys. J.* **198**, L135 (1975).
- [22] K. W. Hinkle, J. J. Keady, and P. F. Bernath, *Science* **241**, 1319 (1988).
- [23] P. F. Bernath, K. W. Hinkle, and J. J. Keady, *Science* **244**, 562 (1989).
- [24] R. J. Hargreaves, K. Hinkle, and P. F. Bernath, *Mon. Not. R. Astron. Soc.* **444**, 3721 (2014).
- [25] J. W. Brault, L. Testerman, N. Grevesse, A. J. Sauval, L. Delbouille, and G. Roland, *Astron. Astrophys.* **108**, 201 (1982).
- [26] W. Huggins, *Proc. R. Soc. London* **33**, 1 (1881).
- [27] A. E. Douglas, *Astrophys. J.* **114**, 446 (1951).
- [28] L. M. Lara, Z.-Y. Lin, R. Rodrigo, and W.-H. Ip, *Astron. Astrophys.* **525**, A36 (2011).
- [29] D. L. Lambert, Y. Sheffer, and S. R. Federman, *Astrophys. J.* **438**, 740 (1995).

-
- [30] G. A. Galazutdinov, F. A. Musaev, and J. Krelowski, *Mon. Not. R. Astron. Soc.* **325**, 1332 (2001).
- [31] J. Cernicharo, J. R. Goicoechea, and Y. Benilan, *Astrophys. J.* **580**, L157 (2002).
- [32] N. L. J. Cox and F. Patat, *Astron. Astrophys.* **565**, A61 (2014).
- [33] E. M. Burbidge, G. R. Burbidge, W. A. Fowler, and F. Hoyle, *Rev. Mod. Phys.* **29**, 547 (1957).
- [34] T. Henning and F. Salama, *Science* **282**, 2204 (1998).
- [35] P. Ehrenfreund and B. H. Foing, *Science* **329**, 1159 (2010).
- [36] P. Ehrenfreund and J. Cami, *Cold Spring Harb. Perspect. Biol.* **2**, 1 (2010).
- [37] J. Cami, J. Bernard-Salas, E. Peeters, and S. E. Malek, *Science* **329**, 1180 (2010).
- [38] N. Sakai and S. Yamamoto, *Chem. Rev.* **113**, 8981 (2013).
- [39] L. Nemes, A. M. Keszler, C. G. Parigger, J. O. Hornkohl, H. A. Michelsen, and V. Stakhursky, *Appl. Opt.* **46**, 4032 (2007).
- [40] P. Gerhardt, S. Löffler, and K. H. Homann, *Chem. Phys. Lett.* **137**, 306 (1987).
- [41] H. W. Kroto and K. McKay, *Nature* **331**, 328 (1988).
- [42] L. Belau, S. E. Wheeler, B. W. Ticknor, M. Ahmed, S. R. Leone, W. D. Allen, H. F. Schaefer, and M. A. Duncan, *J. Am. Chem. Soc.* **129**, 10229 (2007).
- [43] K. E. Yousaf and P. R. Taylor, *Chem. Phys.* **349**, 58 (2008).
- [44] A. J. C. Varandas, *Chem. Phys. Lett.* **471**, 315 (2009).
- [45] C. M. R. Rocha and A. J. C. Varandas, *J. Chem. Phys.* **144**, 064309 (2016).
- [46] H. Massó, M. L. Senent, P. Rosmus, and M. Hochlaf, *J. Chem. Phys.* **124**, 234304 (2006).

-
- [47] H. Massó, V. Veryazov, P. A. Malmqvist, B. O. Roos, and M. L. Senent, *J. Chem. Phys.* **127**, 154318 (2007).
- [48] H. Massó and M. L. Senent, *J. Phys. Chem. A* **113**, 12404 (2009).
- [49] M. M. Al-Mogren, M. L. Senent, and M. Hochlaf, *J. Chem. Phys.* **139**, 064301 (2013).
- [50] D. Sharapa, A. Hirsch, B. Meyer, and T. Clark, *ChemPhysChem* **16**, 2165 (2015).
- [51] M. Born and R. Oppenheimer, *Ann. Phys.* **389**, 457 (1927).
- [52] M. Born, *Gött. Nachr. Akad. Wiss. Math. Phys. Kl.* **6**, 1 (1951).
- [53] M. Born and K. Huang, *Dynamical Theory of Crystal Lattices* (Clarendon Press, Oxford, 1954).
- [54] J. N. Murrell, S. Carter, S. C. Farantos, P. Huxley, and A. J. C. Varandas, *Molecular Potential Energy Functions* (John Wiley & Sons, Chichester, 1984).
- [55] A. J. C. Varandas, *Mol. Phys.* **53**, 1303 (1984).
- [56] A. J. C. Varandas, *J. Mol. Struct.: THEOCHEM* **120**, 401 (1985).
- [57] A. J. C. Varandas, *Adv. Chem. Phys.* **74**, 255 (1988).
- [58] C. M. R. Rocha and A. J. C. Varandas, *J. Chem. Phys.* **143**, 074302 (2015).
- [59] C. M. R. Rocha and A. J. C. Varandas, submitted (2017).
- [60] B. R. L. Galvão, V. C. Mota, and A. J. C. Varandas, *J. Phys. Chem. A* **119**, 1415 (2015).
- [61] B. R. L. Galvão, V. C. Mota, and A. J. C. Varandas, *Chem. Phys. Lett.* **660**, 55 (2016).
- [62] C. M. R. Rocha and A. J. C. Varandas, submitted (2017).
- [63] A. J. C. Varandas, *J. Chem. Phys.* **105**, 3524 (1996).
- [64] A. J. C. Varandas, *J. Chem. Phys.* **119**, 2596 (2003).

-
- [65] K. Ahmed, G. G. Balint-Kurti, and C. M. Western, *J. Chem. Phys.* **121**, 10041 (2004).
- [66] B. Schröder and P. Sebald, *J. Chem. Phys.* **144**, 044307 (2016).
- [67] A. J. C. Varandas and C. M. R. Rocha, *Phil. Trans. R. Soc. A* (in Press) (2017).

Part I

Theoretical Background

Chapter 1

The concept of potential energy surface

A complete theoretical description of the structure and properties of molecular systems naturally emerges from the laws of electronic and nuclear motion. Yet, molecules are complicated quantum objects, and as such many mathematical difficulties arise in solving the resulting Schrödinger equations [1–4]. Such entanglements led to the introduction of essential approximations in order to justify their quantum mechanical treatment.

The cornerstone of our understanding of chemical processes and molecular structure has been hinted at by Born and Oppenheimer (BO) [5] in the early days of quantum mechanics. In the BO framework, the physical picture behind the approximate separability of electronic and nuclear motion rests on the fact that the latter are much more massive than the former, and therefore fast electrons adjust their positions instantaneously as the slow nuclei move. Thence, in this so-called adiabatic approximation [5–7], one first solve an electronic problem with the nuclear variables treated as parameters. Then, the resulting electronic energies as a function of such parameters, *i.e.*, the potential energy surface (PES), act (to a first approximation) as an effective potential for the nuclear motion. Such a PES therefore carries important insights into the structure, spectroscopy, and reactivity of the molecule.

Although the adiabatic approximation is at the heart the way we think about chemistry,

there are several important situations where it breaks down. One of the most striking example appears whenever two (or more) PESs become degenerate or nearly-degenerate at some points in the nuclear configuration space. In such cases, the non-negligible coupling between electronic and nuclear degrees of freedom is ubiquitous, and hence non-adiabatic phenomena plays a central role.

1.1 The Schrödinger equation

Consider a system of L electrons and H nuclei, interacting through Coulomb forces. The non-relativistic time-dependent Schrödinger equation (TDSE) describing the complete many-body problem assumes the form [1–4]

$$\hat{\mathcal{H}}_T |\Omega_n(\mathbf{r}'', \mathbf{R}'', t)\rangle = i\hbar \frac{\partial}{\partial t} |\Omega_n(\mathbf{r}'', \mathbf{R}'', t)\rangle, \quad (1.1)$$

where $\hat{\mathcal{H}}_T$ is the total non-relativistic Hamiltonian operator and $|\Omega_n(\mathbf{r}'', \mathbf{R}'', t)\rangle$ is the total molecular wave function for a quantum state n which depend explicitly on the time t and the set of all electronic $\mathbf{r}''_i (i=1, 2, \dots, L)$ and nuclear $\mathbf{R}''_i (i=1, 2, \dots, H)$ coordinates¹ measured relative to the laboratory-fixed (LF) frame. In turn, $i = \sqrt{-1}$ is the imaginary unit and $\hbar = h/2\pi$ is the reduced Planck's constant. In the absence of external time-varying fields², the LF form of $\hat{\mathcal{H}}_T$ is then [in atomic units (au); see appendix A]

$$\hat{\mathcal{H}}_T(\mathbf{r}'', \mathbf{R}'') = \hat{\mathcal{T}}_N(\mathbf{R}'') + \hat{\mathcal{T}}_e(\mathbf{r}'') + \hat{\mathcal{U}}(\mathbf{r}'', \mathbf{R}''), \quad (1.2)$$

where $\hat{\mathcal{T}}_N(\mathbf{R}'')$ and $\hat{\mathcal{T}}_e(\mathbf{r}'')$ are the kinetic energy operators for the motion of the nuclei and electrons, respectively, which are defined as

$$\hat{\mathcal{T}}_N(\mathbf{R}'') = -\frac{1}{2} \sum_{i=1}^H \frac{1}{\mathcal{M}_i} \nabla^2(\mathbf{R}''_i), \quad (1.3)$$

and

$$\hat{\mathcal{T}}_e(\mathbf{r}'') = -\frac{1}{2} \sum_{i=1}^L \nabla^2(\mathbf{r}''_i). \quad (1.4)$$

¹It is convenient to regard $\mathbf{r}''_i(\mathbf{R}'')$ as a column matrix of three Cartesian components with $\mathbf{r}''(\mathbf{R}'')$ being, therefore, a 3 by $L(H)$ matrix.

²In such cases, the Hamiltonian is not explicitly time dependent.

In the above equations, $\mathcal{M}_i = M_i/m_e$ is the ratio of the mass of nucleus i (M_i) to the mass of an electron (m_e) and ∇^2 is the usual Laplacian operator expressed in the Cartesian components of \mathbf{r}''_i and \mathbf{r}''_j . In Eq. (1.2), $\hat{\mathcal{U}}(\mathbf{r}'', \mathbf{R}'')$ is the total potential energy operator

$$\hat{\mathcal{U}}(\mathbf{r}'', \mathbf{R}'') = \hat{\mathcal{V}}_{ee}(\mathbf{r}'') + \hat{\mathcal{V}}_{Ne}(\mathbf{r}'', \mathbf{R}'') + \hat{\mathcal{V}}_{NN}(\mathbf{R}''), \quad (1.5)$$

with $\hat{\mathcal{V}}_{ee}(\mathbf{r}'')$, $\hat{\mathcal{V}}_{Ne}(\mathbf{r}'', \mathbf{R}'')$ and $\hat{\mathcal{V}}_{NN}(\mathbf{R}'')$ representing the associated operators arising from the electron-electron, nucleus-electron and nucleus-nucleus interactions

$$\hat{\mathcal{V}}_{ee}(\mathbf{r}'') = \sum_{i=1}^L \sum_{j>i}^L \frac{1}{|\mathbf{r}''_i - \mathbf{r}''_j|}, \quad (1.6)$$

$$\hat{\mathcal{V}}_{Ne}(\mathbf{r}'', \mathbf{R}'') = - \sum_{i=1}^H \sum_{j=1}^L \frac{Z_i}{|\mathbf{R}''_i - \mathbf{r}''_j|}, \quad (1.7)$$

and

$$\hat{\mathcal{V}}_{NN}(\mathbf{R}'') = \sum_{i=1}^H \sum_{j>i}^H \frac{Z_i Z_j}{|\mathbf{R}''_i - \mathbf{R}''_j|}, \quad (1.8)$$

where Z_i is the atomic number of the i -th nucleus.

If $\hat{\mathcal{H}}_T$ does not contain time explicitly, as assumed in Eq. (1.2), then the TDSE [Eq. (1.1)] can be separated from its space and time dependencies by writing [8, 9]

$$|\Omega_n(\mathbf{r}'', \mathbf{R}'', t)\rangle = \mathcal{D}_n(t) |\Psi_n(\mathbf{r}'', \mathbf{R}'')\rangle, \quad (1.9)$$

where

$$\mathcal{D}_n(t) = e^{-iE_n t/\hbar}. \quad (1.10)$$

In Eqs. (1.9) and (1.10), $\mathcal{D}_n(t)$ is the usual dynamic phase factor and $|\Psi_n(\mathbf{r}'', \mathbf{R}'')\rangle$ is the stationary-state molecular wave function which depends on the electronic (\mathbf{r}'') and nuclear coordinates (\mathbf{R}'') only. By inserting the ansatz (1.9) into Eq. (1.1) and multiplying both sides by $1/\mathcal{D}_n(t)$, we obtain [8, 9]

$$\hat{\mathcal{H}}_T |\Psi_n(\mathbf{r}'', \mathbf{R}'')\rangle = E_n |\Psi_n(\mathbf{r}'', \mathbf{R}'')\rangle, \quad (1.11)$$

which is the time-independent Schrödinger equation (TISE) [1–4]. Indeed, the $|\Psi_n(\mathbf{r}'', \mathbf{R}'')\rangle$'s (and also the stationary states³ $|\Omega_n(\mathbf{r}'', \mathbf{R}'', t)\rangle$) are both eigenfunctions of $\hat{\mathcal{H}}_T$ with associated eigenvalues E_n . Such functions, therefore, form a complete set $\{|\Psi_n(\mathbf{r}'', \mathbf{R}'')\rangle\}_{n=1}^N$ of orthonormal [$\langle\Psi_n(\mathbf{r}'', \mathbf{R}'')|\Psi_m(\mathbf{r}'', \mathbf{R}'')\rangle = \delta_{nm}$] eigenkets in the N -dimensional Hilbert space.

1.2 Transformation of the Hamiltonian

1.2.1 Removal of translational motion

It is well established that the full LF Hamiltonian given in Eqs. (1.2)-(1.8) is invariant under coordinate transformations corresponding to uniform translations [10–13]. This means that the molecular center-of-mass (COM) moves through space like a free particle whose spectrum is completely continuous and associated eigenfunctions not square integrable. Thence, if there are $P = L + H$ particles, it is always possible to factorize the variable space \mathbb{R}^{3P} as $\mathbb{R}^3 \otimes \mathbb{R}^{3P-3}$, where the variables in \mathbb{R}^{3P-3} are translation free. This process is called setting up a space-fixed (SF) frame. Such a frame is, therefore, parallel to the LF one but it moves with the COM.

The required linear transformation may be written as

$$\mathbf{P}' = \mathbf{P}''\mathbf{V}, \quad (1.12)$$

where $\mathbf{P}' = (\mathbf{r}'\mathbf{R}'\mathbf{X}_T)$ is a 3 by P matrix whose submatrices are expressed entirely in terms of $3L$ and $3H-3$ SF electronic (\mathbf{r}') and nuclear (\mathbf{R}') degrees of freedom, respectively, as well as 3 COM coordinates (\mathbf{X}_T). In turn, $\mathbf{P}'' = (\mathbf{r}''\mathbf{R}'')$ is the associated LF coordinate matrix and \mathbf{V} is a suitable P by P transformation matrix [14–16]. In the above equation, \mathbf{X}_T assumes the form (in au)

$$\mathbf{X}_T = M_T^{-1} \left(\sum_{i=1}^L \mathbf{r}_i'' + \sum_{i=1}^H \mathcal{M}_i \mathbf{R}_i'' \right), \quad (1.13)$$

³A quantum state is called *stationary* if the probability density $|\Omega_n(\mathbf{r}'', \mathbf{R}'', t)|^2 = |\Psi_n(\mathbf{r}'', \mathbf{R}'')|^2$ is time independent and all observables (and associated quantum mechanical operators) which do not depend explicitly on time have time-independent expectation values.

with

$$M_T = \left(L + \sum_{i=1}^H \mathcal{M}_i \right). \quad (1.14)$$

Thence, the Hamiltonian $\hat{\mathcal{H}}_T$ [Eq. (1.2)] in the new coordinates becomes [11–13]

$$\hat{\mathcal{H}}_T(\mathbf{r}'', \mathbf{R}'') \xrightarrow{\mathbf{V}} \hat{\mathcal{H}}_T(\mathbf{r}', \mathbf{R}', \mathbf{X}_T) = \hat{\mathcal{T}}_{COM}(\mathbf{X}_T) + \hat{\mathcal{H}}_{RI}(\mathbf{r}', \mathbf{R}'), \quad (1.15)$$

where $\hat{\mathcal{T}}_{COM}(\mathbf{X}_T)$ represents the kinetic energy operator for the COM motion

$$\hat{\mathcal{T}}_{COM}(\mathbf{X}_T) = -\frac{1}{2M_T} \nabla^2(\mathbf{X}_T). \quad (1.16)$$

As seen in Eq. (1.15), the COM variable does not enter the SF Hamiltonian $\hat{\mathcal{H}}_{RI}(\mathbf{r}', \mathbf{R}')$, and therefore such a problem may be separated off completely [11]. Indeed, the full solution is of the form⁴

$$|\Psi_n(\mathbf{r}'', \mathbf{R}'')\rangle = |T(\mathbf{X}_T)\rangle |\Psi_n(\mathbf{r}', \mathbf{R}')\rangle, \quad (1.17)$$

where

$$|T(\mathbf{X}_T)\rangle = e^{i\mathbf{p}\mathbf{X}_T}, \quad (1.18)$$

and associated translational energy

$$E_T = \frac{|\mathbf{p}|^2}{2M_T}. \quad (1.19)$$

In the above equations, $\mathbf{p} = [p_x p_y p_z]$ is the COM linear momentum whose components $[p_\alpha = M_T d\alpha/dt (\alpha = x, y, z)]$ are defined with respect to the origin of the LF frame. Note that the translational wave function $|T(\mathbf{X}_T)\rangle$ is not square integrable and the associated translational energy E_T is continuous [12].

The SF (translation-free) Hamiltonian ($\hat{\mathcal{H}}_{RI}$) of Eq. (1.15) is then

$$\hat{\mathcal{H}}_{RI}(\mathbf{r}', \mathbf{R}') = \hat{\mathcal{T}}_N(\mathbf{R}') + \hat{\mathcal{T}}_e(\mathbf{r}') + \hat{\mathcal{T}}_{MP}(\mathbf{r}') + \hat{\mathcal{U}}(\mathbf{r}', \mathbf{R}'), \quad (1.20)$$

⁴By inserting Eqs. (1.15) and (1.17) in Eq. (1.11), dividing both sides by $1/[|T(\mathbf{X}_T)\rangle |\Psi_n(\mathbf{r}', \mathbf{R}')\rangle]$ and solving the resulting differential equations.

with $\hat{\mathcal{T}}_N(\mathbf{R}')$ and $\hat{\mathcal{T}}_e(\mathbf{r}')$ given now by

$$\hat{\mathcal{T}}_N(\mathbf{R}') = -\frac{1}{2} \sum_{i,j=1}^{H-1} \frac{1}{\mu_{ij}} \vec{\nabla}(\mathbf{R}'_i) \cdot \vec{\nabla}(\mathbf{R}'_j), \quad (1.21)$$

and

$$\hat{\mathcal{T}}_e(\mathbf{r}') = -\frac{1}{2\mu_e} \sum_{i=1}^L \nabla^2(\mathbf{r}'_i), \quad (1.22)$$

where μ_{ij} and μ_e are the effective (reduced) masses of the nuclei and electrons, respectively. In Eq. (1.20), $\hat{\mathcal{T}}_{MP}(\mathbf{r}')$ is the so-called mass polarization term [13, 17] expressed as

$$\hat{\mathcal{T}}_{MP}(\mathbf{r}') = -\frac{1}{2\mathcal{M}_T} \sum_{i,j=1}^L \vec{\nabla}(\mathbf{r}'_i) \cdot \vec{\nabla}(\mathbf{r}'_j), \quad (1.23)$$

where $\mathcal{M}_T = \sum_{i=1}^H \mathcal{M}_i$ is the total nuclear mass and $\hat{\mathcal{U}}(\mathbf{r}', \mathbf{R}')$ is defined just as in Eq. (1.5) but using SF coordinates (\mathbf{r}' and \mathbf{R}') instead of LF ones (\mathbf{r}'' and \mathbf{R}''). Note that, depending on the choice of the SF coordinates, mixed electronic-nuclear kinetic energy terms may also appear in Eq. (1.20). Suffice it to say that, in Eq. (1.17), $|\Psi_n(\mathbf{r}', \mathbf{R}')\rangle$ is now eigenfunction of $\hat{\mathcal{H}}_{RI}(\mathbf{r}', \mathbf{R}')$ [Eq. (1.20)].

1.2.2 The body-fixed Hamiltonian

It can be realized that the translation-free problem is still invariant under orthogonal transformations (rotations) of all electronic and nuclear coordinates [10–13]. This means that the variable space \mathbb{R}^{3P-3} [spanned by the SF Hamiltonian of Eq. (1.20)] could, in principle, be further factorized into $\mathbb{S}^3 \otimes \mathbb{R}^{3P-6}$, where \mathbb{R}^{3P-6} defines the space of (rotation- and translation-free) internal coordinates. In turn, \mathbb{S}^3 defines orientation coordinates which are usually characterized by three Eulerian angles $\Theta_i (i = 1, 2, 3)$. Such a factorization could be done by defining a new axis set that rotates in a defined way with the system. This process is called constructing (or embedding) a body-fixed (BF) frame [14–16].

The required (non-linear) transformation from the set of SF coordinates ($\mathbf{r}'\mathbf{R}'$) to BF ones can be defined as [12]

$$\mathbf{Z} = \mathbf{C}^T(\mathbf{r}'\mathbf{R}'), \quad (1.24)$$

where \mathbf{Z} is a 3 by $P-1$ matrix whose components must be writable in terms of $3L$ and $3H-6$ independent electronic (\mathbf{r}) and nuclear (\mathbf{R}) internal coordinates, respectively, and \mathbf{C}

is a 3 by 3 orthogonal matrix expressed entirely in terms of Θ_i . Such a matrix, therefore, specifies the orientation of the BF frame with respect to the SF one. Note that the choice of \mathbf{C} and internal coordinates is, likewise \mathbf{V} and \mathbf{P}' in Eq. (1.12), to a large extent arbitrary [14–16].

Using just these general considerations, and assuming that an internal coordinate and embedding scheme have been previously chosen, the SF Hamiltonian $\hat{\mathcal{H}}_{RI}$ [Eq. (1.20)] in BF form becomes [10–13]

$$\hat{\mathcal{H}}_{RI}(\mathbf{r}', \mathbf{R}') \xrightarrow{\mathbf{C}^T} \hat{\mathcal{H}}_{RI}(\mathbf{r}, \mathbf{R}, \Theta) = \hat{\mathcal{T}}_R(\mathbf{r}, \mathbf{R}, \Theta) + \hat{\mathcal{H}}_I(\mathbf{r}, \mathbf{R}), \quad (1.25)$$

where the term $\hat{\mathcal{T}}_R(\mathbf{r}, \mathbf{R}, \Theta)$ contains angular momentum operators involving Θ_i only as well as operators that couple the electronic and nuclear motions separately to the angular motion. In turn, $\hat{\mathcal{H}}_I(\mathbf{r}, \mathbf{R})$ is the corresponding “internal” part which is expressed as

$$\hat{\mathcal{H}}_I(\mathbf{r}, \mathbf{R}) = \hat{\mathcal{T}}_{Ne}(\mathbf{r}, \mathbf{R}) + \hat{\mathcal{T}}_N(\mathbf{R}) + \hat{\mathcal{T}}_e(\mathbf{r}) + \hat{\mathcal{T}}_{MP}(\mathbf{r}) + \hat{\mathcal{U}}(\mathbf{r}, \mathbf{R}), \quad (1.26)$$

where the operator $\hat{\mathcal{T}}_{Ne}(\mathbf{r}, \mathbf{R})$ is responsible for the proper coupling between electronic and nuclear variables via angular motion and all the remaining terms assume the same form as given in Eqs. (1.21)–(1.23) but now with \mathbf{r} and \mathbf{R} replacing the SF coordinates (\mathbf{r}' and \mathbf{R}').

The formal solutions of the eigenvalue problem specified by the BF Hamiltonian of Eq. (1.25) are of the type

$$|\Psi_n(\mathbf{r}', \mathbf{R}')\rangle \xrightarrow{\mathbf{C}^T} |\Psi_n^{J,M}(\mathbf{r}, \mathbf{R}, \Theta)\rangle = \sum_{k=-J}^J |\Phi_k'(\mathbf{r}, \mathbf{R})\rangle |JMk\rangle. \quad (1.27)$$

Here, $|JMk\rangle$ is a (normalized) angular momentum eigenfunction [18] which is a function of the Euler angles alone, J denotes the total angular momentum, M its component along the SF z -axis and k the corresponding component along the BF z -axis. In the absence of a field [11], the energy eigenvalue does not depend on M so that the “internal” motion function $|\Phi_k'(\mathbf{r}, \mathbf{R})\rangle$, which is a function of internal degrees of freedom alone, need be labeled only by J and k . Although a complete separation between internal and rotational motions is not strictly practicable, as can be seen from Eqs. (1.25) and (1.26), it is thus possible

to eliminate the angular motion from the problem and write an effective BF Hamiltonian within any (J, M, k) rotational manifold that depends only on the internal coordinates. In so doing,⁵ one gets a part of the problem [*i.e.*, $\hat{\mathcal{H}}_I^{\text{eff}}(\mathbf{r}, \mathbf{R}) = \langle JMk | \hat{\mathcal{H}}_I(\mathbf{r}, \mathbf{R}) | JMk \rangle$] which is completely invariant under orthogonal transformation of the translation-free variables and another angular part [*i.e.*, $\hat{\mathcal{F}}_R^{\text{eff}}(\mathbf{r}, \mathbf{R}, \Theta) = \langle JMk | \hat{\mathcal{F}}_R(\mathbf{r}, \mathbf{R}, \Theta) | JMk \rangle$] which vanishes when $J=0$ [19] (for details; see chapter 5).

1.3 Adiabatic approximation

Although the underlying idea of the approximate separability of electronic and nuclear motion has its grounds on the classical paper due to BO [5], the justification of the adiabatic approximation is customarily approached through the arguments of Born [6] and Born and Huang (BH) [7]. As traditional in the BH framework, the derivation of the coupled differential equations for the nuclear motion is made quite formally in terms of a LF Hamiltonian [Eq. (1.2)]. Such a procedure, however, is far from being trivial because of the ubiquitous continuous spectrum arising from the COM motion [20, 21]. This difficulty could be avoided by going to a SF frame [section (1.2.1)] or even to a BF coordinate set [section (1.2.2)] but then several complications arise due to the appearance of cross terms that mixes electronic with nuclear coordinates [see, *e.g.*, Eqs. (1.25) and (1.26)] [11–13, 22]. Fortunately, as shown by Handy and Lee [23] and pointed out by Kutzelnigg [22], “In doing things that, strictly speaking, one should not do, one arrives at the correct adiabatic corrections, and so in a much simpler way than if one had first separated off the COM motion”. Thus, for the sake of simplicity, all the derivations here shown follow the pragmatic formalism of BH.

The adiabatic approximation is based onto the assumption that the operator $\hat{\mathcal{F}}_N(\mathbf{R})$ [Eq. (1.3)] can be considered as a small perturbation [5]. Thence, in zeroth-order approximation, when the mass of the nuclei are infinitely large, the LF Hamiltonian of Eq. (1.2)

⁵By constructing matrix representations of the operators $\hat{\mathcal{F}}_R(\mathbf{r}, \mathbf{R}, \Theta)$ and $\hat{\mathcal{H}}_I(\mathbf{r}, \mathbf{R})$ [Eq. (1.27)] in the angular momentum basis $|JMk\rangle$ and integrating over Θ_i .

takes the form⁶ [24, 25]

$$\hat{\mathcal{H}}_e(\mathbf{r}; \mathbf{R}) = \hat{\mathcal{T}}_e(\mathbf{r}) + \hat{\mathcal{U}}(\mathbf{r}; \mathbf{R}), \quad (1.28)$$

where, for simplicity, we have dropped the explicit distinction between coordinate sets [the LF coordinates $\mathbf{r}''(\mathbf{R}'')$ will be denoted, henceforth, as just $\mathbf{r}(\mathbf{R})$, unless otherwise stated]. In Eq. (1.28), $\hat{\mathcal{H}}_e(\mathbf{r}; \mathbf{R})$ is the familiar electronic (clamped-nuclei) Hamiltonian that depends parametrically (as indicated by the semicolon) on \mathbf{R} . The problem of finding the stationary states of the system reduces then to solving the time-independent electronic Schrödinger equation (TIESE)

$$\hat{\mathcal{H}}_e |\psi_i(\mathbf{r}; \mathbf{R})\rangle = V_i(\mathbf{R}) |\psi_i(\mathbf{r}; \mathbf{R})\rangle \quad (1.29)$$

for fixed values of nuclear coordinates \mathbf{R} . In the TIESE above, $|\psi_i(\mathbf{r}; \mathbf{R})\rangle$ are electronic adiabatic eigenfunctions that form a complete set $\{|\psi_i(\mathbf{r}; \mathbf{R})\rangle\}_{i=1}^I$ of orthonormal [$\langle\psi_j(\mathbf{r}; \mathbf{R})|\psi_i(\mathbf{r}; \mathbf{R})\rangle = \delta_{ji}$] eigenkets in the I -dimensional electronic Hilbert space. Such functions thus characterize states of motion of electrons for infinitely slow (adiabatic) changes in \mathbf{R} . $V_i(\mathbf{R})$ is the associated electronic eigenvalues and, if all possible sets of nuclear coordinates are considered, represents the effective adiabatic PES for nuclear motion.

Of course, we are primarily interested in solving the full TISE [Eq. (1.11)] which describes the electronic plus nuclear motion in the system. To this end, we expand the total wave function $|\Psi_n(\mathbf{r}, \mathbf{R})\rangle$ [Eq. (1.11)] in the electronic eigenfunctions of $\hat{\mathcal{H}}_e$ as

$$|\Psi_n(\mathbf{r}, \mathbf{R})\rangle = \sum_i^I |\chi_i(\mathbf{R})\rangle |\psi_i(\mathbf{r}; \mathbf{R})\rangle. \quad (1.30)$$

The above expression represents the BH expansion [6, 7] with $\{|\chi_i(\mathbf{R})\rangle\}_{i=1}^I$ being the set of (*a priori*, unknown) nuclear wave functions. Substituting Eq. (1.30) into the full TISE [Eq. (1.11)] and taking the inner product with $\langle\psi_j(\mathbf{r}; \mathbf{R})|$, one obtain an infinite set [provided that I in Eq. (1.30) is infinitely large] of coupled differential equations of the form [24, 25]

$$\left[-\sum_{\alpha=1}^H \frac{1}{2\mathcal{M}_\alpha} \nabla^2(\mathbf{R}_\alpha) + V_j(\mathbf{R}) - E_n \right] |\chi_j(\mathbf{R})\rangle = \sum_i^I \Lambda_{ji}(\mathbf{R}) |\chi_i(\mathbf{R})\rangle \quad (1.31)$$

⁶By setting the kinetic energy of the nuclei equal to zero.

where $\mathbf{\Lambda}$ defines the so-called non-adiabatic coupling matrix which describes the dynamical interactions between the electronic and nuclear motion. Its elements $[\Lambda_{ji}(\mathbf{R})]$ are given by

$$\Lambda_{ji}(\mathbf{R}) = \sum_{\alpha=1}^H \frac{1}{2\mathcal{M}_{\alpha}} [2\mathbf{F}_{ji}(\mathbf{R}_{\alpha}) \cdot \vec{\nabla}(\mathbf{R}_{\alpha}) + G_{ji}(\mathbf{R}_{\alpha})], \quad (1.32)$$

with

$$\mathbf{F}_{ji}(\mathbf{R}_{\alpha}) = \left\langle \psi_j(\mathbf{r}; \mathbf{R}) \left| \vec{\nabla}(\mathbf{R}_{\alpha}) \psi_i(\mathbf{r}; \mathbf{R}) \right. \right\rangle \quad (1.33)$$

and

$$G_{ji}(\mathbf{R}_{\alpha}) = \left\langle \psi_j(\mathbf{r}; \mathbf{R}) \left| \nabla^2(\mathbf{R}_{\alpha}) \psi_i(\mathbf{r}; \mathbf{R}) \right. \right\rangle \quad (1.34)$$

being the derivative and scalar coupling terms, respectively. Note that \mathbf{F} is a matrix in electronic space whose elements (\mathbf{F}_{ji}) are, in turn, vectors in nuclear space.⁷ In Eqs. (1.32)-(1.34), if the electronic wave functions are chosen to be real, the derivative coupling elements $\mathbf{F}_{ji}(\mathbf{R}_{\alpha})$ vanishes for $i=j$ [6, 7], and only the scalar coupling terms contribute to the so-called diagonal Born-Oppenheimer correction (DBOC) [22, 23] which, for this case, assume the form

$$\Lambda_{jj}(\mathbf{R}) = \sum_{\alpha=1}^H \frac{G_{jj}(\mathbf{R}_{\alpha})}{2\mathcal{M}_{\alpha}}. \quad (1.35)$$

Suffice it to say that the off-diagonal terms $\Lambda_{ji}(\mathbf{R})$ ($i \neq j$) are responsible for the proper coupling between nuclei and electrons in different states of motion [*i.e.*, between electronic states $|\psi_i(\mathbf{r}; \mathbf{R})\rangle$ and $|\psi_j(\mathbf{r}; \mathbf{R})\rangle$], and hence are generally referred to as non-adiabatic corrections [25].

By applying the grad operator $\vec{\nabla}(\mathbf{R}_{\alpha})$ to the TIESE [Eq. (1.29)] and using the definition (1.33), one can obtain the following expression for the off-diagonal derivative couplings⁸

$$\mathbf{F}_{ji}(\mathbf{R}_{\alpha}) = \frac{\left\langle \psi_j(\mathbf{r}; \mathbf{R}) \left| \vec{\nabla}(\mathbf{R}_{\alpha}) \hat{\mathcal{H}}_e(\mathbf{r}; \mathbf{R}) \right| \psi_i(\mathbf{r}; \mathbf{R}) \right\rangle}{V_i(\mathbf{R}) - V_j(\mathbf{R})} \quad (i \neq j). \quad (1.36)$$

⁷We recall that \mathbf{R}_{α} is a column matrix of three Cartesian components corresponding to the coordinates of the α -th nucleus.

⁸From the definition $G_{ji}(\mathbf{R}_{\alpha}) = \vec{\nabla}(\mathbf{R}_{\alpha}) \cdot \mathbf{F}_{ji}(\mathbf{R}_{\alpha}) + \mathbf{F}_{ji}(\mathbf{R}_{\alpha}) \cdot \mathbf{F}_{ji}(\mathbf{R}_{\alpha})$ the same conclusions also apply to scalar coupling terms.

It is clear from the above definition that $\mathbf{F}_{ji}(\mathbf{R}_\alpha)$ assume substantially large values when the $V_i(\mathbf{R})$ and $V_j(\mathbf{R})$ PESs come quite close in energy. Actually, at a conical intersection (Ci) [where $V_i(\mathbf{R}) = V_j(\mathbf{R})$], the derivative couplings becomes infinite. Such a well-known behavior of the non-adiabatic coupling terms (NACTs) is responsible for numerical computational difficulties when one deals with the adiabatic basis representation [25, 26]. Apart from such situations, if the adiabatic PESs are well separated energetically from all other electronic states, $\Lambda_{ji}(\mathbf{R})$ is expected to be a small (but not vanishing) quantity, inasmuch as $\mathbf{F}_{ji}(\mathbf{R}_\alpha)$ and $G_{ji}(\mathbf{R}_\alpha)$ in Eq. (1.32) are scaled by $1/\mathcal{M}_\alpha$.

Since the set of electronic adiabatic wave functions of Eq. (1.29) is, in principle, complete, Eqs. (1.30) and (1.31) are exact [25]. It is only when the BH expansion is truncated that approximations are made. Indeed, if just one term is retained in the expansion of Eq. (1.30), the total wave function is then

$$|\Psi_n(\mathbf{r}, \mathbf{R})\rangle = |\chi_i(\mathbf{R})\rangle |\psi_i(\mathbf{r}; \mathbf{R})\rangle. \quad (1.37)$$

By inserting such adiabatic anzats [5–7] into Eq. (1.11) and taking the inner product with $\langle\psi_j(\mathbf{r}; \mathbf{R})|$, one obtain

$$\left[-\sum_{\alpha=1}^H \frac{1}{2\mathcal{M}_\alpha} \nabla^2(\mathbf{R}_\alpha) + V_j(\mathbf{R}) - \Lambda_{jj}(\mathbf{R}) - E_n \right] |\chi_j(\mathbf{R})\rangle = 0, \quad (1.38)$$

which is exactly Eq. (1.31) when interstate coupling terms [$\Lambda_{ji}(\mathbf{R})$ for $i \neq j$] are neglected. The above equation is thus called BO approximation [5, 6, 17]. Further approximations could be here introduced if one considers the smallness of the $\Lambda_{jj}(\mathbf{R})$ term. Thence, by neglecting the DBOC in (1.38) gives

$$\left[-\sum_{\alpha=1}^H \frac{1}{2\mathcal{M}_\alpha} \nabla^2(\mathbf{R}_\alpha) + V_j(\mathbf{R}) - E_n \right] |\chi_j(\mathbf{R})\rangle = 0, \quad (1.39)$$

which is the so-called adiabatic approximation [5–7]. In such an anzats, the electronic and nuclei motion are completely decoupled and the latter are only allowed to move in a single adiabatic PES generated by the former.

BO [5] demonstrated that such an uncoupled single-surface treatment is justified due to the small electron-to-nuclei mass ratio. Actually, in the BO perturbational approach [5],

the full TISE [Eq. (1.11)] is addressed by considering $\hat{\mathcal{T}}_N(\mathbf{R})$ [Eq. (1.3)] as a small perturbation on the unperturbed (clamped-nuclei) electronic problem [Eq. (1.29)]. Thence, by expanding the total Hamiltonian [$\hat{\mathcal{H}}_T(\mathbf{r}, \mathbf{R})$] up to the fourth-order [or second-order in the total wave function $|\Psi_n(\mathbf{r}, \mathbf{R})\rangle$] in the expansion parameter $\kappa = (1/\mathcal{M}_0)^{1/4}$, BO showed that the adiabatic approximation and also the adiabatic ansatz of Eq. (1.37) are made possible. Note that \mathcal{M}_0 can be set as the mass of a particular nucleus α ($\mathcal{M}_0 = \mathcal{M}_\alpha$) or their mean [7]. Yet, in proceeding to even higher orders in κ , the simple adiabatic picture is lost and cross terms that couple electronic and nuclear degrees of freedom arise [7, 25].

The adiabatic approximation provides the fundamental link between quantum mechanics and traditional chemistry. It allows the visualization of chemical reactions as paths connecting reactants to products via transition states. In fact, the very notion of stationary points on PESs and the electronic states themselves are also a direct outcome of the approximate separability of slow (nuclei) and fast (electrons) degrees of freedom. However, as stated above, there are several important situations in which Eq. (1.39) does not suffice to properly describe the complexity of the problem at hand. In particular, in the presence of close-in-energy or degenerate PESs, the adiabatic approximation breaks down and the NACTs [Eq. (1.32)] become substantial. Suffice it to add that, in the special case of a Ci, the expected singularities of $\Lambda_{ji}(\mathbf{R})$ is generally addressed by employing appropriate adiabatic-to-diabatic (ATD) transformations [17, 25–27]. As a limiting case, we should also comment on the existence of non-adiabatic processes in which the breaking down of the adiabatic approximation is so complete that the notion of a PES is lost and electronic and nuclear motion must be treated on an equal footing. Such processes generally involve very high nuclear kinetic energies [25].

Bibliography

- [1] E. Schrödinger, Ann. Phys. **384**, 361 (1926).
- [2] E. Schrödinger, Ann. Phys. **384**, 489 (1926).
- [3] E. Schrödinger, Ann. Phys. **385**, 437 (1926).
- [4] E. Schrödinger, Ann. Phys. **386**, 109 (1926).
- [5] M. Born and R. Oppenheimer, Ann. Phys. **389**, 457 (1927).
- [6] M. Born, Gött. Nachr. Akad. Wiss. Math. Phys. Kl. **6**, 1 (1951).
- [7] M. Born and K. Huang, *Dynamical Theory of Crystal Lattices* (Clarendon Press, Oxford, 1954).
- [8] L. D. Landau and L. M. Lifshitz, *Quantum Mechanics Non-Relativistic Theory*, 2nd ed., Vol. 3 (Pergamon Press, Bristol, 1981).
- [9] D. A. McQuarrie and J. D. Simon, *Physical Chemistry A Molecular Approach*, 2nd ed. (University Science Books, Sausalito, 1997).
- [10] A. A. Kiselev, J. Phys. B: Atom. Molec. Phys. **3**, 904915 (1970).
- [11] B. T. Sutcliffe, J. Mol. Struc. THEOCHEM **259**, 29 (1992).
- [12] B. T. Sutcliffe, J. Chem. Soc., Faraday Trans. **89**, 2321 (1993).
- [13] B. T. Sutcliffe, Theor. Chem. Acc. **127**, 121 (2010).

-
- [14] J. Tennyson, *Comput. Phys. Rep.* **4**, 1 (1986).
- [15] B. T. Sutcliffe and J. Tennyson, *Mol. Phys.* **58**, 1053 (1986).
- [16] B. T. Sutcliffe and J. Tennyson, *Int. J. Quantum Chem.* **39**, 183 (1991).
- [17] C. J. Ballhausen and A. E. Hansen, *Annu. Rev. Phys. Chem.* **23**, 15 (1972).
- [18] D. M. Brink and G. R. Satchler, *Angular Momentum*, 3rd ed. (Oxford University Press, Oxford, 1994).
- [19] A. A. Kiselev, *Can. J. Phys.* **56**, 615 (1978).
- [20] P. Schiffels, A. Alijah, and J. Hinze, *Mol. Phys.* **101**, 175 (2003).
- [21] W. Kutzelnigg, *Mol. Phys.* **105**, 2627 (2007).
- [22] W. Kutzelnigg, *Mol. Phys.* **90**, 909 (1997).
- [23] N. C. Handy and A. M. Lee, *Chem. Phys. Lett.* **252**, 425 (1996).
- [24] A. S. Davidov, *Quantum Mechanics*, Vol. 1 (Pergamon Press, Oxford, 1965).
- [25] W. Domcke, D. R. Yarkony, and H. Köppel, *Conical Intersections: Electronic Structure, Dynamics & Spectroscopy*, Advanced Series in Physical Chemistry, Vol. 15 (World Scientific, Singapore, 2004).
- [26] G. A. Worth and L. S. Cederbaum, *Ann. Rev. Phys. Chem.* **55**, 127 (2004).
- [27] C. A. Mead and D. G. Truhlar, *J. Chem. Phys.* **77**, 6090 (1982).

Chapter 2

Conical intersections and their topological implications

While the adiabatic single-surface approximation [Eq. (1.39)] is valid for the preponderance of chemical processes, electronically non-adiabatic effects, which extend nuclear motion to more than one adiabatic PES, are ubiquitous in photochemistry and photobiology [1, 2]. Indeed, some of the nature's most fundamental phenomena such as photosynthesis and vision are of non-adiabatic character [3]. In this context, Cis play a key mechanistic role and provide the means through which such events are actually understood [3–5].

The effects of Cis on molecular processes are usually classified as either direct or indirect, depending on whether or not nuclear motion spreads over the intersecting surfaces. The former is generally exhibited in (ultrafast) radiationless relaxation of excited electronic states [2] as well as in non-adiabatic recrossing events [6, 7]. Clearly, the propensity for such interstate transitions is largest at regions of nuclear configuration space close to the so-called photochemical funnels [2]. The more subtle indirect effect associated with the presence of Cis occurs already in the uncoupled single-surface adiabatic formalism and is closely related to the well-known geometric phase (GP) [8, 9] or Berry's phase [10] effect. Such sign-reversal property of real adiabatic electronic wave functions is naturally manifested whenever these latter transverse a closed path in the parameter space round

a degeneracy point. As a result, the GP effect has dramatic consequences for the corresponding nuclear dynamics even if the system is confined to the lower electronic surface and regardless the energy the Ci itself [11–13].

2.1 Classification of conical intersections

Cis form hyperlines in nuclear configuration space on which two (or more) PESs are degenerate. Such a subspace of continuously connected points is called the seam space [4]. For doubly (triply) degenerate electronic states, it has dimensions $3H-8$ ($3H-11$) [9]. The orthogonal complement of the seam space (or locus of Ci) is generally referred to as branching [14] or (g, b) -space [7] at which degeneracies are lifted linearly (in a first-order approximation) in displacements from the intersection, with a local topology of a double cone [15]. Berry and Wilkinson [16] noted that such a conical topology resembles that of a diaboloid and have referred to it as diabolical points.

It is useful to classify M state Cis into three important groups: (i) symmetry-required (or symmetry-dictated), (ii) accidental symmetry-allowed and (iii) accidental same-symmetry [4]. In the first case, the very nature of Cis rely on the molecular point-groups themselves (such as those addressed by Jahn and Teller (JT) [17, 18]; see later section 2.3) and occur whenever M electronic states (at highly symmetric non-linear arrangements) transform as M -fold degenerate irreducible representations (irreps) [17, 18]. For accidental symmetry-allowed intersections, the involved electronic states transform as distinct one-dimensional irreps. Finally, for accidental same-symmetry Cis, $(M+2)(M-1)/2$ independent nuclear coordinates must be varied [9] in order to accomplish the degeneracy and the intersecting PESs have the same spin and spacial symmetry.

2.2 The non-crossing rule

Apart from symmetry-dictated Cis, the existence of accidental same-symmetry degeneracies has been a matter of deep controversy and debate for many years [8, 9, 19–24]. The conditions for such degeneracies have first been recognized by von Neumann and Wigner [19] in 1929, just two years after the seminal paper of BO [25], with Teller [20], in 1937, first emphasizing their hole in fast radiationless transitions. Herzberg and Longuet-

Higgins [8] and Longuet-Higgins [9] further generalized the concept of same-symmetry Cis and their topological implications for systems with more than one degree of freedom.

For the sake of simplicity, the following discussion will be restricted to the case of two intersecting adiabatic PESs. Let $|\psi_1(\mathbf{r}; \mathbf{R})\rangle$ and $|\psi_2(\mathbf{r}; \mathbf{R})\rangle$ be any two eigenfunctions of the TIESE [Eq. (1.29)] which have the same symmetry and spin. Such adiabatic electronic states can be expressed as linear combinations of two arbitrary, *e.g.*, diabatic [4, 5, 26, 27] basis $|\xi_1(\mathbf{r}; \mathbf{R})\rangle$ and $|\xi_2(\mathbf{r}; \mathbf{R})\rangle$, which are orthogonal to all the remaining eigenstates $|\psi_n(\mathbf{r}; \mathbf{R})\rangle$ ($n \geq 3$) and to one another, as

$$|\psi_1(\mathbf{r}; \mathbf{R})\rangle = c_{11} |\xi_1(\mathbf{r}; \mathbf{R})\rangle + c_{12} |\xi_2(\mathbf{r}; \mathbf{R})\rangle, \quad (2.1)$$

and

$$|\psi_2(\mathbf{r}; \mathbf{R})\rangle = c_{21} |\xi_1(\mathbf{r}; \mathbf{R})\rangle + c_{22} |\xi_2(\mathbf{r}; \mathbf{R})\rangle. \quad (2.2)$$

The matrix representation of the electronic Hamiltonian $[\hat{\mathcal{H}}_e(\mathbf{r}; \mathbf{R})]$ in this new basis is then given by

$$\mathcal{H}_e = \begin{pmatrix} H_{11}(\mathbf{R}) & H_{12}(\mathbf{R}) \\ H_{12}(\mathbf{R}) & H_{22}(\mathbf{R}) \end{pmatrix}, \quad (2.3)$$

where $H_{ji}(\mathbf{R}) = \langle \xi_j(\mathbf{r}; \mathbf{R}) | \hat{\mathcal{H}}_e(\mathbf{r}; \mathbf{R}) | \xi_i(\mathbf{r}; \mathbf{R}) \rangle$. In the above equation, we have considered the practically important case that \mathcal{H}_e is a real and symmetric Hermitian matrix¹ and therefore, $H_{21}(\mathbf{R}) = H_{12}(\mathbf{R})$. Its eigenvalues and the corresponding expansion coefficients c_{ji} of Eqs. (2.1) and (2.2) can then be obtained by the orthogonal transformation

$$\mathbf{V} = \mathbf{U}^\dagger \mathcal{H}_e \mathbf{U} = \begin{pmatrix} V_1(\mathbf{R}) & 0 \\ 0 & V_2(\mathbf{R}) \end{pmatrix}, \quad (2.4)$$

where

$$\mathbf{U} = \begin{pmatrix} \cos \frac{1}{2}\alpha(\mathbf{R}) & \sin \frac{1}{2}\alpha(\mathbf{R}) \\ -\sin \frac{1}{2}\alpha(\mathbf{R}) & \cos \frac{1}{2}\alpha(\mathbf{R}) \end{pmatrix} \quad (2.5)$$

¹A Hermitian matrix \mathbf{A} is a complex square matrix that is equal to its conjugate transpose (adjoint) \mathbf{A}^\dagger . A matrix that has only real elements is Hermitian if and only if it is a symmetric matrix.

is an unitary (or, in this particular case, orthogonal) matrix² expressed entirely in terms of the rotation angle $\alpha(\mathbf{R})$ [15]. The associated expectation values of Eq. (2.4) become [14]

$$V_{1,2}(\mathbf{R}) = \bar{H}(\mathbf{R}) \pm \sqrt{\Delta H(\mathbf{R})^2 + H_{12}(\mathbf{R})^2} \quad (2.6)$$

where $\bar{H}(\mathbf{R}) = [H_{11}(\mathbf{R}) + H_{22}(\mathbf{R})]/2$ and $\Delta H(\mathbf{R}) = [H_{11}(\mathbf{R}) - H_{22}(\mathbf{R})]/2$. Note that the above eigenvalues are obtained by choosing $\alpha(\mathbf{R})$ such that

$$\sin \alpha(\mathbf{R}) = \frac{H_{12}(\mathbf{R})}{\sqrt{\Delta H(\mathbf{R})^2 + H_{12}(\mathbf{R})^2}}, \quad (2.7)$$

and

$$\cos \alpha(\mathbf{R}) = \frac{\Delta H(\mathbf{R})}{\sqrt{\Delta H(\mathbf{R})^2 + H_{12}(\mathbf{R})^2}}, \quad (2.8)$$

which defines therefore the transformation from diabatic to adiabatic states. The two eigenvectors and the expansion coefficients of Eqs. (2.1) and (2.2) are thus given by [14, 28]

$$\begin{pmatrix} |\psi_1(\mathbf{r}; \mathbf{R})\rangle \\ |\psi_2(\mathbf{r}; \mathbf{R})\rangle \end{pmatrix} = \begin{pmatrix} \cos \frac{1}{2}\alpha(\mathbf{R}) & -\sin \frac{1}{2}\alpha(\mathbf{R}) \\ \sin \frac{1}{2}\alpha(\mathbf{R}) & \cos \frac{1}{2}\alpha(\mathbf{R}) \end{pmatrix} \begin{pmatrix} |\xi_1(\mathbf{r}; \mathbf{R})\rangle \\ |\xi_2(\mathbf{r}; \mathbf{R})\rangle \end{pmatrix}. \quad (2.9)$$

According to Eq. (2.6), an intersection between the $V_1(\mathbf{R})$ and $V_2(\mathbf{R})$ PESs occurs for a specified set of nuclear configuration $\mathbf{R} = \mathbf{R}^\times$ at which the two quantities $\Delta H(\mathbf{R}^\times)$ and $H_{12}(\mathbf{R}^\times)$ both vanish (see Figure 2.1). In other words, the two crossing conditions are then defined as [8, 9, 19, 20]

$$H_{11}(\mathbf{R}^\times) - H_{22}(\mathbf{R}^\times) = 0, \quad (2.10)$$

and

$$H_{12}(\mathbf{R}^\times) = 0 \quad (2.11)$$

with the corresponding eigenvalues given by $V_{1,2}(\mathbf{R}^\times) = \bar{H}(\mathbf{R}^\times)$. Teller [20] was the first to draw attention to the fact that if $H_{11}(\mathbf{R}) - H_{22}(\mathbf{R})$ and $H_{12}(\mathbf{R})$ are independent

²A complex square matrix \mathbf{U} is unitary if \mathbf{U}^\dagger is equal to its inverse \mathbf{U}^{-1} , *i.e.*, $\mathbf{U}^\dagger \mathbf{U} = \mathbf{U} \mathbf{U}^\dagger = \mathbf{I}$, where \mathbf{I} is the identity matrix. If \mathbf{U} has only real entries it is usually referred to as orthogonal matrix, and hence $\mathbf{U}^T \mathbf{U} = \mathbf{U} \mathbf{U}^T = \mathbf{I}$.

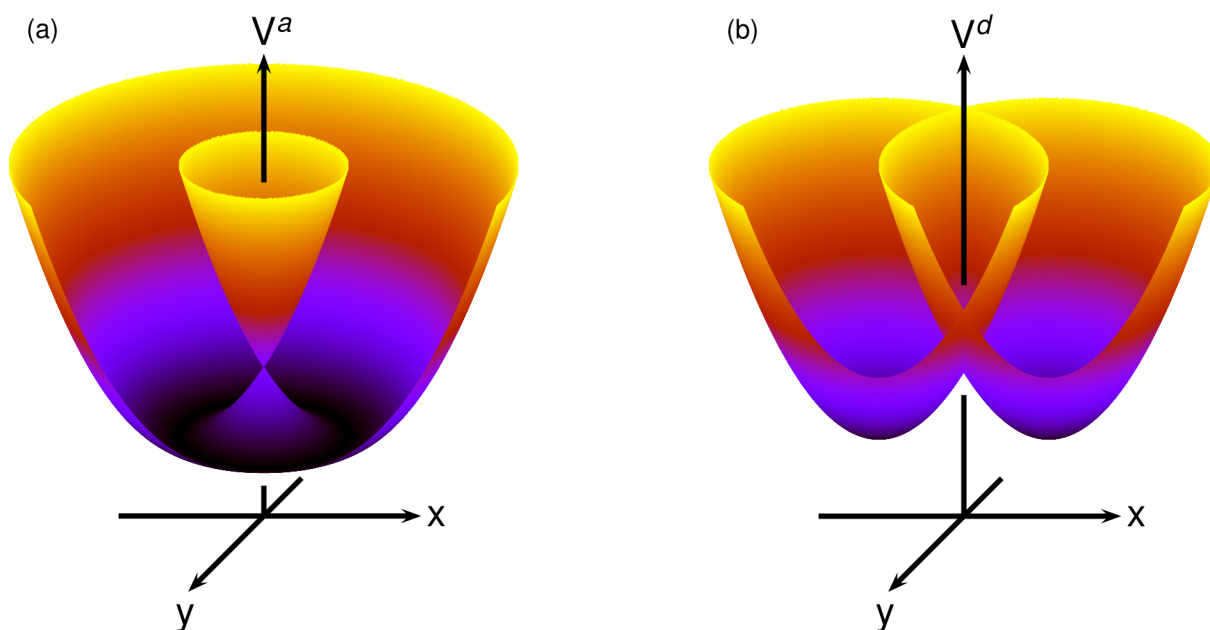


Figure 2.1: (a). Adiabatic and (b). Diabatic PESs around a conical intersection at \mathbf{R}^\times . x and y denotes the two independent nuclear coordinates (the branching plane) with the origin corresponding to the point where $H_{11}(\mathbf{R}^\times) - H_{22}(\mathbf{R}^\times) = 0$ and $H_{12}(\mathbf{R}^\times) = 0$ [8, 20]. Following Herzberg and Longuet-Higgins [8], the adiabatic potentials are given by $V_{1,2}^a(x, y) = k(x^2 + y^2) + lx \pm \sqrt{m^2x^2 + n^2y^2}$, while the diabatic ones by $V_{1,2}^d(x, y) = k(x^2 + y^2) + (l \pm m)x$, with (in arbitrary units) $k=15$, $l=0$ and $m=n=2$.

functions of two nuclear coordinates it is therefore possible, in some situations, to satisfy both (2.10) and (2.11). Indeed, if there are $3H-6$ internal coordinates then such crossing conditions could be satisfied in a space of $3H-8$ dimensions. Thence, for triatomic systems the crossing of PESs for electronic states of the same symmetry can occur in $3 \times 3 - 8 = 1$ dimension, *i.e.*, along a line. As pointed out by Longuet-Higgins [9], for a real and symmetric Hamiltonian matrix \mathcal{H}_e , $(M+2)(M-1)/2$ independent conditions must be satisfied in order to establish a M -fold degeneracy at \mathbf{R}^\times which is expected to occur in a space of $3H-6 - [(M+2)(M-1)/2]$ dimensions.

Since diatomic molecules have only one internal coordinate, for two states of the same irrep, the two conditions (2.10) and (2.11) cannot, in general, be satisfied by adjusting the one available variable. Thence, accidental same-symmetry Cis are very rare events in such systems. This general result is frequently referred to as the “non-crossing rule” and

is strictly limited to diatomic molecules [8, 9, 19, 20].

Despite the present discussion being mainly addressed to accidental same-symmetry intersections, one should bear in mind that the \mathbf{R} -dependence of $\Delta H(\mathbf{R})$ and $H_{12}(\mathbf{R})$ in Eq. (2.6) near \mathbf{R}^\times is the same for all types of Cis aforementioned. Actually, the distinctions are made from the role played by the group theory itself in the determination of the solutions of Eqs. (2.10) and (2.11). Thus, for symmetry-imposed Cis, such requirements are made possible for nuclear configurations \mathbf{R}^\times at which the system carry the highest possible symmetry, *e.g.*, D_{3b} geometries for X_3 -type molecules. In turn, if $|\xi_1(\mathbf{r}; \mathbf{R})\rangle$ and $|\xi_2(\mathbf{r}; \mathbf{R})\rangle$ have different symmetries then $H_{12}(\mathbf{R})$ will be zero for all values of \mathbf{R} (or R in the case of a diatomic molecule). In this case there may be points in nuclear configuration space at which Eq. (2.10) is satisfied by happenstance, and therefore determine the existence of accidental symmetry-allowed Cis. With this in mind, it should be added that accidental same-symmetry intersections are always difficult to predict *a priori* since group theory plays no role in the determination of \mathbf{R}^\times , and therefore both Eqs. (2.10) and (2.11) are always satisfied by happenstance [4, 7, 29, 30].

2.3 The Jahn-Teller vibronic coupling theory

As stated by JT [17, 18], highly symmetric non-linear configurations in degenerate orbital states are not stable structures on adiabatic PESs. At such geometries, there will always exist distorting forces along non-totally symmetric displacements (the JT-active modes) so that any degeneracy can be removed in first order. By making use of degenerate perturbation theory [31] and group theoretical considerations [32], JT examined all types of degenerate terms of all symmetry point groups and determined the corresponding irreps according to which each JT-active mode should transform in order to warrant the existence of non-vanishing perturbation matrix elements. If, for a given molecular symmetry, they are different from zero then the degeneracy is lifted in first order in nuclear displacements and the associated adiabatic electronic states are given as characteristic values of such perturbation matrix.

In what follows, we will stress the main aspects of the so-called JT vibronic coupling theory [33–36] which is the foundation stone for the general understanding of the proper

JT [17, 18], pseudo-Jahn-Teller (PJT) [37, 38] and Renner-Teller (RT) [39–41] effects. The concepts here developed will be further illustrated by considering the simplest JT problem in an X_3 -type system, *i.e.*, a twofold degenerate electronic term E interacting with twofold degenerate e vibrations or, in other words, the well-studied $E \otimes e$ problem.

Consider a molecular system in a high-symmetry reference configuration \mathbf{R}^\times which transform according to the point group S .³ Since we are primarily interested in evaluate the behavior of the adiabatic PESs in the immediate vicinity of \mathbf{R}^\times , the electronic Hamiltonian of Eq. (1.28) can then be expanded as [33, 35, 36]

$$\begin{aligned} \hat{\mathcal{H}}_e(\mathbf{r}; \mathbf{Q}) &= \hat{\mathcal{H}}_e^{(0)}(\mathbf{r}; \mathbf{0}) + \sum_{\bar{\Gamma}\bar{\gamma}} \left(\frac{\partial \hat{\mathcal{U}}(\mathbf{r}; \mathbf{0})}{\partial Q_{\bar{\Gamma}\bar{\gamma}}} \right)_0 Q_{\bar{\Gamma}\bar{\gamma}} \\ &+ \frac{1}{2} \sum_{\bar{\Gamma}\bar{\gamma}} \left\{ \left(\frac{\partial \hat{\mathcal{U}}(\mathbf{r}; \mathbf{0})}{\partial Q_{\bar{\Gamma}_1}} \right)_0 \otimes \left(\frac{\partial \hat{\mathcal{U}}(\mathbf{r}; \mathbf{0})}{\partial Q_{\bar{\Gamma}_2}} \right)_0 \right\}_{\bar{\Gamma}\bar{\gamma}} \{Q_{\bar{\Gamma}_1} \otimes Q_{\bar{\Gamma}_2}\}_{\bar{\Gamma}\bar{\gamma}} + \dots \\ &= \hat{\mathcal{H}}_e^{(0)}(\mathbf{r}; \mathbf{0}) + W^{(1)}(\mathbf{r}; \mathbf{Q}) + W^{(2)}(\mathbf{r}; \mathbf{Q}) + \dots, \end{aligned} \quad (2.12)$$

where \mathbf{Q} are now a set of $3H-6$ (or $3H-5$ for linear molecules) symmetrized nuclear displacements⁴ which transform as the line $\bar{\gamma}$ of the M -fold degenerate irrep $\bar{\Gamma}$ of the point group S .⁵ In turn, $\hat{\mathcal{H}}_e^{(0)}(\mathbf{r}; \mathbf{0})$ is the corresponding zeroth-order Hamiltonian for the nuclei clamped at the origin which satisfies the eigenvalue problem

$$\hat{\mathcal{H}}_e^{(0)} |\Gamma\gamma_i(\mathbf{r}; \mathbf{0})\rangle = V_i(\mathbf{0}) |\Gamma\gamma_i(\mathbf{r}; \mathbf{0})\rangle, \quad (2.13)$$

where $\{|\Gamma\gamma_i(\mathbf{r}; \mathbf{0})\rangle\} \equiv \{|\psi_i(\mathbf{r}; \mathbf{R}^\times)\rangle\}$ [see Eq. (1.29)] is the set of orthonormal eigenfunctions which, under the symmetry operation of the molecular point group S , also transform according to one of its $\Gamma\gamma$ irreps. In Eq. (2.12), $W^{(n)}(\mathbf{r}; \mathbf{Q})$ are vibronic coupling

³In this particular case, S is assumed to have at least one rotational or roto-reflection (improper) axis of order > 2

⁴We assume for the moment that the non-trivial task of separating translational and rotational degrees of freedom has already been accomplished, with any term that couples electronic and nuclear variables via rotation [$\hat{\mathcal{T}}_{Ne}$ in Eq. (1.26)] and mass-polarization effects [$\hat{\mathcal{T}}_{MP}$ in Eq. (1.23)] neglected.

⁵ M -fold degenerate representations Γ have M lines γ . For instance, the two-dimensional irrep $\Gamma = E$ has two lines $\gamma = \theta, \epsilon$, while $\gamma = \xi, \eta, \zeta$ for the threefold degenerate irrep $\Gamma = T$. One-dimensional representations, *e.g.*, $\Gamma = A$ have only one line $\gamma = \iota$ [32].

(n th-order perturbation) operators [35, 36] which involve n th-order derivatives of the electron-nuclear, $\hat{\mathcal{V}}_{Ne}(\mathbf{r}; \mathbf{0})$ [Eq. (1.7)], and nuclear-nuclear, $\hat{\mathcal{V}}_{NN}(\mathbf{0})$ [Eq. (1.8)], interactions with respect to the $Q_{\bar{\Gamma}\bar{\gamma}}$. Note that, similarly to the symmetrized displacements, such derivatives have the same transformation properties of $\bar{\Gamma}\bar{\gamma}$. Indeed, in (2.12), the quantities $\{X_{\bar{\Gamma}_1} \otimes Y_{\bar{\Gamma}_2}\}_{\bar{\Gamma}\bar{\gamma}}$ define irreducible products [32] (or a tensor convolutions [36]) which are *per se* linear combinations of direct products of $X_{\bar{\Gamma}_1}$ and $Y_{\bar{\Gamma}_2}$ (*i.e.*, derivatives or symmetrized displacements) that transform according to the line $\bar{\gamma}$ of the representation $\bar{\Gamma} \in \bar{\Gamma}_1 \otimes \bar{\Gamma}_2$ (for an explicit definition of such quantities see appendix B).

If by solving the TIESE [Eq. (2.13)] one obtains M electronic terms that are degenerate [or, in other words, an eigenstate $|\Gamma\gamma_i(\mathbf{r}; \mathbf{0})\rangle$ that transform as the M -dimensional representation Γ of S], then all such states are vibronically coupled along the JT-active modes and, away from the intersection point, the energy term splits into M branches. In fact, the proper behavior of the M adiabatic PESs in the vicinity of the high-symmetry configuration is only attainable by estimating the effects of the vibronic interaction terms $W^{(n)}(\mathbf{r}; \mathbf{Q})$ in Eq. (2.12) on the eigenvalues $V_i(\mathbf{0})$. To this end, let \mathcal{H}_e be a M by M matrix representation of the operator $\hat{\mathcal{H}}_e(\mathbf{r}; \mathbf{Q})$ [Eq. (2.12)] in the basis of the degenerate electronic term Γ . Its matrix elements are then given by [36]

$$\begin{aligned}
H_{ji}(\mathbf{Q}) &= \left\langle \Gamma' \gamma'_j(\mathbf{r}; \mathbf{0}) \left| \hat{\mathcal{H}}_e^{(0)}(\mathbf{r}; \mathbf{0}) \right| \Gamma \gamma_i(\mathbf{r}; \mathbf{0}) \right\rangle \delta_{ji} \\
&+ \sum_{\bar{\Gamma}\bar{\gamma}} \left\langle \Gamma' \gamma'_j(\mathbf{r}; \mathbf{0}) \left| \left(\frac{\partial \hat{\mathcal{U}}(\mathbf{r}; \mathbf{0})}{\partial Q_{\bar{\Gamma}\bar{\gamma}}} \right)_0 \right| \Gamma \gamma_i(\mathbf{r}; \mathbf{0}) \right\rangle Q_{\bar{\Gamma}\bar{\gamma}} \\
&+ \sum_{\bar{\Gamma}\bar{\gamma}} \frac{1}{2} \left\langle \Gamma' \gamma'_j(\mathbf{r}; \mathbf{0}) \left| \left\{ \left(\frac{\partial \hat{\mathcal{U}}(\mathbf{r}; \mathbf{0})}{\partial Q_{\bar{\Gamma}_1}} \right)_0 \otimes \left(\frac{\partial \hat{\mathcal{U}}(\mathbf{r}; \mathbf{0})}{\partial Q_{\bar{\Gamma}_2}} \right)_0 \right\}_{\bar{\Gamma}\bar{\gamma}} \right| \Gamma \gamma_i(\mathbf{r}; \mathbf{0}) \right\rangle \{Q_{\bar{\Gamma}_1} \otimes Q_{\bar{\Gamma}_2}\}_{\bar{\Gamma}\bar{\gamma}} \\
&+ \dots
\end{aligned} \tag{2.14}$$

Since the orthonormal set $\{|\Gamma\gamma_i(\mathbf{r}; \mathbf{0})\rangle\}_{i=1}^M$ are eigenfunctions of the zeroth-order Hamiltonian $\hat{\mathcal{H}}_e^{(0)}(\mathbf{r}; \mathbf{0})$ [Eq. (2.13)], the first term on the right-hand side (RHS) equals to $V_i(\mathbf{0}) = V^\times(\mathbf{0})$, $i=1, 2, \dots, M$, and hence is different from zero only in diagonal matrix elements. Obviously, at \mathbf{R}^\times , all the remaining terms vanish and $\mathcal{H}_e = V^\times(\mathbf{0})\delta_{ji}$. Nevertheless, for sufficiently small distortions from \mathbf{R}^\times , the non-vanishing nature of the second and third terms on the RHS of Eq. (2.14) warrants the instability of the JT origin, and therefore

the degeneracy is no longer ensured [17, 18]. Such matrix elements define the so-called linear and quadratic vibronic coupling constants (VCCs) which are defined by [35, 36]

$$\begin{aligned} F_{\bar{\Gamma}\bar{\gamma}}^{(\Gamma'\gamma'_j\Gamma\gamma_i)} &= \left\langle \Gamma'\gamma'_j(\mathbf{r}; \mathbf{0}) \left| \left(\frac{\partial \hat{\mathcal{U}}(\mathbf{r}; \mathbf{0})}{\partial Q_{\bar{\Gamma}\bar{\gamma}}} \right)_0 \right| \Gamma\gamma_i(\mathbf{r}; \mathbf{0}) \right\rangle \\ &= F_{\bar{\Gamma}}^{(\Gamma'\Gamma)} \mathbf{V} \begin{pmatrix} \Gamma' & \Gamma & \bar{\Gamma} \\ \gamma'_j & \gamma_i & \bar{\gamma} \end{pmatrix} \end{aligned} \quad (2.15)$$

and

$$\begin{aligned} G_{\bar{\Gamma}\bar{\gamma}}^{(\Gamma'\gamma'_j\Gamma\gamma_i)} &= \frac{1}{2} \left\langle \Gamma'\gamma'_j(\mathbf{r}; \mathbf{0}) \left| \left\{ \left(\frac{\partial \hat{\mathcal{U}}(\mathbf{r}; \mathbf{0})}{\partial Q_{\bar{\Gamma}_1}} \right)_0 \otimes \left(\frac{\partial \hat{\mathcal{U}}(\mathbf{r}; \mathbf{0})}{\partial Q_{\bar{\Gamma}_2}} \right)_0 \right\}_{\bar{\Gamma}\bar{\gamma}} \right| \Gamma\gamma_i(\mathbf{r}; \mathbf{0}) \right\rangle \\ &= \frac{1}{2} G_{\bar{\Gamma}}^{(\Gamma'\Gamma)} \mathbf{V} \begin{pmatrix} \Gamma' & \Gamma & \bar{\Gamma} \\ \gamma'_j & \gamma_i & \bar{\gamma} \end{pmatrix}, \end{aligned} \quad (2.16)$$

respectively. Note that VCCs arising from higher-order ($n > 2$) perturbation operators $W^{(n)}(\mathbf{r}; \mathbf{Q})$ [Eq. (2.12)] will not be considered explicitly here and for most practical purposes can be neglected. Indeed, as clearly seen from Eqs. (2.14)-(2.16), the vibronic constants effectively measure the coupling between electronic structure and nuclear displacements. In particular, linear VCCs in diagonal matrix elements, *i.e.*, $F_{\bar{\Gamma}\bar{\gamma}}^{(\Gamma\gamma_i\Gamma\gamma_i)}$ [see Eq. (2.15)], give a physical insight into (and an estimate of) the distorting forces to which the state $|\Gamma\gamma_i(\mathbf{r}; \mathbf{0})\rangle$ is subjected in the direction of the non-totally symmetric displacement $Q_{\bar{\Gamma}\bar{\gamma}}$.

Following the Wigner-Eckart theorem [32], in Eqs. (2.15) and (2.16), $F_{\bar{\Gamma}}^{(\Gamma'\Gamma)}$ and $G_{\bar{\Gamma}}^{(\Gamma'\Gamma)}$ are reduced matrix elements (which do not depend on γ' , γ and $\bar{\gamma}$) with the last terms defining the so-called V coefficients⁶ [32, 35, 42]. Indeed, the non-vanishing nature of both linear and quadratic VCCs (and therefore the lack of extremum at \mathbf{R}^\times) are clearly

⁶The V coefficients are directly related to the (symmetrized) Clebsch-Gordan coupling coefficients by the equation [32]

$$\mathbf{V} \begin{pmatrix} \Gamma' & \Gamma & \bar{\Gamma} \\ \gamma' & \gamma & \bar{\gamma} \end{pmatrix} = \lambda(\bar{\Gamma})^{-1/2} \langle \Gamma'\Gamma\gamma'\gamma | \Gamma'\Gamma\bar{\Gamma}\bar{\gamma} \rangle, \quad (2.17)$$

where $\lambda(\bar{\Gamma})$ is the dimension of the $\bar{\Gamma}$ irrep in the point group S .

dictated by the symmetry properties of the V coefficients themselves. According to the group-theoretical requirements, such quantities are nonzero if and only if the direct product $\Gamma' \otimes \Gamma$ contains $\bar{\Gamma}$ (or, in other words, if $\Gamma' \otimes \bar{\Gamma} \otimes \Gamma$ contains the totally symmetric irrep A_1) [32, 35]. Indeed, for molecular systems in degenerate electronic terms E and T , the symmetries of the vibronic perturbations should be $E \otimes E \rightarrow A_1 + E$ and $T \otimes T \rightarrow A_1 + E + T_1 + T_2$, respectively [17, 18]. It follows from the above considerations that, besides the E , T_1 and T_2 modes, totally symmetric displacements of A_1 type are also JT-active with (diagonal) linear VCCs [Eq. (2.15)] being different from zero by symmetry. Nevertheless, since displacements along such modes do not remove the degeneracy, they are generally disregarded in the vibronic coupling treatment [35]. Note, however, that the totally symmetric part of the diagonal matrix element in Eq. (2.16), *i.e.*, $G_{a_1 l}^{(\Gamma \gamma_i \Gamma \gamma_i)}$, is an important component of the PES curvature and is often referred to as primary (nonvibronic) force constant $K_0^{(\Gamma)}$. In fact, by setting all the proper linear and quadratic VCCs equal to zero, the M adiabatic PESs near \mathbf{R}^\times assume the simple form of M harmonic oscillators along the JT-active modes.

Once the matrix elements of \mathcal{H}_e [Eq. (2.14)] have been properly determined, the associated eigenvalues (*i.e.*, the adiabatic PESs) can then be obtained by solving the secular determinant

$$\begin{vmatrix} H_{11}(\mathbf{Q}) - V(\mathbf{Q}) & H_{12}(\mathbf{Q}) & \dots & H_{1M}(\mathbf{Q}) \\ H_{21}(\mathbf{Q}) & H_{22}(\mathbf{Q}) - V(\mathbf{Q}) & \dots & H_{2M}(\mathbf{Q}) \\ \vdots & \vdots & \vdots & \vdots \\ H_{M1}(\mathbf{Q}) & H_{M2}(\mathbf{Q}) & \dots & H_{MM}(\mathbf{Q}) - V(\mathbf{Q}) \end{vmatrix} = 0, \quad (2.18)$$

whose solutions assume the form [35, 36]

$$V_i(\mathbf{Q}) = V_i(\mathbf{0}) + \frac{1}{2} \sum_{\bar{\Gamma}\bar{\gamma}} K_0^{(\Gamma)} Q_{\bar{\Gamma}\bar{\gamma}}^2 + \vartheta_i(\mathbf{Q}), \quad i=1, 2, \dots, M \quad (2.19)$$

where $\vartheta_i(\mathbf{Q})$ is the vibronic contribution to the (nonvibronic) harmonic nuclear potential.

Before proceeding with the discussion of the $E \otimes e$ problem, some general remarks are here necessary. The exclusion of linear molecules from the JT statement stems from the fact that only first-order operators $W^{(1)}(\mathbf{r}; \mathbf{Q})$ [see Eq. (2.12)] have been considered

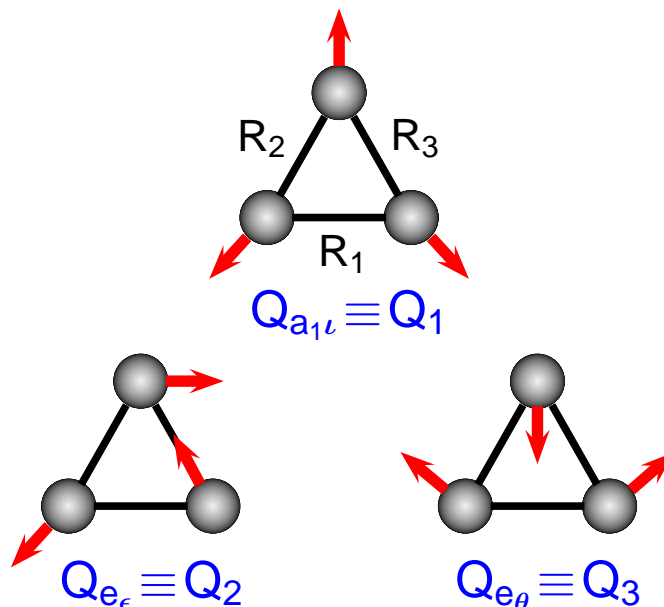


Figure 2.2: Symmetrized nuclear displacements of atoms in a triangular X_3 -type molecular system. $Q_{a_{1g}} \equiv Q_1$ is the symmetry preserving breathing mode, $Q_{e_\epsilon} \equiv Q_2$ is the asymmetric stretch mode which distorts the equilateral triangle into a C_s configuration and $Q_{e_\theta} \equiv Q_3$ takes the D_{3h} structure into a C_{2v} conformation.

in their theoretical perturbational treatment. Indeed, for such systems the non-totally symmetric displacements (*e.g.*, the degenerate bending modes) are of odd type with respect to reflections in the plane containing the molecular axis, while the product of wave functions of the degenerate term (*e.g.*, a Π state with orbital angular momentum quantum number $\Lambda = 1$) is always even with respect to such reflections [43]. It follows that the linear VCCs of Eq. (2.15) vanish and the corresponding adiabatic PESs have an extremum at such arrangements. However, the effect of quadratic terms of Eq. (2.16) is non-negligible. Indeed, for linear molecules, instability arising from quadratic VCCs results in the so-called Renner-Teller effect (RTE) [39–41], but it also takes place in non-linear systems in which the linear VCCs are accidentally zero or negligibly small.

It should be emphasized that, apart from the proper JT and RT effects, the vibronic mixing of two or more close-in-energy (pseudo-degenerate) states under nuclear displacements, *i.e.*, the so-called pseudo-Jahn-Teller effect (PJTE) [37, 38], also occupies an outstanding place in the JT vibronic coupling theory. Indeed, the PJTE is the only source

of instability and distortions of high-symmetry configurations of polyatomic systems in non-degenerate states [38]. Note further that, even in the presence of electronic degeneracy, such additional effects are still very important contributions to the (net) vibronic coupling and interesting topographical features on adiabatic PESs may arise due to such combined problem [44, 45].

Consider now the simplest case of a X_3 -type (D_{3b}) molecule in a doubly degenerate E state. Its component wave functions which are obtained as solutions of the TIESE [Eq. (2.13)] are denoted as $|E_\theta(\mathbf{r}; \mathbf{0})\rangle$ and $|E_e(\mathbf{r}; \mathbf{0})\rangle$ with eigenvalues $V_1(\mathbf{0}) = V_2(\mathbf{0}) = V_E^\times(\mathbf{0})$. Note that, for convenience, the symmetry labels of the point group C_{3v} (subgroup of D_{3b}) will be used henceforth. The corresponding set of symmetrized nuclear displacements and their classification according to irreducible representations are illustrated in Figure 2.2. They are related to the set of internal (bond-length) coordinates $\mathbf{R} = (R_1, R_2, R_3)$ by [46, 47]

$$\begin{pmatrix} Q_{a_{1u}} \\ Q_{e_e} \\ Q_{e_\theta} \end{pmatrix} = \begin{pmatrix} \sqrt{1/3} & \sqrt{1/3} & \sqrt{1/3} \\ 0 & \sqrt{1/2} & -\sqrt{1/2} \\ \sqrt{2/3} & -\sqrt{1/6} & -\sqrt{1/6} \end{pmatrix} \begin{pmatrix} R_1 - R^\times \\ R_2 - R^\times \\ R_3 - R^\times \end{pmatrix}, \quad (2.20)$$

where R^\times defines the D_{3b} JT reference configuration [$\mathbf{R}^\times = (R^\times, R^\times, R^\times)$]. Following appendix B and using the convenient notation introduced in Figure 2.2, the explicit form of $\hat{\mathcal{H}}_e(\mathbf{r}; \mathbf{Q})$ [Eq. (2.12)] for the $E \otimes e$ problem is [35, 36]

$$\hat{\mathcal{H}}_e = \begin{pmatrix} V_E^\times(\mathbf{0}) - F_E Q_3 - G_E(Q_2^2 - Q_3^2) + \kappa_E(\mathbf{Q}) & F_E Q_2 + 2G_E Q_2 Q_3 \\ F_E Q_2 + 2G_E Q_2 Q_3 & V_E^\times(\mathbf{0}) + F_E Q_3 + G_E(Q_2^2 - Q_3^2) + \kappa_E(\mathbf{Q}) \end{pmatrix}. \quad (2.21)$$

where F_E and G_E are the linear and quadratic JT VCCs, respectively, with $\kappa_E(\mathbf{Q})$ being the (nonvibronic) harmonic nuclear potential near \mathbf{R}^\times . In polar coordinates,

$$\begin{aligned} Q_2 &= \rho \cos \phi \\ Q_3 &= \rho \sin \phi, \end{aligned} \quad (2.22)$$

the solution of the secular determinant [Eq. (2.18)] with the present $E \otimes e$ vibronic Hamil-

tonian is given by [35, 36]

$$V_{1,2}(\mathbf{Q}) = V_E^\times(\mathbf{0}) + \frac{1}{2}K_0^{(E)}\rho^2 \pm \rho\sqrt{F_E^2 + G_E^2\rho^2 + 2F_E G_E \rho \sin 3\phi}, \quad (2.23)$$

where $\rho = \sqrt{Q_2^2 + Q_3^2}$ and ϕ define the radial and angular polar coordinates, respectively, and $K_0^{(E)}$ the primary force constant for the E term. It should be pointed out that, since VCCs associated with the breathing normal coordinate are assumed to be identically zero, the adiabatic PESs along sufficiently small Q_1 distortions behave simply as harmonic potentials,

$$V_{1,2}(\mathbf{Q}) = V_E^\times(\mathbf{0}) + \frac{1}{2}K_0^{(E)}Q_1^2. \quad (2.24)$$

From Eq. (2.23), one can see that in the limit of pure linear coupling, *i.e.*, the linear $E \otimes e$ problem [17, 18, 33–36], the PESs simplify to⁷

$$V_{1,2}(\mathbf{Q}) = V_E^\times(\mathbf{0}) + \frac{1}{2}K_0^{(E)}\rho^2 \pm |F_E|\rho, \quad (2.25)$$

and assume the form of a double cone (the Mexican-hat-type PESs) with a Ci at $\rho = 0$ [see Figures 2.3(a) and 2.4(a)]. The radius ρ_{min} of the circle at the bottom of the trough and its well-depth, *i.e.*, the JT stabilization energy E_{JT}^E , are given, respectively, by [37, 48]

$$\rho_{min} = \frac{|F_E|}{K_0^{(E)}}, \quad (2.26)$$

and

$$E_{JT}^E = \frac{F_E^2}{2K_0^{(E)}}. \quad (2.27)$$

As seen from Figures 2.3(b) and 2.4(b), the introduction of the quadratic coupling terms into the vibronic problem [*i.e.*, the linear plus quadratic $E \otimes e$ problem of Eq. (2.23)] reveals the so-called warping of the Mexican hat with the formation three wells (minima) alternating regularly with three humps (saddle points) along the bottom of the trough [49]. Such extrema points (ρ_{min}, ϕ_{min}) on the lowest (ground-state) PES are thus defined by

$$\rho_{min} = \frac{\pm F_E}{K_0^{(E)} \mp (-1)^n 2G_E}, \quad \phi_{min} = (2n + 1)\frac{\pi}{6}, \quad n = 0, \dots, 5, \quad (2.28)$$

⁷By setting $G_E = 0$.

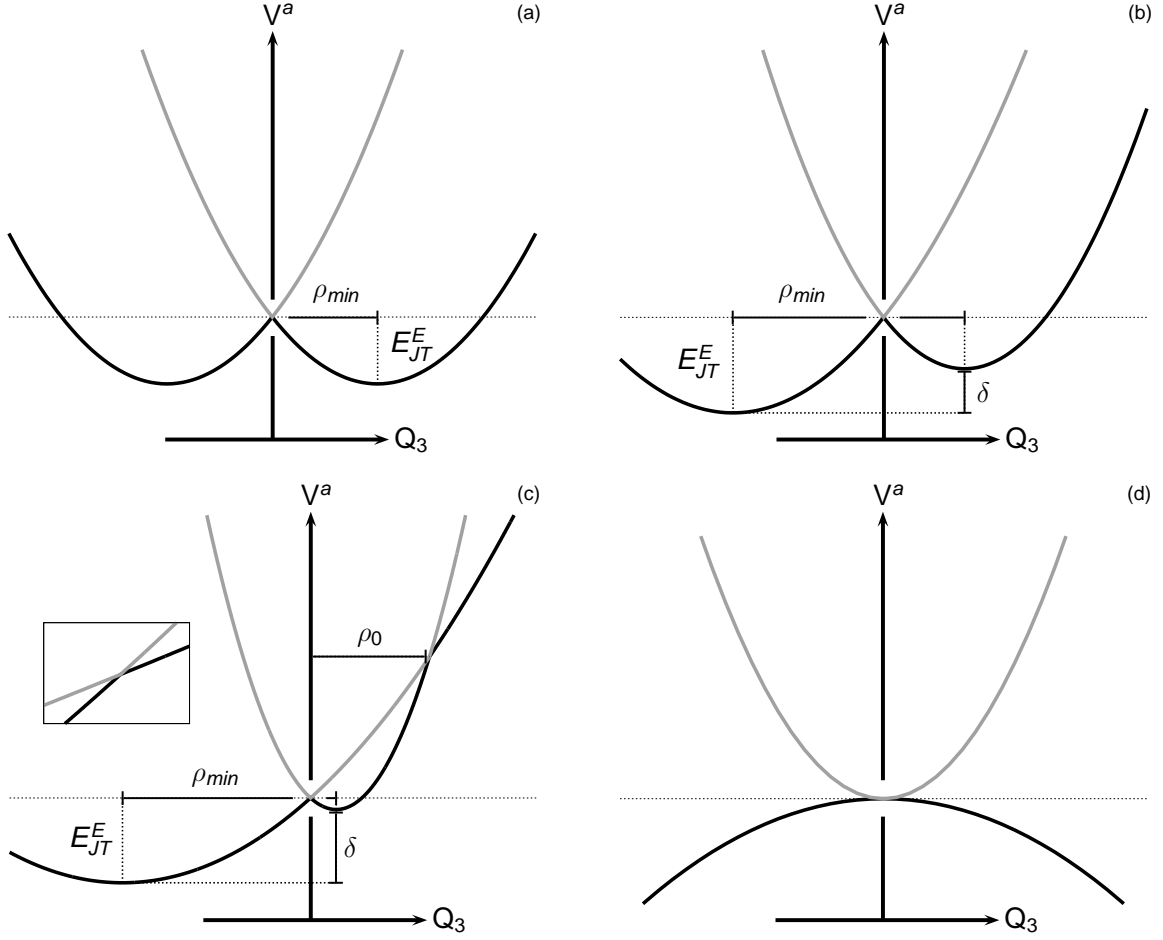


Figure 2.3: Cross sections of the PESs of Eq. (2.23) along the Q_3 mode (with $Q_2 = 0$ and $\phi = \pi/2$) for the various possible $E \otimes e$ coupling regimes. (a). Pure linear coupling with (in arbitrary units) $K_0^{(E)} = 100$, $F_E = 20$ and $G_E = 0$. (b). Linear plus quadratic coupling with $K_0^{(E)} = 100$, $F_E = 20$ and $G_E = 15$. (c). Small linear plus large quadratic coupling with $K_0^{(E)} = 100$, $F_E = 12$ and $G_E = 38$ and (d). Pure quadratic coupling with $K_0^{(E)} = 100$, $F_E = 0$ and $G_E = 80$. The parameters ρ_{min} , E_{JT}^E , δ and ρ_0 are defined in Eqs. (2.26)-(2.30) and (2.33). The dotted lines are the zero of energy defined with respect to $V_1(\mathbf{0}) = V_2(\mathbf{0}) = V_E^\times(\mathbf{0})$, *i.e.*, to the crossing points at $Q_3 = Q_2 = 0$. The inset of panel (c) shows a close view of the additional degeneracy points observed in the large quadratic (and small linear parameter) coupling case.

where the upper and lower signs correspond to the cases $F_E > 0$ and $F_E < 0$, respectively. If $F_E G_E > 0$, the points with $n = 0, 2$ and 4 are minima, whereas those with $n = 1, 3$ and 5 are saddle points [see Figures 2.3(b) and 2.4(b)]. Indeed, for $F_E G_E < 0$, the contrary is the case and the nature of the extrema points interchange. The JT stabilization energy of

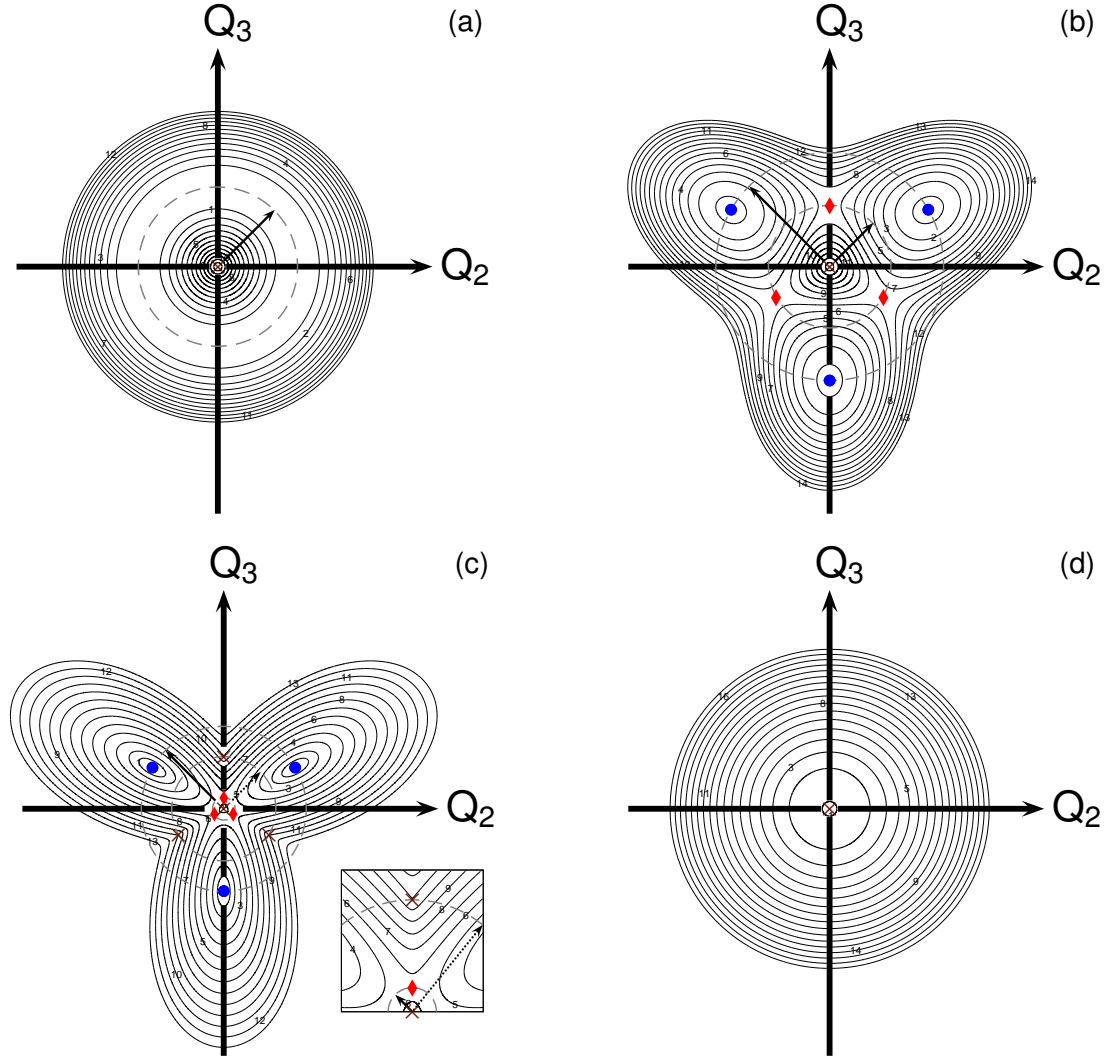


Figure 2.4: Contour plots of the lower (ground-state) PESs of Eq. (2.23) for the various possible $E \otimes e$ coupling regimes shown in Figure 2.3. (a). Pure linear coupling [Figure 2.3(a)]. (b). Linear plus quadratic coupling [Figure 2.3(b)]. (c). Small linear plus large quadratic coupling [Figure 2.3(c)] and (d). Pure quadratic coupling [Figure 2.3(d)]. Minima and saddle points are represented by circles and diamonds, respectively, while Cis are indicated by the “x” symbol. Filled arrows define the ρ_{min} parameters of Eqs. (2.26) and (2.28), whereas the dotted ones represents the radius ρ_0 defined in Eq. (2.33). The angles ϕ_{min} and ϕ_0 are measured counterclockwise starting at the Q_2 axis. The inset of panel (c) shows a close view of the additional degeneracy points observed in the large quadratic (and small linear parameter) coupling case.

the minima with respect to the degeneracy point at $\rho=0$, is

$$E_{JT}^E = \frac{F_E^2}{2(K_0^{(E)} - 2|G_E|)}, \quad (2.29)$$

with the corresponding barrier height δ given by

$$\delta = \frac{4E_{JT}^E |G_E|}{(K_0^{(E)} + 2|G_E|)}. \quad (2.30)$$

It is clear from the above considerations that, in the absence of quadratic couplings [Figures 2.3(a) and 2.4(a)], the nuclei perform free internal rotations (more precisely, pseudo-rotations) along the circle of radius ρ_{min} [50–52]. However, if δ are sufficiently high, such pseudo-rotational motion along the warped trough [Figures 2.3(b) and 2.4(b)] cease to be free and the phenomenon of tunneling between the three symmetry-equivalent minima should be expected [35, 36].

The two eigenvectors which are the solutions of the perturbational problem (2.21), with the corresponding expectation values given by Eq. (2.23), are

$$\begin{pmatrix} |\psi_1(\mathbf{r}; \mathbf{Q})\rangle \\ |\psi_2(\mathbf{r}; \mathbf{Q})\rangle \end{pmatrix} = \begin{pmatrix} \cos \frac{1}{2}\alpha(\mathbf{Q}) & -\sin \frac{1}{2}\alpha(\mathbf{Q}) \\ \sin \frac{1}{2}\alpha(\mathbf{Q}) & \cos \frac{1}{2}\alpha(\mathbf{Q}) \end{pmatrix} \begin{pmatrix} |E_\theta(\mathbf{r}; \mathbf{0})\rangle \\ |E_\epsilon(\mathbf{r}; \mathbf{0})\rangle \end{pmatrix}, \quad (2.31)$$

where $\alpha(\mathbf{Q})$ is defined such that⁸

$$\tan \alpha(\mathbf{Q}) = \frac{F_E \sin \phi - |G_E| \rho \sin 2\phi}{F_E \cos \phi + |G_E| \rho \cos 2\phi}. \quad (2.32)$$

An important aspect of the $E \otimes e$ problem emerged only recently in the literature [53]. For such systems, in addition to the central D_{3b} Ci at $\rho = 0$, the two branches of the adiabatic PESs [Eq. (2.23)] also intersect at

$$\rho_0 = \left| \frac{F_E}{G_E} \right|, \quad \phi_0 = \frac{\pi}{2}, \frac{7\pi}{6} \text{ and } \frac{11\pi}{6}. \quad (2.33)$$

It follows that, if G_E is small, such three additional symmetry-equivalent C_{2v} CIs occur far away from the central intersection. Yet, as shown in Figures 2.3(c) and 2.4(c), for sufficiently large values of G_E (compared to F_E), the radius ρ_0 becomes quite small and the four CIs come quite close together. Indeed, for such molecules, often referred to as small linear parameter (SLP) JT systems [33, 35, 36, 53–55], the presence of these additional topographical features have dramatic implications on the resulting spectral

⁸By considering Eqs. (2.7) and (2.8).

properties of the PESs, in particular, those related to the so-called GP effect [8–11]. As a final remark, we should also comment on the important limiting case for which $F_E = 0$ and $G_E \neq 0$. From Eq. (2.23), the adiabatic PESs become

$$V_{1,2}(\mathbf{Q}) = V_E^\times(\mathbf{0}) + \frac{1}{2}\rho^2 \left(K_0^{(E)} \pm 2|G_E| \right). \quad (2.34)$$

As seen from Figures 2.3(d) and 2.4(d), the two sheets assume the form of tangentially touching parabolas (or, in other words, RT-like PESs) in which the degeneracy is lifted quadratically in displacements from the point of intersection. Interestingly, from Eq. (2.33), $\rho_0 = 0$ in this case which implies therefore that all four degeneracies are assumed to be located at the same point in nuclear configuration space, *i.e.*, at the JT D_{3b} arrangement.

2.4 Geometric phase effect

The most fundamental effect directly related to the presence of Cis has first been recognized in 1963 by Herzberg and Longuet-Higgins [8]. The authors, with the aid of a two-state model Hamiltonian proposed by Teller [20], showed that a real adiabatic electronic wave function undergoes a sign change (*i.e.*, it is a double-valued function) when the nuclear coordinates traverse a closed path round the point at which the associated PESs intersect conically. This signature property of Cis had previously been considered by Longuet-Higgins *et al.* [50] in their treatment of the dynamical $E \otimes e$ JT problem. In fact, it is easy to see from Eqs. (2.9) and (2.31) that as we move round the origin keeping a fixed distance from \mathbf{R}^\times and allowing α to increase from 0 to 2π , both coefficients on the RHS change sign, and so do $|\psi_1\rangle$ and $|\psi_2\rangle$.⁹

Longuet-Higgins [9] further demonstrated, by using topological arguments only, that such sign-reversal condition can be properly utilized to diagnose the presence of intersections between PESs, particularly if the degeneracy is not dictated by symmetry. This well-known Longuet-Higgins' theorem [8, 9] can be formally stated (and generalized) as follows [15]

⁹Note that, in Eq. (2.31), such sign-reversal property can only be achievable for the cases when $F_E \neq 0$ and $G_E = 0$ or $F_E \gg G_E$; see Eq. (2.32).

- (1) On going once around any closed path on the surface that contains the Ci the electronic wave function changes sign.
- (2) If a real adiabatic electronic wave function changes sign when a polyatomic transverse a closed loop on a two-dimensional surface in the $3H-6$ -dimensional nuclear configuration space, then the corresponding electronic state must become discontinuous and degenerate with another one at an odd number of points lying on that surface and within that loop.

Indeed, the physical consequences of the presence of such GP or topological phase are quite remarkable [56]. Overall, Cis can alter the nuclear dynamics even when the collisional or vibrational motions occur far away from the intersection seam, the only requirement though is that the nuclear wave function has appreciable amplitude along an entire path enclosing the degeneracy, regardless of the energy of the Ci itself [11, 13, 57]. Since the total (electron-nuclear) wave function must be continuous and single-valued, the nuclear eigenket must then also change sign to compensate the sign-change of the electronic counterpart. As a result, both $|\psi_i(\mathbf{r}; \mathbf{R})\rangle$ and $|\chi_i(\mathbf{R})\rangle$ in Eq. (1.37) are not single-valued when taken as real. Such observable effects were discussed in a more general sense by Mead and Truhlar [11] who demonstrated that the resulting multiple-valuedness of the electronic part can be removed by attaching to it a complex (multi-valued) geometry-dependent phase factor, although at the cost of introducing a vector-potential-like term into the effective Schrödinger equation for the nuclear motion. The phase factor is chosen in such a way as to cancel out the net change of sign so that the complex electronic wave function is single-valued. Note that this latter also satisfies the same TIESE [Eq. (1.29)] as the real double-valued eigenvector. As pointed by Longuet-Higgins *et al.* [50] and Mead [57], the vector potential so introduced is not a mere mathematical artifact, but has experimental implications such as the appearance of half-odd integral vibronic angular momentum quantum numbers for the pseudorotational motion in certain X_3 -type molecules. In fact, it gives rise to a “fictitious” magnetic field [58] confined at the Ci, which led Mead [57] to further suggest the designation “molecular Aharonov-Bohm effect”¹⁰ for

¹⁰In the Aharonov-Bohm effect [58] the wave function of a charged particle passing around a magnetic

the geometric phase change.

Such a phenomenon has been placed in a wider quantum mechanical context by Berry [10], and hence it also became known as the Berry phase effect [59]. The author showed that any quantum system acquires a geometric phase factor, in addition to the familiar dynamic phase [Eq. (1.10)], when it undergoes an adiabatic time evolution round a circuit C in the parameter space. As pointed out by Berry, the sign-reversal property of electronic eigenfunctions of real symmetric matrices round a degeneracy is a special case of the more general GP problem [12, 59].

In the following, we stress the essential approach to account for the Berry's phase in typical molecular systems and address the main physical consequences of such a phenomena. Since the GP effect manifests itself in the uncoupled single-surface formalism, we also consider the modifications to the standard adiabatic framework which are required in order to access the effects of Cis on nuclear dynamics, *i.e.*, the so-called generalized Born-Oppenheimer (GBO) approximation [4, 11, 13, 29, 60, 61]. To this end, we define, following Mead and Truhlar [11], a gauge transformation of the form [11, 13, 60, 61]

$$|\tilde{\psi}_i(\mathbf{r}; \mathbf{R})\rangle \equiv e^{iA_i(\mathbf{R})} |\psi_i(\mathbf{r}; \mathbf{R})\rangle, \quad (2.35)$$

where $A_i(\mathbf{R})$ is a geometry-dependent phase which is chosen to make the electronic adiabatic eigenstate $|\tilde{\psi}_i(\mathbf{r}; \mathbf{R})\rangle$ single-valued (and complex) and $|\psi_i(\mathbf{r}; \mathbf{R})\rangle$ is a real-valued solution of Eq. (1.29). It should be recalled that both state vectors are actually eigenfunctions of the electronic Hamiltonian. Note that, in (2.35), the wave function index i should not be confused with the imaginary number i .

From (2.35), the BH expansion of Eq. (1.30) can be rewritten in the form

$$|\Psi_n(\mathbf{r}, \mathbf{R})\rangle = \sum_i^I |\chi_i(\mathbf{R})\rangle |\tilde{\psi}_i(\mathbf{r}; \mathbf{R})\rangle. \quad (2.36)$$

By substituting the above anzats into the full TISE [Eq. (1.11)], projecting from the left by $\langle \tilde{\psi}_j(\mathbf{r}; \mathbf{R})|$ and using (2.35), the generalized form of the coupled nuclear equations

flux (a narrow solenoid) experiences a phase shift, even if the field itself is zero everywhere along the path.

[Eq. (1.31)] become [29]

$$\left\{ \sum_{\alpha=1}^H \frac{1}{2\mathcal{M}_\alpha} \left[-i\vec{\nabla}(\mathbf{R}_\alpha) + \vec{\nabla}(\mathbf{R}_\alpha)A_j(\mathbf{R}) \right]^2 + \bar{V}_j(\mathbf{R}) - E_n \right\} |\chi_j(\mathbf{R})\rangle = \sum_{i(\neq j)}^I \Xi_{ji}(\mathbf{R}) |\chi_i(\mathbf{R})\rangle, \quad (2.37)$$

where

$$\begin{aligned} \Xi_{ji}(\mathbf{R}) = e^{i[A_i(\mathbf{R})-A_j(\mathbf{R})]} \sum_{\alpha=1}^H \frac{1}{2\mathcal{M}_\alpha} \left\{ -K_{ji}(\mathbf{R}_\alpha) + i \left[-i\vec{\nabla}(\mathbf{R}_\alpha) + \vec{\nabla}(\mathbf{R}_\alpha)A_j(\mathbf{R}) \right] \cdot \mathbf{F}_{ji}(\mathbf{R}_\alpha) \right. \\ \left. + i\mathbf{F}_{ji}(\mathbf{R}_\alpha) \cdot \left[-i\vec{\nabla}(\mathbf{R}_\alpha) + \vec{\nabla}(\mathbf{R}_\alpha)A_j(\mathbf{R}) \right] \right\} \quad (i \neq j), \end{aligned} \quad (2.38)$$

with $K_{ji}(\mathbf{R}_\alpha)$ being a derivative coupling¹¹ of the form [29]

$$K_{ji}(\mathbf{R}_\alpha) = \left\langle \vec{\nabla}(\mathbf{R}_\alpha)\psi_j(\mathbf{r}; \mathbf{R}) \left| \vec{\nabla}(\mathbf{R}_\alpha)\psi_i(\mathbf{r}; \mathbf{R}) \right. \right\rangle, \quad (2.40)$$

and

$$\begin{aligned} \bar{V}_j(\mathbf{R}) &= V_j(\mathbf{R}) + \sum_{\alpha=1}^H \frac{K_{jj}(\mathbf{R}_\alpha)}{2\mathcal{M}_\alpha} \\ &= V_j(\mathbf{R}) - \sum_{\alpha=1}^H \frac{G_{jj}(\mathbf{R}_\alpha)}{2\mathcal{M}_\alpha} \end{aligned} \quad (2.41)$$

is the effective scalar potential [13, 60, 61]. In the above equations, $\mathbf{F}_{ji}(\mathbf{R}_\alpha)$ and $G_{ji}(\mathbf{R}_\alpha)$ are the usual derivative and scalar couplings defined in Eqs. (1.33) and (1.34), respectively. They are related to the corresponding tilted quantities by¹² [11]

$$\tilde{\mathbf{F}}_{ji}(\mathbf{R}_\alpha) \equiv e^{i[A_i(\mathbf{R})-A_j(\mathbf{R})]} \left[i\delta_{ji}\vec{\nabla}(\mathbf{R}_\alpha)A_i(\mathbf{R}) + \mathbf{F}_{ji}(\mathbf{R}_\alpha) \right], \quad (2.42)$$

and

$$\begin{aligned} \tilde{G}_{ji}(\mathbf{R}_\alpha) \equiv e^{i[A_i(\mathbf{R})-A_j(\mathbf{R})]} \left\{ -\delta_{ji}[\vec{\nabla}(\mathbf{R}_\alpha)A_i(\mathbf{R})]^2 + i\delta_{ji}\nabla^2(\mathbf{R}_\alpha)A_i(\mathbf{R}) \right. \\ \left. + 2i\mathbf{F}_{ji}(\mathbf{R}_\alpha) \cdot \vec{\nabla}(\mathbf{R}_\alpha)A_i(\mathbf{R}) + G_{ji}(\mathbf{R}_\alpha) \right\}. \end{aligned} \quad (2.43)$$

¹¹ $K_{ji}(\mathbf{R}_\alpha)$ is related to $\mathbf{F}_{ji}(\mathbf{R}_\alpha)$ and $G_{ji}(\mathbf{R}_\alpha)$ by [4]

$$K_{ji}(\mathbf{R}_\alpha) = \vec{\nabla}(\mathbf{R}_\alpha) \cdot \mathbf{F}_{ji}(\mathbf{R}_\alpha) - G_{ji}(\mathbf{R}_\alpha). \quad (2.39)$$

¹²By substituting relation (2.35) into Eqs. (1.33) and (1.34), respectively.

Note that, in contrast to $\mathbf{F}_{jj}(\mathbf{R}_\alpha)$ which vanishes for real-valued electronic wave functions, $\tilde{\mathbf{F}}_{jj}(\mathbf{R}_\alpha) = i\vec{\nabla}(\mathbf{R}_\alpha)A_j(\mathbf{R})$. In fact, as can be seen from Eq. (2.37), the appearance of the phase gradients $\vec{\nabla}(\mathbf{R}_\alpha)A_j(\mathbf{R})$, *i.e.*, the well-known gauge or vector potentials [4, 11, 13, 29, 60, 61], is a direct consequence of the presence of Cis. Since such terms are singular at the intersection seam, the resulting (pseudo) magnetic field, $\vec{\nabla}(\mathbf{R}_\alpha) \times [\vec{\nabla}(\mathbf{R}_\alpha)A_j(\mathbf{R})]$, is zero everywhere except at the Ci where it has a delta-function singularity [11, 13]. It is worth mentioning that, if Eq. (2.36) is reassociated as

$$|\Psi_n(\mathbf{r}, \mathbf{R})\rangle = \sum_i^I [e^{iA_i(\mathbf{R})} |\chi_i(\mathbf{R})\rangle] |\psi_i(\mathbf{r}; \mathbf{R})\rangle \equiv \sum_i^I |\tilde{\chi}_i(\mathbf{R})\rangle |\psi_i(\mathbf{r}; \mathbf{R})\rangle, \quad (2.44)$$

then no vector potentials appear and Eq. (2.37) assumes the same form of (1.31) but with $|\tilde{\chi}_i(\mathbf{R})\rangle$ in place of $|\chi_i(\mathbf{R})\rangle$. In this case, both $|\tilde{\chi}_i(\mathbf{R})\rangle$ and $|\psi_i(\mathbf{r}; \mathbf{R})\rangle$ are double-valued. Although being particularly convenient for treating X_3 -type molecules (and their isotopomers) [62], such an alternative approach is often difficult to implement in general systems and computationally cumbersome [63].

Again, if just one term is retained in the expansion (2.36), then Eq. (2.37) becomes

$$\left\{ \sum_{\alpha=1}^H \frac{1}{2\mathcal{M}_\alpha} \left[-i\vec{\nabla}(\mathbf{R}_\alpha) + \vec{\nabla}(\mathbf{R}_\alpha)A_j(\mathbf{R}) \right]^2 + \bar{V}_j(\mathbf{R}) - E_n \right\} |\chi_j(\mathbf{R})\rangle = 0, \quad (2.45)$$

which is a generalized version of Eq. (1.38) or GBO approximation¹³. It is obvious from (2.45) that even when a Ci is not energetically accessible, its presence is certainly reflected on the nuclear dynamics. It should be emphasized, however, that for high-energy collisions and/or vibration motions, the NACTs [Eq. (2.38)] become sizable (and even singular at a Ci) so that the GBO approximation also breaks down.

Of course, in order to account for the proper GP effect in Eqs. (2.37) and (2.45) one must be able to anticipate the existence of Cis prior to the dynamical treatment [11, 13, 29, 62], and then determine the phase accordingly. Indeed, $A_j(\mathbf{R})$ must reflect (by built-in construction) the presence of any discontinuities on adiabatic PESs. Although a general approach for determining $A_j(\mathbf{R})$ has been suggested [63, 64], it remains a nontrivial task.

¹³Obviously, one can also neglect the standard DBOC term in the RHS of Eq. (2.41). In so doing, a generalized version of the adiabatic approximation (1.39) is obtained.

Consider again the linear plus quadratic $E \otimes e$ JT problem for a X_3 -type molecule discussed in section 2.3. As already stated, the eigenkets $|\psi_{1,2}(\mathbf{r}; \mathbf{Q})\rangle$ [Eq. (2.31)] are double-valued, and hence undergo a change of sign when $\alpha(\mathbf{Q})$ [Eq. (2.32)] makes a full circuit from 0 to 2π round the origin.¹⁴ In this case, it is straightforward to show that a phase of the form [11, 53, 57]

$$A_{1,2}(\mathbf{Q}) = \frac{\ell}{2}\alpha(\mathbf{Q}) \quad (2.46)$$

makes the corresponding tilded electronic wave functions single-valued. These latter are thus defined by the following gauge transformation [11, 53, 57]

$$|\tilde{\psi}_{1,2}(\mathbf{r}; \mathbf{Q})\rangle \equiv e^{i\frac{\ell}{2}\alpha(\mathbf{Q})} |\psi_{1,2}(\mathbf{r}; \mathbf{Q})\rangle. \quad (2.47)$$

Note that, in the above equations, $\ell = \pm 1, \pm 3, \pm 5 \dots$ is an odd integer which satisfies the requirement [36]

$$e^{i\frac{\ell}{2}[\alpha(\mathbf{Q})+2\pi]} = -e^{i\frac{\ell}{2}\alpha(\mathbf{Q})}. \quad (2.48)$$

As demonstrated by Mead and Thuhlar [11], the choice of the gauge parameter which is most convenient for the treatment of permutational symmetry is $\ell = \pm 3$.

From Eqs. (2.31), (2.47) and (2.42), one can thus define [53]

$$\begin{aligned} \tilde{\mathbf{F}}_{11} = \tilde{\mathbf{F}}_{22} &= \left\langle \tilde{\psi}_{1,2}(\mathbf{r}; \mathbf{Q}) \left| \vec{\nabla} \tilde{\psi}_{1,2}(\mathbf{r}; \mathbf{Q}) \right. \right\rangle \\ &= i\frac{\ell}{2}\vec{\nabla}\alpha(\mathbf{Q}), \end{aligned} \quad (2.49)$$

where we have used the well-known result $\langle \psi_{1,2}(\mathbf{r}; \mathbf{Q}) | \vec{\nabla} \psi_{1,2}(\mathbf{r}; \mathbf{Q}) \rangle = 0$. Note that the grad operator $\vec{\nabla}$ can be defined such that [36, 53]

$$\vec{\nabla} = \frac{\partial}{\partial \rho} \hat{\rho} + \frac{1}{\rho} \frac{\partial}{\partial \phi} \hat{\phi}. \quad (2.50)$$

Indeed, the quantity $\vec{\nabla}\alpha(\mathbf{Q})$ in (2.49) can be evaluated by applying $\vec{\nabla}$ to Eq. (2.32). In so doing, one obtains [53]

$$\vec{\nabla}\alpha(\mathbf{Q}) = \frac{-F_E|G_E|\sin 3\phi}{F_E^2 + 2F_E|G_E|\rho \cos 3\phi + G_E^2\rho^2} \hat{\rho} + \frac{1}{\rho} \frac{F_E^2 - F_E|G_E|\rho \cos 3\phi - 2G_E^2\rho^2}{F_E^2 + 2F_E|G_E|\rho \cos 3\phi + G_E^2\rho^2} \hat{\phi}. \quad (2.51)$$

¹⁴As we shall see later, this is true only for the cases in which $F_E \neq 0$ and $G_E = 0$ or $F_E \gg G_E$.

Following Berry [10] and Zwanziger and Grant [53], the phase experienced by the wave functions under complete traversal by the nuclei of a circular path C , *i.e.*, for a fixed and arbitrary value of ρ , round the origin is

$$\begin{aligned}
\gamma_{1,2}(C) &= i \oint_C \langle \tilde{\psi}_{1,2}(\mathbf{r}; \mathbf{Q}) | \vec{\nabla} \tilde{\psi}_{1,2}(\mathbf{r}; \mathbf{Q}) \rangle \cdot d\mathbf{Q} \\
&= i \oint_C i \frac{\ell}{2} \vec{\nabla} \alpha(\mathbf{Q}) \cdot d\mathbf{Q} \\
&= -\frac{\ell}{2} \int_0^{2\pi} \frac{\partial \alpha(\mathbf{Q})}{\partial \phi} d\phi \\
&= -\frac{\ell}{2} \int_0^{2\pi} \frac{F_E^2 - F_E G_E \rho \cos 3\phi - 2G_E^2 \rho^2}{F_E^2 + 2F_E G_E \rho \cos 3\phi + G_E^2 \rho^2} d\phi, \tag{2.52}
\end{aligned}$$

where we have taken both F_E and G_E as positive quantities. Note that, in the limit of pure linear coupling, *i.e.*, for $G_E=0$, $\alpha(\mathbf{Q})=\phi$ [see Eq. (2.32)], the integral (2.52) assumes the simple form

$$\gamma_{1,2}(C) = -\frac{\ell}{2} \int_0^{2\pi} 1 d\phi = -\ell\pi, \tag{2.53}$$

which corresponds to a GP factor of

$$e^{-i\ell\pi} = -1. \tag{2.54}$$

Thus, as the electronic wave functions (2.47) are adiabatically transported around any closed path C which encircles the central D_{3b} Ci, they both change sign. This is just the result obtained by Berry in the context of the linear $E \otimes e$ JT problem [10].

Let us now turn to the important case of the SLP JT molecules. As shown in Figures 2.3(c) and 2.4(c), such systems show three additional symmetry-allowed C_{2v} degeneracies in quite close proximity to the central D_{3b} Ci. Zwanziger and Grant [53] evaluated the phase behavior of the adiabatic wave functions (2.47) by solving the integral (2.52) for distinct cyclic paths in the (Q_2, Q_3) branching plane.¹⁵ They demonstrated that for loops defined by $\rho < \rho_0$ [see Eq. (2.33)], *i.e.*, when only the D_{3b} degeneracy is encircled, the electronic wave functions behave much in the same way as those of the purely linear

¹⁵In such circular paths, the perimeter of the triangle is always kept fixed or, in other words, $Q_{a_1} \equiv Q_1$ in Eq. (2.20) equals to zero, with R^\times assuming a particular and fixed value.

$E \otimes e$ problem and change sign under the complete traversal of the path. Furthermore, if the loop encloses just one of the three equivalent C_{2v} Cis, the phase experienced by the eigenkets imparts the same degree of rotation as transport about the origin, but with the opposite sign, *i.e.*,

$$\gamma_{1,2}(C') = \ell\pi. \quad (2.55)$$

Thus, as highlighted by the authors [53], the phase along any path is easily obtained by including $\ell\pi$ for every (counterclockwise) loop around one of the three C_{2v} degeneracies, and $-\ell\pi$ for the origin. Indeed, for paths with $\rho > \rho_0$, *i.e.*, those which include all 4 Cis, we find

$$\gamma_{1,2}(C'') = -\ell\pi + 3(\ell\pi) = 2\ell\pi, \quad (2.56)$$

and

$$e^{i2\ell\pi} = 1. \quad (2.57)$$

In this case, therefore, there is no net sign change and both $|\psi_{1,2}(\mathbf{r}; \mathbf{Q})\rangle$ [Eq. (2.31)] and $|\tilde{\psi}_{1,2}(\mathbf{r}; \mathbf{Q})\rangle$ [Eq. (2.47)] are single-valued everywhere in the $\rho > \rho_0$ region. Finally, consider the RT-like case shown in Figures 2.3(d) and 2.4(d). Again, for such systems $F_E=0$, and therefore, $\alpha(\mathbf{Q})$ in Eq. (2.32) is precisely -2ϕ . Thence, Eq. (2.52) assumes the form

$$\gamma_{1,2}(C''') = -\frac{\ell}{2} \int_0^{2\pi} -2d\phi = 2\ell\pi, \quad (2.58)$$

which is exactly the same solution obtained in (2.56). From such results, one can certainly state that, for SLP JT systems, ρ_0 marks a sharp boundary between (linear) JT- and (quadratic) RT-like behavior. This is so since adiabatic electronic wave functions undergo a sign change upon transport about the origin in the former, but not in the latter.

Bibliography

- [1] J. Michl, "Physical Basis of Qualitative MO Arguments in Organic Photochemistry," in *Photochemistry* (Springer, Berlin, Heidelberg, 1974) pp. 1–59.
- [2] J. Michl and V. Bonačić-Koutecký, *Electronic aspects of organic photochemistry* (John Wiley & Sons, Chichester, 1990).
- [3] S. Matsika and P. Krause, *Annu. Rev. Phys. Chem.* **62**, 621 (2011).
- [4] W. Domcke, D. R. Yarkony, and H. Köppel, *Conical Intersections: Electronic Structure, Dynamics & Spectroscopy.*, Advanced Series in Physical Chemistry, Vol. 15 (World Scientific, Singapore, 2004).
- [5] G. A. Worth and L. S. Cederbaum, *Ann. Rev. Phys. Chem.* **55**, 127 (2004).
- [6] G. C. G. Waschewsky, P. W. Kash, T. L. Myers, D. C. Kitchen, and L. J. Butler, *J. Chem. Soc., Faraday Trans.* **90**, 1581 (1994).
- [7] D. R. Yarkony, *Acc. Chem. Res.* **31**, 511 (1998).
- [8] G. Herzberg and H. C. Longuet-Higgins, *Discuss. Faraday Soc.* **35**, 77 (1963).
- [9] H. C. Longuet-Higgins, *Proc. R. Soc. Ser. A* **344**, 147 (1975).
- [10] M. V. Berry, *Proc. R. Soc.* **392**, 45 (1984).
- [11] C. A. Mead and D. G. Truhlar, *J. Chem. Phys.* **70**, 2284 (1979).
- [12] C. A. Mead, *Rev. Mod. Phys.* **64**, 51 (1992).

-
- [13] B. K. Kendrick, *J. Phys. Chem. A* **107**, 6739 (2003).
- [14] G. J. Atchity, S. S. Xantheas, and K. Ruedenberg, *J. Chem. Phys.* **95**, 1862 (1991).
- [15] A. J. C. Varandas, *Chem. Phys. Lett.* **487**, 139 (2010).
- [16] M. V. Berry and M. Wilkinson, *Proc. R. Soc. Lond. A* **392**, 15 (1984).
- [17] H. A. Jahn and E. Teller, *Proc. R. Soc. Lond. A* **161**, 220 (1937).
- [18] H. A. Jahn, *Proc. R. Soc. Lond. A* **164**, 117 (1938).
- [19] J. von Neumann and E. P. Wigner, *Physik. Z.* **30**, 467 (1929).
- [20] E. Teller, *J. Phys. Chem.* **41**, 109 (1937).
- [21] K. R. Naqvi, *Chem. Phys. Lett.* **15**, 634 (1972).
- [22] A. J. Stone, *Proc. R. Soc. Lond. A* **351**, 141 (1976).
- [23] G. J. Hatton, *Phys. Rev. A* **14**, 901 (1976).
- [24] C. A. Mead, *J. Chem. Phys.* **70**, 2276 (1979).
- [25] M. Born and R. Oppenheimer, *Ann. Phys.* **389**, 457 (1927).
- [26] C. J. Ballhausen and A. E. Hansen, *Annu. Rev. Phys. Chem.* **23**, 15 (1972).
- [27] C. A. Mead and D. G. Truhlar, *J. Chem. Phys.* **77**, 6090 (1982).
- [28] A. Szabo and N. S. Ostlund, *Modern Quantum Chemistry: Introduction to Advanced Electronic Structure Theory*, Vol. 1 (McGraw-Hill Book Co., New York, 1989).
- [29] D. R. Yarkony, *Rev. Mod. Phys.* **68**, 985 (1996).
- [30] D. R. Yarkony, *Chem. Rev.* **112**, 481 (2012).
- [31] L. Pauling and E. B. Wilson, *Introduction to Quantum Mechanics with Applications to Chemistry*, Vol. 1 (McGraw-Hill Book Co., New York, 1935).

- [32] J. S. Griffith, *The Irreducible Tensor Method for Molecular Symmetry Groups* (Prentice-Hall, New Jersey, 1962).
- [33] R. Englman, *The Jahn-Teller Effect* (John Wiley & Sons, New York, 1973).
- [34] I. B. Bersuker and V. Z. Polinger, *Vibronic Interactions in Molecules and Crystals* (Springer-Verlag, Berlin, 1989).
- [35] I. B. Bersuker, Chem. Rev. **101**, 1067 (2001).
- [36] I. B. Bersuker, *The Jahn-Teller Effect* (Cambridge University Press, Cambridge, 2006).
- [37] U. Öpik and M. H. L. Pryce, Proc. R. Soc. Lond. A **238**, 425 (1957).
- [38] I. B. Bersuker, Chem. Rev. **113**, 1351 (2013).
- [39] R. Renner, Z. Phys. **92**, 172 (1934).
- [40] G. Herzberg and E. Teller, Z. Phys. Chem., *Abt. B* **21**, 410 (1933).
- [41] T. J. Lee, D. J. Fox, H. F. Schaefer, and R. M. Pitzer, J. Chem. Phys. **81**, 356 (1984).
- [42] M. D. Sturge, Solid State Physics **20**, 91 (1968).
- [43] T. A. Barckholtz and T. A. Miller, Int. Rev. Phys. Chem. **17**, 435 (1998).
- [44] P. Garcia-Fernandez, I. B. Bersuker, and J. E. Boggs, J. Chem. Phys. **125**, 104102 (2006).
- [45] C. M. R. Rocha and A. J. C. Varandas, J. Chem. Phys. **144**, 064309 (2016).
- [46] A. J. C. Varandas and J. N. Murrell, Chem. Phys. Lett. **84**, 440 (1981).
- [47] J. N. Murrell, S. Carter, S. C. Farantos, P. Huxley, and A. J. C. Varandas, *Molecular Potential Energy Functions* (John Wiley & Sons, Chichester, 1984).
- [48] A. Ceulemans, J. Chem. Phys. **87**, 5374 (1987).
- [49] A. D. Liehr and C. J. Ballhausen, Ann. Phys. **3**, 304 (1958).

-
- [50] H. C. Longuet-Higgins, U. Öpik, M. H. L. Pryce, and R. A. Sack, Proc. R. Soc. Lond. A **244**, 1 (1958).
- [51] W. Moffitt and W. Thorson, Phys. Rev. **108**, 1251 (1957).
- [52] M. C. M. O'Brien, Proc. R. Soc. Lond. A **281**, 323 (1964).
- [53] J. W. Zwanziger and E. R. Grant, J. Chem. Phys. **87**, 2954 (1987).
- [54] H. Köppel and R. Meiswinkel, Z. Phys. D: At., Mol. Clusters **32**, 153 (1994).
- [55] H. Koizumi and I. B. Bersuker, Phys. Rev. Lett. **83**, 3009 (1999).
- [56] D. Xiao, M.-C. Chang, and Q. Niu, Rev. Mod. Phys. **82**, 1959 (2010).
- [57] C. A. Mead, Chem. Phys. **49**, 23 (1980).
- [58] Y. Aharonov and D. Bohm, Phys. Rev. **115**, 485 (1959).
- [59] J. W. Zwanziger, M. Koenig, and A. Pines, Annu. Rev. Phys. Chem. **41**, 601 (1990).
- [60] A. Bohm, B. Kendrick, and M. E. Loewe, Int. J. Quantum Chem. **41**, 53 (1992).
- [61] A. Bohm, B. Kendrick, M. E. Loewe, and L. J. Boya, J. Math. Phys. **33**, 977 (1992).
- [62] A. J. C. Varandas, in *Fundamental World of Quantum Chemistry: A Tribute to the Memory of Per-Olov Löwdin*, Vol. 2, edited by E. J. Brändas and E. S. Kryachko (Kluwer Academic Publishers, Dordrecht, 2003) Chap. 2, pp. 33–92.
- [63] B. Kendrick and R. T. Pack, J. Chem. Phys. **104**, 7475 (1996).
- [64] B. Kendrick and A. C. Mead, J. Chem. Phys. **102**, 4160 (1995).

Chapter 3

Calculation of potential energy surfaces

An essential step toward an accurate representation of PESs consists of finding exact solutions to the TIESE [Eq. (1.29)] for an extensive set of fixed nuclear coordinates. Such a task is central to quantum chemists and, apart from the simplest cases such as H_2^+ (and similar one-electron systems), is hardly achievable. Thus, one frequently has to rely on rigorous (but approximate) quantum-mechanical models in order to approach the exact solutions of the many-electron problem [1–3].

Central to such standard methodologies is the Hartree-Fock (HF) approximation [4, 5] which introduces the simplest and fundamental picture of electrons occupying orbitals and provides a well defined step on the way to more sophisticated theories. By approximating the true electronic wave function as a single antisymmetrized Hartree product (Slater determinant (SD) [6]), the variational principle naturally warrants that the best set of orbitals and the lowest possible electronic energy is achieved for such trial function [7–9]. Obviously, as an independent-particle model, the HF theory accounts only for the average electron-electron interactions, and hence neglects, by its own fundamental nature, the true correlated dynamics of the systems' particles. At higher levels of approximation, one then expects to represent the true wave function for a fully interacting system by a variationally determined superposition of several (if not all) SDs. Although

multi-determinant methods are computationally much more involved than the HF model, they can, in principle, generate results that systematically approach the exact solutions of the TIESE.

Once the best affordable one-electron basis set and electronic structure model, *i.e.*, the L -electron wave function, have been selected and solved for a reasonable set of nuclear arrangements, we are frequently faced with the problem of how to accurately represent such huge table of *ab initio* energies so generated [10, 11]. By selecting a reliable compact analytic model, one is then able to fit such data (interpolate, and possibly extrapolate to regions of the nuclear configuration space not covered by the *ab initio* calculations) and subsequently use the model PES so obtained to solve any nuclear dynamics problem [12–17].

3.1 The Hartree-Fock self-consistent field theory

Following the HF approach [4, 5], the ground-state wave function for an L -electron molecular system can be approximated by the single SD¹

$$|\Theta_0(\mathbf{x}; \mathbf{R})\rangle = \frac{1}{\sqrt{L!}} \begin{vmatrix} \varphi_1(\mathbf{x}_1) & \varphi_2(\mathbf{x}_1) & \dots & \varphi_L(\mathbf{x}_1) \\ \varphi_1(\mathbf{x}_2) & \varphi_2(\mathbf{x}_2) & \dots & \varphi_L(\mathbf{x}_2) \\ \vdots & \vdots & \ddots & \vdots \\ \varphi_1(\mathbf{x}_L) & \varphi_2(\mathbf{x}_L) & \dots & \varphi_L(\mathbf{x}_L) \end{vmatrix}, \quad (3.1)$$

where $\mathbf{x}_j = (\mathbf{r}_j, w)$ is a collective variable defining the three spatial (\mathbf{r}_j) and spin (w) coordinates of the j -th electron and $|\varphi_i(\mathbf{x}_j)\rangle$ specify a set of orthonormal one-electron

¹Slater determinants meet the requirement of the antisymmetry principle [6], *i.e.*, they are antisymmetric with respect to the interchange of the space (\mathbf{r}) and spin (w) coordinates of any two electrons. From Eq. (3.1), this means that, by interchanging any two rows, the determinant changes its sign. Note further that, if two columns are equal, or in other words, if two electrons occupy the same spin orbital, the determinant assumes a null value. This is clearly a direct consequence of the Pauli exclusion principle [6].

wave functions, *i.e.*, spin molecular orbital (MO)s, given by

$$|\varphi_i(\mathbf{x}_j)\rangle = \begin{cases} |\zeta_i(\mathbf{r}_j)\rangle |\alpha(w)\rangle \\ \text{or} \\ |\zeta_i(\mathbf{r}_j)\rangle |\beta(w)\rangle, \end{cases} \quad (3.2)$$

where, $|\alpha(w)\rangle$ and $|\beta(w)\rangle$ are orthonormalized spin functions corresponding to spin up (\uparrow) and spin down (\downarrow), respectively, with $|\zeta_i(\mathbf{r}_j)\rangle$ being the associated spatial part. Before proceeding to the evaluation of the energy of the SD, it is convenient to rewrite the (clamped-nuclei) electronic Hamiltonian of Eq. (1.28) in the form

$$\hat{\mathcal{H}}_e(\mathbf{r}; \mathbf{R}) = \sum_{i=1}^L \hat{h}_i(\mathbf{r}_i; \mathbf{R}) + \sum_{i=1}^L \sum_{j>i}^L \hat{g}_{ij}(\mathbf{r}_i, \mathbf{r}_j; \mathbf{R}) + \hat{\mathcal{V}}_{NN}(\mathbf{R}), \quad (3.3)$$

where

$$\hat{h}_i(\mathbf{r}_i; \mathbf{R}) = -\frac{1}{2} \nabla^2(\mathbf{r}_i) - \sum_{j=1}^H \frac{Z_j}{|\mathbf{R}_j - \mathbf{r}_i|}, \quad (3.4)$$

and

$$\hat{g}_{ij}(\mathbf{r}_i, \mathbf{r}_j; \mathbf{R}) = \frac{1}{|\mathbf{r}_i - \mathbf{r}_j|}. \quad (3.5)$$

In the above equations, $\hat{h}_i(\mathbf{r}_i; \mathbf{R})$ is a one-electron operator which describes the motion of electron i in the field of the nuclei and $\hat{g}_{ij}(\mathbf{r}_i, \mathbf{r}_j; \mathbf{R})$ is the typical electron-electron repulsion term. Note that the nuclear repulsion operator $\hat{\mathcal{V}}_{NN}(\mathbf{R})$ [Eq. (1.8)] is independent of the electronic coordinates, and hence, for a fixed nuclear arrangement, assumes a constant value. Thus, $\hat{\mathcal{V}}_{NN}(\mathbf{R})$ can be immediately integrated out in the evaluation of the matrix elements of $\hat{\mathcal{H}}_e(\mathbf{r}; \mathbf{R})$ in the electronic basis $|\Theta_0(\mathbf{x}; \mathbf{R})\rangle$. For the sake of clarity, here and in the following sections, obvious coordinate dependencies will be suppressed when no confusion result.

By substituting Eqs. (3.1) and (3.3) into the expression

$$\mathcal{E}_0 = \frac{\langle \Theta_0 | \hat{\mathcal{H}}_e | \Theta_0 \rangle}{\langle \Theta_0 | \Theta_0 \rangle}, \quad (3.6)$$

one then obtains the expectation value of $\hat{\mathcal{H}}_e$ in the single-determinantal (trial) wave function $|\Theta_0\rangle$ which yields [1–3]

$$\mathcal{E}_0 = \mathcal{E}'_0 + \mathcal{E}''_0 + \hat{\mathcal{V}}_{NV}, \quad (3.7)$$

where

$$\mathcal{E}'_0 = \sum_{i=1}^L \langle \varphi_i(\mathbf{1}) | \hat{h}_i | \varphi_i(\mathbf{1}) \rangle \quad (3.8)$$

is the expectation value of the one-electron terms and

$$\begin{aligned} \mathcal{E}''_0 &= \frac{1}{2} \sum_{ij}^L \langle \varphi_i(\mathbf{1})\varphi_j(\mathbf{2}) | \hat{g}_{12} | \varphi_i(\mathbf{1})\varphi_j(\mathbf{2}) \rangle - \langle \varphi_i(\mathbf{1})\varphi_j(\mathbf{2}) | \hat{g}_{12} | \varphi_j(\mathbf{1})\varphi_i(\mathbf{2}) \rangle \\ &= \frac{1}{2} \sum_{ij}^L (J_{ij} - K_{ij}) \end{aligned} \quad (3.9)$$

represents the corresponding two-by-two electron repulsion energy. The matrix elements J_{ij} and K_{ij} are the so-called Coulomb and exchange (two-electron) integrals, respectively [1–3]. Clearly, J_{ij} represents the repulsion between two charged particles described by the probability distribution functions $\varphi_i(\mathbf{1})^2$ and $\varphi_j(\mathbf{2})^2$, whereas K_{ij} has no classical interpretation and arises because of the antisymmetric nature of the determinantal wave function [1]. Note that, in Eq. (3.9), the 1/2 factor appears inasmuch as the double summation runs over all electrons, without explicit restrictions on the i and j indexes.²

The total electron-electron repulsion energy \mathcal{E}''_0 [Eq. (3.9)] can be conveniently rewritten in terms of one-electron Coulomb ($\hat{\mathcal{J}}_j$) and exchange ($\hat{\mathcal{K}}_j$) operators. They are defined by their effect when operating on a spin MO, say, $|\varphi_i(\mathbf{1})\rangle$,

$$\hat{\mathcal{J}}_j |\varphi_i(\mathbf{1})\rangle = [\langle \varphi_j(\mathbf{2}) | \hat{g}_{12} | \varphi_j(\mathbf{2}) \rangle] |\varphi_i(\mathbf{1})\rangle \quad (3.10)$$

and

$$\hat{\mathcal{K}}_j |\varphi_i(\mathbf{1})\rangle = [\langle \varphi_j(\mathbf{2}) | \hat{g}_{12} | \varphi_i(\mathbf{2}) \rangle] |\varphi_j(\mathbf{1})\rangle. \quad (3.11)$$

²It can be seen from Eq. (3.9) that the “self-interaction” term J_{ij} is exactly canceled by the corresponding “exchange” element K_{ij} .

By making use of the above operators, Eq. (3.9) assumes the form

$$\mathcal{E}_0'' = \frac{1}{2} \sum_{ij}^L \left[\langle \varphi_i(\mathbf{1}) | \hat{\mathcal{J}}_j | \varphi_i(\mathbf{1}) \rangle - \langle \varphi_i(\mathbf{1}) | \hat{\mathcal{K}}_j | \varphi_i(\mathbf{1}) \rangle \right], \quad (3.12)$$

and, finally, from (3.7), (3.8) and (3.12), the total energy of the single SD wave function [Eq. (3.1)] is

$$\mathcal{E}_0 = \sum_{i=1}^L \langle \varphi_i(\mathbf{1}) | \hat{\mathcal{H}}_i | \varphi_i(\mathbf{1}) \rangle + \frac{1}{2} \sum_{ij}^L \left[\langle \varphi_i(\mathbf{1}) | \hat{\mathcal{J}}_j | \varphi_i(\mathbf{1}) \rangle - \langle \varphi_i(\mathbf{1}) | \hat{\mathcal{K}}_j | \varphi_i(\mathbf{1}) \rangle \right] + \hat{\mathcal{V}}_{NN}. \quad (3.13)$$

We are now primarily interested in obtaining a set of spin MOs $\{|\varphi_i\rangle\}_{i=1}^L$ such that the single determinant (3.1) formed from them is the best possible approximation to the ground-state wave function for the L -electron system. Following the variational principle [7–9], this can only be accomplished by determining those orthonormal orbitals that make the total electronic energy \mathcal{E}_0 [Eq. (3.13)] a minimum. In so doing³, one obtains the usual form of the HF pseudo-eigenvalue equations [1]

$$\hat{\mathcal{F}}_i |\varphi'_i(\mathbf{1})\rangle = \epsilon_i |\varphi'_i(\mathbf{1})\rangle, \quad (3.15)$$

where $\hat{\mathcal{F}}_i$ is the effective one-electron Fock operator

$$\hat{\mathcal{F}}_i = \hat{\mathcal{H}}_i + \sum_j^L (\hat{\mathcal{J}}_j - \hat{\mathcal{K}}_j), \quad (3.16)$$

$|\varphi'_i(\mathbf{1})\rangle$ is the set of canonical⁴ HF eigenvectors (MOs) which warrant that the lowest possible \mathcal{E}_0 is achieved for the single SD and ϵ_i is the corresponding orbital energies. It

³Such a constrained optimization is performed in such a way that the MOs remain orthonormal, and therefore can be reasonably handle by means of the Lagrange multipliers technique [2]. The condition to be fulfilled is that the Lagrange function (L) must be stationary with respect to an orbital variation, *i.e.*,

$$\delta L = \delta \mathcal{E}_0 - \sum_{ij}^L \lambda_{ij} [\langle \delta \varphi_i | \varphi_j \rangle - \langle \varphi_i | \delta \varphi_j \rangle] = 0, \quad (3.14)$$

where λ_{ij} are the Lagrange multipliers.

⁴Canonical orbitals are those that, by an unitary transformation, make the matrix of Lagrange multipliers diagonal. Such diagonal elements are thus the expectation values of the Fock operator in the $\{|\varphi'_i\rangle\}_{i=1}^L$ basis, *i.e.*, have the physical interpretation of the MO energies.

should be emphasized that, apart from atoms and diatomic molecules, the “exact” HF spin orbitals, and hence the exact (numeric) solutions of (3.15) are hardly possible. In practice, one normally expand the MOs as linear combinations of basis functions and then solve the resulting set of matrix equations. It is only when such basis approaches completeness, *i.e.*, at the complete basis set (CBS) or, in this particular case, at the HF limit, will the resulting spin orbitals converge to the correct solutions. By inspecting the ansatz (3.15), it is also clear that, since the Fock operator [Eq. (3.16)] actually depends on its own eigenvectors [via $\hat{\mathcal{F}}$ and $\hat{\mathcal{K}}$ in Eqs. (3.10) and (3.11)], the HF pseudo-eigenvalue problem must then be solved by iterative techniques, *i.e.*, by a self-consistent field (SCF) procedure [1–5].

The minimum value of \mathcal{E}_0 can thus be given in terms of the eigenvalues of the Fock operator, *i.e.*,

$$\begin{aligned}\mathcal{E}_0 &= \mathcal{E}_0^{(0)} + \mathcal{E}_0^{(1)} + \hat{\mathcal{V}}_{NN} \\ &= \sum_{i=1}^L \epsilon_i - \frac{1}{2} \sum_{ij}^L (J_{ij} - K_{ij}) + \hat{\mathcal{V}}_{NN}.\end{aligned}\quad (3.17)$$

Indeed, since the summation over spin orbitals in Eq. (3.16) accounts from the electron-electron repulsion twice, the total energy of the L -electron molecular system is not the sum of MO energies, and hence the corrective term $\mathcal{E}_0^{(1)}$ on the RHS of Eq. (3.17) must be added.

So far we have considered the HF formalism without making any assumptions (or restrictions) about the explicit form of the spin MOs from which the single SD trial wave function [Eq. (3.1)] is built. As stated above, the best set of such orbitals are those that satisfy the Schrödinger-like one-electron equations (3.15). Most stable molecules have singlet ground electronic states (closed-shell species) in which each MO is occupied by a pair of electrons with opposite spins. Thus, for such systems, a reasonable trial SD would be the one in which spin orbitals are constrained to have the same spatial part $|\zeta(\mathbf{r})\rangle$ for $|\alpha(w)\rangle$ and $|\beta(w)\rangle$ spin functions [see Eq. (3.2)]. In an abbreviated notation,

such closed-shell restricted Hartree-Fock (RHF) wave function is thus defined as [1]

$$\begin{aligned} |\Theta_0^{\text{RHF}}\rangle &= \hat{\mathcal{A}} |\varphi_1\varphi_2\varphi_3\varphi_4 \dots \varphi_{L-1}\varphi_L\rangle \\ &= \hat{\mathcal{A}} |\varphi_1\bar{\varphi}_1\varphi_2\bar{\varphi}_2 \dots \varphi_{L/2}\bar{\varphi}_{L/2}\rangle, \end{aligned} \quad (3.18)$$

where $\hat{\mathcal{A}}$ is an antisymmetrizing operator with $|\varphi_i\rangle$ and $|\bar{\varphi}_i\rangle$ denoting the set of restricted spin orbitals having α and β spin functions, respectively. To solve the corresponding (spatial) HF equations [1], one can then expand the unknown set of spatial MOs, *i.e.*, $\{|\varsigma_i\rangle\}_{i=1}^{L/2}$, in terms of a set of K known basis functions [1]

$$|\varsigma_i\rangle = \sum_{\nu=1}^K C_{\nu i} \varrho_{\nu} \quad i = 1, 2 \dots K, \quad (3.19)$$

where $C_{\nu i}$ are the MO expansion coefficients. By making use of the above expansion, the corresponding spatial RHF equations turn into a set of matrix eigenvalue problems [1]

$$\mathbf{FC} = \mathbf{SC}\epsilon \quad (3.20)$$

which is the so-called Roothaan-Hall equations [18, 19]. In the above expression, \mathbf{F} is the matrix representation of the (closed-shell) spatial Fock operator [see Eq. (3.23) below] in the basis $\{|\varrho_{\nu}\rangle\}_{\nu=1}^K$, or the Fock matrix, and \mathbf{S} is the associated overlap matrix [1, 18, 19]. These latter have elements

$$F_{\mu\nu} = \langle \varrho_{\mu} | \hat{\mathcal{F}}_i | \varrho_{\nu} \rangle, \quad (3.21)$$

and

$$S_{\mu\nu} = \langle \varrho_{\mu} | \varrho_{\nu} \rangle, \quad (3.22)$$

with $\hat{\mathcal{F}}_i$ now assuming the form [1]

$$\hat{\mathcal{F}}_i = \hat{h}_i + \sum_j^{L/2} (2\hat{\mathcal{J}}_j - \hat{\mathcal{K}}_j). \quad (3.23)$$

From the definitions of the Coulomb and exchange operators [Eqs. (3.10) and (3.11)] and the above expressions, the element $F_{\mu\nu}$ of the Fock matrix can be further expanded as

[1]

$$\begin{aligned}
F_{\mu\nu} &= \langle \varrho_\mu | \hat{\mathcal{H}}_i | \varrho_\nu \rangle + \sum_j^{L/2} \left[2 \langle \varrho_\mu | \hat{\mathcal{F}}_j | \varrho_\nu \rangle - \langle \varrho_\mu | \hat{\mathcal{H}}_j | \varrho_\nu \rangle \right] \\
&= \langle \varrho_\mu | \hat{\mathcal{H}}_i | \varrho_\nu \rangle + \sum_j^{L/2} \left[2 \langle \varrho_\mu \varsigma_j | \hat{\mathcal{G}}_{12} | \varrho_\nu \varsigma_j \rangle - \langle \varrho_\mu \varsigma_j | \hat{\mathcal{G}}_{12} | \varsigma_j \varrho_\nu \rangle \right] \\
&= \langle \varrho_\mu | \hat{\mathcal{H}}_i | \varrho_\nu \rangle + \sum_j^{L/2} \sum_{\sigma\lambda}^K 2C_{\sigma j} C_{\lambda j}^* \left[\langle \varrho_\mu \varrho_\lambda | \hat{\mathcal{G}}_{12} | \varrho_\nu \varrho_\sigma \rangle - \frac{1}{2} \langle \varrho_\mu \varrho_\lambda | \hat{\mathcal{G}}_{12} | \varrho_\sigma \varrho_\nu \rangle \right] \\
&= \langle \varrho_\mu | \hat{\mathcal{H}}_i | \varrho_\nu \rangle + \sum_{\sigma\lambda}^K P_{\sigma\lambda} \left[\langle \varrho_\mu \varrho_\lambda | \hat{\mathcal{G}}_{12} | \varrho_\nu \varrho_\sigma \rangle - \frac{1}{2} \langle \varrho_\mu \varrho_\lambda | \hat{\mathcal{G}}_{12} | \varrho_\sigma \varrho_\nu \rangle \right], \quad (3.24)
\end{aligned}$$

where

$$P_{\sigma\lambda} = \sum_j^{L/2} 2C_{\sigma j} C_{\lambda j}^* \quad (3.25)$$

is the so-called density matrix [1, 18, 19]. In Eq. (3.20), \mathbf{C} is a K by K matrix of the MO expansion coefficients and ϵ is a diagonal matrix of the orbital energies. The solutions of the Roothaan-Hall equations [Eq. (3.20)] are determined in a self-consistent fashion [1–5] and yield a set of L occupied (restricted) spin orbitals (or $L/2$ doubly occupied MOs) as well as a complementary set of $2K - L$ virtual spin orbitals (or $K - L/2$ unoccupied MOs).

Obviously, not all molecules can be described by pairs of electrons in closed-shell orbitals. Open-shell species are characterized as having one or more unpaired electrons which should then be treated accordingly. Thus, one frequently has to generalize the previous closed-shell approach by allowing each set of α and β spins to be described by a different set of spatial orbitals [20]. Within such open-shell formalism, the single determinantal unrestricted Hartree-Fock (UHF) wave function assumes the form [1]

$$\begin{aligned}
|\Theta_0^{\text{UHF}}\rangle &= \hat{\mathcal{A}} |\varphi_1 \varphi_2 \varphi_3 \varphi_4 \dots \varphi_{L-1} \varphi_L\rangle \\
&= \hat{\mathcal{A}} |\varphi_1^\alpha \bar{\varphi}_1^\beta \varphi_2^\alpha \bar{\varphi}_2^\beta \dots \varphi_{L^\alpha}^\alpha \bar{\varphi}_{L^\beta}^\beta\rangle, \quad (3.26)
\end{aligned}$$

where $|\varphi_i^\alpha\rangle$ and $|\bar{\varphi}_i^\beta\rangle$ now define the set of unrestricted spin orbitals that have different spatial parts $[|\varsigma_i^\alpha\rangle$ and $|\varsigma_i^\beta\rangle]$ for $|\alpha\rangle$ and $|\beta\rangle$ spin functions, respectively. Again, in order to solve the corresponding α and β (spatial) UHF equations [1], we expand the unknown

sets of spatial orbitals, *i.e.*, $\{|\zeta_i^\alpha\rangle\}_{i=1}^{L^\alpha}$ and $\{|\zeta_i^\beta\rangle\}_{i=1}^{L^\beta}$, in terms of a set of K basis functions [1]

$$\begin{aligned} |\zeta_i^\alpha\rangle &= \sum_{\nu=1}^K C_{\nu i}^\alpha \varrho_\nu & i = 1, 2 \dots K \\ |\zeta_i^\beta\rangle &= \sum_{\nu=1}^K C_{\nu i}^\beta \varrho_\nu & i = 1, 2 \dots K, \end{aligned} \quad (3.27)$$

where $C_{\nu i}^\alpha$ and $C_{\nu i}^\beta$ are the coefficients for the distinct sets of α and β MOs. The resulting UHF matrix eigenvalue equations are now split into α and β components [1]

$$\begin{aligned} \mathbf{F}^\alpha \mathbf{C}^\alpha &= \mathbf{S} \mathbf{C}^\alpha \boldsymbol{\epsilon}^\alpha \\ \mathbf{F}^\beta \mathbf{C}^\beta &= \mathbf{S} \mathbf{C}^\beta \boldsymbol{\epsilon}^\beta. \end{aligned} \quad (3.28)$$

The above expressions are the unrestricted generalizations of the Roothaan-Hall equations [Eq. (3.20)] and were first derived by Pople and Nesbet [20]. Note that \mathbf{F}^α and \mathbf{F}^β are matrix representations (in the basis $\{|\varrho_\nu\rangle\}_{\nu=1}^K$) of the unrestricted spatial Fock operators [1, 20]

$$\begin{aligned} \hat{f}_i^\alpha &= \hat{h}_i + \sum_j^{L^\alpha} (\hat{\mathcal{J}}_j^\alpha - \hat{\mathcal{K}}_j^\alpha) + \sum_j^{L^\beta} \hat{\mathcal{J}}_j^\beta \\ \hat{f}_i^\beta &= \hat{h}_i + \sum_j^{L^\beta} (\hat{\mathcal{J}}_j^\beta - \hat{\mathcal{K}}_j^\beta) + \sum_j^{L^\alpha} \hat{\mathcal{J}}_j^\alpha, \end{aligned} \quad (3.29)$$

which include, for an electron of α (β) spin, a coulomb and exchange interactions with all other α (β) electrons plus a coulomb interaction with electrons of β (α) spin. Suffice it to add that, since the $|\alpha\rangle$ and $|\beta\rangle$ spin functions are orthonormal, exchange effects are only effective between electrons of parallel spins [1]. Similarly to Eq. (3.20), the Pople-Nesbet equations [Eq. (3.28)] can be solved with the aid of a SCF procedure. However, inasmuch as \mathbf{F}^α and \mathbf{F}^β depend on both \mathbf{C}^α and \mathbf{C}^β , the solutions of the two eigenvalue problems can only be obtained simultaneously.

Apart from the proper unrestricted treatment, open-shell species can also be described by restricted-type SDs in which all electrons, except those that are explicitly required to occupy open-shell MOs, occupy closed-shell orbitals. In such a restricted open-shell Hartree-Fock (ROHF) formalism [1–3], the orbital space is partitioned into a subset D

which contains doubly occupied orbitals, a subset P that are allowed to be partially occupied and a subset V which are unoccupied (virtual). These three types of orbital spaces give rise to three different spatial Fock operators whose matrices, similarly to Eq. (3.28), must then be diagonalized simultaneously in order to account for the proper mixing between each subset. The advantage of the ROHF procedure is that the associated wave functions are generally eigenfunctions of the total spin angular momentum operator \hat{S}^2 . Indeed, UHF determinants do not meet such a requirement, and therefore suffer from considerable spin contamination, *i.e.*, they have contributions from higher multiplicity components. Nevertheless, one should bear in mind that, by restricting the spatial description of electrons, additional constraints are introduced in the variational problem and the energy of a UHF wave function is always lower than or equal to a corresponding ROHF-type determinant [1–3].

Regardless of the type of spin MOs employed in the construction of the single SD trial wave functions, the essential concept behind the HF approximation, *i.e.*, to transform the L -electron problem into L one-electron Schrödinger-like equations, clearly does not suffice to provide the correct answer. Actually, even at the CBS limit, HF energies are always upper bounds to the exact non-relativistic BO electronic eigenvalues. One then seeks for higher levels of approximations which are capable to properly describe the correlated nature of electrons. Obviously, since the electronic motion in an L -electron system is very complex, such models naturally require elaborate and expensive computational approaches.

3.2 Electron correlation methods

The term “correlation energy” is generally employed to describe all the remaining effects that the mean-field HF theory naturally neglects [21]. It is defined as the difference between the exact non-relativistic BO electronic energy (V_1) and the HF energy obtained

at the CBS limit [1], *i.e.*,⁵

$$\mathcal{E}_{cor} = V_1 - \mathcal{E}_0. \quad (3.30)$$

In practice, however, since the HF limit is hardly reached nor V_1 is known, \mathcal{E}_{cor} is simply determined as the difference in energy between the HF and the lowest possible energy in a given one-electron basis set [2]. Indeed, \mathcal{E}_{cor} represents an essential mathematical quantity which tells us the error of the independent particle model [21].

The HF theory determines (via the variational principle) the best possible single-Slater-determinantal wave function (within the given basis set), so an obvious choice to correct for the remaining deficiencies would be to construct a trial wave function which contains more than one SD, *i.e.*,

$$|\psi_1\rangle = c_0 |\Theta_0\rangle + c_1 |\Theta_1\rangle + c_2 |\Theta_2\rangle + \dots, \quad (3.31)$$

where the coefficients determine the weight of each determinant in the expansion. Clearly, if $|\Theta_0\rangle$ is a reasonable approximation to the ground-state wave function, c_0 will be greater than any other coefficient.

For the majority of chemical systems, the chief error in the mean-field approximation relies on ignoring the (instantaneous) correlated motion of each electron with the others. Such kind of electron correlation is often referred to as dynamical correlation (dc), since it is related to the dynamical character of electron-electron interactions [2]. The dc manifests itself through the small but non-vanishing contributions of other determinants to the total wave function, and hence to the total energy. Several electronic structure methods of varying complexity and accuracy have been proposed in order to account for the dynamical correlation effects; these include the configuration interaction (CI) method [1–3, 22], Møller-Plesset perturbation theory (MPn) [1–3, 23, 24] and coupled cluster (CC) theory [25–27].

In contrast, there will also be situations, particularly for molecules having nearly (or exactly) degenerate frontier orbitals, in which one or more determinants in (3.31) have

⁵Note that, by using the notation V_1 for the exact non-relativistic BO electronic energy, we are here assuming that this is the solution of the TIESE [Eq. (1.29)] for the ground-electronic state of the L -electron molecular system in a particular nuclear configuration.

coefficients of similar magnitude to that of the HF reference wave function. Such near-degeneracy effects are generally referred to as static or non-dynamical correlation (ndc). It reflects the fact that the error in the HF approximation is not only because it ignores the correlated motion of the electrons, but also due to its intrinsic single-determinantal nature [2]. In dealing with such systems, multi-configurational self-consistent field (MCSCF) approaches [28–30] must generally be employed along with multi-reference correlation methods [31–37].

3.2.1 CI method

In our previous discussion, we have addressed the general aspects about the nature and type of trial wave functions that can actually be utilized for improving upon the HF approximation. So far, we did not make any reference on the explicit form of these additional SDs that should be included in (3.31). This will be our main concern here.

Suppose that, by solving the the Roothaan-Hall's equations [Eq. (3.20)] in a finite one-electron basis set, one obtains a set of $2K$ spin orbitals $\{|\varphi_i\rangle\}$. Clearly, the determinant formed from the L lowest spin MOs is $|\Theta_0\rangle$. However, apart from the HF wave function, several other SDs can also be obtained by simply promoting electrons from the set of L occupied spin orbitals, here denoted as $\{|\varphi_a\rangle, |\varphi_b\rangle, |\varphi_c\rangle, |\varphi_d\rangle, \dots\}$, to the set of $2K - L$ virtuals $\{|\varphi_r\rangle, |\varphi_s\rangle, |\varphi_t\rangle, |\varphi_u\rangle, \dots\}$. The possible set of SDs that can be formed include singly $|\Theta_a^r\rangle$, double $|\Theta_{ab}^{rs}\rangle$, triply $|\Theta_{abc}^{rst}\rangle$ up to L -tuply $|\Theta_{abcd\dots}^{rstu\dots}\rangle$ excited determinants. The total number of such possible combinations is given by the binomial coefficient [31]

$$\binom{2K}{L} = \frac{(2K)!}{L!(2K-L)!} \quad (3.32)$$

These SDs so obtained can be taken to represent approximate excited states of the system and form, within a given one-electron basis set, a complete set of L -electron basis in which to expand the exact ground-state wave function $|\psi_1\rangle$. From the above considerations,

Eq. (3.31) can be rewritten as

$$\begin{aligned}
 |\psi_1\rangle = & c_0 |\Theta_0\rangle + \sum_{ar} c_a^r |\Theta_a^r\rangle + \sum_{\substack{a<b \\ r<s}} c_{ab}^{rs} |\Theta_{ab}^{rs}\rangle \\
 & + \sum_{\substack{a<b<c \\ r<s<t}} c_{abc}^{rst} |\Theta_{abc}^{rst}\rangle + \sum_{\substack{a<b<c<d \\ r<s<t<u}} c_{abcd}^{rstu} |\Theta_{abcd}^{rstu}\rangle + \dots, \quad (3.33)
 \end{aligned}$$

which is the so-called full configuration interaction (FCI) wave function [1–3, 22]. Note that the restricted summation indices warrant that a given excited determinant is included only once in the sum. The corresponding coefficients and energies of such trial wave function are obtained by diagonalizing the matrix representation of the electronic Hamiltonian [Eq. (3.3)] in the L -electron basis of Eq. (3.33), *i.e.*, by finding the eigenvectors and eigenvalues of the FCI matrix [31]. The lowest eigenvalue is always an upper bound of the exact non-relativistic BO ground-state energy. Indeed, the difference between the FCI energy and the HF energy within the same finite one-electron basis is often called the basis set correlation energy [31]. Note that, if all possible SDs formed from an infinity set of spin orbitals (at the CBS limit) are included in (3.33), the FCI method provides the “exact” solutions to the TIESE [Eq. (1.29)], with the basis set correlation energy approaching the “true” correlation energy.

Although such an approach is a formally exact theory, FCI calculations becomes computationally prohibitive as the number of electrons and the size of the MO basis set increases. It is therefore a common practice to truncate the CI expansion (3.33) at the double excitation terms (CISD) which already recover a large fraction of the correlation energy. While such truncated approaches make CI computations feasible in practice, the resulting solutions may suffer from size-consistency and size-extensivity problems⁶ [1–3, 22].

⁶An electronic structure method is said to be size consistent when the energy calculated for a supermolecule composed of two identical and noninteracting (infinitely separated) molecules is exactly twice the energy of the (isolated) monomer. In contrast, size extensivity is the property that the fraction of the electron correlation recovered by the model is proportional to the number of electrons present in the molecular system [2].

3.2.2 Multi-configurational SCF theory

For the majority of molecular systems, the HF wave function provides an acceptable starting point for a subsequent (single-reference) correlation treatment. Yet, the most fundamental problem of such an approach is that single SDs become clearly inadequate in describing molecules having near (or exact) degeneracies in their valence MOs. This situation arises particularly in bond-breaking-bond-forming processes in which occupied and unoccupied orbitals come quite close in energy as bond distances are stretched. Obviously, such multi-configurational nature is also preponderant in JT, RT and PJT systems as well as in general avoided crossing situations [28, 29]. Since different regions of the molecular PES are often dominated by different electronic configurations, a qualitatively correct description of these systems can only be attained by including all relevant configuration state function (CSF)s⁷ in the SCF procedure. Such a MCSCF approach can be considered as a CI in which not only the coefficients in the expansion (3.33) are optimized by the variational principle, but also the MOs (via atomic expansion coefficients) used for constructing the corresponding determinants [31].

The fundamental problem with the MCSCF method consists of selecting which CSFs are necessary in (3.33) in order for the total wave function be sufficiently flexible to provide a proper description of the system at hand, but still small enough to be computationally tractable. A successful approach to perform such a task consists in partitioning the MO space into three subsets (spaces)

$$\underbrace{\varphi_1 \dots \varphi_i}_{\text{inactive}} \underbrace{\varphi_{i+1} \dots \varphi_{i+a}}_{\text{active}} \underbrace{\varphi_{i+a+1} \dots \varphi_{i+a+v}}_{\text{virtual}}, \quad (3.34)$$

where the i inactive orbitals are defined as being doubly occupied, the v virtuals as unoccupied, while the a active orbitals have partial occupancy. Within the active MOs a FCI is performed and all the proper CSFs (with the correct spin and spatial symmetry) are included in the MCSCF optimization. Such a model is usually called complete active

⁷Configuration state functions are linear combinations of Slater determinants that have the same spatial-orbital occupations and that are eigenfunctions of the total spin angular momentum operator \hat{S}^2 and the spin projection along the z -axis \hat{S}_z . Note that primitive Slater determinants are typically eigenfunctions only of the \hat{S}_z operator.

space self-consistent field (CASSCF) approach [2, 28–30]. CASSCF active space choices are generally abbreviated as (x, y) where x is the number of electrons and y is the number of orbitals. For small molecules, the core orbitals are frequently treated as inactive, while those orbitals that undergo substantial changes in chemical reactions, *i.e.*, the valence orbitals, as active. In such cases, the CASSCF method is often referred to as full valence complete active space self-consistent field (FVCAS) model [30].

Although MCSCF wave functions have sufficient flexibility to describe bond-breaking-bond-forming processes and also systems that do not have simple one-configurational character, accurate predictions such as reaction energies and barrier heights should not be expected. MCSCF approaches are mainly used for generating a qualitatively correct and balanced wave function across the molecular PES by recovering the non-dynamic part of the electron correlation. Similarly to the single-configuration HF wave functions, they require addition of (dynamical) correlation corrections [2, 28–30].

3.2.3 Multi-reference CI

One of the most powerful quantum-mechanical models for accurate computations of PESs is the multi-reference CI (MRCI) approach [31–35]. Its formalism is quite similar to that for single-reference CI with the exception that, instead of a single-determinantal HF wave function, a set of reference CSFs optimized at MCSCF level is employed as a zeroth-order approximation. In analogy to Eq. (3.33), the (uncontracted) MRCI wave function assumes the general form [31]

$$\begin{aligned}
 |\psi_1\rangle = & \sum_{\nu} c_{\nu} |\Theta_{\nu}\rangle + \sum_{\nu} \sum_{a'r'} c_{(\nu)a'r'}^{r'} |\Theta_{(\nu)a'r'}^{r'}\rangle + \sum_{\nu} \sum_{\substack{a' < b' \\ r' < s'}} c_{(\nu)a'b'}^{r's'} |\Theta_{(\nu)a'b'}^{r's'}\rangle \\
 & + \sum_{\nu} \sum_{\substack{a' < b' < c' \\ r' < s' < t'}} c_{(\nu)a'b'c'}^{r's't'} |\Theta_{(\nu)a'b'c'}^{r's't'}\rangle + \sum_{\substack{a' < b' < c' < d' \\ r' < s' < t' < u'}} c_{(\nu)a'b'c'd'}^{r's't'u'} |\Theta_{(\nu)a'b'c'd'}^{r's't'u'}\rangle + \dots, \quad (3.35)
 \end{aligned}$$

where $\{|\Theta_{\nu}\rangle\}_{\nu=1}^M$ defines the set of orthonormalized reference (internal) configurations (the MCSCF expansion space) from which a complete set of L -electron MRCI basis is

generated, *i.e.*,

$$\begin{aligned}
|\Theta'_{(\nu)a'}\rangle &\equiv \hat{\mathbf{a}}_{r'}^\dagger \hat{\mathbf{a}}_{a'} |\Theta_\nu\rangle \\
|\Theta'^{s'}_{(\nu)a'b'}\rangle &\equiv \hat{\mathbf{a}}_{r'}^\dagger \hat{\mathbf{a}}_{s'}^\dagger \hat{\mathbf{a}}_{a'} \hat{\mathbf{a}}_{b'} |\Theta_\nu\rangle \\
|\Theta'^{s't'}_{(\nu)a'b'c'}\rangle &\equiv \hat{\mathbf{a}}_{r'}^\dagger \hat{\mathbf{a}}_{s'}^\dagger \hat{\mathbf{a}}_{t'}^\dagger \hat{\mathbf{a}}_{a'} \hat{\mathbf{a}}_{b'} \hat{\mathbf{a}}_{c'} |\Theta_\nu\rangle \\
|\Theta'^{s't'u'}_{(\nu)a'b'c'd'}\rangle &\equiv \hat{\mathbf{a}}_{r'}^\dagger \hat{\mathbf{a}}_{s'}^\dagger \hat{\mathbf{a}}_{t'}^\dagger \hat{\mathbf{a}}_{u'}^\dagger \hat{\mathbf{a}}_{a'} \hat{\mathbf{a}}_{b'} \hat{\mathbf{a}}_{c'} \hat{\mathbf{a}}_{d'} |\Theta_\nu\rangle \dots \quad \nu = 1, 2 \dots M, \quad (3.36)
\end{aligned}$$

with $\hat{\mathbf{a}}^\dagger$ and $\hat{\mathbf{a}}$ being the usual spin-orbital creation and annihilation operators, respectively [3, 31]. Note that, in Eqs. (3.35) and (3.36), $\{|\varphi_{a'}\rangle, |\varphi_{b'}\rangle, |\varphi_{c'}\rangle, |\varphi_{d'}\rangle, \dots\}$ now represents the set of internal spin orbitals (containing inactive+active orbitals), while $\{|\varphi_{r'}\rangle, |\varphi_{s'}\rangle, |\varphi_{t'}\rangle, |\varphi_{u'}\rangle, \dots\}$ are the corresponding external or virtuals [see Eq. (3.34)]. Thence, $|\Theta'_{(\nu)a'}\rangle$, $|\Theta'^{s'}_{(\nu)a'b'}\rangle$, $|\Theta'^{s't'}_{(\nu)a'b'c'}\rangle$ and $|\Theta'^{s't'u'}_{(\nu)a'b'c'd'}\rangle$ represent singly, doubly, triply and quadruply excited external configurations, respectively, in which to expand the ground-state eigenket $|\psi_1\rangle$ [Eq. (3.35)].

While large-scale MRCI wave functions can provide a highly accurate and a balanced description of different regions of the ground and excited molecular PESs, the computational cost associated with such calculations can be enormous. Indeed, similarly to single-reference CI approaches, typical multi-reference calculations truncate the CI expansion to include only singles and double excitations out of the MCSCF reference space (MRCISD), and hence are also subjected to size-consistency and size-extensivity problems [31–35].

It should be emphasized that, even for excitation-limited models, the main bottleneck of the MRCI method is the fact that the size of the expansion space and the computational effort rapidly increases with the number of reference configurations. This drastically limit the size of the molecules and/or the size of the one-electron basis sets that can actually be handled. Indeed, different contraction schemes⁸ have been proposed in order to reduce the number of parameters in the variational treatment while allowing the use of much larger reference spaces [33–37]. Additionally, one can also restrict the size of the MCSCF

⁸Among these variants, the internal contraction scheme of Werner and Knowles [33–35] as well as the externally contracted MRCI concept of Siegbahn [36, 37] deserve particular mention.

expansion to something smaller than a CASSCF reference and consider only a reduced number of single and double excitations [23].

3.2.4 Møller-Plesset perturbation theory

CI-based quantum-mechanical models are systematic and convenient procedures in which to improve (and go beyond) the mean-field HF approximation. Clearly, they have the important advantage of being variational in-nature, *i.e.*, the electronic energies so obtained are always upper bounds of the true non-relativistic BO results. The main drawback, however, is that size-consistency and size-extensivity errors are certainly to be expected from them, unless all possible excitations are warranted in the trial wave functions [Eqs. (3.33) and (3.35)]. An alternative method for adding electron correlation, which is not variational but size consistent, is perturbation theory [1–3, 23]. The basic premise of such an approach consists of partitioning the Hamiltonian (in particular, the electronic Hamiltonian $\hat{\mathcal{H}}_e$) into two contributions: a zeroth-order part $\hat{\mathcal{H}}_e^{(0)}$ which has known eigenfunctions and eigenvalues, and a small perturbation $\hat{\mathcal{H}}_e'$. The exact energies, which, in principle, differ only slightly from those of the unperturbed system, are then expressed as a perturbation expansion whose components are entirely defined in terms of the eigenvalues of $\hat{\mathcal{H}}_e^{(0)}$ and matrix elements of $\hat{\mathcal{H}}_e'$ calculated with the zeroth-order wave functions [1–3, 23].

Suppose we wish to solve the TIESE

$$\hat{\mathcal{H}}_e |\psi_i\rangle = \left(\hat{\mathcal{H}}_e^{(0)} + \lambda \hat{\mathcal{H}}_e' \right) |\psi_i\rangle = V_i |\psi_i\rangle, \quad (3.37)$$

where the unperturbed Hamiltonian $\hat{\mathcal{H}}_e^{(0)}$ satisfies the eigenvalue problem

$$\hat{\mathcal{H}}_e^{(0)} |\Theta_i^{(0)}\rangle = \mathcal{E}_i^{(0)} |\Theta_i^{(0)}\rangle. \quad (3.38)$$

In (3.37), λ is a perturbation parameter which connects the reference system ($\lambda = 0$) with the exact physical problem ($\lambda = 1$). Obviously, if the perturbation $\hat{\mathcal{H}}_e'$ is small, one then expects that $|\psi_i\rangle$ and V_i are reasonably close to $|\Theta_i^{(0)}\rangle$ and $\mathcal{E}_i^{(0)}$, respectively. Indeed, if $\lambda = 0$ then $\hat{\mathcal{H}}_e = \hat{\mathcal{H}}_e^{(0)}$, $|\psi_i\rangle = |\Theta_i^{(0)}\rangle$, and hence $V_i = \mathcal{E}_i^{(0)}$. Note that, for the sake of simplicity, we only consider here cases in which $\hat{\mathcal{H}}_e'$ is time-independent and the complete set of orthonormal zeroth-order wave functions $\{|\Theta_i^{(0)}\rangle\}$ is non-degenerate [1].

The exact eigenfunctions and eigenvalues of $\hat{\mathcal{H}}_e$ can now be expanded in a Taylor series in λ , *i.e.*,

$$\begin{aligned} |\psi_i\rangle &= |\Theta_i^{(0)}\rangle + \lambda |\Theta_i^{(1)}\rangle + \lambda^2 |\Theta_i^{(2)}\rangle + \dots + \lambda^n |\Theta_i^{(n)}\rangle \\ V_i &= \mathcal{E}_i^{(0)} + \lambda \mathcal{E}_i^{(1)} + \lambda^2 \mathcal{E}_i^{(2)} + \dots + \lambda^n \mathcal{E}_i^{(n)}, \end{aligned} \quad (3.39)$$

where $|\Theta_i^{(n)}\rangle$ and $\mathcal{E}_i^{(n)}$ define the n th-order perturbation corrections to the electronic wave functions and energies, respectively. The main focus of the so-called Rayleigh-Schrödinger perturbation theory (RSPT) [1–3, 23] consists therefore in expressing these latter quantities in terms of $\{\mathcal{E}_i^{(0)}\}$ and matrix elements of $\hat{\mathcal{H}}_e'$ in the basis $\{|\Theta_i^{(0)}\rangle\}$. To this end, let's substitute Eq. (3.39) into (3.37). In so doing, one obtains [1, 2]

$$\begin{aligned} &\left(\hat{\mathcal{H}}_e^{(0)} + \lambda \hat{\mathcal{H}}_e'\right) \left(|\Theta_i^{(0)}\rangle + \lambda |\Theta_i^{(1)}\rangle + \lambda^2 |\Theta_i^{(2)}\rangle + \dots + \lambda^n |\Theta_i^{(n)}\rangle\right) = \\ &\left(\mathcal{E}_i^{(0)} + \lambda \mathcal{E}_i^{(1)} + \lambda^2 \mathcal{E}_i^{(2)} + \dots + \lambda^n \mathcal{E}_i^{(n)}\right) \left(|\Theta_i^{(0)}\rangle + \lambda |\Theta_i^{(1)}\rangle + \lambda^2 |\Theta_i^{(2)}\rangle + \dots + \lambda^n |\Theta_i^{(n)}\rangle\right). \end{aligned} \quad (3.40)$$

Since the above expression holds for any value of λ (for convenience, this will be later set equal to unit), we can now collect the terms with the same power of λ which yields

$$\begin{aligned} \hat{\mathcal{H}}_e^{(0)} |\Theta_i^{(0)}\rangle &= \mathcal{E}_i^{(0)} |\Theta_i^{(0)}\rangle && \lambda^0 \\ \hat{\mathcal{H}}_e^{(0)} |\Theta_i^{(1)}\rangle + \hat{\mathcal{H}}_e' |\Theta_i^{(0)}\rangle &= \mathcal{E}_i^{(0)} |\Theta_i^{(1)}\rangle + \mathcal{E}_i^{(1)} |\Theta_i^{(0)}\rangle && \lambda^1 \\ \hat{\mathcal{H}}_e^{(0)} |\Theta_i^{(2)}\rangle + \hat{\mathcal{H}}_e' |\Theta_i^{(1)}\rangle &= \mathcal{E}_i^{(0)} |\Theta_i^{(2)}\rangle + \mathcal{E}_i^{(1)} |\Theta_i^{(1)}\rangle + \mathcal{E}_i^{(2)} |\Theta_i^{(0)}\rangle && \lambda^2 \\ &\vdots && \vdots \\ \hat{\mathcal{H}}_e^{(0)} |\Theta_i^{(n)}\rangle + \hat{\mathcal{H}}_e' |\Theta_i^{(n-1)}\rangle &= \sum_{j=0}^n \mathcal{E}_i^{(j)} |\Theta_i^{(n-j)}\rangle && \lambda^n. \end{aligned} \quad (3.41)$$

These latter define the n th-order perturbation equations. Note that the zeroth-order ansatz is just the TIESE for the unperturbed system [Eq. (3.38)]. Multiplying each of these expressions by $\langle \Theta_i^{(0)} |$ and using the orthogonality relation $\langle \Theta_i^{(0)} | \Theta_i^{(n)} \rangle = 0$ [1], we obtain

the following equations for the n th-order energy corrections

$$\begin{aligned}
\mathcal{E}_i^{(0)} &= \langle \Theta_i^{(0)} | \hat{\mathcal{H}}_e^{(0)} | \Theta_i^{(0)} \rangle \\
\mathcal{E}_i^{(1)} &= \langle \Theta_i^{(0)} | \hat{\mathcal{H}}_e' | \Theta_i^{(0)} \rangle \\
\mathcal{E}_i^{(2)} &= \langle \Theta_i^{(0)} | \hat{\mathcal{H}}_e' | \Theta_i^{(1)} \rangle \\
&\vdots \\
\mathcal{E}_i^{(n)} &= \langle \Theta_i^{(0)} | \hat{\mathcal{H}}_e' | \Theta_i^{(n-1)} \rangle.
\end{aligned} \tag{3.42}$$

Thus, to obtain the unknown quantities in Eq. (3.39), one needs first solve the set of equations (3.41) for $|\Theta_i^{(n)}\rangle$ and then determine the n th-order energies using (3.42). Indeed, the first-order correction to the wave function can be obtained by expanding $|\Theta_i^{(1)}\rangle$ in terms of the eigenfunctions of $\hat{\mathcal{H}}_e^{(0)}$

$$|\Theta_i^{(1)}\rangle = \sum_j c_j^{(1)} |\Theta_j^{(0)}\rangle. \tag{3.43}$$

Since $\mathcal{E}_i^{(1)}$ is already known from (3.42), *i.e.*, it is just the average of the perturbation operator over the unperturbed wave function, the coefficients $c_j^{(1)}$ in (3.43) are determined by substituting Eqs. (3.43) and (3.42) into the corresponding first-order perturbation equation (3.41), followed by a multiplication by $\langle \Theta_j^{(0)} |$. In so doing, we find [1, 2]

$$c_j^{(1)} = \frac{\langle \Theta_j^{(0)} | \hat{\mathcal{H}}_e' | \Theta_i^{(0)} \rangle}{\mathcal{E}_i^{(0)} - \mathcal{E}_j^{(0)}} \quad j \neq i. \tag{3.44}$$

Of course, the restriction on the i and j indexes also excludes the term $j = i$ in the summation of Eq. (3.43). Note further that the denominator in (3.44) naturally imposes the constraint that $\{|\Theta_i^{(0)}\rangle\}$ must not involve degenerate states [1].

Starting from the second-order perturbation equation (3.41), analogous formulas can be generated for the second-order corrections. For $\mathcal{E}_i^{(2)}$, one obtains

$$\mathcal{E}_i^{(2)} = \sum_j \frac{\langle \Theta_i^{(0)} | \hat{\mathcal{H}}_e' | \Theta_j^{(0)} \rangle \langle \Theta_j^{(0)} | \hat{\mathcal{H}}_e' | \Theta_i^{(0)} \rangle}{\mathcal{E}_i^{(0)} - \mathcal{E}_j^{(0)}} \quad j \neq i, \tag{3.45}$$

with the associated coefficients $c_j^{(2)}$ for $|\Theta_i^{(2)}\rangle$ being determined as in (3.43). Actually, higher-order corrective terms can be obtained in a similar fashion, with their functional

forms becoming progressively complex as the order of the perturbation increases. For the sake of simplicity, these will be omitted in the present discussion.

Up to now, we have only introduced the main aspects of the RSPT to approach the exact solutions of a general L -electron system. Our main focus here is therefore to use perturbation theory for adding corrections (*i.e.*, correlation energy) to approximate solutions arising from an independent-particle model. For this, one must first select a reasonable form of the zeroth-order Hamiltonian. The most convenient choice is to take the HF Hamiltonian [*i.e.*, a sum over effective one-electron Fock operators; see Eq. (3.16)] as $\hat{\mathcal{H}}_e^{(0)}$. This leads to the infamous MPn methods [1–3, 23, 24]. From Eqs. (3.16), (3.37) and (3.38), we thus define [1, 24]

$$\hat{\mathcal{H}}_e^{(0)} = \sum_i^L \hat{f}_i = \sum_i^L \hat{h}_i + \sum_{ij}^L (\hat{\mathcal{J}}_j - \hat{\mathcal{K}}_j), \quad (3.46)$$

and hence

$$\hat{\mathcal{H}}_e' = \hat{\mathcal{H}}_e - \hat{\mathcal{H}}_e^{(0)} = \sum_{j>i}^L \hat{g}_{ij} - \sum_{ij}^L (\hat{\mathcal{J}}_j - \hat{\mathcal{K}}_j), \quad (3.47)$$

where $\hat{\mathcal{H}}_e$ is the exact electronic Hamiltonian of Eq. (3.3) with all other quantities assuming the same meaning as given in section 3.1. Naturally, as can be seen from (3.47), the perturbation is defined as just the difference between the exact two-electron interaction and the sum of the Coulomb and exchange potentials (*i.e.*, the effective HF potential) [1, 24]. Recall that, for convenience, we have set λ equal to unit. Moreover, since the nuclear repulsion energy $\hat{\mathcal{V}}_{NN}$ [Eq. (1.8)] assumes a constant value for a fixed nuclear arrangement, this have also been omitted in Eq. (3.46) and can be simply added to the total electronic energy in *a posteriori* step; see Eq. (3.17). Obviously, $\hat{\mathcal{V}}_{NN}$ immediately cancels out when calculating the perturbation in (3.47).

The zeroth-order wave function is thus the ground-state HF determinant [Eq. (3.1)] with the corresponding zeroth-order electronic energy given by

$$\mathcal{E}_0^{(0)} = \langle \Theta_0 | \hat{\mathcal{H}}_e^{(0)} | \Theta_0 \rangle = \sum_i^L \langle \Theta_0 | \hat{f}_i | \Theta_0 \rangle = \sum_{i=1}^L \epsilon_i. \quad (3.48)$$

In fact, this latter quantity is just the sum of spin MO energies. From Eqs. (3.42) and

(3.47), the first-order energy is defined as

$$\begin{aligned}
\mathcal{E}_0^{(1)} &= \langle \Theta_0 | \hat{\mathcal{H}}'_e | \Theta_0 \rangle \\
&= \sum_{j>i}^L \langle \Theta_0 | \hat{\mathcal{G}}_{ij} | \Theta_0 \rangle - \sum_{ij}^L \langle \Theta_0 | \hat{\mathcal{J}}_j - \hat{\mathcal{K}}_j | \Theta_0 \rangle \\
&= -\frac{1}{2} \sum_{ij}^L (J_{ij} - K_{ij}).
\end{aligned} \tag{3.49}$$

As one can see, the corrective term $\mathcal{E}_0^{(1)}$ clearly arises due to the double counting of the electron-electron repulsion by the Fock operator [1–3, 23]. Thus, apart from a constant which is simply $\hat{\mathcal{V}}_{NN}$, the HF energy is defined by the sum of the zeroth- and first-order energy terms; see Eq. (3.17). Indeed, within the MPn framework, any correction due to electron correlation starts at order two, or in other words, at the MP2 level.

Let us now turn to the calculation of such $\mathcal{E}_0^{(2)}$ correction. As discussed in connection with the RSPT, the solutions of the unperturbed problem [Eq. (3.38)] yield, in principle, a complete and orthonormal set of eigenfunctions. For the HF case, the lowest possible eigenstate is naturally the single-determinantal wave function formed from occupied HF canonical spin orbitals. As pointed out in section 3.2.1, all other possible members of such a set include those SDs generated by promoting one, two, three, etc., electrons from occupied spin MOs to the virtuals. Thus, the second-order energy correction (3.45) can be readily obtained by considering all possible matrix elements of $\hat{\mathcal{H}}'_e$ that can be formed from the HF reference and such excited states. These latter cannot be singly excited determinants since

$$\begin{aligned}
\langle \Theta_0 | \hat{\mathcal{H}}'_e | \Theta_a^r \rangle &= \langle \Theta_0 | \hat{\mathcal{H}}_e - \hat{\mathcal{H}}_e^{(0)} | \Theta_a^r \rangle \\
&= \langle \Theta_0 | \hat{\mathcal{H}}_e | \Theta_a^r \rangle - \langle \Theta_0 | \hat{\mathcal{H}}_e^{(0)} | \Theta_a^r \rangle \\
&= \langle \Theta_0 | \hat{\mathcal{H}}_e | \Theta_a^r \rangle - \sum_i^L \epsilon_i \langle \Theta_a^r | \Theta_0 \rangle = 0,
\end{aligned} \tag{3.50}$$

where the first bracket on the RHS vanishes due to the well-known Brillouin's theorem [1–3, 23], while the second term is also zero owing to the orthogonality of ground- and excited-state SDs. Moreover, since $\hat{\mathcal{H}}'_e$ is a two-electron operator, the elements between

ground and triple, quadruple, etc., excited determinants also vanish due to the so-called Slater-Condon rules [2]. Therefore, we are left with the possibility of defining the second-order correction (the first contribution to the correlation energy) as a sum over doubly excited determinants

$$\mathcal{E}_0^{(2)} = \sum_{\substack{a < b \\ r < s}} \frac{\langle \Theta_0 | \hat{\mathcal{H}}_e' | \Theta_{ab}^{rs} \rangle \langle \Theta_{ab}^{rs} | \hat{\mathcal{H}}_e' | \Theta_0 \rangle}{\mathcal{E}_0^{(0)} - \mathcal{E}_{ab}^{rs(0)}}. \quad (3.51)$$

Note that the above expression can also be conveniently written in term of two-electron integrals by [1]

$$\mathcal{E}_0^{(2)} = \sum_{\substack{a < b \\ r < s}} \frac{[\langle \varphi_a \varphi_b | \varphi_r \varphi_s \rangle - \langle \varphi_a \varphi_b | \varphi_s \varphi_r \rangle]^2}{\epsilon_a + \epsilon_b - \epsilon_r - \epsilon_s}. \quad (3.52)$$

Thus, the MP2 energy is given by the sum of $\mathcal{E}_0^{(0)}$, $\mathcal{E}_0^{(1)}$, $\mathcal{E}_0^{(2)}$ and $\hat{\mathcal{V}}_{NV}$ [Eqs. (3.48), (3.49), (3.52) and (1.8), respectively]. In fact, because Eq. (3.52) can be efficiently evaluated in actual calculations, MP2 is the most economical method for including electron correlation. Moreover, such an approach, together with all orders of MPn, are size-consistent and size-extensive theories which is a particularly desirable feature when calculating molecular properties.

However, the main limitation of MPn approaches relies therefore in the assumption that the HF determinant is a reasonable approximation of the true wave function and that the perturbation (which is the full electron-electron repulsion energy) is small [1–3, 23]. For this reason, MP2 calculations typically overestimate the correlation energies. Naturally, to improve convergence, one must proceed further and assess the effects of including higher-order corrections such as MP3, MP4, etc [2]. Although ideally the MPn results would show a monotonic convergence as a function of n , in practice, this is by no means the case. Indeed, even for systems where the ground-state wave function is satisfactorily described by a single determinant, an oscillatory behavior of the perturbation series is frequently observed. Clearly, if the system experiences a substantial multi-reference character, one then expects the convergence to be too slow or even erratic. In this direction, generalizations of the MPn theory to the multi-reference case have also been proposed (such as in the CASPT2 approach [38–40]) which involve the natural choice of an MCSCF wave function as a zeroth-order approximation for a subsequent

perturbation treatment.

3.2.5 Coupled cluster methods

CC methods [25, 26] have acquired widespread use in quantum chemistry to calculate electron correlation energy and many other atomic and molecular properties. The idea behind such approaches is to correct the HF reference wave function by using a coupled cluster scheme (or, a cluster operator $\hat{\mathcal{T}}$) which, for most practical purposes, must be truncated at some level of excitation [1–3, 23]. Within the CC framework, the electronic wave function for the L -electron system is expressed in terms of the exponential ansatz

$$|\psi_1\rangle = e^{\hat{\mathcal{T}}} |\Theta_0\rangle, \quad (3.53)$$

where the cluster operator $\hat{\mathcal{T}}$ is defined by

$$\hat{\mathcal{T}} = \hat{\mathcal{T}}_1 + \hat{\mathcal{T}}_2 + \hat{\mathcal{T}}_3 + \hat{\mathcal{T}}_4 + \dots + \hat{\mathcal{T}}_L. \quad (3.54)$$

In the above equation, $\hat{\mathcal{T}}_l$ ($l=1, 2, 3, \dots, L$) are excitation operators which act on the HF wave function to generate all possible l th-excited Slater determinants. For instance,

$$\hat{\mathcal{T}}_1 |\Theta_0\rangle = \sum_{ar} t_a^r |\Theta_a^r\rangle, \quad (3.55)$$

and

$$\hat{\mathcal{T}}_2 |\Theta_0\rangle = \sum_{\substack{a<b \\ r<s}} t_{ab}^{rs} |\Theta_{ab}^{rs}\rangle, \quad (3.56)$$

determines the complete set of singly- and doubly-excited SDs that can be formed from $|\Theta_0\rangle$ (with a given finite one-electron basis set), respectively, with t_a^r and t_{ab}^{rs} being the corresponding cluster amplitudes [which are analogous to the expansion coefficients c_a^r and c_{ab}^{rs} in Eq. (3.33)]. Note that, the exponential operator in Eq. (3.53), is generally written as a Taylor-series expansion

$$e^{\hat{\mathcal{T}}} = 1 + \hat{\mathcal{T}} + \frac{\hat{\mathcal{T}}^2}{2} + \frac{\hat{\mathcal{T}}^3}{6} + \frac{\hat{\mathcal{T}}^4}{24} + \dots = \sum_{k=0}^{\infty} \frac{\hat{\mathcal{T}}^k}{k!}, \quad (3.57)$$

or, by substituting Eqs. (3.54) into (3.57), as

$$e^{\hat{\mathcal{T}}} = 1 + \hat{\mathcal{T}}_1 + \left(\hat{\mathcal{T}}_2 + \frac{\hat{\mathcal{T}}_1^2}{2} \right) + \left(\hat{\mathcal{T}}_3 + \hat{\mathcal{T}}_2 \hat{\mathcal{T}}_1 + \frac{\hat{\mathcal{T}}_1^3}{6} \right) + \left(\hat{\mathcal{T}}_4 + \hat{\mathcal{T}}_3 \hat{\mathcal{T}}_1 + \frac{\hat{\mathcal{T}}_2^2}{2} + \frac{\hat{\mathcal{T}}_2 \hat{\mathcal{T}}_1^2}{2} + \frac{\hat{\mathcal{T}}_1^4}{24} \right) + \dots \quad (3.58)$$

In (3.58), the first term on the RHS generates the HF reference and the second all singly excited states. The first quantities in each parenthesis, *e.g.*, $\hat{\mathcal{T}}_2$, $\hat{\mathcal{T}}_3$, $\hat{\mathcal{T}}_4$, etc., determines the “true” or connected excitations with all the remaining terms (which involve products of lower-order operators) defining the corresponding disconnected excitations.

Obviously, if all cluster operators up to $\hat{\mathcal{T}}_l$ are included in $\hat{\mathcal{T}}$ [Eq. (3.54)], all possible excited SDs are generated and the CC wave function in Eq. (3.53) is equivalent to a full CI [Eq. (3.33)]. Unfortunately, as already stated, such a procedure is impossible for all but the smallest systems. Actually, it is the allowance for simplifications in $\hat{\mathcal{T}}$ that makes CC theory extremely advantageous over excitation-limited CI approaches [25, 26]. As one can see from (3.58), by truncating $\hat{\mathcal{T}}$ at some level, say at $\hat{\mathcal{T}}_2$, there will always remain disconnected terms corresponding to higher-order excitations such as $\hat{\mathcal{T}}_2 \hat{\mathcal{T}}_1$, $\hat{\mathcal{T}}_1^3$, $\hat{\mathcal{T}}_2^2$, $\hat{\mathcal{T}}_2 \hat{\mathcal{T}}_1^2$ and $\hat{\mathcal{T}}_1^4$. In fact, it is exactly the failure to include these additional terms that makes truncated CI approaches non-size-consistent. Thus, by making use of the exponential ansatz (3.53), one can clearly ensure size consistency. Note, however, that truncated CC approaches are not variational [1–3, 23].

The models in most common usage are CC doubles (CCD), where $\hat{\mathcal{T}} = \hat{\mathcal{T}}_2$, and CC with single and double excitations (CCSD), where $\hat{\mathcal{T}} = \hat{\mathcal{T}}_1 + \hat{\mathcal{T}}_2$. Indeed, larger expansions such as in CCSDT make the calculations extremely demanding, and hence are only computationally feasible for relatively small systems. The most practical and sufficiently accurate approach to this problem is the CCSD(T) model, where the effects of the connected triples ($\hat{\mathcal{T}}_3$) are estimated using perturbation theory [27]. This model have acquired great success, becoming a standard method for high accuracy single-reference calculations (sometimes referred to as “the gold standard of quantum chemistry”).

3.3 One-electron basis sets

One of the fundamental approximations inherent in essentially all *ab initio* methods is the introduction of a basis set. Many-electron wave functions such as a single SD or any linear combinations of it are generally made up from atomic or molecular spin orbitals. These *a priori* unknown one-electron eigenkets must therefore be expanded in terms of a known set of basis functions [Eqs. (3.19) and (3.27)] and the optimum coefficients determined in a variational manner. In this regard, the number K and type of functions so employed clearly dictates the level of accuracy that can be attained within a given electronic structure model. Obviously, one can express orbitals as linear combinations of an infinite number of physically motivated functions. Such an approach, however, is impossible in actual calculations and, since *ab initio* methods scale formally as at least K^4 , a balance must be struck between acceptable accuracy and computational efficiency [1–3, 23].

In a strictly mathematical sense many different kinds of one-electron functions could be employed in electronic structure calculations. The most commonly used are the Slater-type orbitals (STOs) [41] and Gaussian-type orbitals (GTOs) [42]. The former have functional form (in atom-centered polar coordinates)

$$\varrho_{\zeta,n,l,m}^{\text{STO}}(r, \theta, \phi) = NY_{l,m}(\theta, \phi)r^{n-1}e^{-\zeta r}, \quad (3.59)$$

where N is a normalization constant, $Y_{l,m}(\theta, \phi)$ are spherical harmonic functions which depend on the angular momentum quantum numbers l and m , n is the principal quantum number and ζ the corresponding orbital exponent. While STOs give the best physical description of the wave function, including the expected singularity (cusp) at $r=0$ and the correct exponential decaying with increasing r , difficulties associated with the calculation of the two-electron multicenter integrals [*i.e.*, the last term on the RHS of Eq. (3.24)] make them impractical for use in anything other than atoms and diatomic species.

In this respect, a significant simplification is made by the use of GTOs. These latter can be written in terms of polar and Cartesian atom-centered coordinates as

$$\varrho_{\zeta,n,l,m}^{\text{GTO}}(r, \theta, \phi) = NY_{l,m}(\theta, \phi)r^{2n-2-l}e^{-\zeta r^2}, \quad (3.60)$$

and

$$\varrho_{\zeta, l_x, l_y, l_z}^{\text{GTO}}(x, y, z) = N x^{l_x} y^{l_y} z^{l_z} e^{-\zeta r^2}, \quad (3.61)$$

respectively. Note that, in (3.61), the sum of l_x , l_y and l_z determines the type of orbital, *i.e.*, $l_x + l_y + l_z = 0$ is an s-orbital, $l_x + l_y + l_z = 1$ an p-orbital, $l_x + l_y + l_z = 2$ an d-orbital and so on. The advantage of GTOs is that the evaluation of the necessary integrals is made simpler and faster than for STOs. This stems largely from the fact that the product of two Gaussian functions on different centers gives a new Gaussian centered on a third position in space, and hence the evaluation of the four-center repulsion integrals reduces to the consideration of only integrals involving two-centers [1].

The use of GTOs, however, does have disadvantages. In particular, they no longer have a cusp at $r=0$ and decay too quickly as $r \rightarrow \infty$. One way around this issue is to use as basis functions a set of contracted Gaussian-type orbitals (CGTOs), *i.e.*, by defining functions that are expressed as fixed linear combinations of primitive Gaussians

$$\varrho_{\nu}^{\text{CGTO}} = \sum_p^C d_{p\nu} \varrho_p^{\text{GTO}}(\zeta_{p\nu}), \quad (3.62)$$

where $d_{p\nu}$ and $\zeta_{p\nu}$ are the contracted coefficients and exponents, respectively, with C determining the length of the contraction. Indeed, a proper choice of the contraction parameters can be made in such a way that CGTOs fit the known behavior of Slater-type functions, reproduce HF atomic orbitals or even based on correlated calculations. Hehre, Stewart and Pople [43] were pioneering in obtaining a series of basis functions for a large number of atoms by fitting STOs to linear combinations of $C=1, 2, 3 \dots 6$ primitive Gaussians. These well-known STO-CG basis are often denoted as minimal since only one CGTO is employed to describe each occupied atomic orbital for a given element. In particular, STO-3G basis sets have come into widespread use in general polyatomic calculations. For first-row atoms, these latter can be denoted as (6s3p)→[2s1p], *i.e.*, as a contraction of 3 primitive GTOs for each atomic basis function.

Overall, basis sets should be flexible enough to account for the inherent changes in electronic density with the formation of more complex chemical environments. This is a general requirement in order for them to be useful in calculations involving atoms,

ions, molecules and solids. Although minimal basis sets should in principle fulfill such requirements, they, in fact, fail to properly describe the changes in orbitals due to bonding nor can they recover much of the correlation energy. One way to increase the flexibility of a basis consists of decontracting it, *i.e.*, by allowing each atomic orbital to be represented by more than one CGTO; this led to the development of the so-called double- ζ , triple- ζ and multiple- ζ basis sets [1–3, 23]. Obviously, at the CBS limit, an infinity- ζ basis would be needed in order to assess the effects of truncating the one-particle space. In practice, however, a compromise must be made between accuracy and feasibility. Naturally, as opposed to the valence orbitals, core orbitals are only weakly affected by chemical bonding. Thus, it is often the case that only valence orbitals are augmented by additional functions, whereas the core continue to be represented by a minimum number of CGTOs. Such basis sets are generally called split valence or valence multiple- ζ [1–3, 23]. The Pople-type basis, such as 3-21G, 6-21G, 4-31G, 6-31G, and 6-311G, are amongst the most widely used split valence basis [44]. For instance, for first-row atoms, the valence triple- ζ basis 6-311G [45] consists of one 1s inner shell function (core) which is a contraction of 6 primitive Gaussians and four more basis functions to represent each valence 2s, 2p_x, 2p_y and 2p_z orbitals. The inner valence functions are a contraction of 3 primitive GTOs, while the outer functions are left uncontracted. This is equivalent to the contraction scheme (11s5p)→[4s3p].

The formation of chemical bonds between two or more elements is clearly accompanied by perturbations of the atomic orbitals. Indeed, even though the involved atoms are individually reasonably well represented by a set of (valence) basis functions, the proper description of MOs requires an extra mathematical flexibility. This is almost always added in the form higher-order angular momentum functions or, in other words, by augmenting basis sets with polarization functions [1–3, 23]. For example, in the 6-311G** basis [45], the first star implies the addition of a set of d functions on first-row atoms, while the second star indicate p functions on hydrogen.⁹ Besides polarization effects, diffuse functions, *i.e.*, GTOs with small exponents, may also be added to a basis set. They are necessary whenever loosely bound electrons are present such as in anions, excited

⁹Such a basis set is also denoted as 6-311G(d,p).

states, hydrogen-bonded and van der Waals complexes [44]. In the Pople family of basis sets, the presence of diffuse functions is indicated by a “+” sign. Thus, 6-311++G** [46] means that heavy atoms have been augmented with an additional one s and one set of p functions with small exponents, while the second plus implies diffuse functions on hydrogen.

For correlated calculations, basis sets requirements are generally more demanding than for mean-field approaches. In such cases, one frequently has to provide a suitable orbital space in order to properly account for the effects of electrons avoiding each other. Dunning and coworkers [47, 48] reported a sequence of correlation consistent (cc) basis in which sets of functions that contribute with similar amounts to the correlation energy are included at the same stage and in a balanced manner. Such basis sets are denoted as cc-pVXZ, where $X=D, T, Q, \dots$ is the associated cardinal number which indicates a systematic improved sequence of double- ζ , triple- ζ , quadruple- ζ and so on. For first-row atoms, these latter have a general contraction scheme¹⁰ of $(9s4p1d) \rightarrow [3s2p1d]$, $(10s5p2d1f) \rightarrow [4s3p2d1f]$ and $(12s6p3d2f1g) \rightarrow [5s4p3d2f1g]$, respectively. Note that the addition of diffuse functions is indicated by the prefix “aug-”, *i.e.*, by referring the basis sets as aug-cc-pVXZ [48].

One of the major advantage of such correlation consistent approach is that on going from aug-cc-pVDZ to aug-cc-pV6Z a significant improvement in the description of the correlation energy is achieved [47, 48]. These latter can be suitably fitted to smooth monotonic functions, and hence approximately extrapolated to the CBS limit (see next section). In conjunction with reliable quantum-mechanical models such as the MRCI approach, these extrapolations can provide highly accurate molecular PESs.

Almost all basis sets currently available employ atom-centered GTOs as expansion functions. This allows for the construction of very compact sets of one-electron basis. In fact, when incomplete basis sets are utilized in electronic structure calculations, it may happen that certain fragments of the system, *e.g.*, a monomer in a complex, benefit from functions located at different centers. Such borrowing of basis functions provides,

¹⁰As opposed to a segmented scheme in which each primitive is allowed to contribute only once in the contracted functions, in a general contraction scheme all primitives appear in all contracted basis [1–3, 23].

therefore, an unphysical lowering of the overall interaction energy. This is so, since this latter are generally calculated by means of the supermolecular approach [49], *i.e.*, by subtracting the energies of the infinitely separated fragments¹¹ (which, in fact, do not suffer from such additional stabilization of the “complex” basis) from the total energy of the system. This basis set superposition error (BSSE) [49] is especially troublesome when dealing with small effects, such as energies of hydrogen-bonded and van der Waals complexes. In these cases, the BSSE is comparable in size to the overall complexation energy, and hence the *ab initio* prediction of PESs with quantitative accuracy is only possible if this error can effectively be removed or avoided. A conceptually simple approach to account for the BSSE is the counterpoise (CP) correction method [50] in which the energies of the constituent parts (in the corresponding geometries adopted in the complex) are also computed in the full basis and subtracted from the energy of the entire system. Naturally, as an alternative to correct for the BSSE, one can also perform extrapolations to the CBS limit either by making use of explicit functional forms or by employing a semiempirical scaling of the *ab initio* energies.

3.4 Extrapolations to the complete basis set limit

An enormous progress in electronic structure calculations arose with the introduction of the so-called cc-type family of basis sets. Such functions provide results that follow a well behaved trend toward some limiting value as the sets are increased in a consistent manner, *i.e.*, for each increment in the cardinal number X . Thus, by performing a sequence of calculations for different values of X , one can then exploit the dependence of the energy \mathcal{E}_X with respect to such cardinal number and search for laws to extrapolate to the CBS limit (\mathcal{E}_∞) [2, 3].

Since the mean-field HF approach treats the electron-electron repulsion in an average sense, the wave function amplitude of a single electron is clearly unaffected by the presence of the others. Nevertheless, for an exact wave function, the probability amplitude for an electron is shifted away from the positions of the other particles, creating therefore a Coulomb hole around them. As is evident from Eqs. (1.28) and (1.5), the

¹¹Of course, we assume that the *ab initio* method so employed is size-consistent.

electronic Hamiltonian possesses singularities whenever two electrons or one electron and one nucleus coincide in space, which imposes an electronic and nuclear Coulomb cusp conditions [3]. With this in mind, one can then expect that the convergence of the HF (and possibly CASSCF) wave function to the CBS limit is achieved much faster than for correlated calculations, inasmuch as no effort is put into the former in describing the electronic Coulomb cusp [51–54]. For this reason, the standard procedure to obtain CBS values is to extrapolate separately the HF (or ndc) and total correlation (or dc) parts of the energy [55–60].

Although the convergence of the correlation energy is rather slow and sets high requirements in both basis sets and computational effort, a simple, yet physically motivated, form to estimate the error ($\Delta\mathcal{E}_\infty^{cor}$) of a calculation with the cc-pVXZ basis sets can be given by [61, 62]

$$\Delta\mathcal{E}_\infty^{cor} \approx A_3 X^{-3}. \quad (3.63)$$

In fact, the above expression allows an *a priori* estimation of the CBS limit as

$$\mathcal{E}_\infty^{cor} \approx \mathcal{E}_X^{cor} + \Delta\mathcal{E}_\infty^{cor} = \mathcal{E}_X^{cor} + A_3 X^{-3}. \quad (3.64)$$

The value of \mathcal{E}_∞^{cor} can then be obtained by simply calculating the correlation energy in two different basis of ranks X and Y [since Eq. (3.64) has just two unknown parameters]

$$\begin{aligned} \mathcal{E}_\infty^{cor} &\approx \mathcal{E}_X^{cor} + A_3 X^{-3} \\ \mathcal{E}_\infty^{cor} &\approx \mathcal{E}_Y^{cor} + A_3 Y^{-3} \end{aligned} \quad (3.65)$$

with the extrapolated energy and linear parameter A_3 being defined by

$$\mathcal{E}_\infty^{cor} \approx \frac{X^3 \mathcal{E}_X^{cor} - Y^3 \mathcal{E}_Y^{cor}}{X^3 - Y^3}, \quad (3.66)$$

and

$$A_3 \approx -\frac{\mathcal{E}_X^{cor} - \mathcal{E}_Y^{cor}}{X^{-3} - Y^{-3}}, \quad (3.67)$$

respectively.

Indeed, the physical motivation behind the ansatz (3.63) comes from the energy increments of partial-wave expansions of atomic correlation energies [63–65] and similar

expressions derived from the convergence behavior of principal expansions [62]. As first demonstrated by Schwartz [63] with the aid of second-order perturbation theory applied to two electron atoms, the energy increments obtained by adding a saturated shell of basis functions of angular momentum l obey the asymptotic formula

$$\delta\mathcal{E}_l^{cor} = \mathcal{E}_l^{cor} - \mathcal{E}_{l-1}^{cor} = -\frac{45}{256} \left(l + \frac{1}{2}\right)^{-4} + \frac{225}{1024} \left(l + \frac{1}{2}\right)^{-6} + \dots \quad (3.68)$$

This result has been later demonstrated by Hill [64] and generalized for atoms with arbitrary number of electrons by Kutzelnigg and Morgan [65]. From these energy increments, one can then assess the basis-set truncation error ($\Delta\mathcal{E}_\infty^{cor}$) due to omission of all basis functions with $l > L$. Thus, by integrating the Schwartz's expansion (3.68) one gets [56, 62]

$$\Delta\mathcal{E}_\infty^{cor} = \sum_{l=L+1}^{\infty} \delta\mathcal{E}_l^{cor} \approx \int_{l=L+1/2}^{\infty} \delta\mathcal{E}_l^{cor} dl = \sum_{m=4} A_{m-1} (L+1)^{-m+1}, \quad (3.69)$$

and hence

$$\mathcal{E}_\infty^{cor} = \mathcal{E}_{L+1}^{cor} + \Delta\mathcal{E}_\infty^{cor} = \mathcal{E}_{L+1}^{cor} + \sum_{m=4} A_{m-1} (L+1)^{-m+1}. \quad (3.70)$$

In the above equations, A_{m-1} are numerical coefficients. Clearly, if we identify $L+1$ with the cardinal number of the cc-pVXZ basis sets and retain only the leading term in Eq. (3.69), formula (3.63) is recovered.

With the aim of developing more accurate extrapolation schemes that follow the well established asymptotic behavior of the Schwartz's series, generalized forms of Eq. (3.64) have also been utilized, in particular, expressions such as [55–57]

$$\mathcal{E}_X^{cor} = \mathcal{E}_\infty^{cor} + \frac{A_3}{(X+\alpha)^{-3}} + \frac{A_n}{(X+\alpha)^{-n}}, \quad (3.71)$$

where A_n (with $n \geq 4$) and α are parameters that may be chosen to approximately account for the effects of higher- X (L) terms in (3.70). Indeed, by choosing $\alpha=0$ and A_n (with $n=4$) to depend on A_3 , Varandas [55] proposed a two-point extrapolation scheme capable of predicting CBS correlation energies with root-mean-square deviation (rmsd) of a few mE_h for a set of 33 systems studied at MP2, CCSD, and CCSD(T) levels. In fact, such a protocol has proved itself very effective in predicting energies that varies little with the pair of cardinal numbers chosen for the extrapolation.

Later on, the same author [56] extended further the method and proposed the use of $\alpha \neq 0$ and $n = 5$ in Eq. (3.71). Since A_3 and A_5 (which is also a function of A_3) explicitly account for the singlet- and triplet pair interactions, respectively, such a novel scheme has been referred to as uniform singlet- and triplet-pair extrapolation (USTE). As usual, \mathcal{E}_∞^{cor} and A_3 (with $A_5 = A_5(0) + cA_3^n$ and $\alpha = -3/8$ [56]) are determined from a fit to *ab initio* energies obtained with cc-pVXZ basis sets of two different ranks. The remaining set of fixed parameters (*i.e.*, $A_5(0)$, c , and n) have been calibrated by fitting total correlation energies in single-reference MP2, CCSD, and CCSD(T) calculations as well as the dynamical counterpart at MRCI level for a set of target atomic and molecular systems. One of the most important features of the USTE method is that it retains the accuracy when extrapolating from smaller $(X, X+1)$ pairs, while the traditional approaches work best when higher pairs of cardinal numbers are employed in the extrapolation procedure. Indeed, this makes such a protocol highly desirable for larger systems where calculations with larger basis sets are computationally prohibitive [56].

More recently, Varandas and co-workers [58, 66] suggested a basis set re-hierarchization scheme in which newly hierarchical (fractional) numbers $x = d, t, q, p, b$, analogous to the cardinal series $X = D : 2, T : 3, Q : 4, 5, 6$, are employed in the extrapolation formulas. These x -numbers are determined from the requirement that the $X \leq 6$ values fall on the straight line obtained by fitting the $X = 5$ and 6 correlation energies with the USTE(5,6) method for each of the 18 molecular systems used for the calibration [58]. Clearly, the aim of the above procedure is to warrant that the results obtained from different pairs of extrapolation, particularly from smaller hierarchical numbers such as d and t , fall close to each other. In such an approach, the USTE($x, x+1$) extrapolation formula assumes the traditional one proposed by Helgaker *et al.* [61] [see Eq. (3.64)] with the exception that the cardinal numbers are replaced by their hierarchical analogues. For the MP2 theory, these latter are defined by $x = d : 2.13, t : 2.90, q : 3.78, p : 4.74$ and $b : 5.72$, while for CC-type methods they read $x = d : 1.91, t : 2.71, q : 3.68, p : 4.71$, and $b : 5.70$. With the above x -hierarchical numbers, the extrapolations of the correlation energy via USTE($x, x+1$) have shown a significant improvement over the original USTE when tested with low hierarchies for a total of 106 target molecules.

To treat the uncorrelated HF and CASSCF energies, one of the two routes is usually followed. The first, and the most obvious, is to consider that the energies obtained from large scale calculations, *e.g.*, with $X = 6$, already represent the converged CBS results. The second though consists of employing exponential or inverse-power-type formulas to extrapolate the SCF energies so obtained with several protocols being devoted to such a task [51–54]. One of the most used form is the exponential law of the type [67, 68]

$$\mathcal{E}_X^{\text{HF}} = \mathcal{E}_\infty^{\text{HF}} + A \exp(-bX), \quad (3.72)$$

where $\mathcal{E}_\infty^{\text{HF}}$, A , and b are parameters to be determined from *ab initio* energies calculated for at least three different values of X . Most recently, Karton and Martin [53], following the work of Jensen [52], proposed the two-point extrapolation formula

$$\mathcal{E}_X^{\text{HF}} = \mathcal{E}_\infty^{\text{HF}} + A(X + 1) \exp(-b\sqrt{X}), \quad (3.73)$$

where $b=9$. The above equation has shown a rmsd of 0.1 mE_h using AVQZ and AV5Z basis sets and of 10 μ E_h using AV5Z and AV6Z basis sets. However, in situations where such large basis are prohibitive, and only AV(T, Q)Z pairs are affordable, it is recommended the use of the inverse power form [53]

$$\mathcal{E}_X^{\text{HF}} = \mathcal{E}_\infty^{\text{HF}} + \frac{A}{X^b}, \quad (3.74)$$

with $b=5.34$. Eq. (3.74) is known to perform very well with rmsd of about 206 μ E_h.

Although Eqs. (3.72)-(3.74) have been specially designed to treat HF energies [53], Varandas [56] suggested that they should also yield accurate CBS values for CASSCF wave functions. Indeed, Pansini *et al.* [54] have recently proposed novel x -hierarchical numbers to be used along with an effective two-parameter form of Eq. (3.72). For the HF theory, these latter assume the values $x=d:2.08$, $t:2.96$, $q:3.87$, $p:5.07$ and $b:6.12$ with $b=1.62$, while for the CASSCF method they are $x=d:2.08$, $t:2.94$, $q:3.87$, $p:5.08$, and $b:6.13$ with $b=1.63$.

3.5 Semiempirical corrections to *ab initio* energies

3.5.1 Size-consistency and size-extensivity errors

As previously stated, one of the most undesirable features of excitation-limited CI approaches is that the resulting electronic energies do not scale properly with the size of molecular systems, *i.e.*, they are not size-extensive. Indeed, higher-order excitations terms become more and more important as the number of electrons increases, and hence truncated CI wave functions tend to recover smaller and smaller fractions of the correlation energy as long as the size of the molecule increases [1, 2, 23]. Another closely related deficiency of such methods rests on the fact the energy of two noninteracting molecules, when placed at infinitely large distances, is not the sum of the energies of each isolated subsystem, *i.e.*, they are not size-consistent either [1]. This handicap becomes particularly dramatic when one aims to obtain accurate predictions of thermochemical data as well as warrant the correct energetics of dissociation channels in global PESs [69].

Several schemes of varying sophistication have been proposed to address this subject [31]. Owing to its simplicity, one of the most popular method to correct for the size-extensivity and size-consistency problems in general CISD calculations is that of Langhoff and Davidson [70] which estimates the energy of the missing quadruple excitations as

$$\mathcal{E}_{cor}^Q = (1 - c_0^2) \mathcal{E}_{cor}^{SD}, \quad (3.75)$$

where c_0 is the coefficient of the HF determinant in the normalized truncated CISD wave function and \mathcal{E}_{cor}^{SD} the corresponding correlation energy, *i.e.*, $\mathcal{E}_{cor}^{SD} = \mathcal{E}_{CISD} - \mathcal{E}_{HF}$. The Davidson correction (DC) is very often extended to the multi-reference case by using the form [71, 72]

$$\mathcal{E}_{cor}^Q = \left(1 - \sum_{\nu} c_{\nu}^2 \right) \mathcal{E}_{cor}^{SD}, \quad (3.76)$$

with c_{ν} now being the associated coefficients of the CSFs in the reference MCSCF expansion and \mathcal{E}_{cor}^{SD} is the dc energy obtained from a truncated MRCI calculation [$\mathcal{E}_{cor}^{SD} = \mathcal{E}_{MRCI} - \mathcal{E}_{MCSCF}$]. In general, the abbreviations CISD(Q) and MRCI(Q) are employed to denote the use of the corrections given by Eqs. (3.75) and (3.76), respectively. Note that, although the validity of the above expressions have been demonstrated by means

of many-body perturbation theory [72], the final justification for the use of the DC is rather empirical, based primarily on a large number of *ab initio* calculations. Suffice it to add that such a correction does not vanish for two-electron systems, where the CISD model becomes equivalent to a FCI, and hence it is expected to overestimate the effects of quadruple excitations in small molecules. Moreover, since there are no useful bounds on the energy expressions, one of the main shortcomings of the Q correction is that some numerical “noises” can be introduced when calculating large sections of PESs which can significantly increase the rmsd for a fitted potential [73].

3.5.2 Scaling of the correlation energy

The fundamental error of excitation-limited CI wave functions, *i.e.*, the lack of size-extensivity and size-consistency, is directly related to the fact that these latter tend to recover only part of the total dynamical or external correlation energy. Brown and Truhlar [74] proposed a scheme to incorporate the remaining deficiencies by recognizing that the fraction of the external correlation energy recovered in a truncated MRCI method (relative to an MCSCF reference and within a given one-electron basis set) is an approximately constant factor of the total external correlation over all nuclear configurations. The authors introduced an scaled external correlation (SEC) energy of the form

$$\mathcal{E}_{\text{SEC}}(\mathbf{R}) = \mathcal{E}_{\text{MCSCF}}(\mathbf{R}) + \frac{\mathcal{E}_{\text{MRCI}}(\mathbf{R}) - \mathcal{E}_{\text{MCSCF}}(\mathbf{R})}{\mathcal{F}} \quad (3.77)$$

as a semiempirical correction to the MRCI energy. Note that the (empirical geometry-independent) parameter \mathcal{F} is taken to be a constant over the entire PES and is chosen in such a way as to reproduce known bond dissociation energies, barrier heights or other available experimental data [74]. As pointed out by Brown and Truhlar [74], an important element of the physical basis of the SEC method is that the MCSCF reference space and the one-electron basis should already be large enough in order to include dominant geometry-dependent internal correlation effects and an appreciable percentage of the external correlation energy. It should be emphasized that, by including information relative to experimental data, the SEC approach, besides extrapolating to the limit of the L -electron basis, also account for the incompleteness of the one-electron basis set [69].

Later on, Varandas [69] proposed a generalization of the SEC approach by recognizing the conceptual relationship between this latter and the double many-body expansion (DMBE) method [75–77] (the DMBE approach is discussed in section 4.3). In such a scheme, denoted as DMBE-SEC [69], the total interaction potential relative to the infinitely separated atoms is thus given by

$$V(\mathbf{R}) = V_{\text{MCSCF}}(\mathbf{R}) + V_{\text{SEC}}(\mathbf{R}), \quad (3.78)$$

where $V_{\text{MCSCF}}(\mathbf{R})$ denotes the internal correlation part and $V_{\text{SEC}}(\mathbf{R})$ the corresponding SEC contribution. Note that, as opposed to the notation used in Eq. (3.77), $V_{\text{SEC}}(\mathbf{R})$ denotes only the scaled external correlation energy component, *i.e.*, the second term on the RHS of (3.77). As usual in the DMBE-SEC approach, each term in Eq. (3.78) are then written in the form of a cluster expansion [10, 78]

$$V_{\text{MCSCF}}(\mathbf{R}) = \sum_{\text{AB}} V_{\text{AB,MCSCF}}^{(2)}(R_{\text{AB}}) + \sum_{\text{ABC}} V_{\text{ABC,MCSCF}}^{(3)}(R_{\text{AB}}, R_{\text{AC}}, R_{\text{BC}}) + \dots \quad (3.79)$$

$$V_{\text{SEC}}(\mathbf{R}) = \sum_{\text{AB}} V_{\text{AB,SEC}}^{(2)}(R_{\text{AB}}) + \sum_{\text{ABC}} V_{\text{ABC,SEC}}^{(3)}(R_{\text{AB}}, R_{\text{AC}}, R_{\text{BC}}) + \dots, \quad (3.80)$$

where the summations run over all subclusters of atoms (*e.g.*, diatomics, triatomics, etc.) that constitute the molecular system. The scaled external correlation contribution of each n -body term in the series is thus given by

$$V_{\text{ABC}\dots\text{H,SEC}}^{(n)}(\mathbf{R}) = \frac{V_{\text{ABC}\dots\text{H,MRCI}}^{(n)}(\mathbf{R}) - V_{\text{ABC}\dots\text{H,MCSCF}}^{(n)}(\mathbf{R})}{\mathcal{F}_{\text{ABC}\dots\text{H}}^{(n)}}, \quad (3.81)$$

where $\mathcal{F}_{\text{ABC}\dots\text{H}}^{(n)}$ is a n -body geometry-independent scaling parameter which, similarly to the SEC method, is judiciously chosen in order to reflect some known (accurate) experimental information. Particularly for diatomic molecules, the two-body factor $\mathcal{F}_{\text{AB}}^{(2)}$ is generally determined in such a way as to reproduce experimental dissociation energies and a similar approach can also be adopted for higher-order terms if accurate atomization energies are known for the relevant subsystems [69]. For the triatomic case, a reasonable approximation for $\mathcal{F}_{\text{ABC}}^{(3)}$ can be obtained by taking the average of the three two-body factors

$$\mathcal{F}_{\text{ABC}}^{(3)} = \frac{1}{3} \left[\mathcal{F}_{\text{AB}}^{(2)} + \mathcal{F}_{\text{AC}}^{(2)} + \mathcal{F}_{\text{BC}}^{(2)} \right]. \quad (3.82)$$

Undoubtedly, enhanced accuracy and better theoretical estimates are obtained when the raw *ab initio* points are corrected by the DMBE-SEC method. Clearly, the chief advantage of such an approach is to warrant the correct exothermicities of all asymptotic channels as well as the proper shape of the potential in the valence region in order for the global PES be useful both for rovibrational calculations and reaction dynamics [69].

Bibliography

- [1] A. Szabo and N. S. Ostlund, *Modern Quantum Chemistry: Introduction to Advanced Electronic Structure Theory*, Vol. 1 (McGraw-Hill Book Co., New York, 1989).
- [2] F. Jensen, *Introduction to Computational Chemistry*, 2nd ed. (John Wiley & Sons, Chichester, 2006).
- [3] T. Helgaker, P. Jørgensen, and J. Olsen, *Molecular Electronic-Structure Theory* (John Wiley & Sons, Chichester, 2000).
- [4] J. C. Slater, *Phys. Rev.* **35**, 210 (1930).
- [5] V. Fock, *Z. Physik* **61**, 126 (1930).
- [6] J. C. Slater, *Phys. Rev.* **34**, 1293 (1929).
- [7] L. D. Landau and L. M. Lifshitz, *Quantum Mechanics Non-Relativistic Theory*, 2nd ed., Vol. 3 (Pergamon Press, Bristol, 1981).
- [8] D. A. McQuarrie and J. D. Simon, *Physical Chemistry A Molecular Approach*, 2nd ed. (University Science Books, Sausalito, 1997).
- [9] L. Pauling and E. B. Wilson, *Introduction to Quantum Mechanics with Applications to Chemistry*, Vol. 1 (McGraw-Hill Book Co., New York, 1935).
- [10] J. N. Murrell, S. Carter, S. C. Farantos, P. Huxley, and A. J. C. Varandas, *Molecular Potential Energy Functions* (John Wiley & Sons, Chichester, 1984).
- [11] G. C. Schatz, *Rev. Mod. Phys.* **61**, 669 (1989).

-
- [12] J. Tennyson, *Comput. Phys. Rep.* **4**, 1 (1986).
- [13] B. T. Sutcliffe and J. Tennyson, *Mol. Phys.* **58**, 1053 (1986).
- [14] B. T. Sutcliffe and J. Tennyson, *Int. J. Quantum Chem.* **39**, 183 (1991).
- [15] P. J. Kuntz, "Features of Potential Energy Surfaces and Their Effect on Collisions," in *Dynamics of Molecular Collisions: Part B* (Springer US, 1976) Chap. 2, pp. 53–120.
- [16] J. S. Wright and S. K. Gray, *J. Chem. Phys.* **69**, 67 (1978).
- [17] J. N. L. Connor, *Comp. Phys. Comm.* **17**, 117 (1979).
- [18] C. C. J. Roothaan, *Rev. Mod. Phys.* **23**, 69 (1951).
- [19] G. G. Hall, *Proc. R. Soc. Lond. A* **205**, 541 (1951).
- [20] J. A. Pople and R. K. Nesbet, *J. Chem. Phys.* **22**, 571 (1954).
- [21] P. O. Löwdin, *Adv. Chem. Phys.* **2**, 207 (1959).
- [22] I. Shavitt, "The Method of Configuration Interaction," in *Methods of Electronic Structure Theory*, edited by H. F. Schaefer (Springer US, Boston, MA, 1977) pp. 189–275.
- [23] C. J. Cramer, *Essentials of Computational Chemistry: Theories and Models*, 2nd ed. (John Wiley & Sons, Chichester, 2005).
- [24] C. Møller and M. S. Plesset, *Phys. Rev.* **46**, 618 (1934).
- [25] J. Čížek, *Adv. Chem. Phys.* **96**, 35 (1969).
- [26] R. J. Bartlett, *J. Phys. Chem.* **93**, 1697 (1989).
- [27] K. Raghavachari, G. W. Trucks, J. A. Pople, and M. Head-Gordon, *Chem. Phys. Lett.* **157**, 479 (1989).
- [28] M. W. Schmidt and M. S. Gordon, *Annu. Rev. Phys. Chem.* **49**, 233 (1998).
- [29] R. Shepard, *Adv. Chem. Phys.* **69**, 63 (1987).

- [30] B. O. Roos, *Adv. Chem. Phys.* **69**, 399 (1987).
- [31] P. G. Szalay, T. Müller, G. Gidofalvi, H. Lischka, and R. Shepard, *Chem. Rev.* **112**, 108 (2012).
- [32] H. J. Werner, *Adv. Chem. Phys.* **69**, 1 (1987).
- [33] H. J. Werner and P. J. Knowles, *J. Chem. Phys.* **89**, 5803 (1988).
- [34] P. J. Knowles and H. J. Werner, *Chem. Phys. Lett.* **145**, 514 (1988).
- [35] P. J. Knowles and H. J. Werner, *Theor. Chim. Acta* **84**, 95 (1992).
- [36] P. E. M. Siegbahn, *Chem. Phys.* **25**, 197 (1977).
- [37] P. E. M. Siegbahn, *Int. J. Quantum Chem.* **23**, 1869 (1983).
- [38] K. Andersson, P. A. Malmqvist, B. O. Roos, A. J. Sadlej, and K. Wolinski, *J. Phys. Chem.* **94**, 5483 (1990).
- [39] K. Andersson, P. A. Malmqvist, and B. O. Roos, *J. Chem. Phys.* **96**, 1218 (1992).
- [40] K. Andersson, *Theor. Chim. Acta* **91**, 31 (1995).
- [41] J. C. Slater, *Phys. Rev.* **36**, 57 (1930).
- [42] S. F. Boys, *Proc. R. Soc. Lond. A* **200**, 542 (1950).
- [43] W. J. Hehre, R. F. Stewart, and J. A. Pople, *J. Chem. Phys.* **51**, 2657 (1969).
- [44] E. R. Davidson and D. Feller, *Chem. Rev.* **86**, 681 (1986).
- [45] R. Krishnan, J. S. Binkley, R. Seeger, and J. A. Pople, *J. Chem. Phys.* **72**, 650 (1980).
- [46] M. J. Frisch, J. A. Pople, and J. S. Binkley, *J. Chem. Phys.* **80**, 3265 (1984).
- [47] T. H. Dunning, *J. Chem. Phys.* **90**, 1007 (1989).
- [48] R. A. Kendall, T. H. Dunning, and R. J. Harrison, *J. Chem. Phys.* **96**, 6796 (1992).

- [49] F. B. van Duijneveldt, J. G. C. M. van Duijneveldt-van de Rijdt, and J. H. van Lenthe, *Chem. Rev.* **94**, 1873 (1994).
- [50] S. F. Boys and F. Bernardi, *Mol. Phys.* **19**, 553 (1970).
- [51] A. Halkier, T. Helgaker, P. Jørgensen, W. Klopper, and J. Olsen, *Chem. Phys. Lett.* **302**, 437 (1999).
- [52] F. Jensen, *Theor. Chem. Acc.* **113**, 267 (2005).
- [53] A. Karton and J. M. L. Martin, *Theor. Chem. Acc.* **115**, 330 (2006).
- [54] F. N. N. Pansini, A. C. Neto, and A. J. C. Varandas, *Theo. Chem. Acc.* **135**, 261 (2016).
- [55] A. J. C. Varandas, *J. Chem. Phys.* **113**, 8880 (2000).
- [56] A. J. C. Varandas, *J. Chem. Phys.* **126**, 244105 (2007).
- [57] A. J. C. Varandas, *J. Phys. Chem. A* **112**, 1841 (2008).
- [58] A. J. C. Varandas and F. N. N. Pansini, *J. Chem. Phys.* **141**, 224113 (2014).
- [59] F. N. N. Pansini and A. J. C. Varandas, *Chem. Phys. Lett.* **631**, 70 (2015).
- [60] F. N. N. Pansini, A. C. Neto, and A. J. C. Varandas, *Chem. Phys. Lett.* **641**, 90 (2015).
- [61] T. Helgaker, W. Klopper, H. Koch, and J. Noga, *J. Chem. Phys.* **106**, 9639 (1997).
- [62] W. Klopper, K. L. Bak, P. Jørgensen, J. Olsen, and T. Helgaker, *J. Phys. B: At. Mol. Opt. Phys.* **32**, R103 (1999).
- [63] C. Schwartz, *Phys. Rev.* **126**, 1015 (1962).
- [64] R. N. Hill, *J. Chem. Phys.* **83**, 1173 (1985).
- [65] W. Kutzelnigg and J. D. Morgan III, *J. Chem. Phys.* **96**, 4484 (1992).
- [66] A. J. C. Varandas, *J. Phys. Chem. A* **114**, 8505 (2010).

-
- [67] D. Feller, *J. Chem. Phys.* **96**, 6104 (1992).
- [68] D. Feller, *J. Chem. Phys.* **98**, 7059 (1993).
- [69] A. J. C. Varandas, *J. Chem. Phys.* **90**, 4379 (1989).
- [70] S. R. Langhoff and E. R. Davidson, *Int. J. Quantum Chem.* **8**, 61 (1974).
- [71] S. Prime, C. Rees, and M. A. Robb, *Mol. Phys.* **44**, 173 (1981).
- [72] K. Jankowski, L. Meissner, and J. Wasilewski, *Int. J. Quantum Chem.* **28**, 931 (1985).
- [73] R. J. Bartlett, I. Shavitt, and G. D. Purvis, *J. Chem. Phys.* **71**, 281 (1979).
- [74] F. B. Brown and D. G. Truhlar, *Chem. Phys. Lett.* **117**, 307 (1985).
- [75] A. J. C. Varandas, *Mol. Phys.* **53**, 1303 (1984).
- [76] A. J. C. Varandas, *J. Mol. Struct.: THEOCHEM* **120**, 401 (1985).
- [77] A. J. C. Varandas, *Adv. Chem. Phys.* **74**, 255 (1988).
- [78] A. J. C. Varandas and J. N. Murrell, *Faraday Discuss. Chem. Soc.* **62**, 92 (1977).

Chapter 4

Analytical modeling of *ab initio* energies

The theoretical study of molecular dynamics (scattering, spectroscopy, etc.) requires precise information about the relevant electronic PES. A common starting point to obtain such interaction potential is to perform pointwise “solutions” to the TIESE [Eq. (1.29)] at sufficiently many nuclear configurations by choosing an appropriate quantum-mechanical method and one-electron basis set. In such *ab initio* electronic structure calculations, the results are mostly given in form of huge tables of energy values for the specific nuclear arrangements so selected and, in order to obtain a realistic global representation of the potential, one must then devise a model function in which to fit such discrete data (see appendix C).

Clearly, the need for developing analytical representations of PESs arises primarily because *ab initio* computations are sufficiently time consuming that the explicit energy and gradients evaluations at every nuclear geometry required in a dynamics study is rarely feasible [1–3]. Thus, by making use of reliable analytic models, one can clearly benefit from their advantages in providing fast, continuous and differentiable representations of the surface. Such an asset is particularly useful if one aims at studying chemical kinetics for a given reaction. Indeed, by integrating the relevant equations of motion with the PES dictating the interactions between the involved species, accurate reaction rate constants

and cross sections can be obtained and compared to experimental data [4]. Although direct dynamics methods [5] have been proposed to couple dynamics and electronic structure calculations (avoiding, therefore, a global functional form), the computational effort for evaluating *ab initio* all the nuclear geometries needed dramatically restricts the usefulness of such an approach. Similar drawbacks are also encountered when calculating rovibrational energy levels of polyatomic systems (see chapter 5). In fact, apart from the simplest cases of diatomic molecules, the direct evaluation of the electronic energies required to solve the corresponding bound-state problem in molecular systems with large number of nuclear degrees of freedom is extremely demanding. Again, the fitted potentials provide the main route toward the spectroscopic characterization of the underlying species.

It should be recalled that, due to the unavoidable errors associated to the truncation of CI expansions and incompleteness of the one-electron basis sets, *ab initio* energies themselves seldom fulfill the standards of spectroscopic ($\lesssim 1 \text{ cm}^{-1}$) or even chemical accuracy ($\lesssim 4 \text{ kJ mol}^{-1}$). To overcome such difficulties some corrections, such as the use of CBS extrapolation schemes and/or the DMBE-SEC method, must be generally made prior to the calibration procedure [6]. Of course, one can also improve the quality of the final PES by employing an iterative process in which the potential parameters are further refined in such a way as to minimize the differences between calculated and experimental data [7–10]. Other approaches also exist in which global analytic forms are actually merged with experimentally-determined local potentials. These latter are often referred to as the energy-switching (ES) methods [11, 12].

4.1 General rules and strategies

Wright and Gray [2], following a suggestion by Kuntz [1], enumerated ten criteria that a potential form should satisfy to be successful. These can be stated as follows [1, 2]

- (1) It should accurately characterize the asymptotic reactant and product molecules.
- (2) It should have the correct symmetry properties of the system.

- (3) It should represent the true potential accurately in interaction regions for which experimental or theoretical data are available.
- (4) It should behave in a physically reasonable manner in those parts of the interaction region for which no experimental or theoretical data are available.
- (5) It should smoothly connect the asymptotic and interaction region in a physically reasonable way.
- (6) The target function and its derivatives should have as simple an algebraic form as possible consistent with the desired goodness of fit.
- (7) It should require as small a number of data points as possible to achieve an accurate fit.
- (8) It should converge to the true surface as more data become available.
- (9) It should indicate where it is most meaningful to compute the data points.
- (10) It should have a minimal amount of *ad hoc* or “patched up” character.

As noted by Connor [3], the criteria (1)-(5) are essential for a global PES to be useful for reaction dynamics studies, while the remaining five are less essential but highly desirable. Schatz [13] emphasized that the Wright and Gray criteria may lead to some conflicting strategies, inasmuch as simplicity and accuracy are seldom fulfilled at once. Obviously, in order to maximize the compromise between such concepts, the use of physically motivated fitting forms are always advocated.

Several strategies have been suggested to analytically represent PESs of small polyatomic systems [1–3, 6, 13–17]. These approaches can generally be categorized into two distinct classes, *i.e.*, global and local methods [3]. In the former, the potential is determined at each point by all the data that are used as input for the calibration procedure. Among these, several approaches can be highlighted such as diatomics-in-molecules (DIM) [18–20], many-body expansion-type forms [14, 17, 21–23], reproducing kernel Hilbert space [24, 25] and ES methods [11, 12]. Conversely, in local schemes, the

value of the potential at a specified nuclear arrangement depends only on *ab initio* data that are available for geometries close to that point. Some examples include standard cubic-spline interpolations [26, 27], Shepard interpolation [28] and moving least-squares methods [29]. Indeed, local interpolation schemes are useful when sufficiently detailed information is available about the interaction potential under study [15]. Therefore, they require an extremely dense and equidistant grid of *ab initio* data that cover large sections of the PESs [27]. In turn, global approaches are more attractive when little detailed information is known about the PES [6]. Their main advantages relies on the fact that a lesser amount of input data points are needed in the calibration procedure and that the resulting analytic forms have physically meaningful extrapolation capabilities.

Amongst the most reliable global interpolation schemes, the many-body expansion (MBE) [14] and, its improved variant, the DMBE [17, 21, 22] methods play a prominent role and have acquired the greatest popularity. In such methodologies, the total interaction potential of a molecular system is defined by making an expansion in the energy of all its sub-clusters of atoms [14]. Besides accurately describing valence interactions, one of the main advantages of such approaches relies, therefore, on the possibility to account for the correct asymptotic behavior of each n -body term in the series so that all dissociation limits (as well as long-range interactions in the case of the DMBE approach) are naturally warranted. Indeed, once the potentials of all the fragments have been obtained, the many-body expansion also enables one to built a first estimate of the PES of a target polyatomic system [14, 30]. Note that, even if the series converges rapidly, chemical accuracy is only attainable by including the highest-order (*i.e.*, the non-pairwise-additive) contributions to the potential [14, 17]. A practical advantage of such methods over those based on semiempirical valence-bond theories such as the DIM approach is that simpler and more flexible functional forms can actually be employed to fit *ab initio* and/or experimental information, and hence accurate and realistic global potentials are often obtained.

Before proceeding to the discussion of the underlying theories, it is safe here to highlight an important point not addressed by the Wright and Gray criteria, *i.e.*, the issue of the multi-sheeted PESs. Although chemical reactions may be viewed as proceeding on

an approximate single-sheeted potential, the formation and breaking of chemical bonds frequently involves several (coupled) electronic states. As noted by Varandas [6], two distinct approaches to modeling a multi-sheeted problem can be advocated. The first consists of fitting the involved adiabatic PESs arising from a proper diagonalization of a diabatic electronic potential matrix, either separated [31, 32] or simultaneously [33, 34]. The second approach is to fit instead the various (diagonal and off-diagonal) elements of such a matrix which yields, when diagonalized, the required adiabatic potentials [35]. One of the main drawbacks of this latter methodology consists of finding a proper ATD similarity transformation in such a way that the diagonal adiabatic PESs (strictly speaking, *ab initio* energies) are replaced by a potential matrix whose elements are smooth functions of the nuclear coordinates [14, 35–38]. Indeed, for molecules other than diatomics, strictly diabatic basis which exactly diagonalize the nuclear kinetic energy operators do not exist [39], and hence one may speak at most of quasi-diabatic PESs. However, if the aim is to solve adiabatically the nuclear equations of motion [Eq. (1.31)], the first strategy may be more advantageous. Note that, by adopting such a coupled multi-sheet approach, one generally requires precise knowledge of the NACTs [Eq. (1.32)]. Alternatively, if the proper topological properties are to be warranted [see Eq. (2.45)], one can also ensure the expected cusp behavior on single-sheeted adiabatic PESs by making use of polynomial forms containing special non-analytic coordinates [30, 40–42]. As we shall see later, this will be the main strategy employed throughout the present thesis.

4.2 The MBE method

According to the MBE method, the molecular PES for an H -atom system can be expressed by the cluster expansion [14]

$$V_{\text{ABC}\dots\text{H}}(\mathbf{R}) = \sum_{\text{A}} V_{\text{A}}^{(1)} + \sum_{\text{AB}} V_{\text{AB}}^{(2)}(R_{\text{AB}}) + \sum_{\text{ABC}} V_{\text{ABC}}^{(3)}(R_{\text{AB}}, R_{\text{AC}}, R_{\text{BC}}) + \dots + V_{\text{ABC}\dots\text{H}}^{(n)}(\mathbf{R}), \quad (4.1)$$

where the one-body term $V_{\text{A}}^{(1)}$ is the energy of atom A in the state produced by adiabatically removing it from the cluster. If the energy zero is chosen with all atoms in their ground states, $V_{\text{A}}^{(1)}$ is only non-zero when, on dissociation, A is left in an excited state. In turn, $V_{\text{AB}}^{(2)}(R_{\text{AB}})$ is a two-body term and corresponds to the diatomic in-

teraction potential of the subsystem AB. $V_{\text{ABC}}^{(3)}(R_{\text{AB}}, R_{\text{AC}}, R_{\text{BC}})$ is the corresponding ABC three-body energy, and so on. Note that, in (4.1), the summations run over all possible $H!/n!(H-n)!$ n -body terms, each depending on the set of $\mathbf{R}^n \equiv \{R_1, R_2, \dots, R_{n(n-1)/2}\}$ nuclear coordinates which, in turn, is a subset of the total number of interatomic separations $\mathbf{R}^H \equiv \{R_1, R_2, \dots, R_{H(H-1)/2}\}$. Thus, we can rewrite Eq. (4.1) in a more compact form as

$$V(\mathbf{R}^H) = \sum_{n=1}^H \sum_{\mathbf{R}^n \subset \mathbf{R}^H} V^{(n)}(\mathbf{R}^n). \quad (4.2)$$

As already mentioned, in the MBE method, each n -body term in the series vanishes as any one of its constituent atoms is adiabatically removed to infinity. Such a requirement is generally satisfied by writing the corresponding terms in Eq. (4.2) as

$$V^{(n)}(\mathbf{R}^n) = P(\mathbf{R}^n)T(\mathbf{R}^n), \quad (4.3)$$

where $P(\mathbf{R}^n)$ is an n -body polynomial in the interparticle coordinates and $T(\mathbf{R}^n)$ is a range determining factor which decreases to zero when any of the coordinates belonging to \mathbf{R}^n becomes infinite [14].

4.3 The DMBE method

A commonly accepted and conceptually convenient approach in obtaining realistic functional forms for molecular PESs is to make a further partition of the potential by splitting each n -body term of Eq. (4.2) into extended Hartree-Fock (EHF) and dc energy-type components [17, 21, 22]. In such a DMBE approach, originally proposed by Varandas [21], the molecular PESs are thus represented by

$$V(\mathbf{R}^H) = \sum_{n=1}^H \sum_{\mathbf{R}^n \subset \mathbf{R}^H} \left[V_{\text{EHF}}^{(n)}(\mathbf{R}^n) + V_{\text{dc}}^{(n)}(\mathbf{R}^n) \right]. \quad (4.4)$$

One of the major advantages of the DMBE method over the conceptually simple MBE approach relies therefore in the allowance for the different convergence rates of the n -body terms at short separations, where the EHF energy is the dominant contribution, and at large distances, where the dispersion (or dc) energy component dominates. It is also fair to say that by performing such a double decomposition of the interaction energy,

one can naturally add physical insight into the origin of the potential [17, 21, 22]. To this end, it is convenient, for modeling purposes, to carry out a further partition of these two energy components as

$$V_{\text{EHF}}^{(n)}(\mathbf{R}^n) = V_{\text{exc}}^{(n)}(\mathbf{R}^n) + V_{\text{ele}}^{(n)}(\mathbf{R}^n) + V_{\text{ind}}^{(n)}(\mathbf{R}^n), \quad (4.5)$$

and

$$V_{\text{dc}}^{(n)}(\mathbf{R}^n) = V_{\text{intra}}^{(n)}(\mathbf{R}^n) + V_{\text{inter}}^{(n)}(\mathbf{R}^n) + V_{\text{res}}^{(n)}(\mathbf{R}^n), \quad (4.6)$$

where the subscripts ele and ind indicate the electrostatic and induction energies, exc denotes the exponentially decaying short-range exchange energy, intra and inter are the intra- and inter-fragment components of the dc energy, and res denotes the residual intra-inter dc coupling terms. Indeed, at the valence (short-range) interaction regions of the potential, where the EHF component prevails, its exponentially decaying behavior can be reasonably modeled *ab initio* by employing conventional polynomial expansions such as (4.3) [14, 17, 21, 22]. Conversely, at long-range distances, where the interaction potential are mainly determined by means of the Rayleigh-Schrödinger perturbation approach [17], the inter-fragment dc energy (here, identified as the dispersion energy arising in second-order of perturbation theory) are modeled semiempirically from the dispersion coefficients for the various separate and united-atom limits [43–46]. Note that a similar approach may also be used to represent the long-range contributions to the electrostatic and induction energies which find their formal definitions in first- and second-order of perturbation theory, respectively [43, 47]. Of course, for regions of the potential where charge-overlap and exchange effects are appreciable (*i.e.*, at intermediate separations), the usual asymptotic multipolar series expansions for the (long-range) interaction energy becomes divergent, and hence convenient damping functions must be introduced to approximate such effects [14, 17, 21, 22, 44]. Suffice it to add that, in these regions of the nuclear configurations space, ambiguities also arise in the formal definition of the various energy contributions (4.5) and (4.6), but any errors caused by such inadequate representations are commonly absorbed into the various n -body energy terms which contribute to EHF. Moreover, the terms $V_{\text{intra}}^{(n)}(\mathbf{R}^n)$ and $V_{\text{res}}^{(n)}(\mathbf{R}^n)$ are generally not explicitly considered and, for most practical purposes, can be incorporated into $V_{\text{EHF}}^{(n)}(\mathbf{R}^n)$.

Varandas and coworkers proposed simple, yet reliable, physically motivated forms for the various n -body terms of Eq. (4.4). For the simplest case, *i.e.*, for a diatomic potential energy curve, the DMBE method finds its usefulness in the well-known extended Hartree-Fock approximate correlation energy for two-body interactions (EHFACE2) [48] and the EHFACE2U (EHFACE2 including united atom limit) [49] models. For the three-body energy terms, several approaches have also been advocated in obtaining realistic and flexible functional representations [17, 22, 23, 50]. Note that a suitable analytical form should reflect the intrinsic complexities of the molecule at hand, and hence must be modeled accordingly (*i.e.*, is system-specific) [30, 40–42, 51]. In fact, for small polyatomic systems, the main features of their PESs appear to be contained in the two- and three-body terms, with the four-body (and higher-order) terms being regarded as a fine tuning to give chemical accuracy [14]. Thus, it is expected that only a simple and approximate representation of these latter will generally be required.

4.4 Modeling of multi-sheeted potentials

It is a well known fact that the modeling of global PESs is dramatically complicated by the presence of Cis. At such regions of the nuclear configuration space both ground- and excited-state potentials show a cusp and possess discontinuous first derivatives that cannot be mimicked by standard analytic forms [30, 40]. One way around this issue is to employ appropriate diabatic matrix representations where the adiabats (which vary drastically and in a discontinuous manner near these regions) are replaced by functions that behave smoothly at the neighborhood of Cis. Such diabatic states, once properly obtained and conveniently modeled by some functional form, can be back transformed to adiabatic ones, yielding therefore the expected cusp behavior in the vicinity of the crossing seams [41, 42].

For the two-state case, the adiabatic energies $V_1(\mathbf{R})$ and $V_2(\mathbf{R})$, which are obtained as pointwise solutions to the TIESE [Eq. (1.29)], can be resolved into diabatic ones by the

following ATD transformation [14, 52]

$$\begin{pmatrix} H_{11}(\mathbf{R}) & H_{12}(\mathbf{R}) \\ H_{12}(\mathbf{R}) & H_{22}(\mathbf{R}) \end{pmatrix} = \begin{pmatrix} \cos \alpha'(\mathbf{R}) & \sin \alpha'(\mathbf{R}) \\ -\sin \alpha'(\mathbf{R}) & \cos \alpha'(\mathbf{R}) \end{pmatrix} \begin{pmatrix} V_1(\mathbf{R}) & 0 \\ 0 & V_2(\mathbf{R}) \end{pmatrix} \begin{pmatrix} \cos \alpha'(\mathbf{R}) & -\sin \alpha'(\mathbf{R}) \\ \sin \alpha'(\mathbf{R}) & \cos \alpha'(\mathbf{R}) \end{pmatrix}, \quad (4.7)$$

where $\alpha'(\mathbf{R}) = (1/2)\alpha(\mathbf{R})$ [see Eqs. (2.3)-(2.5)] is the so-called diabaticization or mixing angle [35] which is responsible for the proper “rotation” between one representation to the other. From the above expression, the diabatic potential matrix elements $H_{ji}(\mathbf{R})$ can be further defined by the relations [35]

$$\begin{aligned} H_{11}(\mathbf{R}) &= V_1(\mathbf{R}) \cos^2 \alpha'(\mathbf{R}) + V_2(\mathbf{R}) \sin^2 \alpha'(\mathbf{R}) \\ H_{22}(\mathbf{R}) &= V_1(\mathbf{R}) \sin^2 \alpha'(\mathbf{R}) + V_2(\mathbf{R}) \cos^2 \alpha'(\mathbf{R}) \\ H_{12}(\mathbf{R}) &= [V_2(\mathbf{R}) - V_1(\mathbf{R})] \cos \alpha'(\mathbf{R}) \sin \alpha'(\mathbf{R}). \end{aligned} \quad (4.8)$$

Note that such ATD transformations are not unique and strictly depend on the functional form for $\alpha'(\mathbf{R})$. Although several approaches [14, 35–39, 53–56] have been devoted to obtain appropriate global (or local) representations for the mixing angle, the resolution in term of diabatic states is generally a non-trivial matter.

Once this transformation has been accomplished, the diabatic energies obtained for $H_{11}(\mathbf{R})$ and $H_{22}(\mathbf{R})$ can then be fitted to polynomial forms of the MBE or DMBE-type [57, 58]. In turn, the non-diagonal element $[H_{12}(\mathbf{R})]$ is problem-specific and must be modeled in such a way as to vanish at all the dissociation limits as well as in regions of the nuclear configuration space at which the intersection occurs. Following Murrell *et al.* [14, 57, 59], this term is usually written as a polynomial times a specially designed function that becomes zero at the desired molecular arrangements.

After convenient analytic forms have been obtained for the diabatic elements in (4.8), the functional representation of the whole adiabatic surfaces (or sheets), including the non-analytic behavior at the intersection seam, can be expressed as the lowest eigenvalues of the 2 by 2 matrix (4.7) [see also Eq. (2.3)] giving

$$V_{1,2}(\mathbf{R}) = \frac{1}{2} [H_{11}(\mathbf{R}) + H_{22}(\mathbf{R})] \pm \frac{1}{2} \sqrt{[H_{11}(\mathbf{R}) - H_{22}(\mathbf{R})]^2 + 4H_{12}(\mathbf{R})^2}, \quad (4.9)$$

which has exactly the same form as (2.6). Suffice it to add that, apart from the proper diabaticization schemes, the modeling of the multi-sheeted problem can also be accomplished by first employing a semiempirical diabatic-type formalism such as DIM theory, which has built-in the desired cusps, followed by the introduction of additional terms to accommodate as much flexibility as possible to fit directly adiabatic *ab initio* energies [12, 57, 58, 60].

4.5 Modeling cusps in adiabatic potentials

Alternative and efficient approaches to describe the characteristic cusps on adiabatic PESs have been put forward after the pioneering work due to Varandas and Murrell [30]. The authors proposed the use of the so-called JT-type coordinate $\sqrt{\Gamma_2} = (Q_2^2 + Q_3^2)^{1/2}$ [see, *e.g.*, Eq. (2.25)] together with suitable additional polynomial terms to introduce the required nonanalyticity into the lowest adiabatic PES of $\text{H}_3(1^2A')$ which shows a symmetry-dictated intersection at D_{3b} geometries. Later on, Varandas and coworkers [31–33] extended further the above methodology and showed that it can be used not only to cause the cusp but also to fit simultaneously both ground- and excited-state sheets, hence ensuring degeneracy over the entire crossing seam. Undoubtedly, this was the first approach to correctly mimic the two adiabatic sheets without the need of any diabatic representation. Accordingly, the lower [$V_1(\mathbf{R})$] and upper [$V_2(\mathbf{R})$] surfaces are written as [33]

$$\begin{aligned} V_1(\mathbf{R}) &= V^{(2)}(\mathbf{R}) + V_{\text{dc}}^{(3)}(\mathbf{R}) + \left[P_1'(\mathbf{R}) - \sqrt{\Gamma_2} P_1''(\mathbf{R}) \right] T(\mathbf{R}) \\ V_2(\mathbf{R}) &= V^{(2)}(\mathbf{R}) + V_{\text{dc}}^{(3)}(\mathbf{R}) + \left[P_2'(\mathbf{R}) + \sqrt{\Gamma_2} P_2''(\mathbf{R}) \right] T(\mathbf{R}), \end{aligned} \quad (4.10)$$

where, as usual in the DMBE framework, $V^{(2)}(\mathbf{R})$ is the sum of two-body potentials, $V_{\text{dc}}^{(3)}(\mathbf{R})$ is the three-body dc term, $P(\mathbf{R})$ are appropriate polynomial functions and $T(\mathbf{R})$ the corresponding range-decaying factors. It is seen from (4.10) that the two-body fragments must be equal on both sheets (or forced to vanish at equilateral triangular conformations [33]) in order to make the adiabatic PESs degenerate along the D_{3b} line. Moreover, since $\sqrt{\Gamma_2} = 0$ at D_{3b} arrangements, one must also warrant that the polynomials $P'(\mathbf{R})$ assume the same values at these crossing geometries. Such a requirement can actually be accomplished by making those coefficients that depend only on the breathing normal

mode Q_1 [see Figure 2.2] be the same, *i.e.*, $c'_{i00}{}^{(1)} = c'_{i00}{}^{(2)} \forall i$. Since Eq. (4.10) ensures that the two sheets behave as a linear function of the $\sqrt{\Gamma_2}$ coordinate in the neighborhood of the intersection seam, the only additional constraint is to impose the same slope, *i.e.*, $c'_{000}{}^{(1)} = c'_{000}{}^{(2)}$.

Apart from the specific case of X_3 -type JT systems, Varandas *et al.* [41, 42] recently suggested the use of a generalized JT-type coordinate (Δ) to cause the desired singularities on adiabatic single-sheeted PESs of any triatomic molecule, including those having accidental Cis. Indeed, such a novel scheme has been proved very effective in accurately modeling the locus of intersection of several molecules such as $N_3(1^2A')$, $NO_2(1^2A'')$, $HN_2(1^2A')$ and $C_3(1^1A')$ [41, 42, 51].

4.6 The energy-switching approach

Following the Wright and Gray criteria (section 4.1), a global PES should attain spectroscopic accuracy at regions where such an information is available. With this in mind, Varandas [11] proposed a simple, yet reliable, scheme in which a local polynomial expansion that is capable of predicting experimental spectroscopic information is actually morphed with a global form that warrants a realistic description of the whole surface. Because these latter potentials are switched smoothly between one to the other as a function of the energy only, the method has been referred to as energy-switching. Labeling the spectroscopically accurate surface by $V_2(\mathbf{R})$ and the global one as $V_1(\mathbf{R})$, the final ES potential [$V_{ES}(\mathbf{R})$] can be cast in the form [11]

$$V_{ES}(\mathbf{R}) = f(\Delta E) V_1(\mathbf{R}) + [1 - f(\Delta E)] V_2(\mathbf{R}), \quad (4.11)$$

with

$$f(\Delta E) = \frac{1}{2} \{1 + \tanh[(\gamma_0 + \gamma_1 \Delta E^m) \Delta E]\}, \quad (4.12)$$

where $\Delta E = E - E_0$ is the displacement from some reference energy E_0 at which $V_1(\mathbf{R})$ and $V_2(\mathbf{R})$ are equally reliable, and $f(\Delta E)$ is a switching function that approaches zero for large negative energy displacements (*i.e.*, at the absolute minimum) and +1 for large positive ones (*i.e.*, at the atom-diatom dissociation limits). Note that γ_i ($i = 0, 1$) are disposable parameters to be optimized for a selected even power of m [11].

Recently, the same author [12] suggested further refinements onto the approach and introduced a generalized multiple energy-switching (MES) variant. In fact, such a novel methodology has been particularly designed to convey spectroscopic accuracy for systems in which the switching from $V_2(\mathbf{R})$ to $V_1(\mathbf{R})$ takes place in a rather narrow energy window. In this case, $V_{\text{ES}}(\mathbf{R})$ assumes the form [12]

$$V_{\text{ES}}(\mathbf{R}) = f_i \dots f_3 f_2 f_1 [V_1(\mathbf{R}) - V_2(\mathbf{R})] + V_2(\mathbf{R}), \quad (4.13)$$

with the switching functions $f_i(\Delta E)$ being given by [12]

$$f_i(\Delta E) = \begin{cases} \exp \left[-\beta_i \left(\frac{\Delta E_0}{\Delta E + \xi} - 1 \right)^{n_i} \right] & \text{if } \Delta E < \Delta E_0 \\ 1 & \text{if } \Delta E \geq \Delta E_0, \end{cases} \quad (4.14)$$

where $\Delta E = E - E_{\text{min}}$ is the energy displacement with respect to the absolute minimum of the global PES, while $\Delta E_0 = E_0 - E_{\text{min}}$ measures the energy difference between E_{min} and some cutoff energy E_0 [12]. Usually, E_0 can be wisely chosen so as to keep unaltered some topological feature of $V_1(\mathbf{R})$ or simply represent the energy range at which the Taylor-series-type expansion $V_2(\mathbf{R})$ is physically meaningful. Note that, in (4.14), β_i is a trial-and-error parameter, n_i is an even integer and ξ is a small number chosen to avoid numerical overflows at $E = E_{\text{min}}$.

The ES and MES schemes have been successfully applied to obtain PESs of several triatomic [11, 61, 62] and tetratomic [63–65] molecules, including multi-sheeted ones [12, 66–68], and have provided some of the most accurate global form thus far reported for those systems.

Bibliography

- [1] P. J. Kuntz, “Features of Potential Energy Surfaces and Their Effect on Collisions,” in *Dynamics of Molecular Collisions: Part B* (Springer US, 1976) Chap. 2, pp. 53–120.
- [2] J. S. Wright and S. K. Gray, *J. Chem. Phys.* **69**, 67 (1978).
- [3] J. N. L. Connor, *Comp. Phys. Comm.* **17**, 117 (1979).
- [4] N. E. Henriksen and F. Y. Hansen, *Theories of Molecular Reaction Dynamics: The Microscopic Foundation of Chemical Kinetics* (Oxford University Press, New York, 2008).
- [5] K. Bolton, W. L. Hase, and G. H. Peslherbe, in *Modern Methods for Multidimensional Dynamics Computations in Chemistry*, edited by G. M. Sukker, N. Wazzan, A. Ahmed, and R. Hilal (World Scientific Publishing, Singapore, 1998) Chap. 5, pp. 143–189.
- [6] A. J. C. Varandas, in *Conical Intersections: Electronic Structure, Dynamics & Spectroscopy*, Advanced Series in Physical Chemistry, Vol. 15, edited by W. Domcke, D. R. Yarkony, and H. Köppel (World Scientific Publishing, Singapore, 2004) Chap. 5, pp. 205–270.
- [7] A. J. C. Varandas, S. P. J. Rodrigues, and V. M. O. Batista, *Chem. Phys. Lett.* **424**, 425 (2006).
- [8] A. J. C. Varandas and S. P. J. Rodrigues, *Spectrochim. Acta Mol. Biomol. Spectrosc.* **58**, 629 (2002).

- [9] A. J. C. Varandas and S. P. J. Rodrigues, *J. Phys. Chem. A* **110**, 485 (2006).
- [10] S. P. J. Rodrigues, A. C. G. Fontes, Y. Q. Li, and A. J. C. Varandas, *Chem. Phys. Lett.* **516**, 17 (2011).
- [11] A. J. C. Varandas, *J. Chem. Phys.* **105**, 3524 (1996).
- [12] A. J. C. Varandas, *J. Chem. Phys.* **119**, 2596 (2003).
- [13] G. C. Schatz, *Rev. Mod. Phys.* **61**, 669 (1989).
- [14] J. N. Murrell, S. Carter, S. C. Farantos, P. Huxley, and A. J. C. Varandas, *Molecular Potential Energy Functions* (John Wiley & Sons, Chichester, 1984).
- [15] N. Sathyamurthy, *Comput. Phys. Rep.* **3**, 1 (1985).
- [16] D. G. Truhlar, R. Steckler, and M. S. Gordon, *Chem. Rev.* **87**, 217 (1987).
- [17] A. J. C. Varandas, *Adv. Chem. Phys.* **74**, 255 (1988).
- [18] F. O. Ellison, *J. Am. Chem. Soc.* **85**, 3540 (1963).
- [19] J. C. Tully, *Adv. Chem. Phys.* **42**, 63 (1980).
- [20] P. J. Kuntz, "Interaction Potentials II: Semiempirical Atom-Molecule Potentials for Collision Theory," in *Atom-Molecule Collision Theory: A Guide for the Experimentalist*, edited by R. B. Bernstein (Springer US, Boston, MA, 1979) pp. 79–110.
- [21] A. J. C. Varandas, *Mol. Phys.* **53**, 1303 (1984).
- [22] A. J. C. Varandas, *J. Mol. Struct.: THEOCHEM* **120**, 401 (1985).
- [23] A. J. C. Varandas, *J. Chem. Phys.* **138**, 054120 (2013).
- [24] T.-S. Ho and H. Rabitz, *J. Chem. Phys.* **104**, 2584 (1996).
- [25] T. Hollebeek, T.-S. Ho, and H. Rabitz, *Annu. Rev. Phys. Chem.* **50**, 537 (1999).
- [26] D. R. McLaughlin and D. L. Thompson, *J. Chem. Phys.* **59**, 4393 (1973).

- [27] N. Sathyamurthy and L. M. Raff, *J. Chem. Phys.* **63**, 464 (1975).
- [28] K. C. Thompson, M. J. T. Jordan, and M. A. Collins, *J. Chem. Phys.* **108**, 564 (1998).
- [29] T. Ishida and G. C. Schatz, *Chem. Phys. Lett.* **314**, 369 (1999).
- [30] A. J. C. Varandas and J. N. Murrell, *Faraday Discuss. Chem. Soc.* **62**, 92 (1977).
- [31] M. Cernei, A. Alijah, and A. J. C. Varandas, *J. Chem. Phys.* **118**, 2637 (2003).
- [32] L. P. Viegas, M. Cernei, A. Alijah, and A. J. C. Varandas, *J. Chem. Phys.* **120**, 253 (2004).
- [33] A. J. C. Varandas, A. Alijah, and M. Cernei, *Chem. Phys.* **308**, 285 (2005).
- [34] B. R. L. Galvão and A. J. C. Varandas, *J. Phys. Chem. A* **115**, 12390 (2011).
- [35] V. C. Mota and A. J. C. Varandas, *J. Phys. Chem. A* **112**, 3768 (2008).
- [36] A. J. C. Varandas, *J. Chem. Phys.* **129**, 234103 (2008).
- [37] A. J. C. Varandas, *Chem. Phys. Lett.* **471**, 315 (2009).
- [38] B. R. L. Galvão, P. J. S. B. Caridade, and A. J. C. Varandas, *J. Chem. Phys.* **137**, 22A515 (2012).
- [39] C. A. Mead and D. G. Truhlar, *J. Chem. Phys.* **77**, 6090 (1982).
- [40] R. N. Porter, R. M. Stevens, and M. Karplus, *J. Chem. Phys.* **49**, 5163 (1968).
- [41] B. R. L. Galvão, V. C. Mota, and A. J. C. Varandas, *J. Phys. Chem. A* **119**, 1415 (2015).
- [42] B. R. L. Galvão, V. C. Mota, and A. J. C. Varandas, *Chem. Phys. Lett.* **660**, 55 (2016).
- [43] A. J. C. Varandas, *Mol. Phys.* **60**, 527 (1987).
- [44] A. J. C. Varandas, *Chem. Phys. Lett.* **194**, 333 (1992).
- [45] A. J. C. Varandas and S. P. J. Rodrigues, *Chem. Phys. Lett.* **245**, 66 (1995).

- [46] M. A. Matías and A. J. C. Varandas, *Mol. Phys.* **70**, 623 (1990).
- [47] S. P. J. Rodrigues and A. J. C. Varandas, *Phys. Chem. Chem. Phys.* **2**, 435 (2000).
- [48] A. J. C. Varandas and J. D. Silva, *J. Chem. Soc., Faraday Trans. 2* **82**, 593 (1986).
- [49] A. J. C. Varandas and J. D. Silva, *J. Chem. Soc., Faraday Trans.* **88**, 941 (1992).
- [50] E. Martínez-Núñez and A. J. C. Varandas, *J. Phys. Chem. A* **105**, 5923 (2001).
- [51] C. M. R. Rocha and A. J. C. Varandas, *J. Chem. Phys.* **143**, 074302 (2015).
- [52] W. Domcke, D. R. Yarkony, and H. Köppel, *Conical Intersections: Electronic Structure, Dynamics & Spectroscopy*, Advanced Series in Physical Chemistry, Vol. 15 (World Scientific, Singapore, 2004).
- [53] T. Pacher, L. S. Cederbaum, and H. Köppel, *Adv. Chem. Phys.* **87**, 293 (1993).
- [54] J. G. Atchity and K. Ruedenberg, *Theor. Chem. Acc.* **97**, 47 (1997).
- [55] A. J. Doblynn and P. J. Knowles, *Mol. Phys.* **91**, 1107 (1997).
- [56] A. Thiel and H. Köppel, *J. Chem. Phys.* **110**, 9371 (1999).
- [57] J. N. Murrell and A. J. C. Varandas, *Mol. Phys.* **57**, 415 (1986).
- [58] A. J. C. Varandas and A. I. Voronin, *Mol. Phys.* **85**, 497 (1995).
- [59] J. N. Murrell, S. Carter, I. M. Mills, and M. F. Guest, *Mol. Phys.* **42**, 605 (1981).
- [60] A. J. C. Varandas, in *Reaction and Molecular Dynamics*, Lecture Notes in Chemistry, Vol. 75, edited by A. Laganà and A. Riganelli (Springer Berlin Heidelberg, 2000) pp. 33–56.
- [61] R. Prosmiti, O. L. Polyansky, and J. Tennyson, *Chem. Phys. Lett.* **273**, 107 (1997).
- [62] O. L. Polyansky, R. Prosmiti, W. Klopper, and J. Tennyson, *Mol. Phys.* **98**, 261 (2000).

-
- [63] A. J. C. Varandas, S. P. J. Rodrigues, and P. A. J. Gomes, Chem. Phys. Lett. **297**, 458 (1998).
- [64] H. G. Yu and A. J. C. Varandas, Chem. Phys. Lett. **334**, 173 (2001).
- [65] W. H. Ansari and A. J. C. Varandas, J. Phys. Chem. A **106**, 9338 (2002).
- [66] A. J. C. Varandas, J. Chem. Phys. **107**, 867 (1997).
- [67] A. J. C. Varandas, A. I. Voronin, and P. J. S. B. Caridade, J. Chem. Phys. **108**, 7623 (1998).
- [68] B. R. L. Galvão, S. P. J. Rodrigues, and A. J. C. Varandas, J. Chem. Phys. **129**, 044302 (2008).

Chapter 5

Exploring potential energy surfaces via rovibrational calculations

Once a reliable and physically motivated form for the PES have been acquired, an essential step to obtain dynamical observables such as those related to molecular spectroscopy and chemical dynamics involves the solution of the nuclear Schrödinger equation [Eq. (1.31)]. Similarly to the electronic-motion case, such a problem is also subjected to some approximations [1, 2]; the most obvious is the adiabatic ansatz (1.39). One of the most fundamental differences between electronic structure and nuclear dynamics problems is that, in the former, we are interested only in the ground and possibly in a few excited states, while in the latter we often want to compute many hundreds or even thousands of excited states. This is particularly true when dealing with molecular rotation-vibration motion [3].

The theoretical calculation of rovibrational energy levels is characterized by a fruitful interplay between state-of-the-art molecular spectroscopy and quantum-mechanics. Obviously, what brings them together is the very notion of PESs. As noted previously, such *ab initio* potentials seldom meet the standards of spectroscopic accuracy, specially if more extended, high-energy regions of the nuclear configuration space are of interest. Although experimental spectra cannot in general be directly inverted to yield PESs, it does provide the most stringent test for the theoretically obtained potentials and the

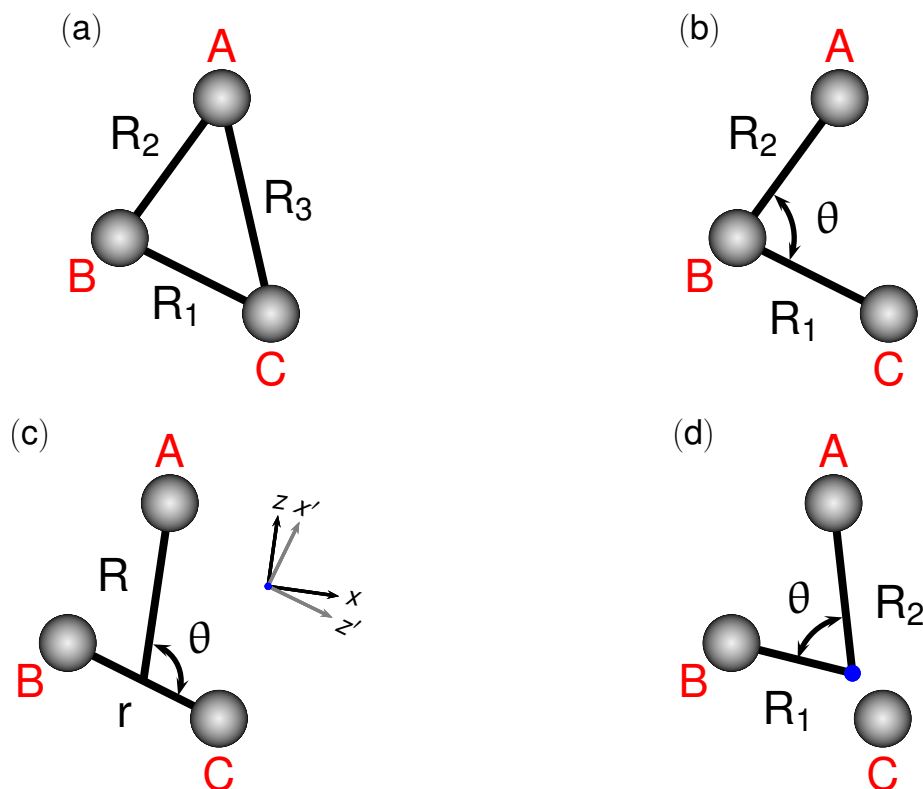


Figure 5.1: Internal coordinate systems for a triatomic molecule ABC. (a). Bond-length coordinates. (b). Bond-length-bond-angle or valence coordinates. (c). Jacobi or scattering coordinates and (d). Radau coordinates. Panel (c) illustrates different embedding schemes for Jacobi coordinates which place R (R embedding) or r (r embedding) along the body-fixed z -axis.

properties derived from them. Thus, the only practical way of improving potentials is to minimize the difference between experimental and predicted observables [4–6].

5.1 Coordinate systems and embedding schemes

It is useful to consider the nuclear motion in a molecular system as falling into three categories

- (1) Translation of the whole molecule through space.
- (2) Rotation of the molecule.
- (3) Internal or vibrational motion.

As noted in section 1.2, the translational motion of the system gives a continuous spectrum which is unattractive if one is interested in spectroscopy. Thus, it is often possible to separate off the center-of-mass motion and setting up a space-fixed frame, *i.e.*, by defining a moving axis with origin at the COM [3, 7–10]. The remaining $3H-3$ translation-free nuclear coordinates are a mixture of those representing vibration and rotation. In order to formulate any theoretical treatment of the bond state problem, it is generally desirable to distinguish between these latter degrees of freedom by setting up the so-called body-fixed frame. Although there is no unique way of fixing the rotating axis to the molecule [11–13], the BF representation allows the introduction of several decoupling approximations (*i.e.*, by minimizing rovibrational interactions) so that the resulting equations are generally simpler than those obtained from the SF Hamiltonian [14]. In this regard, the choice of the coordinate system appropriate to the molecule under study plays a central role. For instance, it is well known that the use of orthogonal coordinates such as Jacobi and Radau coordinates¹ (see Figure 5.1) generate rather simple and general internal kinetic energy operators which contains no cross-derivative terms [5, 14]. Indeed, an optimal set of coordinates must take advantage of the highest symmetry present in the system as well as span all of the nuclear configuration space accessible for the molecule of interest [16].

Once a suitable coordinate system have been judiciously chosen, the process of deriving a BF Hamiltonian also requires the specification of a set of Cartesian axes defined in the frame of the molecule [see Figure 5.1(c)]. This process is often called “embedding” [4–6]. Apart from the proper choice of internal coordinates, a suitable embedding scheme may shift away the inherent singularities of the BF Hamiltonian to regions of the nuclear configuration space not physically accessible to the problem at hand. The rotational motions are then represented by the three Euler angles $\Theta_i (i = 1, 2, 3)$ which determine the

¹Jacobi coordinates are suitable for describing atom-diatom complexes and systems with large amplitude motion. In such a coordinate system, r is the bond length of the BC diatomic, R is the distance from the atom A to the center-of-mass of BC and θ is the included angle. Conversely, in the Radau coordinate system, R_1 and R_2 measure the distance of the two light atoms from the so-called canonical point [15], which for light-heavy-light systems lies very close to the center of the heavy atom C.

orientation of the BF frame with respect to the SF one. Note that the actual definition of the BF axes is only relevant for rotationally excited states since the Hamiltonian for $J=0$ is independent of this choice. After setting on some definitions of the molecule-fixed frame, $3H-6$ (or $3H-5$ for linear molecules) translation- and rotation-free vibrational degrees of freedom remain which can be readily employed in the construction of the internal-coordinate Hamiltonian.

5.2 Hamiltonians

Early approaches to the nuclear-motion problem were primarily based on an approximate separability of the vibrational and rotational degrees of freedom (the so-called Eckart conditions [17]) and a harmonic expansion of the PES around an equilibrium geometry [18, 19]. In such normal mode Hamiltonians, the reference configuration is rigidly attached to the BF axes so that the nuclear motions consist essentially of rigid rotations and small amplitude vibrations [3]. Among these, the Watson's Hamiltonian [20, 21] has been the most widely used form for calculating low-lying rovibrational energy states of (semi-) rigid triatomic molecules. Its success owes much to the pioneering variational method due to Whitehead and Handy [22]. However, it has long been recognized that, for highly anharmonic systems containing large-amplitude bending motions such as CH_2^+ [23, 24], the Watson's Hamiltonian gives rise to unphysical, spurious solutions. This is an expected result since the Eckart's embedding scheme is only valid in the small amplitude limit [24]. Note that, as demonstrated by Watson himself, the originally proposed form has an inherent singularity at linear geometries [21].

Expressions for the full vibration-rotation Hamiltonian for non-rigid triatomic species, which do not rely on the Eckart conditions nor in the concept of an equilibrium geometry, have been extensively discussed in the literature by Sutcliffe and Tennyson [4, 11–13, 24–27]. These authors proposed [11, 12] a rather general BF Hamiltonian which is expressed in terms of two lengths and an included angle and that includes as limiting cases those previously derived in Jacobi [26, 27] and valence [28, 29] coordinates. Suffice it to add that the first Hamiltonians especially designed for calculating rovibrational states in floppy triatomic molecules were those based on the (non- and semi-) rigid bender method of

Bunker and Jensen [30, 31]. In such an approach, the small amplitude vibrations (normal coordinates) are handled by means of standard perturbation theory, whereas the large amplitude motion is treated in a separate (and accurate) manner by defining a suitable bending vibrational coordinate.

Regardless the set of internal coordinates so chosen, the general expression for the rotation-vibration BF Hamiltonian ($\hat{\mathcal{H}}_{RV}$) can be cast in the form² [4, 28]

$$\hat{\mathcal{H}}_{RV} = \hat{\mathcal{T}}_{RV} + \hat{\mathcal{T}}_V + V, \quad (5.1)$$

where $\hat{\mathcal{T}}_{RV}$ and $\hat{\mathcal{T}}_V$ are the rotation-vibration and purely vibrational kinetic energy operators, respectively, with V being the corresponding potential for the molecule (and electronic state) under consideration. Note that, for a non-rotating ($J=0$) system, the term $\hat{\mathcal{T}}_{RV}$ vanishes. Derivation of the kinetic energy operators in Eq. (5.1), in any coordinate set, can be accomplished by using the well-known Podolsky transformation [32] or by means of the increasingly popular method of Sutcliffe [33]. For a triatomic molecule A-BC, $\hat{\mathcal{T}}_V$ can be written in Jacobi coordinates as [26, 27]

$$\begin{aligned} \hat{\mathcal{T}}_V(r, R, \theta) = & -\frac{1}{2\mu R^2} \frac{\partial}{\partial R} \left(R^2 \frac{\partial}{\partial R} \right) - \frac{1}{2\mu_d r^2} \frac{\partial}{\partial r} \left(r^2 \frac{\partial}{\partial r} \right) \\ & - \frac{1}{2} \left(\frac{1}{\mu R^2} + \frac{1}{\mu_d r^2} \right) \frac{1}{\sin \theta} \frac{\partial}{\partial \theta} \left(\sin \theta \frac{\partial}{\partial \theta} \right), \end{aligned} \quad (5.2)$$

where r is the bond length of the BC diatomic, R is the distance from the atom A to the COM of BC and θ is the included angle [see Figure 5.1(c)]. The reduced masses are [4]

$$\mu = \frac{1}{\mathcal{M}_A} + \frac{1}{\mathcal{M}_B + \mathcal{M}_C} \quad \text{and} \quad \mu_d = \frac{1}{\mathcal{M}_B} + \frac{1}{\mathcal{M}_C}. \quad (5.3)$$

In contrast to $\hat{\mathcal{T}}_V$, the expression for the rotation-vibration kinetic energy operator $\hat{\mathcal{T}}_{RV}$ depends on the embedding scheme chosen. If a R embedding is assumed [see Figure 5.1(c)],

²Eq. (5.1) can be readily obtained from the general forms (1.25) and (1.26) by considering the approximate separability of the electronic and nuclear degrees of freedom as well as by neglecting mass polarization terms. In so doing, one can define $\hat{\mathcal{H}}_{RI} \approx \hat{\mathcal{H}}_{RV}$ with $\hat{\mathcal{T}}_R \approx \hat{\mathcal{T}}_{RV}$ and $\hat{\mathcal{H}}_I \approx \hat{\mathcal{T}}_V + V$.

its form is given by [26]

$$\begin{aligned} \hat{\mathcal{T}}_{RV}(r, R, \theta) = & \frac{1}{2} \left[\frac{1}{\mu R^2} \left(\hat{\Pi}_x^2 + \hat{\Pi}_y^2 \right) + \left(\frac{1}{\mu R^2 \tan^2 \theta} + \frac{1}{\mu_d r^2 \sin^2 \theta} \right) \hat{\Pi}_z^2 \right. \\ & \left. - \frac{1}{\mu R^2 \tan \theta} \left(\hat{\Pi}_x \hat{\Pi}_z + \hat{\Pi}_z \hat{\Pi}_x \right) \right] - \frac{i}{\mu R^2} \left(\frac{\partial}{\partial \theta} + \frac{1}{2 \tan \theta} \right) \hat{\Pi}_y, \end{aligned} \quad (5.4)$$

where the quantities $\hat{\Pi}_\alpha$ ($\alpha = x, y, z$) are the components of total angular momentum operator which depend only on the three Euler angles. Note that, if the r embedding is considered, the resulting $\hat{\mathcal{T}}_{RV}$ operator is simply obtained by making the changes $R \rightarrow r$ and $\mu \rightarrow \mu_d$ in Eq. (5.4).

In fact, the solutions of the eigenvalue problem specified by the Hamiltonian (5.1) can be written as a sum of products of internal functions and angular momentum eigenfunctions³

$$|\chi\rangle = \sum_{k=-J}^J |\xi_k^J(r, R, \theta)\rangle |JMk\rangle. \quad (5.5)$$

By allowing (5.1) [with the form given in (5.2) and (5.4)] to operate on Eq. (5.5), multiplying from the left by $\langle JMk'|$ and integrating over Euler angles, one can then obtain an effective Hamiltonian [11, 12, 26]

$$\hat{\mathcal{H}}_{RV}^{eff} = \hat{\mathcal{T}}_{RV}^{eff} + \delta_{k'k} \hat{\mathcal{T}}_V + \delta_{k'k} V, \quad (5.6)$$

that depends only on the internal coordinates and is block-diagonal in J . The part arising from $\hat{\mathcal{T}}_{RV}^{eff}$ assumes the form [26]

$$\begin{aligned} \hat{\mathcal{T}}_{RV}^{eff} = & \delta_{k'k} \left[\frac{J(J+1) - 2k^2}{2\mu R^2} + \frac{k^2}{2 \sin^2 \theta} \left(\frac{1}{\mu R^2} + \frac{1}{\mu_d r^2} \right) \right] \\ & + \delta_{k'k+1} \frac{1}{2\mu R^2} C_{Jk}^+ \left(-\frac{\partial}{\partial \theta} + \frac{k}{\tan \theta} \right) \\ & + \delta_{k'k-1} \frac{1}{2\mu R^2} C_{Jk}^- \left(\frac{\partial}{\partial \theta} + \frac{k}{\tan \theta} \right), \end{aligned} \quad (5.7)$$

where $C_{Jk}^\pm = [J(J+1) - k(k \pm 1)]^{1/2}$. Clearly, $\hat{\mathcal{T}}_{RV}^{eff}$ is diagonal in J but not in k . Note that, because the PES and the vibrational kinetic energy operator are functions of the internal coordinates only, they are naturally diagonal in both J and k [see Eq. (5.6)].

³Eq. (5.5) can also be obtained from the general form (1.27) by setting $|\Phi_k^J\rangle \approx |\psi\rangle |\xi_k^J\rangle$ and noting that $|\psi\rangle$ which is a solution of the clamped-nuclei electronic problem do not depend on J .

It is worth pointing out that, differently from the purely vibrational part, both $\hat{\mathcal{H}}_{RV}$ and $\hat{\mathcal{H}}_{RV}^{eff}$ operators have singularities at linear arrangements for which $\theta = 0$ or π . This issue can be further addressed by choosing a convenient angular basis and constructing another effective (radial) Hamiltonian in which all angular variables (including θ) are integrated out [11, 12, 26]. As noted by Tennyson [4], the explicit coupling between polynomials depending on θ (such as normalized associated Legendre functions) and the rotational functions $|JMk\rangle$ by means of their common index k allows the cancellation of singular terms in Eqs. (5.4) and (5.7).

5.3 Solutions to the bound-state problem

Likewise the electronic-motion case, the solutions to the bound-state problem are generally obtained by making use of two main strategies, *i.e.*, by means of perturbation methods or variational approaches [14, 34]. The first involves the expansion of the exact rotation-vibration Hamiltonian into a Taylor series about the equilibrium geometry whose components are clearly identified as a zeroth-order part and a small perturbation. This former contribution, which has known eigenfunctions and eigenvalues, is generally associated to the standard harmonic-oscillator rigid-rotor Hamiltonian, while the corrections due to anharmonicities of the potential, Coriolis and centrifugal distortion effects are self-contained in the higher-order perturbation terms [18, 34, 35]. Although being of fundamental importance to any interpretation of rotation-vibration data⁴, the solutions based on perturbation approaches are primarily obtained from the basic assumption that the vibrational displacements in the molecule are of small amplitude compared to the equilibrium bond lengths and bond angles. Thus, for molecules with large amplitude vibrational motion (or in highly excited states), the application of such standard treatment is known to generate an oscillatory or even a non-convergent perturbation series,

⁴As a result of such perturbation theoretic approach the energies become expressed as a power series in the rotation and vibration quantum numbers [*i.e.*, $J(J+1)$ and $(v+1/2)$] whose coefficients are determined from a fit to the experimental and/or *ab initio* data. Additionally, perturbation theory also gives expressions for the rotation-vibration constants in terms of the equilibrium geometry, harmonic and anharmonic constants of the molecular PESs.

and hence meaningful results can only be accomplished by employing a fully variational procedure [4, 22, 28, 29, 34, 36].

As usual in methodologies based on the variational principle, one generally provides a trial wave function which, for the particular case under consideration, can be readily defined as a sum of products of suitably chosen vibrational and rotational basis functions. Rotation-vibration energy levels can then be obtained by diagonalizing the resulting matrix representation of the Hamiltonian in this basis which, as naturally warranted by any variational treatment, are always upper bounds to the true solutions [34]. The variational method has proved very effective in calculating many rovibrational energy levels of non-rigid triatomic species [4, 28, 29, 36]. However, extensive applications to floppy molecules have shown that such an approach has also several shortcomings, particularly when dealing with highly excited vibrational states which cover large, anharmonic regions of the PESs [14]. Pointwise representations of the internal degrees of freedom such as the discrete variable representation (DVR) method [37–39] have also been developed that are more appropriate for delocalized wave functions of large amplitude vibrational states than the usual bases.

5.3.1 The variational method

As discussed previously, the eigenvalues and eigenvectors of the effective Hamiltonian (5.6) can be readily obtained by means of the linear variational method [40–43], *i.e.*, one introduces a set of basis functions and the Hamiltonian matrix \mathcal{H}_{RV}^{eff} in this basis is build and then diagonalized. A suitably chosen trial wave function for the i th rovibrational state of a triatomic molecule can be written (in Jacobi coordinates) as [4, 28, 34, 36]

$$|\chi_i^{J,M}\rangle = \sum_{k=-J}^J \sum_l \sum_m \sum_n c_{n,m,l}^{J,k,i} |X_n(r)\rangle |Y_m(R)\rangle |Z_{l,k}(\theta)\rangle |JMk\rangle, \quad (5.8)$$

where $|X_n(r)\rangle$ and $|Y_m(R)\rangle$ are some convenient one-dimensional, orthogonal radial basis functions, $|Z_{l,k}(\theta)\rangle$ is generally associated Legendre polynomials and $|JMk\rangle$ represent the usual normalized Wigner rotation matrix elements $[\mathcal{D}_{Mk}^J(\Theta)]$ [44]. Clearly, the success of any variational method depends upon the selection of a suitable basis for representing

the radial degrees of freedom and the ability to evaluate the matrix elements [4]

$$\begin{aligned} H_{ji} &= \left\langle X_{n'}(r)Y_{m'}(R)Z_{l',k'}(\theta) \left| \mathcal{H}_{RV}^{\text{eff}} \right| X_n(r)Y_m(R)Z_{l,k}(\theta) \right\rangle \\ &= \langle X_{n'}(r)Y_{m'}(R)Z_{l',k'}(\theta) | \langle JMk' | \mathcal{H}_{RV} | JMk \rangle | X_n(r)Y_m(R)Z_{l,k}(\theta) \rangle, \end{aligned} \quad (5.9)$$

so that the secular equation problem can be accurately solved. The main strategy therefore is to use known analytic solutions of model one-dimensional vibrational problems that contain parameters which can be adjusted to the current potential, yielding therefore a compact basis set representation [14]. Indeed, the most commonly used forms for $|X_n(r)\rangle$ and $|Y_m(R)\rangle$ in Eq. (5.8) are Morse oscillator-like wave functions and spherical oscillator functions [4, 22, 28, 29, 34, 36]. Note that, in analogy to electronic structure theory, one can also determine in advance the best simple product functions (and their parameters) by means of a SCF step in which some effective (zeroth-order) model Hamiltonian is considered. Since these functions form, in principle, a complete and orthonormal set, they can be used *a posteriori* as expansion basis in the CI-like trial wave function (5.8) [34, 45–47].

Once the type and size of the weighted orthogonal polynomial basis have been determined, the evaluation of the matrix elements (5.9) can be accomplished numerically by using convenient Gaussian quadrature formulas [48]. Note that, as emphasized by Sutcliffe and Tennyson [4, 11, 12], all the angular matrix elements can be computed analytically, with the exception of those involving angular integration over the potential⁵ which are usually obtained by means of Gauss-Legendre quadrature rules [36]. Additionally, for both the Morse oscillator and the spherical oscillator functions, the matrix elements of the differential terms in $\hat{\mathcal{T}}_V$ [the first and second terms on the RHS of Eq. (5.2)] can be evaluated analytically, with all the remaining radial integrals being computed by using M -point Gauss-Laguerre quadrature schemes [4].

For fully coupled rovibrational calculations, the size of the secular problem to be solved increases largely with J and makes therefore the computation of rotationally excited states prohibitively expensive. This is so since every product of internal coordinate

⁵In fact, if the PES is assumed to be represented by a Legendre expansion [see later Eq. (29) of chapter 6] then angular integration over the potential can be performed analytically [4].

functions in Eq. (5.8) must be associated with $2J+1$ rotational functions. To obviate these limitations, Sutcliffe and Tennyson [25, 49] proposed the use of a two-step variational procedure which has extended the range of J s that can be covered in practical variational calculations [14]. In such an approach, one first obtains the solutions of a Coriolis decoupled problem, *i.e.*, by neglecting the off-diagonal terms in Eq. (5.7), for which k , the projection of J onto the body-fixed z -axis, is a good quantum number. The resulting eigenfunctions can then be used in a subsequent step as basis for the construction (and diagonalization) of the full Hamiltonian matrix [25, 49]. Note that the main advantage of such a procedure is that the solutions of the decoupled Hamiltonian provide a well-adapted and compact basis for the full problem, and hence not all of them are actually required to obtain fully converged rovibrational states [24].

Indeed, the feasibility of any variational treatment is clearly dictated by the size of the final Hamiltonian matrix that must be handled. This is particularly critical when highly excited vibrational states are envisaged. For them, one generally needs a large number of oscillator basis functions in order to ensure convergence of the band origins, which makes the calculation computationally unfeasible [14]. Such entanglements can often be tackled on going from the usual finite basis representation (FBR) to a “pointwise representation” of the bound-state problem [37–39].

5.3.2 Discrete variable representation

As noted above, in the FBR, the Hamiltonian operator is represented in terms of a (finite) set of “diffuse” basis functions whose elements are generally determined by numerical quadrature. Suffice it to highlight that, as opposed to the FBR, in the so-called variational basis representation (VBR) [14], all the required matrix elements are computed exactly, and hence the only source of error is due to basis set incompleteness.

DVRs, on the other hand, are representations in which the associated basis functions are in some sense “localized” about grid points on a coordinate space [37, 39]. The fundamental assumption behind the use of DVRs is that matrix representations of coordinate-dependent operators are always diagonal and their matrix elements are given simply by the value of this latter quantity at the DVR grid points. In this sense, DVR-based

approaches have acquired great success in providing efficient and accurate numerical solutions to nuclear dynamics problems, inasmuch as they greatly simplify the evaluation of Hamiltonian operators. Indeed, since kinetic energy matrices can efficiently be computed, potential matrix elements are merely the value of the PESs at the DVR pivots [37–39].

To construct a DVR, one should first determine an appropriate set of finite global basis functions and then establish the proper transformational relationship between point and function space. As first demonstrated by Harris *et al.* [50], such a task can be accomplished by simply diagonalizing the matrix representation (in the VBR) of the position operator whose eigenvalues and eigenvectors are nothing but the DVR points and basis functions, respectively. Dickinson and Certain [51] provided the formal basis for the technique, and proved that, for sets of M classical orthogonal polynomials times their appropriate weight functions, the diagonal elements of the coordinate matrix in the DVR were in fact the points of the Gaussian quadrature associated to the FBR. Indeed, Gaussian quadrature DVRs became the standard representation in which to base discrete variable approaches [37, 39].

Consider a general (non-rotating) one-dimensional system with Hamiltonian defined simply by

$$\hat{\mathcal{H}} = \hat{\mathcal{T}} + V. \quad (5.10)$$

Again, to obtain the desired eigenvalues and eigenfunctions, one could then express $\hat{\mathcal{H}}$ in terms of a truncated orthonormal basis function $\{f_i(x)\}_{i=1}^M$ having the form of a classical polynomial times the square root of a weight function $\omega(x)$ [5]

$$f_i(x) = \sqrt{\omega(x)} p_i(x). \quad (5.11)$$

For instance, if $f_i(x)$ are chosen to be harmonic oscillator wave functions, $\omega(x) = \exp(-x^2)$ and $p_i(x) = N_i H_i(x)$ are normalized Hermite polynomials [42]. With the above basis, the M by M Hamiltonian matrix can then be diagonalized. One of the main drawback of such an approach is that, while the matrix representation of the kinetic energy operator $\hat{\mathcal{T}}$ are computed only once for a chosen basis, the corresponding $M(M+1)/2$ elements

(integrals) of \mathbf{V} should be recalculated for each choice of $V(x)$. In fact, if these latter can be evaluated exactly, then

$$V_{ji}^{\text{VBR}} = \langle f_j(x) | V(x) | f_i(x) \rangle \quad (5.12)$$

is the matrix elements of \mathbf{V} expressed in the VBR [5]. Recall that, in such a representation, the only source of error is due to the truncation of the basis [39].

Conversely, we can also choose to evaluate all the integrals necessary to build \mathbf{V} in an approximate way by using for each of them an M -point Gaussian quadrature formula [48]

$$V_{ji}^{\text{VBR}} \approx V_{ji}^{\text{FBR}} = \sum_{\alpha=1}^M \frac{w_{\alpha}}{\omega(x_{\alpha})} f_j^*(x_{\alpha}) V(x_{\alpha}) f_i(x_{\alpha}), \quad (5.13)$$

where, $\{x_{\alpha}\}_{\alpha=1}^M$ and $\{w_{\alpha}\}_{\alpha=1}^M$ are the set of Gaussian points and weights, respectively, associated to the polynomial basis. Note that, in the above equation, the number of quadrature points is set equal to the number of basis functions. Thus, in addition to the basis set incompleteness error, in such FBR, approximations inherent to the use of Gaussian quadratures are also introduced.

Dickinson and Certain [51] have shown that, for a basis of M classical orthogonal polynomials times their associated weight functions $\{f_i(x)\}$, there will always be an orthogonal transformation that switches between representations in the M -quadrature points (the DVR) and the one in the M -dimensional function space (the FBR). Thus, from Eq. (5.13), we can then define the elements of a M by M transformation matrix \mathbf{T} as [39]

$$T_{\alpha i} = \sqrt{\frac{w_{\alpha}}{\omega(x_{\alpha})}} f_i(x_{\alpha}), \quad (5.14)$$

and the diagonal matrix

$$\mathbf{V}^{\text{DVR}} = \text{diag}(V(x_1), V(x_2), V(x_3), \dots, V(x_M)). \quad (5.15)$$

By making use of the above expressions, one can now rewrite the anzats (5.13) in matrix form as [37–39]

$$\mathbf{V}^{\text{VBR}} \approx \mathbf{V}^{\text{FBR}} = \mathbf{T}^{\dagger} \mathbf{V}^{\text{DVR}} \mathbf{T}. \quad (5.16)$$

As clearly seen from the above relations, the matrix representation of the potential energy operator $V(x)$ in the DVR basis is always diagonal and the associated matrix elements are

given simply by the value of the potential itself at the quadrature points (or, equivalently, at the DVR pivots) [51]. In fact, one of the main advantages of DVR-based approaches is that \mathbf{V}^{VBR} can be approximately calculated without making any integral at all [5]. The orthonormal set of DVR basis $\{g_\alpha(x)\}_{\alpha=1}^M$ can then be defined from the DVR-to-FBR transformation (unitary) matrix \mathbf{T} as [39]

$$g_\alpha(x) = \sum_{i=1}^M T_{\alpha i} f_i(x). \quad (5.17)$$

An important property of such functions is that they are strongly localized around their respective focal points x_α and vanish for all $x_\beta \neq x_\alpha$ [39].

As noted above, differently from \mathbf{V} , kinetic energy matrices can, in principle, be evaluated (sometimes even analytically) in the M function space. In this case, the transformation from, say, VBR to DVR can be usually performed [52]. With this in mind, one can define the matrix representation of the Hamiltonian (5.10) in the DVR basis as [39]

$$\mathcal{H}^{\text{VBR}} \approx \mathcal{H}^{\text{DVR}} = \mathcal{T}^{\text{DVR}} + \mathbf{V}^{\text{DVR}}, \quad (5.18)$$

where $\mathcal{T}^{\text{DVR}} = \mathbf{T}\mathcal{T}^{\text{VBR}}\mathbf{T}^\dagger$. Suffice it to add that the use of DVRs, as made explicit in Eq. (5.16), introduce the same approximation to the VBR as that implied by the use of quadrature schemes in evaluating matrix elements (the FBR). For this reason, DVRs are generally said to be isomorphic with the corresponding FBRs [37]. One of the main disadvantages in DVRs, however, is that the solutions of the eigenvalue equations dictated by the Hamiltonian (5.18) are not strictly variational, inasmuch as the quadrature error so introduced may cause some of the eigenvalues to be lower than their true BO values [53].

Up to this point, we have stressed the main aspects and convenience in the use of DVR-based approaches in dealing with general one-dimensional bound-state problems. Clearly, these advantages should become even more flagrant when higher dimensions are envisaged [5, 39]. The simplest way of introducing multi-dimensional DVRs is as direct products of one-dimensional DVRs for each of the coordinates. The required \mathbf{T} matrix is thus given by a direct product of 1D transformation matrices (5.14) [54–56]. A

major attraction of such an approach is that the resulting transformed Hamiltonians (in DVR) are very sparse so that efficient algorithms can be applied along with sequential diagonalization/truncation schemes⁶ [54, 55]. It should also be emphasized on passing the possibility that only one or two (large-amplitude) vibrational coordinates be treated in the DVR. For triatomic molecules, this concept led to the introduction of the so-called DVR-DGB methodology [38]. In this approach, the DVR is generally used to represent the bending coordinate, while a separate distributed Gaussian basis (DGB) is employed at each angle (*i.e.*, at the DVR grid points) to describe the motion of the radial degrees of freedom.

⁶In such schemes, low-dimensional Hamiltonian matrices are first diagonalized and the solutions with eigenvalues above certain cutoff energy are then used as a basis for subsequent higher-dimensional problems.

Bibliography

- [1] B. T. Sutcliffe, *Adv. Quantum Chem.* **28**, 65 (1997).
- [2] P. O. Löwdin, *J. Mol. Struc. THEOCHEM* **230**, 13 (1991).
- [3] E. B. Wilson, J. C. Decius, and P. C. Cross, *Molecular Vibrations: The Theory of Infrared and Raman Vibrational Spectra*, Vol. 1 (McGraw-Hill, 1955).
- [4] J. Tennyson, *Comput. Phys. Rep.* **4**, 1 (1986).
- [5] L. Lodi and J. Tennyson, *J. Phys. B: At. Mol. Opt. Phys.* **43**, 133001 (2010).
- [6] J. Tennyson, “High Accuracy Rotation-Vibration Calculations on Small Molecules,” in *Handbook of High-resolution Spectroscopy* (John Wiley & Sons, Ltd., 2011) pp. 551–571.
- [7] A. A. Kiselev, *J. Phys. B: Atom. Molec. Phys.* **3**, 904915 (1970).
- [8] B. T. Sutcliffe, *J. Mol. Struc. THEOCHEM* **259**, 29 (1992).
- [9] B. T. Sutcliffe, *J. Chem. Soc., Faraday Trans.* **89**, 2321 (1993).
- [10] B. T. Sutcliffe, *Theor. Chem. Acc.* **127**, 121 (2010).
- [11] B. T. Sutcliffe and J. Tennyson, *Mol. Phys.* **58**, 1053 (1986).
- [12] B. T. Sutcliffe and J. Tennyson, *Int. J. Quantum Chem.* **39**, 183 (1991).
- [13] J. Tennyson and B. T. Sutcliffe, *Int. J. Quantum Chem.* **42**, 941 (1992).

-
- [14] Z. Bačić and J. C. Light, *Annu. Rev. Phys. Chem.* **40**, 469 (1989).
- [15] B. R. Johnson and W. P. Reinhardt, *J. Chem. Phys.* **85**, 4538 (1986).
- [16] J. P. Leroy and R. Wallace, *Chem. Phys.* **111**, 11 (1987).
- [17] C. Eckart, *Phys. Rev.* **47**, 552 (1935).
- [18] E. B. Wilson and J. B. Howard, *J. Chem. Phys.* **4**, 260 (1936).
- [19] B. T. Darling and D. M. Dennison, *Phys. Rev.* **57**, 128 (1940).
- [20] J. K. G. Watson, *Mol. Phys.* **15**, 479 (1968).
- [21] J. K. G. Watson, *Mol. Phys.* **19**, 465 (1970).
- [22] R. J. Whitehead and N. C. Handy, *J. Mol. Spectrosc.* **55**, 356 (1975).
- [23] R. Bartholomae, D. Martin, and B. T. Sutcliffe, *J. Mol. Spectrosc.* **87**, 367 (1981).
- [24] B. T. Sutcliffe and J. Tennyson, *J. Chem. Soc., Faraday Trans. 2* **83**, 1663 (1987).
- [25] J. Tennyson and B. T. Sutcliffe, *Mol. Phys.* **58**, 1067 (1986).
- [26] J. Tennyson and B. T. Sutcliffe, *J. Chem. Phys.* **77**, 4061 (1982).
- [27] J. Tennyson and B. T. Sutcliffe, *J. Chem. Phys.* **79**, 43 (1983).
- [28] S. Carter and N. C. Handy, *Comput. Phys. Rep.* **5**, 117 (1986).
- [29] S. Carter and N. C. Handy, *Mol. Phys.* **57**, 175 (1986).
- [30] P. R. Bunker, *Annu. Rev. Phys. Chem.* **34**, 59 (1983).
- [31] P. Jensen, *Comput. Phys. Rep.* **1**, 1 (1983).
- [32] B. Podolsky, *Phys. Rev.* **32**, 812 (1928).
- [33] B. T. Sutcliffe, *Adv. Chem. Phys.* **114**, 1 (2000).

- [34] G. D. Carney, L. L. Sprandel, and C. W. Kern, *Adv. Chem. Phys.* , 305 (1978).
- [35] H. H. Nielsen, *Rev. Mod. Phys.* **23**, 90 (1951).
- [36] S. Carter and N. C. Handy, *Mol. Phys.* **47**, 1445 (1982).
- [37] J. C. Light, I. P. Hamilton, and J. V. Lill, *J. Chem. Phys.* **82**, 1400 (1985).
- [38] Z. Bačić and J. C. Light, *J. Chem. Phys.* **85**, 4594 (1986).
- [39] J. C. Light and T. Carrington, *Adv. Chem. Phys.* **114**, 263 (2000).
- [40] L. D. Landau and L. M. Lifshitz, *Quantum Mechanics Non-Relativistic Theory*, 2nd ed., Vol. 3 (Pergamon Press, Bristol, 1981).
- [41] D. A. McQuarrie and J. D. Simon, *Physical Chemistry A Molecular Approach*, 2nd ed. (University Science Books, Sausalito, 1997).
- [42] L. Pauling and E. B. Wilson, *Introduction to Quantum Mechanics with Applications to Chemistry*, Vol. 1 (McGraw-Hill Book Co., New York, 1935).
- [43] A. Szabo and N. S. Ostlund, *Modern Quantum Chemistry: Introduction to Advanced Electronic Structure Theory*, Vol. 1 (McGraw-Hill Book Co., New York, 1989).
- [44] D. M. Brink and G. R. Satchler, *Angular Momentum*, 3rd ed. (Oxford University Press, Oxford, 1994).
- [45] J. M. Bowman, *Acc. Chem. Res.* **19**, 202 (1986).
- [46] T. C. Thompson and D. G. Truhlar, *J. Chem. Phys.* **77**, 3031 (1982).
- [47] M. A. Ratner and R. B. Gerber, *J. Phys. Chem.* **90**, 20 (1986).
- [48] A. H. Stroud and D. Secrest, *Gaussian Quadrature Formulas* (Prentice-Hall, Englewood Cliffs, 1966).
- [49] B. T. Sutcliffe, S. Miller, and J. Tennyson, *Comput. Phys. Commun.* **51**, 73 (1988).

-
- [50] D. O. Harris, G. G. Engerholm, and W. D. Gwinn, *J. Chem. Phys.* **43**, 1515 (1965).
- [51] A. S. Dickinson and P. R. Certain, *J. Chem. Phys.* **49**, 4209 (1968).
- [52] V. Szalay, *J. Chem. Phys.* **99**, 1978 (1993).
- [53] H. Wei, *J. Chem. Phys.* **106**, 6885 (1997).
- [54] J. R. Henderson, S. Miller, and J. Tennyson, *J. Chem. Soc., Faraday Trans.* **86**, 1963 (1990).
- [55] J. R. Henderson, C. R. L. Sueur, S. G. Pavett, and J. Tennyson, *Comput. Phys. Commun.* **74**, 193 (1993).
- [56] J. Tennyson, M. A. Kostin, P. Barletta, G. J. Harris, O. L. Polyansky, J. Ramanlal, and N. F. Zobov, *Comput. Phys. Commun.* **163**, 85 (2004).

Part II

Case Studies



Accurate *ab initio*-based double many-body expansion potential energy surface for the adiabatic ground-state of the C₃ radical including combined Jahn-Teller plus pseudo-Jahn-Teller interactions

C. M. R. Rocha and A. J. C. Varandas^{a)}

Departamento de Química, and Centro de Química, Universidade de Coimbra, 3004-535 Coimbra, Portugal

(Received 9 May 2015; accepted 30 July 2015; published online 18 August 2015)

A fully *ab initio*-based potential energy surface is first reported for the ground electronic state of the C₃ radical using the double many-body expansion (DMBE) method. The DMBE form so obtained mimics the full set of energies calculated at the multireference configuration interaction level of theory with chemical accuracy. To account for the incompleteness of the one- and \mathcal{N} -electron bases, the calculated external correlation energies have been scaled prior to the fitting procedure via DMBE-scaled external correlation method. Furthermore, the novel potential energy surface reproduces accurately dissociation energies, diatomic potentials, long-range interactions at all asymptotic channels, and the correct topological behavior at the region of 4 conical intersections with the partner state of the same symmetry near equilateral triangular geometries due to combined Jahn-Teller ($E' \otimes e'$) plus pseudo-Jahn-Teller [$(E' + A'_1) \otimes e'$] interactions. Rovibrational calculations have also been performed, unveiling a good match of the vibrational spectrum of C₃ for 53 calculated levels. The present DMBE form is, therefore, commended for both spectroscopic and reaction dynamics studies, some also performed in the present work. © 2015 AIP Publishing LLC. [http://dx.doi.org/10.1063/1.4928434]

I. INTRODUCTION

The $\tilde{A}^1\Pi_u - \tilde{X}^1\Sigma_g^+$ emission spectrum of the C₃ radical, near 4050 Å, was initially detected in the tail of a comet by Huggins as early as 1881.¹ These so-called Swings emission bands² of C₃ were first reproduced in the laboratory by Herzberg³ in 1942, although the final assignment of the rovibronic spectra was attributed to Douglas⁴ and Gausset *et al.*^{5,6} Since then, the C₃ radical has been observed in a wide range of astrophysical sources,^{7,8} including circumstellar shells of carbon stars,^{9–11} interstellar molecular clouds,^{12–15} and comets.^{1,10} As the most abundant small pure carbon molecule in the interstellar medium,^{16–18} C₃ along with its smaller congener C₂ are the central key to the formation of more complex carbon clusters, long-chain cyanopolynes, carbon dust, and polycyclic aromatic hydrocarbons.^{2,19,20} Mebel and Kaiser²¹ provided alternative pathways, besides the $C(^3P_j) + C_2H_2(X^1\Sigma_g^+)$ reaction,²² through which linear C₃($\tilde{X}^1\Sigma_g^+$) would be formed in interstellar environments, i.e., in the reactions $CH(X^2\Pi_u) + C_2(X^1\Sigma_g^+)$ and $C(^3P_j) + C_2H(X^2\Sigma^+)$, the latter being most relevant in interstellar space.²³ C₃ is also the predominant carbon cluster in equilibrium hot carbon vapor,^{19,24} hydrocarbon flames,^{2,19} and plasmas generated through energetic processing of carbon containing materials.^{19,25,26} The relevance of the C₃ molecule in space²⁷ as well as in terrestrial sooting flames and combustion processes^{2,19} has motivated many experimental^{28–30} and theoretical^{17,18,31–41} studies both in the ground ($1^1A'$) as well as in some low-lying excited singlet ($1^1A''$) and triplet

($3^1A'/3^1A''$) electronic manifolds.^{23,38–40} It is worth pointing out that, from the theoretical perspective, much effort has been devoted to obtain local (near-equilibrium) ground state potential energy surfaces⁴² (PESs) for C₃ aiming to explore its spectroscopy, notably the unusual large amplitude bending motion and related speculations concerning its *quasi*-linearity (for a comprehensive review, see Refs. 2 and 19, and references therein).

Early *ab initio* calculations by Kraemer *et al.*³² using configuration interaction with single and double excitations including the Davidson correction for quadruple excitations⁴³ (CISDQ) and a triple- ζ -plus-polarization (TZP) basis set³² yielded a PES which has been expressed as a force field expansion.⁴⁴ Its minimum shows the C₃ radical as a bent species with an equilibrium bond angle of about 162° and a barrier to linearity of 21 cm⁻¹.³² The results so obtained seemed to indicate the title system to be *quasi*-linear (i.e., with a barrier to linearity much smaller than the bending frequency of $\nu_2 = 63.42$ cm⁻¹).^{40,45} This has been reinforced by Jensen³³ who used the MORBID (Morse Oscillator-Rigid Bender Internal Dynamics) Hamiltonian⁴⁶ along with experimentally determined bend-stretch term values to derive an analytic PES for the ground electronic state of the C₃ radical.³³ However, these studies were soon superseded by high level *ab initio* PESs obtained from complete active space self-consistent field⁴⁷ (CASSCF) calculations by Jørgensen *et al.*,³⁴ and Jensen *et al.*,³⁵ as well as large scale coupled cluster calculations with single and double excitations and a *quasi*-perturbative treatment of the connected triple substitutions⁴⁸ [CCSD(T)] by Mladenović *et al.*³⁶ Accordingly,^{34–36} it was stated that C₃ is not *quasi*-linear as had previously

^{a)}Author to whom correspondence should be addressed. Electronic mail: varandas@uc.pt

been discussed but possesses instead an exceptionally flat bending potential. Such a controversy was rationalized by means of its strong stretch-bend coupling: as noted by Northrup *et al.*⁴⁹ and Špirko *et al.*,³⁶ a lower barrier to linearity and an increase in floppiness is observed when the antisymmetric stretch (ν_3) is excited, while a more rigid linear configuration prevails upon excitation of the symmetric stretch (ν_1).⁴⁹ More recently, Ahmed *et al.*³⁹ and Saha *et al.*⁴⁰ employed internally contracted multireference configuration interaction⁴⁷ (MRCI) calculations with the cc-pVTZ basis set of Dunning⁵⁰ to model near-equilibrium PESs for both the ground and excited $\tilde{A}^1\Pi_u$ and $\tilde{D}^1\Delta_g$ electronic states of the C_3 radical which potential parameters were, subsequently, least-squares fitted to experimental data.^{39,40} From these studies,^{39,40} several important features were highlighted, notably the strong Renner-Teller vibronic interactions^{51,52} for the Π and Δ excited states, already reported by Gausset *et al.*^{5,6} and Jungen *et al.*,⁵³ in which the degeneracy at linear configurations is lifted closely proportional to the square and fourth power of the bending coordinate, respectively.^{5,6,53} Furthermore, as previously noted,^{54,55} Ahmed *et al.*³⁹ emphasized the presence of a symmetry-required conical intersection^{42,56} between the ground and the excited adiabatic $\tilde{B}^1\Delta_u$ state at equilateral triangular geometries where both correlate with the degenerate $^1E'$ irreducible representation in D_{3h} symmetry (see also Figure 1 of the supplementary material⁵⁷).

The first global PES and, to the best of our knowledge, the only one reported so far for the ground state of $C_3(1^1A')$ radical is due to Carter, Mills, and Murrell³¹ (CMM). The authors employed the many-body expansion^{31,42,58} (MBE) with an experimentally determined harmonic force field⁶ and 40 *ab initio* energies^{55,59} to obtain an analytic form of the PES that exactly reproduces an early experimental heat of formation, geometry, and force constants of the linear equilibrium configuration of C_3 . Additionally, it describes other relevant topographical attributes such as the C_{2v} transition-states for the isomerization between the three equivalent symmetry-related minima, in addition to accurately characterize the atom+diatom asymptotic limits which correlate adiabatically with^{31,42,60,61} $C_2(a^3\Pi_u) + C(^3P)$.

Despite its astrophysical significance and importance as a key intermediate for the formation of more complex carbon clusters,^{2,19} there is not as yet an *ab initio*-based global PES for the title system. Thus, the main goal of this work is to provide such a PES for $C_3(1^1A')$. For this, we use double many-body expansion (DMBE) theory^{62–66} (for recent developments on the methodology, see Refs. 67 and 68). As usual in DMBE theory,^{63,66} the present form must ensure the proper permutational symmetry and correct behavior at conical intersections. Given the close resemblance to the PES of⁵⁸ H_3 and^{69–71} $H_3^+(1^3A'/2^3A')$, a similar methodological scheme will be here adopted. Naturally, the DMBE function so obtained will correctly reproduce the dissociation energies, diatomic potentials, and long-range interactions at all asymptotic channels (a long-standing feature of DMBE theory^{62–66}), as well as all topological features in the valence region in order to be useful both for rovibrational calculations (hopefully with minor adjustments) and reaction dynamics.^{69,70,72}

The paper is organized as follows. Section II summarizes the *ab initio* calculations and provides an overview on the singlet electronic manifold of the C_3 radical. The scaling of the external (dynamical) correlation is examined in Section III. Section IV is devoted to details of the analytical functions employed for the modeling, while the results and the main topographical features of the PES are discussed in Section V. Its quality is further judged via rovibrational calculations in Section VI. Some conclusions are gathered in Section VII.

II. AB INITIO CALCULATIONS AND SYNOPSIS ON THE SINGLET MANIFOLD

Although the paper is primarily concerned with the $1^1A'$ state of C_3 , a survey of the main features of some low-lying excited singlet states for C_{2v} conformations, and their correlations with distinct dissociation limits, is summarized in Figures 1 and 2. For this, we have performed full valence CASSCF⁴⁷ (FVCAS) constrained optimizations with a triple- ζ augmented correlation consistent basis set of Dunning^{50,73} (aug-cc-pVTZ or AVTZ) for a grid of angles ϕ , i.e., by fixing C_{2v} symmetry with the bond distance R optimized at each angle. Single-point calculations employing the internally contracted MRCI⁴⁷ method, as implemented in MOLPRO,⁷⁴ have subsequently been done. Thus, the C_{2v} cuts are effectively obtained at the MRCI/AVTZ//FVCAS/AVTZ level of theory, following an efficient scheme for accurate treatment of bond-breaking/forming reactions proposed elsewhere.⁷⁵ Note that for small angles ($\phi < 30^\circ$), the optimization leads to the asymptotic channels, as the optimum bond lengths correspond to widely separated atom+diatom fragments (e.g., for $\phi = 15^\circ$, $R \approx 9.624 a_0$).

According to the spin-spatial Wigner-Witmer correlation rules,^{76,77} six singlet states correlate in C_{2v} (C_s) symmetry with the lowest dissociation limit $C_2(a^3\Pi_u) + C(^3P)$,

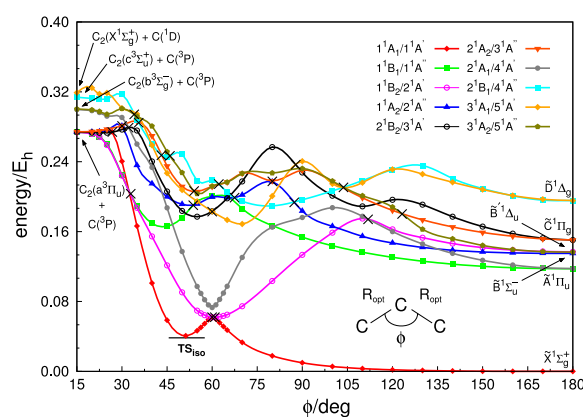


FIG. 1. Optimized bending potential for the ground and some low-lying excited singlet states of C_3 obtained at the MRCI/AVTZ//CASSCF/AVTZ level of theory for a grid of fixed angles. The key shows the irreducible representation, in C_{2v} symmetry, for each electronic state and its correlation with C_s point group. Also shown in panel are the associated correlations, for linear geometries, with $D_{\infty h}$ symmetry as well as the corresponding dissociation limits. Conical intersections are indicated by the “x” symbol; for details in C_s symmetry, see Figure 1 of the supplementary material.⁵⁷

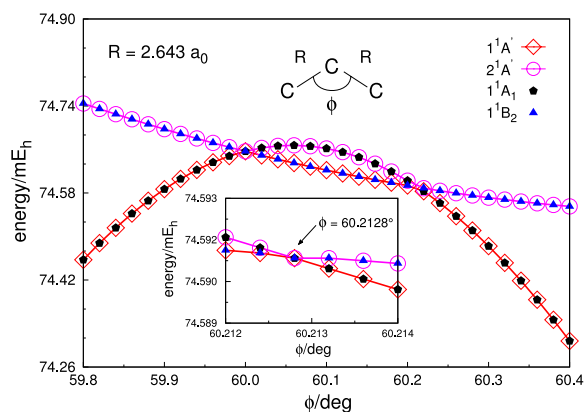


FIG. 2. FVCAS/AVTZ description of the region close to the conical intersection regions with two equal bond lengths fixed at $R = 2.643 a_0$. The solid symbols correspond to points calculated in the 1^1A_1 and 1^1B_2 states of C_{2v} symmetry, while the open symbols connected by smooth splines correspond to calculations with A' symmetry in the C_s point group. The energies are given with respect to the global minimum of C_3 with $D_{\infty h}$ symmetry.

namely, 1^1A_1 ($1^1A'$), 1^1B_1 ($1^1A''$), 1^1B_2 ($2^1A'$), 1^1A_2 ($2^1A''$), 2^1B_2 ($3^1A'$), and 2^1A_2 ($3^1A''$). In turn, the four other electronic states here considered [2^1A_1 ($4^1A'$), 2^1B_1 ($4^1A''$), 3^1A_1 ($5^1A'$), and 3^1A_2 ($5^1A''$)] correlate with triplet states of the fragments [$C_2(b^3\Sigma_g^-) + C(^3P)$ and $C_2(c^3\Sigma_u^+) + C(^3P)$] or $C_2(X^1\Sigma_g^+) + C(^1D)$. Suffice to add that other dissociation limits correlate with higher excited singlet states: $C_2(b^3\Sigma_g^-) + C(^3P)$ correlates with 1^1A_1 (A'), 1^1A_2 (A''), and 1^1B_2 (A'); $C_2(c^3\Sigma_u^+) + C(^3P)$ with 1^1A_1 (A'), 1^1A_2 (A''), and 1^1B_1 (A''); $C_2(X^1\Sigma_g^+) + C(^1D)$ with 1^1A_1 (A'), 1^1A_2 (A''), 1^1A_1 (A'), 1^1B_1 (A''), and 1^1B_2 (A').⁷⁷ However, as seen from Figure 1, some have not been considered in our test calculations. As noted by Murrell and co-workers,^{31,42,60,61} the ground state of $C_3(\tilde{X}^1\Sigma_g^+/1^1A_1/1^1A')$ does not dissociate adiabatically to ground state fragments [$C_2(X^1\Sigma_g^+) + C(^3P)$], since either C_2 or C must be in an excited state to satisfy the spin correlation rules. Such considerations will be discussed in relation to the PES in Section IV.

In order to characterize the dissociation limits in Figure 1, we have computed the optimized equilibrium bond distances for the diatomic fragments ($R_{e,asym}$) in the asymptotic channels (for $\phi = 15^\circ$) and compared the results with the ones obtained from FVCAS/AVTZ and MRCI/AVTZ geometry optimizations for the isolated diatomic molecules ($R_{e,diat}$). The results are gathered in Table I. Also given are the relative energies (ΔE) between the dissociation channels at FVCAS/AVTZ and MRCI/AVTZ//FVCAS/AVTZ levels of theory as well as experimental values. Note that the latter were estimated considering the equilibrium experimental electronic term values (T_e) for each diatomic ($T_e[C_2(X^1\Sigma_g^+)] = 0 \text{ kJ mol}^{-1}$, $T_e[C_2(a^3\Pi_u)] = 8.59 \text{ kJ mol}^{-1}$, $T_e[C_2(b^3\Sigma_g^-)] = 77.00 \text{ kJ mol}^{-1}$, and $T_e[C_2(c^3\Sigma_u^+)] = 109.13 \text{ kJ mol}^{-1}$)⁷⁸⁻⁸⁰ and the $1^1D - ^3P$ separation of the carbon atom ($121.96 \text{ kJ mol}^{-1}$).⁸¹

As shown, excellent agreements have been obtained between the equilibrium bond distances for the diatomic fragments ($R_{e,asym}$) and those from geometry optimizations for the isolated molecules ($R_{e,diat}$) as well as experimental ones.^{78,80} In fact, as shown in the fifth column of Table I, the calculated rela-

TABLE I. Optimized equilibrium bond distances of diatomic fragments in dissociation channels shown in Figure 1 ($R_{e,asym}$), and corresponding attributes in the bare diatomics ($R_{e,diat}$) as obtained at the FVCAS/AVTZ and MRCI/AVTZ levels of theory. ΔE is the relative energy between dissociation channels.

Channel	Method	$R_{e,asym}/a_0$	$R_{e,diat}/a_0$	$\Delta E/\text{kJ mol}^{-1}$
$C_2(a^3\Pi_u) + C(^3P)$	FVCAS/AVTZ ^a	2.512 ^b	2.513	0 ^c
	MRCI/AVTZ ^a	...	2.498	0 ^c
	Expt.	...	2.479 ^d	0 ^e
$C_2(b^3\Sigma_g^-) + C(^3P)$	FVCAS/AVTZ ^a	2.618 ^b	2.616	80.08 ^c
	MRCI/AVTZ ^a	...	2.606	67.25 ^c
	Expt.	...	2.587 ^d	68.41 ^e
$C_2(c^3\Sigma_u^+) + C(^3P)$	FVCAS/AVTZ ^a	2.316 ^b	2.313	75.84 ^c
	MRCI/AVTZ ^a	...	2.299	103.91 ^c
	Expt.	...	2.283 ^d	100.54 ^e
$C_2(X^1\Sigma_g^+) + C(^1D)$	FVCAS/AVTZ ^a	2.372 ^b	2.372	108.93 ^c
	MRCI/AVTZ ^a	...	2.366	117.71 ^c
	Expt.	...	2.348 ^d	113.37 ^e

^aThis work.

^bCalculated in this work as $R_{e,asym} = R\sqrt{2(1-\cos\phi)}$, where $\phi = 15^\circ$.

^cFVCAS/AVTZ and MRCI/AVTZ//FVCAS/AVTZ energies for each asymptotic channel with respect to $C_2(a^3\Pi_u) + C(^3P)$.

^dReferences 78 and 80.

^eRelative energies from experimental electronic term values (T_e)⁷⁸⁻⁸⁰ for each diatomic and $1^1D - ^3P$ separation of C atom.⁸¹

tive energies (ΔE) at the asymptote yield results in good agreement with the experimental estimates. Of course, although the correct wave function at (near-) dissociation regions has been ensured by our multireference scheme,⁴⁷ the calculations are subject to errors due to the incompleteness of the one-electron basis and truncation of the N -electron expansion. Additionally, spin-orbit couplings are intrinsic to experimental data both for the $C(^1D) - C(^3P_{J=0})$ energy separation (with spin-orbit coupling constant $A \approx 14.47 \text{ cm}^{-1}$)⁷⁸ and C_2 in the $^3\Pi_\Omega$ state (which splits into a multiplet of 3 equidistant components: $\Omega = 0, 1, 2$, with $A \approx -15.25 \text{ cm}^{-1}$).⁷⁸ Because they should be minor, such effects have not been considered.

As shown in Figure 1, and by others,^{5,6,39,40,53} all degenerate excited states at linear geometries (namely, $\tilde{A}^1\Pi_u$, $\tilde{B}^1\Delta_u$, $\tilde{C}^1\Pi_g$, and $\tilde{D}^1\Delta_g$) are subject to strong Renner-Teller vibronic interactions^{51,52} which are manifested as splittings into symmetric (A') and antisymmetric (A'') components as the molecule bends. Such electronic excited states show numerous crossings between themselves for $\phi < 140^\circ$. They are indicated by a "x" symbol in Figure 1; for details on the conical intersections and avoided crossings in C_s symmetry, see Figure 1 of the supplementary material.⁵⁷ However, an appreciable gap (up to 377 kJ mol^{-1}) is visible between them and the ground state for $\phi \geq 100^\circ$.

Figure 1 allows a comprehensive picture of the topological features for the lowest ten singlet surfaces of C_3 (for a T-shaped path). However, in as much as the present work is focused on the ground state of C_3 , special relevance will be given to electronic states that correlate with the A' irreducible representation in C_s symmetry, in particular, the 1^1A_1 and 1^1B_2 states. The following discussion will therefore be devoted to them.

As seen from Figure 1, the ground state equilibrium geometry of C_3 is linear with $R_e = 2.474 a_0$ at this level, in good agreement with the experimental value of $2.451 a_0$.⁹ As already remarked,^{5,6,39,40,53} the ground state bending potential is exceptionally flat with a low bending frequency and hence a large amplitude motion. In fact, only $25.81 \text{ kJ mol}^{-1}$ are required to bend C_3 up to $\phi = 90^\circ$.

A region that deserves close attention refers to near equilateral triangular ($\phi = 60^\circ$) geometries. As shown in Figure 1, there appears to be a single conical intersection at geometries with D_{3h} symmetry ($R = 2.643 a_0$). However, a close inspection (see Figure 2) indicates that there are two such intersections which may be attributed to what is commonly referred to as a combined JT [$E' \otimes e'$] plus pseudo-JT (PJT) [$(E' + A'_1) \otimes e'$] interactions.⁸²⁻⁸⁵ Rather than a single symmetry-dictated ${}^1E \otimes e$ intersection, one has instead a strong mixing of two 1A_1 states which pushes down the lower term to cross twice the 1B_2 state at valence angles of $\phi = 60^\circ$ and 60.2128° for D_{3h} and C_{2v} conformations, respectively. Such an interesting feature is then due to one of the components of the twofold degenerate ${}^1E'$ which gets vibronically mixed with the next electronic state of ${}^1A'_1$ symmetry (note that the separation between the ${}^1E'$ and ${}^1A'_1$ states at $\phi = 60^\circ$ is only $29.29 \text{ kJ mol}^{-1}$).^{84,85} Thus, for typical systems with e^2 or t^3 configurations in high-symmetry geometries, e.g., the C_3 congener Si_3 ,⁸⁵ such a JT + PJT vibronic effect is known to generate four conical intersections^{85,86} (see Figures 10 and 11) at which the wave function and associated energy levels may not be subjected to the topological (Longuet-Higgins,⁸⁷⁻⁸⁹ also called Berry⁹⁰) phase.

Distortion of the D_{3h} structure maintaining C_{2v} symmetry and $\phi < 60^\circ$ leads to stabilization of the lower sheet and formation of a saddle point, Figure 1 at $\phi \approx 50^\circ$. This represents the transition state (TS_{iso} for future reference) for the isomerization between the three equivalent $D_{\infty h}$ minima in the ground state PES. In turn, C_{2v} distortions with $\phi > 60^\circ$ lead ultimately to the absolute $D_{\infty h}$ minima of C_3 ; see Section V.

III. SCALING OF THE EXTERNAL CORRELATION

To calibrate the DMBE PES, we have performed *ab initio* calculations at the MRCI⁴⁷ level of theory using the FVCAS⁴⁷ wave function as reference. The AVTZ basis of Dunning^{50,73} has been employed, with the calculations performed using the MOLPRO⁷⁴ package. Due to inadequacies of a single-reference treatment in the description of surface crossings (or avoided crossings) and regions of the PES dominated by a multistate character^{47,56} (e.g., at dissociation regions characterized by electronic degeneracies), a FVCAS wave function has been utilized as reference by employing state averaged CASSCF⁴⁷ in which three electronic states of A' symmetry (in the C_s point group) were simultaneously treated. Such a reference wave function involves 12 correlated electrons in 12 active orbitals ($9a' + 3a''$) and amounts to a total of 113 904 configuration state functions (CSFs). For the MRCI calculations, all single and double excitations (FVCAS-CISD) have been considered, yielding a total of 21 580 857 contracted configurations with the AVTZ basis. The three lowest molecular orbitals ($3a'$) have been treated

as inactive in all calculations. A total of 629 symmetry unrelated grid points has been chosen to map the entire PES defined by $1.5 \leq R_{C_2}/a_0 \leq 6.0$, $0.0 \leq r_{C-C_2}/a_0 \leq 10.0$, and $0 \leq \theta/\text{deg} \leq 90$. Note that R_{C_2} , r_{C-C_2} , and θ are Jacobi coordinates (see inset of Figure 12). The diatomic potential energy curve for the $C_2(a^3\Pi_u)$ molecule and the corresponding static dipole polarizabilities have also been obtained at the same MRCI/AVTZ level of theory.

To account for excitations beyond singles and doubles and also the incompleteness of the one-electron basis set, all raw *ab initio* energies have been scaled with the double many-body expansion-scaled external correlation (DMBE-SEC)⁹¹ method, which is a generalization of the SEC⁹² method. Thus, the total interaction energy relative to the separated atoms assumes the form

$$V_{\text{DMBE-SEC}}(\mathbf{R}) = V_{\text{FVCAS}}(\mathbf{R}) + V_{\text{SEC}}(\mathbf{R}), \quad (1)$$

where

$$V_{\text{FVCAS}}(\mathbf{R}) = \sum_{\text{AB}} V_{\text{AB,FVCAS}}^{(2)}(R_{\text{AB}}) + V_{\text{ABC,FVCAS}}^{(3)}(\mathbf{R}) \quad (2)$$

and

$$V_{\text{SEC}}(\mathbf{R}) = \sum_{\text{AB}} V_{\text{AB,SEC}}^{(2)}(R_{\text{AB}}) + V_{\text{ABC,SEC}}^{(3)}(\mathbf{R}). \quad (3)$$

Note that both the FVCAS [$V_{\text{FVCAS}}(\mathbf{R})$] and scaled external correlation [$V_{\text{SEC}}(\mathbf{R})$] energy contributions are written as a sum of two- and three-body terms, where $\mathbf{R} = \{R_{\text{AB}}, R_{\text{BC}}, R_{\text{CA}}\}$ is a collective variable defining the three interparticle distances. The first two terms in the SEC series expansion [Eq. (3)] are written as

$$V_{\text{AB,SEC}}^{(2)}(R_{\text{AB}}) = \frac{V_{\text{AB,FVCAS-CISD}}^{(2)}(R_{\text{AB}}) - V_{\text{AB,FVCAS}}^{(2)}(R_{\text{AB}})}{\mathcal{F}_{\text{AB}}^{(2)}} \quad (4)$$

and

$$V_{\text{ABC,SEC}}^{(3)}(\mathbf{R}) = \frac{V_{\text{ABC,FVCAS-CISD}}^{(3)}(\mathbf{R}) - V_{\text{ABC,FVCAS}}^{(3)}(\mathbf{R})}{\mathcal{F}_{\text{ABC}}^{(3)}}. \quad (5)$$

According to the DMBE-SEC method,⁹¹ the two-body scaling parameter $\mathcal{F}_{\text{AB}}^{(2)}$ in Eq. (4) is chosen such as to reproduce the experimental dissociation energy (D_e) of the diatomic fragment, while $\mathcal{F}_{\text{ABC}}^{(3)}$ is defined as the average of the two-body \mathcal{F} factors.⁹¹ A value of $\mathcal{F}_{C_2(a^3\Pi_u)}^{(2)} = 0.4905$ has been obtained (at MRCI/AVTZ level) in such a way as to reproduce the experimental dissociation energy of $C_2(a^3\Pi_u)$, which has been defined as⁹³

$$D_e[C_2(a^3\Pi_u)] = D_0[C_2(X^1\Sigma_g^+)] + E_{\text{ZPE}}[C_2(X^1\Sigma_g^+)] - T_e[C_2(a^3\Pi_u)] \quad (6)$$

and

$$E_{\text{ZPE}}[C_2(X^1\Sigma_g^+)] = \frac{1}{2} \omega_e - \frac{1}{4} \omega_e x_e + \frac{1}{8} \omega_e y_e, \quad (7)$$

where $D_0[C_2(X^1\Sigma_g^+)] = 607.47 \text{ kJ mol}^{-1}$ is the accurate experimental dissociation energy of Ref. 94 $C_2(X^1\Sigma_g^+)$, and $T_e[C_2(a^3\Pi_u)] = 8.59 \text{ kJ mol}^{-1}$ (or 716.24 cm^{-1}) is the electronic term value of the first excited triplet state.⁷⁸⁻⁸⁰ The

zero-point energy (ZPE) correction for the ground state of C_2 ($E_{\text{ZPE}}[C_2(X^1\Sigma_g^+)] = 11.10 \text{ kJ mol}^{-1}$) has been determined based on experimental spectroscopic constants:⁹⁵ $\omega_e = 1854.71 \text{ cm}^{-1}$, $\omega_e x_e = 13.34 \text{ cm}^{-1}$, and $\omega_e y_e = -0.172 \text{ cm}^{-1}$. It should be pointed out that both the ground-singlet and first excited-triplet states of C_2 dissociate to the same limit, $C(^3P) + C(^3P)$. In turn, the three-body scaling parameter has been defined⁹¹ as the average of the two-body \mathcal{F} factors so obtained which yields $\mathcal{F}_{C_3(^3\Pi_u)}^{(2)} = \mathcal{F}_{C_3}^{(3)}$ for C_3 . Although an experimental value is available for the dissociation energy of C_3 ,²⁴ which could therefore be used in estimating $\mathcal{F}_{C_3}^{(3)}$, we have decided not to bias further the *ab initio* results since the uncertainties associated to such an experimental value are²⁴ $\approx 13.01 \text{ kJ mol}^{-1}$ (note the much smaller experimental uncertainty in $D_e[C_2(a^3\Pi_u)]$:⁹⁴ $\approx 2.09 \text{ kJ mol}^{-1}$).

IV. DMBE MODELING

According to the spin-spatial Wigner-Witmer correlation rules,^{76,77} the ground state $C_3(^1A')$ dissociates adiabatically into $C_2(X^1\Sigma_g^+) + C(^1D)$ or $C_2(a^3\Pi_u) + C(^3P)$ fragments. As noted elsewhere,^{31,42,60,61} the first excited triplet state of C_2 lies only 8.59 kJ mol^{-1} ($T_e[C_2(a^3\Pi_u)] = 8.59 \text{ kJ mol}^{-1}$)^{78–80} above the corresponding ground state, whereas the energy separation between the 3P state of atomic carbon and its first excited state $C(^1D)$ is $121.96 \text{ kJ mol}^{-1}$.⁸¹ Thus, as Figure 1 (see also Table I) shows, the lowest asymptotic channel $C_2(a^3\Pi_u) + C(^3P)$ is $113.37 \text{ kJ mol}^{-1}$ more stable than the dissociation limit $C_2(X^1\Sigma_g^+) + C(^1D)$. Thus, to model the present DMBE^{62,63,65,66} form, we have adopted as $V^{(2)}(R)$ the potential energy curve of $C_2(a^3\Pi_u)$. Because all $C - C_2$ channels dissociate to $C(^3P) + C(^3P) + C(^3P)$, no use of the switching function formalism⁹⁶ is required.

Within the DMBE^{62,63,65,66} framework, the PES is written as a sum of one-, two-, and three-body terms,

$$V(\mathbf{R}) = V^{(1)} + \sum_{i=1}^3 [V_{\text{EHF}}^{(2)}(R_i) + V_{\text{dc}}^{(2)}(R_i)] + [V_{\text{EHF}}^{(3)}(\mathbf{R}) + V_{\text{dc}}^{(3)}(\mathbf{R})], \quad (8)$$

where the atom pairs AB, BC, and AC have been labeled for convenience by $i = 1-3$, thence $\mathbf{R} = \{R_1, R_2, R_3\}$. In turn, EHF stands for extended Hartree-Fock type energy, and dc for dynamical correlation.

Following previous work on the N_3 system,^{72,97} the zero of energy is defined as $C_2(a^3\Pi_u)$ at its equilibrium geometry (R_e) with the $C(^3P)$ atom infinitely separated. Thus, we impose that the (pseudo-) one-body term equals $V^{(1)} = D_e$. Such a strategy ensures the correct energetics of the PES at all asymptotic limits: $V(R_e, \infty, \infty) = 0$ and $V(\infty, \infty, \infty) = D_e$. As usual, every term in Eq. (8) is expressed as a sum of EHF and dc energy contributions, with the details of the analytical forms employed in such a cluster expansion given in Subsections IV A-IV C (see also the supplementary material⁵⁷). We emphasize that the DMBE form here reported warrants by built-in construction the cusped behavior of the adiabatic ground-state PES at both D_{3h} and C_{2v} conical intersections without resorting to diabaticization schemes,⁹⁸ thus ensuring a realistic representation of

such nonanalytic features. The terms required to be added to the three-body EHF [$V_{\text{EHF}}^{(3)}(\mathbf{R})$] energy are given in Sections IV C 1 and IV C 2.

A. Two-body energy terms

The diatomic potential energy curve of $C_2(a^3\Pi_u)$ has been modeled using the extended Hartree-Fock approximate correlation energy method for diatomic molecules including the united-atom limit⁹⁹ (EHFACE2U), which has built-in the correct behavior both at long-range distances and in regions close to the united-atom limit ($R \rightarrow 0$); the reader is addressed to Ref. 62, 63, 99–104 (see also the supplementary material⁵⁷) for a complete description of the analytical functions here employed.

Figure 3 shows that the EHFACE2U potential accurately reproduces the DMBE-SEC interaction energies [with a root mean square deviation (rmsd) of 4.8 cm^{-1} for 116 calculated points] while exhibiting quite good ability for extrapolation to regions not covered by the *ab initio* data. Also shown in the inset of panel (b) are the RKR (Rydberg-Klein-Rees) turning points.¹⁰⁵ For comparison, we have also computed RKR points using the RKR1 code¹⁰⁶ and accurate spectroscopic constants¹⁰⁷ ($\omega_e = 1641.3463 \text{ cm}^{-1}$, $\omega_e x_e = 11.6595 \text{ cm}^{-1}$, $\omega_e y_e = -0.00079 \text{ cm}^{-1}$, $B_e = 1.632355 \text{ cm}^{-1}$, $\alpha_e = 0.016582 \text{ cm}^{-1}$, and $\gamma_e = -0.000273 \text{ cm}^{-1}$) for the Dunham expansion.⁴² Note that both data sets differ by no more than $5.764 \times 10^{-4} a_0$ and 3.8 cm^{-1} for both inner and outer turning points. As seen in Figure 3, the potential curve reproduces quite well the

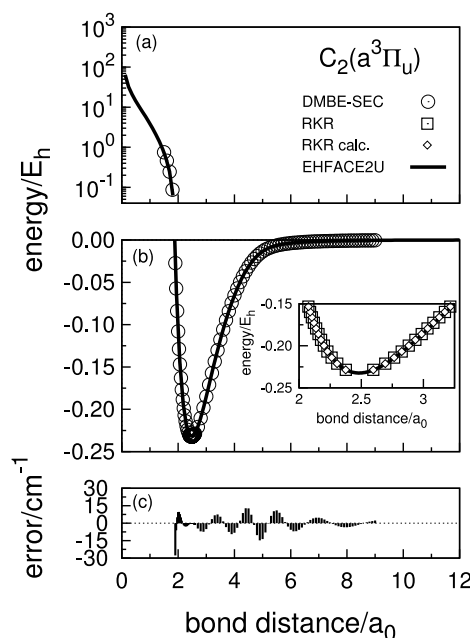


FIG. 3. Potential energy curve for $C_2(a^3\Pi_u)$ as obtained from a least-squares fit to the DMBE-SEC energies. The energy differences between the predicted and fitted values are shown in panel (c). Also shown in the inset of panel (b) are the RKR (Rydberg-Klein-Rees) turning points of Read *et al.*¹⁰⁵ and the ones calculated from accurate spectroscopic constants of Brooke *et al.*¹⁰⁷ with the RKR1 computer code.¹⁰⁶ The key is in panel (a).

TABLE II. Equilibrium geometries (R_e), dissociation energies (D_e), and vibrational frequencies (w_e) of C_2 .

$C_2(a^3\Pi_u)$			
Method	R_e/a_0	$D_e/\text{kJ mol}^{-1}$	w_e/cm^{-1}
EHFAC2U ^a	2.483	610.03	1638.3
FVCAS/AVTZ ^b	2.513	558.35	1592.9
MRCI/AVTZ ^b	2.498	583.50	1618.4
CCSD(T)/PVQZ ^c	2.477	596.30	1653.0
W4 ^d	2.486	605.76	1639.8
MRCI/CBS ^e	2.487	598.31	1632.3
MRCI+Q/CBS ^e	2.487	598.73	1629.8
MRCI+Q+CV/AV6Z ^f	2.480	...	1641.6
MRCI+Q+CV+Rel/AV6Z ^f	2.480	...	1641.1
MRCI+[2] _{R12} + [2] _S /AVQZ ^g	2.487	601.24	...
Expt. ^h	2.479	609.99	1641.35

^aThis work.^bThis work. From *ab initio* points at FVCAS and MRCI levels of theory.^cReference 108.^dReference geometry at CCSD(T)/VQZ level of theory.¹⁰⁹^eCBS limit obtained⁹³ as $A(X) = A_\infty + B \exp(-CX)$ using MRCI(+Q)/VXZ energies with cardinal numbers $X = 2, 3, 4, 5$.^fReference 110. Dissociation energies not reported.^gReference 111. Harmonic vibrational frequency not reported.^hReferences 78, 94, and 95.

experimental RKR classical turning points with a rmsd that amounts to ca. 231.8 cm^{-1} . It must be stressed that the RKR points have not been included in the fitted data set, and therefore such discrepancies may partly be due to the fact that the error margin associated to the fitted (see above) experimental dissociation energy is $\approx 174.9 \text{ cm}^{-1}$.⁹⁴ The computed equilibrium geometry (R_e), dissociation energy (D_e), and harmonic vibrational frequencies (w_e) are given in Table II, together with available results from the literature. As seen, excellent agreement is found between the structural properties of the EHFAC2U curve and the experimental data, with deviations of $0.004 a_0$, 0.04 kJ mol^{-1} , and -3.1 cm^{-1} for the equilibrium geometry, dissociation energy, and harmonic vibrational frequency, respectively. Indeed, the enhanced accuracy and reliability of the results when the raw *ab initio* points are corrected by scaling of the dynamical correlation are remarkable. It should be pointed out that excellent correlations were also found between the present model potential and the best available theoretical results^{93,109,111} (see Table II). Note that these^{93,109–111} include extrapolations to the one- and/or \mathcal{N} -electron basis sets, core and core-valence correlation contributions, and also relativistic corrections, effects implicitly accounted for in the SEC⁹² and DMBE-SEC⁹¹ methods. All numerical coefficients in the $C_2(a^3\Pi_u)$ potential curve and other contributions to the DMBE PES are given as the supplementary material.⁵⁷

B. Three-body dynamical correlation energy

Following the DMBE^{62,63,65,66} formalism, the three-body energy term [$V^{(3)}(\mathbf{R})$], likewise $V^{(2)}(R)$ in Eq. (8), is split into EHF and dc contributions,

$$V^{(3)}(\mathbf{R}) = V_{\text{EHF}}^{(3)}(\mathbf{R}) + V_{\text{dc}}^{(3)}(\mathbf{R}). \quad (9)$$

The three-body dc energy term assumes the form^{112,113}

$$V_{\text{dc}}^{(3)}(\mathbf{R}) = - \sum_{i=1}^3 \sum_{n=6,8,10} f_i(\mathbf{R}) C_n^{(i)}(R_i, \theta_i) \chi_n(r_i) r_i^{-n}, \quad (10)$$

where R_i , r_i , and θ_i are Jacobi coordinates, with i labeling the associated atom-diatom (I – JK) arrangement channel for a defined set of interparticle distances $\mathbf{R} = \{R_1, R_2, R_3\}$. The switching function $f_i(\mathbf{R})$ is chosen from the requirement that its value must be +1 for $R_i = R_e$ and $r_i \rightarrow \infty$, and 0 when $R_i \rightarrow \infty$. As proposed elsewhere,¹¹² a suitable functional form is

$$f_i(\mathbf{R}) = \frac{1}{2} \left\{ 1 - \tanh[\xi(\eta R_i - R_j - R_k)] \right\}, \quad (11)$$

where $\xi = 1 a_0^{-1}$ and $\eta = 6$ are fixed parameters,¹¹⁴ and the indices (i, j, k) are to be understood as cyclic permutations of (1,2,3). In turn, the damping functions $\chi_n(r_i)$ in Eq. (10) assume the same functional form as employed in EHFAC2U model⁹⁹ [see Eq. (3) of the supplementary material⁵⁷], but with R_i replaced by the center-of-mass separation r_i for the appropriate atom-diatom channel. To determine the scaling parameter ρ in the damping functions $\chi_n(r_i)$ [see Eqs. (3) and (6) of the supplementary material⁵⁷], the associated Le Roy radius¹¹⁵ (R_0) has been estimated as for the Mg – C diatomic (the Mg atom corresponds to the united-atom for the collapsed C_2 fragment) which yields $R_0 = 10.983 a_0$ and $\rho = 19.230 a_0$.¹⁰¹

In Eq. (10), $C_n^{(i)}(R_i, \theta_i)$ are atom-diatom long-range dispersion coefficients given by¹¹³

$$C_n^{(i)}(R_i, \theta_i) = \sum_L C_n^L(R_i) P_L(\cos \theta_i), \quad (12)$$

where $P_L(\cos \theta_i)$ denotes the L th term of the Legendre polynomial expansion. Note that this expansion has been truncated by considering only $C_6^0(R_i)$, $C_6^2(R_i)$, $C_8^0(R_i)$, $C_8^2(R_i)$, $C_8^4(R_i)$, and $C_{10}^0(R_i)$; all other components are assumed to make negligible contributions and hence neglected. In order to estimate the dependence of such coefficients on the diatomic vibrational coordinate¹¹⁶ (R_i), the generalized Slater-Kirkwood approximation¹¹⁷ has been employed, with the isotropic [$\alpha_0(R_i)$] and anisotropic [$\alpha_2(R_i)$] static dipole polarizabilities¹¹⁶ calculated at the MRCI/AVTZ level using the finite field method.¹¹⁶ Note that the dipole polarizability for the carbon atom has been here estimated *ab initio* to be $\alpha_{C(\delta P)} = 11.31 a_0^3$, with the corresponding polarizability for the united-atom of the coalescent $C_2(a^3\Pi_u)$ diatomic as $\alpha_{Mg(\delta P)} = 101.26 a_0^3$. It should also be pointed out that the isotropic dispersion energy coefficients $C_8^0(R_i)$ and $C_{10}^0(R_i)$ have been obtained from $C_6^0(R_i)$ by the generalized correlation approach,¹¹⁶ while the associated anisotropic components $C_6^2(R_i)$, $C_8^2(R_i)$, and $C_8^4(R_i)$ were estimated using an adaptation of Pack's formalism based on the harmonic oscillator model.¹¹⁸

The atom-diatom dispersion coefficients so obtained for a set of internuclear distances were then fitted to the form

$$C_n^{L,C_1-C_2C_3}(R) = C_n^{L,C_1C_2} + C_n^{L,C_1C_3} + D_M \left(1 + \sum_{i=1}^3 a_i r^i \right) \exp \left(- \sum_{i=1}^3 b_i r^i \right), \quad (13)$$

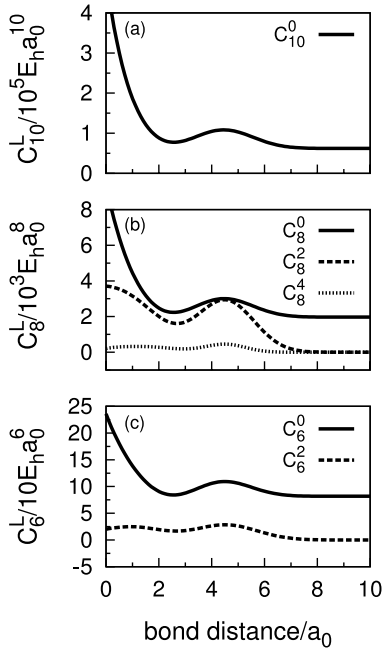


FIG. 4. Dispersion coefficients for the atom-diatom asymptotic channel as a function of the $C_2(a^3\Pi_u)$ internuclear distance.

where $C_n^{L,C_1C_2} = C_n^{L,C_1C_3}$ is the atom-atom dispersion coefficients for $L = 0$ and $C_n^{L,C_1C_2} = C_n^{L,C_1C_3} = 0$ for $L \neq 0$, a_i and b_i are fitting parameters with $a_1 = b_1$, and $r = R - R_M$ is the displacement from the internuclear distance (R_M) associated with the maximum value (D_M) of the corresponding atom-diatom coefficient. The dependence of such coefficients on the internuclear distance of $C_2(a^3\Pi_u)$ is shown in Figure 4. As noted elsewhere,¹¹⁴ Eq. (10) causes an overestimation of the dynamical correlation energy at the atom-diatom dissociation channel. To correct this, we have multiplied the two-body dynamical correlation energy for the i th pair by $\prod_{j \neq i} [1 - f_j(\mathbf{R})]$, correspondingly for channels j and k . This ensures¹¹⁴ that the only two-body contribution at the i th channel is that of jk .

C. Three-body extended Hartree-Fock energy

Once the one- [$V^{(1)} = D_e$], two- [$V^{(2)}(R_i)$], and three-body dc [$V_{dc}^{(3)}(\mathbf{R})$] energy terms are obtained, the three-body EHF interaction energy [$\epsilon_{EHF}(\mathbf{R}_n)$] is given as^{69,70}

$$\epsilon_{EHF}(\mathbf{R}_n) = E_{DMBE-SEC}(\mathbf{R}_n) - V^{(1)} - \sum_{i=1}^3 V^{(2)}(R_{i,n}) - V_{dc}^{(3)}(\mathbf{R}_n), \quad (14)$$

where $E_{DMBE-SEC}(\mathbf{R}_n)$ is the DMBE-SEC interaction energy for the n th *ab initio* point. Since the title radical is composed by three identical carbon atoms, the DMBE PES must ensure the proper permutational symmetry (see Refs. 42 and 119, and references therein), which is warranted by built-in construction. Such a requirement is generally satisfied by expressing the three-body EHF term [$V_{EHF}^{(3)}(\mathbf{R})$ —see Eq. (9)] as a sum of

polynomials in the integrity basis,¹¹⁹

$$\Gamma_1 = Q_1, \quad (15)$$

$$\Gamma_2 = Q_2^2 + Q_3^2, \quad (16)$$

$$\Gamma_3 = Q_3(Q_3^2 - 3Q_2^2), \quad (17)$$

where the Q_i are symmetry adapted displacement coordinates from a D_{3h} configuration of bond length R_0 ,^{58,119}

$$\begin{pmatrix} Q_1 \\ Q_2 \\ Q_3 \end{pmatrix} = \begin{pmatrix} \sqrt{1/3} & \sqrt{1/3} & \sqrt{1/3} \\ 0 & \sqrt{1/2} & -\sqrt{1/2} \\ \sqrt{2/3} & -\sqrt{1/6} & -\sqrt{1/6} \end{pmatrix} \begin{pmatrix} R_1 - R_0 \\ R_2 - R_0 \\ R_3 - R_0 \end{pmatrix}. \quad (18)$$

Note that Q_1 , Q_2 , and Q_3 transform as irreducible representations of the S_3 permutation group⁴² and, in Eqs. (15)-(17), Γ_i are totally symmetric combinations of the Q_i . Hence, any polynomial built from the Γ_i also transforms as the totally symmetric representation of S_3 . In this work, the modelling of both D_{3h} and C_{2v} crossing seams has been accomplished by expressing the three-body EHF [$V_{EHF}^{(3)}(\mathbf{R})$] energy as a sum of two terms,

$$V_{EHF}^{(3)}(\mathbf{R}) = V_{EHF}'^{(3)}(\mathbf{R}) + V_{EHF}''^{(3)}(\mathbf{R}), \quad (19)$$

where $V_{EHF}'^{(3)}(\mathbf{R})$ is the component which adequately describes the symmetry-required JT conical intersection along the D_{3h} symmetry line and $V_{EHF}''^{(3)}(\mathbf{R})$ is an extra term that accounts for the three equivalent conical intersections at C_{2v} symmetries which occur for a valence angle of $\phi = 60.2128^\circ$. The details of the forms used along with the two-step fitting procedure are described next.

1. Crossing seam with D_{3h} symmetry

Following previous work for the H_3 ,¹²⁰ H_3^+ ,⁶⁹⁻⁷¹ and N_3^{72} systems, the $V_{EHF}'^{(3)}(\mathbf{R})$ term is written as

$$V_{EHF}'^{(3)}(\mathbf{R}) = \left[P_1^{N'}(\Gamma_1, \Gamma_2, \Gamma_3) - \sqrt{\Gamma_2} P_2^{M'}(\Gamma_1, \Gamma_2, \Gamma_3) \right] T'(\mathbf{R}), \quad (20)$$

where the $P_n^I(n = 1, 2)$ are polynomials of order I that assume the form

$$P_n^I(\Gamma_1, \Gamma_2, \Gamma_3) = \sum_{i+2j+3k \leq I} c_{ijk}^n \Gamma_1^i \Gamma_2^j \Gamma_3^k. \quad (21)$$

In turn, $T'(\mathbf{R})$ in Eq. (20) is a range-determining factor that ensures the proper asymptotic behavior of the three-body term as any of the three atoms is removed to infinity [$V_{EHF}'^{(3)}(\infty, R_2, R_3) = 0$] and is given by

$$T'(\mathbf{R}) = \prod_{i=1}^3 \{1 - \tanh[\alpha(R_i - R_0)]\}. \quad (22)$$

As remarked by Varandas and Murrell,⁵⁸ the second polynomial in Eq. (20) warrants that the present DMBE form behaves as a linear function of the JT coordinate⁸² $\sqrt{\Gamma_2}$ in the vicinity of the intersection seam.⁵⁸ Thus, it is responsible for the proper representation of the nonanalytic part of the potential at the line of D_{3h} symmetry;⁵⁸ see elsewhere⁹⁸ for an extension to non-symmetrical seams. Finally, the numerical

parameters in Eq. (20) are obtained by minimizing the sum of squared residuals

$$\chi^2 = \sum_{n=1}^N [\epsilon_{\text{EHF}}(\mathbf{R}_n) - V'_{\text{EHF}}(\mathbf{R}_n)]^2, \quad (23)$$

where $\epsilon_{\text{EHF}}(\mathbf{R}_n)$ is the three-body EHF interaction energy previously defined in Eq. (14), with the summation extended over the whole data set of *ab initio* points. Thus, the complete set of parameters (86 in all: 84 c_{ijk}^n , α , and R_0) has been obtained from a fit to the 575 calculated points covering 1/6 of the physically accessible space (see Figure 10) due to symmetry requirements. Following the usual procedure,⁴² the reference geometry (R_0) used to define the displacement coordinates of Eq. (18) was taken as a D_{3h} triangle with perimeter equal to that of C_3 at linear equilibrium geometry, $R_0 = 3.268 a_0$. Due to the symmetry restrictions, the range-determining factor $T'(\mathbf{R})$ [see Eq. (22)] has been obtained with $\alpha_1 = \alpha_2 = \alpha_3 = \alpha = 0.620 a_0^{-1}$ and selected by a trial-and-error procedure where the total rmsd is minimized; the optimal numerical values are given in the supplementary material.⁵⁷ Suffice it to emphasize that the *ab initio* data cover a range of up to 2510 kJ mol⁻¹ above the C_3 global minimum, and that larger weights were attributed to the most important regions of the PES, namely, the linear minimum, the isomerization transition state, and the van der Waals complexes.

2. Crossing seams with C_{2v} symmetry

Following recent work on NO_2 ($^1A''$) and N_3 ($^2A'$) systems,⁹⁸ the cusps at C_{2v} symmetry can be modelled by adding an extra term [$V''_{\text{EHF}}(\mathbf{R})$] on the three-body EHF energy [see Eq. (19)] defined as⁹⁸

$$V''_{\text{EHF}}(\mathbf{R}) = [P_3^{N''}(\Gamma_1, \Gamma_2, \Gamma_3) - \Delta_1 \Delta_2 \Delta_3 P_4^{M''}(\Gamma_1, \Gamma_2, \Gamma_3)] T''(\mathbf{R}), \quad (24)$$

where P_n^l ($n = 3, 4$) are two other polynomials that assume the form given in Eq. (21) and Δ_c ($c = 1, 2, 3$) is the distance from any point in \mathbf{R} space (R_1, R_2 , and R_3) to the three permutationally equivalent C_{2v} crossing seams.⁹⁸ Focussing on one of these lines, we define⁹⁸

$$\Delta_1 = \sqrt{(R_1 - t_0)^2 + (R_2 - t_0)^2 + [R_3 - t_0 \sqrt{2(1 - \cos \phi)}]^2}, \quad (25)$$

with

$$t_0 = \frac{R_1 + R_2 + R_3 \sqrt{2(1 - \cos \phi)}}{4 - 2 \cos \phi}. \quad (26)$$

Note that $\phi = 60.2128^\circ$ is the corresponding valence angle and t_0 defines the point $[(t_0, t_0, t_0 \sqrt{2(1 - \cos \phi)})]$ in the parametric line $r_1 = (t, t, t \sqrt{2(1 - \cos \phi)})$ [i.e., in the C_{2v} crossing line] at which the distance is being calculated. Similarly, Δ_2 and Δ_3 are quantities obtained by considering the parametric equations for the other permutationally equivalent lines [$r_2 = (t \sqrt{2(1 - \cos \phi)}, t, t)$ and $r_3 = (t, t \sqrt{2(1 - \cos \phi)}, t)$, respectively]; the reader is addressed to Ref. 98 for more details.

In turn, $T''(\mathbf{R})$ in Eq. (24) is a range-decaying Gaussian function suitably centered at each of the minima of the crossing

TABLE III. Stratified root-mean-square deviations (in kJ mol⁻¹) of the final DMBE PES.

Energy ^a	N^b	Maximum deviation ^c	rmsd	$N_{>\text{rmsd}}^d$
42	105	2.93	0.67	27
84	168	3.56	0.79	35
126	250	5.02	0.88	45
167	310	9.08	1.00	48
209	327	13.22	1.21	49
251	338	13.22	1.46	47
293	347	13.22	1.67	47
335	366	14.85	2.34	38
377	367	14.85	2.51	39
418	372	14.85	2.72	39
628	396	14.85	2.85	45
837	484	14.85	2.93	66
1255	572	16.61	3.56	67
1674	623	16.61	3.81	75
2092	626	16.61	3.97	75
2510	629	16.61	4.14	76

^aThe units of energy are kJ mol⁻¹. Energy strata are defined relative to the absolute minimum of the DMBE PES, i.e., the linear C_3 structure with an energy of $-0.2904 E_h$.

^bNumber of calculated points up to indicated energy range.

^cMaximum deviation up to indicated energy range.

^dNumber of calculated points with an energy deviation larger than the rmsd.

seam (R_1^0, R_2^0 , and R_3^0) and written as⁹⁸

$$T''(\mathbf{R}) = \exp\{-\beta[(R_1 - R_1^0)^2 + (R_2 - R_2^0)^2 + (R_3 - R_3^0)^2]\} \\ + \exp\{-\beta[(R_1 - R_2^0)^2 + (R_2 - R_3^0)^2 + (R_3 - R_1^0)^2]\} \\ + \exp\{-\beta[(R_1 - R_3^0)^2 + (R_2 - R_1^0)^2 + (R_3 - R_2^0)^2]\}, \quad (27)$$

where β is a rate decaying parameter which ensures that the above function avoids any influence of the $V''_{\text{EHF}}(\mathbf{R})$ term at regions of the configuration space far from the crossing seam.⁹⁸ The complete set of parameters in Eq. (24) [20 in all: 15 c_{ijk}^n , R_0 , β , R_1^0 , R_2^0 , and R_3^0] have been obtained by subtracting the sum of one- [$V^{(1)} = D_e$], two- [$V^{(2)}(R_i)$], three-body dc [$V_{\text{dc}}^{(3)}(\mathbf{R})$], and $V'_{\text{EHF}}(\mathbf{R})$ energy terms from an extra set of 54 scaled *ab initio* points covering the region defined by $59.88^\circ \leq \phi \leq 60.40^\circ$ with bond lengths fixed at $R_1 = R_2 = 2.643 a_0$ and also FVCAS/AVTZ optimized distances ($2.644 a_0 \leq R_1 = R_2 \leq 2.639 a_0$ —see inset of Figure 11). These could be least-squared fitted to Eq. (24) with a rmsd of 0.06 kJ mol⁻¹; the numerical values of the corresponding optimum parameters are given in the supplementary material.⁵⁷ Table III displays the stratified rmsd values of the final PES with respect to all fitted points. Accordingly, the fit shows a maximum unweighted rmsd of 4.14 kJ mol⁻¹ up to the highest repulsive energy stratum.

V. FEATURES OF THE DMBE POTENTIAL ENERGY SURFACE

All major topographical features of the PES are depicted in Figures 5-12, while the corresponding structural parameters of the relevant stationary points are collected in Table IV. The most salient feature relates to the fact that the present DMBE PES for the C_3 ($^1A'$) radical shows three equivalent,

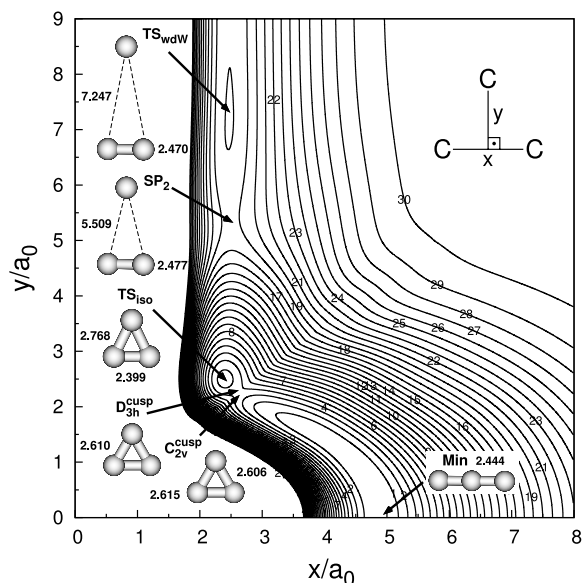


FIG. 5. Contour plot for C_{2v} insertion of the C atom into the C_2 fragment. Contours equally spaced by $0.01 E_h$, starting at $-0.2904 E_h$.

symmetry related minima (referred to as Min) at symmetric linear configurations with a characteristic bond length of $R_1/2 = R_2 = R_3 = 2.444 a_0$ in excellent agreement with the experimental value reported by Hinkle *et al.*⁹ of $2.451 a_0$. As seen in Table IV, this is no doubt obtained by virtue of the DMBE-SEC⁹¹ scheme employed in the present work. Table IV also gathers the best available results reported in the literature as well as our own *ab initio* values obtained at the FVCAS/AVTZ and MRCI/AVTZ levels of theory. For comparison, we have also computed scaled MRCI + Q/AVQZ (with $\mathcal{F}_{C_2}^{(2)} = \mathcal{F}_{C_3}^{(3)}$

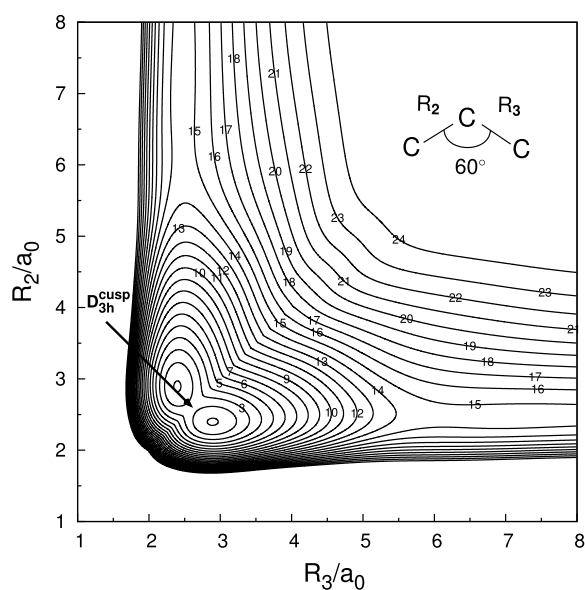


FIG. 6. Contour plot for the C–C–C bond stretching keeping the included angle fixed at 60° . Contours equally spaced by $0.012 E_h$, starting at $-0.2588 E_h$.

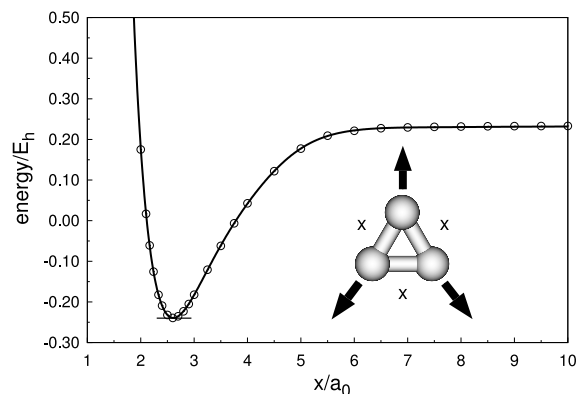


FIG. 7. Cut along the D_{3h} intersection line as a function of the characteristic bond length. The dots indicate the *ab initio* points included in the fit.

$= 0.6738$ at this level) and CBS extrapolated energies^{121,122} at the stationary structures predicted by the DMBE PES. Note that the latter were estimated by treating separately the FVCAS and dc components of the energy as obtained from MRCI + Q/AVXZ ($X = T, Q$) calculations.^{121,122} Thence, for FVCAS energies, a two-point extrapolation scheme due to Karton-Martin¹²¹ has been employed, while the dc components have been obtained following the USTE(T, Q)¹²² protocol. Although the DMBE PES yields an accurate equilibrium structure for the $C_3(1^1A')$ radical, the harmonic vibrational frequencies so obtained deviate by ca. 20.0 cm^{-1} , -0.1 cm^{-1} , and -86.5 cm^{-1} for the symmetric (w_1), bending (w_2), and antisymmetric (w_3) motions, respectively, relative to the observed fundamentals. Such a discrepancy is most likely due to large anharmonicity and large-amplitude motion, which are especially manifested in the bending frequency, thence explaining why deviations

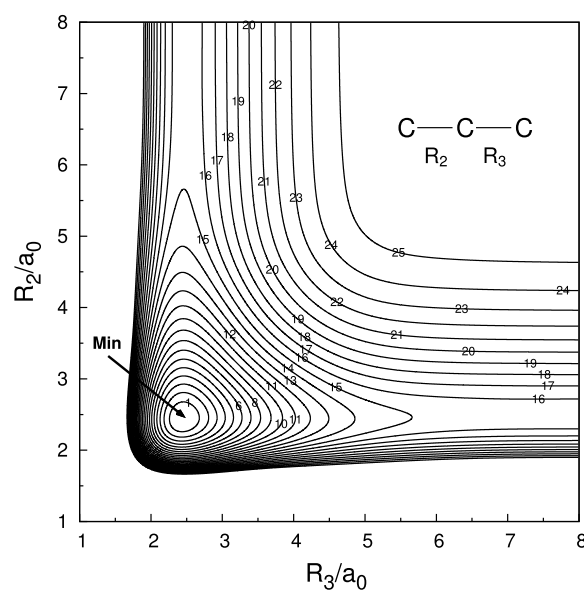


FIG. 8. Contour plot for the C–C–C bond stretching for linear configuration. Contours equally spaced by $0.012 E_h$, starting at $-0.2904 E_h$.

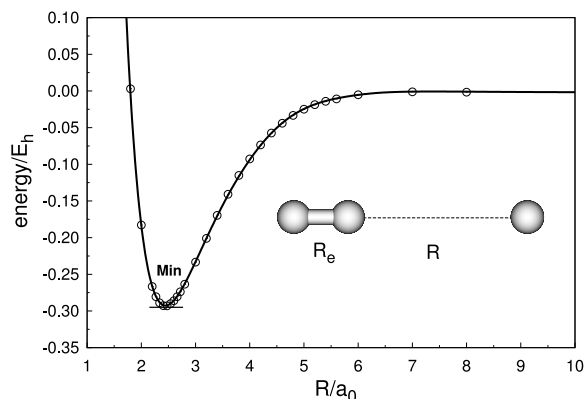


FIG. 9. Cut for $C_{\infty v}$ insertion of the C atom into the C_2 diatomic with an internuclear distance fixed at $R_e = 2.444 a_0$. The dots indicate the *ab initio* points included in the fit.

from the normal mode and small-amplitude models may take place.²

A notable feature of the present DMBE PES, thus far unreported, is the transition structure (hereinafter referred to as TS_{wdw}) at regions of the PES dominated by long range interactions. As clearly visible from Figure 5, which depicts the insertion of a C atom into the C_2 fragment for C_{2v} configurations, such a structure is predicted to be located at $R_1 = 2.470 a_0$ and $R_2 = R_3 = 7.247 a_0$ with a well depth of $-6.49 \text{ kJ mol}^{-1}$ relative to the $C_2(a^3\Pi_u) + C(^3P)$ dissociation channel. Although it is a typical first-order saddle point whose imaginary frequency ($136.7i \text{ cm}^{-1}$) corresponds to the distortion of the isosceles triangle to a C_s configuration, such a TS_{wdw} structure manifests as a minimum in two dimensions, one corresponding to the perpendicular approach of the C atom to $C_2(a^3\Pi_u)$ and the other to the diatomic C–C stretching. The saddle-point nature of this stationary state is perhaps best understood from the plot shown later in Figure 12. In fact, this transition state is connected by another saddle point of index 2 (or second-order), SP_2 , with characteristic bond

lengths of $R_1 = 2.477 a_0$ and $R_2 = R_3 = 5.509 a_0$, which lies about $32.46 \text{ kJ mol}^{-1}$ and $38.95 \text{ kJ mol}^{-1}$ above $C + C_2$ and TS_{wdw} , respectively. Note from Table IV that SP_2 is actually a second-order saddle point with imaginary frequencies of $453.3i \text{ cm}^{-1}$ and $542.7i \text{ cm}^{-1}$ which correspond to the insertion of the C atom into C_2 , and distortion of the isosceles triangle to a C_s configuration, respectively. This now appears as a maximum in the C around C_2 contour plot of Figure 12. Although stationary structures with more than one negative curvature along the principal axes have, generally, no chemical significance, such a feature may reflect an avoided intersection with an upper electronic state. As first remarked by Carter *et al.*³¹ and Whiteside *et al.*,⁵⁴ the isomerization between the three symmetry related C_3 global minima (i.e., the degenerate arrangement which exchanges the central carbon atom to a terminal position and vice versa) occurs via a C_{2v} transition state TS_{iso} located at $R_1 = 2.399 a_0$ and $R_2 = R_3 = 2.768 a_0$ with a frequency of $1039.3i \text{ cm}^{-1}$. Note that due to the low dimensionality of the contour plot in Figure 5, such a structure shows itself as a local minimum with an energy of $-673.01 \text{ kJ mol}^{-1}$ with respect to the $C_2(a^3\Pi_u) + C(^3P)$ asymptote. Note further that the TS_{iso} arises from a non-totally symmetric distortion of the D_{3h} equilateral triangle (D_{3h}^{cusp} structure — see Table IV), as implied by the Jahn-Teller theorem,^{82,83} with a stabilization energy relative to the D_{3h}^{cusp} of $-45.98 \text{ kJ mol}^{-1}$. The classical barrier height predicted from the present DMBE form is $89.58 \text{ kJ mol}^{-1}$ relative to the linear minima. In fact, excellent agreements were found between this value and the corresponding barriers predicted from the DMBE-SEC/MRCI+Q/AVQZ ($89.43 \text{ kJ mol}^{-1}$) and CBS extrapolation schemes ($82.22 \text{ kJ mol}^{-1}$). It should be pointed out that scaling of the dynamical correlation via DMBE-SEC⁹² reduces the activation barrier for the isomerization process in about $32.34 \text{ kJ mol}^{-1}$ and $17.82 \text{ kJ mol}^{-1}$ with respect to the values actually predicted from the FVCAS/AVTZ and MRCI/AVTZ energies, respectively (see Table IV). Note that the corresponding barrier predicted from the CMM³¹ PES is rather low ($25.19 \text{ kJ mol}^{-1}$) compared with the results reported by Whiteside *et al.*⁵⁴ at the MP4/6-31G* level of theory

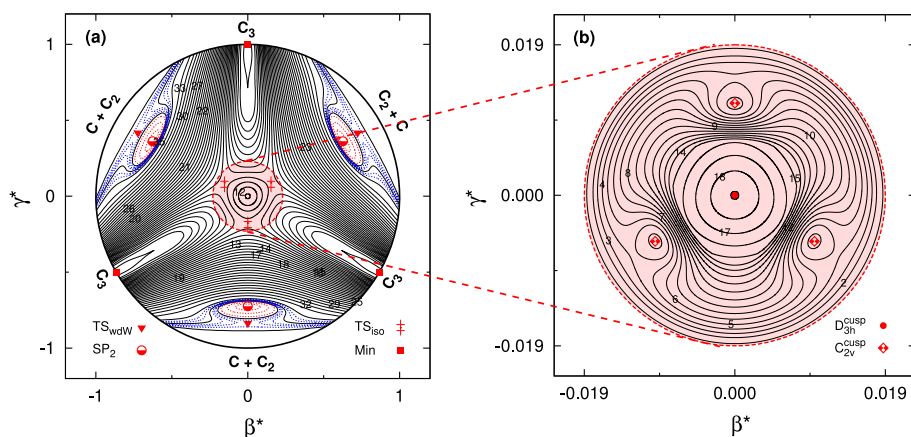


FIG. 10. (a) Relaxed triangular plot in hyperspherical coordinates depicting the location and symmetry of all stationary points discussed in the present work for the ground state of C_3 . Solid black lines are equally spaced by $0.005 E_h$, starting at $-0.2904 E_h$. Dashed red and blue lines are equally spaced by $0.001 E_h$, starting at $0.00067 E_h$ and $-0.0206 E_h$, respectively. (b) Close view of the conical intersection region showing the minimum of the crossing seam at D_{3h} symmetry as well as the minimum of the three equivalent symmetry related C_{2v} crossing lines. Contours are equally spaced by $0.00004 E_h$, starting at $-0.240085 E_h$.

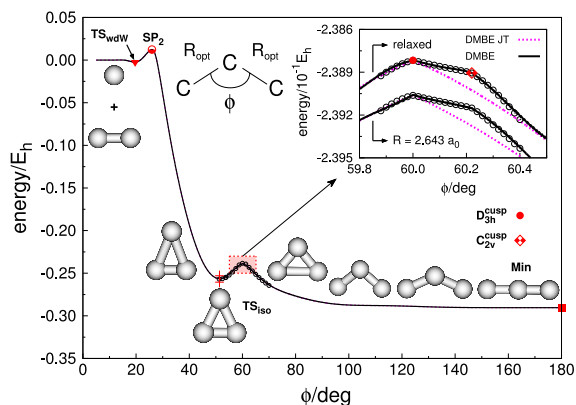


FIG. 11. Minimum energy path with bond lengths relaxed along the bending angle ϕ . The plot starts at $\phi = 5^\circ$ which corresponds to the $C+C_2$ limit and leads to the linear global minimum at $\phi = 180^\circ$ via the conical intersection region. The inset shows an amplified region of the configuration space, with the correct cusped behavior at both D_{3h} and C_{2v} crossing seams. The dots indicate the *ab initio* points included in the fit, with the ones related to a fixed bond-length shifted by $-0.0025 E_h$. In the key, DMBE JT indicates the present PES without the contributions of the $V_{EHF}^{(3)}(\mathbf{R})$ term.

(125.14 kJ mol $^{-1}$) as well as our own *ab initio* calculations. Figures 5–11 show that the present DMBE form ensures the correct behavior at the 4 conical intersections. This is a result of using the Jahn-Teller type coordinate $^{82} \sqrt{F_2}$ in the second polynomial of Eq. (20), and the term $V_{EHF}^{(3)}$ in Eq. (24). Note that the D_{3h}^{cusp} structure shown in Table IV and emphasized in Figure 7 is not a stationary point on the global PES: it is a minimum only for A_1 distortions. Conversely to the C_{2v} case, the linear insertion of $C(^3P)$ into $C_2(a^3\Pi_u)$, shown in Figures 8 and 9, encounters no barrier for forming ground-state linear C_3 (denoted as Min). Suffice it to say that this minimum structure has a well depth of -762.58 kJ mol $^{-1}$ relative to $C+C_2$, and an energy of -1372.60 kJ mol $^{-1}$ ($\equiv -D_e[C_3(\bar{X}^1\Sigma_g^+)]$) with respect to the three infinitely separated $C(^3P)$ atoms. This

result agrees quite well with the experimental values reported by Gingerich *et al.* 24 (-1323.27 kJ mol $^{-1}$) as well as the *ab initio* W4 result of Karton *et al.* 109 (-1342.65 kJ mol $^{-1}$). As above, the global minima (Min) arises due to distortion of the D_{3h}^{cusp} and C_{2v}^{cusp} unstable configurations to form a linear structure with a stabilization energy of -135.56 kJ mol $^{-1}$.

All major topographical features of the DMBE PES are probably better viewed in a relaxed triangular plot 123 using scaled hyperspherical coordinates ($\beta^* = \beta/Q$ and $\gamma^* = \gamma/Q$),

$$\begin{pmatrix} Q \\ \beta \\ \gamma \end{pmatrix} = \begin{pmatrix} 1 & 1 & 1 \\ 0 & \sqrt{3} & -\sqrt{3} \\ 2 & -1 & -1 \end{pmatrix} \begin{pmatrix} R_1^2 \\ R_2^2 \\ R_3^2 \end{pmatrix}. \quad (28)$$

As shown in Figure 10, such a plot depicts in a physical way all the stationary points discussed above. Two significant features also visible from Figure 10 are the TS_{wdw} and SP_2 structures in the entrance channel associated to $C+C_2$. Following the C_{2v} line, the transition state for the isomerization between the three symmetry related global minima is apparent and signaled by a red double dagger symbol (\ddagger). From here, the title system may attain the C_3 structure by following down to the right or left until reaching the equator of the hypersphere. Instead, if continuing to move forward along the C_{2v} axis, one encounters first the minimum of the C_{2v} conical seam and finally the minimum of the D_{3h} conical seam. On moving further on along the C_{2v} axis, one finally encounters the $D_{\infty h}$ absolute minimum as it is visible from Figure 10(a). For collinear arrangements, the $C+C_2$ system may reach directly the C_3 minima by following any direction along the equator (see Figure 9).

Figure 11 shows a minimum energy cut for C_{2v} arrangements and corresponds, in Figure 10, to a path from the equator ($C+C_2$) to the pole of the North or South hemispheres (i.e., center of the shown physical circle 123), D_{3h}^{cusp} , and then again to the equator at the opposite side (C_3). Note that similar sections exist for rotations by $\pm 120^\circ$. As already remarked by others, 5,6,39,40,53 and clearly visible from Figure 11, the ground

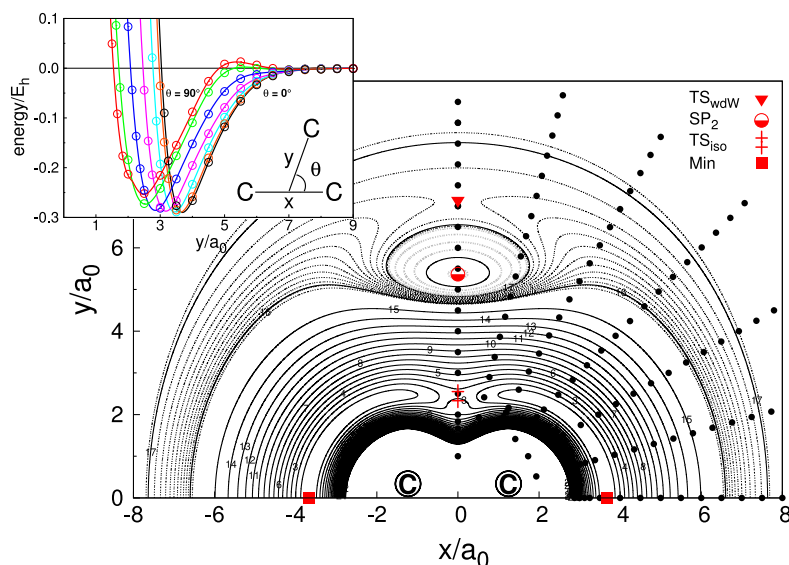


FIG. 12. Contour plot for the C atom moving around a partially relaxed C_2 diatom ($2.2 \leq R_{C_2}/a_0 \leq 2.6$), which lies along the x axis with the center of the bond fixed at the origin. Solid black lines are equally spaced by $0.01 E_h$, starting at $-0.2906 E_h$. Dashed gray and black lines are equally spaced by 0.001 and $0.00025 E_h$, starting at zero and $-0.0206 E_h$, respectively. Also shown by the black solid dots are the calculated *ab initio* points for the C atom moving around a C_2 diatomic fixed at the equilibrium geometry. Similarly indicated by other symbols are various stationary points. In turn, the inset shows cuts along the atom-(equilibrium)/diatom radial coordinate for selected values of the Jacobi angle.

TABLE IV. Properties of stationary points and other relevant structures on the $C_3(1^1A')$ DMBE PES.

	Method	R_1/a_0	R_2/a_0	R_3/a_0	$E/\text{kJ mol}^{-1}$	w_1/cm^{-1}	w_2/cm^{-1}	w_3/cm^{-1}
Min	DMBE ^a	4.888	2.444	2.444	0 ^b	1204.2	63.5	2126.5
	FVCAS/AVTZ ^a	4.948	2.474	2.474	0	1171.0	56.1	2060.9
	MRCI/AVTZ ^a	4.922	2.461	2.461	0	1190.0	75.8	2085.1
	DMBE-SEC/MRCI+Q/AVQZ ^a	4.888	2.444	2.444	0
	CBS ^a	4.888	2.444	2.444	0
	FVCAS/ANO ^c	4.948	2.474	2.474	...	1192.0	70.2	2007.3
	CCSD(T)/177 cGTOs ^d	4.906	2.453	2.453	...	1219.0	64.3	2040.6
	MRCI+Q/VTZ ^e	4.924	2.462	2.462	...	1212.6	84.8	2044.6
	CASSCF(10, 8)/VQZ ^f	4.920	2.460	2.460	...	1178.9	132.3	2067.7
	CMM ^g	4.838	2.419	2.419	0	1278.0	106.0	1950.0
	Expt. ^h	4.902	2.451	2.451	0	1224.20	63.42	2040.02
TS _{iso}	DMBE ^a	2.399	2.768	2.768	89.58	1257.2	1873.3	1039.3 <i>i</i>
	FVCAS/AVTZ ^a	2.424	2.808	2.808	121.92	1193.8	1747.0	997.7 <i>i</i>
	MRCI/AVTZ ^a	2.413	2.787	2.787	107.40	1211.1	1774.0	1011.1 <i>i</i>
	DMBE-SEC/MRCI+Q/AVQZ ^a	2.399	2.768	2.768	89.43
	CBS ^a	2.399	2.768	2.768	82.22
	MP4/6-31G ^{si}	2.362	2.761	2.761	125.14	1339.0	2013.0	1402.0 <i>i</i>
CMM ^g	2.268	3.053	3.053	25.19	
SP ₂	DMBE ^a	2.477	5.509	5.509	795.04	1354.4	453.3 <i>i</i>	542.7 <i>i</i>
	DMBE-SEC/MRCI+Q/AVQZ ^a	2.477	5.509	5.509	799.83
	CBS ^a	2.477	5.509	5.509	771.17
TS _{wdw}	DMBE ^a	2.470	7.247	7.247	756.09	1613.1	160.0	136.7 <i>i</i>
	DMBE-SEC/MRCI+Q/AVQZ ^a	2.470	7.247	7.247	755.93
	CBS ^a	2.470	7.247	7.247	729.75
D _{3h} ^{cusp}	DMBE ^a	2.610	2.610	2.610	135.56
	FVCAS/AVTZ ^a	2.643	2.643	2.643	181.08
	MRCI/AVTZ ^a	2.627	2.627	2.627	159.20
	DMBE-SEC/MRCI+Q/AVQZ ^a	2.610	2.610	2.610	137.97
	CBS ^a	2.610	2.610	2.610	154.43
C _{2v} ^{cusp}	DMBE ^a	2.615	2.606	2.606	135.31
	FVCAS/AVTZ ^a	2.648	2.639	2.639	180.96
	MRCI/AVTZ ^a	2.628	2.620	2.620	159.12
	DMBE-SEC/MRCI+Q/AVQZ ^a	2.615	2.606	2.606	137.40
	CBS ^a	2.615	2.606	2.606	154.12
C ₂ ($a^3\Pi_u$) + C(3P)	DMBE ^a	2.483	50.000	52.483	762.58
	FVCAS/AVTZ ^a	2.513	50.000	52.513	667.31
	MRCI/AVTZ ^a	2.498	50.000	52.498	714.79
	DMBE-SEC/MRCI+Q/AVQZ ^a	2.483	50.000	52.483	761.67
	CBS ^a	2.483	50.000	52.483	733.66
	CMM ^g	2.479	50.000	52.479	877.93
	W4 ^j	736.89
Expt. ^k	713.29	

^aThis work.^bRelative to the absolute minimum of C_3 , $-0.2904 E_h$.^cReference 35. Dissociation energy not reported.^dReference 37. Dissociation energy not reported.^eReferences 39 and 40. Dissociation energy not reported.^fReference 34. Dissociation energy not reported.^gReference 31. Harmonic vibrational frequencies for TS_{iso} not reported.^hReferences 9 and 40.ⁱReference 54.^jReference 109.^kReferences 78, 94, 95, and 24. Estimated as $E = -D_e[C_2(a^3\Pi_u)] + \{D_0[C_3(\tilde{X}^1\Sigma_g^+)] + E_{ZPE}[C_3(\tilde{X}^1\Sigma_g^+)]\}$.

state bending potential is exceptionally flat with a very low bending frequency and large amplitude motion. Indeed, as predicted from the present DMBE form, linear C_3 requires only $16.36 \text{ kJ mol}^{-1}$ to reach a bending angle of 90° . Additionally,

the inset of Figure 11 reinforces the fact that the present DMBE PES has the correct behavior at the conical intersection region.

Figure 12 illustrates the PES for a C atom moving around a C_2 fragment and summarizes, in a comprehensive manner,

all the stationary structures discussed in the present work. For inelastic and reactive quantum scattering calculations, it is often advantageous to express the interaction potential by a Legendre expansion^{120,124,125}

$$V(R_e, r, \theta) = \sum_L V_L(R_e, r) P_L(\cos \theta), \quad (29)$$

where R_e is the diatomic internuclear distance of C_2 , here fixed at its equilibrium value of $2.483 a_0$, r and θ are Jacobi coordinates, and $P_L(\cos \theta)$ are Legendre polynomials.¹²⁵ The leading terms $V_L(R_e, r)$, shown in Figure 13, are obtained from $V(\mathbf{R})$ by the integral⁴²

$$V_L(R_e, r) = (2L + 1) \times \int_0^{\pi/2} V(R_e, R_2, R_3) P_L(\cos \theta) \sin \theta d\theta. \quad (30)$$

Only even terms are presented, since odd ones vanish by symmetry reasons.¹²⁵ Of particular relevance in scattering processes^{97,125} are the spherically averaged (or isotropic) [$V_0(R_e, r)$] and leading anisotropic [$V_2(R_e, r)$] terms. Generally, the magnitude of $V_0(R_e, r)$ determines how close, on the average, the atom and the diatomic fragment can get together, while the sign of $V_2(R_e, r)$ indicates whether or not the molecule prefers to orient its axis along the incoming atom:^{97,125} a negative value favors a collinear approach, whereas a positive one favors the approach through C_{2v} configurations. As seen in Figure 13, the average distance where $V_0(R_e, r)$ attains its lowest value is $\langle r \rangle = 3.172 a_0$ and corresponds to a region of maximum interaction between the C atom and C_2 diatomic (at its equilibrium distance). Note that in regions dominated by long-range interactions (see inset of Figure 13), the $V_2(R_e, r)$ term changes twice sign for values of the atom-diatom separation equal to $r = 12.495 a_0$ and $7.478 a_0$, distance from which it remains negative until the next sign change at $r = 3.172 a_0$. Note that the third sign change of $V_2(R_e, r)$ coincides with the distance at which $V_0(R_e, r)$ assumes its minimum value. All such features may be rationalized from a close inspection of Figures 10 and 12. Accordingly, the collinear approach of the C atom to the C_2 molecule is energetically more favorable at large values of r and changes as the fragments get together following the sequence: collinear,

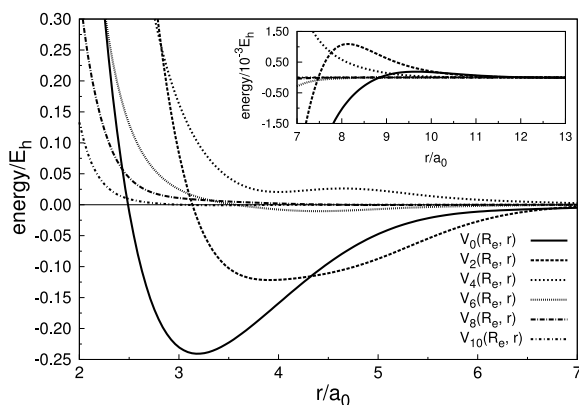


FIG. 13. Isotropic [$V_0(R_e, r)$], leading anisotropic [$V_2(R_e, r)$], and higher order terms of the Legendre expansion in Eq. (29).

perpendicular (first sign change at $r = 12.495 a_0$), collinear (second sign change at $r = 7.478 a_0$), and perpendicular (third sign change at $r = 3.172 a_0$). Note that the first sign change ($r = 12.495$) is most likely induced by the energy stabilization of $\approx 6.49 \text{ kJ mol}^{-1}$ due to formation of the TS_{wdw} structure. Subsequently, the system undergoes a distortion to $D_{\infty v}$ conformation (second sign change) following the imaginary normal mode of TS_{wdw} in order to avoid spending $38.95 \text{ kJ mol}^{-1}$ to overcome the SP_2 stationary point. This is seen from Figure 12, which shows that the depth of the van der Waals potential is the largest for the perpendicular approach and decreases smoothly as one approaches collinear arrangements.

VI. ROVIBRATIONAL ENERGY LEVELS

To judge the quality of the current DMBE PES, we have performed rovibrational calculations for the first 53 levels using the multidimensional discrete variable representation (DVR) method^{126,127} as implemented in Tennyson's¹²⁸ DVR3D code. All calculations have employed Jacobi coordinates with the molecular body-fixed z -axis embedded along the C–C center-of-mass separation (r). This embedding scheme and choice of (orthogonal) internal coordinates are particularly advantageous^{129,130} to achieve simple (in the sense that no cross-derivative terms are present) and general kinetic energy operators. Details concerning the analytical expression of the body-fixed Hamiltonian operator in Jacobi coordinates can be found elsewhere.^{126,131,132}

As noted by Ahmed *et al.*³⁹ and Mladenović *et al.*,³⁷ the strong stretch-bend coupling and the large-amplitude bending motion in C_3 set high requirements to a proper treatment of the intramolecular motion, in as much as vibrational modes are sufficiently highly excited and significant portions of the PES far from the equilibrium are accessible.¹²⁶ In this sense, DVR-based methods^{126,127} have enjoyed great success in obtaining accurate solutions of a variety of rovibrational problems for such floppy systems.^{37,126,127}

The rotation-vibration wave function assumes the form^{129,130}

$$|nJp\rangle = \sum_{k=0}^J |Jkp\rangle \sum_{m_1 m_2 m_3} c_{km_1 m_2 m_3}^{nJp} P_{m_1}^k(R) P_{m_2}^k(r) P_{m_3}^k(\theta), \quad (31)$$

where $|nJp\rangle$ is the wave function of the n th rotation-vibration state with rotational symmetry defined by the total rotational angular momentum quantum number J and the parity p .¹³⁰ The $|Jkp\rangle$ are the symmetrized rotational functions^{129,130} and depend on the three Euler angles (α , β , and γ) which specify the orientation of the body-fixed coordinate with respect to the space-fixed frame. Finally, $P_{m_i}^k$ are the vibrational basis functions, which may depend on the projection of the total angular momentum along the body-fixed z -axis, k , and are functions of a single internal Jacobi coordinate (R , r , or θ). In turn, $c_{km_1 m_2 m_3}^{nJp}$ are expansion coefficients which are determined by diagonalizing the Hamiltonian matrix.^{129,130}

For given (J , p) values, the Hamiltonian matrix of the body-fixed operator in Jacobi coordinates, \hat{H}^{Jac} , is defined as follows:^{129,130}

TABLE V. Calculated (G_{cal}) and experimental (G_{exp}) vibrational term values (in cm^{-1}) for the ground state of $\text{C}_3(1^1\text{A}')$ radical. The quantum numbers v_1 , v_2 , and v_3 refer to symmetric, bending, and antisymmetric motions, respectively, and $l_2=0, 1, 2$ is the vibrational angular momentum quantum number. J is the total rotational angular momentum quantum number.

v_1	$v_2^{l_2}$	v_3	J	$G_{\text{cal}}^{\text{a}}$	$G_{\text{exp}}^{\text{b}}$	Observed — calculated			
						DMBE ^a	Jensen <i>et al.</i> ^c	Ahmed <i>et al.</i> ^d	Mladenović <i>et al.</i> ^e
0	2 ⁰	0	0	140.8	132.80	-8.0	-21.5	15.5	-0.5
0	4 ⁰	0	0	328.5	286.11	-42.4	-47.1	-5.0	2.7
0	6 ⁰	0	0	522.9	461.09	-61.8	-66.7	-16.7	11.0
0	8 ⁰	0	0	691.8	647.59	-44.2	-87.9	-29.5	15.1
0	10 ⁰	0	0	862.8	848.40	-14.4	-106.8	-40.0	19.1
0	12 ⁰	0	0	1085.3	1061.96	-23.3	-118.4	-49.2	...
1	0 ⁰	0	0	1161.0	1224.20	63.2	32.2	60.4	5.3
1	2 ⁰	0	0	1330.0	1404.10	74.1	26.1	32.4	1.0
1	4 ⁰	0	0	1606.7	1592.05	-14.7	5.3	13.1	2.0
1	6 ⁰	0	0	1812.3	1785.11	-27.1	-20.1	-2.2	2.4
1	8 ⁰	0	0	1954.7	1990.52	35.8	-42.1	-14.9	6.6
1	10 ⁰	0	0	2169.7	2210.50	40.8	-57.3	-21.9	15.3
0	0 ⁰	1	0	1986.1	2040.02	53.9	32.7	44.2	-0.6
0	2 ⁰	1	0	2126.9	2133.88	6.9	3.2	13.9	-4.7
0	4 ⁰	1	0	2314.6
0	6 ⁰	1	0	2509.0
0	8 ⁰	1	0	2678.0
0	10 ⁰	1	0	2848.9
2	0 ⁰	0	0	2422.8	2435.20	12.4	60.8	69.5	10.5
2	2 ⁰	0	0	2616.8	2656.30	39.5	65.7	46.0	3.9
2	4 ⁰	0	0	2826.9	2876.90	50.0	49.3	30.6	0.4
2	6 ⁰	0	0	3010.5	3099.90	89.4	29.6	18.7	1.6
2	8 ⁰	0	0	3364.4
2	10 ⁰	0	0	3445.2
0	1 ¹	0	1	61.6	63.42	1.8	-6.8	27.3	-0.9
0	3 ¹	0	1	231.9	207.30	-24.6	-33.0	3.0	0.8
0	5 ¹	0	1	426.0
0	7 ¹	0	1	612.3
0	9 ¹	0	1	769.8
1	1 ¹	0	1	1201.9
1	3 ¹	0	1	1463.7
1	5 ¹	0	1	1754.2
1	7 ¹	0	1	2042.1
1	9 ¹	0	1	2219.9
0	1 ¹	1	1	2075.7	2078.50	2.8	19.7	21.6	-4.4
0	3 ¹	1	1	2279.9	2191.10	-88.8	-10.3	1.0	-5.7
0	5 ¹	1	1	2427.3	2330.00	-97.3	-34.5	-12.9	-2.1
0	7 ¹	1	1	2571.6	2489.70	-81.9	-54.7	-23.3	3.3
0	2 ²	0	2	121.2	133.06	11.8	-16.9	...	-1.2
0	4 ²	0	2	323.3	286.80	-36.5	-44.6	...	2.2
0	6 ²	0	2	516.4	462.10	-54.3	-64.8	...	10.7
0	8 ²	0	2	688.7	648.80	-39.9	-86.2	...	15.0
0	10 ²	0	2	857.1	849.70	-7.4	-104.7	...	19.0
1	2 ²	0	2	1321.4	1410.50	89.1	-31.5	...	3.5
1	4 ²	0	2	1597.5	1596.00	-1.5	-8.0	...	2.0
1	6 ²	0	2	1905.7	1995.80	90.1	-37.7	...	8.6
1	8 ²	0	2	2239.8
1	10 ²	0	2	2305.3
0	2 ²	1	2	2125.9	2127.41	1.5	1.8	...	-7.0
0	4 ²	1	2	2239.8
0	6 ²	1	2	2405.3
0	8 ²	1	2	2606.7

TABLE V. (Continued.)

v_1	$v_2^{l_2}$	v_3	J	G_{cal}^a	$G_{\text{expt.}}^b$	Observed — calculated			
						DMBE ^a	Jensen <i>et al.</i> ^c	Ahmed <i>et al.</i> ^d	Mladenović <i>et al.</i> ^e
0	10 ²	1	2	2808.3
		rmsd				50.4	53.1	31.2	8.0

^aThis work. G_{cal} is given with respect to the zero point level at 1728.8 cm⁻¹.

^bReferences 35, 37, 39, 45, and 49.

^cReference 35.

^dReference 39. Vibrational term values for $J = 2$ not reported.

^eReference 37.

$$H_{S'S}^{Jp} = \langle Jk'p | \langle m'_1 m'_2 m'_3 | \hat{H}^{Jac} | m_1 m_2 m_3 \rangle | Jkp \rangle, \quad (32)$$

where the S (S') index has been used to represent the quantum numbers k , m_1 , m_2 , and m_3 (k' , m'_1 , m'_2 , and m'_3) and $|m_1 m_2 m_3\rangle$ ($|m'_1 m'_2 m'_3\rangle$) denote the purely vibrational part in Eq. (31). In the present work, we have employed Morse oscillator-like functions¹²⁸ as radial vibrational basis [$P_{m_1}^k(R)$ and $P_{m_2}^k(r)$] whose parameters were initially obtained by taking cuts through the PES at the region defined by the $D_{\infty h}$ global minimum (Min structure). Such parameters have been subsequently optimized in initial test calculations, yielding $R = 2.585 a_0$, $D_e = 0.562 E_h$, and $w_e = 0.011 E_h$ for the CC diatomic stretching coordinate and $r = 3.695 a_0$, $D_e = 0.305 E_h$, and $w_e = 0.008 E_h$ for C–CC center-of-mass coordinate. Note that associated Legendre polynomials¹²⁹ have been used for angular vibrational basis [$P_{m_3}^k(\theta)$], as defined in the DVR3D software suite.¹²⁸ With the above set of orthogonal polynomials and their associated Gaussian quadratures,^{129,130} our final DVR transformation has been accomplished by using 100 grid points for each single internal Jacobi coordinate with the diagonalization problem solved in the order $r \rightarrow R \rightarrow \theta$. An energy cutoff of 3000 cm⁻¹ (here, the global minimum is the zero of the potential) has been used for the 1D solutions, and 1000 2D solutions utilized for building the final 3D matrix of dimension 2000. It should be pointed out that the above procedure provided a large number of converged levels up to 3500 cm⁻¹ above the zero point level at 1728.8 cm⁻¹, typically converged to within 0.1 cm⁻¹ or better.

The rovibrational levels for the ground state of the C₃(1¹A') radical were obtained for $J \leq 2$ both for even(e)-parity ($p = 0$) and odd(f)-parity ($p = 1$). The term values so obtained (G_{cal}) are gathered in Table V together with the available experimental measurements^{35,37,39,45,49} ($G_{\text{expt.}}$). Also shown in Table V are the differences between experimental and calculated term energies ($G_{\text{expt.}} - G_{\text{cal}}$) obtained in the present work as well as those reported in the most recent purely *ab initio* (near-equilibrium) surfaces of Jensen *et al.*,³⁵ Mladenović *et al.*,³⁷ and Ahmed *et al.*³⁹ Note that all vibrational term energies, G_v , are assigned according to four approximate quantum numbers ($v_1, v_2^{l_2}, v_3$), where v_1 , v_2 , and v_3 refer to symmetric, bending, and antisymmetric motions, respectively, and $l_2 = 0, 1, 2$ is the vibrational angular momentum quantum number.³⁵

A close inspection of Table V shows that the present global DMBE PES reproduces quite well the vibrational

energy spectrum of C₃ with a rmsd of 50.4 cm⁻¹ for 53 calculated levels. Note that to achieve such an accuracy, a relatively dense grid of 149 scaled *ab initio* points has been generated in the region defined by $2.145 a_0 \leq R_{1,2}/R_e \leq 2.745 a_0$ in steps of $0.15 a_0$ for a range of selected ϕ angles (180°, 177°, 174°, 171°, 168°). Note further that R_1 , R_2 , and ϕ are valence coordinates⁴² with $R_e = 2.444 a_0$ and $\phi_e = 180^\circ$ referring to the bond length and bond angle equilibrium values, respectively, at the $D_{\infty h}$ global minimum (Min structure) predicted by our DMBE-SEC⁹¹ approach. Such a grid has been included in the whole data set of scaled *ab initio* points and could be least-squares fitted to the analytical function here employed [see Eqs. (8), (20), and (21)] with a rmsd of 19.8 cm⁻¹ up to 3000 cm⁻¹ above the equilibrium geometry (corresponding to 92 points), which is about the range to which our present rovibrational calculations have been restricted. It should also be pointed out that attempts were made to achieve an even smaller rmsd in this region of configuration space by attributing larger weights to the selected grid points. Such a procedure, however, leads to spurious features at other regions of configuration space, and hence has not been pursued. Of course, small numerical uncertainties in the raw energies themselves may support such an attitude. In spite of this, the present DMBE PES shows slightly better results when compared with the near-equilibrium FVCAS/ANO surface of Jensen *et al.*³⁵ whose rmsd amounts to ca. 53.1 cm⁻¹ for the selected levels.

Regarding the local, purely *ab initio*, surface of Ahmed *et al.*³⁹ obtained at MRCI+Q/VTZ level, this shows a somewhat better rmsd of 31.2 cm⁻¹ for the selected levels. Note, however, that the authors have employed a much denser grid (384 *ab initio* points) at regions of configuration space up to 8000 cm⁻¹ (≈ 96 kJ mol⁻¹) above the equilibrium geometry, which corresponds to an energy cutoff of about 42 kJ mol⁻¹ below the conical intersection region. This contrasts with the global nature of the current PES. The best fit of the rovibrational data (rmsd = 8.0 cm⁻¹) is obtained with the PES reported by Mladenović *et al.*³⁷ which has been calculated at the CCSD(T) level of theory with a basis set of 177 contracted Gaussian-type orbitals (cGTOs). Unfortunately, this too is of the local type. In summary, we judge the fit of the present work as quite satisfactory particularly because it does not involve any fitting to the observed vibrational data. Moreover, it may provide the required input for later improvement to true spectroscopy accuracy either via a direct fit^{114,133,134} to spectroscopic data or by morphing the current PES with a spectroscopically accurate local potential via energy-switching.^{112,135,136}

VII. CONCLUSIONS

We report the first global accurate *ab initio*-based PES for the ground state of the $C_3(1^1A')$ radical, thus including all relevant stationary points some of which unreported thus far to our best knowledge. Because C_3 shows a combined Jahn-Teller [$E' \otimes e'$] plus pseudo-Jahn-Teller [$(E' + A'_1) \otimes e'$] interaction, the adiabatic DMBE PES here reported must describe four conical intersections. To account for excitations beyond singles and doubles in the MRCI calculations, and also incompleteness of the one-electron basis set, all calculated energies have been fine-tuned with the DMBE-SEC method such as to reproduce the experimental dissociation energy of $C_2(a^3\Pi_u)$. The PES has then been modeled to the scaled data points according to DMBE theory, and the fit shown to accurately reproduce dissociation energies, diatomic potentials, and long-range interactions at all asymptotic channels. The proper permutational symmetry and correct behavior at the four conical intersections have also been warranted by built-in construction. Rovibrational calculations also performed have shown that the present PES reproduces the vibrational energy spectrum of C_3 with a rmsd of 50.4 cm^{-1} for the 53 considered levels. The novel DMBE form here reported is therefore commended for spectroscopic as well as reaction dynamics studies on C_3 . Moreover, the new potential energy surface should be useful, and indeed is currently being utilized, as a building block for constructing the potential energy surfaces of larger carbon clusters. Of course, being single-sheeted, it cannot be used for non-adiabatic dynamics where other adiabatic sheets can be visited.

ACKNOWLEDGMENTS

This work has the support of Fundação para a Ciência e a Tecnologia, Portugal, under Contract Nos. PTDC/CEQ-COM3249/2012 and PTDC/AAG-MAA/4657/2012, as well as the support to the Coimbra Chemistry Centre through the Project No. PEst-OE/UI0313/2014. C.M. thanks also the CAPES Foundation (Ministry of Education of Brazil) for a scholarship (Process No. BEX 0417/13-0).

- ¹W. Huggins, Proc. R. Soc. London **33**, 1 (1881).
- ²W. Weltner and R. J. Van Zee, Chem. Rev. **89**, 1713 (1989).
- ³G. Herzberg, Astrophys. J. **96**, 314 (1942).
- ⁴A. E. Douglas, Astrophys. J. **114**, 446 (1951).
- ⁵L. Gausset, G. Herzberg, A. Lagerqvist, and B. Rosen, Discuss. Faraday Soc. **35**, 113 (1963).
- ⁶L. Gausset, G. Herzberg, A. Lagerqvist, and B. Rosen, Astrophys. J. **142**, 45 (1965).
- ⁷T. Oka, J. A. Thorburn, B. J. McCall, S. D. Friedman, L. M. Hobbs, P. Sonnentrucker, D. E. Welty, and D. G. York, Astrophys. J. **582**, 823 (2003).
- ⁸M. Ádámkóvics, G. A. Blake, and B. J. McCall, Astrophys. J. **595**, 235 (2003).
- ⁹K. W. Hinkle, J. J. Keady, and P. F. Bernath, Science **241**, 1319 (1988).
- ¹⁰J. Cernicharo, J. R. Goicoechea, and E. Caux, Astrophys. J., Lett. **534**, L199 (2000).
- ¹¹B. Mookerjee, T. Giesen, J. Stutzki, J. Cernicharo, J. R. Goicoechea, M. De Luca, T. A. Bell, H. Gupta, M. Gerin, C. M. Persson, P. Sonnentrucker, Z. Makai, J. Black, F. Boulanger, A. Coutens, E. Dartois, P. Encrenaz, E. Falgarone, T. Geballe, B. Godard, P. F. Goldsmith, C. Gry, P. Hennebelle, E. Herbst, P. Hily-Blant, C. Joblin, M. Kazmierczak, R. Koos, J. Kreowski, D. C. Lis, J. Martin-Pintado, K. M. Menten, R. Monje, J. C. Pearson, M. Perault, T. G. Phillips, R. Plume, M. Salez, S. Schlemmer, M. Schmidt, D. Teysseier, C. Vastel, S. Yu, P. Dieleman, R. Göusten, C. E. Honingh, P. Morris, P. Roelfsema, R. Schieder, A. G. G. M. Tielens, and J. Zmuidzinas, Astron. Astrophys. **521**, L13 (2010).
- ¹²R. E. S. Clegg and D. L. Lambert, Mon. Not. R. Astron. Soc. **201**, 723 (1982).
- ¹³J. P. Maier, N. M. Lakin, G. A. H. Walker, and D. A. Bohlender, Astrophys. J. **553**, 267 (2001).
- ¹⁴E. Roueff, P. Felenbok, J. H. Black, and C. Gry, Astron. Astrophys. **384**, 629 (2002).
- ¹⁵N. L. J. Cox and F. Patat, Astron. Astrophys. **565**, A61 (2014).
- ¹⁶I. Savić, I. Čermák, and D. Gerlich, Int. J. Mass Spectrom. **240**, 139 (2005).
- ¹⁷M. M. Al Mogren, O. Denis-Alpizar, D. B. Abdallah, T. Stoecklin, P. Halvick, M. L. Senent, and M. Hochlaf, J. Chem. Phys. **141**, 044308 (2014).
- ¹⁸O. Denis-Alpizar, T. Stoecklin, and P. Halvick, J. Chem. Phys. **140**, 084316 (2014).
- ¹⁹A. Van Orden and R. J. Saykally, Chem. Rev. **98**, 2313 (1998).
- ²⁰R. I. Kaiser, T. N. Le, T. L. Nguyen, A. M. Mebel, N. Balucani, Y. T. Lee, F. Stahl, P. R. Schleyer, and H. F. Schaefer III, Faraday Discuss. **119**, 51 (2002).
- ²¹A. M. Mebel and R. I. Kaiser, Chem. Phys. Lett. **360**, 139 (2002).
- ²²R. I. Kaiser, C. Ochsenfeld, M. Head-Gordon, Y. T. Lee, and A. G. Suits, Science **274**, 1508 (1996).
- ²³A. Terentyev, R. Scholz, M. Schreiber, and G. Seifert, J. Chem. Phys. **121**, 5767 (2004).
- ²⁴K. A. Gingerich, H. C. Finkbeiner, and R. W. Schmude, J. Am. Chem. Soc. **116**, 3884 (1994).
- ²⁵L. Nemes, A. M. Keszler, C. G. Parigger, J. O. Hornkohl, H. A. Michelsen, and V. Stakhursky, Appl. Opt. **46**, 4032 (2007).
- ²⁶I. Lopez-Quintas, M. Oujja, M. Sanz, M. Martín, R. A. Ganeev, and M. Castillejo, Appl. Surf. Sci. **278**, 33 (2013).
- ²⁷J. Tennyson and S. N. Yurchenko, Mon. Not. R. Astron. Soc. **425**, 21 (2012).
- ²⁸C. Chen, A. J. Merer, J. Chao, and Y. Hsu, J. Mol. Spectrosc. **263**, 56 (2010).
- ²⁹J. Krieger, V. Lutter, C. P. Endres, I. H. Keppeler, P. Jensen, M. E. Harding, J. Vázquez, S. Schlemmer, T. F. Giesen, and S. Thorwirth, J. Phys. Chem. A **117**, 3332 (2013).
- ³⁰Y. Sych, P. Bornhauser, G. Knopp, Y. Liu, T. Gerber, R. Marquardt, and P. Radi, J. Chem. Phys. **139**, 154203 (2013).
- ³¹S. Carter, I. M. Mills, and J. N. Murrell, J. Mol. Spectrosc. **81**, 110 (1980).
- ³²W. Kraemer, P. Bunker, and M. Yoshimine, J. Mol. Spectrosc. **107**, 191 (1984).
- ³³P. Jensen, Collect. Czech. Chem. Commun. **54**, 1209 (1989).
- ³⁴U. G. Jørgensen, J. Almlöf, and P. E. M. Siegbahn, Astrophys. J. **343**, 554 (1989).
- ³⁵P. Jensen, C. M. Rohlfing, and J. Almlöf, J. Chem. Phys. **97**, 3399 (1992).
- ³⁶V. Špirko, M. Mengel, and P. Jensen, J. Mol. Spectrosc. **183**, 129 (1997).
- ³⁷M. Mladenović, S. Schmatz, and P. Botschwina, J. Chem. Phys. **101**, 5891 (1994).
- ³⁸H. Fueno and Y. Taniguchi, Chem. Phys. Lett. **312**, 65 (1999).
- ³⁹K. Ahmed, G. G. Balint-Kurti, and C. M. Western, J. Chem. Phys. **121**, 10041 (2004).
- ⁴⁰S. Saha and C. M. Western, J. Chem. Phys. **125**, 224307 (2006).
- ⁴¹D. G. A. Smith, K. Patkowski, D. Trinh, N. Balakrishnan, T. Lee, R. C. Forrey, B. H. Yang, and P. C. Stancil, J. Phys. Chem. A **118**, 6351 (2014).
- ⁴²J. N. Murrell, S. Carter, S. C. Farantos, P. Huxley, and A. J. C. Varandas, *Molecular Potential Energy Functions* (John Wiley & Sons, Chichester, 1984).
- ⁴³J. M. L. Martin, J. P. Franois, and R. Gijbels, Chem. Phys. Lett. **172**, 346 (1990).
- ⁴⁴W. P. Kraemer and P. R. Bunker, J. Mol. Spectrosc. **101**, 379 (1983).
- ⁴⁵K. Kawaguchi, K. Matsumura, H. Kanamori, and E. Hirota, J. Chem. Phys. **91**, 1953 (1989).
- ⁴⁶P. Jensen, J. Mol. Spectrosc. **128**, 478 (1988).
- ⁴⁷P. G. Szalay, T. Müller, G. Gidofalvi, H. Lischka, and R. Shepard, Chem. Rev. **112**, 108 (2012).
- ⁴⁸K. Raghavachari, G. W. Trucks, J. A. Pople, and M. Head-Gordon, Chem. Phys. Lett. **157**, 479 (1989).
- ⁴⁹F. J. Northrup, T. J. Sears, and E. A. Rohlfing, J. Mol. Spectrosc. **145**, 74 (1991).
- ⁵⁰T. H. Dunning, J. Chem. Phys. **90**, 1007 (1989).
- ⁵¹G. Herzberg and E. Teller, Z. Phys. Chem. B **21**, 410 (1933).
- ⁵²R. Renner, Z. Phys. **92**, 172 (1934).
- ⁵³C. Jungen and A. J. Merer, Mol. Phys. **40**, 95 (1980).
- ⁵⁴R. A. Whiteside, R. Krishnan, M. J. Frisch, J. A. Pople, and P. V. R. Schleyer, Chem. Phys. Lett. **80**, 547 (1981).
- ⁵⁵D. H. Liskow, C. F. Bender, and H. F. Schaefer, J. Chem. Phys. **56**, 5075 (1972).

- ⁵⁶W. Domcke, D. R. Yarkony, and H. Köppel, in *Conical Intersections: Electronic Structure, Dynamics & Spectroscopy*, Advanced Series in Physical Chemistry Vol. 15 (World Scientific, Singapore, 2004).
- ⁵⁷See supplementary material at <http://dx.doi.org/10.1063/1.4928434> for a detailed overview on the C₃ bending profile in C_s symmetry and to access all the parameters necessary to construct the DMBE PES function here reported.
- ⁵⁸A. J. C. Varandas and J. N. Murrell, *Faraday Discuss. Chem. Soc.* **62**, 92 (1977).
- ⁵⁹J. Römelt, S. D. Peyerimhoff, and R. J. Buenker, *Chem. Phys. Lett.* **58**, 1 (1978).
- ⁶⁰S. Carter, I. M. Mills, and R. N. Dixon, *J. Mol. Spectrosc.* **106**, 411 (1984).
- ⁶¹J. N. Murrell, *Int. J. Quantum Chem.* **37**, 95 (1990).
- ⁶²A. J. C. Varandas, *J. Mol. Struct.: THEOCHEM* **120**, 401 (1985).
- ⁶³A. J. C. Varandas, *Adv. Chem. Phys.* **74**, 255 (1988).
- ⁶⁴A. J. C. Varandas and A. I. Voronin, *Mol. Phys.* **85**, 497 (1995).
- ⁶⁵A. J. C. Varandas, in *Reaction and Molecular Dynamics*, Lecture Notes in Chemistry Vol. 75, edited by A. Laganà and A. Riganelli (Springer, Berlin, Heidelberg, 2000), pp. 33–56.
- ⁶⁶A. J. C. Varandas, in *Conical Intersections: Electronic Structure, Dynamics & Spectroscopy*, Advanced Series in Physical Chemistry Vol. 15, edited by W. Domcke, D. R. Yarkony, and H. Köppel (World Scientific, 2004), Chap. 5, pp. 205–270.
- ⁶⁷A. J. C. Varandas, *J. Chem. Phys.* **138**, 054120 (2013).
- ⁶⁸A. J. C. Varandas and B. R. L. Galvão, *J. Phys. Chem. A* **118**, 10127 (2014).
- ⁶⁹M. Cernei, A. Alijah, and A. J. C. Varandas, *J. Chem. Phys.* **118**, 2637 (2003).
- ⁷⁰L. P. Viegas, M. Cernei, A. Alijah, and A. J. C. Varandas, *J. Chem. Phys.* **120**, 253 (2004).
- ⁷¹A. J. C. Varandas, A. Alijah, and M. Cernei, *Chem. Phys.* **308**, 285 (2005).
- ⁷²B. R. L. Galvão and A. J. C. Varandas, *J. Phys. Chem. A* **115**, 12390 (2011).
- ⁷³R. A. Kendall, T. H. Dunning, and R. J. Harrison, *J. Chem. Phys.* **96**, 6796 (1992).
- ⁷⁴H. J. Werner, P. J. Knowles, G. Knizia, F. R. Manby, M. Schütz *et al.*, MOLPRO, version 2010.1, a package of *ab initio* programs, 2010, see <http://www.molpro.net>.
- ⁷⁵A. J. C. Varandas, *J. Chem. Theory Comput.* **8**, 428 (2012).
- ⁷⁶E. Wigner and E. E. Witmer, *Z. Phys.* **51**, 859 (1928).
- ⁷⁷G. Herzberg, *Molecular Spectra and Molecular Structure III. Electronic Spectra and Electronic Structure of Polyatomic Molecules* (Van Nostrand, New York, 1966), Vol. III.
- ⁷⁸K. P. Huber and G. Herzberg, *Molecular Spectra and Molecular Structure IV. Constants of Diatomic Molecules* (Van Nostrand, New York, 1979), Vol. IV.
- ⁷⁹M. Martin, *J. Photochem. Photobiol.*, A **66**, 263 (1992).
- ⁸⁰M. Boggio-Pasqua, A. I. Voronin, P. Halvick, and J. C. Rayez, *J. Mol. Struct.: THEOCHEM* **531**, 159 (2000).
- ⁸¹A. Kramida, Y. Ralchenko, J. Reader, and NIST ASD Team, NIST Atomic Spectra Database version 5.2 (Online), National Institute of Standards and Technology, Gaithersburg, MD, 2014. Available: <http://physics.nist.gov/asd> (4 November 2014).
- ⁸²H. A. Jahn and E. Teller, *Proc. R. Soc. A* **161**, 220 (1937).
- ⁸³A. J. C. Varandas, *Chem. Phys. Lett.* **487**, 139 (2010).
- ⁸⁴I. B. Bersuker, *Chem. Rev.* **113**, 1351 (2013).
- ⁸⁵P. Garcia-Fernandez, I. B. Bersuker, and J. E. Boggs, *J. Chem. Phys.* **125**, 104102 (2006).
- ⁸⁶J. J. Dillon and D. R. Yarkony, *J. Chem. Phys.* **126**, 124113 (2007).
- ⁸⁷H. C. Longuet-Higgins, *Adv. Spectrosc.* **2**, 429 (1961).
- ⁸⁸H. C. Longuet-Higgins, U. Öpik, M. H. L. Pryce, and R. A. Sack, *Proc. R. Soc. A* **244**, 1 (1958).
- ⁸⁹H. C. Longuet-Higgins, *Proc. R. Soc. A* **344**, 147 (1975).
- ⁹⁰M. V. Berry, *Proc. R. Soc. A* **392**, 45 (1984).
- ⁹¹A. J. C. Varandas, *J. Chem. Phys.* **90**, 4379 (1989).
- ⁹²F. B. Brown and D. G. Truhlar, *Chem. Phys. Lett.* **117**, 307 (1985).
- ⁹³K. A. Peterson, *J. Chem. Phys.* **102**, 262 (1995).
- ⁹⁴R. S. Urdahl, Y. Bao, and W. M. Jackson, *Chem. Phys. Lett.* **178**, 425 (1991).
- ⁹⁵I. R. Marenin and H. R. Johnson, *J. Quant. Spectrosc. Radiat. Transfer* **10**, 305 (1970).
- ⁹⁶A. J. C. Varandas and L. A. Poveda, *Theor. Chem. Acc.* **116**, 404 (2006).
- ⁹⁷B. R. L. Galvão and A. J. C. Varandas, *J. Phys. Chem. A* **113**, 14424 (2009).
- ⁹⁸B. R. L. Galvão, V. C. Mota, and A. J. C. Varandas, *J. Phys. Chem. A* **119**, 1415 (2015).
- ⁹⁹A. J. C. Varandas and J. D. Silva, *J. Chem. Soc., Faraday Trans.* **88**, 941 (1992).
- ¹⁰⁰A. J. C. Varandas, *Mol. Phys.* **60**, 527 (1987).
- ¹⁰¹J. P. Desclaux, *At. Data Nucl. Data Tables* **12**, 311 (1973).
- ¹⁰²A. J. C. Varandas, *J. Chem. Phys.* **129**, 234103 (2008).
- ¹⁰³A. J. C. Varandas, *Chem. Phys. Lett.* **471**, 315 (2009).
- ¹⁰⁴F. E. Cummings, *J. Chem. Phys.* **63**, 4960 (1975).
- ¹⁰⁵S. M. Read and J. T. Vanderslice, *J. Chem. Phys.* **36**, 2366 (1962).
- ¹⁰⁶R. J. Le Roy, RKR1 2.0: A computer program implementing the first-order RKR method for determining diatomic molecule potential energy functions. (2014), University of Waterloo Chemical Physics Research Report CP-657R, 2004. The source code and manual for this program may be obtained from the Computer Programs link at <http://leroy.uwaterloo.ca>.
- ¹⁰⁷J. S. A. Brooke, P. F. Bernath, T. W. Schmidt, and G. B. Bacskay, *J. Quant. Spectrosc. Radiat. Transfer* **124**, 11 (2013).
- ¹⁰⁸J. D. Watts and R. J. Bartlett, *J. Chem. Phys.* **96**, 6073 (1992).
- ¹⁰⁹A. Karton, A. Tarnopolsky, and J. M. L. Martin, *Mol. Phys.* **107**, 977 (2009).
- ¹¹⁰D. L. Kokkin, G. B. Bacskay, and T. W. Schmidt, *J. Chem. Phys.* **126**, 084302 (2007).
- ¹¹¹L. B. Roskop, L. Kong, E. F. Valeev, M. S. Gordon, and T. L. Windus, *J. Chem. Theory Comput.* **10**, 90 (2014).
- ¹¹²A. J. C. Varandas, *J. Chem. Phys.* **105**, 3524 (1996).
- ¹¹³A. J. C. Varandas, *Chem. Phys. Lett.* **194**, 333 (1992).
- ¹¹⁴A. J. C. Varandas and S. P. J. Rodrigues, *J. Phys. Chem. A* **110**, 485 (2006).
- ¹¹⁵R. J. Le Roy, in *Molecular Spectroscopy*, edited by R. F. Barrow, D. A. Long, and D. J. Millen (The Royal Society of Chemistry, 1973), Vol. 1, pp. 113–176.
- ¹¹⁶A. J. C. Varandas and S. P. J. Rodrigues, *Chem. Phys. Lett.* **245**, 66 (1995).
- ¹¹⁷M. A. Matías and A. J. C. Varandas, *Mol. Phys.* **70**, 623 (1990).
- ¹¹⁸A. J. C. Varandas, in *Dynamical Processes in Molecular Physics*, edited by G. Delgado-Barrio (IOP, 1993), Vol. 1, pp. 3–28.
- ¹¹⁹A. J. C. Varandas and J. N. Murrell, *Chem. Phys. Lett.* **84**, 440 (1981).
- ¹²⁰A. J. C. Varandas, F. B. Brown, C. A. Mead, D. G. Truhlar, and N. C. Blais, *J. Chem. Phys.* **86**, 6258 (1987).
- ¹²¹A. Karton and J. M. L. Martin, *Theor. Chem. Acc.* **115**, 330 (2006).
- ¹²²A. J. C. Varandas, *J. Chem. Phys.* **126**, 244105 (2007).
- ¹²³A. J. C. Varandas, *Chem. Phys. Lett.* **138**, 455 (1987).
- ¹²⁴A. J. C. Varandas and J. Tennyson, *Chem. Phys. Lett.* **77**, 151 (1981).
- ¹²⁵A. J. C. Varandas, *J. Chem. Phys.* **70**, 3786 (1979).
- ¹²⁶Z. Băcić and J. C. Light, *Annu. Rev. Phys. Chem.* **40**, 469 (1989).
- ¹²⁷J. C. Light and T. Carrington, “Discrete-variable representations and their utilization,” in *Advances in Chemical Physics* (John Wiley & Sons, Inc., 2007), pp. 263–310.
- ¹²⁸J. Tennyson, M. A. Kostin, P. Barletta, G. J. Harris, O. L. Polyansky, J. Ramanlal, and N. F. Zobov, *Comput. Phys. Commun.* **163**, 85 (2004).
- ¹²⁹J. Tennyson, “High accuracy rotation-vibration calculations on small molecules,” *Handbook of High-resolution Spectroscopy* (John Wiley & Sons, Ltd., 2011), pp. 551–571.
- ¹³⁰L. Lodi and J. Tennyson, *J. Phys. B* **43**, 133001 (2010).
- ¹³¹B. T. Sutcliffe and J. Tennyson, *Mol. Phys.* **58**, 1053 (1986).
- ¹³²O. L. Polyansky and J. Tennyson, *J. Chem. Phys.* **110**, 5056 (1999).
- ¹³³A. J. C. Varandas and S. P. J. Rodrigues, *Spectrochim. Acta A. Mol. Biomol. Spectrosc.* **58**, 629 (2002).
- ¹³⁴A. J. C. Varandas, S. P. J. Rodrigues, and V. M. O. Batista, *Chem. Phys. Lett.* **424**, 425 (2006).
- ¹³⁵A. J. C. Varandas, *J. Chem. Phys.* **107**, 867 (1997).
- ¹³⁶A. J. C. Varandas, A. I. Voronin, and P. J. S. B. Caridade, *J. Chem. Phys.* **108**, 7623 (1998).



The Jahn-Teller plus pseudo-Jahn-Teller vibronic problem in the C_3 radical and its topological implications

C. M. R. Rocha and A. J. C. Varandas^{a)}

Departamento de Química and Centro de Química, Universidade de Coimbra, 3004-535 Coimbra, Portugal

(Received 21 December 2015; accepted 20 January 2016; published online 12 February 2016)

The combined Jahn-Teller plus pseudo-Jahn-Teller $[(E' + A'_1) \otimes e']$ problem is discussed for the tricarbon radical (C_3) by means of *ab initio* calculations at the multireference configuration interaction level of theory. For the ${}^1E'$ electronic state arising from a e'^2 valence configuration, three additional symmetry-equivalent C_{2v} seams are found to lie in close proximity to the D_{3h} symmetry-required seam over the entire range of the breathing coordinate here considered. As the perimeter of the molecule increases, the C_{2v} disjoint seams approach the D_{3h} one almost linearly and ultimately coalesce with it at $Q_1 = 5.005 a_0$, thence forming an intersection node or confluence. By further increasing the size of the molecular triangle, the C_{2v} seams get rotated by $\pm\pi$ in the g - h plane. A three-state vibronic Hamiltonian is also proposed to model locally the title system and shown to accurately mimic the calculated data over the region close to the minimum energy crossing point. No net geometric phase effect is observed when the associated electronic wave functions are adiabatically transported along closed paths encircling the four singularity points. For all paths enclosing the intersection node, the sign reversal criterion is shown to be not fulfilled, even for infinitesimal loops. The results so obtained are expected to be valid for other ring systems experiencing similar topological attributes. © 2016 AIP Publishing LLC. [<http://dx.doi.org/10.1063/1.4941382>]

I. INTRODUCTION

Homonuclear triatomic (X_3 -type) molecules have enjoyed a great theoretical interest for many decades and still provide a tempting target for electronic structure calculations (Refs. 1–10 and references therein). At high-symmetry nuclear configurations, such elemental clusters assume equilateral triangular geometries (threefold axial symmetry) with some of the electronic states transforming according to the twofold degenerate $E'(E'')$ irreducible representation (irrep) of the D_{3h} point group.^{1,11} Not surprisingly, therefore, symmetry-required conical intersections¹² (CIs) between the associated potential energy surfaces¹ (PESs) are often realized and have been extensively characterized for a variety of such systems.^{12–17}

According to the Jahn-Teller (JT) theorem,^{18–25} highly symmetric non-linear geometries in degenerate electronic states are not stable equilibrium configurations but instead singularity points on adiabatic PESs.²⁶ As such, the system lowers its symmetry so that any electronic degeneracy can be lifted.^{21–24} By means of first-order perturbation theory and group-theoretical arguments, Jahn and Teller¹⁸ proved that for non-linear molecules experiencing a symmetry imposed CI there will exist non-vanishing perturbation matrix elements along certain non-totally symmetric nuclear displacements, thence implying the instability at the JT origin.^{18,19} Accordingly, the associated electronic energies of the distorted configurations are the characteristic values

of the perturbation matrix, the elements of which define the nonadiabatic electronic-nuclear interactions (vibronic interactions).^{18–25} Specifically for X_3 -type molecules, the simplest JT case consists of a twofold degenerate electronic term E interacting with twofold degenerate e vibrations, i.e., the well-studied linear $E \otimes e$ problem.^{3,12–17,20–25} Generally, systems with e or e^3 electron configurations²⁷ behave as linear JT molecules with the adiabatic PESs assuming the well-known form of a “Mexican hat.”^{22–24} The simplest prototype of such a class of molecules is $H_3^+(1^3A'/2^3A')$,⁷ with the locus of CI having D_{3h} symmetry. Yet, the introduction of quadratic terms of vibronic interactions in the perturbation theoretic approach, i.e., the linear plus quadratic JT problem,^{18–25} reveals the so-called warping of the Mexican-hat-type PESs²³ (the “tricorn”) with the formation of three wells (alternating regularly with three bumps, topographically saddle points or transition states) along the bottom of the trough.^{23,24} Although the linear plus quadratic JT problem encompasses a large spectrum of possibilities²⁸ [ranging from the pure linear to pure Renner-Teller^{22–24} (RT) case], systems in which small linear and large quadratic coupling terms succeed are in general a much more entangled subject. Indeed, as pointed out by Zwanziger and Grant,²⁸ in such systems, referred to as small linear parameter (SLP) JT molecules,^{21,28–30} the locus of points of CI is quite peculiar. Thus, in addition to the symmetry-required D_{3h} crossing seam, there are three symmetry-equivalent C_{2v} seams in close proximity to the central one.^{27,28,30,31} In general, ring systems with principal electron configurations e^2 and e^3 tend to produce SLP JT molecules^{16,27} with³¹ $Si_3(1^1E')$ and^{27,32} $N_3^+(1^1E'')$ providing well established prototypes.

^{a)}Author to whom correspondence should be addressed. Electronic mail: varandas@uc.pt

In addition to the JT effect, the vibronic mixing of two (or several) nearly degenerate electronic states under nuclear displacements, the well-known pseudo-JT (PJT) effect,²⁵ is expected to play a crucial role in the structural instability of X_3 -type systems are cases where relatively close-in-energy E and A states emerge, as is the case in $C_3(1^1E'/1^1A_1)^{10}$ and $Si_3(1^1E'/1^1A_1)^{31}$. Overall, such combined JT plus PJT effects introduce drastic changes in the structure and properties of adiabatic PESs near equilateral triangular geometries as reported for the alkali metal trimers $Li_3(2^2E')^{33}$ and $Na_3(2^2E')^{34-37}$.

One of the most fundamental topological phenomenons directly related to the JT effect has been hinted at by Herzberg and Longuet-Higgins³⁸ and Longuet-Higgins.³⁹ These authors, with the aid of a linear $E \otimes e$ JT Hamiltonian, have shown that real-valued electronic wave functions change sign when adiabatically transported around a closed circuit (in nuclear configuration space) enclosing the intersection point.^{38,39} Such a geometric (also known as topological or Berry's⁴⁰) phase (GP) effect³⁸⁻⁴¹ naturally emerges whenever the Born-Oppenheimer (BO) approximation¹² which separates the fast moving electrons from the slow nuclei degrees of freedom is employed in the study of the coupled electron-vibrational (vibronic) system.^{26,28} For general JT problems, such a sign flip of the electronic adiabatic wave functions occurs only when an odd number of CIs is encircled and hence, the net GP effect may be readily suppressed by the existence of marginal crossing seams in the vicinity of the central one.^{23,24,28}

The present work is primarily concerned with C_3 , an astrophysically important radical which has been detected in stellar atmospheres, interstellar molecular clouds, and cometary tails.^{42,43} Being the most abundant X_3 -type carbon molecule in the interstellar medium, the title system plays a major role in the formation of more involved carbon clusters and carbon-chain molecules;⁴⁴ the reader is addressed to Refs. 10, 42, and 43 for a comprehensive review and updated bibliography regarding the target system. Recently, we have reported¹⁰ the first global *ab initio*-based PES for the ground state of the $C_3(1^1A')$ radical using the double many-body expansion (DMBE) method.¹¹ In this study, we outlined the existence of three symmetry-equivalent C_{2v} crossing seams in quite close proximity to the symmetry-required one, an attribute which had been previously overlooked for the title species. Such an interesting topographical feature (4 CIs) has been ascribed to combined JT plus PJT vibronic effects involving the first three $1A'$ states of C_3 , with the proper cusped behavior warranted by built-in construction.⁴⁵

Although a huge body of information regarding JT and PJT effects for systems with equilateral triangular geometries is available in the literature,^{24,25} studies involving systems in which such combined problems clearly succeed, as it happens in the one here reported, and SLP JT molecules are much less advanced.^{10,27,31-37} The main goal of this work is therefore to provide a comprehensive analysis of the JT plus PJT vibronic effects in C_3 where they have profound topological implications both for ground and excited states. Despite the present discussion being mainly addressed to C_3 ,

the results here reported should be applicable to a whole class of molecules experiencing similar features.

The paper is organized as follows. Section II summarizes the *ab initio* calculations. The molecular orbital picture and the nature of the low-lying excited states are examined in Section III. Section IV gathers the main topological aspects induced by such combined vibronic effects, while the proper $(E' + A_1') \otimes e'$ problem is discussed and analyzed in Section V. The topological-phase implications are then discussed in Section VI. Some conclusions are gathered in Section VII.

II. COMPUTATIONAL DETAILS

All electronic structure calculations have been performed at the multireference configuration interaction⁴⁶ (MRCI) level of theory using the complete active space self-consistent field⁴⁶ (CASSCF) wave functions as reference. The triple- ζ augmented correlation consistent basis set of Dunning^{47,48} (aug-cc-pVTZ or AVTZ) has been employed, with the calculations performed using the MOLPRO⁴⁹ package. Due to the strong vibronic interactions between the ground and first two excited singlet states near equilateral triangular geometries¹⁰ [$1^1E'(1^1A_1, 1^1B_2)$ and $1^1A_1'(2^1A_1)$ states in $D_{3h}(C_{2v})$ symmetry], a coherent picture of such a region is only attainable by including all three relevant A' states of C_s symmetry in state-averaged CASSCF calculations, and hence in the reference state for the internally contracted MRCI wave functions.

For C_3 , a total of 15 molecular orbitals are of interest. The three lowest arise from carbon 1s orbitals [$1a_1'(a_1) + 1e'(a_1, b_2)$] and have been treated as inactive throughout all calculations. The remaining 12 orbitals [$2a_1'(a_1) + a_2'(b_2) + 3e'(a_1, b_2) + a_2''(b_1) + e''(a_2, b_1)$] resulting from 2s and 2p atomic orbitals have all been included in the CASSCF active space (full valence CASSCF or FVCAS⁴⁶), yielding a reference wave function which involves 12 correlated electrons in 12 active orbitals.

In order to characterize the major topological features of the relevant PESs near D_{3h} equilateral triangular conformations, we have performed *ab initio* calculations along the standard (symmetry-adapted) JT coordinates [$\mathbf{Q} = (Q_1, Q_2, Q_3)$] which are defined in terms of the internuclear distances [$\mathcal{R} = (R_1, R_2, R_3)$] by^{1,11}

$$\begin{pmatrix} Q_1 \\ Q_2 \\ Q_3 \end{pmatrix} = \begin{pmatrix} \sqrt{1/3} & \sqrt{1/3} & \sqrt{1/3} \\ 0 & \sqrt{1/2} & -\sqrt{1/2} \\ \sqrt{2/3} & -\sqrt{1/6} & -\sqrt{1/6} \end{pmatrix} \begin{pmatrix} R_1 \\ R_2 \\ R_3 \end{pmatrix}. \quad (1)$$

Here, Q_1 is associated with the totally symmetric representation $a_1'(a_1)$ or breathing mode, while the pair (Q_2, Q_3) constitutes the $e'(b_2, a_1)$ JT active degenerate vibration associated with the asymmetric stretch and bending normal modes, respectively (see Figure 1). Thus, nuclear configurations with $\mathbf{Q}_s = (Q_1, 0, 0)$ define the symmetry-required (D_{3h}) intersection line along which the degeneracy of the E' electronic term is preserved.²⁶ In turn, the two-dimensional coordinate space defined by $\mathbf{Q}_b(Q_1) = (Q_2, Q_3)$ [i.e., for a fixed value of Q_1] forms the so-called branching¹⁴ or g - h plane¹⁵ in which the degeneracy is lifted due to the coupling between electronic and nuclear motions (vibronic effects).²¹⁻²⁵

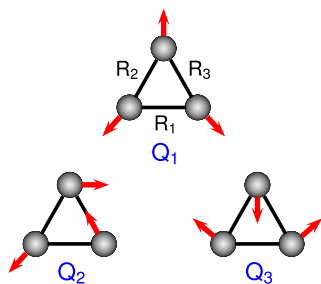


FIG. 1. Displacements associated with the Q coordinates. Q_1 is the D_{3h} preserving breathing mode, Q_2 is the asymmetric stretch mode which distorts the equilateral triangle into a C_s configuration and Q_3 takes the D_{3h} structure into a C_{2v} conformation.

III. MOLECULAR ORBITAL PICTURE AND EXCITED STATES

As noted elsewhere,^{10,50,51} both the ground [$1^1A'(1^1A_1)$] and first excited [$2^1A'(1^1B_2)$] singlet states of the C_3 radical correlate with the twofold E' irrep at D_{3h} equilateral triangular geometries, thus yielding the e^2 valence configuration. Figure 2 shows a molecular orbital (MO) diagram (valence orbitals only) for the 1A_1 (in C_{2v}) electronic state component of the $^1E'$ term. Note that MOs are labeled according to the D_{3h} irreps, while the corresponding correlations with the C_{2v} point group are given in parentheses. Also shown are the natural orbitals obtained from a state-averaged FVCAS/AVTZ reference wave function. Accordingly, 9 MOs arise from 2s, 2p_x, and 2p_y

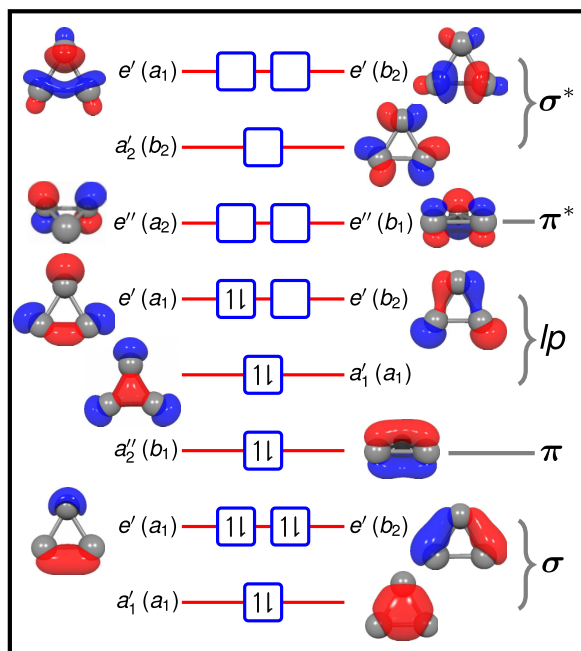


FIG. 2. Molecular orbital diagram and valence electronic configuration for the 1A_1 (in C_{2v}) component of the $^1E'$ term (in D_{3h}). Molecular orbitals are labeled according to D_{3h} irreps with the corresponding correlations with the C_{2v} point group given in parentheses. Up and down arrows denote α and β spin states, respectively. Natural orbitals obtained from a state-averaged FVCAS/AVTZ wave function are also depicted.

atomic orbitals (AOs), i.e., 3 σ -bonding, 3 σ^* -antibonding, and 3 lone-pair (lp) orbitals which are depicted in Figure 2. The remaining three 2p_z AOs originate a π -bonding and two π^* -antibonding orbitals. A remarkable aspect of such a system, as already emphasized for the cyclic N_3^+ molecule,^{27,32} is that both highest occupied molecular orbital (HOMO- lp MO) and lowest unoccupied molecular orbital (LUMO- π^* MO) are degenerate and transform as $E'(A_1, B_2)$ and $E''(A_2, B_1)$ irreps of $D_{3h}(C_{2v})$ point group, respectively. Thus, along $C_{2v}(C_s)$ distortions [i.e., for $Q_3(Q_2) > 0$ or $Q_3(Q_2) < 0$], both split into $a_1(a')/b_2(a')$ and $a_2(a'')/b_1(a'')$ orbital pairs, respectively.

At D_{3h} configurations, four electronic states arise from HOMO \rightarrow HOMO excitations (see Figure 2), i.e.,

$$e' \otimes e' \xrightarrow{D_{3h}} A'_1 + A'_2 + (E') \xrightarrow{C_{2v}} A_1 + B_2 + (A_1 + B_2). \quad (2)$$

Note that all states here considered correlate with the A' irrep in C_s symmetry. It should be pointed out that higher excited states can be obtained from HOMO-1 \rightarrow HOMO [$a'_1 \otimes e' \xrightarrow{D_{3h}} (E') \xrightarrow{C_{2v}} (A_1 + B_2)$], HOMO \rightarrow LUMO [$e' \otimes e'' \xrightarrow{D_{3h}} A''_1 + A''_2 + (E'') \xrightarrow{C_{2v}} A_2 + B_1 + (A_2 + B_1)$] and HOMO-2 \rightarrow HOMO [$a'_2 \otimes e' \xrightarrow{D_{3h}} (E'') \xrightarrow{C_{2v}} (A_2 + B_1)$] excitations, each of which being either singlet or triplet. Such a manifold, however, will not be considered in the present work (for a comprehensive picture on the singlet manifold, see Figure 1 of Ref. 10).

Figure 3 schematically shows the relevant Slater determinants arising from HOMO \rightarrow HOMO excitations in a e^2 valence configuration. The leading (spin-spatial symmetry adapted) configuration state functions (CSFs) for each electronic term of Eq. (2) are thus given by

$$|\Psi_1 \ ^3A'_2(1^3B_2)\rangle = |\alpha\rangle, \quad (3)$$

$$|\Psi_2 \ ^1E'(1^1A_1)\rangle = \frac{1}{\sqrt{\mathcal{A}^2 + \mathcal{B}^2}}[\mathcal{A}|\beta\rangle - \mathcal{B}|\gamma\rangle], \quad (4)$$

$$|\Psi_3 \ ^1E'(1^1B_2)\rangle = \frac{1}{\sqrt{\mathcal{C}^2 + \mathcal{D}^2}}[\mathcal{C}|\delta\rangle - \mathcal{D}|\epsilon\rangle], \quad (5)$$

$$|\Psi_4 \ ^1A'_1(2^1A_1)\rangle = \frac{1}{\sqrt{\mathcal{E}^2 + \mathcal{F}^2}}[\mathcal{E}|\beta\rangle + \mathcal{F}|\gamma\rangle], \quad (6)$$

where \mathcal{A} , \mathcal{B} , \mathcal{C} , \mathcal{D} , \mathcal{E} , and \mathcal{F} are coefficients that determine the relative contributions of each determinant in the associated CSF. At D_{3h} geometries, their ratios are approximately equal to one, with $|\mathcal{A}| = |\mathcal{B}| \approx |\mathcal{C}| = |\mathcal{D}| \approx |\mathcal{E}| = |\mathcal{F}| \approx 1$. However, as shown later in Section IV B, along non-totally symmetric distortions, the ratio of each determinant changes as much as different CSFs belonging to the same spin and spatial symmetry can mix.

As seen from Eqs. (3)-(6), along with $^1E'(1^1A_1, 1^1B_2)$ and $^1A'_1(2^1A_1)$, a spin-triplet $^3A'_2(1^3B_2)$ term, lower in energy, is observed.^{50,52,53} Such a state depicts a minimum at an equilateral triangular geometry,^{50,52,53} which is non-JT in nature; see Figure 4. In turn, the PJT effect between the excited $^1A'_1(2^1A_1)$ electronic state and the $^1E'(1^1A_1, 1^1B_2)$ one reinforces the stabilization (by strengthening the PES curvature) and generates a minimum at this geometry. The computed equilibrium geometries (in valence coordinates¹) and harmonic vibrational frequencies for such structures as

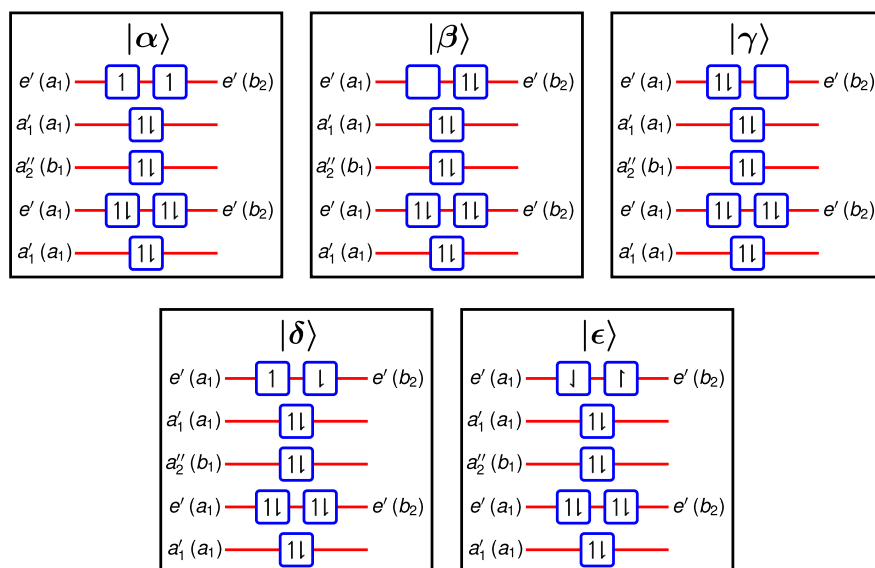


FIG. 3. Slater determinants arising from HOMO \rightarrow HOMO excitations in a e^2 valence configuration. Molecular orbitals are labeled according to D_{3h} irreps with the corresponding correlations with C_{2v} point group given in parentheses. Up and down arrows denote α and β spin states, respectively.

obtained from FVCAS/AVTZ calculations are given in Table I, together with results from the literature. Note that the relative energies are given with respect to the absolute minimum on the adiabatic ground state PES [lin- $C_3(^1\Sigma_g^+/1^1A_1)$] and have been obtained from single-point MRCI/AVXZ ($X = T, Q$) calculations as well as complete basis set (CBS) extrapolated energies; the reader is addressed to Refs. 10, 54, and 55 for more details. Vertical excitation energies from the cyc- $C_3(^3A_2'/1^3B_2)$ structure [i.e., for equilateral triangular conformations with $\mathbf{Q}_s = (4.554 a_0, 0, 0)$] are in Table II.

Accordingly, the most stable electronic state corresponds to the spin-triplet $^3A_2'(1^3B_2)$ with a stabilization energy relative to the $^1E'(1^1A_1, 1^1B_2)$ term of 70.2, 69.4, and 66.7 kJ mol $^{-1}$ at MRCI/AVTZ, MRCI/AVQZ and CBS levels

of theory, respectively. However, as emphasized by Garcia-Fernandez *et al.*,³¹ the structural instability and distortion of the high-symmetry D_{3h} configuration in the $^1E'(1^1A_1, 1^1B_2)$ term, associated with the JT plus PJT vibronic coupling between the latter and $^1A_1'(2^1A_1)$ state, strongly stabilizes the 1^1A_1 component (153.6 kJ mol $^{-1}$ as predicted from the CBS extrapolation scheme) and generates a distorted (linear) global minimum on the adiabatic ground state PES.¹⁰ Indeed, as shown in Table I, the (low-spin distorted) lin- $C_3(^1\Sigma_g^+/1^1A_1)$ structure is 84.2 kJ mol $^{-1}$ more stable than the (high-spin undistorted) cyc- $C_3(^3A_2'/1^3B_2)$ conformation at CBS//FVCAS/AVTZ level. The corresponding topological attributes induced by such combined vibronic effects are of primary concern in the present work and will be addressed in Secs. IV, V, and VI.

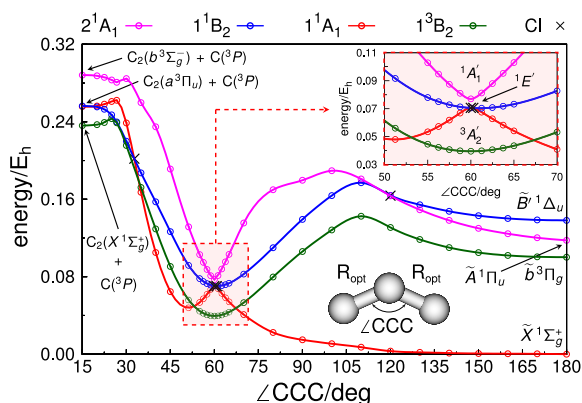


FIG. 4. Optimized FVCAS/AVTZ bending potential for the four electronic states of C_3 radical arising from HOMO \rightarrow HOMO excitations in the e^2 valence configuration [see Eqs. (2)–(6)]. The key shows the irreducible representation, in C_{2v} symmetry, for each electronic state. Also shown in panel are the associated correlations, for linear geometries, with $D_{\infty h}$ symmetry as well as the corresponding dissociation limits. Conical intersections are indicated by the symbol \times , and the bending angle by $\angle CCC$.

IV. TOPOLOGICAL ASPECTS INDUCED BY JT PLUS PJT VIBRONIC EFFECTS

A. The symmetry-required D_{3h} seam

The topology of the PESs along the breathing normal coordinate Q_1 [$\mathbf{Q}_s = (Q_1, 0, 0)$] is illustrated in Figure 5 for the $^1E'(1^1A_1, 1^1B_2)$ and $^1A_1'(2^1A_1)$ electronic states of the C_3 radical. Note that the *ab initio* calculations have been performed at the FVCAS/AVTZ [Figure 5(a)] and MRCI/AVTZ [Figure 5(b)] levels of theory and covered a region defined by $3.65 a_0 \leq Q_1/Q_1^{\text{cusp}} \leq 5.55 a_0$ in steps of 0.1 a_0 (or less when convenient — see insets of Figure 5), where Q_1^{cusp} [$\mathbf{Q}_s^{\text{cusp}} = (Q_1^{\text{cusp}}, 0, 0)$] corresponds to the minimum of equilateral triangular conformations (this is not a stationary point on the $^1E'(1^1A_1, 1^1B_2)$ PES but is for Q_1 distortions).

As Figure 5 shows, the $^1E'$ and $^1A_1'$ states are quite close in energy over the range of equilateral triangular geometries here considered, notably for $Q_1 > 4.750 a_0$. Suffice it to say that

TABLE I. Properties and energetics of stationary points on the ground and excited state PESs of C_3 radical. Structures are labeled according to their respective point group irreps with the corresponding correlations with C_{2v} symmetry given also in parentheses. Energies are given with respect to the $D_{\infty h}$ absolute minimum [$\text{lin-}C_3(^1\Sigma_g^+/1^1A_1)$] of the ground state adiabatic PES of C_3 .

	Method	R/a ₀	∠CCC/deg	ΔE/kJ mol ⁻¹	w ₁ /cm ⁻¹	w ₂ /cm ⁻¹	w ₃ /cm ⁻¹
lin- $C_3(^1\Sigma_g^+/1^1A_1)$	FVCAS/AVTZ ^a	2.474	180.0	0 ^b	1171.0	56.1	2060.9
	MRCI/AVTZ ^a			0			
	MRCI/AVQZ ^a			0			
	CBS ^a			0			
	DMBE ^c	2.444	180.0		1204.2	63.5	2126.5
	MP4/6-31G ^{†d}	2.415	180.0	0	1367.0	154.0	2311.0
	CISD/6-311+G ^{†e}	2.477	180.0	0			
cyc- $C_3(^3A_2'/1^3B_2)$	CCSD(T)/AVTZ ^f	2.440	180.0	0			
	Expt. ^g	2.451	180.0		1224.20	63.42	2040.02
	FVCAS/AVTZ ^a	2.629	60.0	114.6	1508.3	1064.2	1064.2
	MRCI/AVTZ ^a			91.3			
	MRCI/AVQZ ^a			89.2			
	CBS ^a			84.2			
	MP4/6-31G ^{†d}	2.544	60.0	102.3	1774.0	1091.0	1091.0
cyc- $C_3(^1A_1'/2^1A_1)$	CISD/6-311+G ^{†e}	2.632	60.0	96.5			
	CCSD(T)/AVTZ ^f	2.589	60.0	85.4			
	FVCAS/AVTZ ^a	2.678	60.0	213.0	1456.3	5069.5	5069.5
	MRCI/AVTZ ^a			191.2			
	MRCI/AVQZ ^a			189.7			
	CBS ^a			185.6			

^aThis work.

^bRelative to the FVCAS/AVTZ optimized minimum of lin- $C_3(^1\Sigma_g^+/1^1A_1)$.

^cReference 10.

^dReference 50. Geometries optimized at the HF/6-31G^{*} level of theory.

^eReference 52. Geometries optimized at the CASCF/6-31G^{*} level of theory. Harmonic vibrational frequencies not reported.

^fReference 53. Geometries optimized at the B3LYP/6-311G^{*} level of theory. Harmonic vibrational frequencies not reported.

^gReferences 56 and 57. Separation between origin level and lowest $v_n = 1$ level.

the components of the E' term are found to remain degenerate in the *ab initio* calculations to better than $1.0 \times 10^{-7} E_h$. A region that deserves close attention in Figure 5(a) refers to near $Q_s = (5.005 a_0, 0, 0)$ [highlighted by a filled circle in

TABLE II. Vertical excitation energies (ΔE) for the three lowest states of the C_3 radical at equilateral triangular conformations. The electronic states are labeled according to D_{3h} irreps with the corresponding correlations with C_{2v} point group given in parentheses. Energies are given with respect to the D_{3h} minimum [cyc- C_3] of $^3A_2'(1^3B_2)$ electronic state.

State	Method	ΔE/kJ mol ⁻¹
$^3A_2'(1^3B_2)$	FVCAS/AVTZ ^a	0 ^b
	MRCI/AVTZ ^a	0
	MRCI/AVQZ ^a	0
	CBS ^a	0
$^1E'(1^1A_1, 1^1B_2)$	FVCAS/AVTZ ^a	81.7
	MRCI/AVTZ ^a	70.2
	MRCI/AVQZ ^a	69.4
	CBS ^a	66.7
$^1A_1'(2^1A_1)$	FVCAS/AVTZ ^a	101.7
	MRCI/AVTZ ^a	100.7
	MRCI/AVQZ ^a	100.1
	CBS ^a	100.3

^aThis work.

^bRelative to the FVCAS/AVTZ optimized minimum of $^3A_2'(1^3B_2)$ state at the D_{3h} equilateral triangular conformation with $Q_s = (4.554 a_0, 0, 0)$.

Figure 5(a)]. At this point, the $^1E'$ and $^1A_1'$ electronic states are remarkably close in energy, with the former being predicted from our *ab initio* calculations to be only $1.1 \times 10^{-5} E_h$ (at FVCAS/AVTZ level) more stable than the latter. Such a feature [near (triple) degeneracy] has been reported in the literature for alkali metal trimers Li_3 ³³ and Na_3 ^{34,35} as well as the N_3^+ cation.^{27,32} Note that, for $Q_1 > 5.005 a_0$, the FVCAS/AVTZ calculations predict an inversion of the $^1E'$ and $^1A_1'$ states [see Figure 5(a)], i.e., the twofold degenerate E' term appears to have as its components the 2^1A_1 and 1^1B_2 electronic states. The aforementioned picture changes, however, by the inclusion of dynamical correlation in MRCI/AVTZ calculations. Thence, as seen in Figure 5(b), the degenerate $^1E'(1^1A_1, 1^1B_2)$ term and its components remain unchanged over the range of geometries here considered. Still, as the inset of Figure 5(b) shows, the energy difference between the $^1E'$ and $^1A_1'$ states is $\approx 3.0 mE_h$ (at MRCI/AVTZ level) over the range of $5.400 a_0 \leq Q_1 \leq 6.200 a_0$.

B. The g-h plane and the symmetry-equivalent C_{2v} seams

Figures 6 and 7 show cuts of the relevant PESs along the asymmetric stretch [$Q_b(Q_1) = (Q_2, 0)$] and bending [$Q_b(Q_1) = (0, Q_3)$] normal modes, respectively, for a fixed value of symmetric stretching coordinate $Q_1 = 4.576 a_0$ (note that fixed Q_1 does not imply fixed bond lengths; see Figure 1). It

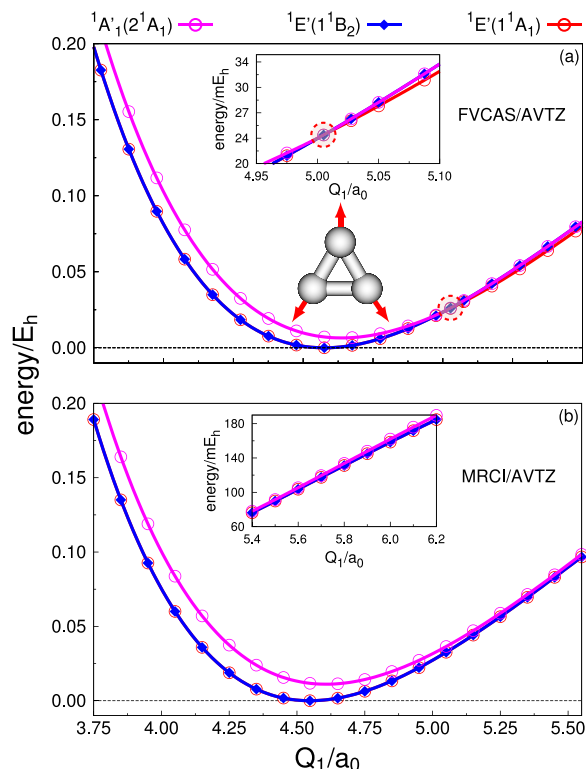


FIG. 5. PES cuts along the breathing normal coordinate Q_1 [$\mathbf{Q}_s = (Q_1, 0, 0)$] for the $1E'(1^1A_1, 1^1B_2)$ and $1A_1'(2^1A_1)$ electronic states of C_3 radical at (a) FVCAS/AVTZ and (b) MRCI/AVTZ levels of theory over the range of $3.750 a_0 \leq Q_1/Q_1^{\text{cusp}} \leq 5.550 a_0$ in which a near (triple) degeneracy is predicted from FVCAS/AVTZ calculations. Energies relative to: $\mathcal{E}_{1E'}(\mathbf{Q}_s^{\text{cusp}}) = -113.5104816 E_h$ at $Q_1^{\text{cusp}} = 4.576 a_0$ and $\mathcal{E}_{1A_1'}(\mathbf{Q}_s^{\text{cusp}}) = -113.7605899 E_h$ at $Q_1^{\text{cusp}} = 4.548 a_0$ for FVCAS/AVTZ and MRCI/AVTZ levels, respectively.

must be emphasized that for equilateral triangular geometries [$\mathbf{Q}_b(Q_1) = (0, 0), \forall Q_1$], the $1^1A'$, $2^1A'$ and $3^1A'$ electronic states correlate with $1E'(1^1A_1, 1^1B_2)$ and $1A_1'(2^1A_1)$ states in $D_{3h}(C_{2v})$ symmetry, respectively. Note that the *ab initio* calculations covered a region defined by $-0.020 a_0 \leq Q_n (n = 2, 3) \leq 0.020 a_0$ in steps of at most $0.0025 a_0$.

Figures 6 and 7 illustrate the structural instability (with respect to JT active displacements) of the high-symmetry D_{3h} geometry in the $1E'$ term. Thence, along $C_s(C_{2v})$ distortions [i.e., for $Q_2(Q_3) > 0$ or $Q_2(Q_3) < 0$], the adiabatic PES splits into two $1A'$ branches.^{21–25} In fact, a close inspection of the cross-sectional cuts here shown for the three lowest singlet states of the C_3 radical gives insights into the real nature of the JT problem at hand. Obviously, instead of a typical linear $E' \otimes e'$ JT problem^{21–25} in which only linear JT vibronic coupling constants ($F_{E'}$) are taken into account, the non-negligible contribution of the quadratic coupling constants ($G_{E'}$) is key for the title system (linear plus quadratic JT problem^{27,28,32–35}). Additionally, an interaction^{23,25} occurs due to strong vibronic mixing between the close lying $1E'$ and $1A_1'$ states, which are linearly coupled by the non-vanishing constant $H_{E'/A_1'}$;³¹ see Figures 5–7 and Table II. Thence, such a combined JT plus PJT vibronic problem introduces

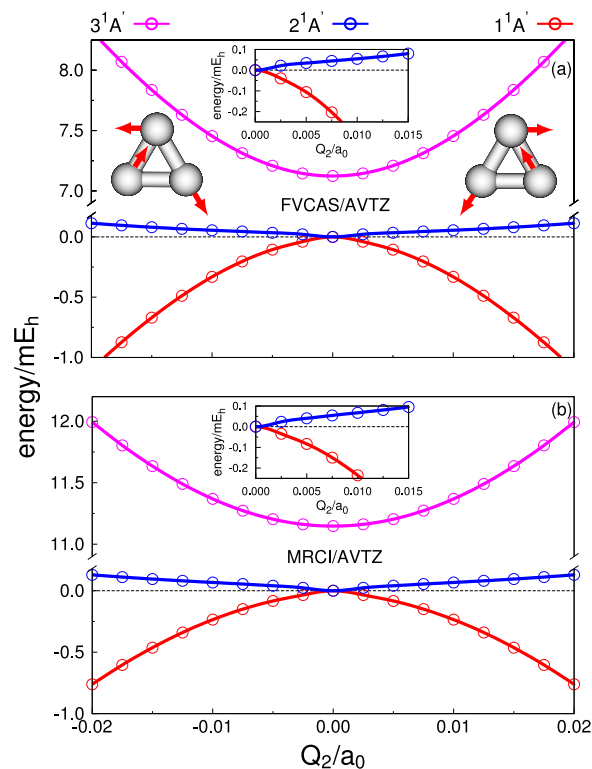


FIG. 6. PES cuts along the asymmetric stretch normal coordinate Q_2 [$\mathbf{Q}_b(Q_1) = (Q_2, 0)$ with Q_1 fixed at $4.576 a_0$] for the three lowest $1A'$ electronic states of C_3 radical at (a) FVCAS/AVTZ and (b) MRCI/AVTZ levels of theory over the range of $-0.020 a_0 \leq Q_2 \leq 0.020 a_0$. Energies relative to $\mathcal{E}_{1E'}(\mathbf{Q}_1, 0, 0) = -113.5104816 E_h$ and $\mathcal{E}_{1A_1'}(\mathbf{Q}_1, 0, 0) = -113.7604536 E_h$ at FVCAS/AVTZ and MRCI/AVTZ levels, respectively.

profound changes on the topology of the PESs near equilateral triangular geometries.¹⁰ Indeed, as shown in Figure 7, besides the D_{3h} symmetry-required crossing seam at $\rho(Q_1) = 0 \forall Q_1$, where $\rho(Q_1) = \sqrt{Q_2^2 + Q_3^2}$ (Refs. 11 and 58) is the radial polar coordinate in the two dimensional g - h plane,²⁶ there are three symmetry-equivalent C_{2v} seams in close proximity to the reference seam.^{16,28} Such additional CIs (highlighted by filled circles in Figure 7 for $Q_1 = 4.576 a_0$) are located at $\rho_0(Q_1) = 0.007 a_0$ and $\rho_0(Q_1) = 0.011 a_0$ at FVCAS/AVTZ and MRCI/AVTZ levels of theory, respectively, with $\rho_0(Q_1)$ defining the radius on which the C_{2v} disjoint seams¹⁶ are located with respect to the central one. Although not visible in Figure 7, two other symmetry related C_{2v} seams exist for similar cross sections rotated by $\pm 2\pi/3$. Thence, on a circle of radius ρ_0 in the two dimensional g - h plane, the 4 CIs are defined by $\mathbf{Q}_b(Q_1) = (0, 0)$, and $\mathbf{Q}_b(Q_1) = (0, \rho_0), (-\sqrt{3}\rho_0/2, -\rho_0/2), (\sqrt{3}\rho_0/2, -\rho_0/2)$. Suffice it to say that the three additional C_{2v} CIs between the $1^1A'$ and $2^1A'$ states are found degenerate to within $1.0 \times 10^{-7} E_h$ in the *ab initio* calculations here reported. Note further that, over the range of $-0.020 a_0 \leq Q_3 \leq \rho_0(Q_1)$, the $1^1A'$ and $2^1A'$ electronic states correlate with $1^1B_2(1^1A_1)$ and $1^1A_1(1^1B_2)$ states, respectively, for $Q_3 > 0 (< 0)$; see Figure 7. Nevertheless, over the entire interval of Q_3 , the C_{2v} character of the upper and lower states remains unchanged on passing

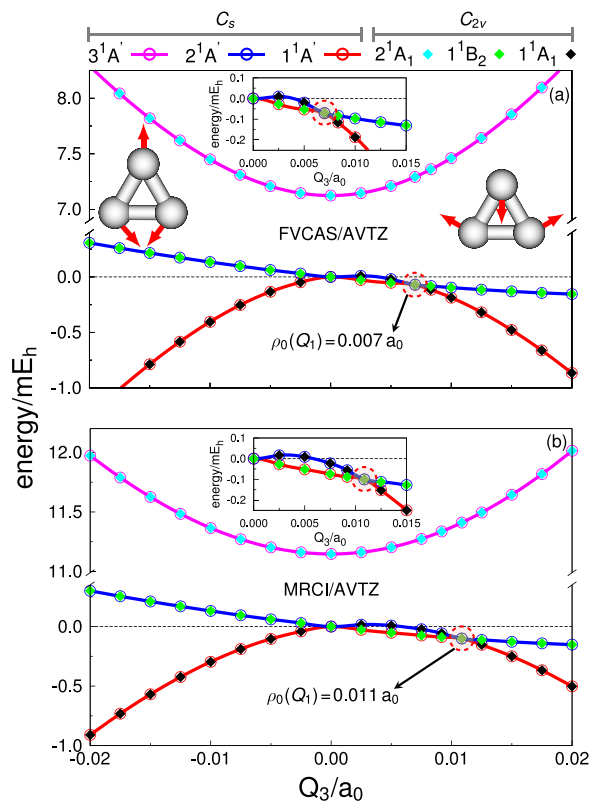


FIG. 7. PES cuts along the bending normal coordinate Q_3 [$\mathbf{Q}_b(Q_1) = (0, Q_3)$] with Q_1 fixed at $4.576 a_0$ for the three lowest $1A'$ electronic states of C_3 radical at (a) FVCAS/AVTZ and (b) MRCI/AVTZ levels of theory over the range of $-0.020 a_0 \leq Q_3 \leq 0.020 a_0$. Solid symbols correspond to points calculated in the 1^1A_1 , 1^1B_2 , and 2^1A_1 states of C_{2v} symmetry, while the open symbols connected by smooth splines correspond to calculations with A' symmetry in C_s point group. Filled circles highlight the additional C_{2v} CIs obtained from FVCAS/AVTZ and MRCI/AVTZ calculations and located at $\rho_0(Q_1) = 0.007 a_0$ and $\rho_0(Q_1) = 0.011 a_0$, respectively, with respect to the symmetry-required seam. Reference energies as in Figure 6.

from both crossing seams. Figure 8 schematically illustrates the evolution of the dominant CSFs shown in Eqs. (4)-(6) for the 1^1A_1 , 1^1B_2 , and 2^1A_1 electronic states (in C_{2v}) along the bending normal coordinate Q_3 [$\mathbf{Q}_b(Q_1) = (0, Q_3)$]. As noted in Section III, at D_{3h} geometries, the ratio between the Slater determinants (see Figure 3) in the associated leading CSF is approximately equal to one, with $|\mathcal{A}| = |\mathcal{B}| \approx |\mathcal{C}| = |\mathcal{D}| \approx |\mathcal{E}| = |\mathcal{F}| \approx 1$. Displacements along the bending normal coordinate changes the ratio between the $|\beta\rangle/|\gamma\rangle$ determinants in the $|\Psi_2^1 E'(1^1A_1)\rangle$ and $|\Psi_4^1 A_1'(2^1A_1)\rangle$ CSFs. Thence, for $Q_3 > 0$, $\mathcal{A} > \mathcal{B}$ and $\mathcal{E} < \mathcal{F}$, leading ultimately to the collapsed $|\Psi_2^1 A_1\rangle \rightarrow |\beta\rangle$ and $|\Psi_4^1 2^1A_1\rangle \rightarrow |\gamma\rangle$ wave functions (see Figure 8). Conversely, for $Q_3 < 0$, $\mathcal{A} < \mathcal{B}$ and $\mathcal{E} > \mathcal{F}$, and the associated CSFs collapse into $|\Psi_2^1 1^1A_1\rangle \rightarrow |\gamma\rangle$ and $|\Psi_4^1 2^1A_1\rangle \rightarrow |\beta\rangle$. Note that for the $|\Psi_3^1 E'(1^1B_2)\rangle$ CSF (which correlates to $|\Psi_3^1 1^1B_2\rangle$ for $Q_3 \neq 0$), the coefficients \mathcal{C} and \mathcal{D} remain approximately constant under small displacements from the reference D_{3h} geometry as schematically shown in Figure 8. It is worth noting that the changes in the $|\beta\rangle/|\gamma\rangle$ ratios [and therefore, in the coefficients of Eqs. (4) and (6)] arise due

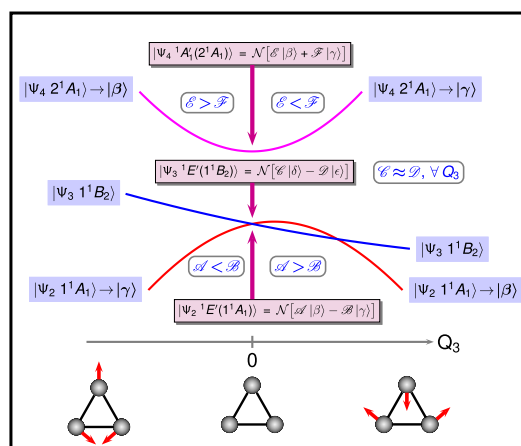


FIG. 8. Evolution of the dominant CSFs shown in Eqs. (4)-(6) for the 1^1A_1 , 1^1B_2 , and 2^1A_1 electronic states (in C_{2v}) along the bending normal coordinate Q_3 . The Slater determinants $|\beta\rangle$, $|\gamma\rangle$, $|\delta\rangle$ and $|\epsilon\rangle$ are schematically shown in Figure 3. $N = 1/\sqrt{X^2 + Y^2}$ is the normalization factor for each CSF, where $X = \{\mathcal{A}, \mathcal{C}, \mathcal{E}\}$ and $Y = \{\mathcal{B}, \mathcal{D}, \mathcal{F}\}$ are the associated coefficients.

to the mixing of $|\Psi_2^1 E'(1^1A_1)\rangle$ and $|\Psi_4^1 A_1'(2^1A_1)\rangle$ CSFs (which have the same spin and irrep at C_{2v} geometries) in the 1^1A_1 and 2^1A_1 electronic states as the molecule bends, i.e., $|\Psi_2^1 1^1A_1\rangle = a|\Psi_2^1 E'(1^1A_1)\rangle + b|\Psi_4^1 A_1'(2^1A_1)\rangle$ and $|\Psi_4^1 2^1A_1\rangle = c|\Psi_2^1 E'(1^1A_1)\rangle + d|\Psi_4^1 A_1'(2^1A_1)\rangle$. Therefore, the CSFs shown in Eqs. (4)-(6) may be considered to represent an approximate diabatic (perhaps more precisely, crude adiabatic) basis through which the three-state JT plus PJT problem can be conveniently formulated.³² Note further in passing that for C_s geometries [e.g., for $\mathbf{Q}_b(Q_1) = (Q_2, 0)$ nuclear configurations, see Figure 6], the adiabatic wave functions for the $1^1A'$, $2^1A'$, and $3^1A'$ electronic states are given by a linear combination of all the $|\Psi_2^1 E'(1^1A_1)\rangle$, $|\Psi_3^1 E'(1^1B_2)\rangle$, and $|\Psi_4^1 A_1'(2^1A_1)\rangle$ CSFs, since the latter correlate with the same spin and irrep in the C_s point group.

Figures 9 and 10 show cross sections of the 1^1A_1 , 1^1B_2 , and 2^1A_1 PESs (in C_{2v}) along Q_3 [$\mathbf{Q}_b(Q_1) = (0, Q_3)$] for different values of symmetric stretching coordinate Q_1 as obtained from FVCAS/AVTZ and MRCI/AVTZ calculations, respectively. The energies are given with respect to the associated value at equilateral triangular geometries $\mathcal{E}_{1E'}(\mathbf{Q}_s)$ of the $1E'$ term. Note that such graphical representations correspond to orthogonal cuts (in the Q_3 direction) of the seam space¹² (i.e., the continuously connected points of degeneracy shown in Figure 5) for distinct Q_1 values. As clearly seen from Figures 9 and 10 (see also Figure 11), as the perimeter $P = \sqrt{3}Q_1$ of the molecule increases, the C_{2v} disjoint seam (highlighted by filled circles) approaches the symmetry-required D_{3h} seam almost linearly and ultimately coalesces [$\rho_0(Q_1) = 0$] with the central one at $Q_1 = 5.005 a_0$ [Figures 9(c) and 10(c)]. Such a point at the junction of the seams is referred to as the intersection node⁵⁹ or confluence^{17,60} and has been reported in the literature for Li_3 ,³³ Na_3 ,³⁵ and N_3^{+27} as well as for less symmetrical seams (C_{2v}/C_s confluences) in O_3 ,⁶¹ AlH_2 ,⁶² CH_2 ,⁶³ and BH_2 .⁶⁰ A close view of such a confluence of the D_{3h} and C_{2v} seams is illustrated in Figure 11 which depicts the dependence of $\rho_0(Q_1)$ as a

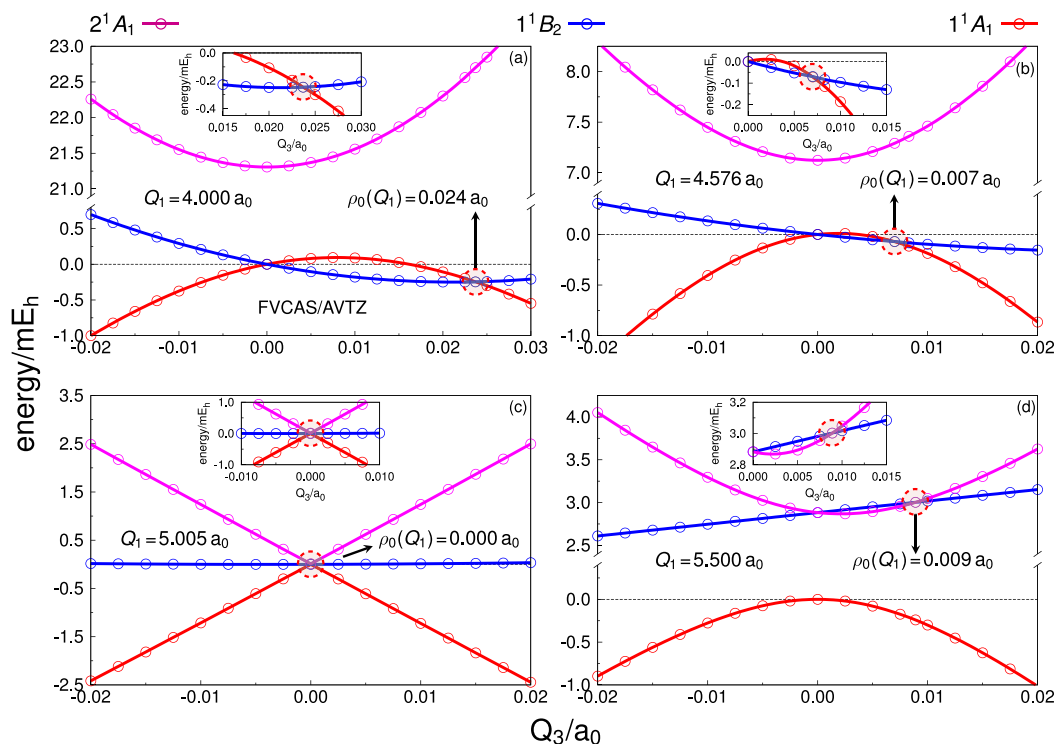


FIG. 9. Cross-sectional cuts of the 1^1A_1 , 1^1B_2 , and 2^1A_1 PESs (in C_{2v}) along Q_3 [$Q_b(Q_1) = (0, Q_3)$] for different values of symmetric stretching coordinate Q_1 as obtained from FVCAS/AVTZ calculations. (a) $Q_1 = 4.000 a_0$, (b) $Q_1 = 4.576 a_0$, (c) $Q_1 = 5.005 a_0$, and (d) $Q_1 = 5.500 a_0$. Filled circles highlight the dependence of $\rho_0(Q_1)$ as a function of Q_1 .

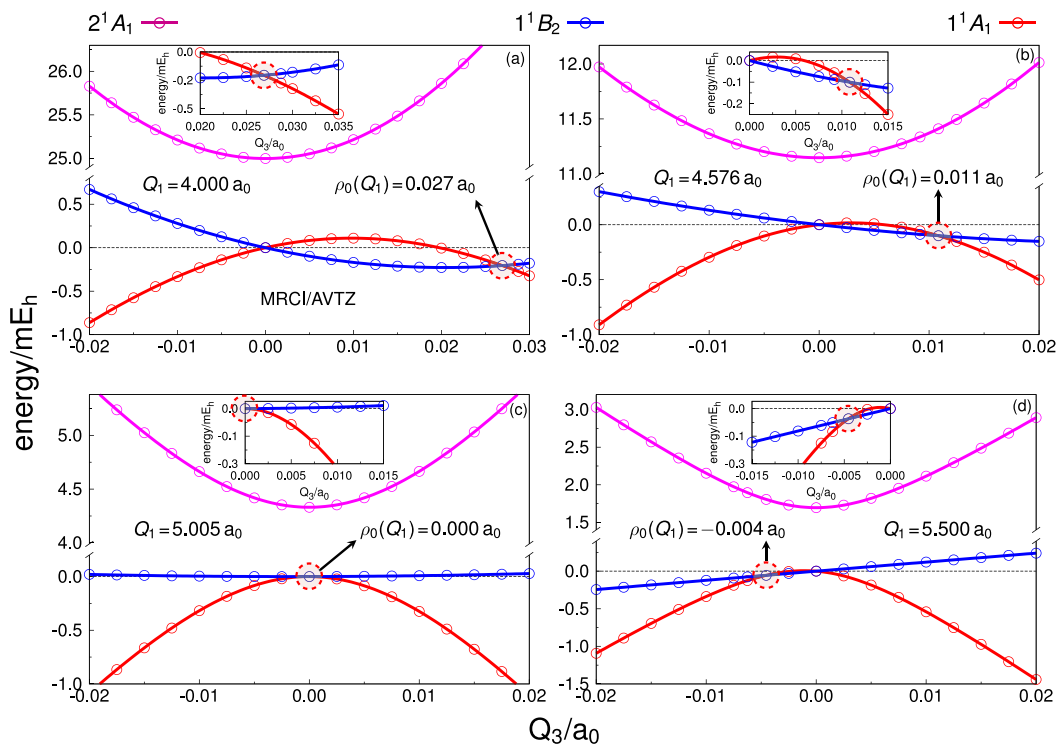


FIG. 10. Cross-sectional cuts of the 1^1A_1 , 1^1B_2 , and 2^1A_1 PESs (in C_{2v}) along Q_3 [$Q_b(Q_1) = (0, Q_3)$] for different values of symmetric stretching coordinate Q_1 as obtained from MRCI/AVTZ calculations. (a) $Q_1 = 4.000 a_0$, (b) $Q_1 = 4.576 a_0$, (c) $Q_1 = 5.005 a_0$, and (d) $Q_1 = 5.500 a_0$. Filled circles highlight the dependence of $\rho_0(Q_1)$ as a function of Q_1 .

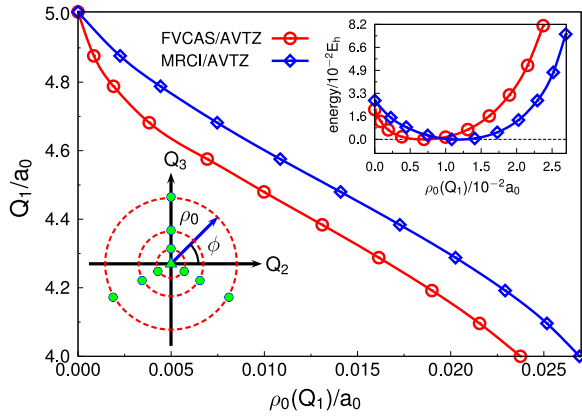


FIG. 11. Dependence of $\rho_0(Q_1)$ as a function of the symmetric stretching coordinate Q_1 over the range of $4.000 a_0 \leq Q_1 \leq 5.005 a_0$ as obtained from FVCAS/AVTZ and MRCl/AVTZ calculations. The inset depicts the energy of the associated disjoint seam point with respect to the minimum of the C_{2v} crossing seams located at $\phi = \pi/2, 7\pi/6$, and $11\pi/6$ on a circle of radius $\rho_0(Q_1)$ in the two dimensional g - h plane.

function of the symmetric stretching coordinate Q_1 over the range of $4.000 a_0 \leq Q_1 \leq 5.005 a_0$. It should be recalled that although only one seam is emphasized in Figures 9-11 [i.e., $\mathbf{Q}_b(Q_1) = (0, \rho_0)$], the three symmetry-equivalent C_{2v} disjoint seams are located at $\phi = \pi/2, 7\pi/6$, and $11\pi/6$ on a circle of radius $\rho_0(Q_1)$, where ϕ is the polar (or pseudo-rotation) angle^{11,26,58} (see Figure 11).

In fact, as Figure 11 shows, the radial distances $\rho_0(Q_1)$ predicted from FVCAS/AVTZ calculations are ≈ 0.003 - $0.004 a_0$ shorter than those obtained at the MRCl/AVTZ level of theory. Nevertheless, at regions of configuration space near the intersection node [i.e., $\rho_0(Q_1) \rightarrow 0$ for $Q_1 \leq 5.005 a_0$], $\rho_0(Q_1)$ is a rapidly decreasing function of Q_1 with both curves shown in Figure 11 converging toward a null value. As emphasized by Zwanziger and Grant²⁸ with the aid of a linear plus quadratic JT $E' \otimes e'$ Hamiltonian, $\rho_0(Q_1) \approx F_{E'}/G_{E'}$ (here, the approximate sign follows due to the non-negligible PJT effect between the close-in-energy ${}^1E'$ and ${}^1A'_1$ states). Thence, as noted elsewhere,^{27,31} configuration interactions including excited states with large linear JT parameters may increase the value of $F_{E'}$ and therefore the associated radius $\rho_0(Q_1)$ on which the three equivalent C_{2v} degeneracies occur. Interestingly enough from the seminal work of Zwanziger and Grant,²⁸ there are important limiting cases which follow naturally from the above treatment of the quadratic JT problem (see Refs. 21–24, 27, 28, and 32–35 for a detailed description). The first is the well-studied linear $E' \otimes e'$ JT system for which $F_{E'} \neq 0$ and $G_{E'} = 0$. In this case the PESs in the vicinity of the high-symmetry configuration \mathbf{Q}_0 assume the simple form $E_{\pm} = \frac{1}{2}K_{E'}\rho^2 \pm F_{E'}\rho$ ($K_{E'}$ is the so-called primary force constant²⁴) with the three C_{2v} crossing seams pushed off to ∞ [$\rho_0(Q_1) \rightarrow \infty$]. Conversely, for $F_{E'} = 0$ and $G_{E'} \neq 0$ (i.e., the pure Renner-Teller case), the PESs take the form $E_{\pm} = \frac{1}{2}K_{E'}\rho^2(1 \pm G_{E'})$, and the three additional degeneracies are located at $\rho_0(Q_1) = 0$. On the other hand and more relevant to the current work are the cases in which $G_{E'} > F_{E'}$, the SLP JT molecules.^{21,28–30} Thus, in such systems, the

three symmetry-equivalent C_{2v} disjoint seams lie close to the central one with the associated distance depending on the ratio between the linear and quadratic JT parameters for a given Q_1 , i.e., $\rho_0(Q_1) = F_{E'}/G_{E'}$. As noted elsewhere,^{27,60} at the point of confluence of the D_{3h} and C_{2v} crossing seams (here at $Q_1 \approx 5.005 a_0$), the linear JT parameter $F_{E'}$ dies off and the conical nature of the intersection is lost. Therefore, as in the case where $F_{E'} = 0$ and $G_{E'} \neq 0$, the intersection topology appears to behave Renner-Teller-like rather than conical [see Figure 10(c)]. Obviously, for the title system, the non-negligible PJT effect between the ${}^1E'$ and ${}^1A'_1$ states [note that in Figure 10(c) the energy gap (Δ) between the latter is only 4.3 mE_h] alters significantly the curvature $K = K_{E'} + K_v$ of the PESs near \mathbf{Q}_0 , where $K_v = -2|H_{E'}/A'_1}|^2/\Delta$ is an additional contribution to the primary force constant.^{23–25}

Figure 9(c) illustrates the cut $\mathbf{Q}_b(Q_1) = (0, Q_3)$ of the seam space through the point ($Q_1 = 5.005 a_0$) where the near triple degeneracy between the ${}^1E'(1^1A_1, 1^1B_2)$ and ${}^1A'_1(2^1A_1)$ electronic states is predicted at the FVCAS/AVTZ level; see Figure 5(a). As emphasized in Section IV A, for $Q_1 > 5.005 a_0$ [see Figure 9(d)], the non-degenerate ${}^1A'_1$ state becomes the ground state singlet, with the degenerate ${}^1E'$ term taking the 2^1A_1 and 1^1B_2 electronic states as its components. Nevertheless, as Figure 9(d) shows, the additional C_{2v} crossing seam between the 2^1A_1 and 1^1B_2 states still occurs with $\rho_0(Q_1) = 0.009 a_0$ for $Q_1 = 5.500 a_0$. However, the aforementioned picture changes somewhat by inclusion of the dynamical correlation in MRCl/AVTZ calculations. Indeed, as Figure 10(d) shows, for $Q_1 > 5.005 a_0$, the degenerate ${}^1E'$ term remains the ground state singlet of C_3 at geometries with D_{3h} symmetry. Instead, as seen from Figure 10(d), the three symmetry-equivalent C_{2v} disjoint seams (see illustration in Figure 11) are rotated by $\pm\pi$ (i.e., $\phi' = \phi \pm \pi$) in the two dimensional g - h plane, and hence are given by $\mathbf{Q}_b(Q_1) = (0, -\rho_0)$, $(\sqrt{3}\rho_0/2, \rho_0/2)$ and $(-\sqrt{3}\rho_0/2, \rho_0/2)$. Such an interesting feature may be attributed to the sign change of the ratio between the linear and quadratic JT parameters $F_{E'}/G_{E'}$ on passing through the confluence point. As addressed later in Section VI, the combined JT plus PJT vibronic effects between the first three ${}^1A'$ states of C_3 radical (4 CIs) jointly with the occurrence of an intersection node have a dramatic impact on the adiabatic evolution of the wave functions along a closed circuit C enclosing such points, thence on the so-called GP effect.^{38–41}

V. THE $(E' + A'_1) \otimes e'$ PROBLEM IN C_3

The electronic Hamiltonian (H_e) of the system can be expanded as a Taylor series in terms of small nuclear displacements from the high-symmetry reference configuration \mathbf{Q}_0 as^{21–25}

$$\begin{aligned}
 H_e(\mathbf{r}, \mathbf{Q}) &= H_e^{(0)}(\mathbf{r}, \mathbf{0}) + \sum_{\Gamma_\gamma} \left(\frac{\partial V}{\partial Q_{\Gamma_\gamma}} \right)_0 Q_{\Gamma_\gamma} \\
 &+ \frac{1}{2} \sum_{\Gamma_\gamma} \sum_{\Gamma_1 \Gamma_2} \left\{ \left(\frac{\partial^2 V}{\partial Q_{\Gamma_1} \partial Q_{\Gamma_2}} \right)_0 \right\}_{\Gamma_\gamma} \{Q_{\Gamma_1} \otimes Q_{\Gamma_2}\}_{\Gamma_\gamma} + \dots \\
 &= H_e^{(0)}(\mathbf{r}, \mathbf{0}) + W(\mathbf{r}, \mathbf{Q}).
 \end{aligned} \tag{7}$$

where the zeroth-order Hamiltonian $H_e^{(0)}(\mathbf{r}, \mathbf{0}) = H(\mathbf{r}) + V(\mathbf{r}, \mathbf{0})$ includes the purely electronic part $[H(\mathbf{r})]$ and the electron-nuclear plus nuclear-nuclear interactions $[V(\mathbf{r}, \mathbf{0})]$ with the nuclei fixed at origin; \mathbf{r} is the set of electronic coordinates, and $Q_{\Gamma\gamma}$ are symmetrized nuclear displacements (see Figure 1) which transform according to the line γ of the D_{3h} irrep Γ . In turn, $W(\mathbf{r}, \mathbf{Q})$ is the vibronic coupling (perturbation) operator whose matrix elements (vibronic coupling constants) measure the effect of changes in electronic structure upon nuclear dynamics.^{21–25} In the current analysis, the expansion in Eq. (7) has been truncated at the quadratic terms (second-order perturbation treatment). The starting point consists of the solution of the electronic Schrödinger equation in the field of the nuclei fixed at the origin

$$H_e^{(0)}(\mathbf{r}, \mathbf{0})|\varphi_k(\mathbf{r}, \mathbf{0})\rangle = \mathcal{E}_k(\mathbf{0})|\varphi_k(\mathbf{r}, \mathbf{0})\rangle, \quad (8)$$

where $\{|\varphi_k\rangle\}$ (or, in symmetry representations, $\{|\Gamma\gamma_k\rangle\}$) defines an orthonormal set of static eigenvectors (with associated eigenvalues $\{\mathcal{E}_k(\mathbf{0})\}$) which span the complete electronic function space with the nuclei clamped at \mathbf{Q}_0 .⁶⁴ Due to the strong vibronic interactions between the ground and first two ${}^1A'$ excited states near \mathbf{Q}_0 and given that such terms are well separated from all other ones, only the subspace spanned by them needs to be considered in the formulation of the current JT plus PJT problem. Thus, we employ the BO states in Eqs. (4)-(6) as electronic basis: $\{|\varphi_k\rangle\} \equiv \{|\Psi_2 {}^1E'(1^1A_1)\rangle, |\Psi_3 {}^1E'(1^1B_2)\rangle, |\Psi_4 {}^1A'_1(2^1A_1)\rangle\}$. The appropriate picture of the adiabatic PESs near \mathbf{Q}_0 will therefore be obtained by diagonalizing the 3×3 potential matrix \mathbf{H}_e . Since the above orthonormal basis sets are eigenfunctions of the zeroth-order electronic Hamiltonian $H_e^{(0)}(\mathbf{r}, \mathbf{0})$, the associated matrix is diagonal, with elements $(\mathbf{H}_e^{(0)})_{kl} = \mathcal{E}_k(\mathbf{0})\delta_{kl}$. The potential matrix \mathbf{H}_e , however, is nondiagonal in this basis, except at \mathbf{Q}_0 .

Consider the coefficients of the expansion in Eq. (7), which are derivatives of the operator of electron-nuclear interaction $V(\mathbf{r}, \mathbf{0})$. As noted above, the associated matrix elements \mathbf{W}_{kl} define the vibronic coupling constants.^{23,24} Let us first examine the linear vibronic constants $F_{\overline{\Gamma}\overline{\gamma}}^{(\Gamma\gamma\Gamma'\gamma')}$ which are given by^{21–25}

$$F_{\overline{\Gamma}\overline{\gamma}}^{(\Gamma\gamma\Gamma'\gamma')} = \langle \Gamma\gamma | \left(\frac{\partial V}{\partial Q_{\overline{\Gamma}\overline{\gamma}}} \right)_0 | \Gamma'\gamma' \rangle = F_{\overline{\Gamma}}^{(\Gamma\Gamma')} \mathbf{V} \begin{pmatrix} \Gamma & \Gamma' & \overline{\Gamma} \\ \gamma & \gamma' & \overline{\gamma} \end{pmatrix}, \quad (9)$$

where $\gamma(\gamma')$ and $\overline{\gamma}$ are the lines of the D_{3h} irreps $\Gamma(\Gamma')$ and $\overline{\Gamma}$ according to which the electronic wave functions and symmetrized displacements transform, respectively. Note that, similarly to $Q_{\overline{\Gamma}\overline{\gamma}}$, the derivative $(\partial V / \partial Q_{\overline{\Gamma}\overline{\gamma}})_0$ possess the transformation properties of $\overline{\Gamma}\overline{\gamma}$. According to the Wigner-Eckart theorem,^{22,23,65} $F_{\overline{\Gamma}}^{(\Gamma\Gamma')} = \langle \Gamma || (\partial V / \partial Q_{\overline{\Gamma}}) || \Gamma' \rangle$ is the reduced matrix element (which does not depend on γ, γ' , and $\overline{\gamma}$) and the last term of Eq. (9) defines the associated V coefficient (directly related to the Clebsch-Gordan coupling coefficient^{22,23}) for the D_{3h} point group.⁶⁵

Selection rules for $F_{\overline{\Gamma}\overline{\gamma}}^{(\Gamma\gamma\Gamma'\gamma')}$ can be readily determined from group-theoretic considerations^{22,23,65} and therefore, are naturally incorporated by the V coefficient.⁶⁵ Thence, for

nondegenerate states in which $\Gamma\gamma \equiv \Gamma$, $\Gamma'\gamma' \equiv \Gamma'$ and hence $\overline{\Gamma}\overline{\gamma} \equiv \overline{\Gamma}$, $F_{\overline{\Gamma}}^{(\Gamma\Gamma')}$ is nonzero if and only if the triple direct product $\Gamma \otimes \overline{\Gamma} \otimes \Gamma'$ contains the totally symmetric irrep A_1 . In turn, if Γ or Γ' are nondegenerate (e.g., Γ or $\Gamma' = A'_1$), then $F_{\overline{\Gamma}\overline{\gamma}}^{(\Gamma\gamma\Gamma'\gamma')}$ is nonzero only if the doubly degenerate electronic term and symmetrized displacement transform as the same line of the E' irrep in D_{3h} . Indeed, if $\Gamma = A'_1$, $\Gamma' = \overline{\Gamma} = E'$ and $\gamma' = \overline{\gamma} = \epsilon$ (or θ), $A'_1 \otimes E' \otimes E' \supset A'_1$ and $\mathbf{V} = 1/\sqrt{2}$. In this case, $F_{\overline{\Gamma}\overline{\gamma}}^{(\Gamma\gamma\Gamma'\gamma')}$ is referred to as linear PJT vibronic constants. Finally, if Γ and Γ' are both doubly degenerate with $\Gamma \equiv \Gamma'$, $F_{\overline{\Gamma}\overline{\gamma}}^{(\Gamma\gamma\Gamma'\gamma')}$ is nonzero if $\Gamma \otimes \overline{\Gamma} \otimes \Gamma \supset A_1$ (or, in other words, if the symmetric square $[\Gamma^2]$ contains $\overline{\Gamma}$). Clearly, for $\Gamma = \Gamma' = \overline{\Gamma} = E'$, the associated linear JT vibronic constant vanishes for $\gamma = \gamma' = \overline{\gamma} = \epsilon$ or any combination of θ, θ , and ϵ lines, since in these cases $\mathbf{V} = 0$. It should be mentioned here that, following the rules of group theory,^{22,23,65} the linear vibronic constants between states of the same symmetry (i.e., the diagonal elements of \mathbf{W}) are nonzero along the breathing normal coordinate $Q_1 \equiv Q_{A'_1}$, e.g., $F_{A'_1}^{(E'E'E)}$, $F_{A'_1}^{(E'_\theta E'_\theta)}$, and $F_{A'_1}^{(A'_1 A'_1)}$. However, since the degeneracy of the E' term is only lifted along the JT active displacements ($Q_2 \equiv Q_{E'_\epsilon}$ and $Q_3 \equiv Q_{E'_\theta}$), the vibronic perturbations associated with Q_1 are assumed to be unimportant, and hence neglected. Thus, by means of Eq. (9), the linear JT and PJT vibronic coupling constants in the electronic basis of Eqs. (4)-(6) are defined by

$$\begin{aligned} \langle \Psi_2 {}^1E'(1^1A_1) | \left(\frac{\partial V}{\partial Q_3} \right)_0 | \Psi_2 {}^1E'(1^1A_1) \rangle &= -F_{E'} \\ \langle \Psi_2 {}^1E'(1^1A_1) | \left(\frac{\partial V}{\partial Q_2} \right)_0 | \Psi_3 {}^1E'(1^1B_2) \rangle &= F_{E'} \\ \langle \Psi_3 {}^1E'(1^1B_2) | \left(\frac{\partial V}{\partial Q_2} \right)_0 | \Psi_2 {}^1E'(1^1A_1) \rangle &= F_{E'} \\ \langle \Psi_3 {}^1E'(1^1B_2) | \left(\frac{\partial V}{\partial Q_3} \right)_0 | \Psi_3 {}^1E'(1^1B_2) \rangle &= F_{E'} \end{aligned} \quad (10)$$

and

$$\begin{aligned} \langle \Psi_2 {}^1E'(1^1A_1) | \left(\frac{\partial V}{\partial Q_3} \right)_0 | \Psi_4 {}^1A'_1(2^1A_1) \rangle &= H_{E'/A'_1} \\ \langle \Psi_3 {}^1E'(1^1B_2) | \left(\frac{\partial V}{\partial Q_2} \right)_0 | \Psi_4 {}^1A'_1(2^1A_1) \rangle &= H_{E'/A'_1} \\ \langle \Psi_4 {}^1A'_1(2^1A_1) | \left(\frac{\partial V}{\partial Q_3} \right)_0 | \Psi_2 {}^1E'(1^1A_1) \rangle &= H_{E'/A'_1} \\ \langle \Psi_4 {}^1A'_1(2^1A_1) | \left(\frac{\partial V}{\partial Q_2} \right)_0 | \Psi_3 {}^1E'(1^1B_2) \rangle &= H_{E'/A'_1} \end{aligned}, \quad (11)$$

where $F_{E'}$ and H_{E'/A'_1} are the associated reduced matrix elements; see Eq. (9). Note that, in Eqs. (10) and (11), the following symmetry correlations have been employed: $|\Psi_2 {}^1E'(1^1A_1)\rangle \equiv |E'_\theta\rangle$, $|\Psi_3 {}^1E'(1^1B_2)\rangle \equiv |E'_\epsilon\rangle$, and $|\Psi_4 {}^1A'_1(2^1A_1)\rangle \equiv |A'_1\rangle$.

Let us now turn to the analysis of the quadratic vibronic constants. As shown in the expansion of Eq. (7), the quantity $\{(\partial^2 V / \partial Q_{\Gamma_1} \partial Q_{\Gamma_2})_0\}_{\Gamma\gamma}$ defines an irreducible product⁶⁵ (or a tensor convolution^{22,23}) which, in fact, is a linear combination of second derivatives with respect to Q_{Γ_1} and Q_{Γ_2} that transforms according to the line γ of the D_{3h} irrep $\Gamma \subset \Gamma_1 \otimes \Gamma_2$. Such combinations can be found by

means of group-theoretical transformations, together with the Wigner-Eckart theorem,^{22,23,65} see, e.g., Eq. (5.1) of Ref. 65. Likewise, $\{Q_{\Gamma_1} \otimes Q_{\Gamma_2}\}_{\Gamma\gamma}$ denotes the irreducible product for the corresponding symmetrized coordinates. The quadratic vibronic constants are then given by^{21–25}

$$\begin{aligned} G_{\bar{\Gamma}\bar{\gamma}}^{(\Gamma\gamma\Gamma'\gamma')} &= \frac{1}{2} \langle \Gamma\gamma | \left\{ \left(\frac{\partial^2 V}{\partial Q_{\Gamma_1} \partial Q_{\Gamma_2}} \right)_0 \right\}_{\bar{\Gamma}\bar{\gamma}} | \Gamma'\gamma' \rangle \\ &= \frac{1}{2} G_{\bar{\Gamma}}^{(\Gamma\Gamma')} \mathbf{V} \begin{pmatrix} \Gamma & \Gamma' & \bar{\Gamma} \\ \gamma & \gamma' & \bar{\gamma} \end{pmatrix}, \end{aligned} \quad (12)$$

where $G_{\bar{\Gamma}}^{(\Gamma\Gamma')} = \langle \Gamma | \left\{ \left(\frac{\partial^2 V}{\partial Q_{\Gamma_1} \partial Q_{\Gamma_2}} \right)_0 \right\}_{\bar{\Gamma}} | \Gamma' \rangle$ is the associated reduced matrix element^{22,23,65} with all other quantities assuming the same meaning as above. Suffice it to say that, as for the linear case, the same group-theoretical selection rules can be used to evaluate the matrix elements of Eq. (12). Thence, diagonal elements (for which $\Gamma\gamma \equiv \Gamma'\gamma'$) evaluated at totally symmetric irreducible products $\{(\partial^2 V / \partial Q_{\Gamma}^2)_0\}_{A_1}$ are nonzero, since $\Gamma \otimes A_1 \otimes \Gamma \supset A_1$ and, for degenerate terms, $\gamma \equiv \gamma'$.^{21–25} Indeed, such elements are the (nonvibronic) force constants of the adiabatic PESs at \mathbf{Q}_0 ^{22,23,65} and within the basis set under consideration are defined by

$$\begin{aligned} \langle \Psi_2 {}^1E'(1^1A_1) | \left(\frac{\partial^2 V}{\partial Q_2^2} \right)_0 + \left(\frac{\partial^2 V}{\partial Q_3^2} \right)_0 | \Psi_2 {}^1E'(1^1A_1) \rangle &= K_{E'} \\ \langle \Psi_3 {}^1E'(1^1B_2) | \left(\frac{\partial^2 V}{\partial Q_2^2} \right)_0 + \left(\frac{\partial^2 V}{\partial Q_3^2} \right)_0 | \Psi_3 {}^1E'(1^1B_2) \rangle &= K_{E'}. \\ \langle \Psi_4 {}^1A'_1(2^1A_1) | \left(\frac{\partial^2 V}{\partial Q_2^2} \right)_0 + \left(\frac{\partial^2 V}{\partial Q_3^2} \right)_0 | \Psi_4 {}^1A'_1(2^1A_1) \rangle &= K_{A'_1} \end{aligned} \quad (13)$$

Here, $K_{E'}$ and $K_{A'_1}$ are the primary force constants (without vibronic coupling) for the ${}^1E'$ and ${}^1A'_1$ electronic states, respectively. The remaining terms and the off-diagonal elements of \mathbf{W} comprise the quadratic JT vibronic coupling constants which are given by

$$\begin{aligned} \langle \Psi_2 {}^1E'(1^1A_1) | \left(\frac{\partial^2 V}{\partial Q_2^2} \right)_0 - \left(\frac{\partial^2 V}{\partial Q_3^2} \right)_0 | \Psi_2 {}^1E'(1^1A_1) \rangle &= -G_{E'} \\ \langle \Psi_2 {}^1E'(1^1A_1) | \left(\frac{\partial^2 V}{\partial Q_2 Q_3} \right)_0 | \Psi_3 {}^1E'(1^1B_2) \rangle &= 2G_{E'} \\ \langle \Psi_3 {}^1E'(1^1B_2) | \left(\frac{\partial^2 V}{\partial Q_2 Q_3} \right)_0 | \Psi_2 {}^1E'(1^1A_1) \rangle &= 2G_{E'} \\ \langle \Psi_3 {}^1E'(1^1B_2) | \left(\frac{\partial^2 V}{\partial Q_2^2} \right)_0 - \left(\frac{\partial^2 V}{\partial Q_3^2} \right)_0 | \Psi_3 {}^1E'(1^1B_2) \rangle &= G_{E'} \end{aligned}, \quad (14)$$

where $G_{E'}$ is the reduced matrix element. Note that, for the sake of simplicity, only the quadratic parameters $G_{E'}$ associated with the JT effect have been included in the vibronic coupling matrix \mathbf{W} , and hence the nonadiabatic corrections due to PJT interaction are here accounted up to first-order (H_{E'/A'_1}). Using Eq. (10)–Eq. (14), the potential matrix \mathbf{H}_e , within the basis $\{|\Psi_2 {}^1E'(1^1A_1)\rangle, |\Psi_3 {}^1E'(1^1B_2)\rangle, |\Psi_4 {}^1A'_1(2^1A_1)\rangle\}$, assumes the form³¹

$$\mathbf{H}_e = \mathbf{H}_e^{(0)} + \mathbf{W} = \begin{pmatrix} -F_{E'} Q_3 + \kappa_{E'}(\mathbf{Q}) - G_{E'}(Q_2^2 - Q_3^2) & F_{E'} Q_2 + 2G_{E'} Q_2 Q_3 & H_{E'/A'_1} Q_3 \\ F_{E'} Q_2 + 2G_{E'} Q_2 Q_3 & F_{E'} Q_3 + \kappa_{E'}(\mathbf{Q}) + G_{E'}(Q_2^2 - Q_3^2) & H_{E'/A'_1} Q_2 \\ H_{E'/A'_1} Q_3 & H_{E'/A'_1} Q_2 & \Delta + \kappa_{A'_1}(\mathbf{Q}) \end{pmatrix}, \quad (15)$$

where $\kappa_{E'}(\mathbf{Q}) = \frac{1}{2} K_{E'}(Q_2^2 + Q_3^2)$ and $\kappa_{A'_1}(\mathbf{Q}) = \frac{1}{2} K_{A'_1}(Q_2^2 + Q_3^2)$ are the corresponding harmonic nuclear interaction potentials about \mathbf{Q}_0 for the ${}^1E'$ and ${}^1A'_1$ electronic states, respectively. It is worth pointing out that the zero of energy in Eq. (15) is taken from the ${}^1E'$ term at the reference configuration [$\mathcal{E}_{E'}(\mathbf{0}) = 0$, see Eq. (8)], and hence Δ denotes the energy gap between the vibronically mixed terms at the origin. For sufficiently small $Q_{\Gamma\gamma}$ (for which the present perturbation approach is valid), the roots of Eq. (15) are then obtained by solving the secular determinant $|\mathbf{H}_e - \mathcal{E}(\mathbf{Q})\mathbf{I}| = 0$ whose solutions assume the form^{21–25}

$$\mathcal{E}_k(\mathbf{Q}) = \kappa_k(\mathbf{Q}) + \vartheta_k(\mathbf{Q}), \quad (16)$$

where $\vartheta_k(\mathbf{Q})$ is the vibronic contribution which—added to the harmonic (nonvibronic part) term $\kappa_k(\mathbf{Q})$ —produces the appropriate picture of the adiabatic PESs near \mathbf{Q}_0 , including the expected cusped behavior at electronic degeneracies and the vibronic mixing between close-in-energy terms. Suffice it to add that since the vibronic coupling constants associated with Q_1 are assumed to be identically zero, the corresponding adiabatic PESs along sufficiently small Q_1 distortions behave simply as harmonic potentials, i.e., $\mathcal{E}_k(\mathbf{Q}) = \frac{1}{2} K Q_1^2$ with $\vartheta_k(\mathbf{Q}) = 0$ and $K = \langle \Gamma\gamma | (\partial^2 V / \partial Q_1^2)_0 | \Gamma\gamma \rangle$.

The solutions of the vibronic coupling equations with the present JT plus PJT Hamiltonian [Eq. (15)] are illustrated

in Figure 12 for cross-sectional cuts of the $1^1A'$, $2^1A'$, and $3^1A'$ PESs along Q_3 [$\mathbf{Q}_b(Q_1) = (0, Q_3)$]. Note that the *ab initio* points have been obtained from MRCI/AVTZ calculations and covered a region defined by $-0.020 a_0 \leq Q_3 \leq 0.020 a_0$ in steps of $0.00125 a_0$ for Q_1 fixed at the minimum of the equilateral triangular conformation; $\mathbf{Q}_s^{cusp} = (Q_1^{cusp}, 0, 0)$ with $Q_1^{cusp} = 4.548 a_0$. The numerical parameters in Eq. (15), [$F_{E'}$, $G_{E'}$, H_{E'/A'_1} , $K_{E'}$ and $K_{A'_1}$] have been estimated by minimizing the sum of squared residuals

$$\chi_{\text{total}}^2 = \chi_{1^1A'}^2 + \chi_{2^1A'}^2 + \chi_{3^1A'}^2 \quad (17)$$

in which each electronic state is treated democratically with χ_k^2 , the corresponding sum of squared residuals for the term k , given by

$$\chi_k^2 = \sum_{n=1}^{N_k} [\mathcal{E}_{k,ab\text{ initio}}(\mathbf{Q}_n) - \mathcal{E}_{k,\text{num}}(\mathbf{Q}_n)], \quad (18)$$

where $\mathcal{E}_{k,ab\text{ initio}}(\mathbf{Q}_n)$ is the corresponding *ab initio* energy of the electronic state k at nuclear configuration \mathbf{Q}_n [given with respect to $\mathcal{E}_{1E'}(\mathbf{Q}_0) = \mathcal{E}_{1E'}(\mathbf{Q}_s^{cusp})$] and $\mathcal{E}_{k,\text{num}}(\mathbf{Q}_n)$ is the associated eigenvalue obtained by numerical diagonalization of the potential matrix \mathbf{H}_e with the aid of the Jacobi method.^{66,67} In Eq. (18), the summation is extended over the whole set of *ab initio* points for each electronic state ($N_k = 34$ and therefore, $N_{\text{total}} = 102$) with all minimizations performed by means of the Levenberg-Marquardt algorithm.^{68,69} As Figure 12 shows, the present JT plus PJT potential matrix [Eq. (15)] yields eigenvalues which accurately mimic the adiabatic energies obtained from MRCI/AVTZ calculations, with an unweighted root mean square deviation (rmsd) of only 2.6 cm^{-1} for the total number of fitted *ab initio* points. The fitting parameters are: $K_{E'} = 351.3 \text{ mE}_h a_0^{-2}$, $K_{A'_1} = 399.0 \text{ mE}_h a_0^{-2}$, $F_{E'} = 11.8 \text{ mE}_h a_0^{-1}$, $G_{E'} = 1940.0 \text{ mE}_h a_0^{-2}$, $H_{E'/A'_1} = 150.8 \text{ mE}_h a_0^{-1}$, and $\Delta = 11.7 \text{ mE}_h$. Accordingly, we see that the linear JT vibronic constant ($F_{E'}$) is extremely small and

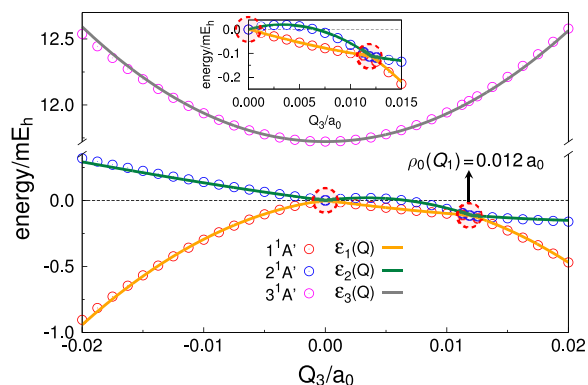


FIG. 12. PES cuts along the bending normal coordinate Q_3 [$\mathbf{Q}_b(Q_1^{cusp}) = (0, Q_3)$] for the three lowest $1^1A'$ electronic states of C_3 radical over the range of $-0.020 a_0 \leq Q_3 \leq 0.020 a_0$. Open symbols correspond to points calculated at MRCI/AVTZ level of theory, while the solid lines are the associated eigenvalues of Eq. (15) as obtained from the least-squares fitting procedure. Filled circles highlight the central and additional C_{2v} Cls. The zero of energy is $\mathcal{E}_{1E'}(\mathbf{Q}_s^{cusp}) = -113.7605899 \text{ E}_h$.

about 1 and 2 orders of magnitude smaller than H_{E'/A'_1} and $G_{E'}$, respectively. Dillon and Yarkony²⁷ reported a similar ratio between the linear and quadratic JT parameters for N_3^+ . Because $G_{E'} \gg F_{E'}$, exceptionally small values of $\rho_0(Q_1)$ are then expected in this region of configuration space, as seen in Figures 7 and 9-12. In spite of that, for the present case $F_{E'}/G_{E'} \approx 0.006 a_0$ and therefore, the PJT vibronic effect operates in such a way as to increase twice the value of $\rho_0(Q_1)$, i.e., as seen in Figure 12, $\rho_0(Q_1^{cusp}) = 0.012 a_0$. Indeed, the relatively large magnitude of the linear PJT parameter (H_{E'/A'_1}) gives insights into the relevance and influence of such combined JT plus PJT vibronic effects in the proper description of the title system.

Interestingly, as shown in Figure 13, the current three state JT plus PJT model Hamiltonian predicts the existence of a stationary point [hereafter, denoted as $c_{2v}\text{-}C_3(1^1B_2)$] in the $2^1A'$ electronic state PES for $Q_3 = 0.025 a_0$. Indeed, such a structure has been confirmed by *ab initio* FVCAS/AVTZ geometry optimizations and shown itself as a minimum on the $2^1A'$ adiabatic PES. The computed equilibrium geometry (in valence coordinates¹) and harmonic vibrational frequencies are given in Table III. Also shown are the relative energies (ΔE) given with respect to the absolute minimum on the adiabatic ground state PES [lin- $C_3(1^1\Sigma_g^+/1^1A_1)$] as well as JT plus PJT stabilization energies (ΔE_v) with respect to the minimum of the equilateral triangular geometry \mathbf{Q}_s^{cusp} . Accordingly, excellent correlations are found between the predicted structure and the one actually obtained from the *ab initio* calculations. In fact, the $c_{2v}\text{-}C_3(1^1B_2)$ distorted minimum arises from the structural instability associated to the high-symmetry D_{3h} configuration with a JT plus PJT stabilization energy of -38.0 , -38.8 and -40.0 cm^{-1} as obtained from MRCI/AVTZ, MRCI/AVQZ and CBS/MRCI calculations, respectively. Suffice it to say that such stabilization energies compare quite well with the value of -34.4 cm^{-1} predicted from the JT plus PJT model Hamiltonian here considered.

Note that, in the $3^1A'$ electronic state PES, the PJT vibronic effect provides an additional stabilization of the

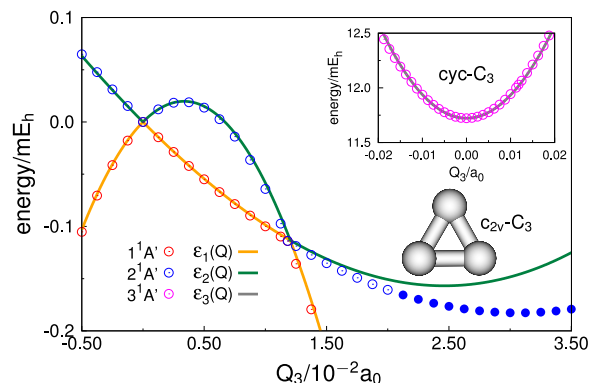


FIG. 13. PES cuts along the bending normal coordinate Q_3 [$\mathbf{Q}_b(Q_1^{cusp}) = (0, Q_3)$] near the minimum structure predicted by the three state JT plus PJT model Hamiltonian for the $2^1A'$ PES of C_3 radical. Open symbols correspond to points calculated at MRCI/AVTZ level of theory, while the solid lines are the associated eigenvalues of Eq. (15) as obtained from the least-squares fitting procedure. Solid symbols correspond to non-fitted *ab initio* points.

TABLE III. Properties and energetics of the c_{2v} - $C_3(1^1B_2)$ minimum on the first excited state ($2^1A'$) PES of the C_3 radical. The structure is labeled according to its point group irrep in C_{2v} symmetry (given in parentheses). Energies are given with respect to the $D_{\infty h}$ absolute minimum [$\text{lin-C}_3(1^1\Sigma_g^+/1^1A_1)$] of the ground state adiabatic PES of C_3 (see Table I) as well as with respect to the minimum of the equilateral triangular geometry Q_s^{cusp} .

	Method	R/a ₀	∠CCC/deg	ΔE/kJ mol ⁻¹	ΔE _v /cm ⁻¹	ω ₁ /cm ⁻¹	ω ₂ /cm ⁻¹	ω ₃ /cm ⁻¹
	FIT ^{a,b}	2.616	60.8		-34.4 ^c			
	FVCAS/AVTZ ^a	2.629	60.9	195.5 ^d	-38.7	1512.7	1124.7	3690.7
c_{2v} - $C_3(1^1B_2)$	MRCI/AVTZ ^a			161.4	-38.0			
	MRCI/AVQZ ^a			158.8	-38.8			
	CBS ^a			151.3	-40.0			

^aThis work.

^bPredicted by the three state JT plus PJT model Hamiltonian of Eq. (15).

^cRelative to $Q_s^{\text{cusp}} = (Q_1^{\text{cusp}}, 0, 0)$ with $Q_1^{\text{cusp}} = 4.548 a_0$.

^dRelative to the FVCAS/AVTZ optimized minimum of $\text{lin-C}_3(1^1\Sigma_g^+/1^1A_1)$ [see Table I].

undistorted D_{3h} configuration and therefore, a minimum at this geometry [$\text{cyc-C}_3(1^1A'_1/2^1A_1)$] is observed for $Q_s = (4.638 a_0, 0, 0)$, as noted in Section III (see inset of Figure 13 and Table I). Such a strengthening of the PES curvature is perceived by inspection to the magnitude of the harmonic vibrational frequency: 5069.5 cm⁻¹ for the degenerate e' normal mode of $\text{cyc-C}_3(1^1A'_1/2^1A_1)$, as shown in Table I [compare with the corresponding value of 1091.0 cm⁻¹ of the $\text{cyc-C}_3(3^1A'_2/1^3B_2)$ triplet structure where neither JT nor PJT effects are observed]. As emphasized by Rocha and Varandas,¹⁰ in the $1^1A'$ ground state singlet, distortions from the D_{3h} structure toward $Q_3 > 0$ give rise to the distorted (linear) global minimum on the adiabatic ground state PES [$\text{lin-C}_3(1^1\Sigma_g^+/1^1A_1)$; see Table I]. Instead, if displacements along $Q_3 < 0$ take place the title system actually attains a saddle point structure which is, indeed, the transition state for the isomerization between the three symmetry-equivalent $D_{\infty h}$ global minima.¹⁰

VI. TOPOLOGICAL IMPLICATIONS

Following the Longuet-Higgins' (LH) theorem:³⁹ if a real-valued electronic wave function changes sign when adiabatically transported around a closed circuit C in the two-dimensional g - h plane, then it must become discontinuous and degenerate with another state at an odd number of points lying on that surface and within that loop.^{26,38-41} Varandas *et al.*⁵⁸ first demonstrated the numerical validity of such sign reversal criterion in the unsymmetrical LiNaK system by following the variation of the dominant coefficients, c_i , of the ground-state electronic wave function along a path (in the two-dimensional branching space) that encircles the crossing point.⁵⁸

In this spirit, we have performed state-averaged FVCAS/AVTZ calculations in which the adiabatic evolution of the $1^1A'$, $2^1A'$, and $3^1A'$ electronic wave functions along a chosen (circular) path was attended by following the leading components (c_0) of the associated CASSCF vectors. Note that such (counterclockwise) paths in the two dimensional g - h plane²⁶ were judiciously chosen by fixing the radial polar coordinate $\rho(Q_1) = \sqrt{Q_2^2 + Q_3^2}$ (hereafter, denoted simply as ρ) at a convenient value, while varying the pseudo-rotation angle $\phi = \arctan(Q_3/Q_2)$ from 0 to 2π in steps of $\pi/18$.^{11,26,58}

Suffice it to say that the associated coordinates in the two dimensional branching space are given by $Q_2 = \rho \cos \phi$ and $Q_3 = \rho \sin \phi$, i.e., $Q_b(Q_1) = (\rho \cos \phi, \rho \sin \phi)$. Figure 14 depicts such closed loops in nuclear configuration space together with the associated coefficients (c_0) in the leading determinants (or CSFs) of the FVCAS/AVTZ wave functions for the $1^1A'$, $2^1A'$, and $3^1A'$ electronic states of the C_3 radical. It should be emphasized that in Figures 14(a) and 14(d), the circular paths are centered at the minimum of the D_{3h} crossing seam, i.e., $Q_s^{\text{cusp}} = (Q_1^{\text{cusp}}, 0, 0)$ with $Q_1^{\text{cusp}} = 4.576 a_0$ ($Q_1^{\text{cusp}} = 4.548 a_0$ at MRCI/AVTZ level), while in Figure 14(b), the minimum of the C_{2v} seam is set as the origin, i.e., $Q_b^{\text{cusp}} = (Q_1^{\text{cusp}}, 0, Q_3^{\text{cusp}})$ with $Q_3^{\text{cusp}} = 0.007 a_0$ ($Q_3^{\text{cusp}} = 0.012 a_0$ at MRCI/AVTZ level). In turn, the path illustrated in Figure 14(c) is centered at the midpoint between Q_s^{cusp} and Q_b^{cusp} , i.e., at $Q = (Q_1^{\text{cusp}}, 0, Q_3^{\text{cusp}}/2)$.

As first pointed out by Zwanziger and Grant,²⁸ and later by others,^{10,27,31,33,35-37} for SLP JT molecules and systems in which a strong JT plus PJT interactions occur such as the one here reported, the additional three symmetry-equivalent C_{2v} seams may prevent the associated electronic wave function of changing sign when transported around a loop enclosing the four CIs. In other words, the net GP effect³⁸⁻⁴¹ is largely suppressed.

Consider first the case in which a circular path in the g - h plane is chosen such that $\rho < \rho_0(Q_1)$ [see Figure 14(a) and the insetted illustration]. In this case, only one CI (the central one) is enclosed and the adiabatic wave function changes sign along this loop, as seen in Figure 14(a) for the $1^1A'$ and $2^1A'$ electronic states. In fact, a similar sign change is expected when only one of the three equivalent degeneracies of C_{2v} symmetry is encircled [see Figure 14(b)]. Conversely, as Figure 14(c) shows, a closed circuit which encloses both the central CI and one of the C_{2v} degeneracy points is sign-preserving, i.e., the adiabatic wave functions experience no sign change. Indeed, for more general cases in which circular paths are chosen in such a way that $\rho > \rho_0(Q_1)$ [Figure 14(d)], the associated adiabatic wave functions do not change sign, since upon transport along this loop the four CIs are encircled. It should be emphasized at this point that $\rho_0(Q_1)$ marks an important transition region between a Jahn-Teller- and Renner-Teller-like behavior in the sense that the adiabatic wave functions for the $1^1A'$ and $2^1A'$ electronic

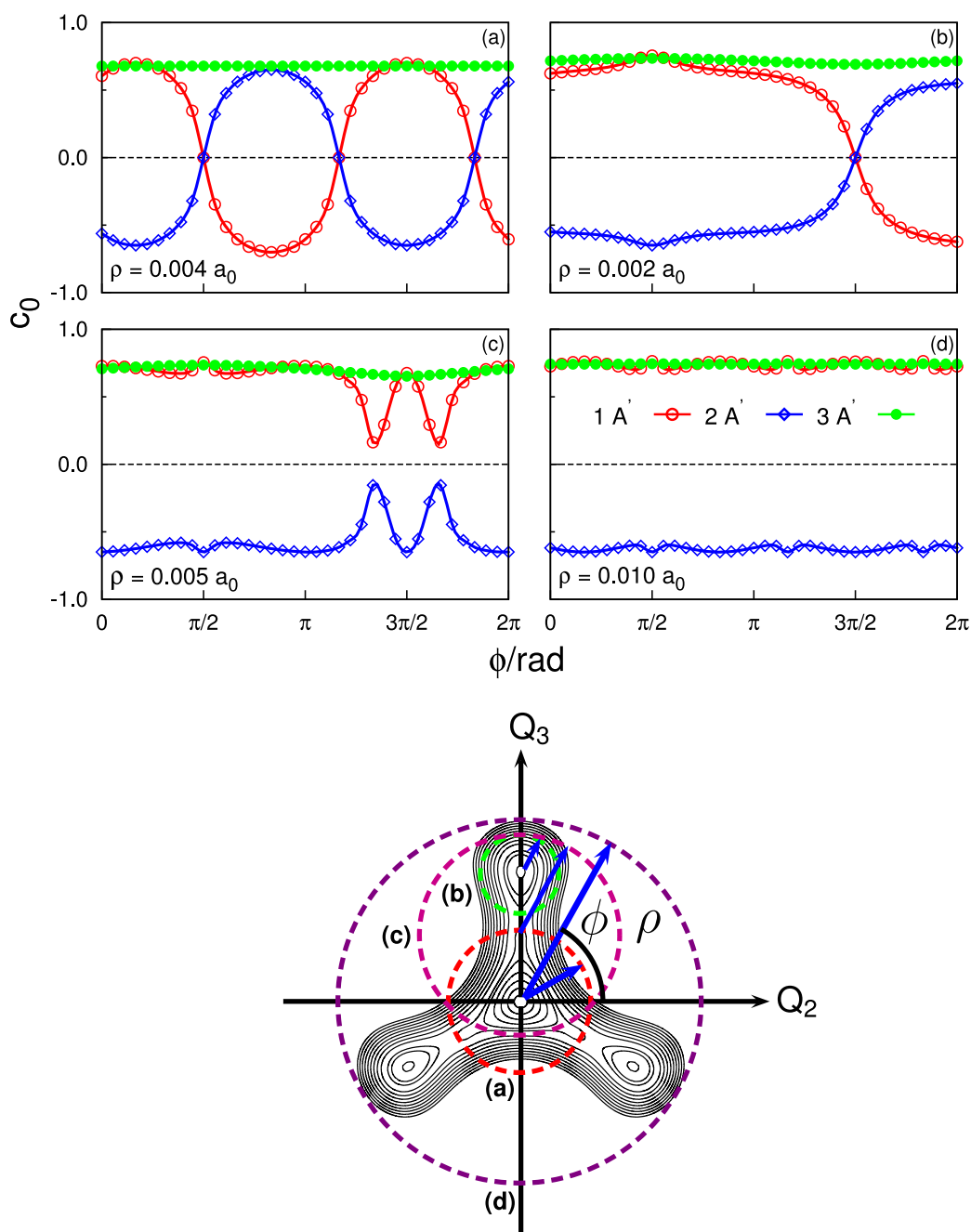


FIG. 14. Adiabatic evolution of the $1^1A'$, $2^1A'$, and $3^1A'$ electronic wave functions of C_3 radical along a closed circuit C in the two dimensional $g-h$ plane encircling one or multiple conical intersections (see illustration). c_0 is the associated coefficient in the leading determinant (or CSF) of the FVCAS/AVTZ electronic wave function for each state considered. The sign changes are observed by considering four closed loops which encircle (a) the central (D_{3h}) conical intersection with origin at Q_s^{cusp} and fixed radius of $\rho = 0.004 a_0$ (b) one C_{2v} conical intersection with origin at Q_b^{cusp} and fixed radius of $\rho = 0.002 a_0$ (c) two conical intersections with origin at $Q = (Q_1^{cusp}, 0, Q_3^{cusp}/2)$ and fixed radius of $\rho = 0.005 a_0$ and (d) four conical intersections with origin at Q_s^{cusp} and fixed radius of $\rho = 0.010 a_0$.

states experience a sign change upon adiabatic transport about the origin (the D_{3h} reference seam) in the case $\rho < \rho_0(Q_1)$, but not for $\rho > \rho_0(Q_1)$.²⁸ Note that, in Figure 14, the adiabatic wave function for the $3^1A'$ state does not change sign in any of the cases here considered since it is non-JT in nature.

Figure 15 illustrates the adiabatic evolution the $1^1A'$, $2^1A'$, and $3^1A'$ electronic wave functions along closed paths encircling the point of confluence between the D_{3h} and C_{2v} crossing seams or the intersection node^{17,59,60} at $Q_s = (5.005 a_0, 0, 0)$; see Figures 9(c) and 10(c). As highlighted

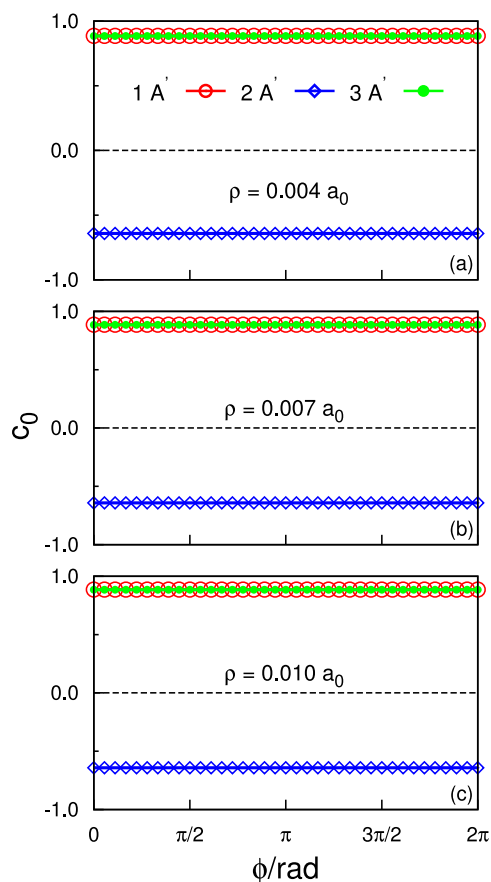


FIG. 15. Adiabatic evolution of the $1^1A'$, $2^1A'$, and $3^1A'$ electronic wave functions of C_3 radical along a closed circuit C in the two dimensional g - h plane encircling the point of confluence between the D_{3h} and C_{2v} crossing seams or the intersection node. c_0 is the associated coefficient in the leading determinant (or CSF) of the FVCAS/AVTZ electronic wave function for each state considered. The circular paths are centered at $Q_s = (5.005 a_0, 0, 0)$ with fixed radius of (a) $\rho = 0.004 a_0$, (b) $\rho = 0.007 a_0$, and (c) $\rho = 0.010 a_0$.

in Section IV B, at such a point in nuclear configuration space, the predominance of quadratic coupling constants $G_{E'}$ is remarkable [see for instance Figure 10(c)] and therefore, the situation can be drawn on the same grounds as that for the $F_{E'} = 0$ and $G_{E'} \neq 0$ (i.e., the pure Renner-Teller) case in which the three additional degeneracies coincide with the central one, $\rho_0(Q_1) \rightarrow 0$.^{28,59} Indeed, as seen from Figure 15, the adiabatic states exhibit no sign changes after a complete transversal of the loops. As noted by Dillon and Yarkony²⁷ and Schuurman and Yarkony,¹⁶ the intersection node is the only point in the nuclear configuration space at which the topological phase effect is suppressed even for infinitesimal loops.

VII. CONCLUSIONS

The combined JT plus PJT problem in the C_3 radical has been here fully accounted for by means of *ab initio* calculations obtained at the multireference configuration interaction level of theory. For the $1^1E'$ electronic state, arising from a e'^2 valence configuration, it is found that the three additional

symmetry-equivalent C_{2v} seams are in extremely close proximity to the symmetry-required one over the range of breathing coordinate here considered. Clearly, as the perimeter of the molecule increases, the C_{2v} disjoint seams approach the D_{3h} crossing seam almost linearly and ultimately coalesce with the central one at $Q_1 = 5.005 a_0$ thus forming an intersection node or confluence of the seams. By further increasing the size of the triangle, however, the marginal C_{2v} seams are rotated by $\pm\pi$ in the g - h plane. A three-state JT plus PJT vibronic Hamiltonian is then proposed for the title system, and shown to accurately mimic the region defined by the minimum energy crossing point. No net geometric phase effect is observed, e.g., when the associated electronic wave functions are adiabatically transported along closed paths encircling the four singularity points. For paths enclosing the intersection node it is also realized that the sign-reversal criterion is not fulfilled, even for infinitesimal loops. The results so obtained are clearly applicable to other ring systems experiencing similar topological attributes.

ACKNOWLEDGMENTS

This work has the support of Fundação para a Ciência e a Tecnologia, Portugal, under Contract Nos. PTDC/CEQ-COM3249/2012 and PTDC/AAG-MAA/4657/2012, as well as the support to the Coimbra Chemistry Centre through Project No. PEst-OE/UI0313/2014. C.M. thanks also the CAPES Foundation (Ministry of Education of Brazil) for a scholarship (Process No. BEX 0417/13-0).

- ¹J. N. Murrell, S. Carter, S. C. Farantos, P. Huxley, and A. J. C. Varandas, *Molecular Potential Energy Functions* (John Wiley & Sons, Chichester, 1984).
- ²A. J. C. Varandas and V. M. F. Morais, *Mol. Phys.* **47**, 1241 (1982).
- ³A. J. C. Varandas, F. B. Brown, C. A. Mead, D. G. Truhlar, and N. C. Blais, *J. Chem. Phys.* **86**, 6258 (1987).
- ⁴J. N. Murrell, *Int. J. Quantum Chem.* **37**, 95 (1990).
- ⁵A. J. C. Varandas and A. A. C. C. Pais, *J. Chem. Soc., Faraday Trans.* **89**, 1511 (1993).
- ⁶A. J. C. Varandas, in *Conical Intersections: Electronic Structure, Dynamics & Spectroscopy*, Advanced Series in Physical Chemistry Vol. 15, edited by W. Domcke, D. R. Yarkony, and H. Köppel (World Scientific Publishing, Singapore, 2004), Chap. 5, pp. 205–270.
- ⁷A. J. C. Varandas, A. Alijah, and M. Cernei, *Chem. Phys.* **308**, 285 (2005).
- ⁸L. P. Viegas, A. Alijah, and A. J. C. Varandas, *J. Chem. Phys.* **126**, 074309 (2007).
- ⁹B. R. L. Galvão, P. J. S. B. Caridade, and A. J. C. Varandas, *J. Chem. Phys.* **137**, 22A515 (2012).
- ¹⁰C. M. R. Rocha and A. J. C. Varandas, *J. Chem. Phys.* **143**, 074302 (2015).
- ¹¹A. J. C. Varandas, *Adv. Chem. Phys.* **74**, 255 (1988).
- ¹²W. Domcke, D. R. Yarkony, and H. Köppel, *Conical Intersections: Electronic Structure, Dynamics & Spectroscopy*, Advanced Series in Physical Chemistry (World Scientific Publishing, Singapore, 2004), Vol. 15.
- ¹³D. R. Yarkony, *Rev. Mod. Phys.* **68**, 985 (1996).
- ¹⁴G. J. Atchity, S. S. Xantheas, and K. Ruedenberg, *J. Chem. Phys.* **95**, 1862 (1991).
- ¹⁵D. R. Yarkony, *Acc. Chem. Res.* **31**, 511 (1998).
- ¹⁶M. S. Schuurman and D. R. Yarkony, *J. Chem. Phys.* **126**, 044104 (2007).
- ¹⁷D. R. Yarkony, *Theor. Chem. Acc.* **98**, 197 (1998).
- ¹⁸H. A. Jahn and E. Teller, *Proc. R. Soc. A* **161**, 220 (1937).
- ¹⁹H. A. Jahn, *Proc. R. Soc. A* **164**, 117 (1938).
- ²⁰A. Ceulemans, *J. Chem. Phys.* **87**, 5374 (1987).
- ²¹R. Englman, *The Jahn-Teller Effect* (John Wiley & Sons, New York, 1973).
- ²²I. B. Bersuker and V. Z. Polinger, *Vibronic Interactions in Molecules and Crystals* (Springer-Verlag, Berlin, 1989).
- ²³I. B. Bersuker, *The Jahn-Teller Effect* (Cambridge University Press, Cambridge, 2006).

- ²⁴I. B. Bersuker, Chem. Rev. **101**, 1067 (2001).
- ²⁵I. B. Bersuker, Chem. Rev. **113**, 1351 (2013).
- ²⁶A. J. C. Varandas, Chem. Phys. Lett. **487**, 139 (2010).
- ²⁷J. J. Dillon and D. R. Yarkony, J. Chem. Phys. **126**, 124113 (2007).
- ²⁸J. W. Zwanziger and E. R. Grant, J. Chem. Phys. **87**, 2954 (1987).
- ²⁹H. Köppel and R. Meiswinkel, Z. Phys. D: At., Mol. Clusters **32**, 153 (1994).
- ³⁰H. Koizumi and I. B. Bersuker, Phys. Rev. Lett. **83**, 3009 (1999).
- ³¹P. Garcia-Fernandez, I. B. Bersuker, and J. E. Boggs, J. Chem. Phys. **125**, 104102 (2006).
- ³²V. A. Mozhayskiy, D. Babikov, and A. I. Krylov, J. Chem. Phys. **124**, 224309 (2006).
- ³³R. G. Sadygov and D. R. Yarkony, J. Chem. Phys. **110**, 3639 (1999).
- ³⁴F. Cocchini, T. H. Upton, and W. Andreoni, J. Chem. Phys. **88**, 6068 (1988).
- ³⁵D. R. Yarkony, J. Chem. Phys. **111**, 4906 (1999).
- ³⁶A. K. Paul, S. Ray, D. Mukhopadhyay, and S. Adhikari, Chem. Phys. Lett. **508**, 300 (2011).
- ³⁷A. K. Paul, S. Ray, D. Mukhopadhyay, and S. Adhikari, J. Chem. Phys. **135**, 034107 (2011).
- ³⁸G. Herzberg and H. C. Longuet-Higgins, Discuss. Faraday Soc. **35**, 77 (1963).
- ³⁹H. C. Longuet-Higgins, Proc. R. Soc. A **344**, 147 (1975).
- ⁴⁰M. V. Berry, Proc. R. Soc. A **392**, 45 (1984).
- ⁴¹C. A. Mead and D. G. Truhlar, J. Chem. Phys. **70**, 2284 (1979).
- ⁴²W. Weltner and R. J. Van Zee, Chem. Rev. **89**, 1713 (1989).
- ⁴³A. Van Orden and R. J. Saykally, Chem. Rev. **98**, 2313 (1998).
- ⁴⁴N. Sakai and S. Yamamoto, Chem. Rev. **113**, 8981 (2013).
- ⁴⁵B. R. L. Galvão, V. C. Mota, and A. J. C. Varandas, J. Phys. Chem. A **119**, 1415 (2015).
- ⁴⁶P. G. Szalay, T. Müller, G. Gidofalvi, H. Lischka, and R. Shepard, Chem. Rev. **112**, 108 (2012).
- ⁴⁷T. H. Dunning, J. Chem. Phys. **90**, 1007 (1989).
- ⁴⁸R. A. Kendall, T. H. Dunning, and R. J. Harrison, J. Chem. Phys. **96**, 6796 (1992).
- ⁴⁹H. J. Werner, P. J. Knowles, G. Knizia, F. R. Manby, M. Schütz *et al.*, MOLPRO, version 2010.1, a package of *ab initio* programs, 2010, see <http://www.molpro.net>.
- ⁵⁰R. A. Whiteside, R. Krishnan, M. J. Frisch, J. A. Pople, and P. V. R. Schleyer, Chem. Phys. Lett. **80**, 547 (1981).
- ⁵¹K. Ahmed, G. G. Balint-Kurti, and C. M. Western, J. Chem. Phys. **121**, 10041 (2004).
- ⁵²H. Fueno and Y. Taniguchi, Chem. Phys. Lett. **312**, 65 (1999).
- ⁵³A. M. McAnoy, S. Dua, D. Schroder, J. H. Bowie, and H. Schwarz, J. Chem. Soc., Perkin Trans. 2 **2002**, 1647.
- ⁵⁴A. Karton and J. M. L. Martin, Theor. Chem. Acc. **115**, 330 (2006).
- ⁵⁵A. J. C. Varandas, J. Chem. Phys. **126**, 244105 (2007).
- ⁵⁶K. W. Hinkle, J. J. Keady, and P. F. Bernath, Science **241**, 1319 (1988).
- ⁵⁷S. Saha and C. M. Western, J. Chem. Phys. **125**, 224307 (2006).
- ⁵⁸A. J. C. Varandas, J. Tennyson, and J. N. Murrell, Chem. Phys. Lett. **61**, 431 (1979).
- ⁵⁹G. J. Atchity and K. Ruedenberg, J. Chem. Phys. **110**, 4208 (1999).
- ⁶⁰S. Matsika and D. R. Yarkony, J. Phys. Chem. A **106**, 2580 (2002).
- ⁶¹G. J. Atchity, K. Ruedenberg, and A. Nanayakkara, Theor. Chem. Acc. **96**, 195 (1997).
- ⁶²G. Chaban, M. S. Gordon, and D. R. Yarkony, J. Phys. Chem. A **101**, 7953 (1997).
- ⁶³D. R. Yarkony, J. Chem. Phys. **109**, 7047 (1998).
- ⁶⁴C. J. Ballhausen and A. E. Hansen, Annu. Rev. Phys. Chem. **23**, 15 (1972).
- ⁶⁵J. S. Griffith, *The Irreducible Tensor Method for Molecular Symmetry Groups* (Prentice-Hall, New Jersey, 1962).
- ⁶⁶A. Schönhage, Numer. Math. **6**, 410 (1964).
- ⁶⁷G. H. Golub and H. A. Van der Vorst, J. Comput. Appl. Math. **123**, 35 (2000).
- ⁶⁸K. Levenberg, Q. Appl. Math. **2**, 164 (1944).
- ⁶⁹D. W. Marquardt, SIAM J. Appl. Math. **11**, 431 (1963).

Cite this: DOI: 10.1039/xxxxxxxxxx

Multiple conical intersections in small linear parameter Jahn-Teller systems: the DMBE potential energy surface of ground-state C_3 revisited[†]

C. M. R. Rocha and A. J. C. Varandas^{*a}Received Date
Accepted Date

DOI: 10.1039/xxxxxxxxxx

www.rsc.org/journalname

A new single-sheeted DMBE potential energy surface for ground-state C_3 is reported. The novel analytical form describes accurately the three symmetry-equivalent C_{2v} disjoint seams, in addition to the symmetry-required D_{3h} one, over the entire configuration space. The present formalism warrants by built-in construction the confluence of the above crossings, and the rotation-in-plane of the C_{2v} seams when the perimeter of the molecule fluctuates. Up to 1050 *ab initio* energies have been employed in the calibration procedure, of which 421 map the loci of intersection. The calculated energies have been scaled to account for incompleteness of the basis set and truncation of the MRCI expansion, and fitted analytically with chemical accuracy. The novel form is shown to mimic accurately the region defined by the 4 conical intersections, while exhibiting similar attributes to the one previously reported [*J. Chem. Phys.* 2015, **143**, 074302] at regions of configuration space away from the crossing seams. Despite being mainly addressed to C_3 , the present approach should be applicable to adiabatic PESs of any X_3 system experiencing similar topological attributes, in particular the small-linear-parameter Jahn-Teller molecules.

1 Introduction

Conical intersections (Cis) form hyperlines in nuclear configuration space where two (or more) adiabatic potential energy surfaces (PESs) are degenerate.¹ Such hyperlines are referred to as seams (or locus) of Cis. Their orthogonal complements define the so-called branching² or (*g*,*h*)-plane³ at which degeneracies are linearly lifted in displacements from the intersection, assuming a local topology of a double cone.⁴ Conventionally, degeneracies on PESs are classified as normal (or symmetry-required), when they are naturally dictated by the molecular point group [as in the Jahn-Teller (JT) case^{5–9}] and accidental.^{1,3,10} These include both symmetry-allowed Cis (if the symmetries of the involved states carry distinct one-dimensional irreducible representations) and degeneracies involving two states of the same symmetry, which can only occur when two independent conditions are satisfied.^{11–14} Although often considered a theoretical curiosity, the conditions for electronic degeneracies have long been recognized by von Neumann and Wigner¹¹, with Teller¹² emphasizing 80 years ago their role in fast radiationless transitions. Rather than the “non-crossing rule”,^{11–14} Herzberg and Longuet-Higgins¹³ and Longuet-Higgins¹⁴ have shown that intersections

of PESs are possible in systems with the same spin and spatial symmetries as long as they involve 2 or more configurational degrees of freedom. When dictated by symmetry, Jahn and Teller⁵ demonstrated that the very nature of Cis relies on the molecular point groups, thus occurring whenever two electronic states (at highly symmetric non-linear arrangements) transform as twofold degenerate irreducible representations.⁵ Cis lie also at the heart of nonadiabatic processes,^{1,10} and related phenomena associated with the so-called geometric phase (GP) effect.^{13–16}

Regardless the nature of the Cis, they make the task of modeling an accurate global PES increasingly cumbersome. This is so, since standard analytic functions are inappropriate to describe the characteristic cusp behavior of the involved electronic states in the vicinity of the degeneracy seam.^{17,18} Given the divergent nature of the nonadiabatic couplings terms (NACTs) and the pronounced electronic interstate couplings [the breakdown of the Born-Oppenheimer (BO) approximation^{19,20}] at the locus of intersection and immediacies,¹ one could then resort to appropriate diabatization schemes.^{21–30} By employing an adiabatic-to-diabatic (ATD) unitary transformation so that the leading terms of the NACTs are partially removed, the diagonal adiabatic PESs (strictly speaking, *ab initio* energies) are replaced by a potential matrix whose elements are smooth functions of the nuclear coordinates.^{22,27–30} Such diabatic states, once properly obtained and conveniently modeled by some smooth functional form, can be back transformed to adiabatic ones, yielding therefore the ex-

^a Departamento de Química, and Centro de Química, Universidade de Coimbra 3004-535 Coimbra, Portugal. E-mail: varandas@uc.pt

[†] Electronic Supplementary Information (ESI) available. See DOI: 10.1039/b000000x/

pected cusp behavior in the vicinity of the crossing seams. Despite its advantages, the resolution in terms of diabatic basis is nontrivial and, together with the need for a proper modeling of the potential matrix, turns the process of obtaining accurate global PESs increasingly complex.^{17,18} Actually, for molecules other than diatomics, strictly diabatic basis which exactly diagonalize the nuclear kinetic energy operators do not exist²¹ and hence, any attempt to minimize NACTs often leads to arbitrariness in the construction of the (quasi)-diabatic states.^{21,23–26}

Another possibility to describe a cusp on adiabatic PESs has been proposed by Varandas and Murrell.³¹ The authors employed the so-called JT-type coordinate^{31,32} ($\sqrt{\Gamma_2}$) together with suitable additional polynomial terms such as to introduce the required nonanalyticity into the adiabatic PESs of $H_3(1^2A')$ which shows the symmetry-required Ci for D_{3h} arrangements.^{31,33} Indeed, $\sqrt{\Gamma_2}$ has been especially designed to model adiabatic PESs of X_3 -type JT molecules in which a doubly degenerate pair of electronic states (E) are coupled by a doubly degenerate normal mode (e) [the well-studied linear $E \otimes e$ JT systems^{2–4,6–9}]. As such, the approach has been successfully applied to model accurate global PESs for^{34–36} $H_3^+(1^3A'/2^3A')$ and³⁷ $N_3(1^2A''/2^2A'')$ molecules without the need of any ATD transformation. As stated in Ref. 17, the JT coordinate is simply the distance from a given point in the branching plane³ to the corresponding origin (the D_{3h} crossing seam) and hence ensures, by built-in construction, the correct linear dependence of the potential (the conical shape) along non-totally symmetric distortions.^{31,32,34–37}

Recently, Galvão, Mota and Varandas (GMV)^{17,18} extended the above methodology to include cusps on adiabatic single-sheeted PESs of any triatomic system exhibiting accidental Cis.¹⁷ Such an approach relies on finding the appropriate parametric equation which characterizes the locus of intersection and, from simple geometric considerations, define the distance from any point in \mathbf{R} -space to the seam.^{17,18} The GMV scheme has been employed to accurately model the C_{2v} degeneracy line (${}^2A_2/{}^2B_1$) of^{38,39} $NO_2(1^2A'')$ as well as the three permutationally equivalent seams of³⁰ $N_3(1^2A')$. Further progress on the methodology has recently been reported.¹⁸ The authors suggested the use of a generalized JT-type coordinate (Δ) to mimic the desired singularities on PESs of any triatomic system, including molecules having strongly curved (accidental) seams, as is the case of^{18,27,40} $HN_2(1^2A')$; the reader is addressed to Refs 17 and 18 for details.

For general X_3 -type JT molecules, it is widely known that the introduction of quadratic terms in the vibronic coupling perturbation operator (the linear plus quadratic $E \otimes e$ problem^{6–9}) reveals the so-called warping of the Mexican-hat-type PESs with the formation of three-equivalent minima connected by three pseudo-rotation saddle points along the bottom of the “tricorn”.^{7–9} Yet, for molecules with small linear (F_E) and large quadratic (G_E) vibronic coupling constants, the locus of Ci and hence, the topology of the PESs near equilateral triangular arrangements is rather intricate.^{41,42} For such systems, referred to as small linear parameter (SLP) JT molecules,^{6,41–43} besides the usual symmetry-required D_{3h} seam, three additional symmetry-allowed Cis along the line of C_{2v} symmetry are found in quite close proximity to the D_{3h} one. Such unusual topological fea-

tures have been reported in literature for elemental clusters such as $Li_3(2^2E')$,⁴⁴ $Na_3(2^2E')$,^{43,45,46} $K_3(2^2E')$,⁴⁷ $Si_3(1^1E')$,⁴⁸ $N_3^+(1^1E'')$,⁴⁹ and $C_3(1^1E')$.^{50,51} Suffice it to add that, in addition to the proper JT effect,^{5–9} the presence of close-in-energy A states near D_{3h} conformations are ubiquitous,^{44–51} so the overall problem at hand is effectively a three state one, *i.e.*, a combined JT plus pseudo-JT (PJT) case.^{48,50,51}

In previous work,⁵⁰ we have reported a single-sheeted DMBE PES (hereinafter referred to as DMBE I) for ground-state $C_3(1^1A')$. There, we first outlined the presence of the 4 Cis characteristic of SLP JT systems. Because a third electronic state of $1^1A'$ symmetry ($1^1A'_1$ in D_{3h}) comes close in energy to the pair of intersecting states ($1^1E'$ in D_{3h}) near equilateral triangular arrangements,⁵¹ such unusual topological attributes have been ascribed to combined JT plus PJT vibronic effects.⁵⁰ Modeling of the D_{3h} and C_{2v} seams has then been accomplished by employing the JT coordinate and the GMV approach, respectively, along with suitable additional polynomial terms.⁵⁰ Since the term responsible for introducing the required singularities at C_{2v} degeneracies dies-off Gaussian-like,¹⁷ the cusps are warranted only near the region defined by the minimum energy crossing point (MeX).⁵⁰

Most recently, the combined JT plus PJT [$(E' + A'_1) \otimes e'$] problem in C_3 has been further exploited⁵¹ with somewhat unexpected results. Accordingly, the three additional symmetry-allowed C_{2v} seams are not static objects with respect to the symmetry-required (D_{3h}) one but evolve in location with varying perimeter of the molecule. In so doing, such degeneracy points approach the central D_{3h} Ci almost linearly and ultimately coalesce with it forming an intersection node⁵² or confluence.^{53,54} Additionally, by increasing the size of the molecular triangle, the C_{2v} disjoint seams get rotated by $\pm\pi$ in the branching plane.⁵¹ We have also proposed a three-state vibronic Hamiltonian that, once diagonalized, naturally mimics the 4 singularity points near the MeX of D_{3h} and C_{2v} symmetries as well as highlighted the implications of such multiple Cis on the net GP effect.

Our aim in this work is to devise a form (DMBE II) capable of accurately modeling the three symmetry-equivalent C_{2v} disjoint seams, in addition to the seam of D_{3h} symmetry, over the entire range of nuclear configuration space. Special attention is paid in developing a form that warrants by built-in construction the confluence of the above crossings and the rotation in the branching plane of the C_{2v} seams as the perimeter of the molecule fluctuates. The approach, which follows the original formalism should in principle be applicable to other cusps of any X_3 -type SLP JT system without the need of diabatization.

The paper is organized as follows. Section 2 summarizes the *ab initio* calculations. The strategy and analytical forms used in DMBE I PES are briefly reviewed in section 3. In section 4, we devise an alternative scheme capable of accurately mimicking the symmetry-related C_{2v} seams over the entire configuration space, while in section 5 the approach is used to get the DMBE II form. The major topological features of the current PES are discussed in section 6 whereas section 7 gathers the conclusions.

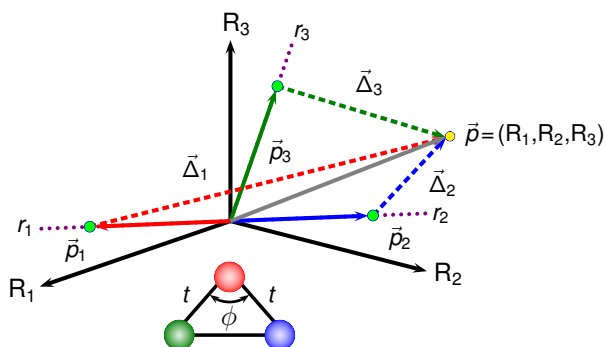


Fig. 1 Permutationally equivalent C_{2v} crossing seams for a fixed valence angle ϕ . The seams are shown in dotted, with the distances from any point in \mathbf{R} -space (\vec{p} vector) to the corresponding crossings points (\vec{p}_1 , \vec{p}_2 and \vec{p}_3 vectors) indicated by the $\vec{\Delta}_1$, $\vec{\Delta}_2$ and $\vec{\Delta}_3$ vectors. The dummy variable t defines the associated parametric lines r_1 , r_2 and r_3 (see text).

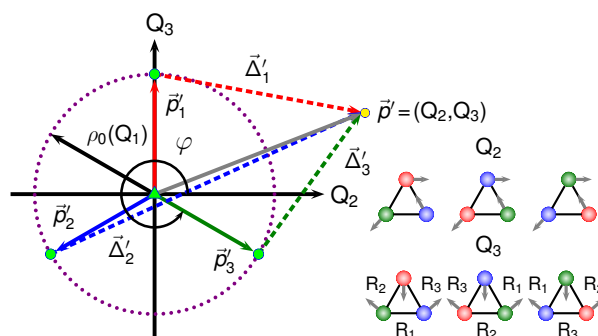


Fig. 2 Symmetry-equivalent C_{2v} crossing seams lying at $\phi = \pi/2$, $7\pi/6$ and $11\pi/6$ on a circle of radius $\rho_0(Q_1)$ in the (Q_2, Q_3) branching plane. Also shown at the origin, $(0, 0)$, is the D_{3h} symmetry-required seam. The distances from any point in \mathbf{Q} -space (\vec{p}' vector) to the corresponding C_{2v} crossings points (\vec{p}'_1 , \vec{p}'_2 and \vec{p}'_3 vectors) are indicated by the $\vec{\Delta}'_1$, $\vec{\Delta}'_2$ and $\vec{\Delta}'_3$ vectors.

2 Ab initio calculations

All calculations have been performed at the multireference configuration interaction (MRCI) level using the full-valence complete active space self-consistent field [CASSCF(12,12) or FVCAS] wave functions as reference.⁵⁵ The triple- ζ augmented correlation consistent basis set of Dunning^{56,57} (aug-cc-pVTZ or AVTZ) has been employed, and the calculations done with MOLPRO.⁵⁸ To account for the incompleteness of the one- and \mathcal{N} -electron bases, all raw *ab initio* energies have been scaled using the double many-body expansion-scaled external correlation (DMBE-SEC)⁵⁹ method, a methodology also utilized in Ref. 50. All computations have been performed by considering cuts of the PES along symmetry-adapted coordinates [$\mathbf{Q} = (Q_1, Q_2, Q_3)$] defined by^{22,60}

$$\begin{pmatrix} Q_1 \\ Q_2 \\ Q_3 \end{pmatrix} = \begin{pmatrix} \sqrt{1/3} & \sqrt{1/3} & \sqrt{1/3} \\ 0 & \sqrt{1/2} & -\sqrt{1/2} \\ \sqrt{2/3} & -\sqrt{1/6} & -\sqrt{1/6} \end{pmatrix} \begin{pmatrix} R_1 \\ R_2 \\ R_3 \end{pmatrix}, \quad (1)$$

where Q_1 is related to the perimeter of the triatomic, and the pair (Q_2, Q_3) defines the shape of the molecular triangle; $\mathbf{R} = (R_1, R_2, R_3)$ are internuclear distances.⁵¹

To obtain a realistic PES in which both D_{3h} and C_{2v} seams are accurately modeled, a total of 421 grid points have been chosen to map the region defined by $4.000a_0 \leq Q_1 \leq 5.750a_0$ and $-0.040a_0 \leq Q_i (i=2, 3) \leq 0.040a_0$. An extra 629 *ab initio* energies⁵⁰ have been considered, which amounts to a total of 1050 points used for the calibration process.

3 The DMBE I potential energy surface: a brief survey

The adiabatic ground-state PES reported elsewhere⁵⁰ for the $C_3(1^1A')$ radical assumes the following form:

$$V_1(\mathbf{R}) = V^{(1)} + V^{(2)}(\mathbf{R}) + V_{\text{dc}}^{(3)}(\mathbf{R}) + V_{\text{L,EHF}}^{(3)}(\mathbf{R}), \quad (2)$$

where as usual^{60–63} $V^{(1)}$ is a one-body term equal to the dissociation energy (D_e) of $C_2(a^3\Pi_u)$, $V^{(2)}(\mathbf{R})$ is the sum of the two-body

potentials, and $V_{\text{dc}}^{(3)}(\mathbf{R})$ is the three-body dynamical correlation; see Ref. 50 and Electronic Supplementary Information (ESI). To ensure the proper cusp behavior,^{17,18} the three-body extended Hartree-Fock (EHF) energy, $V_{\text{L,EHF}}^{(3)}(\mathbf{R})$, is expressed as a sum of two terms⁵⁰

$$V_{\text{L,EHF}}^{(3)}(\mathbf{R}) = V'_{\text{L,EHF}}(\mathbf{R}) + V''_{\text{L,EHF}}(\mathbf{R}), \quad (3)$$

where

$$V'_{\text{L,EHF}}(\mathbf{R}) = \left[P_1^{N'}(\Gamma_1, \Gamma_2, \Gamma_3) - \sqrt{\Gamma_2} P_2^{M'}(\Gamma_1, \Gamma_2, \Gamma_3) \right] T_1'(\mathbf{R}), \quad (4)$$

and

$$V''_{\text{L,EHF}}(\mathbf{R}) = \left[P_3^{N''}(\Gamma_1, \Gamma_2, \Gamma_3) - \Delta_1 \Delta_2 \Delta_3 P_4^{M''}(\Gamma_1, \Gamma_2, \Gamma_3) \right] T_1''(\mathbf{R}). \quad (5)$$

In Eqs. (4) and (5), $P_n^J(\Gamma_1, \Gamma_2, \Gamma_3)$ [$n = 1, \dots, 4$ and $J = N', M', N'', M''$] are polynomials of order J expressed as

$$P_n^J(\Gamma_1, \Gamma_2, \Gamma_3) = \sum_{i+2j+3k \leq J} c_{ijk}^n \Gamma_1^i \Gamma_2^j \Gamma_3^k, \quad (6)$$

where $\Gamma_1 = Q_1$, $\Gamma_2 = Q_2^2 + Q_3^2$, and $\Gamma_3 = Q_3(Q_3^2 - 3Q_2^2)$ define the integrity basis.⁶⁴ In turn, $T_1'(\mathbf{R})$ and $T_1''(\mathbf{R})$ are range-decaying factors.⁵⁰ As noted elsewhere,^{17,31,32,50} the polynomial in Eq. (4) warrants that the DMBE form behaves as a linear function of the radial polar coordinate⁴ $\rho(Q_1) \equiv \sqrt{\Gamma_2} = \sqrt{Q_2^2 + Q_3^2}$ in the two dimensional branching plane [here denoted for a given value of Q_1 as $\mathbf{Q}_b(Q_1) = (Q_2, Q_3)$]. In turn, following Ref. 17, the polynomials in Eq. (5) provide the expected cusp behavior at C_{2v} degeneracies which, in Ref. 50, have been first modeled for a fixed valence angle of $\phi = 60.2128^\circ$. Thus, in Eq. (5), Δ_c ($c = 1, 2, 3$) are the distances (or the corresponding norms $|\vec{\Delta}_c|$ in Figure 1) from any point in \mathbf{R} -space [say, $\vec{p} = (R_1, R_2, R_3)$] to the three permutation-

ally equivalent C_{2v} crossing seams

$$\|\vec{\Delta}_1\| = \sqrt{[R_1 - t_0 \sqrt{2(1 - \cos \phi)}]^2 + (R_2 - t_0)^2 + (R_3 - t_0)^2} \quad (7)$$

$$\|\vec{\Delta}_2\| = \sqrt{(R_1 - t_0)^2 + [R_2 - t_0 \sqrt{2(1 - \cos \phi)}]^2 + (R_3 - t_0)^2} \quad (8)$$

$$\|\vec{\Delta}_3\| = \sqrt{(R_1 - t_0)^2 + (R_2 - t_0)^2 + [R_3 - t_0 \sqrt{2(1 - \cos \phi)}]^2}, \quad (9)$$

where t_0 is the reference distance in $\vec{p}_1 = (t_0 \sqrt{2(1 - \cos \phi)}, t_0, t_0)$, $\vec{p}_2 = (t_0, t_0 \sqrt{2(1 - \cos \phi)}, t_0)$, and $\vec{p}_3 = (t_0, t_0, t_0 \sqrt{2(1 - \cos \phi)})$ along the parametric lines $r_1 = (t \sqrt{2(1 - \cos \phi)}, t, t)$, $r_2 = (t, t \sqrt{2(1 - \cos \phi)}, t)$, and $r_3 = (t, t, t \sqrt{2(1 - \cos \phi)})$; Figure 1. Suffice to say that t_0 is obtained from the requirement that $\vec{\Delta}_c$ is orthogonal to the seam, which is equivalent to solve $\vec{\Delta}_c \cdot \vec{p}_c = 0$ for t_0 . This yields

$$t_0 = \frac{R_1 \sqrt{2(1 - \cos \phi)} + R_2 + R_3}{4 - 2 \cos \phi}, \quad (10)$$

for $\vec{\Delta}_1 \cdot \vec{p}_1 = 0$, and

$$t_0 = \frac{R_1 + R_2 \sqrt{2(1 - \cos \phi)} + R_3}{4 - 2 \cos \phi} \quad (11)$$

$$t_0 = \frac{R_1 + R_2 + R_3 \sqrt{2(1 - \cos \phi)}}{4 - 2 \cos \phi}, \quad (12)$$

for $\vec{\Delta}_2 \cdot \vec{p}_2 = 0$ and $\vec{\Delta}_3 \cdot \vec{p}_3 = 0$, respectively; see elsewhere^{17,18} for details. Note that the parameters of Eqs. (4) and (5) have been obtained⁵⁰ from a fit to 629 scaled *ab initio* energies with a total unweighted root mean square deviation (rmsd) of 4.14 kJ mol⁻¹. It should be recalled that, unlike $V_{1,EHF}^{(3)}(\mathbf{R})$, $V_{1,EHF}^{(3)}(\mathbf{R})$ in Eq. (5) dies-off Gaussian-like, and therefore is expected to be valid in a limited portion of configuration space, namely at the region defined by the minima of the C_{2v} crossings.^{17,50}

4 Modeling the C_{2v} disjoint seams

Consider the 2D branching plane $\mathbf{Q}_b(Q_1) = (Q_2, Q_3)$ in Figure 2 defined by the coordinates Q_2 and Q_3 , for a fixed Q_1 . Clearly, $\forall Q_1$, $\mathbf{Q}_b(Q_1) = (0, 0)$ defines equilateral triangular arrangements where the ground ($1^1A'$) and first excited ($2^1A'$) PESs of C_3 show a symmetry-dictated Ci.^{50,51} The C_{2v} crossings points are then defined by

$$\vec{p}_c' \equiv (Q_2^c, Q_3^c) = (\rho_0 \cos(\varphi_c \pm n\pi), \rho_0 \sin(\varphi_c \pm n\pi)), \quad (13)$$

where the parametric dependences of $Q_2^c(Q_1)$, $Q_3^c(Q_1)$ and $\rho_0(Q_1)$ on Q_1 is eliminated thereof for convenience of notation. In turn, $\rho_0 = [(Q_2^c)^2 + (Q_3^c)^2]^{1/2}$ denotes the radius at which the three symmetry-equivalent disjoint seams are located with respect to the central Ci⁵¹ and φ_c ($c = 1, 2, 3$) is the polar angle^{4,60,65} that explicitly defines the positions of the crossings; $\varphi_1 = \pi/2$, $\varphi_2 = 7\pi/6$ and $\varphi_3 = 11\pi/6$. In Eq. (13), $n = 0$ or 1 is an integer that accounts for the proper rotation-in-plane of the C_{2v} seams on passing through the confluence point.⁵¹ Thus, the distance from any point $\vec{p}' = (Q_2, Q_3)$ in \mathbf{Q} -space to the three permutationally equiv-

alent C_{2v} crossing points (see Figure 2) is defined by^{17,18}

$$\vec{\Delta}_c' = \vec{p}' - \vec{p}_c' = (Q_2 - Q_2^c, Q_3 - Q_3^c) \quad (14)$$

and hence

$$\|\vec{\Delta}_c'\| = \sqrt{(Q_2 - Q_2^c)^2 + (Q_3 - Q_3^c)^2}. \quad (15)$$

Thus, the only requirement to determine the norm $\|\vec{\Delta}_c'\|$, thence the cusp behavior of the adiabatic PESs, is to find the appropriate equation of the seam that relates the positions of the disjoint crossing points [Q_2^c , Q_3^c or ρ_0 ; see Eq. (13)] and the size of the molecular triangle. In principle, such a requirement can be fulfilled by any type of well-behaved function of Q_1 . To accomplish this, we have performed *ab initio* calculations along $\mathbf{Q}_b(Q_1) = (0, Q_3)$ for different values of Q_1 ($4.000 a_0 \leq Q_1 \leq 5.750 a_0$). This allows to determine the C_{2v} points of degeneracy between the $1^1A'$ and $2^1A'$ states along the line $(Q_2^c, Q_3^c) \equiv (0, Q_3^c)$; see Figure 2. Various perspectives of the current results are illustrated in Figure 3.

As shown in Figure 3(a), the Cis at C_{2v} symmetry occur not only for fixed valence angles of⁵⁰ $\phi = 60.2128^\circ$, but also for angles varying between 59.7447° ($R = 3.324 a_0$) and 60.9511° ($R = 2.298 a_0$). The crossing geometries lie therefore in close proximity to the D_{3h} Ci ($\phi = 60.0^\circ$), with the valence angles deviating by less than 1.0° . Actually, as depicted in Figure 3, such geometries ultimately coalesce with an equilateral triangular one at $R \approx 2.890 a_0$ or $Q_1 \approx 5.005 a_0$ (see Figure 3) forming an intersection node or confluence of seams. In fact, following recent work¹⁷ for $\text{NO}_2(1A'')$, the equation of the seam could be well modeled in \mathbf{R} -space by a straight line [Figure 3(b)] of the form $R_1 = f(R) = a + bR$ where $R_2 = R_3 = R$, $a = 0.134 a_0$ and $b = 0.954$; see elsewhere¹⁸ for generalizations employing non-linear functions. As shown, the errors in R_1 amount to $\approx 10^{-3} a_0$. However, preliminary tests indicated that even such small deviations prevent an accurate fit of the proper C_{2v} cusp location in \mathbf{Q} -space, especially for geometries with stretched bond distances where the deviations from the simple straight line would be of the same order of magnitude as the difference between the geometries themselves [see inset of Figure 3(b)]. Thus, we have chosen an analytic form in ρ_0 that accurately mimics all C_{2v} crossing seams. This has been accomplished through a 1D fit of the various $(0, Q_3^c)$ crossing points obtained for each Q_1 , with ρ_0 extracted from the relation:

$$\rho_0 = |Q_3^c|. \quad (16)$$

As Figure 3(c) shows, Q_3^c can be accurately modeled by the form

$$Q_3^c = \rho - \delta \tanh \left[\sum_{i=1}^5 \zeta_i (Q_1 - Q_1^0)^i \right], \quad (17)$$

which contains 8 adjustable parameters. Note that the linear fit in panel (b) deviates quite significantly from the points in panel (c) when plotted onto the same scale (not shown for simplicity).

In fact, as seen in the inset of Figure 3(c), the errors in the crossing geometries predicted by Eq. (17) amount to $\approx 10^{-5} a_0$ at most. Clearly, the advantage of such a procedure, *i.e.*, fit first Q_3^c and subsequently extract the associated radii from Eq. (16),

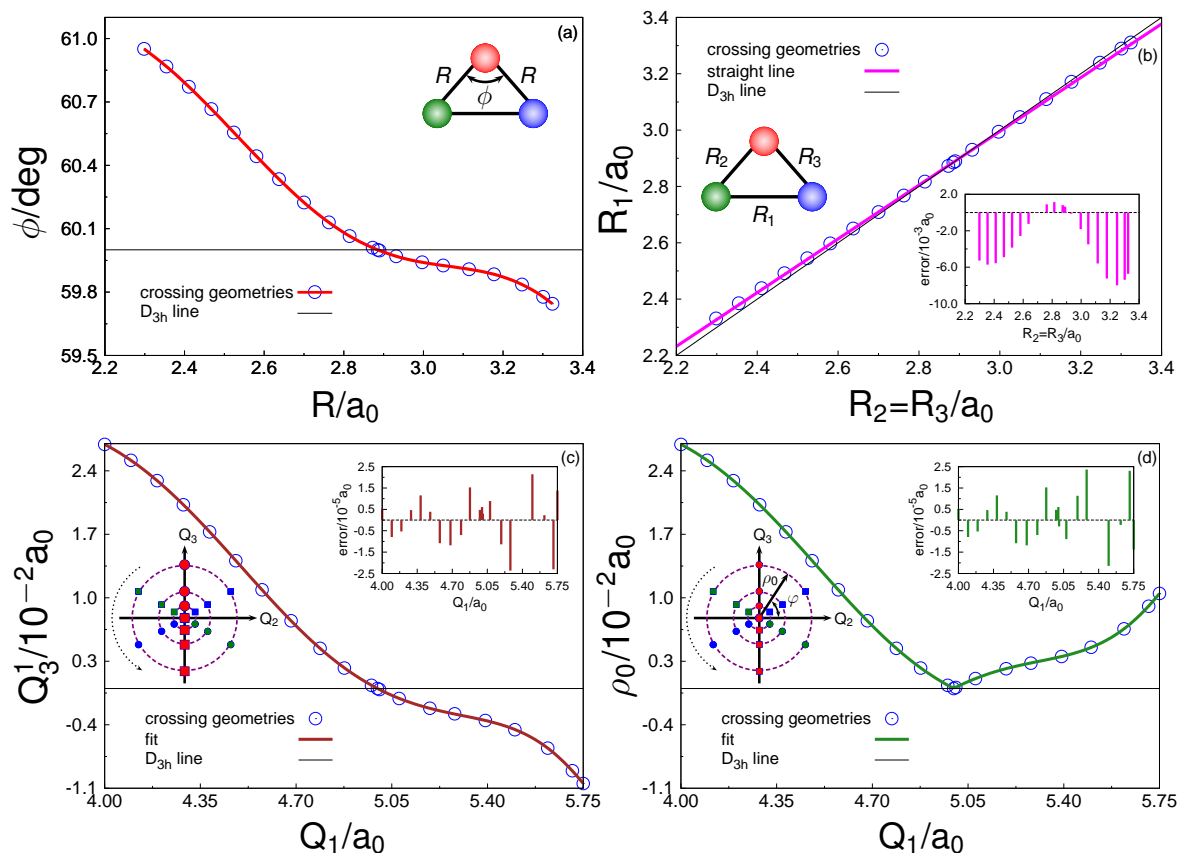


Fig. 3 Location of the C_{2v} crossing seam $(Q_2^1, Q_3^1) \equiv (0, Q_3^1)$ for distinct values of Q_1 . The seam is shown in different perspectives and coordinate systems: (a) in valence coordinates R and ϕ ; (b) in triangular coordinates R_1 , R_2 and R_3 ; (c) Q_3^1 with respect to Q_1 [Eq. (17)]; (d) ρ_0 with respect to Q_1 [Eq. (16)].

may circumvent problems with the analytic representation of the “cusp-like” behavior of ρ_0 near the intersection node, as seen from Figure 3(d). Note that this latter is predicted from the analytical form (17) to be located at $Q_1 = 4.997a_0$. The numerical coefficients of Eq. (17) are given as ESI.

Once the value of ρ_0 is known, the distances to the three equivalent C_{2v} crossing seams $\Delta_1' \equiv \|\vec{\Delta}_1'\|$, $\Delta_2' \equiv \|\vec{\Delta}_2'\|$ and $\Delta_3' \equiv \|\vec{\Delta}_3'\|$ can then be determined from Eqs. (13)–(15). Note that, unlike Refs. 17 and 18, no orthogonality relations between $\vec{\Delta}_c'$ and \vec{p}_c' , i.e., $\vec{\Delta}_c' \cdot \vec{p}_c' = 0$, are here needed inasmuch as \vec{p}_c' is uniquely defined in the (Q_2, Q_3) plane and so will be $\|\vec{\Delta}_c'\|$.

In Refs. 50 and 17, the desired cusp behavior on the adiabatic PESs has been accomplished by using the product of such distances [see Eq. (5)] such as to ensure the permutational nature of the crossings. Clearly, as Figure 4(a) shows, $-\Delta_1'\Delta_2'\Delta_3'$ behaves nonlinearly as one moves away from the intersection point. So, we define instead a set of symmetrized combinations of Δ_1' , Δ_2' and Δ_3' ,

$$\begin{pmatrix} S_1 \\ S_2 \\ S_3 \end{pmatrix} = \begin{pmatrix} \sqrt{1/3} & \sqrt{1/3} & \sqrt{1/3} \\ 0 & \sqrt{1/2} & -\sqrt{1/2} \\ \sqrt{2/3} & -\sqrt{1/6} & -\sqrt{1/6} \end{pmatrix} \begin{pmatrix} \Delta_1' \\ \Delta_2' \\ \Delta_3' \end{pmatrix}, \quad (18)$$

This journal is © The Royal Society of Chemistry 2017

and also

$$\Delta = \sqrt{S_2^2 + S_3^2}. \quad (19)$$

It is seen from Figure 4 that Δ causes the desired cusps at C_{2v} geometries. Suffice it to say that Eq. (19) is analogous to the JT coordinate ($\sqrt{\Gamma_2}$) yielding the proper linear dependence of the potential energy along non-totally symmetric distortions. Note that Δ has built-in the permutational equivalency of the seams, thus allowing to create cusps on adiabatic PESs of any X_3 -type system; see Figure 5. This approach is here utilized to develop a novel DMBE form for $C_3(1^1A')$, thus ensuring the correct topological description of the 4 conical intersections. The details of the new analytical form here employed is discussed next.

5 The DMBE II potential energy surface

All terms in the novel PES have the same functional form as previously used,⁵⁰ with the exception of the three-body EHF term. Such a potential is then written as

$$V_{II}(\mathbf{R}) = V^{(1)} + V^{(2)}(\mathbf{R}) + V_{dc}^{(3)}(\mathbf{R}) + V_{II,EHF}^{(3)}(\mathbf{R}), \quad (20)$$

where $V^{(1)}$, $V^{(2)}(\mathbf{R})$, and $V_{dc}^{(3)}(\mathbf{R})$ assume the same meaning as in Eq. (2); the details of the corresponding analytical forms are in

Phys. Chem. Chem. Phys. 1–13 | 5

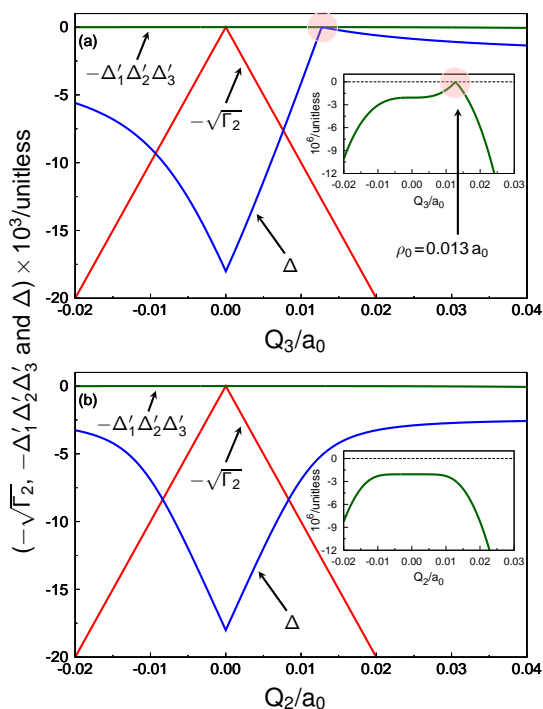


Fig. 4 Behavior of $-\sqrt{\Gamma_2}$, $-\Delta'_1\Delta'_2\Delta'_3$ and Δ along: (a) the bending [$\mathbf{Q}, (Q_1) = (0, Q_3)$]; (b) asymmetric stretch [$\mathbf{Q}, (Q_1) = (Q_2, 0)$] normal modes for $Q_1 = 4.520a_0$. The curve related to the Δ function is shifted by $-\sqrt{2}\rho_0$. Shaded red circles highlight the cusps at C_{2v} symmetry.

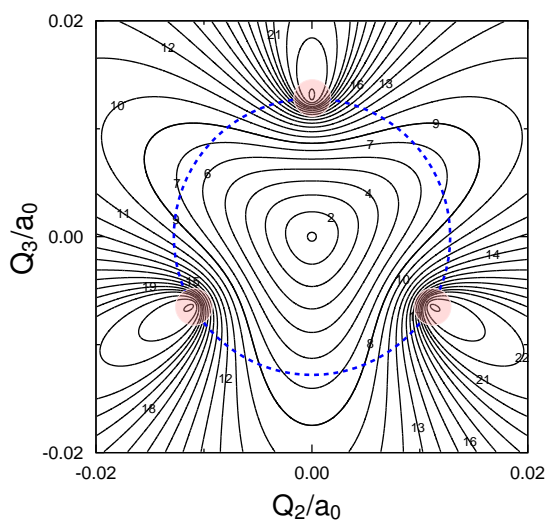


Fig. 5 Contour plot of Δ [Eq. (19)] for $Q_1 = 4.520a_0$. As in Figure 4, Δ is shifted by $-\sqrt{2}\rho_0$. Contours are equally spaced by 3.00×10^{-4} starting at -203.34×10^{-4} . Shaded red circles highlight the three C_{2v} symmetry-equivalent cusps.

Table 1 Stratified rmsd, in kJ mol^{-1} , of the DMBE I and DMBE II PESs.

Energy ^c	DMBE I ^a		DMBE II ^b	
	N^d	rmsd	N^d	rmsd
42	105	0.67	105	0.66
84	168	0.79	168	0.82
126	250	0.88	250	0.84
167	310	1.00	518	0.62
209	327	1.21	596	0.89
251	338	1.46	651	0.87
293	347	1.67	680	0.89
335	366	2.34	747	1.53
377	367	2.51	748	1.85
418	372	2.72	773	2.03
628	396	2.85	817	2.26
837	484	2.93	905	2.66
1255	572	3.56	993	3.14
1674	623	3.81	1044	3.70
2092	626	3.97	1047	3.90
2510	629	4.14	1050	4.07

^aRef. 50. ^bThis work. ^cThe units of energy are kJ mol^{-1} . Energy strata defined relative to the $C_3(^1\Sigma_g^+)$ global minimum. ^dNumber of calculated points up to indicated energy range.

Ref. 50. In turn, the new three-body EHF component, $V_{\text{II,EHF}}^{(3)}(\mathbf{R})$, assumes the form

$$V_{\text{II,EHF}}^{(3)}(\mathbf{R}) = V'_{\text{II,EHF}}(\mathbf{R}) + V''_{\text{II,EHF}}(\mathbf{R}) + V'''_{\text{II,EHF}}(\mathbf{R}). \quad (21)$$

Note that, similarly to Eq. (3), $V'_{\text{II,EHF}}(\mathbf{R})$ is the component which adequately describes the symmetry-imposed Ci at D_{3h} symmetry, while the additional terms $V''_{\text{II,EHF}}(\mathbf{R})$ and $V'''_{\text{II,EHF}}(\mathbf{R})$ warrant the correct cusp behavior at C_{2v} degeneracies over the whole configuration space. They are given by

$$V'_{\text{II,EHF}}(\mathbf{R}) = \left[P_1^{N'}(\Gamma_1, \Gamma_2, \Gamma_3) - \mathcal{F}_{nJT}(\mathbf{R}) \sqrt{\Gamma_2} P_2^M(\Gamma_1, \Gamma_2, \Gamma_3) \right] T_{\text{II}}'(\mathbf{R}), \quad (22)$$

$$V''_{\text{II,EHF}}(\mathbf{R}) = \left[P_3^{N''}(\Gamma_1, \Gamma_2, \Gamma_3) - \mathcal{F}_{nJT}(\mathbf{R}) \sqrt{\Gamma_2} P_4^{M''}(\Gamma_1, \Gamma_2, \Gamma_3) \right. \\ \left. - \Delta P_5^{P''}(\Gamma_1, \Gamma_2, \Gamma_3) \right] T_{\text{II}}''(\mathbf{R}), \quad (23)$$

and

$$V'''_{\text{II,EHF}}(\mathbf{R}) = \left[P_6^{N'''}(\Gamma_1, \Gamma_2, \Gamma_3) - \mathcal{F}_{nJT}(\mathbf{R}) \sqrt{\Gamma_2} P_7^{M'''}(\Gamma_1, \Gamma_2, \Gamma_3) \right. \\ \left. - \Delta P_8^{P'''}(\Gamma_1, \Gamma_2, \Gamma_3) \right] T_{\text{II}}'''(\mathbf{R}). \quad (24)$$

In Eqs. (22)-(24), $P_n^j(\Gamma_1, \Gamma_2, \Gamma_3)$ are polynomials that assume the same form as in Eq. (6) and are suitably centered at D_{3h} geometries with bond lengths of R'_0 , R''_0 and R'''_0 , respectively. $T_{\text{II}}'(\mathbf{R})$, $T_{\text{II}}''(\mathbf{R})$ and $T_{\text{II}}'''(\mathbf{R})$ are range-determining factors defined by

$$T_{\text{II}}^j(\mathbf{R}) = \prod_{i=1}^3 \{1 - \tanh[\alpha'(R_i - R'_0)]\}, \quad (25)$$

Table 2 Properties of stationary points and other relevant structures on the $C_3(1^1A')$ DMBE PESs.

	Method	R_1/a_0	R_2/a_0	R_3/a_0	$\Delta E/\text{kJ mol}^{-1}$	w_1/cm^{-1}	w_2/cm^{-1}	w_3/cm^{-1}
Min	DMBE II ^a	4.888	2.444	2.444	0 ^b	1203.9	61.0	2125.5
	DMBE I ^c	4.888	2.444	2.444	0	1204.2	63.5	2126.5
	Expt.	4.902	2.451	2.451 ^d	...	1224.49 ^e	63.42 ^e	2040.02 ^e
		4.890	2.445	2.445 ^f	...			
TS _{iso}	DMBE II	2.401	2.771	2.771	89.46	1295.2	1840.5	1047.3i
	DMBE I	2.399	2.768	2.768	89.58	1257.2	1873.3	1039.3i
SP ₂	DMBE II	2.478	5.511	5.511	795.35	1345.3	459.5i	546.5i
	DMBE I	2.477	5.509	5.509	795.04	1354.4	453.3i	542.7i
TS _{vdw}	DMBE II	2.470	7.249	7.249	755.80	1618.1	160.1	129.7i
	DMBE I	2.470	7.247	7.247	756.09	1613.1	160.0	136.7i
D_{3h}^{cusp}	DMBE II	2.610	2.610	2.610	135.50
	DMBE I	2.610	2.610	2.610	135.56
C_{2v}^{cusp}	DMBE II	2.620	2.604	2.604	135.18
	DMBE I	2.615	2.606	2.606	135.31

^aThis work. ^bRelative to the $C_3(1^1\Sigma_g^+)$ global minimum. ^cRef. 50. ^dRef. 69. ^eRefs. 70 and 71. Separation between origin level and lowest $v_n = 1$ level. ^fMixed theoretical/experimental approaches of Refs. 72 and 73.

$$T_{\text{II}}''(\mathbf{R}) = \sum_{(i,j,k)} \left\{ \left\{ 1 - \tanh[\beta''(R_i - R_1''^0)] \right\} \right. \\ \left. \left\{ 1 - \tanh[\beta''(R_j - R_2''^0)] \right\} \right. \\ \left. \left\{ 1 - \tanh[\beta''(R_k - R_3''^0)] \right\} \right\}, \quad (26)$$

and

$$T_{\text{II}}'''(\mathbf{R}) = \sum_{(i,j,k)} \left\{ \left\{ 1 - \tanh[\gamma'''(R_i - R_1'''^0)] \right\} \right. \\ \left. \left\{ 1 - \tanh[\gamma'''(R_j - R_2'''^0)] \right\} \right. \\ \left. \left\{ 1 - \tanh[\gamma'''(R_k - R_3'''^0)] \right\} \right\}, \quad (27)$$

where the summations in Eqs. (26) and (27) extend over all possible cyclic permutations of (1,2,3), and the symbols are defined later in the text.

As remarked elsewhere,^{49,51,54} at the confluence point between the D_{3h} and C_{2v} crossing seams (or, in other words, at the point where the three additional degeneracies coincide with the central one), the conical nature of the intersection is lost with the locus of degeneracy assuming the form of tangentially touching parabolas rather than cones placed apex to apex.⁵¹ Thence, in order mimic such topological feature, the JT-type coordinates of Eqs. (22)-(24) have all been multiplied by a “non-JT” factor

$$\mathcal{F}_{\text{JT}}(\mathbf{R}) = 1 - \exp \left\{ -\zeta \left[(R_1 - R_0^{cP})^2 + (R_2 - R_0^{cP})^2 + (R_3 - R_0^{cP})^2 \right] \right\} \quad (28)$$

where $R_0^{cP} = 2.885a_0$ is the bond length of the confluence point predicted by the analytical function of Eq. (17) with $\zeta = 1 \times 10^4 a_0^{-2}$ being the associated decaying parameter. Indeed, the

$\mathcal{F}_{\text{JT}}(\mathbf{R})$ term in Eq. (28) guarantees that any singularity on the adiabatic PES due to $\sqrt{\Gamma_2}$ is canceled out at such a point. Suffice it to highlight that the Δ coordinate [Eq. (19)] naturally vanishes at the intersection node, since $\rho_0 = 0$ [see Figures 3(c) and 3(d)], $\Delta'_1 = \Delta'_2 = \Delta'_3 = \|\vec{p}'\|$ and hence, $S_2 = S_3 = 0$; see Eqs (13-19).

The strategy employed for calibration of the $V_{\text{II,EHF}}^{(3)}(\mathbf{R})$ term in Eq. (21) is similar to the one used for the DMBE I PES,⁵⁰ and we summarize next only the basic approach. Following usual practice,⁶⁰⁻⁶³ the three-body EHF interaction energy for the extra set of 421 grid points was obtained by first removing, for a given triatomic geometry, the one-body $[V^{(1)}]$ and the sum of the two-body energy terms $[V^{(2)}(\mathbf{R})]$ from the corresponding *ab initio* DMBE-SEC interaction energy [defined with respect to infinitely separated $C(3P)$ atoms]. One then subtracts the dynamical correlation term $[V_{\text{dc}}^{(3)}(\mathbf{R})]$ from the total three-body energy. It is the remaining energy so calculated that we adjust to the three-body polynomial form $V_{\text{II,EHF}}^{(3)}(\mathbf{R})$. Note that the same procedure has been adopted⁵⁰ in the calibration of the $V_{\text{I,EHF}}^{(3)}(\mathbf{R})$ term in Eq. (3) [previously denoted as $V_{\text{EHF}}^{(3)}(\mathbf{R})$]. For the fit, a version of the nonlinear Levenberg-Marquardt^{66,67} set of programs reported by Press *et al.*⁶⁸ has been used, with larger weights given to the most important regions of the PES, including the stationary points and the crossing geometries of D_{3h} and C_{2v} symmetry.

As a first step in the least-squares fitting procedure, the parameters of the $V_{\text{II,EHF}}^{(3)}(\mathbf{R})$ component [Eq. (22)] have been kept fixed (including the non-linear ones) to those values reported in Ref. 50, while allowing all the coefficients of the $V_{\text{II,EHF}}^{(3)}(\mathbf{R})$ and $V_{\text{II,EHF}}^{(3)}(\mathbf{R})$ terms to vary (to these extra parameters, small initial guesses have been assigned). Note that the non-linear coefficients β'' , γ''' and ζ of Eqs. (26), (27) and (28), respectively, have been

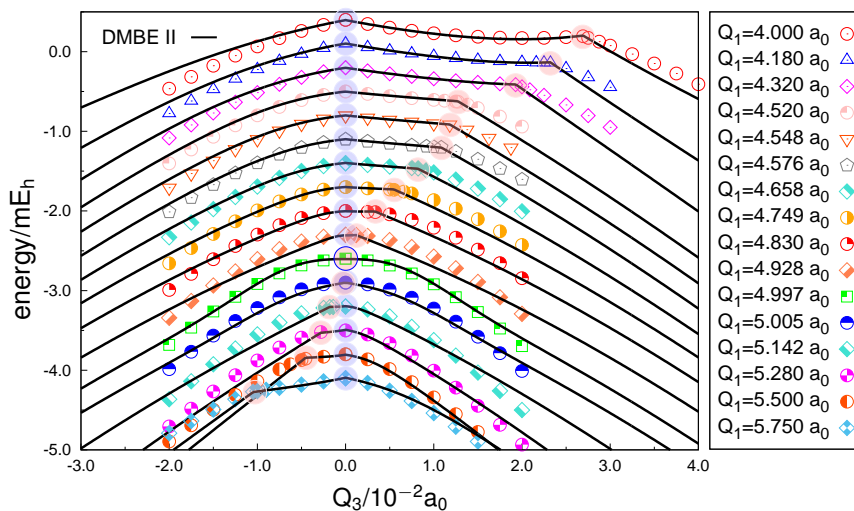


Fig. 6 Cross-sectional cuts of the DMBE II PES along Q_3 [$\mathbf{Q}_b(Q_1) = (0, Q_3)$] for different values of symmetric stretching coordinate Q_1 ($4.000a_0 \leq Q_1 \leq 5.750a_0$). The dots indicate the DMBE-SEC points included in the fit of the present work. The energies are given with respect to the associated value at equilateral triangular geometries and shifted by multiples of $\pm 0.03mE_h$. Filled blue and red circles highlight the D_{3h} and C_{2v} crossing points, respectively.

selected by a trial-and-error fit where the total rmsd is minimized. It should be emphasized at this point that the advantage of using such a double set of polynomials is to guarantee the continuation of the C_{2v} disjoint seams as one moves way from the corresponding MeX, an overall improvement over the DMBE I PES. Indeed, the $V_{\text{II,EHF}}^{(3)}(\mathbf{R})$ and $V_{\text{II,EHF}}^{(3)}(\mathbf{R})$ polynomials are centered at $Q_1 = 4.520a_0$ ($R_0'' = 2.610a_0$) and $Q_1 = 5.750a_0$ ($R_0''' = 3.320a_0$) with the range-functions $T_{\text{II}}''(\mathbf{R})$ and $T_{\text{II}}'''(\mathbf{R})$ defined with respect to the associated C_{2v} crossing geometries $R_1'' = 2.620a_0$, $R_2'' = R_3'' = 2.604a_0$ and $R_1''' = 3.311a_0$, $R_2''' = R_3''' = 3.324a_0$, respectively.

Once a reasonable set of initial coefficients for the $V_{\text{II,EHF}}^{(3)}(\mathbf{R})$ and $V_{\text{II,EHF}}^{(3)}(\mathbf{R})$ terms have been generated, the second step consisted of relaxing all involved parameters. It turns out that this often yields solutions with unphysical features, notably in highly repulsive regions of the PES and structures with C_{2v} symmetries. In fact, this behavior should be expected due to the added flexibility at such a narrow region of the configuration space.⁷⁴ However, a smooth PES could be obtained by performing a series of constrained optimizations in which blocks of coefficients are floated while keeping the others fixed. Such a strategy was carried out until chemical accuracy (4.07kJ mol^{-1}) was achieved. By employing such a procedure, all coefficients in Eqs. (22)-(24) [146 in total: $134 c_{ijk}^n$, R_0' , α' , R_0'' , β'' , R_1'' , $R_2'' = R_3''$, R_0''' , γ''' , R_1''' , $R_2''' = R_3'''$, ζ and R_0^{cp}] have been determined from a fit to the 1050 *ab initio* points; the optimal numerical values are given as ESI. The quality of the current fit may be judged from its stratified rmsd in Table 1. For comparison, we also give the corresponding rmsd obtained in DMBE I.⁵⁰ Accordingly, a good overall fit to the *ab initio* points has been achieved for the whole PES, notably in the regions containing the D_{3h} and C_{2v} crossing seams (typically, $135\text{-}490\text{kJ mol}^{-1}$ above the global minimum). As expected, the novel PES exhibits a similar accuracy to DMBE I in describing other relevant regions of the configuration space.

6 Features of the novel DMBE potential energy surface

The major features of the current DMBE PES are shown in Figures 6-10, while the properties of the stationary points and other relevant structures are in Table 2. Clearly, our approach allows an accurate description of both D_{3h} and C_{2v} crossings seams over the entire range of nuclear configuration space, a significant improvement over the previously reported PES.⁵⁰ As Figure 6 shows, such a procedure has proven very effective in reducing the discrepancies between the *ab initio* data and the single-sheeted DMBE form of Eq. (20) in the crossing regions. As noted elsewhere⁵¹ and depicted in Figures 6 and 7, when the size of the molecular triangle increases (*i.e.*, from $Q_1 = 4.000a_0$ to $Q_1 \lesssim 4.997a_0$) the C_{2v} disjoint seams approach the symmetry-required D_{3h} Ci almost linearly and ultimately coalesce with the latter at $Q_1 = 4.997a_0$. In fact, as noted in section 5 and seen from Figure 7(c), at such a confluence point the quadratic nature of the PES is remarkable and the intersection appears to be a Renner-Teller-like^{49,51} rather than a conical one. This is a result of using the “non-JT” factor of Eq. (28) in the three-body terms $V_{\text{II,EHF}}^{(3)}(\mathbf{R})$, $V_{\text{II,EHF}}^{(3)}(\mathbf{R})$ and $V_{\text{II,EHF}}^{(3)}(\mathbf{R})$ [Eqs. (22)-(24)]. Indeed, as Figures 6 and 7 show, any further increase of the perimeter leads to a rotation of the C_{2v} seams by $\pm\pi$ in the (Q_2, Q_3) -plane, thence becoming located at $\mathbf{Q}_b(Q_1) = (0, -\rho_0)$, $(\sqrt{3}\rho_0/2, \rho_0/2)$ and $(-\sqrt{3}\rho_0/2, \rho_0/2)$.⁵¹ Clearly, this is accomplished by Eq. (13) with the integer n being responsible for the shift of the disjoints seams when passing the confluence point.

The seam space¹ of D_{3h} and C_{2v} symmetries is best visualized in Figure 8 which depicts the continuously connected points of degeneracy for distinct values of Q_1 and Q_3 , respectively. Also shown are the *ab initio* crossing geometries highlighted in Figure 6 as well as those obtained in Ref. 50. Accordingly, the

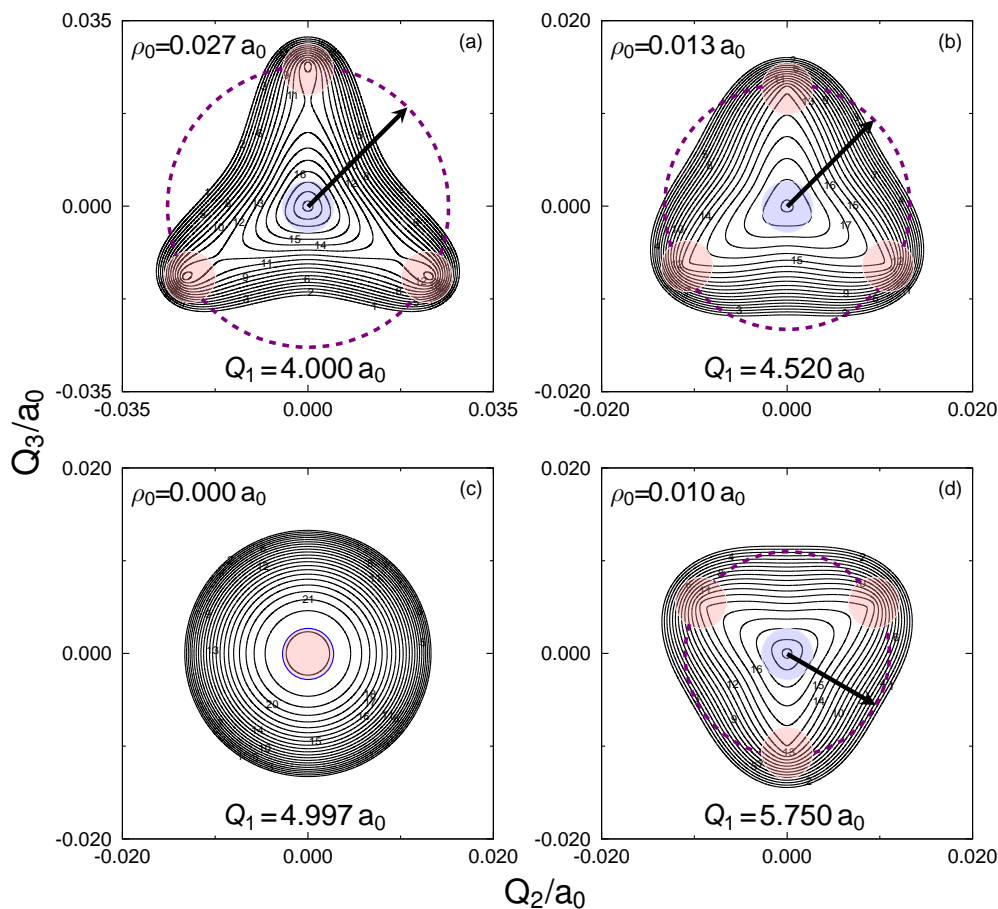


Fig. 7 Contour plots of the (Q_2, Q_3) -plane for fixed values of Q_1 coordinate. (a). $Q_1 = 4.000 a_0$. Contours are equally spaced by $0.000025 E_h$ starting at $-0.1710 E_h$, (b). $Q_1 = 4.520 a_0$. Contours are equally spaced by $0.000015 E_h$ starting at $-0.2392 E_h$, (c). $Q_1 = 4.997 a_0$. Contours are equally spaced by $0.000012 E_h$ starting at $-0.2081 E_h$ and (d). $Q_1 = 5.750 a_0$. Contours are equally spaced by $0.000022 E_h$ starting at $-0.1048 E_h$. Filled blue and red circles highlight the D_{3h} and C_{2v} crossing points, respectively.

MeX for equilateral triangular arrangements (D_{3h}^{cusp}) is predicted to be located at $R_1 = R_2 = R_3 = 2.610 a_0$ ($Q_1^{\text{cusp}} = 4.520 a_0$) and lies $135.50 \text{ kJ mol}^{-1}$ above the linear global minimum (referred to as Min). As Table 2 shows, excellent agreement is found between such a structure and the one actually predicted from the DMBE I PES. In turn, the MeX for C_{2v} conformations (C_{2v}^{cusp}) shows a characteristic bond lengths of $R_1 = 2.620 a_0$ and $R_2 = R_3 = 2.604 a_0$ [$\mathbf{Q}_b(Q_1^{\text{cusp}}) = (0, 0.013 a_0)$ with $Q_1^{\text{cusp}} = 4.520 a_0$] which lies $135.18 \text{ kJ mol}^{-1}$ higher in energy with respect to the Min structure. Note that two other symmetry-related MeXs of C_{2v} symmetry exist for similar cross-sections rotated by $\pm 2\pi/3$. Such structures are predicted to be located at $R_2 = 2.620 a_0$, $R_1 = R_3 = 2.604 a_0$ [$\mathbf{Q}_b(Q_1^{\text{cusp}}) = (0.011 a_0, -0.006 a_0)$] and $R_3 = 2.620 a_0$, $R_1 = R_2 = 2.604 a_0$ [$\mathbf{Q}_b(Q_1^{\text{cusp}}) = (-0.011 a_0, -0.006 a_0)$]. Suffice to say that the C_{2v}^{cusp} structure here obtained is also in excellent agreement with the corresponding MeX previously reported⁵⁰ with bond lengths and relative energy deviating by less than $0.005 a_0$ and $-0.13 \text{ kJ mol}^{-1}$, respectively; see Table 2. It should be pointed out that the range of geometries here considered ($4.000 a_0 \leq Q_1 \leq$

$5.750 a_0$ and $-0.040 a_0 \leq Q_i (i=2,3) \leq 0.040 a_0$) is satisfactory to accurately mimic the C_{2v} disjoint seams at low-to-intermediate energy regimes of the adiabatic ground-state PES, typically up to $\approx 490 \text{ kJ mol}^{-1}$ above the D_{3h} global minima; their validity range gets drastically limited by the extrapolation capability of the Q_1^3 function in Eq. (17) as well as the range-determining factors $T_{\text{II}}''(\mathbf{R})$ and $T_{\text{II}}'''(\mathbf{R})$ [Eqs. (26)-(27)]. In fact, by decreasing the size of the equilateral triangle (e.g., for $Q_1 \ll 4.000 a_0$), highly repulsive regions of the PES are accessible with both D_{3h} and C_{2v} crossing geometries ultimately coalescing to the $C(^3P)+C(^3P)+C(^3P)$ united-(Ar)-atom limit; see Figures 8 and 9. Of course, at such regions of configuration space, the intrinsic accuracy of the *ab initio* calculations themselves is expected to be poor. Conversely, for $Q_1 \gg 5.750 a_0$, the D_{3h} and C_{2v} crossing geometries collapse naturally into infinitely separated carbon atoms placed at the vertices of equilateral and isosceles triangles, respectively.

The global topography of the current DMBE PES is summarized in Figure 9 which shows the C_{2v} insertion of a C atom into C_2 . Also shown in panel (b) are close views of the crossing re-

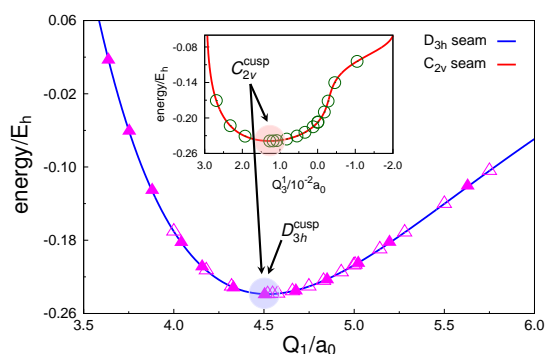


Fig. 8 Cuts along the D_{3h} and C_{2v} intersection lines as a function of Q_1 and Q_3 . The solid symbols correspond to DMBE-SEC points calculated in Ref. 50, while the open ones refer to the present work. Filled blue and red circles highlight the minimum energy crossing points at D_{3h} and C_{2v} symmetries, respectively.

gions illustrated in Figures 6-8, together with the corresponding crossing geometries and representative degeneracy lines. Such a plot rationalizes in a comprehensive way all the relevant details. The most salient feature of Figure 9(a), already remarked elsewhere,^{50,51,72,75,76} relates to the fact that the ground-state of C_3 shows its global minimum at $D_{\infty h}$ configurations with a characteristic bond length of $R_1/2 = R_2 = R_3 = 2.444 a_0$. Such a structure matches the one predicted from the DMBE I PES with the harmonic vibrational frequencies deviating by -0.3 cm^{-1} , -2.5 cm^{-1} and -1.0 cm^{-1} for the symmetric (w_1), bending (w_2) and antisymmetric (w_3) motions, respectively.

Note that the Min structure arises from structural JT+PJT instabilities and distortions of the D_{3h}^{cusp} and C_{2v}^{cusp} MeXs toward a valence angle $\phi > 60.0^\circ$, with a stabilization energy of $135.18 \text{ kJ mol}^{-1}$ (with respect to C_{2v}^{cusp}). As seen from Figure 9(b), if displacements toward $\phi < 60.0^\circ$ take place, the title system attains the saddle point TS_{iso} with a stabilization energy of $46.04 \text{ kJ mol}^{-1}$. Such a structure (visible as a minimum in the 2D plot of Figure 9) is therefore related to the isomerization between the three symmetry-equivalent C_3 global minima and is actually a transition state for pseudo-rotation.⁷⁻⁹ This is perhaps best seen from the plot shown later in Figure 10. Note that, due to large contributions of the quadratic JT vibronic coupling constant G_E ,⁵¹ the associated minima (Min) are shifted away from the intersection region⁷⁷ as can be seen from Figures 9(a) and Figure 10. The classical barrier height for the isomerization process is $89.46 \text{ kJ mol}^{-1}$, which agrees well with the previously reported barrier of⁵⁰ $89.58 \text{ kJ mol}^{-1}$. Although the current PES predicts bond lengths and energy for TS_{iso} in reasonable agreement with the DMBE I form, the harmonic vibrational frequencies deviate by 38.0 cm^{-1} , -32.8 cm^{-1} and $8.0 i \text{ cm}^{-1}$ for the symmetric (w_1), bending (w_2) and antisymmetric (w_3) motions, respectively; see Table 2. This is most likely due to the proximity of such stationary point to the locus of intersections [see Figure 9(b)] where small discrepancies between the current and previous fit are expected to manifest. In contrast, as shown in Table 2, at regions of configuration space far away from the crossing seams, namely at regions of the PES dominated by long range interactions, the

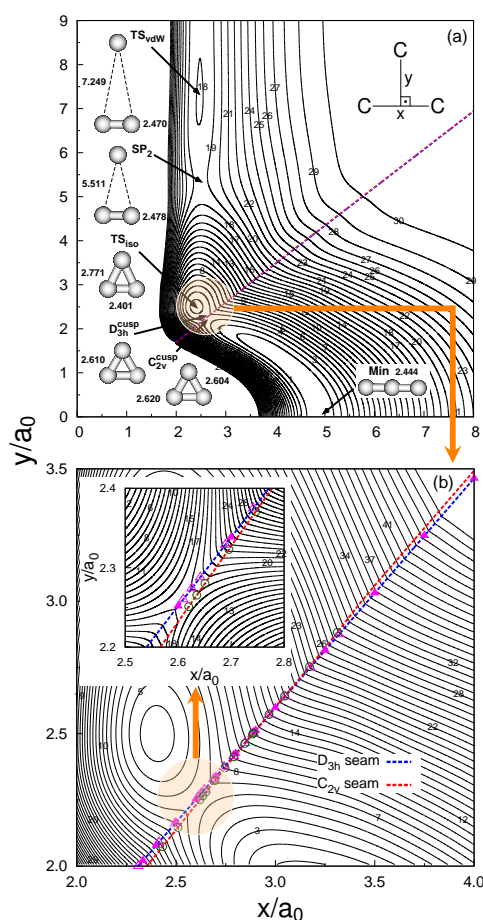


Fig. 9 Contour plots for C_3 , insertion of a C atom into the C_2 fragment. (a). Contours are equally spaced by $0.01 E_h$ starting at $-0.2904 E_h$. (b). Close view of the region defined by the D_{3h} and C_{2v} crossing seams. Contours are equally spaced by $0.004 E_h$ starting at $-0.2800 E_h$. In the inset of panel (b), contours are equally spaced by $0.0007 E_h$ starting at $-0.2520 E_h$. Key for *ab initio* crossing points as in Figure 8.

properties of the stationary structures SP_2 and TS_{vdW} are essentially the same as predicted⁵⁰ from DMBE I; for a detailed discussion of all stationary structures and corresponding properties, see Ref. 50. (Note that there is a misprint in Ref. 50 concerning the subscript “vdW” in TS_{vdW} , which stands for “van der Waals”.)

As seen from the inset of Figure 9(b), the novel DMBE PES here obtained provides not only an improvement in the description of the crossing region but also displays the expected sharp nature in the vicinity of the D_{3h} and C_{2v} crossings seams. This is a result of using the $\sqrt{\Gamma_2}$ and Δ coordinates. Because the present form guarantees by built-in construction the correct cusp behavior over an extended region of the nuclear configuration space, one expects that the net GP effect is largely suppressed for any path in the (Q_2, Q_3) -plane that encircles the four singularity points. Obviously, no sign change is expected when looping around the confluence point in panel (c) of Figure 7. Note that, in view of Figure 9, the intersection node corresponds to the point in config-

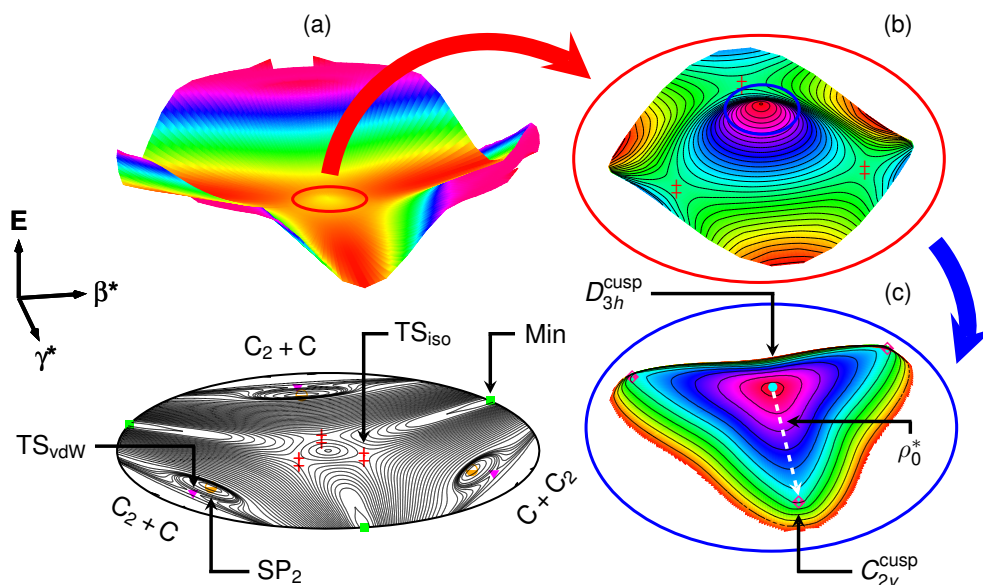


Fig. 10 Relaxed triangular plot in hyperspherical coordinates depicting the location and symmetry of all stationary points and other relevant structures discussed in the present work for the ground state of C_3 . (a). Contours are equally spaced by $0.005 E_h$, starting at $-0.2904 E_h$. (b). Close view of the region defined by the three-symmetry related TS_{iso} structures, and delimited by the bold red circle. Contours are equally spaced by $0.001 E_h$, starting at $-0.2700 E_h$. (c). Close view of the conical intersection region showing the minimum of the crossing seam at D_{3h} symmetry as well as the minimum of the three equivalent symmetry related C_{2v} crossing points (inside the bold blue circle). Contours are equally spaced by $0.00002 E_h$, starting at $-0.2390 E_h$.

uration space where the D_{3h} and C_{2v} intersection lines cross each other: $x = 2.885 a_0$ and $y = \sqrt{3}x/2 = 2.498 a_0$. Up to this point, the C_{2v} disjoint line lies below that of D_{3h} symmetry, with the opposite being the case for regions above it; see Figure 9(b).

The major topographical features of the DMBE II PES are best viewed in a relaxed triangular plot⁷⁸ using hyperspherical coordinates:¹⁵

$$\begin{pmatrix} Q \\ \beta \\ \gamma \end{pmatrix} = \begin{pmatrix} 1 & 1 & 1 \\ 0 & \sqrt{3} & -\sqrt{3} \\ 2 & -1 & -1 \end{pmatrix} \begin{pmatrix} R_1^2 \\ R_2^2 \\ R_3^2 \end{pmatrix}. \quad (29)$$

By relaxing the “size” Q of the molecular triangle so as to minimize the energy for fixed values of β and γ (or the “shape”), the scaled β^* and γ^* coordinates, plotted in Figure 10, are given by⁷⁸

$$\beta^* = \beta/Q \quad (30)$$

$$\gamma^* = \gamma/Q. \quad (31)$$

As Figure 10(a) shows, all major topographical attributes of the current PES can be perceived through a close inspection of the line $\beta^* = 0$ and $\gamma^* \neq 0$ (the C_{2v} axis), with the associated symmetry-equivalent structures obtained for similar cuts rotated by $\pm 2\pi/3$. Note that linear geometries lie at the border of the physical circle, while the equilateral triangular conformation (D_{3h}) is located at the origin ($\beta^* = 0$ and $\gamma^* = 0$). Also shown in panels (b) and (c) are close views of the regions containing the three symmetry equivalent transition states TS_{iso} and MeXs, respectively. In addition to accurately reproducing the diatomic potentials, long-range forces at all asymptotic channels and valence interactions over the

whole configuration space [already achieved by DMBE I⁵⁰], the novel DMBE II PES shows the correct topological behavior in the vicinity of the MeXs; see Figure 10(c).

As shown in Figure 10(c), the minima of the C_{2v} crossings lie at $\rho_0^* = 0.008 a_0$, where ρ_0^* is the (scaled-) radial polar coordinate in the (β^*, γ^*) plane. Thence, on this circle of radius ρ_0^* in such a 2D plane, the four MeXs are uniquely defined by the coordinates $(0, 0)$, $(0, \rho_0^*)$, $(-\sqrt{3}\rho_0^*/2, -\rho_0^*/2)$ and $(\sqrt{3}\rho_0^*/2, -\rho_0^*/2)$. Note that the C_{2v}^{cusp} structures lie only 0.32 kJ mol^{-1} below the corresponding MeX of D_{3h} symmetry.

The probability of observing the GP effect (P_{GP}) may be speculated to be given by

$$P_{GP} \lesssim \frac{A_{ci}}{A_{tot}} \times 100 = (\rho_0^*)^2 \times 100 \quad (32)$$

where $A_{ci} = \pi(\rho_0^*)^2$ is the area of the circle defined by ρ_0^* , and $A_{tot} = \pi(\rho^*)^2$ with $\rho^* = 1$ the radius of the physical circle in Figure 10(a). For ground-state C_3 , this would yield $P_{GP} \lesssim 0.0064\%$, thus implying a very small number of paths that may sign-flip the electronic adiabatic wave function when looping an odd number of times the D_{3h} Ci.⁵¹ In most adiabatic energy regimes, one then expects the wave function to encircle the 4 Cis (classically, if having an energy above the barrier for pseudo-rotation) or not encircle any, which amounts basically to 100% of the cases.

7 Conclusions

A new single-sheeted DMBE II PES for ground-state $C_3(1^1A')$ has been reported. For this, we have suggested a form capable of accurately modeling the three symmetry-equivalent C_{2v} disjoint

seams, in addition to the symmetry-required D_{3h} one, over the full configuration space. The present formalism warrants by built-in construction the confluence of the above crossings and the change-in-phase of the C_{2v} seams when the size of the molecular perimeter fluctuates. Up to 1050 *ab initio* energies have been employed in the calibration procedure, of which 421 were used to map the loci of intersection. The calculated energies have been scaled to account for the incompleteness of the basis set and truncation of the MRCI expansion and fitted analytically with chemical accuracy. The novel DMBE form is shown to accurately mimic the region defined by the 4 CIs, while exhibiting attributes similar to the ones predicted from the previously reported DMBE I PES at regions away from the crossing seams. Despite focusing on C_3 , the present approach should be applicable to any adiabatic PES of X_3 -type systems experiencing similar topological effects, in particular for so-called small linear parameter JT molecules.

Acknowledgments

This work is supported by Fundação para a Ciência e a Tecnologia and Coimbra Chemistry Centre, Portugal, through the project UI0313/QUI/2013, also co-funded by FEDER/COMPETE 2020-EU. C.M. thanks also the CAPES Foundation (Ministry of Education of Brazil) for a scholarship (Process BEX 0417/13-0)

References

- W. Domcke, D. R. Yarkony and H. Köppel, *Conical Intersections: Electronic Structure, Dynamics & Spectroscopy*, World Scientific Publishing, Singapore, 2004, vol. 15.
- G. J. Atchity, S. S. Xantheas and K. Ruedenberg, *J. Chem. Phys.*, 1991, **95**, 1862–1876.
- D. R. Yarkony, *Acc. Chem. Res.*, 1998, **31**, 511–518.
- A. J. C. Varandas, *Chem. Phys. Lett.*, 2010, **487**, 139–146.
- H. A. Jahn and E. Teller, *Proc. R. Soc. Lond. A*, 1937, **161**, 220–235.
- R. Englman, *The Jahn-Teller Effect*, John Wiley & Sons, New York, 1973.
- I. B. Bersuker and V. Z. Polinger, *Vibronic Interactions in Molecules and Crystals*, Springer-Verlag, Berlin, 1989.
- I. B. Bersuker, *The Jahn-Teller Effect*, Cambridge University Press, Cambridge, 2006.
- I. B. Bersuker, *Chem. Rev.*, 2001, **101**, 1067–1114.
- D. R. Yarkony, *Chem. Rev.*, 2012, **112**, 481–498.
- J. von Neumann and E. P. Wigner, *Physik. Z.*, 1929, **30**, 467–470.
- E. Teller, *J. Phys. Chem.*, 1937, **41**, 109–116.
- G. Herzberg and H. C. Longuet-Higgins, *Discuss. Faraday Soc.*, 1963, **35**, 77–82.
- H. C. Longuet-Higgins, *Proc. R. Soc. Lond. A*, 1975, **344**, 147–156.
- C. A. Mead and D. G. Truhlar, *J. Chem. Phys.*, 1979, **70**, 2284–2296.
- M. V. Berry, *Proc. R. Soc. Lond. A*, 1984, **392**, 45–57.
- B. R. L. Galvão, V. C. Mota and A. J. C. Varandas, *J. Phys. Chem. A*, 2015, **119**, 1415–1421.
- B. R. L. Galvão, V. C. Mota and A. J. C. Varandas, *Chem. Phys. Lett.*, 2016, **660**, 55–59.
- M. Born and R. Oppenheimer, *Ann. Phys.*, 1927, **389**, 457–484.
- M. Born and K. Huang, *Dynamical Theory of Crystal Lattices*, Oxford, Clarendon Press, 1954.
- C. A. Mead and D. G. Truhlar, *J. Chem. Phys.*, 1982, **77**, 6090–6098.
- J. N. Murrell, S. Carter, S. C. Farantos, P. Huxley and A. J. C. Varandas, *Molecular Potential Energy Functions*, John Wiley & Sons, Chichester, 1984.
- T. Pacher, L. S. Cederbaum and H. Köppel, *Adv. Chem. Phys.*, 1993, **87**, 293–391.
- J. G. Atchity and K. Ruedenberg, *Theor. Chem. Acc.*, 1997, **97**, 47–58.
- A. J. Doblyn and P. J. Knowles, *Mol. Phys.*, 1997, **91**, 1107–1124.
- A. Thiel and H. Köppel, *J. Chem. Phys.*, 1999, **110**, 9371–9383.
- V. C. Mota and A. J. C. Varandas, *J. Phys. Chem. A*, 2008, **112**, 3768–3786.
- A. J. C. Varandas, *J. Chem. Phys.*, 2008, **129**, 234103–234116.
- A. J. C. Varandas, *Chem. Phys. Lett.*, 2009, **471**, 315–321.
- B. R. L. Galvão, P. J. S. B. Caridade and A. J. C. Varandas, *J. Chem. Phys.*, 2012, **137**, 22A515–22A527.
- A. J. C. Varandas and J. N. Murrell, *Faraday Discuss. Chem. Soc.*, 1977, **62**, 92–109.
- R. N. Porter, R. M. Stevens and M. Karplus, *J. Chem. Phys.*, 1968, **49**, 5163–5178.
- A. J. C. Varandas, F. B. Brown, C. A. Mead, D. G. Truhlar and N. C. Blais, *J. Chem. Phys.*, 1987, **86**, 6258–6269.
- M. Cernei, A. Alijah and A. J. C. Varandas, *J. Chem. Phys.*, 2003, **118**, 2637–2646.
- L. P. Viegas, M. Cernei, A. Alijah and A. J. C. Varandas, *J. Chem. Phys.*, 2004, **120**, 253–259.
- A. J. C. Varandas, A. Alijah and M. Cernei, *Chem. Phys.*, 2005, **308**, 285–295.
- B. R. L. Galvão and A. J. C. Varandas, *J. Phys. Chem. A*, 2011, **115**, 12390–12398.
- V. C. Mota, P. J. S. B. Caridade and A. J. C. Varandas, *Int. J. Quantum Chem.*, 2011, **111**, 3776–3785.
- V. C. Mota, P. J. S. B. Caridade and A. J. C. Varandas, *J. Phys. Chem. A*, 2012, **116**, 3023–3034.
- V. C. Mota and A. J. C. Varandas, *J. Phys. Chem. A*, 2007, **111**, 10191–10195.
- J. W. Zwanziger and E. R. Grant, *J. Chem. Phys.*, 1987, **87**, 2954–2964.
- H. Koizumi and I. B. Bersuker, *Phys. Rev. Lett.*, 1999, **83**, 3009–3012.
- H. Köppel and R. Meiswinkel, *Z. Phys. D: At., Mol. Clusters*, 1994, **32**, 153–156.
- R. G. Sadygov and D. R. Yarkony, *J. Chem. Phys.*, 1999, **110**, 3639–3642.
- D. R. Yarkony, *J. Chem. Phys.*, 1999, **111**, 4906–4912.

- 46 S. Mukherjee, S. Bandyopadhyay, A. K. Paul and S. Adhikari, *J. Phys. Chem. A*, 2013, **117**, 3475–3495.
- 47 S. Mukherjee and S. Adhikari, *Chem. Phys.*, 2014, **440**, 106–118.
- 48 P. Garcia-Fernandez, I. B. Bersuker and J. E. Boggs, *J. Chem. Phys.*, 2006, **125**, 104102–104112.
- 49 J. J. Dillon and D. R. Yarkony, *J. Chem. Phys.*, 2007, **126**, 124113–124119.
- 50 C. M. R. Rocha and A. J. C. Varandas, *J. Chem. Phys.*, 2015, **143**, 074302–074318.
- 51 C. M. R. Rocha and A. J. C. Varandas, *J. Chem. Phys.*, 2016, **144**, 064309–064324.
- 52 G. J. Atchity and K. Ruedenberg, *J. Chem. Phys.*, 1999, **110**, 4208–4212.
- 53 D. R. Yarkony, *Theor. Chem. Acc.*, 1998, **98**, 197–201.
- 54 S. Matsika and D. R. Yarkony, *J. Phys. Chem. A*, 2002, **106**, 2580–2591.
- 55 P. G. Szalay, T. Müller, G. Gidofalvi, H. Lischka and R. Shepard, *Chem. Rev.*, 2012, **112**, 108–181.
- 56 T. H. Dunning, *J. Chem. Phys.*, 1989, **90**, 1007–1023.
- 57 R. A. Kendall, T. H. Dunning and R. J. Harrison, *J. Chem. Phys.*, 1992, **96**, 6796–6806.
- 58 H. J. Werner, P. J. Knowles, G. Knizia, F. R. Manby, M. Schütz and *et al.*, *MOLPRO, a package of ab initio programs, version 2010.1*, 2010, see: <http://www.molpro.net>, Cardiff, U.K., 2010.
- 59 A. J. C. Varandas, *J. Chem. Phys.*, 1989, **90**, 4379–4391.
- 60 A. J. C. Varandas, *Adv. Chem. Phys.*, 1988, **74**, 255–338.
- 61 A. J. C. Varandas, *J. Mol. Struct.: THEOCHEM*, 1985, **120**, 401–424.
- 62 A. J. C. Varandas, in *Reaction and Molecular Dynamics*, ed. A. Laganà and A. Riganelli, Springer Berlin Heidelberg, 2000, vol. 75, pp. 33–56.
- 63 A. J. C. Varandas, in *Conical Intersections: Electronic Structure, Dynamics & Spectroscopy*, ed. W. Domcke, D. R. Yarkony and H. Köppel, World Scientific, 2004, vol. 15, ch. 5, pp. 205–270.
- 64 A. J. C. Varandas and J. N. Murrell, *Chem. Phys. Lett.*, 1981, **84**, 440–445.
- 65 A. J. C. Varandas, J. Tennyson and J. N. Murrell, *Chem. Phys. Lett.*, 1979, **61**, 431–434.
- 66 K. Levenberg, *Quart. Applied Math.*, 1944, **2**, 164–168.
- 67 D. W. Marquardt, *SIAM J. Appl. Math.*, 1963, **11**, 431–441.
- 68 W. H. Press, S. A. Teukolsky, W. T. Vetterling and B. P. Flannery, *Numerical Recipes in Fortran: The Art of Scientific Computing*, Cambridge University Press, New York, NY, USA, 2nd edn., 1993.
- 69 K. W. Hinkle, J. J. Keady and P. F. Bernath, *Science*, 1988, **241**, 1319–1322.
- 70 G. Zhang, K. Chen, A. J. Merer, Y. Hsu, W. Chen, S. Shaji and Y. Liao, *J. Chem. Phys.*, 2005, **122**, 244308–244315.
- 71 J. Krieg, V. Lutter, C. P. Endres, I. H. Keppeler, P. Jensen, M. E. Harding, J. Vázquez, S. Schlemmer, T. F. Giesen and S. Thorwirth, *J. Phys. Chem. A*, 2013, **117**, 3332–3339.
- 72 B. Schröder and P. Sebald, *J. Chem. Phys.*, 2016, **144**, 044307–044318.
- 73 A. A. Breier, T. Büchling, R. Schnierer, V. Lutter, G. W. Fuchs, K. M. T. Yamada, B. Mookerjee, J. Stutzki and T. F. Giesen, *J. Chem. Phys.*, 2016, **145**, 234302–234311.
- 74 A. J. C. Varandas, *J. Chem. Phys.*, 2013, **138**, 054120–054133.
- 75 M. Mladenović, S. Schmatz and P. Botschwina, *J. Chem. Phys.*, 1994, **101**, 5891–5899.
- 76 K. Ahmed, G. G. Balint-Kurti and C. M. Western, *J. Chem. Phys.*, 2004, **121**, 10041–10051.
- 77 T. A. Barckholtz and T. A. Miller, *Int. Rev. Phys. Chem.*, 1998, **17**, 435–524.
- 78 A. J. C. Varandas, *Chem. Phys. Lett.*, 1987, **138**, 455–461.

Energy-switching potential energy surfaces for ground-state C₃

C. M. R. Rocha, A. J. C. Varandas*

*Departamento de Química, and Centro de Química, Universidade de Coimbra
3004-535 Coimbra, Portugal.***Abstract**

The multiple energy switching scheme [J. Chem. Phys. 119 (2003) 2596] is utilized to improve the potential energy surface of C₃ near its linear global minima by morphing it with Taylor-series expansions of Ahmed, Balint-Kurti and Western [J. Chem. Phys. 121 (2004) 10041] and Schröder and Sebald [J. Chem. Phys. 144 (2016) 044307]. Near spectroscopic accuracy is conveyed to the final global forms up to 4000 cm⁻¹ above zero-point energy, while keeping unaltered all key attributes of the original potential, namely the topology at conical intersections and dissociative channels. Both ES forms are commended for spectroscopic and reaction dynamics.

Keywords: C₃, potential energy surfaces, energy switching, rovibrational spectroscopy

1. Introduction

In principle, a global potential energy surface (PES) is expected to reproduce experimental data at regions of the nuclear configuration space where such information is available, and behave in a physically reasonable manner elsewhere (namely, at intermediate and long-range regions) [1–4]. In practice, such a requirement is seldom fulfilled. Despite all recent computational/methodological developments, the above problem still poses a challenge to both *ab initio* theory and analytical modeling [5], particularly if aiming at spectroscopic accuracy [6–9].

This led one of us [6] to suggest a simple, yet reliable, scheme in which two potential forms [$V_1(\mathbf{R})$ and $V_2(\mathbf{R})$] optimal at distinct energy regimes can be merged together and switched smoothly from one to the other as a function of energy such that the final energy switching (ES) form is accurate everywhere [6–9]. As usual, $V_1(\mathbf{R})$ is a double many-body expansion (DMBE)-type [4, 10–12] function or any global form that warrants a realistic description of the whole surface including the location and well depth of the potential minimum(a). In turn, $V_2(\mathbf{R})$ is a local-type form that attains spectroscopic accuracy near such minimum(a). The ES potential (V_{ES}) is then given by [6]

$$V_{\text{ES}} = f(\Delta E)V_1(\mathbf{R}) + [1 - f(\Delta E)]V_2(\mathbf{R}), \quad (1)$$

with

$$f(\Delta E) = \frac{1}{2} \{1 + \tanh[(\gamma_0 + \gamma_1 \Delta E^m) \Delta E]\}, \quad (2)$$

where $\Delta E = E - E_0$ is the displacement from some reference energy E_0 at which $V_1(\mathbf{R})$ and $V_2(\mathbf{R})$ are equally

reliable, and $f(\Delta E)$ is a switching function that ensures $V_{\text{ES}} \equiv V_2(\mathbf{R})$ for large negative energy displacements (at the absolute minimum) and $V_{\text{ES}} \equiv V_1(\mathbf{R})$ for large positive ones (at the atom-diatom dissociation limits). In turn, γ_i ($i = 0, 1$) are disposable parameters to be optimized for a selected even power of m [6]. Clearly, V_{ES} benefits from the advantages of both individual forms, while avoiding their limitations [6–8]. The ES scheme has proved effective in obtaining spectroscopically accurate global PESs for H₂O [6–8, 13], H₃⁺ [14, 15] and also for systems such as ArHCN [16], HO₃ [17] and HeHCN [18].

Recently, Varandas suggested further refinements onto the approach by introducing the multiple ES (MES) scheme [9]. The novel methodology is particularly useful to convey spectroscopic accuracy for systems in which the switching from $V_2(\mathbf{R})$ to $V_1(\mathbf{R})$ takes place in a narrow energy window, as is the case for NO₂(1²A') [9]. Accordingly, the ES potential (V'_{ES}) assumes the form [9]

$$V'_{\text{ES}} = f'_i \dots f'_3 f'_2 f'_1 [V_1(\mathbf{R}) - V_2(\mathbf{R})] + V_2(\mathbf{R}), \quad (3)$$

with the switching functions f'_i being defined by [9]

$$f'_i(\Delta E') = \begin{cases} \exp \left[-\beta_i \left(\frac{\Delta E'_0}{\Delta E' + \xi} - 1 \right)^{n_i} \right] & \text{if } \Delta E' < \Delta E'_0 \\ 1 & \text{if } \Delta E' \geq \Delta E'_0. \end{cases} \quad (4)$$

In the above equation, $\Delta E' = E - E_{\text{min}}$ is the energy displacement with respect to the absolute minimum of the global PES, while $\Delta E'_0 = E'_0 - E_{\text{min}}$ measures the energy difference between E_{min} and some cutoff energy E'_0 [9]. Typically, E'_0 can be judiciously chosen in such a way as to keep unaltered some chosen topological feature of $V_1(\mathbf{R})$ (e.g., a conical intersection [9]) or simply represent the energy threshold at which the Taylor-series-expansion-type form $V_2(\mathbf{R})$ is valid. In turn, β_i is a trial-and-error param-

*Corresponding author

Email address: varandas@uc.pt (A. J. C. Varandas)

eter, n_i is an even integer and ξ is a small number chosen to avoid numerical overflows at $E = E_{\min}$.

The present work is concerned with $C_3(1^1A')$, an astrophysically relevant species that plays a central role in the chemistry of cometary and interstellar atmospheres [19]. Recently, the authors reported [20] an *ab initio*-based global PES (DMBE I) for the ground electronic state of the title species. A total of 629 *ab initio* energies calculated at the multireference configuration interaction (MRCI) level of theory and the aug-cc-pVTZ (AVTZ) [21] basis have been employed. The input *ab initio* data have been there also scaled to account for the incompleteness the one- and \mathcal{N} -electron basis via DMBE-scaled external correlation (DMBE-SEC) method [22] and subsequently fitted with a root mean square deviation (rmsd) of 4.14 kJ mol⁻¹ [20]. To judge the quality of the potential form so obtained, exploratory rovibrational energy calculations have been performed. As shown in the original paper [20], the DMBE I PES reproduces the vibrational energy spectrum of C_3 with a rmsd of 50.4 cm⁻¹ for 53 calculated levels up to about 3000 cm⁻¹ above zero point energy (ZPE) [20]. Most recently, the authors reported [23] a refined form (DMBE II) which has been especially designed to properly mimic the region defined by the 4 conical intersections in the title molecule, which are due to combined Jahn-Teller plus pseudo-Jahn-Teller [$(E' + A'_1) \otimes e'$] vibronic effects [20, 23, 24]. For this, the *ab initio* data set was extended to a total of 1050 grid points and least-squares fitted to the DMBE II form with a rmsd of 4.07 kJ mol⁻¹.

As stated elsewhere [20], the above global PESs could provide the required input for further improvements to true spectroscopic accuracy via the ES scheme [6, 9]. Of course, the first step toward such an approach consists of selecting available local forms that fulfill the desired requirements. As emphasized by van Order and Saykally [19], the carbon trimer is one of the most well-characterized nonrigid triatomics in existence and such a wealth of experimental and theoretical effort has been devoted in obtaining accurate near-equilibrium ground-state PESs for the title species [25–29].

Of special relevance here is the local form due to Ahmed, Balint-Kurti and Western (ABW) [28]. The authors employed internally contracted MRCI calculations including the Davidson correction and a basis set of VTZ quality [21]. By using a total of 384 *ab initio* energies up to 8000 cm⁻¹ above the equilibrium geometry, they have least-squares fitted the data to a Taylor-series-type expansion with a rmsd of 13.2 cm⁻¹. The *ab initio* surface so obtained has subsequently been refined by fitting a few of the potential coefficients to the experimental data. As noted by the authors [28], the ground-state fit covers a range of ≈ 8713 cm⁻¹ above the ZPE level and reproduces 100 observed rovibrational levels to within 3 cm⁻¹.

More recently, Schröder and Sebald (SS) [29] reported a near-equilibrium ground-state PES for C_3 employing a composite approach. The potential has been calibrated from *ab initio* data obtained at fc-CCSD(T*)-F12b/AV5Z

(“fc” stands for frozen core) level of theory [30]. The raw *ab initio* energies have then been corrected additively hoping to incorporate higher-order correlations (up to iterative pentuples CCSDTQP [29]), core-core/core-valence effects and also scalar relativistic contributions. All calculated energies have been fitted to a polynomial form with a standard deviation of only 0.05 cm⁻¹ [29]. It should be pointed out that the work is primarily concerned with the low-lying rotation-vibration energies obtained for $J \leq 30$ (where J is the rotational angular momentum quantum number) and a few vibrational term energies up to ≈ 3500 cm⁻¹ above the ZPE were reported. As shown by the authors [29], these are reproduced to better than 1 cm⁻¹.

In the present work, the ABW [28] and SS [29] local forms are merged with the novel DMBE II PES [23] by following Varandas’ [9] MES scheme [Eqs. (3) and (4)]. Inspired by the graphical abstract, the resulting ES potentials will be called DMBE-II/ES/ABW and DMBE-II/ES/SS, although we will remove “II” here for simplicity.

The plan of the paper is as follows. In section 2, we provide some aspects of the current ES methodology employed for ground-state C_3 and also show the main topographical features of the resulting ES potentials. The details of the rovibrational energy calculations here performed are described in section 3, while the results and discussion are in section 4. Section 5 gathers the conclusions.

2. The ES potential energy surface

Since the ABW/SS [28, 29] and DMBE II [23] potentials are exceptionally flat near the region defined by the linear global minimum (Min) [see Figure 1], only a single switching function $f'_1(\Delta E') \equiv f'(\Delta E')$ with $n_1 \equiv n = 2$ [see Eqs. (3) and (4)] suffices to smoothly connect the above PESs (for brevity, the corresponding functional forms will not be given here, with the reader being addressed to the original papers [23, 28, 29] for details). As usual, the $\beta_1 \equiv \beta$ parameter has been determined from the requirement that V'_{ES} should approach the accuracy of the original local PESs in reproducing the rovibrational data (see later), while avoiding the appearance of wrinkles at energies close to E'_0 [9]. Such a procedure yielded $\beta = 12$ and 15 for the DMBE/ES/ABW and DMBE/ES/SS PESs, respectively.

The topographical features of the final ES PESs are depicted in Figures 1 and 2, together with the corresponding local potentials. For comparison, in Figure 2, the near-equilibrium PESs reported by Mladenović *et al.* (MSB) [26] and Špirko *et al.* (SMJ) [27] are also shown; see Table 1 to assess the structural parameters of the Min structures predicted from the potential forms here considered. To warrant invariance with respect to permutation of the C atoms, we have ensured that all sets of coordinates $[(R_1, R_2, R_3), (R_2, R_3, R_1), \text{ and } (R_3, R_1, R_2)]$ project onto the valence coordinates $(R_1, R_2 \text{ and } \phi)$ utilized by the ABW and SS potential energy surfaces [28, 29].

Some comment is due on the determination of the cut-off energies E'_0 in Eq. (4). Obviously, one wishes to keep

Table 1: Structural parameters of the $C_3(^1\Sigma_g^+)$ global minima (Min structures) predicted from the ES and other potential forms.

Potential	R_1/a_0	R_2/a_0	R_3/a_0	w_1/cm^{-1}	w_2/cm^{-1}	w_3/cm^{-1}
DMBE/ES/ABW ^a	4.920	2.460	2.460	1214.5	64.6	2109.8
ABW ^b	4.920	2.460	2.460	1214.5	64.6	2109.8
DMBE/ES/SS ^a	4.890	2.445	2.445	1206.7	42.8	2101.3
SS ^c	4.890	2.445	2.445	1206.7	42.8	2101.3
DMBE II ^d	4.888	2.444	2.444	1203.9	61.0	2125.5
DMBE I ^e	4.888	2.444	2.444	1204.2	63.5	2126.5
MSB ^f	4.906	2.453	2.453	1201.3	41.5	2098.2
SMJ ^g	4.881	2.447	2.447	1195.6	32.2	2072.7
Expt.	4.902	2.451	2.451 ^h	1224.49 ⁱ	63.42 ⁱ	2040.02 ⁱ
	4.890	2.445	2.445 ^j			

^aThis work. ^bRef. 28. ^cRef. 29. ^dRef. 23. ^eRef. 20. ^fRef. 26. ^gRef. 27. ^hRef. 31. ⁱRefs. 32 and 33. Separation between origin level and lowest $v_n=1$ level. ^jFrom mixed theoretical/experimental approaches of Refs. 29 and 34.

unaltered the original crossing seams with D_{3h} and C_{2v} symmetries [20, 23, 24] which occur at an energy of $E_{Ci} = 135.2 \text{ kJ mol}^{-1} \approx 11302 \text{ cm}^{-1}$ above the Min structure (actually the minimum energy crossing point of C_{2v} symmetry). Additionally, as seen in Figure 1(b) and (d), neither the ABW nor the SS local representations properly describe the isomerization transition state TS_{iso} located at $E_{\text{TS}} = 89.5 \text{ kJ mol}^{-1} \approx 7482 \text{ cm}^{-1}$ with respect to the global minimum. Thence, we should warrant that the switching from the ABW/SS to the DMBE II forms has already been accomplished at such a limit. In fact, as shown in Figure 1, the near-equilibrium forms show several spurious holes at regions close to equilateral triangular conformations; see the regions delimited by the magenta triangles.

As remarked by Ahmed *et al.* [28], geometries up to $\phi = 70^\circ$ have been considered in their fit; thence fall into the physically acceptable energy range ($\lesssim 7400 \text{ cm}^{-1}$). This is the limit which we have used ourselves in determining E'_0 . Regarding the SS potential [29], the range of geometries covered by the *ab initio* calculations are slightly lower (up to $\phi = 80^\circ$) and we judged convenient to define $E'_0 = 6500 \text{ cm}^{-1}$. Such energy limits are shown by the blue dashed lines in Figures 1(a) and (c) as well as by black dotted lines in the one-dimensional cuts depicted in Figure 2. Note that E_{min} in Eq. (4) is set as the energy of the $D_{\infty h}$ global minimum with respect to the $C_2(a^3\Pi_u)+C(^3P)$ dissociation channel ($E_{\text{min}} = -0.2904 E_h$) with E being evaluated at the global DMBE II form.

3. Rovibrational calculations

The rovibrational energy calculations have been carried out using the multidimensional discrete variable representation (DVR) method [36] as implemented in the DVR3D and ROTLEV3 suite of programs of Tennyson and co-workers [37]. All calculations employed orthogonal Jacobi coordinates with the molecular body-fixed z -axis embedded along r_1 (this is the CC diatomic distance, r_2 the C-CC center-of-mass separation, and θ the included angle).

In setting the so-called finite basis representation (FBR) [36], we have used Morse oscillator-like functions as radial vibrational basis whose parameters are summarized in Table S1 of Supplementary Information (SI). For the angular basis, (associated) Legendre polynomials have been utilized [37]. With the above set of weighted orthogonal polynomials and their associated Gaussian quadratures (see Table S1 for the number of DVR pivots), the FBR-to-DVR transformation ($\mathbf{H}^{\text{DVR}} = \mathbf{T}\mathbf{H}^{\text{FBR}}\mathbf{T}^\dagger$) has been accomplished by the so-called quadrature approximation [36, 37] with the corresponding kinetic energy integrals evaluated analytically prior to the transformation process. The final solutions are obtained from a series of diagonalizations and truncations of the transformed Hamiltonian (\mathbf{H}^{DVR}) occurring in the order $r_2 \rightarrow r_1 \rightarrow \theta$. The energy cutoff of $E_{\text{max}}^{\text{1D}} = 70000 \text{ cm}^{-1}$ (the global minima are the zero of the potentials) has been utilized for 1D problems and solutions with eigenenergies $\leq E_{\text{max}}^{\text{1D}}$ were then used to construct 2D problems with maximum dimension of 1500. To built the final 3D matrix, such a dimension has been increased to 2500. All calculations were restricted to the levels reported in Ref. 28 for $J \leq 1$. They cover a range up to $\approx 8713 \text{ cm}^{-1}$ above the corresponding ZPEs and are here typically converged to within 0.1 cm^{-1} or better. Excellent agreement (within 0.2 cm^{-1} or less) has been found between the calculated levels and those reported in the literature [28, 29]. For $J = 1$, the two-step variational procedure of Tennyson and Sutcliffe [38] is employed. This uses the solutions of Coriolis decoupled “vibrational” problems (where the projection of J onto the body fixed z -axis, k , is assumed to be a good quantum number) as basis functions for the fully coupled rovibrational one [38], both for even(*e*) and odd(*f*)-parities. Note that we have not attempted to calculate rotational or l -type doubling constants and hence, small discrepancies (up to about 0.5 cm^{-1}) between experimental band centers and calculated data for $J = 1$ should be expected (only *f* levels are here reported). As stated in section 2 and seen in Figure 1, the ABW and SS forms show several unphysical

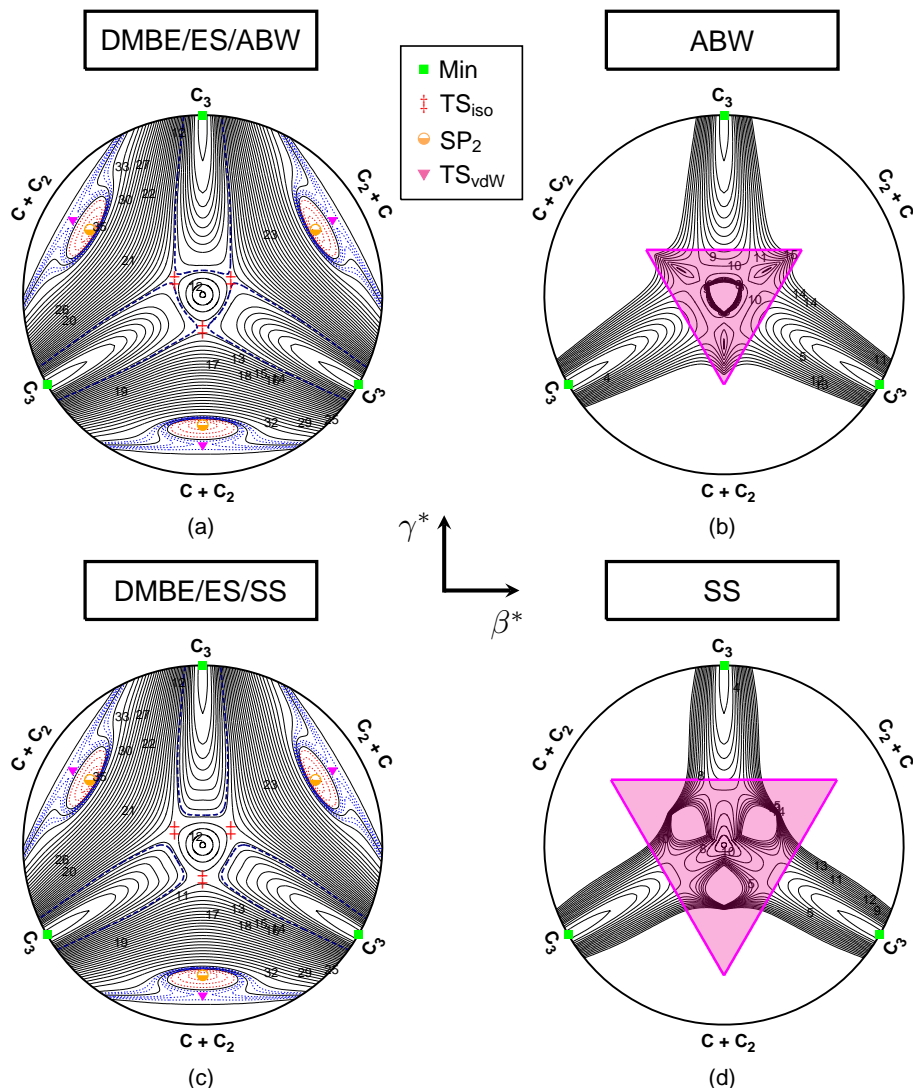


Figure 1: Relaxed triangular plots in hyperspherical coordinates [35] of the ground-state C_3 PES. (a). DMBE/ES/ABW. Black solid lines are equally spaced by $0.005 E_h$, starting at $-0.2904 E_h$. Red and blue dashed lines are equally spaced by $0.001 E_h$, starting at $0.00067 E_h$ and $-0.0206 E_h$, respectively. (b). ABW [28]. Contours are equally spaced by $0.005 E_h$, starting at $-0.2904 E_h$. (c). DMBE/ES/SS. Contours as in (a). (d). SS [29]. Contours as in (b). In panels (a) and (c), the blue dashed lines define the associated cutoff energies (E'_0) in Eq. (4), while the magenta triangles in panels (b) and (d) establish the limits beyond which the corresponding local potentials were delimited by a high repulsive wall. Note that the ABW and SS PESs have been shifted by $-0.2904 E_h$. See Refs. 20 and 23 for the stationary points.

features near D_{3h} arrangements and therefore, the rovibrational calculations could only be attained by cutting them with a high-energy wall near this region. The assumed borderlines are highlighted by the colored triangles in Figure 1(b) and (d).

4. Results and discussion

Table S2 of the SI shows the differences between the observed ($G_{\text{expt.}}$) [33, 39–45] and calculated vibrational

levels for the ES PESs and their associated local potentials. Also shown, for comparison, are the corresponding values from the DMBE I [20] and DMBE II [23] PESs as well as those (when available) reported by Mladenović *et al.* [26] and Špirko *et al.* [27]. As usual, all calculated energy levels are assigned according to four approximate quantum numbers (v_1, v_2^l, v_3) , where v_1 , v_2 and v_3 refer to symmetric, bending and antisymmetric vibrational modes, respectively, and l_2 is the vibrational angular momentum quantum number. One should now comment on the assign-

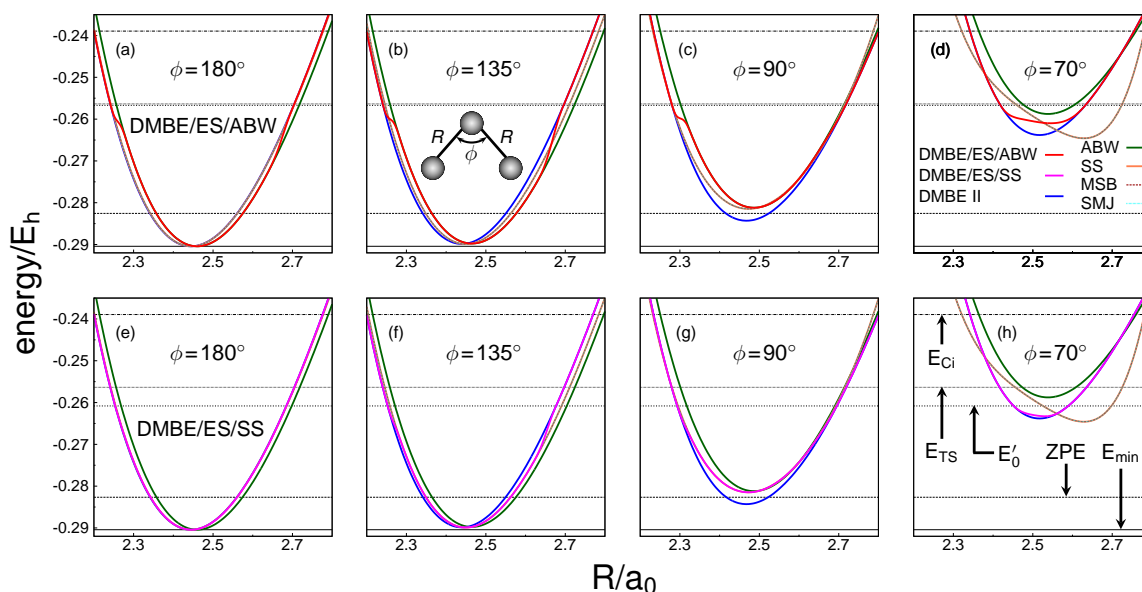


Figure 2: Cuts of the DMBE/ES/ABW [panels (a)-(d)], DMBE/ES/SS [panels (e)-(h)], DMBE II, and corresponding local potentials along the symmetric stretching coordinate for fixed valence angles of $\phi = 180^\circ$, 135° , 90° and 70° .

ment process. Although automated approaches have been successfully employed for triatomic molecules [46–48], the relatively modest number of states here considered (100 levels) allowed us to perform such assignments by visual inspection of the wave function plots (see Figure 5). However, for excited overtones (typically, levels $> 6000 \text{ cm}^{-1}$) such an approach can become cumbersome (even for automated assignments) as the wave functions show complex nodal structures. In fact, such intricate patterns of the eigenfunctions are specially manifested in the global PESs and can be attributed either to delocalization of the states or presence of “junctions” particularly at regions where the local and global forms mix together. Indeed, for the most complicated cases, assignments have been done in such a way as to minimize the discrepancies between the calculated and observed data. Table 2 gathers the stratified rmsds for all 100 calculated levels up to 9000 cm^{-1} (the last level is actually $\approx 8713 \text{ cm}^{-1}$ above ZPE).

Clearly, the vibrational wave numbers calculated from the ES potentials agree well with those obtained using the corresponding local PESs up to 4000 cm^{-1} above ZPE (this is best seen from the plots in Figures 3 and 4). As seen, the DMBE/ES/ABW and DMBE/ES/SS potentials show rmsds with respect to experimental term values of 8.2 and 13.2 cm^{-1} , respectively. Indeed, Figure 2, shows that the agreement between the ES and local forms is best in this region. Unfortunately, as remarked elsewhere [7] and clearly seen in Table 2, discrepancies quickly appear with increasing energy. This is particularly true for the DMBE/ES/ABW PES whose counterparts (the DMBE II and ABW potentials) exhibit remarkable differences be-

tween themselves at some geometries [see Figure 2(c) and Table 1]. In fact, Figure 1(a) shows the scars of their merging together, with the switching from one to the other occurring in a more “severe” way. In contrast, for the DMBE/ES/SS potential, the global and local constituents differ only slightly from each other and hence such scars are less marked. Actually, as Figure 2(e) depicts, the DMBE II [23], SS [29], MSB [26] and SMJ [27] potentials are practically indistinguishable at linear geometries (the last three are hardly distinguishable in all plots shown) and, apart from the SMJ PES [27], have essentially the same equilibrium structures; Table 1. Suffice to add that the experimentally-merged SMJ surface [27] has its equilibrium configuration at non-linear geometries [$R_1 = R_2 = 2.447 a_0$ and $\phi = 171.6^\circ$] despite reproducing 207 vibrational term values below 9000 cm^{-1} with a rmsd of 26 cm^{-1} .

Of course, one would like to enhance the accuracy of the global DMBE/ES potentials by bringing them into coincidence with the ABW or SS surfaces at regions where they are physically acceptable. This might be achieved by following two routes: (i) increasing the value of E'_0 and/or (ii) the value of β in Eq. (4). The first cannot be considered due to spurious features arising in the local forms. As for (ii), a few attempts have been done to improve the DMBE/ES spectroscopies at higher energy strata by increasing β . However, this leads to the appearance of more marked scars, which may affect the smoothness of the resulting forms close to E'_0 . After all, a reduction of 20 cm^{-1} or so in the final rmsd for levels up to 9000 cm^{-1} is already a significant asset of the ES approach which brings

Table 2: Stratified rmsd (in cm^{-1}) for the 100 calculated rovibrational energy levels ($J \leq 1$).

Energy ^a	N^b	rmsd					
		DMBE/ES/ABW	ABW	DMBE/ES/SS	SS	DMBE II	DMBE I
1000	8	3.3	3.2	2.5	2.3	24.5	32.5
2000	17	3.3	2.8	7.3	6.9	38.9	41.8
3000	35	4.2	2.6	9.7	9.1	37.5	47.0
4000	49	8.2	2.7	13.2	11.1	40.1	48.1
5000	70	17.2	2.7	17.6	13.5	42.6	49.4
6000	83	18.0	3.0	19.8	13.4	42.2	49.0
7000	89	24.9	3.0	22.9	13.0	43.0	50.4
8000	94	26.4	2.9	27.4	12.9	44.5	52.1
9000	100	26.9	2.9	31.0	12.5	45.7	53.4

^aUnits of energy are cm^{-1} . Energy strata defined relative to the corresponding zero point energy level. ^bNumber of vibrational states up to indicated energy range.

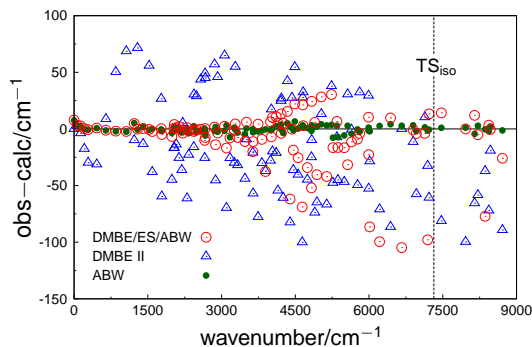


Figure 3: Scatter plot of the errors between the observed and calculated energy levels for the DMBE/ES/ABW, DMBE II and ABW PESs as a function of the experimental band centers. The vertical line highlights the location of the isomerization transition state TS_{iso} .

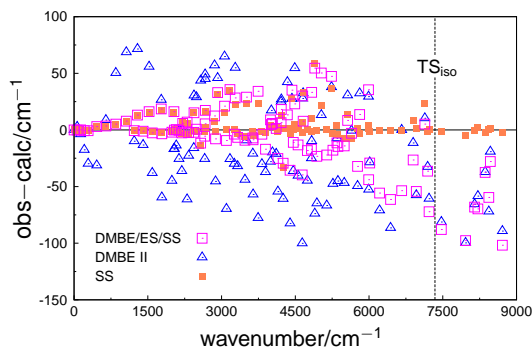


Figure 4: As in Figure 3, but for the DMBE/ES/SS and SS PESs.

an unprecedented improvement over the global PES.

Naturally, the accuracy of the ES PESs hinges on the quality of the corresponding local forms. Although not being spectroscopically accurate ($\text{rmsd} \leq 1 \text{ cm}^{-1}$), the ABW [28] local PES is certainly the most reliable so far in reproducing experimental rovibrational levels for ground-state C_3 at high energy regimes [49]. Recall that the lowest level $(0,0^0,0)$ of the ABW potential form has been treated [28] as an adjustable parameter; see Table S2. Thence, as highlighted by the authors [28], the ZPE level (at 1728.1 cm^{-1} with respect to the bottom of the well) is artificial when compared with the experimental value. A comment goes also to the SS potential [28]. This is undoubtedly the best purely *ab initio* local PES. However, one should bear in mind that, despite significant improvements over the previous fully *ab initio* MSB form [26] in reproducing spectroscopic constants and term energies for the low-lying states, some deficiencies remain, particularly in describing excited bending overtones [the deviation here obtained for the $(0,18^0,0)$ state is as high as 17.6 cm^{-1}]. Note that the near-equilibrium PES of Mladenović *et al.* [26] is equally reliable in reproducing experimental band centers and rotational manifolds up to 3000 cm^{-1} . Nevertheless, as noted elsewhere [49], its behavior is increasingly erratic for levels above such a limit.

As already noted, neither the ABW nor the SS near-equilibrium forms describe the saddle point TS_{iso} which is responsible for the proper isomerization between the three symmetry related $\text{C}_3(1^1\Sigma_g^+)$ global minima [20, 23]. Although such potentials adequately account for the large amplitude vibrational motion in C_3 at low-to-intermediate energies, one should expect inadequacies related to the proper delocalization of highly excited rovibrational eigenstates lying close to or above the isomerization barrier. As noted elsewhere [50] such effects are particularly relevant in studying unimolecular reactions and intramolecular vibrational redistribution processes in floppy systems.

Figure 5 shows sample vibrational wave functions obtained from the ES potentials and the corresponding local

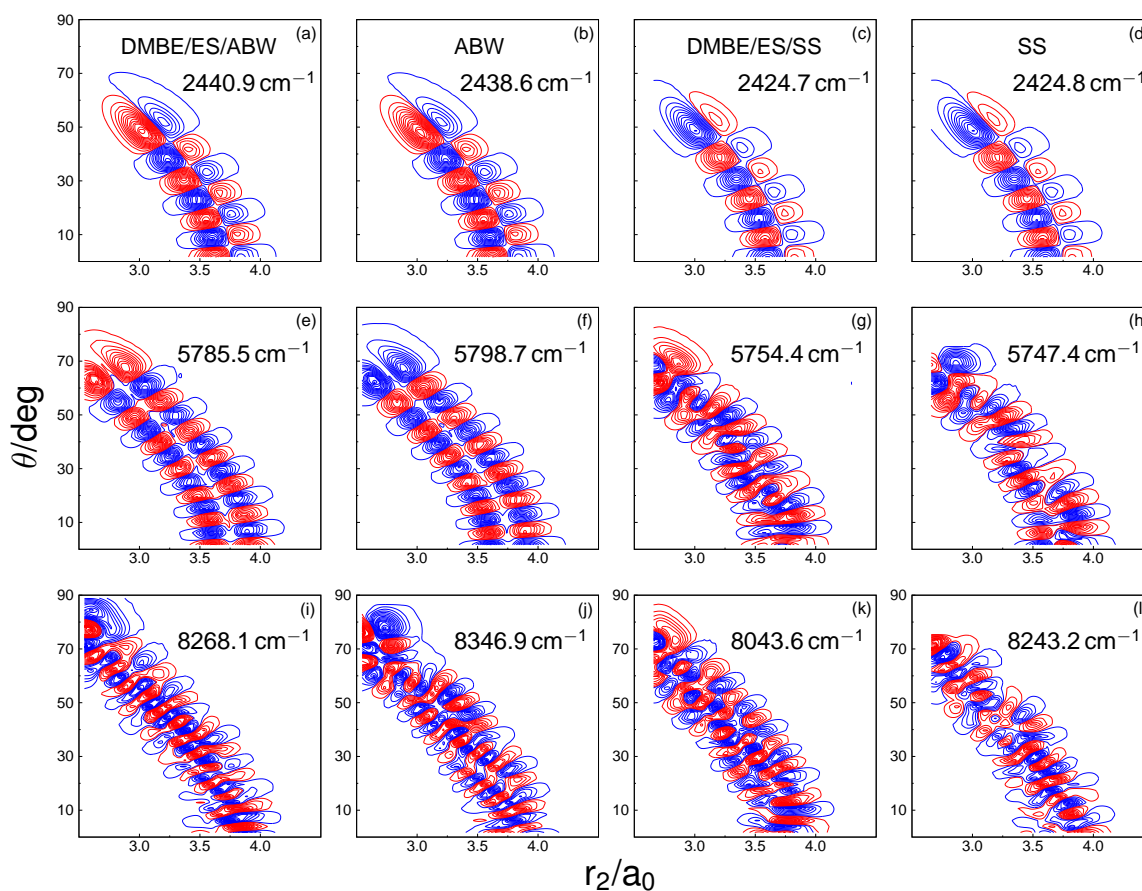


Figure 5: Contour plots of sample vibrational wave functions for $J=0$ calculated from the DMBE/ES/ABW [panels (a), (e) and (i)], ABW [panels (b), (f) and (j)], DMBE/ES/SS [panels (c), (g) and (k)] and SS [panels (d), (h) and (l)] PESs at distinct energy regimes. Panels (a)-(d) depict wave functions for the $(1,12^0,0)$ and (e)-(h) for $(1,24^0,1)$ levels. For comparison, panels (i)-(l), sample wave functions with similar nodal structures in the energy range of $8000\text{-}8500\text{ cm}^{-1}$ above ZPE. Blue and red lines are for positive and negative contours, respectively.

forms at distinct energy regimes. Note that, in panels (i)-(j), we did not attempt to make any assignments and only wave functions with similar nodal structures (in the energy range of $8000\text{-}8500\text{ cm}^{-1}$ above the ZPE level) are shown. Overall, for low-to-intermediate excitation energies, the vibrational wave functions so obtained from both ES and local potentials exhibit quite close behavior; see panels (a)-(f). However, as seen in Figure 5(g) and (h), the eigenfunctions calculated from the DMBE/ES/SS and SS PESs already exhibit a slightly distorted nodal structure with the former showing itself more disperse over the nuclear configuration space. The very delocalized nature of the vibrational wave functions can be best seen in the plots shown in panels (i) and (k). In contrast to their ABW or SS counterparts, these eigenfunctions can actually surpass (or tunnel through) the potential barriers and delocalize themselves over all three symmetry related minima at once. Indeed, the task of calculating accurately energies and wave functions for such high-lying states can be a

rather difficult one, particularly when these cover regions of the nuclear configuration space at which crossings between surfaces are known to exist. At such regions, nonadiabatic effects are ubiquitous and therefore, the accuracy of adiabatic calculations are somewhat limited. Specifically for ground-state $C_3(1^1A')$, it is fair to think that many of the rovibrational states lying half-way between ZPE and the conical intersections (5000 cm^{-1} above ZPE) are perturbed by interactions with the first excited $2^1A'$ state [20, 23, 24]. For this reason, we judge the present methodology and the results so obtained quite satisfactory. Of course, one might struggle for a more accurate spectroscopic PES by employing an hybrid approach [9] through which the Taylor-series-type expansions are refined (by fitting experimental rovibrational data) once embedded in the global DMBE PES. In so doing, we must bear in mind that the final PESs will lie beyond the strict adiabatic approximation (as it is actually the case for the ABW form [28]) since nonadiabatic effects are implicitly accounted.

5. Conclusions

A simplified version of the multiple energy switching scheme [9] is here utilized to improve the previously reported DMBE II PES of ground-state C_3 in the vicinity of its linear global minima by morphing it with the best Taylor-series expansions due to Ahmed *et al.* [28] and Schröder and Sebald [29]. Near spectroscopic accuracy is conveyed to both global forms up to about 4000 cm^{-1} above zero-point energy, while keeping unaltered all attributes of the original DMBE II PES, namely atom-diatom dissociation channels and the region defined by the 4 conical intersections with the partner state of the same symmetry. Both forms so obtained are therefore commended for both spectroscopic and reaction dynamics studies.

Acknowledgments

This work is supported by Fundação para a Ciência e a Tecnologia and Coimbra Chemistry Centre, Portugal, through the project UI0313/QUI/2013, also co-funded by FEDER/COMPETE 2020-EU. C.M. thanks also the CAPES Foundation (Ministry of Education of Brazil) for a scholarship (Process BEX 0417/13-0).

Appendix A. Supplementary information

Supplementary data associated with this article can be found in the online version

References

- [1] P. J. Kuntz, Features of Potential Energy Surfaces and Their Effect on Collisions, Springer US, 1976, Ch. 2, pp. 53–120.
- [2] J. S. Wright, S. K. Gray, Rotated Morse Curve-Spline Potential Function for A+BC Reaction Dynamics: Application to (Cl, HBr), (F, H₂), and (H⁺, H₂), J. Chem. Phys. 69 (1978) 67–81.
- [3] J. N. L. Connor, Reactive Molecular Collision Calculations, Comp. Phys. Comm. 17 (1979) 117–143.
- [4] A. J. C. Varandas, Intermolecular and Intramolecular Potentials: Topographical Aspects, Calculation, and Functional Representation via A Double Many-Body Expansion Method, Adv. Chem. Phys. 74 (1988) 255–338.
- [5] A. J. C. Varandas, Combined-Hyperbolic-Inverse-Power-Representation of Potential Energy Surfaces: A Preliminary Assessment for H₃ and HO₂, J. Chem. Phys. 138 (2013) 054120–054133.
- [6] A. J. C. Varandas, Energy Switching Approach to Potential Surfaces: An Accurate Single-Valued Function for the Water Molecule, J. Chem. Phys. 105 (1996) 3524–3531.
- [7] A. J. C. Varandas, Energy Switching Approach to Potential Surfaces. II. Two-Valued Function for the Water Molecule, J. Chem. Phys. 107 (1997) 867–878.
- [8] A. J. C. Varandas, A. I. Voronin, P. J. S. B. Caridade, Energy Switching Approach to Potential Surfaces. III. Three-Valued Function for the Water Molecule, J. Chem. Phys. 108 (1998) 7623–7630.
- [9] A. J. C. Varandas, A Realistic Multi-Sheeted Potential Energy Surface for NO₂(²A′) from the Double Many-Body Expansion Method and a Novel Multiple Energy-Switching Scheme, J. Chem. Phys. 119 (2003) 2596–2613.
- [10] A. J. C. Varandas, A general approach to the potential energy functions of small polyatomic systems: Molecules and van der Waals molecules, J. Mol. Struct.: THEOCHEM 120 (1985) 401–424.
- [11] A. J. C. Varandas, Multivalued Potential Energy Surfaces for Dynamics Studies, in: A. Laganà, A. Riganelli (Eds.), Reaction and Molecular Dynamics, Vol. 75 of Lecture Notes in Chemistry, Springer Berlin Heidelberg, 2000, pp. 33–56.
- [12] A. J. C. Varandas, Modeling and Interpolation of Global Multi-Sheeted Potential Energy Surfaces, in: W. Domcke, D. R. Yarkony, H. Köppel (Eds.), Conical Intersections: Electronic Structure, Dynamics & Spectroscopy, Vol. 15 of Advanced Series in Physical Chemistry, World Scientific, 2004, Ch. 5, pp. 205–270.
- [13] B. R. L. Galvão, S. P. J. Rodrigues, A. J. C. Varandas, Energy-Switching Potential Energy Surface for the Water Molecule Revisited: A Highly Accurate Singled-Sheeted Form, J. Chem. Phys. 129 (2008) 044302–044308.
- [14] R. Prosimiti, O. L. Polyansky, J. Tennyson, A Global Potential Energy Surface for the H₃⁺ Molecule, Chem. Phys. Lett. 273 (1997) 107–114.
- [15] O. L. Polyansky, R. Prosimiti, W. Klopper, J. Tennyson, An Accurate, Global, *Ab Initio* Potential Energy Surface for the H₃⁺ Molecule, Mol. Phys. 98 (2000) 261–273.
- [16] A. J. C. Varandas, S. P. J. Rodrigues, P. A. J. Gomes, Energy Switching Potential Energy Surfaces and Spectra of the Van der Waals Modes for the ArHCN Molecule, Chem. Phys. Lett. 297 (1998) 458–466.
- [17] H. G. Yu, A. J. C. Varandas, *Ab Initio* Theoretical Calculation and Potential Energy Surface for Ground-State HO₃, Chem. Phys. Lett. 334 (2001) 173–178.
- [18] W. H. Ansari, A. J. C. Varandas, Six-Dimensional Energy-Switching Potential Energy Surface for HeHCN, J. Phys. Chem. A 106 (2002) 9338–9344.
- [19] A. Van Orden, R. J. Saykally, Small Carbon Clusters: Spectroscopy, Structure, and Energetics., Chem. Rev. 98 (1998) 2313–2358.
- [20] C. M. R. Rocha, A. J. C. Varandas, Accurate *Ab Initio*-Based Double Many-Body Expansion Potential Energy Surface for the Adiabatic Ground-State of the C₃ Radical Including Combined Jahn-Teller plus Pseudo-Jahn-Teller Interactions, J. Chem. Phys. 143 (2015) 074302–074318.
- [21] T. H. Dunning Jr., A road map for the calculation of molecular binding energies, J. Phys. Chem. A 104 (2000) 9062–9080.
- [22] A. J. C. Varandas, A Semiempirical Method for Correcting Configuration Interaction Potential Energy Surfaces, J. Chem. Phys. 90 (1989) 4379–4391.
- [23] C. M. R. Rocha, A. J. C. Varandas, Multiple Conical Intersections in Small Linear Parameter Jahn-Teller Systems: the DMBE Potential Energy Surface for Ground-State C₃ Revisited, (submitted)
- [24] C. M. R. Rocha, A. J. C. Varandas, The Jahn-Teller plus Pseudo-Jahn-Teller Vibronic Problem in the C₃ Radical and its Topological Implications, J. Chem. Phys. 144 (2016) 064309–064324.
- [25] P. Jensen, C. M. Rohlfing, J. Almlöf, Calculation of the Complete-Active-Space Self-Consistent-Field Potential-Energy Surface, the Dipole Moment Surfaces, the Rotation-Vibration Energies, and the Vibrational Transition Moments for C₃($\tilde{X}^1\Sigma_g^+$), J. Chem. Phys. 97 (1992) 3399–3411.
- [26] M. Mladenović, S. Schmatz, P. Botschwina, Large-Scale *Ab Initio* Calculations for C₃, J. Chem. Phys. 101 (1994) 5891–5899.
- [27] V. Špirko, M. Mengel, P. Jensen, Calculation of Rotation-Vibration Energy Levels in Ground State C₃ by a Born-Oppenheimer-Type Separation of the Vibrational Motions, J. Mol. Spectrosc. 183 (1997) 129–138.
- [28] K. Ahmed, G. G. Balint-Kurti, C. M. Western, *Ab Initio* Calculations and Vibrational Energy Level Fits for the Lower Singlet Potential-Energy Surfaces of C₃, J. Chem. Phys. 121 (2004) 10041–10051.
- [29] B. Schröder, P. Sebald, High-Level Theoretical Rovibrational

- Spectroscopy beyond fc-CCSD(T): The C₃ molecule, *J. Chem. Phys.* 144 (2016) 044307–044318.
- [30] G. Knizia, T. B. Adler, H.-J. Werner, Simplified CCSD(T)-F12 Methods: Theory and Benchmarks, *J. Chem. Phys.* 130 (2009) 054104–054123.
- [31] K. W. Hinkle, J. J. Keady, P. F. Bernath, Detection of C₃ in the Circumstellar Shell of IRC+10216., *Science* 241 (1988) 1319–1322.
- [32] G. Zhang, K. Chen, A. J. Merer, Y. Hsu, W. Chen, S. Shaji, Y. Liao, The 4051-Å Band of C₃ ($\tilde{A}^1\Pi_u - \tilde{X}^1\Sigma_g^+$, 000-000): Perturbed Low-J Lines and Lifetime Measurements, *J. Chem. Phys.* 122 (2005) 244308–244315.
- [33] J. Krieg, V. Lutter, C. P. Endres, I. H. Keppeler, P. Jensen, M. E. Harding, J. Vázquez, S. Schlemmer, T. F. Giesen, S. Thorwirth, High-Resolution Spectroscopy of C₃ Around 3 μm, *J. Phys. Chem. A* 117 (2013) 3332–3339.
- [34] A. A. Breier, T. Büchling, R. Schnierer, V. Lutter, G. W. Fuchs, K. M. T. Yamada, B. Mookerjee, J. Stutzki, T. F. Giesen, Lowest Bending Mode of ¹³C-Substituted C₃ and an Experimentally Derived Structure, *J. Chem. Phys.* 145 (2016) 234302–234311.
- [35] A. J. C. Varandas, A Useful Triangular Plot of Triatomic Potential Energy Surfaces, *Chem. Phys. Lett.* 138 (1987) 455–461.
- [36] J. C. Light, T. Carrington, Discrete-Variable Representations and their Utilization, John Wiley & Sons, Inc., 2007, Ch. 4, pp. 263–310.
- [37] J. Tennyson, M. A. Kostin, P. Barletta, G. J. Harris, O. L. Polyansky, J. Ramanlal, N. F. Zobov, DVR3D: A Program Suite for the Calculation of Rotation-Vibration Spectra of Triatomic Molecules, *Comput. Phys. Commun.* 163 (2004) 85–116.
- [38] J. Tennyson, B. T. Sutcliffe, Highly Rotationally Excited States of Floppy Molecules: H₂D⁺ with J ≤ 20, *Mol. Phys.* 58 (1986) 1067–1085.
- [39] K. Kawaguchi, K. Matsumura, H. Kanamori, E. Hirota, Diode Laser Spectroscopy of C₃: The $\nu_2 + \nu_3 - \nu_2$, $2\nu_2 + \nu_3 - 2\nu_2$, and $2\nu_2 + \nu_3$ Bands, *J. Chem. Phys.* 91 (1989) 1953–1957.
- [40] E. A. Rohlfling, Laser-Induced-Fluorescence Spectroscopy of Jet-Cooled C₃, *J. Chem. Phys.* 91 (1989) 4531–4542.
- [41] C. A. Schmuttenmaer, R. C. Cohen, N. Pugliano, J. R. Heath, A. L. Cooksy, K. L. Busarow, R. J. Saykally, Tunable Far-IR Laser Spectroscopy of Jet-Cooled Carbon Clusters: the ν_2 bending vibration of C₃, *Science* 249 (1990) 897–900.
- [42] E. A. Rohlfling, J. E. M. Goldsmith, Stimulated-Emission Pumping Spectroscopy of Jet-Cooled C₃: Antisymmetric Stretch-Bend Levels, *J. Opt. Soc. Am. B* 7 (1990) 1915–1923.
- [43] F. J. Northrup, T. J. Sears, Stimulated-Emission Pumping Spectroscopy Study of Jet-Cooled C₃: Pure Bending Levels and Bend-Symmetric-Stretch Combination Levels of $X^1\Sigma_g^+$, *J. Opt. Soc. Am. B* 7 (1990) 1924–1934.
- [44] J. Baker, S. K. Bramble, P. A. Hamilton, A Hot Band LIF Study of the $A^1\Pi_u - X^1\Sigma_g^+$ transition in C₃, *Chem. Phys. Lett.* 213 (1993) 297–302.
- [45] J. Baker, S. K. Bramble, P. A. Hamilton, Observation of New Bands in the $A^1\Pi_u - X^1\Sigma_g^+$ Laser Induced Fluorescence Spectrum of C₃, *J. Mol. Spec.* 183 (1997) 6–11.
- [46] M. Menou, C. Leforestier, Labeling the HCN Vibrational States in the Regular Spectrum, *Chem. Phys. Lett.* 210 (1993) 294–302.
- [47] A. J. C. Varandas, S. P. J. Rodrigues, A Realistic Double Many-Body Expansion Potential Energy Surface for SO₂(\tilde{X}^1A') from a Multiproperty Fit to Accurate *Ab Initio* Energies and Vibrational Levels, *Spectrochim. Acta Mol. Biomol. Spectrosc.* 58 (2002) 629–647.
- [48] A. J. C. Varandas, S. P. J. Rodrigues, New Double Many-Body Expansion Potential Energy Surface for Ground-State HCN from a Multiproperty Fit to Accurate *Ab Initio* Energies and Rovibrational Calculations, *J. Phys. Chem. A* 110 (2006) 485–493.
- [49] J. Tennyson, G. J. Harris, R. J. Barber, S. Delfa, B. A. Voronin, B. M. Kaminsky, Y. V. Pavlenko, Molecular Line Lists for Modelling the Opacity of Cool Stars, *Mol. Phys.* 105 (2007) 701–714.
- [50] Z. Băcić, Accurate Calculation and Assignment of Highly Excited Vibrational Levels of Floppy Triatomic Molecules in a Basis of Adiabatic Vibrational Eigenstates, *J. Chem. Phys.* 95 (1991) 3456–3466.



Article submitted to journal

Subject Areas:

electronic structure, potential energy surfaces, spectroscopy

Keywords:

carbon clusters, C_2 , C_3 , C_4 , many-body expansion, double many-body expansion, potential energy surfaces

Author for correspondence:

A. J. C. Varandas
e-mail: varandas@uc.pt

C_n ($n = 2 - 4$): current status

A. J. C. Varandas and C. M. R. Rocha

Department of Chemistry and Coimbra Chemistry Center, University of Coimbra 3004-535 Coimbra, Portugal.

A detailed survey of the major aspects of the C_2 , C_3 and C_4 elemental carbon clusters is presented. For the dimer, a summary of its current status is addressed. For C_3 , the most recent results obtained in our group are reviewed with special emphasis onto the modeling of its potential energy surface (PES) which is particularly complicated due to the presence of multiple conical intersections. Regarding C_4 , the most stable isomeric forms for both triplet and singlet PESs and their possible interconversion pathways are here examined afresh by means of high-level *ab initio* calculations. The main strategies toward a global modeling of the ground-state PES of triplet C_4 have also been discussed. Starting from an approximate cluster expansion of the molecular potential that utilizes previously reported function for C_3 , an approximate four-body term has been calibrated using accurate *ab initio* energies. The resulting fully six-dimensional global DMBE form here reported reproduces all known topographical aspects of the title system as well as its linear-rhombic isomerization path accurately and is, therefore, commended for both spectroscopic and reaction dynamics studies.

1. Introduction and historical remarks

The study of pure carbon chains has fascinated chemists and physicists over the years [1,2]. They were first identified more than a century ago [3] in astrophysical objects but still are today a topic of increasing interest. Small C_n clusters play a major role in the chemistry of carbon stars [4,5], comets [3,6], and interstellar molecular clouds [7,8], while acting as building blocks for formation of complex carbon-containing compounds [9,10]. Besides such an astrophysical significance, C_n chains can be chief intermediates in chemical vapor deposition systems for production of carbon-rich thin films [11], and be predominant species in terrestrial sooting flames [1,2]. Their fascinating physicochemical properties find justification on the exceptional bonding flexibility of carbon as demonstrated by its unique ability to form single, double, and triple (even speculations of quadruple for $C_2(X^1\Sigma_g^+)$ [12–19]) bonds.

The richness of the carbon chemistry is clearly evinced by the structural diversity of carbon allotropes, which include [20] diamond, graphite, fullerenes [21], nanotubes [22], graphenes [23] and other elusive periodic scaffolds [24], all with outstanding electronic, material or biological properties. Elucidation of possible mechanisms for formation of such aggregates (*i.e.*, their evolution from linear to monocyclic/polycyclic rings to fullerene/cage-like structures) is only attainable once the properties of their precursors (smallest clusters) have been clarified [25–29].

Small C_n clusters are highly reactive species which makes their experimental characterization cumbersome [1,2]. On the other hand, the existence of several (nearly isoenergetic) isomers, a high-density of low-lying singlet/triplet electronic states, and a significant multi-reference (MR) character, makes their study theoretically challenging [30–39]. Clearly, a detailed knowledge of the structure and energetics of such species requires a faithful interplay between state-of-the-art experimental techniques and high-level *ab initio* calculations.

Most of our knowledge on the title molecules began with the seminal work of Pitzer and Clementi [40]. They first recognized that linear C_n molecules are low energy isomeric forms with odd- and even-numbered chains (for $n > 2$) attaining $^1\Sigma_g^+$ and $^3\Sigma_g^-$ ground electronic states, respectively. Typically, for such systems, cumulenic structures ($\text{:C=C}\cdots\text{C=C:}$) are lower in energy than acetylenic ($\text{:C}\equiv\text{C}-\text{C}\cdots\text{C}\equiv\text{C:}$) bonding configurations [1,2,40,41]. More recently, supported by *ab initio* calculations, low-lying monocyclic isomers have also been conjectured as being isoenergetic or even more stable than linear arrangements [25–29,39]. In this work, we survey the current status on the smallest clusters (C_2 , C_3 and C_4) but keeping the focal point on the trimer and tetramer. For C_3 , we review our recent work in section 2, while in section 3(a) high-level *ab initio* calculations are reported anew for C_4 . A global 6D potential energy surface (PES; see Glossary at end of the paper for all acronyms) of ground-state triplet C_4 is also provided for the first time in section 3(b).

(a) The carbon dimer: the best studied carbon cluster

The most abundant molecules in carbon vapor produced by laser vaporization of graphite are C_2 and C_3 [42–44], with the former being widely quoted as important stacking sub-units during formation (growth) of medium to large-sized fullerenes [45]. Their spectroscopy has been extensively studied over the years, making them by far the best characterized carbon clusters [1,2].

As first observed by Wollaston [46] and Swan [47], C_2 is responsible for the blue glow emanating from hydrocarbon flames. These well-known $d^3\Pi_g-a^3\Pi_u$ Swan bands (the spectroscopic notation employed throughout is the updated one [48]) at 19380.1 cm^{-1} have long been recognized in cometary spectra [49]. Despite previous knowledge of the Phillips ($A^1\Pi_u-X^1\Sigma_g^+$) and Mulliken ($D^1\Sigma_u^+-X^1\Sigma_g^+$) bands involving singlet states [50], the prominence of the Swan emission/absorption features in the laboratory and astrophysical sources led to consider $a^3\Pi_u$ as the ground state of C_2 . This changed with Ballik and Ramsay in 1959 [50] during investigations of the $b^3\Sigma_g^- - a^3\Pi_u$ system (so-called Ballik-Ramsay band). They observed perturbations in the rotational levels of the $^3\Sigma_g^-$ state which were attributed to the presence of a neighboring singlet state. From the analysis of the spectral lines, the authors first confirmed that $^1\Sigma_g^+$ is the ground state of the carbon dimer. In fact, it lies only 603.8 cm^{-1} below the $a^3\Pi_u$ state [48]. Later on, several other singlet, triplet, quintet and intercombination band systems of the carbon dimer have been reported in the literature [1,2,48,51]. At present, C_2 has a total of 23 identified band systems, covering the spectral range $0\text{--}55000\text{ cm}^{-1}$, and 21 spectroscopically characterized electronic states; see Refs. 1, 2, 51, and 48 for a review. Guided by this well-known and rich rovibronic line list, the identification C_2 was made possible in a plethora of astrophysical sources, including carbon stars, comets, interstellar medium, and the sun [1,2,48]. Such a wealth of spectroscopic information has been recently utilized [48] to obtain highly accurate partition functions and thermodynamic data of C_2 up to 4000 K.

The first theoretical work on carbon dimer dates back to 1939 by Mulliken [52]. Using known experimental information on C_2 , molecular orbital arguments and an empirical formula for

estimating internuclear distances (R_0), he predicted mean relative energies and R_0 values for various low-lying states. Besides assigning the observed band system at 43239.8 cm^{-1} due to $^1\Sigma_g^+ - ^1\Sigma_g^+$ transition (now known under his name), Mulliken commented on the possibility that $^1\Sigma_g^+$ could be the “normal state” of carbon dimer. Apart from the pioneering semiempirical work of Araki *et al.* [53], the first VB calculations on C_2 were performed by Clementi and Pitzer [54]. The authors expanded the wave functions of the six lowest states arising from $2\sigma_g^2 2\sigma_u^2 1\pi_u^4$ ($^1\Sigma_g^+$), $2\sigma_g^2 2\sigma_u^2 1\pi_u^3 3\sigma_g^1$ ($^3\Pi_u, ^1\Pi_u$) and $2\sigma_g^2 2\sigma_u^2 1\pi_u^2 3\sigma_g^2$ ($^3\Sigma_g^-, ^1\Delta_g, ^1\Sigma_g^+$) valence configurations in terms of covalent, ionic and double-ionic components whose contributions have been variationally determined. Although the results agreed reasonably with the experimental data at that time (the $^3\Pi_u$ curve turned out to be lowest in energy), the authors recognized the need of a more refined theory to fully understand the inherent complexities of the system. Read and Vanderslice were the first to report PECs of C_2 using the RKR method [55]. Based on the findings of Ballik and Ramsay [50] concerning the true ground state of the system, the authors also tentatively calculated dissociation energies for the 9 upper-lying electronic states [55]. To our knowledge, the first purely *ab initio* calculations performed on the dimer are due to Fraga [56], Fougere [57] and Kirby [58] using CI wave functions with Slater-type orbitals. In the most complete work in these series, Kirby and Liu reported PECs for 62 valence states of C_2 , including 28 singlets, 28 triplets, and 6 quintets that correlate with carbon atoms in their $^3P, ^1D$ and 1S states [58]. Such calculations rendered the identification of 19 possible bound states not yet observed experimentally at that time together with the determination of their spectroscopic constants. In turn, Watts and Bartlett [59] performed CCSD(T) calculations with several Dunning’s correlation consistent basis sets [60,61]. The discrepancies found in the prediction of the $^1\Sigma_g^+ / ^3\Pi_u$ energy splittings have been attributed to the strong MR character of ground-state. Such aspect has previously been emphasized by Bauschlicher and Langhoff [62] by means of CASSCF and MRCI calculations.

Since then, C_2 has been the subject of extensive *ab initio* MRCI [30–32,63–71], full CI [72,73], quantum Monte Carlo [74] and explicit correlated MR [75] calculations aiming at obtaining accurate analytic representations of the various PECs (and their avoided crossings [30–32]), electronic excitation energies, dissociation energies and spectroscopic parameters. Note that these latter approaches frequently rely on extrapolations to the one- and/or \mathcal{N} -electron basis sets, core and core-valence correlation contributions, and also relativistic corrections. As argued several times [72–75], the presence of various low-lying excited electronic states and its unusual bonding behavior makes C_2 a notoriously challenging benchmark test for quantum chemical methods. Recently, with the aid of high-level MR calculations and state-of-the-art experimental techniques, Krechkivska *et al.* reported the existence of novel $4^3\Pi_{g-a} - ^3\Pi_u$ [69] and $3^3\Pi_{g-a} - ^3\Pi_u$ [71] systems (referred to as Krechkivska-Schmidt bands) and provided an accurate value for the carbon dimer ionization energy [70].

$\text{C}_2(X^1\Sigma_g^+)$ is one of the most strongly bonded diatomic molecule in nature [14,18,19]. Besides being the simplest possible carbon cluster, its bonding has eluded chemists over the years and continues to render extensive debate [12–19]. The simple assumption of a $2\sigma_g^2 2\sigma_u^2 1\pi_u^4$ valence configuration and molecular orbital arguments would suggest a bond order of two [52] ($:\text{C}=\text{C}:$), while qualitative VB considerations (*e.g.*, assuming two *sp*-hybridized carbons) yield a triply-bonded species, $\cdot\text{C}\equiv\text{C}\cdot$ [12]. Recently, using high-level VB calculations, Shaik and co-workers [13,14,18,19] proposed the existence of a fourth σ -bond on ground-state C_2 (first contemplated by Mulliken [52] and Schleyer *et al.* [76] for excited states). It arises from the interactions between the “residual” singlet odd pair, pointing outwards on the *sp* hybrids, *i.e.*, $\overline{\text{C}\equiv\text{C}}$. This additional “inverted” bond would contribute $\approx 70\text{--}90 \text{ kJ mol}^{-1}$ to the overall interaction. This has been disputed [15–18], with no consensus yet reached about the C_2 bonding nature.

(b) The carbon trimer

The smallest cluster capable of forming cyclic structures is C_3 . Its well-known $\tilde{A}^1\Pi_u - \tilde{X}^1\Sigma_g^+$ emission spectrum was first recorded by Huggins in 1881, while investigating unknown cometary emission features near 24675.6 cm^{-1} [3]. These so-called Swings emission bands [1] were first

reproduced in laboratory by Herzberg [77]. Although the emitter was initially thought to be CH₂ [77], the unambiguous assignment to linear C₃ is due to Douglas [78] and Gausset *et al.* [79,80], who performed spectroscopic investigations on discharges through ¹³C-substituted methane and flash photolysis of diazomethane, respectively. From the high resolution spectra, Gausset *et al.* first emphasized the unusual low bending frequency of *l*-C₃($\tilde{X}^1\Sigma_g^+$) with $\nu_2 \approx 63 \text{ cm}^{-1}$ as well as the strong RT vibronic interactions of the excited *l*-C₃($\tilde{A}^1\Pi_u$). Such features are responsible for the observed intricate vibrational spectrum [79,80]. Several gas-phase and matrix studies of C₃ have subsequently been devoted to its spectroscopic characterization, resulting in the assignment of the most ground and upper state vibrational frequencies of the $\tilde{A}^1\Pi_u$ - $\tilde{X}^1\Sigma_g^+$ band [81–85] and the discovery of a low-lying triplet electronic state manifold [86–88]. In fact, the carbon trimer is perhaps one of the best characterized nonrigid triatomics in existence [2,89].

C₃ has been observed in a wide range of astrophysical sources [90,91], including circumstellar shells of carbon stars [4,92,93], interstellar molecular clouds [7,94–96], and comets [3,92]. Its mid-IR spectrum (ν_3 antisymmetric stretching mode) was measured in the circumstellar envelope of the C-rich star IRC+10216 by Hinkle *et al.* [4], and the far-IR one (ν_2) detected in the direction of Sgr B2 by Cernicharo *et al.* [92]. The abundance of C₃ were determined in translucent clouds by Maier *et al.* [95], Roueff *et al.* [96] and Oka *et al.* [90] through its Swings' electronic transition. As the most abundant small pure carbon molecule in the interstellar medium, C₃ along with C₂ are key to formation of more complex carbon clusters, long-chain cyanopolyynes, carbon dust and polycyclic aromatic hydrocarbons [1,2]. In addition to its astrophysical importance, it is the predominant carbon cluster in equilibrium hot carbon vapor [2,42,44], hydrocarbon flames [1,2], and plasmas generated through energetic processing of carbon-containing materials [2,97,98].

The relevance of C₃ in space as well as in terrestrial sooting flames and combustion processes has motivated many theoretical [34–36,40,99–117] studies both in the ground and low-lying excited singlet and triplet electronic manifolds [33,114,118]. In particular, much effort has been devoted to obtain local (near-equilibrium) ground-state PESs [119] with a view to explore its *quasi*-linearity and unusual large amplitude bending motions.

Early *ab initio* SCF studies due to Pitzer and Clementi *et al.* [40,99,100] agree on an electronic structure of the form :C=C=C: with C₃ assumed linear. Hoffmann [101] reported extended Hückel calculations and predicted it to be nonlinear with an equilibrium CCC bond angle of $\approx 160^\circ$ and a barrier to linearity of only $\approx 63 \text{ cm}^{-1}$. Motivated by the discrepancies found in the calculated and experimental entropy values of C₃ as well as the proposition by Gausset and co-workers that the molecule could be *quasi*-linear, Liskow *et al.* [102] have subsequently performed SCF and CI studies. They highlighted for the first time the unusual bending potential of C₃ as well as the importance of adding d functions to the basis set. In turn, Perić-Radić and co-workers [103] used MRCI calculations and a double- ζ -plus-polarization basis set to report curves for the symmetric, bending and antisymmetric stretching of the ground and first excited ^{1,3} Π_u trimeric states. The strong RT vibronic interactions to which the Π_u states are subjected was pointed out for the first time [103]. To the best of our knowledge, the first global PES for the ground state of C₃(¹ A') has been reported by Carter, Mills and Murrell [105]. The authors employed the MBE [105,119,120] formalism jointly with the experimentally determined force field of Gausset *et al.* and 40 *ab initio* energies [102,104] to obtain an analytic form that exactly reproduces an early experimental heat of formation, geometry, and force constants of *l*-C₃($\tilde{X}^1\Sigma_g^+$). Additionally, other relevant topographical attributes such as the C_{2v} transition-states for isomerization between the three equivalent symmetry-related minima are described, as well as an accurate characterization of the adiabatic atom+diatom asymptotic limits, C₂(³ Π_u)+C(³ P) [105–107,119].

Following a previous observation due to Liskow *et al.* that ground-state *l*-C₃ correlates with an ¹ E' term at equilateral triangular geometries, Whiteside *et al.* [121] used MP4SDQ/6-31G*//HF/6-31G* to understand the JT nature of the PES. They noted for the first time that both C_{2v} transition-state and linear minimum arise from JT distortions of the D_{3h} structure; the corresponding isomerization barrier was predicted to be about 125.1 kJ mol⁻¹. Additionally,

they have pointed out that a triplet ${}^3A'_2$ term arises from the e'^2 valence configuration, with its minimum occurring at equilateral triangular geometries.

Kraemer *et al.* [108] using CISD(Q) and a triple- ζ -plus-polarization basis set reported a local PES which has been expressed as a force field expansion. Its minimum shows the C_3 radical as a bent species with an equilibrium bond angle of $\sim 162^\circ$ and a barrier to linearity of 21 cm^{-1} . The results suggested C_3 to be *quasi-linear*. Such a finding was reinforced by Jensen [109] who used the MORBID Hamiltonian [122] along with experimentally determined bend-stretch term values to obtain an analytic PES for the ground electronic state of C_3 [109]. These earlier PESs were soon superseded by *ab initio* ones from CASSCF calculations [110,111] which suggested C_3 to be non-*quasi-linear* but possessing an exceptionally flat bending potential.

Mladenović *et al.* [113] published an extensive theoretical study of C_3 based on SR CCSD(T) calculations and a basis set of near AVQZ quality. An analytical local PES has also been calibrated from a total of 108 *ab initio* energies up to about 3000 cm^{-1} above the equilibrium geometry by least-squares fitting a Taylor-series-type expansion. With a rmsd of $\sim 2\text{ cm}^{-1}$, such a form reproduces the rovibrational spectrum of C_3 within 8 cm^{-1} up to the specified energy range.

Ahmed, Balint-Kurti and Western (ABW) [34] and Saha *et al.* [114] employed MRCI(Q) calculations with the VTZ basis set to model local near-equilibrium PESs for both the ground and excited $\tilde{A}^1\Pi_u$ and $\tilde{D}^1\Delta_g$ electronic states of the C_3 trimer, with the fitted parameters subsequently altered to mimic the experimental data. From these studies, important features were highlighted such as strong RT vibronic interactions for the Π and Δ excited states as well as the presence of a symmetry-required Ci between the ground and first excited singlet states of C_3 at D_{3h} geometries. Suffice to add that a total of 384 *ab initio* energies up to 8000 cm^{-1} above the equilibrium geometry has been employed to fit the ABW Taylor-series expansion for the ground state, which shows a rmsd of 13.2 cm^{-1} . As noted by the authors, their fit covers a range of $\approx 8713\text{ cm}^{-1}$ above ZPE and mimics 100 rovibrational levels within 3 cm^{-1} . Note that the purely *ab initio* PES shows a rmsd of about 61.6 cm^{-1} for the same levels.

Schröder and Sebald (SS) [115] reported a local PES for C_3 employing a quantum mechanical composite approach. Their form was obtained from fc-CCSD(T*)-F12b/AV5Z calculations, with the raw *ab initio* energies corrected additively such as to approximate higher-order correlations, core-core/core-valence effects and also scalar relativistic contributions. All calculated points were then fitted by a polynomial form with a standard deviation of 0.05 cm^{-1} [115]. From it, low-lying rotation-vibration energies for $J \leq 30$ and a few vibrational term energies up to $\approx 3500\text{ cm}^{-1}$ above ZPE have been reported, and shown to agree within 1 cm^{-1} with the observed values.

In Ref. 35, we have reported the first purely *ab initio*-based global PES for $C_3(1^1A')$ [known as DMBE I]. A total of 629 *ab initio* energies at MRCI/AVTZ level of theory have been employed to calibrate a DMBE [123–125] form. To account for the incompleteness of the basis set and truncation of the MRCI expansion, all calculated external correlation energies have been scaled prior to calibration via DMBE-SEC method [126], and fitted with a rmsd of 4.1 kJ mol^{-1} [35]. In this study, we outlined for the first time the existence of three symmetry-equivalent C_{2v} crossing seams in close proximity to the symmetry-required D_{3h} Ci. Because a third electronic state of $1^1A'$ symmetry ($1^1A'_1$ in D_{3h}) comes quite close in energy to the pair of intersecting states ($1^1E'$ in D_{3h}) near D_{3h} arrangements [36], such unusual topographical attributes have been ascribed to combined JT+PJT vibronic effects $[(E' + A'_1) \otimes e']$ with the proper cusped behavior modeled accordingly [127,128]. Exploratory rovibrational energy calculations have also been performed, and the DMBE I form shown to reproduce the vibrational energy spectrum of C_3 with a rmsd of 50.4 cm^{-1} for 53 calculated levels up to about 3000 cm^{-1} above ZPE [35]. The combined JT+PJT problem in C_3 has been further exploited by us [36] with intriguing results. We will come to it later on section 2, where other recent results from our group are also discussed for C_3 .

(c) The carbon tetramer

The existence of two low-lying isomeric structures of C_4 is widely accepted: the cumulenic linear chain [l - $C_4({}^3\Sigma_g^-)$], and the bicyclic rhombic [r - $C_4(1^1A_g)$] structures [37,38,129–141]. Along

with C_2 and C_3 , the title species is likely an important molecule in astrophysics and an abundant one in carbon-rich stars as well as interstellar molecular clouds [8,9]. Cernicharo *et al.* [8] reported a pattern of bands at 173.9 cm^{-1} observed in Sgr B2, IRC+10216, CRL 618, CRL 2688 and NGC 7027 which was tentatively assigned to the ν_5 cis-bending mode of $l\text{-C}_4(^3\Sigma_g^-)$. Motivated by the observation of C_3 in interstellar clouds [95], Maier *et al.* [142] were the first to attempt the detection of $l\text{-C}_4(^3\Sigma_g^-)$ in the ζ Ophiuchi star by measuring the origin bands of its well-known electronic transitions $^3\Sigma_u^- - ^3\Sigma_g^-$ at 26384.9 cm^{-1} [143]. Unfortunately, as stated by the authors [142], such a detection has not been pursued. Triplet C_4 has been first observed experimentally by Weltner *et al.* [144] and Graham *et al.* [145] using IR and electron spin resonance spectroscopy of graphite vapor trapped in inert-gas matrices. Heath and Saykally [146] first characterized such a species in gas phase through its antisymmetric CC stretching fundamental (ν_3) at 1548.9 cm^{-1} by means of tunable IR diode laser spectroscopy. Subsequently, Moazzen-Ahmadi *et al.* [147] revisited the rotational constant for the ν_3 mode. From this parameter and the associated averaged C=C bond length ($\approx 2.458\text{ a}_0$) [147], triplet C_4 was confirmed to be linear with a cumulenic structure [2,147]. A wealth of other experimental efforts have been done to characterize the title species [2,8,140,148,149]. As noted by Senent *et al.* [140], relatively large errors affect other modes besides the ν_3 fundamental, which makes a definitive assignment of $l\text{-C}_4$ in interstellar bands a rather difficult task. Apart from the linear isomer, experimental evidence for $r\text{-C}_4(^1A_g)$ was reported with the Coulomb explosion imaging technique [150–152]. Kella *et al.* [152], observed three distinct photodetachment wavelengths, and conjectured the existence of a third 3D isomer which has been attributed to a tetrahedral structure. However, this has not been supported by any other experimental or theoretical evidence [38,140]. More recently, Blanksby *et al.* [138] performed mass spectrometric studies on isotopically labeled C_4^- . Upon neutralization of the incident anions and based on the peak abundances of the spectra so obtained, they reported evidence of isotopic scrambling of both singlet ($^1\Sigma_g^+$) and triplet ($^3\Sigma_g^-$) neutral $l\text{-C}_4$ due to formation of the corresponding rhombic isomers [138].

C_4 has also been the subject of many theoretical studies [37,38,40,41,129–141], starting with the pioneering *ab initio* SCF calculations of Clementi [41]. To our knowledge and apart from semiempirical MINDO/2 studies of Slanina and Zahradnik [153], the first correlated *ab initio* calculations of the relative energies of $l\text{-C}_4(^3\Sigma_g^-)$ and $r\text{-C}_4(^1A_g)$ are due to Whiteside *et al.* [129] at MP4SDQ/6-31G*//HF/6-31G* level of theory. They have predicted the singlet rhombic structure to be 2.9 kJ mol^{-1} more stable than the linear chain, and hence the ground state of C_4 . The same authors further highlighted the existence of a C_{2v} planar isomeric form (a capped triangle) on the singlet PES which was found to lie $\sim 123.4\text{ kJ mol}^{-1}$ above the $r\text{-C}_4(^1A_g)$ [129]. Subsequent *ab initio* studies by Magers *et al.* [130], Bernholdt *et al.* [133], Martin *et al.* [136] and Watts *et al.* [137] employing the CC method, as well as CI calculations by Ritchie *et al.* [131] and Pacchioni *et al.* [132], have indicated the two isomers to be essentially isoenergetic, with the linear-rhombic energy difference being extremely sensitive to the basis set and correlation treatment [136,137]. In turn, Parasuk and Almöf [37] performed MRCI calculations using CAS wave functions as reference and ANO-type basis sets. At the highest level of theory, *i.e.*, 16-electron MRCI in a (13s8p4d)/[5s4p2d] ANO basis, with 5 dominant configurations in the CAS(10,10) wave function being included in the reference set [37], $l\text{-C}_4(^3\Sigma_g^-)$ was predicted to be the ground-state structure with a stabilization energy of $\sim 6.8\text{ kJ mol}^{-1}$ with respect to the 1A_g state. Motivated by earlier experimental results of Cheung and Graham [154] who conjectured the existence of triplet C_4 as a bent structure, Parasuk and Almöf [37] investigated the PES of $l\text{-C}_4(^3\Sigma_g^-)$ along the cis (ν_5)- and trans (ν_4)-bending modes whose frequencies have been estimated to be 211.0 and 428.0 cm^{-1} in the same order. In contrast to the floppy nature of C_3 [35,116,117], the authors were the first to point out the stiffness of the bending potential of C_4 , thence refuting any evidence for a bent structure in the gas phase [37]. In an attempt to assign some of the unknown transitions in the IR spectrum of carbon clusters trapped in Ar matrices [144], Martin *et al.* [135,136,155] suggested that the observed band at 1284 cm^{-1} was due to the ν_6 mode of $r\text{-C}_4(^1A_g)$. Subsequently, the authors [155] computed a QFF for such a species using 116 CCSD(T) energies with a VTZ basis [60,61].

Their best ν_6 estimate (including the strong Fermi resonance with the $\nu_3 + \nu_5$ combination band) was $1320 \pm 10 \text{ cm}^{-1}$, thence casting doubts on Martin's earlier statement [135,136,155]. As noted by the authors themselves [155], the correct assignment would then imply an unusual large matrix red shift in argon. Recently, Massó *et al.* [38] performed MRCI(Q)/VTZ calculations on C_4 keeping all configurations with coefficients larger than 0.03 in the CAS(8,12) wave function as the reference set. The results so obtained have shown $l\text{-}C_4(^3\Sigma_g^-)$ to be favored by about $100.7 \text{ kJ mol}^{-1}$ over $r\text{-}C_4(^1A_g)$, thus supporting the general trend that the linear triplet structure is the most stable form in MRCI calculations [37,38,132]. Besides various structural parameters of both singlet and triplet PESs, the authors evaluated isomerization pathways between such forms and reported other low-lying excited singlet, triplet and quintet electronic states [38]. To determine new spectroscopic parameters for C_4 and attempt a definitive assignment of the astrophysical band observed by Cernicharo *et al.* [8], Senent *et al.* [140] reported local PESs for both $l\text{-}C_4(^3\Sigma_g^-)$ and $r\text{-}C_4(^1A_g)$ isomers using about 1050 non-redundant energies calculated at MRCI(Q)/VTZ level [38]. The *ab initio* data so obtained has then been least squares fitted to a Taylor series expansion with a rmsd of 43 cm^{-1} , with spectroscopic parameters determined by standard vibrational perturbation theory (VPT2) [140]. Most recently, Wang *et al.* [141] reported a new QFF PES for $r\text{-}C_4(^1A_g)$ by fitting 255 CCSD(T)/CV5Z energies. A local PES covering a wider range of geometries has also been obtained using 2914 grid points at CCSD(T)-F12b/AVTZ level of theory, and updated sets of spectroscopic parameters reported for the rhombic isomer using VPT2 and vibrational configuration interaction calculations [141].

Despite the immense theoretical work done on C_4 [37,38,40,41,129–141,143], it is clear from such studies that only some very limited portions of the PES are well understood, namely regions close to the $l\text{-}C_4(^3\Sigma_g^-)$ and $r\text{-}C_4(^1A_g)$ minima. While knowledge of structural and spectroscopic parameters as well as the energetics are key for the identification of C_4 [especially, $r\text{-}C_4(^1A_g)$] in experimental analysis and astrophysical sources, many other important issues remain to assess. Of particular relevance is the determination of other stable (or even transient) isomeric forms and their interconversion pathways, which provide valuable information for understanding reactive collision processes and formation of C_n clusters in the interstellar medium [9]. In view of the above, we report new results on C_4 in section 3. By exploring the isomerization pathways between linear and rhombic structures on both singlet and triplet PESs, several other isomers of this species are unraveled, some reported for the first time. Based on the results so obtained and the many-body expansion, an approximate four-body term will be calibrated using high-level *ab initio* data and hence a global $6D$ PES for triplet C_4 .

2. Further on carbon trimer

(a) Electronic structure

Figure 1 shows the optimized bending potential for ground- and low-lying excited singlet states of C_3 at MRCI/AVTZ//CASSCF/AVTZ level of theory [35]. Note that for acute $\angle CCC$ angles ($< 30^\circ$), the optimization process leads naturally to the asymptotic channels, as the optimum bond length corresponds to widely separated atom+diatom fragments. As first pointed out by Murrell and coworkers [105–107,119], the ground state of C_3 does not dissociate adiabatically to ground-state fragments [$C_2(X^1\Sigma_g^+) + C(^3P)$], inasmuch as either C_2 or C must be on an excited state to satisfy the spin-spatial Wigner-Witmer correlation rules [156,157]; see section 2(d). As Figure 1 shows, all degenerate excited states at linear geometries ($\tilde{A}^1\Pi_u, \tilde{B}'^1\Delta_u, \tilde{C}^1\Pi_g, \tilde{D}^1\Delta_g$, etc) are subjected to strong RT vibronic interactions which are manifested as splittings into symmetric (A') and antisymmetric (A'') components as the molecule bends. Such electronic excited states show also numerous crossings between themselves for bending angles smaller than 140° . These are indicated by the symbol “ \times ” in Figure 1. However, an appreciable gap (up to 377 kJ mol^{-1}) is visible between the excited and ground-states for $\angle CCC \geq 100^\circ$. Note that the $\tilde{B}^1\Sigma_u^-$ and $\tilde{B}'^1\Delta_u$ states are close in energy, with the former predicted from our *ab initio* calculations to be $\approx 1.2 \text{ kJ mol}^{-1}$ more stable than the latter. As indicated by Ahmed *et al.* [34] and Saha *et al.* [114]

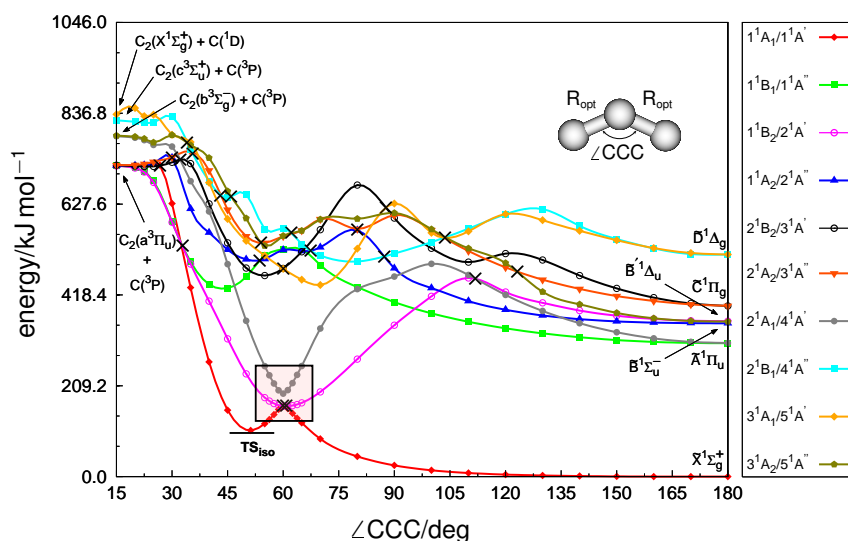


Figure 1. Optimized bending potentials for C_3 at MRCI/AVTZ//FVCAS/AVTZ level of theory as a function of the $\angle CCC$ angle. Shown in the key are the irreducible representations in C_{2v} symmetry for each state, and correlations within the C_s point group. Also shown are the associated correlations for linear geometries in $D_{\infty h}$ symmetry, and corresponding dissociation limits. Cis are indicated by the symbol “ \times ”. Energies are given with respect to the global minimum of C_3 of $D_{\infty h}$ symmetry.

such energetic proximity (near degeneracy) is expected to be of the same order of magnitude as the accuracy of the *ab initio* calculations themselves, and therefore a proper examination of their relative stability requires a higher level of theory. Recall [34,79,80,114] that the ground state bending potential is exceptionally flat, and hence large amplitude bending vibrations are expected: only 25.8 kJ mol^{-1} are required to bend C_3 up to $\angle CCC=90^\circ$.

A region that deserves attention refers to near equilateral triangular geometries ($\angle CCC=60^\circ$). As we have first noted [35,36], the C_3 PES shows there intriguing topographical attributes (highlighted in Figure 1 by the shaded square): rather than a single symmetry-dictated Ci, a strong mixing of two 1A_1 states occurs which pushes down the lowest to cross twice the 1B_2 state. Since similar cross-sections of Figure 1 exist for rotations by $\pm 120^\circ$, such a combined JT+PJT [$(E' + A_1') \otimes e'$] effect creates 4 Cis in the ground-state PES; see section 2(b). Note that distortions of the D_{3h} structure maintaining C_{2v} symmetry with bend angles $< 60^\circ$ lead to stabilization of the lower sheet and formation of a saddle point; see Figure 1. This represents the transition state (TS_{iso}) for isomerization between the three equivalent $D_{\infty h}$ minima in the ground state PES. Conversely, C_{2v} distortions with angles $> 60^\circ$ lead ultimately to the absolute $D_{\infty h}$ minima of C_3 .

(b) The Jahn-Teller plus pseudo-Jahn-Teller problem

As shown in Figure 1 and noted elsewhere [34–36,121], both the ground [$1^1A'(1^1A_1)$] and first excited [$2^1A'(1^1B_2)$] singlet states of C_3 correlate with the twofold E' irrep at D_{3h} geometries, thus yielding an e'^2 valence configuration (see Figure 2). At such geometries, four electronic states arise from HOMO→HOMO excitations

$$e' \otimes e' \xrightarrow{D_{3h}} A_1' + A_2' + (E') \xrightarrow{C_{2v}} A_1 + B_2 + (A_1 + B_2). \quad (2.1)$$

All of them correlate with the A' irrep in C_s symmetry. Similarly, higher excited states can be obtained from the HOMO−1→HOMO, HOMO→LUMO, and HOMO−2→HOMO excitations, but they are not here considered. At FVCAS/AVTZ, the leading (spin-spatial symmetry adapted)

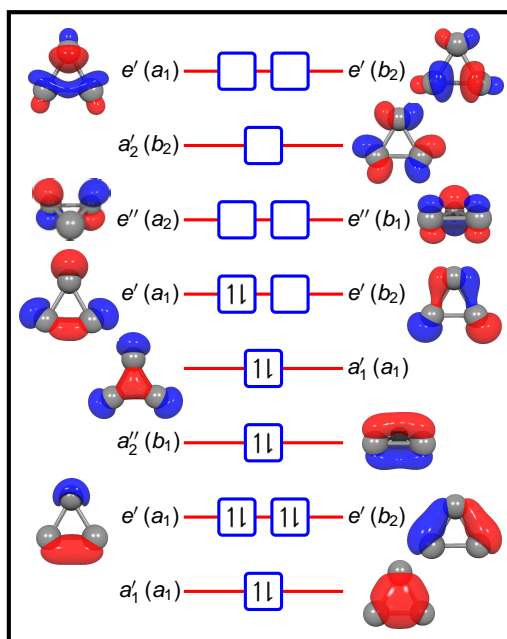


Figure 2. MO diagram and valence electronic configuration of C_3 at equilateral triangular geometries. The 1A_1 (in C_{2v}) component of the ${}^1E'$ term (in D_{3h}) is schematically shown. MOs are labeled according to D_{3h} irreps with the corresponding correlations with C_{2v} point group in parentheses. Up and down arrows denote as usual α and β spin states. Natural orbitals obtained from a state-averaged FVCAS/AVTZ wave function are also shown.

CSFs for each electronic term of Eq. (2.1) are then given by [36]

$$|\Psi_1 {}^3A_2'({}^3B_2)\rangle = |\alpha\rangle \quad (2.2)$$

$$|\Psi_2 {}^1E'({}^1A_1)\rangle = \frac{1}{\sqrt{\mathcal{A}^2 + \mathcal{B}^2}} [\mathcal{A} |\beta\rangle - \mathcal{B} |\gamma\rangle] \quad (2.3)$$

$$|\Psi_3 {}^1E'({}^1B_2)\rangle = \frac{1}{\sqrt{\mathcal{C}^2 + \mathcal{D}^2}} [\mathcal{C} |\delta\rangle - \mathcal{D} |\epsilon\rangle] \quad (2.4)$$

$$|\Psi_4 {}^1A_1'({}^2A_1)\rangle = \frac{1}{\sqrt{\mathcal{E}^2 + \mathcal{F}^2}} [\mathcal{E} |\beta\rangle + \mathcal{F} |\gamma\rangle], \quad (2.5)$$

where $|\alpha\rangle, |\beta\rangle, |\gamma\rangle, |\delta\rangle$ and $|\epsilon\rangle$ are Slater determinants schematically shown in Figure 3: $\mathcal{A}, \mathcal{B}, \mathcal{C}, \mathcal{D}, \mathcal{E}$ and \mathcal{F} are coefficients that weight the relative contributions in the associated CSF. At D_{3h} geometries, their ratios are approximately equal to one, with $|\mathcal{A}|=|\mathcal{B}|\approx|\mathcal{C}|=|\mathcal{D}|\approx|\mathcal{E}|=|\mathcal{F}|\approx 1$. However, if any distortion of the molecular triangle occur, the ratio of each determinant changes inasmuch as different CSFs belonging to the same spin and spatial symmetry can mix. As seen from Eqs. (2.2)-(2.5) and Figure 4, an ${}^3A_2'({}^3B_2)$ term lower than the ${}^1E'({}^1A_1, {}^1B_2)$ and ${}^1A_1'({}^2A_1)$ states also arises from the HOMO→HOMO excitations. Such a triplet state shows the minimum at a geometry with D_{3h} symmetry [$e-C_3({}^3A_2')$; see Table 1] and hence is non-JT [36,121].

A close inspection of Figures 1 and 4 gives an insight into the real nature of the vibronic problem. Clearly, instead of a typical linear $E' \otimes e'$ JT problem [158] in which only linear JT vibronic coupling constants are taken into account, the non-negligible contribution of the quadratic coupling constants is key for the title system (linear plus quadratic JT problem [158,159]). Additionally, an interaction occurs due to strong vibronic mixing between the close lying ${}^1E'$ and ${}^1A_1'$ states [158,160]. Such a JT+PJT [$(E' + A_1') \otimes e'$] vibronic problem introduces profound changes on the topology of the PESs near equilateral triangular geometries. Indeed, as

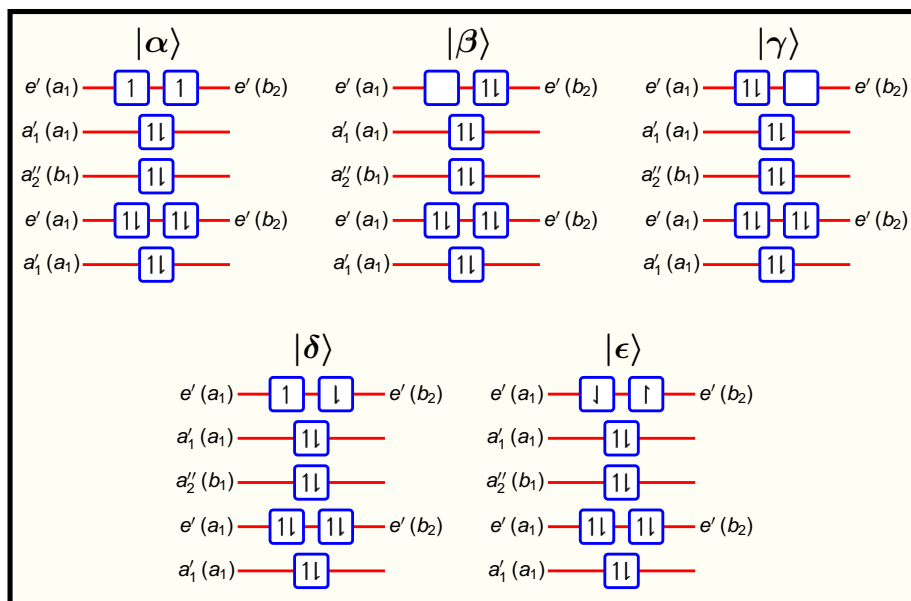


Figure 3. Slater determinants arising from HOMO→HOMO excitations in the e'^2 valence configuration of C_3 (Figure 2). All MOs are labeled according to D_{3h} irreps with the corresponding C_{2v} correlations given in parentheses. Up and down arrows denote α and β spin states.

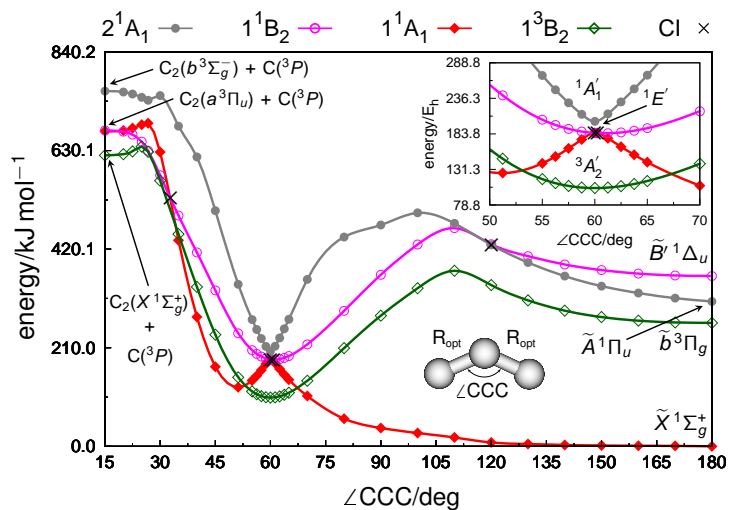


Figure 4. Optimized FVCAS/AVTZ bending potential for the four electronic states of C_3 arising from HOMO→HOMO excitations in the e'^2 configuration [see Eqs. (2.1)-(2.5)]. Shown in the key are the irreps, in C_{2v} symmetry, for each state. Cis are indicated by the symbol \times .

we have first shown [36] for both the ground ($1^1A'$) and first excited ($2^1A'$) singlet states of C_3 radical, besides the D_{3h} symmetry-required crossing seam there are three symmetry-equivalent C_{2v} seams in close proximity to the former central Ci. A cross-sectional cut of such a region is shown in Figure 5 at MRCI/AVTZ level of theory [36]. Note that $\mathbf{Q}=(Q_1, Q_2, Q_3)$ defines the

Table 1. Properties of stationary points on ground and excited PESs of C_3 . Structures are labeled by the irrep, and energies (in kJ mol^{-1}) are relative to the $D_{\infty h}$ absolute minimum [$l\text{-}C_3(^1\Sigma_g^+)$] of the ground state PES. Bond lengths (R), bond angles ($\angle CCC$) and harmonic vibrational frequencies (w_i) are in a_0 , degrees, and cm^{-1} .

Structure	Method ^a	R	$\angle CCC$	ΔE	w_1	w_2	w_3
$l\text{-}C_3(^1\Sigma_g^+)$	FVCAS/AVTZ	2.474	180.0	0.0	1171.0	56.1	2060.9
	CBS			0.0			
$c\text{-}C_3(^3A_2')$	FVCAS/AVTZ	2.629	60.0	114.6	1508.3	1064.2	1064.2
	CBS			84.2			
$d\text{-}C_3(^1B_2)$	FVCAS/AVTZ	2.629	60.9	195.5	1512.7	1124.7	3690.7
	CBS			151.3			
	Eq. (2.9)	2.616	60.8				
$c\text{-}C_3(^1A_1')$	FVCAS/AVTZ	2.678	60.0	213.0	1456.3	5069.5	5069.5
	CBS			185.6			
	Eq. (2.9)	2.626	60.0				

^a Data retrieved from Ref. 36.

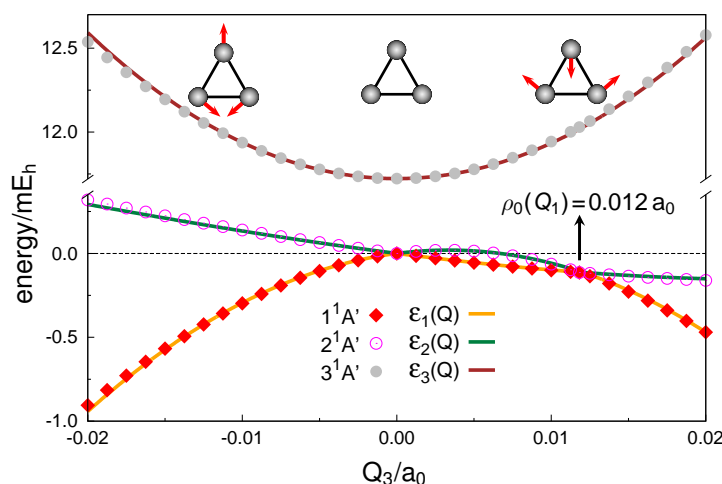


Figure 5. PES cuts along the bending coordinate Q_3 [for $Q_2=0$ and $Q_1=4.548 a_0$] for the three lowest $^1A'$ electronic states of C_3 over the range of $-0.020 a_0 \leq Q_3 \leq 0.020 a_0$. Symbols indicate MRCI/AVTZ points, and the solid lines the associated eigenvalues of Eq. (2.9) as obtained from the least-squares fitting procedure.

standard (symmetry-adapted) JT coordinates in terms of the internuclear distances by [119,125]

$$\begin{pmatrix} Q_1 \\ Q_2 \\ Q_3 \end{pmatrix} = \begin{pmatrix} \sqrt{1/3} & \sqrt{1/3} & \sqrt{1/3} \\ 0 & \sqrt{1/2} & -\sqrt{1/2} \\ \sqrt{2/3} & -\sqrt{1/6} & -\sqrt{1/6} \end{pmatrix} \begin{pmatrix} R_1 \\ R_2 \\ R_3 \end{pmatrix}, \quad (2.6)$$

where Q_1 is the totally symmetric representation $a_1(a_1)$ or breathing mode, and (Q_2, Q_3) is the pair of $e(b_2, a_1)$ JT active vibrations associated with the asymmetric stretch and bending normal modes, respectively. As noted above, cross-sections similar to Figure 5 exist for rotations by $\pm 120^\circ$, with $\rho(Q_1) = \sqrt{Q_2^2 + Q_3^2}$ being the radial polar coordinate in the 2D branching plane [$Q_b(Q_1) = (Q_2, Q_3)$]. Thus, for the circle of radius ρ_0 , the 4 CIs are defined by $Q_b(Q_1) = (0, 0)$, and $Q_b(Q_1) = (0, \rho_0)$, $(-\sqrt{3}\rho_0/2, -\rho_0/2)$, $(\sqrt{3}\rho_0/2, -\rho_0/2)$.

To model the above JT+PJT $[(E' + A'_1) \otimes e']$ vibronic problem, we write the electronic Hamiltonian (H_e) as a Taylor series expansion in the nuclear displacements from the high-symmetry D_{3h} configuration, [158,160]

$$\begin{aligned} H_e(\mathbf{r}, \mathbf{Q}) &= H_e^{(0)}(\mathbf{r}, \mathbf{0}) + \sum_{\bar{\Gamma}\bar{\gamma}} \left(\frac{\partial V}{\partial Q_{\bar{\Gamma}\bar{\gamma}}} \right)_0 Q_{\bar{\Gamma}\bar{\gamma}} \\ &+ \frac{1}{2} \sum_{\bar{\Gamma}\bar{\gamma}} \sum_{\bar{\Gamma}_1\bar{\Gamma}_2} \left\{ \left(\frac{\partial^2 V}{\partial Q_{\bar{\Gamma}_1} \partial Q_{\bar{\Gamma}_2}} \right)_0 \right\}_{\bar{\Gamma}\bar{\gamma}} \{Q_{\bar{\Gamma}_1} \otimes Q_{\bar{\Gamma}_2}\}_{\bar{\Gamma}\bar{\gamma}} + \dots \\ &= H_e^{(0)}(\mathbf{r}, \mathbf{0}) + W(\mathbf{r}, \mathbf{Q}), \end{aligned} \quad (2.7)$$

where the zeroth-order Hamiltonian $H_e^{(0)}(\mathbf{r}, \mathbf{0}) = H(\mathbf{r}) + V(\mathbf{r}, \mathbf{0})$ includes the purely electronic part $[H(\mathbf{r})]$ and the electron-nuclear plus nuclear-nuclear interactions $[V(\mathbf{r}, \mathbf{0})]$ with the nuclei fixed at origin (\mathbf{Q}_0); \mathbf{r} is the set of electronic coordinates, and $Q_{\bar{\Gamma}\bar{\gamma}}$ symmetrized nuclear displacements [see Eq. (2.6)] which transform according to the line $\bar{\gamma}$ of the D_{3h} irrep $\bar{\Gamma}$. In turn, $W(\mathbf{r}, \mathbf{Q})$ is the vibronic coupling perturbative operator whose matrix elements (vibronic constants) measure the effect of changes in the electronic structure upon nuclear motion [158,160]. Note that $\{(\partial^2 V / \partial Q_{\bar{\Gamma}_1} \partial Q_{\bar{\Gamma}_2})_0\}_{\bar{\Gamma}\bar{\gamma}}$ defines an irreducible product [161] (tensor convolution [158]); this is a linear combination of second derivatives with respect to $Q_{\bar{\Gamma}_1}$ and $Q_{\bar{\Gamma}_2}$, which transforms according to the line $\bar{\gamma}$ of the D_{3h} irrep $\bar{\Gamma} \subset \bar{\Gamma}_1 \otimes \bar{\Gamma}_2$. Likewise, $\{Q_{\bar{\Gamma}_1} \otimes Q_{\bar{\Gamma}_2}\}_{\bar{\Gamma}\bar{\gamma}}$ denotes the irreducible product for the corresponding symmetrized coordinates.

The starting point consists therefore of solving the electronic Schrödinger equation with the nuclei fixed at the origin

$$H_e^{(0)}(\mathbf{r}, \mathbf{0})|\varphi_k(\mathbf{r}, \mathbf{0})\rangle = \mathcal{E}_k(\mathbf{0})|\varphi_k(\mathbf{r}, \mathbf{0})\rangle \quad (2.8)$$

where $\{|\varphi_k\rangle\} \equiv \{|\Psi_2^1 E'(1^1 A_1)\rangle, |\Psi_3^1 E'(1^1 B_2)\rangle, |\Psi_4^1 A'_1(2^1 A_1)\rangle\}$ is the orthonormal set of eigenvectors (the eigenvalues are $\{\mathcal{E}_k(\mathbf{0})\}$) here utilized to approximate the electronic function space with the nuclei clamped at \mathbf{Q}_0 . The corresponding matrix representation of the electronic Hamiltonian H_e [Eq. (2.7)] in such a basis assumes the form [36,162]

$$\mathbf{H}_e = \begin{pmatrix} -F_{E'} Q_3 + \kappa_{E'} - G_{E'}(Q_2^2 - Q_3^2) & F_{E'} Q_2 + 2G_{E'} Q_2 Q_3 & H_{E'/A'_1} Q_3 \\ F_{E'} Q_2 + 2G_{E'} Q_2 Q_3 & F_{E'} Q_3 + \kappa_{E'} + G_{E'}(Q_2^2 - Q_3^2) & H_{E'/A'_1} Q_2 \\ H_{E'/A'_1} Q_3 & H_{E'/A'_1} Q_2 & \Delta + \kappa_{A'_1} \end{pmatrix}, \quad (2.9)$$

where $\kappa_{E'}(\mathbf{Q}) = \frac{1}{2} K_{E'}(Q_2^2 + Q_3^2)$ and $\kappa_{A'_1}(\mathbf{Q}) = \frac{1}{2} K_{A'_1}(Q_2^2 + Q_3^2)$ are harmonic potentials for the $^1 E'$ and $^1 A'_1$ electronic states centered at \mathbf{Q}_0 , with force constants $K_{E'}$ and $K_{A'_1}$. In turn, $F_{E'}$ and $G_{E'}$ are linear and quadratic JT vibronic coupling constants, respectively, and H_{E'/A'_1} is the associated linear PJT parameter [36,162]. Correspondingly, Δ denotes the energy gap (at the origin) between the vibronically mixed $^1 E'$ and $^1 A'_1$ terms. Note that the vibronic coupling constants of Eq. (2.9) can be obtained from group-theoretic considerations [158,161]; see Appendix. They were all determined from a fit to *ab initio* MRCI/AVTZ energies, with the numerical values and definition given in Table 2. As seen, the linear JT vibronic constant ($F_{E'}$) is small: about 1 and 2 orders of magnitude smaller than H_{E'/A'_1} and $G_{E'}$, respectively. This is the signature of so-called small linear parameter (SLP) JT molecules [159,163].

The solutions of the present JT+PJT vibronic problem are shown in Figures 5 and 6. Clearly, the model reproduces the full picture of the adiabatic PESs near D_{3h} symmetry, including the cusped behavior at all electronic degeneracies and vibronic mixing between close-in-energy terms. Interestingly, the current three state JT+PJT model Hamiltonian also predicts a stationary point [labeled $d\text{-}C_3(^1 B_2)$] in the $2^1 A'$ electronic state. Such a structure has been confirmed by *ab initio* FVCAS/AVTZ optimizations, and shown to be a minimum; see Table 1. Note that the PJT vibronic effect provides an additional stabilization of the undistorted D_{3h} minimum of the $3^1 A'$ state. Note also from Table 1 that the predicted structures agree well with the *ab initio* ones.

Table 2. Vibronic coupling constants and parameters in Eq. (2.9). The numerical data was obtained from a fit to the *ab initio* MRCI/AVTZ energies in Figure 5.

Parameter ^a	Expression ^b	Value ^a
$K_{E'}$	$\langle {}^1E'_{\theta/\epsilon} \left(\frac{\partial^2 V}{\partial Q_2^2} \right)_0 + \left(\frac{\partial^2 V}{\partial Q_3^2} \right)_0 {}^1E'_{\theta/\epsilon} \rangle$	351.3 ^c
$K_{A'_1}$	$\langle {}^1A'_1 \left(\frac{\partial^2 V}{\partial Q_2^2} \right)_0 + \left(\frac{\partial^2 V}{\partial Q_3^2} \right)_0 {}^1A'_1 \rangle$	399.0 ^c
$F_{E'}$	$\langle {}^1E'_\epsilon \left(\frac{\partial V}{\partial Q_3} \right)_0 {}^1E'_\epsilon \rangle$	11.8 ^d
$G_{E'}$	$\langle {}^1E'_\epsilon \left(\frac{\partial^2 V}{\partial Q_2^2} \right)_0 - \left(\frac{\partial^2 V}{\partial Q_3^2} \right)_0 {}^1E'_\epsilon \rangle$	1940.0 ^c
H_{E'/A'_1}	$\langle {}^1E'_\epsilon \left(\frac{\partial V}{\partial Q_2} \right)_0 {}^1A'_1 \rangle$	150.8 ^d
Δ		11.7 ^e

^aRef. 36. ^bThe following symmetry correlations have been employed: $|\Psi_2 {}^1E'(1^1A_1)\rangle \equiv |{}^1E'_\theta\rangle$, $|\Psi_3 {}^1E'(1^1B_2)\rangle \equiv |{}^1E'_\epsilon\rangle$ and $|\Psi_4 {}^1A'_1(2^1A_1)\rangle \equiv |{}^1A'_1\rangle$. ^cUnits in $\text{mE}_h \text{a}_0^{-2}$. ^dUnits in $\text{mE}_h \text{a}_0^{-1}$. ^eUnits in mE_h .

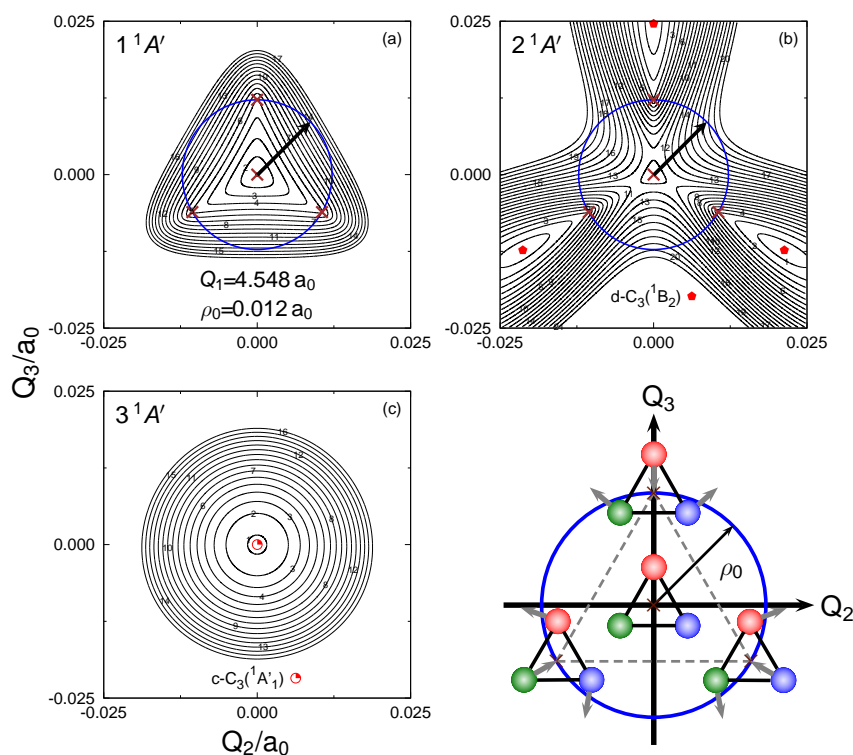


Figure 6. Contour plot of the lowest eigenvalues of the JT+PJT vibronic Hamiltonian of C_3 [Eq. (2.9)] for $Q_1=4.548 \text{a}_0$; (a) $1^1A'$; (b) $2^1A'$; (c) $3^1A'$. Contours in (a) are equally spaced by -0.0300mE_h starting at 0.0000mE_h , with values of 0.0168mE_h and -0.2000mE_h for (b), and 0.0500mE_h and 11.7224mE_h for (c). Cis are indicated by crosses (\times).

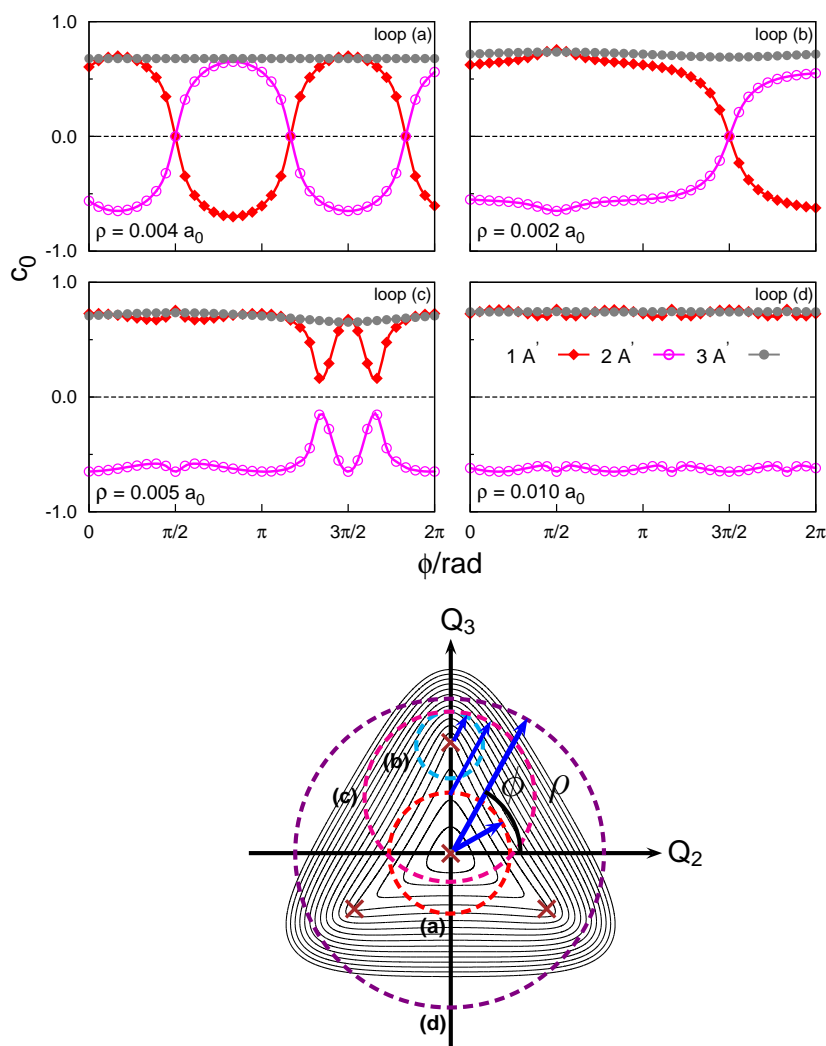


Figure 7. Adiabatic evolution of the $1^1 A'$, $2^1 A'$ and $3^1 A'$ wave functions of C_3 along a closed circuit C in the two dimensional branching plane encircling one or more Cis. c_0 is the coefficient of the leading determinant (CSF) of the FVCAS/AVTZ wave function for each state. Four closed loops are considered that encircle: (a) the central (D_{3h}) Ci; (b) one C_{2v} Ci; (c) two Cis; (d) four Cis. See also text.

(c) The Longuet-Higgins sign-change theorem

As stated by the Longuet-Higgins' theorem [164]: if a real-valued electronic wave function changes sign when adiabatically transported around a closed circuit C in the two-dimensional branching plane, then it must become discontinuous and degenerate with another state at an odd number of points lying on that surface and within that loop [164–166]. Varandas, Tennyson and Murrell [167] were the first to demonstrate the numerical validity of such sign-reversal criterion for LiNaK by following the variation of the dominant coefficients in the ground-state wave function along a path that encircles the crossing point [167]. We have followed the same approach with state-averaged FVCAS/AVTZ calculations. The results are shown in Figure 7.

As first pointed out by Zwanziger and Grant [159], for SLP JT molecules the additional three symmetry-equivalent C_{2v} seams may prevent the associated electronic wave function of changing sign when transported around a loop enclosing the four Cis. In other words, the net geometric

Table 3. Functional representation of the three-body EHF energy terms shown in Eq. (2.12) for the DMBE I and DMBE II PESs.

X	$V_{x,\text{EHF}}^{J(3)}$	$V_{x,\text{EHF}}^{J''(3)}$	$V_{x,\text{EHF}}^{J'''(3)}$
I^a	$(P_1^{N'} - \sqrt{T_2} P_2^{M'}) T_1'$	$(P_3^{N''} - \Delta_1 \Delta_2 \Delta_3 P_4^{M''}) T_1''$	0
II^b	$(P_1^{N'} - \mathcal{F}_{nJT} \sqrt{T_2} P_2^{M'}) T_1'$	$(P_3^{N''} - \mathcal{F}_{nJT} \sqrt{T_2} P_4^{M''} - \Delta P_5^{P''}) T_1''$	$(P_6^{N'''} - \mathcal{F}_{nJT} \sqrt{T_2} P_7^{M'''} - \Delta P_8^{P'''}) T_1'''$

^aDMBE I of Ref. 35. ^bDMBE II of Ref. 116.

phase (GP) effect [164–166] is largely suppressed. Consider first the case in which a circular path is chosen such that $\rho < \rho_0(Q_1)$ [see Figure 7(a)]. In this case, only one Ci (the central one) is enclosed and the adiabatic wave function changes sign along this loop, as seen in Figure 7(a) for the $1^1A'$ and $2^1A'$ electronic states. In fact, a similar sign change is expected when only one of the three equivalent degeneracies of C_{2v} symmetry is encircled [see Figure 7(b)]. Conversely, as Figure 7(c) shows, a closed circuit enclosing both the central and one of the C_{2v} Cis is sign-preserving. By the same token, when $\rho > \rho_0(Q_1)$ [Figure 7(d)], the associated electronic adiabatic wave function is sign-unchanged upon transportation along the corresponding loop. Note that $\rho_0(Q_1)$ marks the important transition between a JT- and RT-like behavior in the sense that the adiabatic wave functions for the $1^1A'$ and $2^1A'$ electronic states experience a sign change upon adiabatic transportation about the origin (D_{3h} seam) in the case $\rho < \rho_0(Q_1)$, but not for $\rho > \rho_0(Q_1)$ [159]. Note also from Figure 7 that the adiabatic wave function for the $3^1A'$ state does not change sign in any of the cases mentioned above: it is non-JT in nature.

(d) Global potential energy surfaces

(i) Accurate DMBE forms

According to the spin-spatial Wigner-Witmer correlation rules [156,157], $l\text{-}C_3(\tilde{X}^1\Sigma_g^+)$ dissociates adiabatically into

$$l\text{-}C_3(\tilde{X}^1\Sigma_g^+) \rightarrow \begin{cases} C_2(a^3\Pi_u) + C(^3P) & (2.10a) \\ C_2(X^1\Sigma_g^+) + C(^1D). & (2.10b) \end{cases}$$

As noted elsewhere [105–107,119], the first excited triplet state of C_2 lies only 8.6 kJ mol^{-1} (this is actually the equilibrium electronic term value T_e) above the corresponding ground state [48], whereas the energy separation between the 3P state of atomic carbon and its first excited state $C(^1D)$ is 122.0 kJ mol^{-1} [168]. Thus, as Figures 1 and 4 show, the lowest channel $C_2(a^3\Pi_u) + C(^3P)$ is favored by 113.4 kJ mol^{-1} relative to $C_2(X^1\Sigma_g^+) + C(^1D)$. In Refs. 35 and 116, we modeled the adiabatic ground-state PES of C_3 by

$$V_{I/II}(\mathbf{R}) = V^{(1)} + V^{(2)}(\mathbf{R}) + V_{\text{dc}}^{(3)}(\mathbf{R}) + V_{I/II,\text{EHF}}^{(3)}(\mathbf{R}), \quad (2.11)$$

where [124,125] $V^{(1)}$ is a one-body term equal to the dissociation energy (D_e) of $C_2(a^3\Pi_u)$, $V^{(2)}(\mathbf{R})$ the sum of the two-body potentials, and $V_{\text{dc}}^{(3)}(\mathbf{R})$ the three-body dc. In both DMBE I and DMBE II potentials, the three-body EHF energy assumes the form [35,116]

$$V_{I/II,\text{EHF}}^{(3)}(\mathbf{R}) = V_{I/II,\text{EHF}}^{J(3)}(\mathbf{R}) + V_{I/II,\text{EHF}}^{J''(3)}(\mathbf{R}) + V_{I/II,\text{EHF}}^{J'''(3)}(\mathbf{R}), \quad (2.12)$$

where $V_{I/II,\text{EHF}}^{J(3)}(\mathbf{R})$ is responsible for introducing nonanalyticity into the potential along the line of D_{3h} symmetry, and the remaining terms provide the required cusp behavior at the C_{2v} degeneracies. The corresponding forms are shown in Table 3; for simplicity, obvious coordinate dependences have been eliminated. Note that $P_n^J(\Gamma_1, \Gamma_2, \Gamma_3)$ are J -th order polynomials expressed in the integrity basis [169] and the $T(\mathbf{R})$'s are range-decaying factors. In turn,

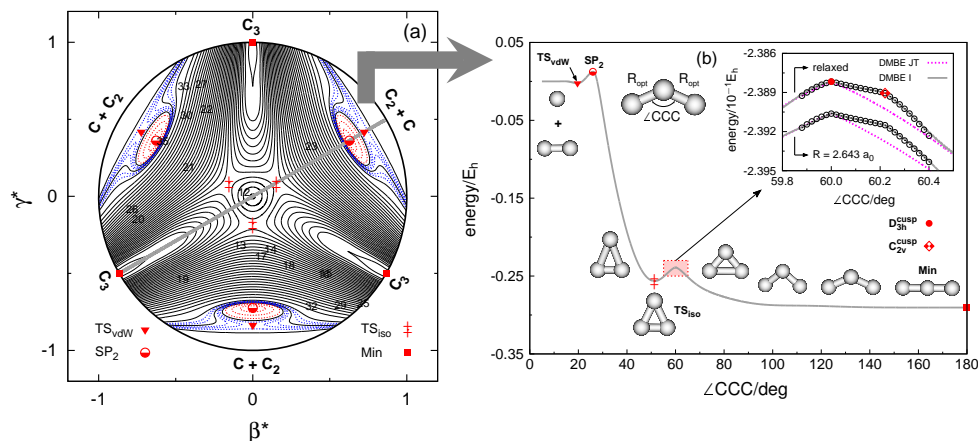


Figure 8. (a) Relaxed triangular plot in hyperspherical coordinates [171] depicting the location and symmetry of all stationary points of the DMBE I PES for ground-state C_3 . Solid black lines are equally spaced by $0.005 E_h$, starting at $-0.2904 E_h$. Dashed red and blue lines are equally spaced by $0.001 E_h$, starting at $0.00067 E_h$ and $-0.0206 E_h$, respectively. (b) Optimized reaction path along C_{2v} arrangements. The plot starts at $\angle CCC = 5^\circ$, which corresponds to the $C + C_2$ limit and leads to the linear global minimum at $\angle CCC = 180^\circ$ via the C_i region. The insert shows an amplified view of the nuclear configuration space illustrating the correct cusped behavior at D_{3h} and C_{2v} crossing seams. The dots indicate fitted points, with the lowest curve shifted by $-0.0025 E_h$ for visibility. Indicated by DMBE JT is PES without the $V_{I,EHF}^{(3)}(\mathbf{R})$ contributions in Table 3.

$\sqrt{T_2} = (Q_2^2 + Q_3^2)^{1/2}$ is the so-called JT-type coordinate [120,170] which essentially measures the distance from any point in the (Q_2, Q_3) -plane to the D_{3h} Ci [where $Q_b(Q_1) = (0, 0), \forall Q_1$] [127,128]. Likewise, $\Delta_1 \Delta_2 \Delta_3$ is the (product of) distances from any point in \mathbf{R} -space to the three permutationally equivalent C_{2v} crossing seams. Note that $V_{I,EHF}^{(3)}(\mathbf{R})$ dies-off Gaussian-like [127] in DMBE I, and hence the cusps at such geometries are warranted only close to the minimum of crossing seam [35]. All major topographical features are shown in Figure 8.

As we have shown elsewhere [36], the three C_{2v} seams are not static with respect to the D_{3h} Ci but evolve instead with the size of the molecule. In so doing, such degeneracy points approach the central D_{3h} Ci almost linearly and ultimately coalesce with it, thence forming a node of confluence. Indeed, by increasing the size of the molecular triangle, the C_{2v} disjoint seams get rotated by $\pm \pi$ in the branching plane [36]. In order to mimic such a behavior, we have proposed a revisited DMBE II form [116] and a novel coordinate (Δ in Table 3) that incorporates by built-in construction the exact equation of the seam as a function of Q_1 . Likewise the JT coordinate, Δ assumes the form [116]

$$\Delta = \sqrt{S_2^2 + S_3^2}, \quad (2.13)$$

where S_2 and S_3 are symmetrized coordinates made of the distances $\Delta = \{\Delta'_1, \Delta'_2, \Delta'_3\}$ from an arbitrary point to the C_{2v} Cis [116]:

$$\Delta'_c = \sqrt{(Q_2 - Q_2^c)^2 + (Q_3 - Q_3^c)^2} \quad c=1, 2, 3, \quad (2.14)$$

with the disjoint crossings points (Q_2^c, Q_3^c) given by

$$(Q_2^c, Q_3^c) = (\rho_0 \cos(\varphi_c \pm n\pi), \rho_0 \sin(\varphi_c \pm n\pi)). \quad (2.15)$$

As in sections 2(b) and 2(c), ρ_0 denotes the radius at which the disjoint seams are located with respect to the central Ci and φ_c ($c=1, 2, 3$) is the polar angle that explicitly defines the positions of the crossings: $\varphi_1 = \pi/2$, $\varphi_2 = 7\pi/6$ and $\varphi_3 = 11\pi/6$ (see Figure 7). In Eq. (2.15), $n=0$ or 1 is an integer that accounts for the proper rotation-in-plane of the C_{2v} seams on passing through the

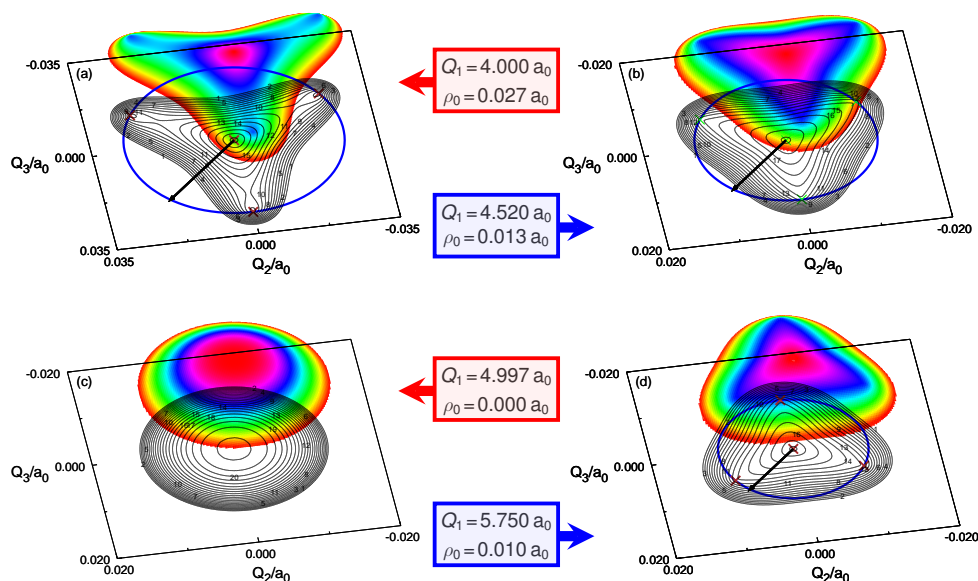


Figure 9. Evolution of D_{3h} and C_{2v} crossing seams versus Q_1 as predicted from the DMBE II PES for ground-state C_3 : (a) $Q_1 = 4.000 a_0$; (b) $Q_1 = 4.520 a_0$; (c) $Q_1 = 4.997 a_0$; (d) $Q_1 = 5.750 a_0$. Contours are spaced as follows [from (a) to (d)]: 0.025 mE_h , starting at -0.1710 E_h ; 0.015 mE_h , starting at -0.2392 E_h ; 0.012 mE_h , starting at -0.2081 E_h and 0.022 mE_h , starting at -0.1048 E_h . Cis are indicated by \times .

confluence point [116]. The equation of the seam is self-contained in the proper definition of ρ_0 , and is accurately represented by

$$\rho_0(Q_1) = \left| \varrho - \delta \tanh \left[\sum_{i=1}^5 \zeta_i (Q_1 - Q_1^0)^i \right] \right|, \quad (2.16)$$

where ϱ , δ , ζ_i and Q_1^0 are adjustable parameters; the details are given elsewhere [116]. As Figure 9 shows, Δ is capable of accurately modeling the three symmetry-equivalent C_{2v} disjoint seams, in addition to the symmetry-required D_{3h} one, over the entire configuration.

One wonders at this stage about the topographical form of the PES when all Cis meet each other. As shown in Figure 9, at this point of all confluences the PESs become tangentially touching paraboloids rather than two cones connected by the vertex. In order to mimic such a behavior, it suffices to add a term $\mathcal{F}_{nJT}(\mathbf{R})$ (non-JT factor) that warrants the $\sqrt{T_2}$ singularity on the adiabatic PESs to be canceled out (see Table 3). The result, obtained from the DMBE II PES, is illustrated in Figure 9 which shows the evolution of such crossings versus Q_1 . Table 4 shows only the properties of the linear global minima. The agreement with experimental data is good, while the properties of other stationary points (not shown) agree well with the corresponding *ab initio* attributes [35,116].

(ii) Realistic ES/DMBE forms

To improve the C_3 DMBE II PES at the linear global minima, we used [117] a simplified version of Varandas' ES scheme [173] to morph DMBE II and the ABW [34] and SS [115] local functions. Both DMBE/ES/ABW and DMBE/ES/SS PESs so obtained [117] read

$$V_{\text{DMBE/ES}/x} = f(\Delta E) [V_{\text{DMBE II}}(\mathbf{R}) - V_x(\mathbf{R})] + V_x(\mathbf{R}), \quad (2.17)$$

Table 4. Properties of the global linear minima on the $C_3(1^1A')$ DMBE PESs. Relative energies (ΔE), bond lengths (R_i) and harmonic frequencies (w_i) are in kJ mol^{-1} , a_0 and cm^{-1} , respectively.

Method	R_1	R_2	R_3	ΔE	w_1	w_2	w_3
DMBE I ^a	4.888	2.444	2.444	0.0 ^b	1204.2	63.5	2126.5
DMBE II ^c	4.888	2.444	2.444	0.0	1203.9	61.0	2125.5
DMBE/ES/ABW ^d	4.920	2.460	2.460	0.0	1214.5	64.6	2109.8
DMBE/ES/SS ^d	4.890	2.445	2.445	0.0	1206.7	42.8	2101.3
Expt.	4.902	2.451	2.451 ^e		1224.49 ^f	63.42 ^f	2040.02 ^f
	4.890	2.445	2.445 ^g				

^aRef. 35. ^bRelative to the $C_3(1^1\Sigma_g^+)$ global minimum. ^cRef. 116. ^dRef. 117. ^eRef. 4. ^fRefs. 172 and 84. Separation between origin level and lowest $v_n=1$ level. ^gMixed theoretical/experimental approach of Refs. 115 and 85.

Table 5. Stratified root-mean-square deviations (in cm^{-1}) obtained for 100 calculated energy levels for $J \leq 1$.

Energy ^a	N^b	rmsd					
		DMBE/ES/ABW	ABW	DMBE/ES/SS	SS	DMBE II	DMBE I
1000	8	3.3	3.2	2.5	2.3	24.5	32.5
2000	17	3.3	2.8	7.3	6.9	38.9	41.8
3000	35	4.2	2.6	9.7	9.1	37.5	47.0
4000	49	8.2	2.7	13.2	11.1	40.1	48.1
6000	83	18.0	3.0	19.8	13.4	42.2	49.0
9000	100	26.9	2.9	31.0	12.5	45.7	53.4

^aThe units of energy are cm^{-1} . Energy strata defined relative to the corresponding zero point energy level.

^bNumber of vibrational states up to indicated energy range.

where $x=ABW$ or SS , and $f(\Delta E)$ is defined by [173]

$$f(\Delta E) = \begin{cases} \exp\left[-\beta\left(\frac{\Delta E_0}{\Delta E + \xi} - 1\right)^n\right] & \text{if } \Delta E < \Delta E_0 \\ 1 & \text{if } \Delta E \geq \Delta E_0. \end{cases} \quad (2.18)$$

In turn, $\Delta E = E - E_{\min}$ is the energy displacement with respect to the absolute global minima of the DMBE II PES, and $\Delta E_0 = E_0 - E_{\min}$ the energy difference between E_{\min} and the cutoff energy E_0 . Finally, β is a trial-and-error parameter, n is an even integer and ξ a small number chosen to avoid numerical overflows at $E = E_{\min}$. Clearly, $f(\Delta E)$ ensures that the resulting PESs converge to the local potentials at energy ranges near E_{\min} , while smoothly changing to the global PES as long as the energy approaches E_0 . The topographical features of the final ES PESs are shown in Figure 10, together with the utilized local potentials. Clearly, the ES scheme allows a convenient merge of the global and local forms while eliminating spurious holes in the latter near equilateral triangular geometries. Additionally, they allow an extension of such spectroscopic forms to the dissociative regions. Their reliability is shown in Table 5, which summarizes stratified rmsds for 100 rovibrational energy levels up to 9000 cm^{-1} above ZPE. As seen, near spectroscopic accuracy is conveyed to both global forms up to 4000 cm^{-1} above ZPE, while keeping unaltered all attributes of the original DMBE II PES (Table 4). Not surprisingly, discrepancies appear with increasing energy, particularly for DMBE/ES/ABW since the original PESs differ most. Despite this, a reduction of $\sim 20 \text{ cm}^{-1}$ in levels up to 9000 cm^{-1} is already an asset of the ES method [173].

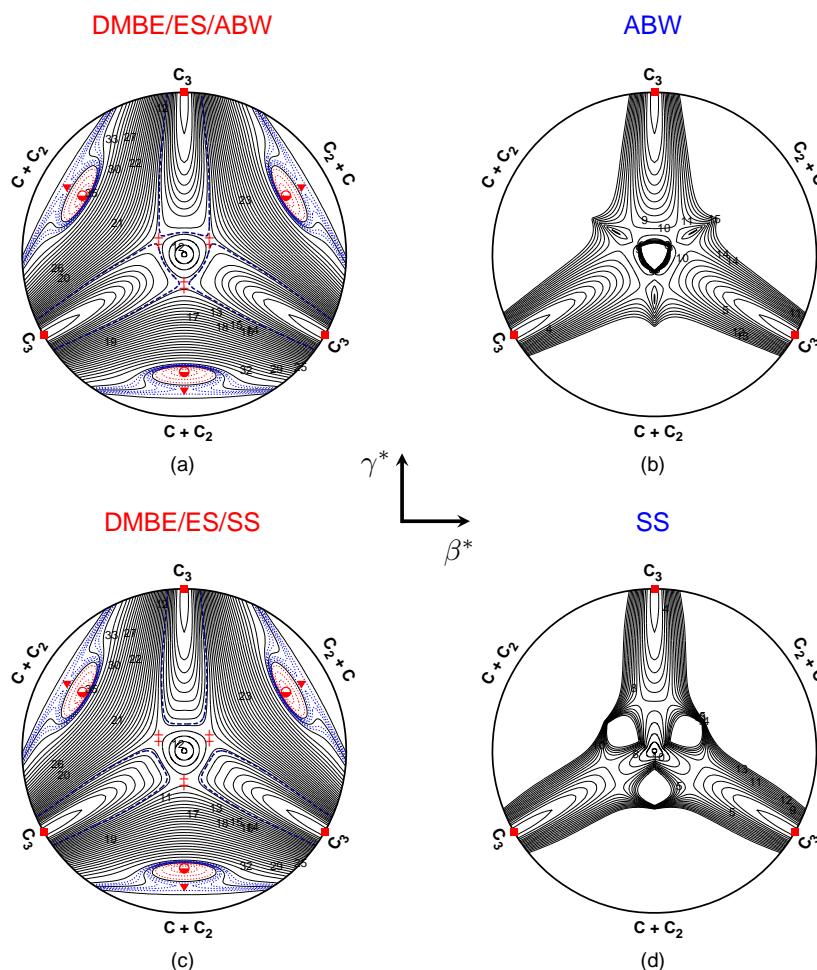


Figure 10. Relaxed triangular plot in hyperspherical coordinates [171] for C_3 : (a) DMBE/ES/ABW [117]; (b) ABW [34]; (c) DMBE/ES/SS [117]; (d) SS [115]. Key for all global forms are as in Figure 8. For local forms, contours are equally spaced by $0.005 E_{h_1}$, starting at $-0.2904 E_{h_1}$. Navy dashed lines in panels (a) and (c) define cutoff energies (E_0) of Eq. (2.18).

3. Further on carbon tetramer

(a) Electronic structure

All structures have been optimized with MOLPRO [174] at CASSCF (or, simply, CAS) level of theory [175] in C_1 symmetry with the AVTZ basis set [60,61]. The reference wave functions have then been obtained using the largest possible active space, which involves 8 correlated electrons in 12 orbitals [CAS(8,12)]; 8 orbitals were treated as inactive, but optimized, throughout all calculations. Geometry optimizations were also done, and followed by harmonic vibrational analysis to confirm the nature of the stationary point as minima (only real frequencies) or transition-state structures (only one imaginary frequency). To understand the connections between the predicted transition states and associated minima, calculations along convenient ORC paths [176,177] have further been carried out. This involves a selection of a single reactive coordinate, *i.e.*, the one that determines the bond-breaking/bond-forming process, with all other degrees of freedom fully optimized at each point of the predefined grid for the active coordinate.

Such a process has proven very effective in obtaining accurate reaction dissociation profiles for HO₃ [176], HO₂ and HS₂ [177] as well as for the Li₃N-CO₂ complex [178]. For every point of the various ORCs, an enhanced estimate of the energetics has then been obtained at MRCI(Q) level [175] with AVTZ and AVQZ basis sets, followed by extrapolation to the CBS limit [179,180]. Suffice it to add that all CAS(8,12) vectors were included in the reference space for the 8-electron MRCI(Q)-8 calculations; the 8 inner orbitals were left uncorrelated.

For CBS extrapolation of the CAS energies, a double-level protocol developed in our group [179] has been utilized,

$$E_X^{\text{CAS}(8,12)}(\mathbf{R}) = E_\infty^{\text{CAS}(8,12)}(\mathbf{R}) + Ae^{-1.63x}, \quad (3.1)$$

where $x=t(2.94)$, $q(3.87)$ are hierarchical numbers [181,182] associated with the $X=T:3$, $Q:4$ cardinals and \mathbf{R} is a six-dimensional coordinate vector; $E_\infty^{\text{CAS}(8,12)}(\mathbf{R})$ and A are parameters obtained from the fit to the CAS(8,12)/AVXZ ndc energies.

In turn, the extrapolated dc contribution [$E_\infty^{\text{dc-8}}(\mathbf{R})$] is obtained with Varandas' USTE protocol [180]

$$E_X^{\text{dc-8}}(\mathbf{R}) = E_\infty^{\text{dc-8}}(\mathbf{R}) + \frac{A_3}{(X-3/8)^3} + \frac{A_5(0) + cA_3^{5/4}}{(X-3/8)^5}, \quad (3.2)$$

where $A_5(0)$ and c are universal parameters [180], and $E_\infty^{\text{dc-8}}(\mathbf{R})$ and A_3 are obtained by fitting the raw MRCI(Q)-8/AVXZ dc energies:

$$E_X^{\text{dc-8}}(\mathbf{R}) = E_X^{\text{MRCI(Q)-8}}(\mathbf{R}) - E_X^{\text{CAS}(8,12)}(\mathbf{R}). \quad (3.3)$$

For a specified nuclear arrangement \mathbf{R} , the total energy is then obtained as

$$E_\infty^{\text{CASDC/CBS-8}}(\mathbf{R}) = E_\infty^{\text{CAS}(8,12)}(\mathbf{R}) + E_\infty^{\text{dc-8}}(\mathbf{R}), \quad (3.4)$$

and denoted CASDC/CBS-8 as suggested elsewhere [177].

As noted by Parasuk and Almöf [37], the inclusion of all valence electrons in the correlation treatment is key to obtain the best energy differences between the linear and cyclic forms. Thence, we carried out FVCAS geometry optimizations with the AVTZ basis set, followed by single-point AVQZ computations. Such calculations involve correlating the 16 electrons in 16 orbitals, which are affordable only by including point-group symmetry in the wave function. Because this could not be pursued for stationary points of symmetry lower than C_{2v} , single-point FVCAS/AVXZ calculations were performed at the optimum CAS(8,12)/AVTZ geometries. To obtain a reliable estimate of the total CBS energy, the ndc extrapolated components $E_\infty^{\text{CAS}(16,16)}(\mathbf{R})$ were added to the $E_\infty^{\text{dc-8}}(\mathbf{R})$ contributions, with the energies so obtained denoted as ve-CASDC/CBS. Figure 11 shows the minimum energy pathways for interconversion between the linear and rhombic C_4 for both triplet and singlet isomers. The corresponding structural parameters, harmonic vibrational frequencies and relative energies are given in Tables 6 and 7.

We begin the present discussion with some remarks on the $l\text{-}C_4(^3\Sigma_g^-)$ and $r\text{-}C_4(^1A_g)$ energetics. As noted in the Introduction, it appears to be a common trend [37,38,132] that the singlet vs triplet relative positioning, hence the true ground-state structure, depends on whether one utilizes SR vs MR methodologies: $r\text{-}C_4(^1A_g)$ is more stable than $l\text{-}C_4(^3\Sigma_g^-)$ for SR, while the contrary is the case for MR. Indeed, as noted by Parasuk and Almöf [37], SR approaches may not be sufficient to treat adequately the high density of electronic states present in C_4 which occur already for very low internal energies [38]. Our own calculations at the CASDC/CBS-8 level suggest from Tables 6 and 7 that $l\text{-}C_4(^3\Sigma_g^-)$ lies about 25.9 kJ mol⁻¹ lower in energy than the corresponding rhombic singlet structure. However, at our highest level of theory, *i.e.*, ve-CASDC/CBS, the linear-rhombic energy difference is reduced to only 9.1 kJ mol⁻¹ (positive signs favors the linear form). These results are in good agreement with those obtained by Parasuk and Almöf in their 16-electron MRCI/G[542] calculations (6.8 kJ mol⁻¹) [37]. Although such relative quantity certainly converges to different values for distinct correlation methods, extrapolations to the CBS limit tend to level their relative positioning; the isomer with larger correlation

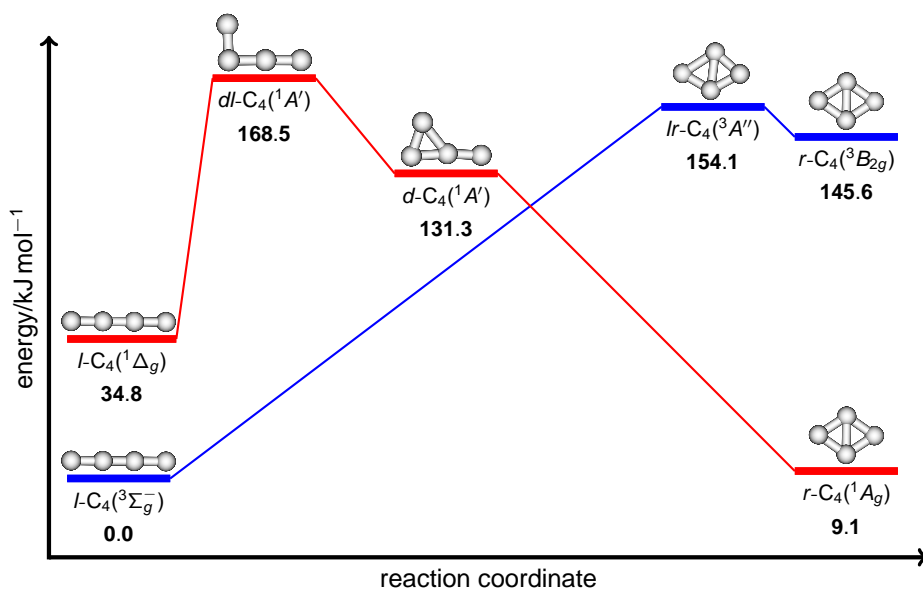


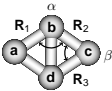
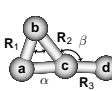
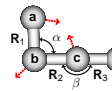
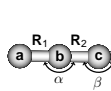
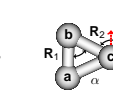
Figure 11. Minimum energy paths for interconversion of linear and rhombic C_4 in both the triplet (in blue) and singlet (in red) ground-state PESs. Energies are given with respect to the $l-C_4(^3\Sigma_g^-)$ form and have been obtained at ve-CASDC/CBS level of theory. Structural parameters and vibrational frequencies for each structure are in Tables 6 and 7.

Table 6. Structural parameters (distances R_i in a_0 , angles in degrees) and vibrational frequencies (in cm^{-1}) of the stationary points on the ground-state triplet PES of C_4 . Energies (in kJ mol^{-1}) relative to $l-C_4(^3\Sigma_g^-)$.

Feature/Method	$l-C_4(^3\Sigma_g^-)$ $D_{\infty h}$	$lr-C_4(^3A'')$ C_s	$r-C_4(^3B_{2g})$ D_{2h}
CAS(8,12)/AVTZ ^a	0.0	229.0	220.9
FVCAS/AVTZ ^a	0.0	122.5	105.5
CASDC/CBS-8 ^a	0.0	262.4	261.0
ve-CASDC/CBS ^a	0.0	154.1	145.6
R_1 ^b	2.458(2.506)	3.076	2.698(2.744) ^c
R_2	2.449(2.463) ^c	2.604	2.698(2.744) ^c
R_3	2.458(2.506) ^c	2.637	2.698(2.744) ^c
α	180.0(180.0) ^c	105.6	111.4(112.8) ^c
β	180.0(180.0) ^c	70.4	68.6(67.2) ^c
w_1 ^b	2165.0(2057.0) ^e	1347.1	1316.2
w_2	949.3	1325.9	1038.4
w_3	1667.2(1548.9) ^e	992.0	877.3
w_4	538.8(323.0) ^e	706.0	665.5
w_5	216.0(174.0) ^e	552.2	618.2
w_6		392.1 ⁱ	608.8

^aThis work. ^bObtained at CAS(8,12)/AVTZ level of theory. ^cFVCAS/AVTZ optimized values. ^dThe experimentally averaged C=C bond length is 2.458 a_0 (see Ref. 2). ^eExperimental band origins taken from Refs. 8, 146 and 148.

Table 7. Structural parameters (distances R_i in a_0 , angles in degrees) and vibrational frequencies (in cm^{-1}) of the stationary points on the ground-state singlet PES of C_4 . Energies (in kJ mol^{-1}) relative to $l\text{-}C_4(^3\Sigma_g^-)$.

Feature/Method	 $r\text{-}C_4(^1A_g)$ D_{2h}	 $d\text{-}C_4(^1A')$ C_s	 $dl\text{-}C_4(^1A')$ C_s	 $l\text{-}C_4(^1\Delta_g)$ $D_{\infty h}$	 $dd\text{-}C_4(^1A_1)$ C_{2v}
CAS(8,12)/AVTZ ^a	29.8	127.0	156.8	27.5	130.2
FVCAS/AVTZ ^a	12.7	124.4	158.2	32.0	126.5
CASDC/CBS-8 ^a	25.9	137.6	168.3	38.7	138.8
ve-CASDC/CBS ^a	9.1	131.3	168.5	34.8	133.5
R_1^b	2.725(2.758) ^c	2.616	2.507	2.467(2.509) ^c	2.655(2.643)
R_2	2.725(2.758) ^c	2.938	2.583	2.457(2.484) ^c	2.785(2.778)
R_3	2.725(2.758) ^c	2.496	2.488	2.467(2.509) ^c	2.480(2.556)
α	115.9(116.7) ^c	56.6	91.7	180.0(180.0) ^c	61.5(61.6) ^c
β	64.4(63.3) ^c	130.8	179.5	180.0(180.0) ^c	151.5(151.6) ^c
w_1^b	1271.9	1643.0	1796.3	2021.8	1739.8
w_2	964.1	1296.1	1561.1	936.5	1269.6
w_3	983.3	902.6	1103.7	1643.0	818.1
w_4	406.3	689.3	1065.6	406.4/375.2	628.7
w_5	514.2	287.5	284.8	209.6/194.1	257.2
w_6	1445.0	211.8	475.5i		238.0i

^aThis work. ^bObtained at CAS(8,12)/AVTZ level of theory. ^cFVCAS/AVTZ optimized values.

energy, *i.e.*, $r\text{-}C_4(^1A_g)$ tends to be favoured. Indeed, the energy splittings predicted from our (FVCAS+dc-8)/AVTZ, (FVCAS+dc-8)/AVQZ and ve-CASDC/CBS calculations are 14.7, 11.2 and 9.1 kJ mol^{-1} , respectively. A similar basis-set effect is also observed in the MRCI(Q)-8/AVTZ, MRCI(Q)-8/AVQZ and CASDC/CBS-8 series (*i.e.*, 31.2, 27.9 and 25.9 kJ mol^{-1} , respectively). Suffice it to add that the corresponding (harmonic) ZPE contribution is about -4.2 kJ mol^{-1} at CAS(8,12)/AVTZ level which, in turn, reduces the corresponding energy differences even further. As noted by Massó *et al.* [38], such energetic proximity ($\approx 4.9 \text{ kJ mol}^{-1}$) between the $l\text{-}C_4(^3\Sigma_g^-)$ and $r\text{-}C_4(^1A_g)$ isomers is expected to be of the same order of accuracy of the *ab initio* calculations themselves, and hence any statement about the true ground-state of C_4 is possibly risky at present.

Unquestionably, the triplet ground-state is the $^3\Sigma_g^-$ structure. Its cumulenitic nature is evidenced by the nearly equal C=C bond lengths which are predicted from our FVCAS/AVTZ calculations to be 2.506 and 2.463 a_0 for the outer ($R_1=R_3$) and inner (R_2) distances, respectively. Such values agree well with the experimental (averaged) bond length of 2.458 a_0 [2]. As first remarked by Parasuk and Almöf [37], the corresponding acetylenic form is of $^3\Sigma_u^+$ symmetry and lies well above in energy ($\approx 107.6 \text{ kJ mol}^{-1}$). This state of C_4 has characteristic bond distances of an acetylenic-like molecule, *i.e.*, the outer C=C bonds are about 0.3 a_0 shorter than the inner R_1 distance [37]. It should be noted that, at linear geometries, two low-lying $^1\Delta_g$ and $^1\Sigma_g^+$ excited states also arise from the π_g^2 configuration [see Figure 12(a)]. These have been measured in anion photoelectron spectra [148] to be about 32.0 and 48.2 kJ mol^{-1} , respectively, above the $^3\Sigma_g^-$ state. The corresponding adiabatic excitation energies predicted from our ve-CASDC/CBS calculations are 34.8 and 50.2 kJ mol^{-1} , respectively.

Figure 11 shows that the ground singlet is the rhombic 1A_g structure, thence an a_g^2 electronic configuration [see Figure 12(b)]. At the FVCAS/AVTZ level of theory, this molecule shows

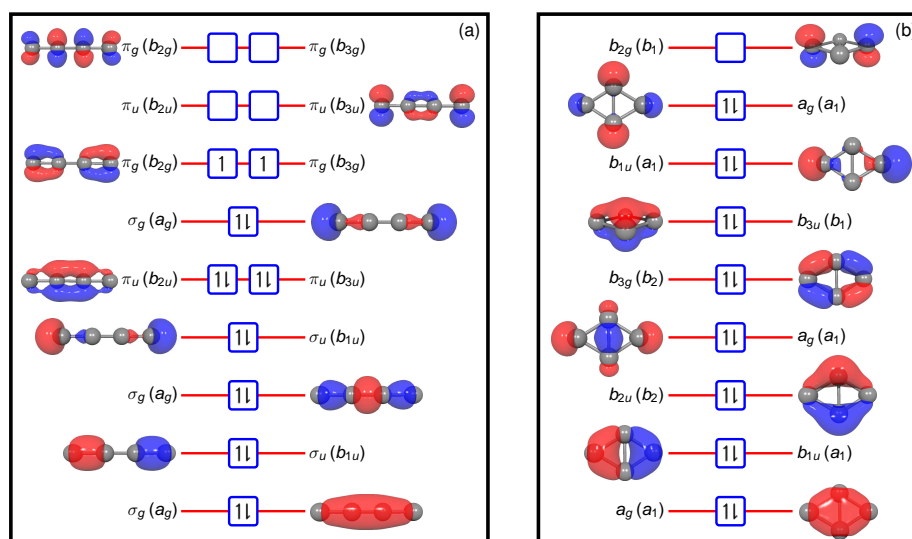


Figure 12. Molecular orbital diagrams and valence electronic configurations for (a). $l\text{-C}_4(^3\Sigma_g^-)$ and (b). $r\text{-C}_4(^1A_g)$. Molecular orbitals are labeled according to $D_{\infty h}$ and D_{2h} irreps, respectively, with the corresponding correlations with D_{2h} and C_{2v} point groups given in parentheses. Up and down arrows denote α and β spin states, respectively. Natural orbitals obtained from a FVCAS/AVTZ wave functions are also depicted.

characteristic peripheral and intrannular (cross-ring) C–C bond lengths of 2.758 and 2.895 a_0 , respectively. Such quantities agree nicely with the most recent *ab initio* values of 2.739 and 2.855 a_0 reported by Wang *et al.* [141] at CCSD(T)-F12b/AVTZ level of theory as well as those obtained from ve-MRCI(Q)/VTZ calculations by Senent *et al.* [140] (2.742 and 2.873 a_0). Actually, as seen in Tables 6 and 7, all stationary structures optimized at CAS(8,12)/AVTZ level differ by less than $\approx 0.05 a_0$ and $\approx 1^\circ$ for bond lengths and bond angles, from those obtained when all valence electrons are included in the ndc treatment. This situation clearly reflects the general observation that geometries are often less sensitive to the theoretical level than relative energies [176,177].

Figure 11 further depicts an additional (local) minimum on the lowest triplet PES of C_4 , namely $r\text{-C}_4(^3B_{2g})$. At CASDC/CBS-8 level, such a structure lies about 261.0 kJ mol^{-1} higher in energy relative to the $^3\Sigma_g^-$ isomer and is located well above the corresponding 1A_g rhombic partner; see Tables 6 and 7. Note that, although the optimized structures predicted from the CAS(8,12)/AVTZ calculations are in excellent agreement with those obtained at FVCAS/AVTZ level, the inclusion of all valence space in the ndc treatment reduces the energy difference between $l\text{-C}_4(^3\Sigma_g^-)$ and $r\text{-C}_4(^3B_{2g})$ by about 115.4 kJ mol^{-1} . In fact, at ve-CASDC/CBS level, these latter forms are separated by 145.6 kJ mol^{-1} . Note that the energy splitting between the $^3B_{2g}$ and 1A_g rhombic structures is predicted to be 136.5 kJ mol^{-1} at this level. Such a result is in reasonable agreement with the corresponding vertical excitation energy of 187.2 kJ mol^{-1} reported by Massó *et al.* [38] at ve-MRCI(Q)/VTZ level. As emphasized by the authors, their value would be decreased if one considers the relaxation of all nuclear coordinates.

The isomerization of $l\text{-C}_4(^3\Sigma_g^-)$ into $r\text{-C}_4(^3B_{2g})$ structure occurs via a C_s transition state $lr\text{-C}_4(^3A'')$; see Figures 11 and 13. At CASDC/CBS-8 level, the latter is about 262.4 kJ mol^{-1} above the corresponding linear minimum. The full valence ndc treatment reduces that value by about 108.3 kJ mol^{-1} . Indeed, the classical barrier height predicted from our ve-CASDC/CBS protocol is 154.1 kJ mol^{-1} . The corresponding ORC path for such a isomerization reaction is depicted in Figure 13. For this we performed CAS(8,12)/AVTZ constrained optimizations in which a single peripheral bond length of the $r\text{-C}_4(^3B_{2g})$ structure (R) is treated as inactive, with all other degrees freedom (two bond lengths and two bond angles) optimized at each grid point. Single-point MRCI(Q)-8/AVXT ($X=T, Q$) calculations along the optimized CAS(8,12)/AVTZ

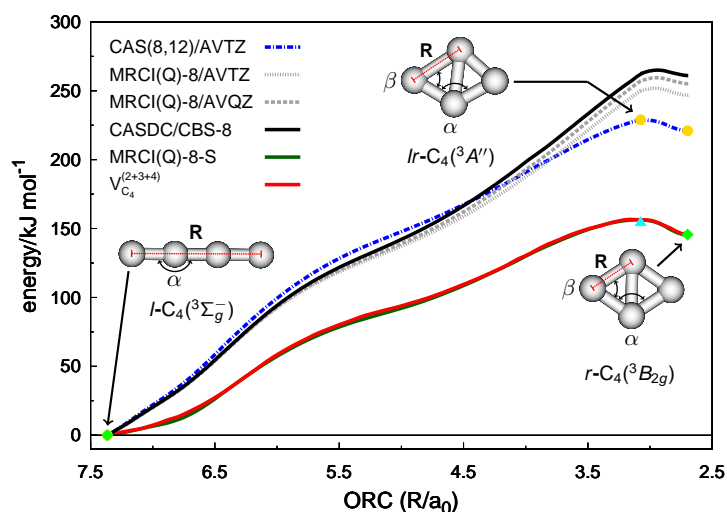


Figure 13. ORC paths for interconversion of $l\text{-C}_4(^3\Sigma_g^-)$ and $r\text{-C}_4(^3B_{2g})$ via $lr\text{-C}_4(^3A'')$ transition state. The inactive coordinate corresponds to the peripheral bond length of the $r\text{-C}_4(^3B_{2g})$ structure (R), with all other degrees of freedom optimized at each grid point. Stationary structures at CAS(8,12)/AVTZ, ve-CASDC/CBS and ve-CASDC/CBS/CAS(8,12)/AVTZ levels are shown by dots, diamonds and triangles, respectively. Energies are relative to $l\text{-C}_4(^3\Sigma_g^-)$. The MRCI(Q)-8-S and $V_{C_4}^{(2+3+4)}$ curves are discussed in section 3(b).

path have subsequently been performed, followed by extrapolations to the CASDC/CBS-8 limit. To check the proper convergence of the CAS wave function, all ORCs have been performed in both “forward” and “backward” directions. Unfortunately, at FVCAS/AVXZ level, such paths are unaffordable with the means at our disposal, and hence not pursued. However, as emphasized in section 3(b), an alternative approach can be employed that brings MRCI(Q)-8/AVTZ energies in close agreement with the predicted linear-rhombic energy splittings at ve-CASDC/CBS.

Figure 13 shows that, although the predicted potential barriers increase by 21.0, 28.3 and 33.5 kJ mol^{-1} with the MRCI(Q)-8/AVTZ, MRCI(Q)-8/AVQZ and CASDC/CBS-8 correlation treatments, respectively, the structure of the transition state differs only slightly from the CAS(8,12)/AVTZ one. Overall, the addition of dynamical correlation shifts the location of $lr\text{-C}_4(^3A'')$ TS toward the rhombic isomer. Suffice to highlight that, although only a single peripheral bond has been followed in the ORC path, the above isomerization process clearly involves the formation/breaking of both peripheral and intramolecular bonds.

To the best of our knowledge, the only *ab initio* study on such a reaction path for C_4 is that of Blanksby *et al.* [138]. The authors, used CCSD(T)/AVDZ//B3LYP/6-31G* to report a value of $108.1 \text{ kJ mol}^{-1}$ for the isomerization barrier of $l\text{-C}_4(^3\Sigma_g^-)$ into $r\text{-C}_4(^3B_{2g})$. Suffice to add that the rhombic 1A_g structure is 11.7 kJ mol^{-1} more stable than $l\text{-C}_4(^3\Sigma_g^-)$ at their level of theory [138].

In contrast to the triplet ground-state surface, the isomerization between rhombic and linear forms on the singlet PES occurs in a stepwise manner; see Figures 11 and 14. Starting from the 1A_g global minimum, the system attains an intermediate C_s monocyclic ring [$d\text{-C}_4(^1A')$] via a ring-opening (barrierless) process in which only a single peripheral bond is broken. Indeed, $d\text{-C}_4(^1A')$ shows itself as a local minimum on the singlet ground-state PES and lies about 111.7 and $122.2 \text{ kJ mol}^{-1}$ above the $r\text{-C}_4(^1A_g)$ structure at CASDC/CBS-8 and ve-CASDC/CBS levels of theory, respectively. As we shall see, the discrepancies between full-valence and truncated-space correlation approaches are generally smaller for the singlet than the triplet states. This stems from a higher multi-configurational character of the latter [141]. In fact, because the isomerization process in the singlet PES occurs in a stepwise manner, reactants and products are somewhat similar in nature, thus allowing for some error compensation in the *ab initio* calculations.

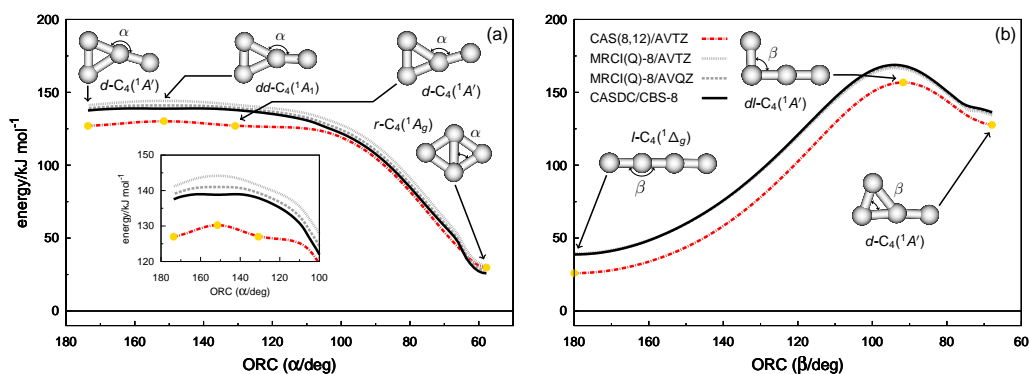


Figure 14. ORC paths for the *r*-C₄(¹A_g) and *l*-C₄(¹Δ_g) isomerization. (a) Interconversion of *r*-C₄(¹A_g) and *d*-C₄(¹A'). The inactive coordinate corresponds to the angle formed between peripheral and cross-ring bond lengths (α). (b) Interconversion of *d*-C₄(¹A') and *l*-C₄(¹Δ_g) via *dl*-C₄(¹A') transition state. The inactive coordinate corresponds to the ring-opening angle β. Stationary structures at CAS(8,12)/AVTZ level are indicated by solid dots. Energies are relative to *l*-C₄(³Σ_g⁻).

The ORC path for interconversion of *r*-C₄(¹A_g) and *d*-C₄(¹A') is depicted in Figure 14(a). The salient feature relates to the appearance of a small barrier at α=151.5° in the CAS(8,12)/AVTZ optimized curve. Indeed, such a geometry corresponds to a C_{2v} capped triangle [*dd*-C₄(¹A₁) in Table 7] which was first identified by Whiteside *et al.* [129] At CAS(8,12)/AVTZ level, this form represents a transition state with an imaginary frequency of only 238.0i cm⁻¹. A close inspection of Figure 14(a) reveals that *dd*-C₄(¹A₁) is responsible for the degenerate isomerization between symmetrically equivalent *d*-C₄(¹A') structures (one with α=130.8°, the other α=173.6°). The isomerization barrier is only 3.2 kJ mol⁻¹ at this level. However, as first noted by Massó *et al.* [38] and clearly seen in Figure 14(a), extrapolations to the CBS limit make the appearance of a very shallow minimum at such a geometry. At CASDC/CBS-8 and *ve*-CASDC/CBS levels of theory, *dd*-C₄(¹A₁) is found to be 112.9 and 124.4 kJ mol⁻¹ higher in energy than the singlet rhombus, respectively. Note from Figure 14(a) that if one increases α up to about 244.1°, a symmetry-equivalent conformer of *r*-C₄(¹A_g) (in which the intrannular bond is converted to peripheral and vice versa) is obtained. Suffice to say that Blanksby *et al.* predicted a CCSD(T)/AVDZ//B3LYP/6-31G* transition state of C_s symmetry for interconversion of *r*-C₄(¹A_g) and *d*-C₄(¹A') but, surprisingly, lying below the latter. In our preliminary CAS(8,12)/AVTZ geometry searches, a similar transition state has been found but the IRC revealed discontinuities. Such an unphysical behavior is removed using the ORC method.

The ultimate path in the isomerization process consists of converting *d*-C₄(¹A') into the more stable *l*-C₄(¹Δ_g) form. As Figure 14(b) shows, this is the rate determining step, which occurs via a *L*-type transition structure *dl*-C₄(¹A') with a *ve*-CASDC/CBS barrier height of about 37.2 kJ mol⁻¹ relative to *d*-C₄(¹A'). This compares with the value 58.6 kJ mol⁻¹ predicted by Blanksby *et al.* A final remark goes to work by Ngandjong *et al.* [183] who studied the above cyclization pathway for singlet C₄ at M06-2X/AVDZ level of theory. The authors suggested a one-step isomerization process where *r*-C₄(¹A_g) is directly attained from *l*-C₄(¹Δ_g) via a C_s transition structure similar to *dl*-C₄(¹A'). Clearly, their result differs dramatically from our own MR result. In fact, as noted by the authors themselves, the use of DFT on electronic structure calculations of carbon clusters can be notoriously complicated due to their intrinsic multi-state character [183].

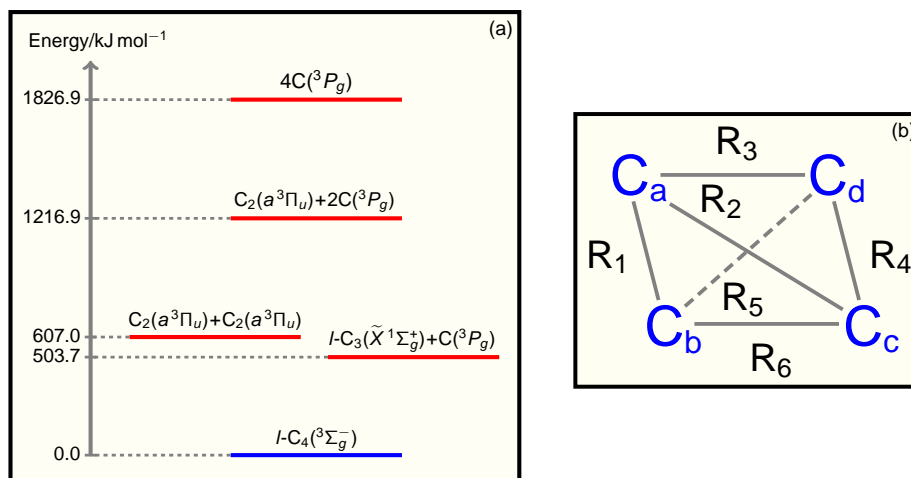


Figure 15. (a). Energetics of the various asymptotic channels of $l\text{-C}_4(^3\Sigma_g^-)$ shown in Eq. (3.5). The atomization energy (at 0K) for C_4 is taken from Ref. 42 with the zero-point vibrational energy retrieved from Ref. 184. The corresponding experimental data for $\text{C}_3(\tilde{X}^1\Sigma_g^+)$ and $\text{C}_2(a^3\Pi_u)$ are from Ref. 35. (b). Interparticle coordinate system employed in the construction of the DMBE-(2+3) and DMBE-(2+3+4) PESs.

(b) A novel DMBE for triplet C_4

Following the Wigner-Witmer rules [156,157], one has

$$l\text{-C}_4(^3\Sigma_g^-) \longrightarrow \begin{cases} \text{C}_2(a^3\Pi_u) + \text{C}_2(a^3\Pi_u) & (3.5a) \\ l\text{-C}_3(\tilde{X}^1\Sigma_g^+) + \text{C}(^3P) & (3.5b) \\ \text{C}_2(a^3\Pi_u) + 2\text{C}(^3P) & (3.5c) \\ 4\text{C}(^3P). & (3.5d) \end{cases}$$

Likewise $\text{C}_3(\tilde{X}^1\Sigma_g^+)$ [35,105,106,119], the title species does not correlate to ground-state C_2 fragments, with the asymptote (3.5a) lying [51] 17.2 kJ mol^{-1} above the $\text{C}_2(X^1\Sigma_g^+) + \text{C}_2(X^1\Sigma_g^+)$ spin-forbidden channel. As noted by Ritchie *et al.* [131], this latter correlates with the excited $l\text{-C}_4(^1\Sigma_g^+)$ form. Figure 15(a) shows that the dissociation process into $\text{C}_2(a^3\Pi_u)$ occurs with an endothermicity of about 607.0 kJ mol^{-1} . In turn, the dissociation into unlike species gives both C_3 and C fragments into their ground electronic states. As pointed out by Wakelam *et al.* [9], such a collinear reaction is the lowest energy path yielding $l\text{-C}_4(^3\Sigma_g^-)$ which according to Figure 15(a), is exothermic by about 503.7 kJ mol^{-1} . Note that the first excited asymptotic channel $\text{C}_3(\tilde{a}^3\Pi_u) + \text{C}(^3P)$ lies [86,88] 202.8 kJ mol^{-1} above the asymptote (3.5b) and correlates with higher excited electronic states such as $l\text{-C}_4(^3\Pi_u)$ [9] and $l\text{-C}_4(^1\Sigma_g^+)$. Suffice to say that the exit channels (3.5c) and (3.5d) arise from the dissociation of $\text{C}_3(\tilde{X}^1\Sigma_g^+)$ [in channel (3.5b)] into $\text{C}_2(a^3\Pi_u) + \text{C}(^3P)$, with subsequent fragmentation into $\text{C}(^3P) + \text{C}(^3P)$ [35].

Among the most reliable approaches to obtain a realistic representation of a global PES, the MBE [119,120] and DMBE [123–125] methods play a prominent role and have acquired popularity. Accordingly, the PES of a molecular system is expanded in sub-clusters of atoms [119], thus warranting by built-in construction the correct asymptotic behavior in any fragmentation. Indeed, once the potentials of all fragments have been obtained, the key MBE development enables a first estimate of the PES for the target polyatomic [119,120]. One should bear in mind that, even if the series converges rapidly, chemical accuracy is only attainable by including the highest-order (*i.e.*, beyond pairwise-additivity) possible contributions [119,125]. Since the potentials of $\text{C}_3(\tilde{X}^1\Sigma_g^+)$

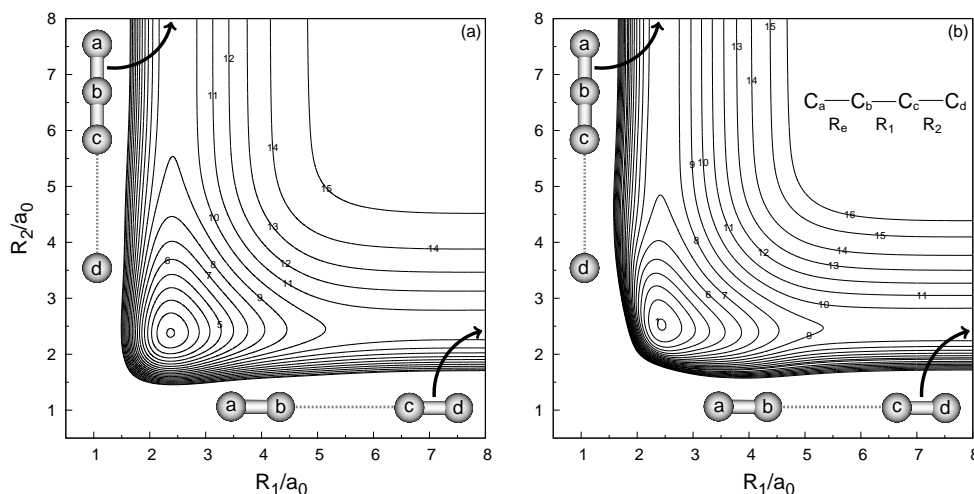


Figure 16. Partially relaxed ($2.2 \leq R_e/a_0 \leq 2.6$) contour plot for $C_{\infty v}$ insertion of C atom into a C_3 triatomic. (a). DMBE/ES/SS-(2+3) PES. (b) DMBE/ES/SS-(2+3+4) PES. Contours in panel (a) are equally spaced by $0.03 E_h$, starting at $-0.8370 E_h$. In (b), they are $0.03 E_h$, and $-0.7127 E_h$ in the same order.

and $C_2(a^3 \Pi_u)$ are already known [section 2(d)], one can proceed to *a priori* estimate of the C_4 triplet PES.

Following the DMBE method [123–125] and Eq. (3.5), the approximate cluster expansion for the title species including two- and three-body contributions only assumes the form

$$\begin{aligned}
 V_{C_4}^{(2+3)}(\mathbf{R}) = & V_{C_a C_b}^{(2)}(R_1) + V_{C_a C_c}^{(2)}(R_2) + V_{C_a C_d}^{(2)}(R_3) + V_{C_c C_d}^{(2)}(R_4) + V_{C_b C_d}^{(2)}(R_5) \\
 & + V_{C_b C_c}^{(2)}(R_6) + V_{C_a C_b C_c}^{(3)}(R_1, R_2, R_6) + V_{C_a C_c C_d}^{(3)}(R_2, R_3, R_4) \\
 & + V_{C_a C_b C_d}^{(3)}(R_1, R_3, R_5) + V_{C_b C_c C_d}^{(3)}(R_4, R_5, R_6), \quad (3.6)
 \end{aligned}$$

where $\mathbf{R} = \{R_1, R_2, R_3, R_4, R_5, R_6\}$ is a collective variable of the interparticle distances in Figure 15(b). As usual [123–125], each n -body term is split into EHF and dc energy contributions [35,116]: $V^{(n)} = V_{\text{EHF}}^{(n)} + V_{\text{dc}}^{(n)}$. Note that all fragments dissociate into ground-state C atoms, and hence there is no need for one-body terms; the zero of energy is the exit channel (3.5d). Because the DMBE/ES/SS [117] form of C_3 is here utilized to obtain such an approximate potential, the C_4 PES will be denoted as DMBE/ES/SS-(2+3). The required three-body terms have been obtained by subtracting the sum of two-bodies from the total energy,

$$V_{C_3}^{(3)}(R_i, R_j, R_k) = V_{\text{ES}}(R_i, R_j, R_k) - \left[V_{C_2}^{(2)}(R_i) + V_{C_2}^{(2)}(R_j) + V_{C_2}^{(2)}(R_k) \right]. \quad (3.7)$$

Similar topographical features are obtained when using any other of our functions. Figures 16(a) and 17(a) show relevant aspects of the purely *ab initio*-based DMBE/ES/SS-(2+3) expansion.

As expected, the DMBE/ES/SS-(2+3) PES provides a realistic representation of the potential both in the valence and long-range interaction regions. In fact, as Figures 16(a) and 17(a) show, the current DMBE has the correct asymptotic behavior, which is a well established asset of MBE theory [119,123–125]. It should be stressed that, although the truncated potentials give a good representation of the triplet linear global minimum, $l-C_4(^3 \Sigma_g^-)$ is predicted to be a saddle point of index 4, with imaginary frequencies corresponding to the degenerate trans- (w_4) and cis-bending (w_5) modes. This result stems largely from the lack of the four-body term which, according to Figure 15(a) and the DMBE/ES/SS-(2+3) PES, is estimated to be as repulsive as 376 kJ mol^{-1} at this geometry. Similar magnitudes of four-body interaction energies have been reported for X_4 -type elemental clusters such as H_4 [120,185] and O_4 [186]. In fact, for ground-state C_3 , the

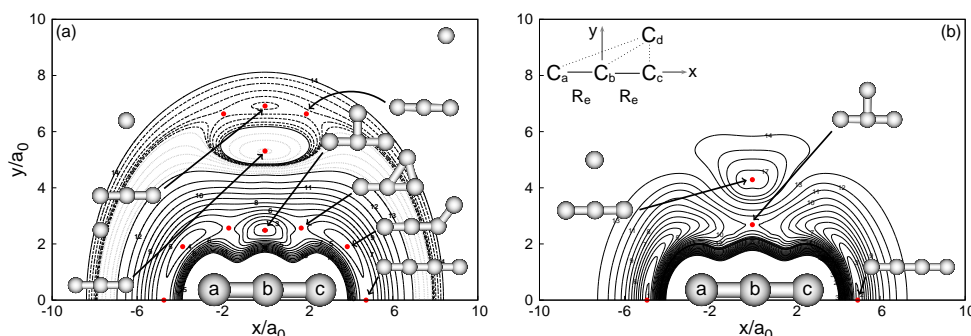


Figure 17. As in Figure 16, but for a partially relaxed ($2.2 \leq R_e/a_0 \leq 2.6$) contour plot for the C atom moving around C_3 which lies along the x axis with the origin fixed at the central carbon atom. Solid black lines are in panel (a) equally spaced by $0.01 E_h$, starting at $-0.8864 E_h$. In panel (b), the corresponding values are $0.015 E_h$ and $-0.7127 E_h$. Dotted gray and dashed black lines are equally spaced by 0.005 and $0.0002 E_h$, starting at -0.5624 and $-0.5326 E_h$, respectively.

three-body energy is known [35,116,185] to strongly favor the linear structure: it is attractive in this region, but repulsive (or less attractive) as the molecule bends, in such a way as to counteract the increased attraction of the two-body terms. Thus, at D_{3h} geometries, a minimum of the latter is accompanied by a maximum in energy of the former. On going from C_3 to C_4 , the two-body terms are doubled in number, while the three-body terms are quadrupled. If the four-body energy is ignored *a priori*, one expects, therefore, an over-stabilization of the linear structure due to the three-body terms, with highly symmetric geometries such as T_d forms being greatly destabilized. Obviously, there are cases in which the gain in two-body energy on passing from chains to rings will compensate for the loss of three-body interaction so that cyclic structures can be almost isoenergetic or even more stable than $l-C_4(^3\Sigma_g^-)$. However, such forms are predicted from our *ab initio* calculations to be high-lying stationary structures on the triplet ground-state PES. This is mostly attributed to the generally repulsive nature of the four-body term: although this contributes significantly to the total energy, it is a well accepted trend that the two- and three-body terms are predominantly structure determining in elemental clusters [119,120,185,186].

In an attempt to improve the above PES, an approximate four-body term has been added to the DMBE/ES/SS-(2+3) potential in Eq. (3.6). For this, we employed a distributed Gaussian approach [187,188] in which sets of correcting locally-valid functions are centered at convenient geometries; see also Ref. 189 for the original n -body distributed polynomial method. The effective four-body term is then written as

$$V_{C_4}^{(4)}(\mathbf{R}) = \sum_{i=1}^7 P_i^{(4)}(\boldsymbol{\Gamma}) G_i(\boldsymbol{\Gamma}), \quad (3.8)$$

where $P_i^{(4)}(\boldsymbol{\Gamma})$ are cubic polynomials of the form

$$P_i^{(4)}(\boldsymbol{\Gamma}) = (c_0 + c_1 \Gamma_1 + c_2 \Gamma_1^2 + c_3 \Gamma_2 + c_4 \Gamma_3 + c_5 \Gamma_1^3 + c_6 \Gamma_1 \Gamma_2 + c_7 \Gamma_1 \Gamma_3 + c_8 \Gamma_4 + c_9 \Gamma_5 + c_{10} \Gamma_6), \quad (3.9)$$

and $G_i(\boldsymbol{\Gamma}) = \exp[-\gamma_i(\Gamma_1)^2]$ are Gaussian factors that quickly die-off away from the origin point. Following Varandas and Murrell [119,169,186], Γ_i ($i=1-6$) are totally symmetric combinations of the Q_i ($i=1-6$) coordinates (see Table 8), which are written as symmetrized displacements

Table 8. Integrity basis used for the representation of the triplet C_4 PES.

$\Gamma_1 = Q_1$	$\Gamma_4 = Q_2 Q_3 Q_4$
$\Gamma_2 = Q_2^2 + Q_3^2 + Q_4^2$	$\Gamma_5 = Q_6^3 - 3Q_6 Q_5^2$
$\Gamma_3 = Q_5^2 + Q_6^2$	$\Gamma_6 = Q_6(2Q_2^2 - Q_3^2 - Q_4^2) + \sqrt{3}Q_5(Q_3^2 - Q_4^2)$

from a T_d geometry of side R_0 [119,169,186]

$$\begin{pmatrix} Q_1 \\ Q_2 \\ Q_3 \\ Q_4 \\ Q_5 \\ Q_6 \end{pmatrix} = \begin{pmatrix} \sqrt{1/6} & \sqrt{1/6} & \sqrt{1/6} & \sqrt{1/6} & \sqrt{1/6} & \sqrt{1/6} \\ \sqrt{1/2} & 0 & 0 & -\sqrt{1/2} & 0 & 0 \\ 0 & \sqrt{1/2} & 0 & 0 & -\sqrt{1/2} & 0 \\ 0 & 0 & \sqrt{1/2} & 0 & 0 & -\sqrt{1/2} \\ 0 & 1/2 & -1/2 & 0 & 1/2 & -1/2 \\ \sqrt{1/3} & -\sqrt{1/12} & -\sqrt{1/12} & \sqrt{1/3} & -\sqrt{1/12} & -\sqrt{1/12} \end{pmatrix} \begin{pmatrix} \Delta R_1 \\ \Delta R_2 \\ \Delta R_3 \\ \Delta R_4 \\ \Delta R_5 \\ \Delta R_6 \end{pmatrix}, \quad (3.10)$$

where $\Delta R_i = R_i - R_0$. Thus, using symmetry labels of T_d point group, Q_1 , (Q_2, Q_3, Q_4) , and (Q_5, Q_6) transform as A_1 , T_2 and E irreps, respectively. To calibrate Eq. (3.8), a total of 663 *ab initio* points has been employed as follows. First, a set of 53 (constrained) optimized geometries for collinear approximations of the C_3+C and C_2+C_2 fragments has been obtained at ve-CASDC/CBS level using C_{2v} and D_{2h} symmetries, respectively (Figure 18). The corresponding four-body interaction energies have then been determined from the requirement that they vanish at all dissociation limits (assumed as $R_{bc} = R_{cd} = 10.0 a_0$) and by further subtracting the energies predicted from DMBE/ES/SS-(2+3). An additional set of 76 nuclear arrangements related to the ORC path shown in Figure 13 has also been included. To give them ve-CASDC/CBS quality, we have scaled the corresponding MRCI(Q)-8/AVTZ energies in such a way as to reproduce the correct splitting between the $l-C_4(^3\Sigma_g^-)$ and $r-C_4(^3B_{2g})$ forms at ve-CASDC/CBS level, *i.e.*, $\Delta E_{lr} = 0.0555 E_h$ (see Table 6). Such a factor has been determined with

$$\mathcal{F} = \frac{[E_3^{\text{MRCI(Q)-8}}(\mathbf{R}_r) - E_3^{\text{MRCI(Q)-8}}(\mathbf{R}_l)]}{\Delta E_{lr}}, \quad (3.11)$$

where $E_3^{\text{MRCI(Q)-8}}(\mathbf{R}_r)$ and $E_3^{\text{MRCI(Q)-8}}(\mathbf{R}_l)$ denote the MRCI(Q)-8/AVTZ absolute energies of the rhombic and linear isomers, yielding $\mathcal{F} = 1.7010$. From (3.11), the total interaction energy, with respect to $l-C_4(^3\Sigma_g^-)$, for any structure x can be expressed by

$$E(\mathbf{R}_x) = \frac{[E_3^{\text{MRCI(Q)-8}}(\mathbf{R}_x) - E_3^{\text{MRCI(Q)-8}}(\mathbf{R}_l)]}{\mathcal{F}} + E(\mathbf{R}_l), \quad (3.12)$$

where $E(\mathbf{R}_l) = -0.7127 E_h$ is the total interaction energy of the linear global minima (relative to the infinitely separated atoms) predicted from ve-CASDC/CBS calculations. Note that this is in excellent agreement with the experimental estimate of $-0.6958 E_h$ [35,42,184]; Figure 15(a). The ORC path obtained from Eq. (3.12) and denoted MRCI(Q)-8-S is shown in Figure 13. Clearly, the present approach brings MRCI(Q)-8/AVTZ energies in close agreement with the predicted linear-rhombic energy separations at ve-CASDC/CBS, while reasonably describing the region defined by the transition state $lr-C_4(^3A'')$.

With the aid of Eq. (3.12), an extra set of 534 *ab initio* points calculated at MRCI(Q)-8/AVTZ level has further been added in the least-squares fitting procedure. Note that the effective four-body energies have been determined simply by subtracting the total interaction energies predicted by Eq. (3.12) from the ones estimated with the DMBE/ES/SS-(2+3) form. Suffice to say that, differently from the set of linear coefficients [Eq. (3.9)] in which small initial guesses have been freely varied, the origin points (R_0) and range-decaying parameters (γ_i) of every Gaussian have been optimized by trial-and-error. Table 9 displays the stratified rmsd values of the final PES

Table 9. Stratified rmsd (in kJ mol^{-1}) of the DMBE/ES/SS-(2+3+4) PES.

Energy ^a	N ^b	rmsd	Energy ^a	N ^b	rmsd
41	54	0.4	334	245	5.2
83	90	0.8	460	320	6.2
125	133	1.2	878	582	6.2
167	169	2.2	1297	616	8.1
209	182	2.3	2133	633	9.3
251	207	2.9	2552	640	10.2
292	221	3.1	6317	663	12.6

^aEnergy strata defined relative to the $l\text{-C}_4(^3\Sigma_g^-)$ structure. ^bNumber of calculated points up to indicated energy range.

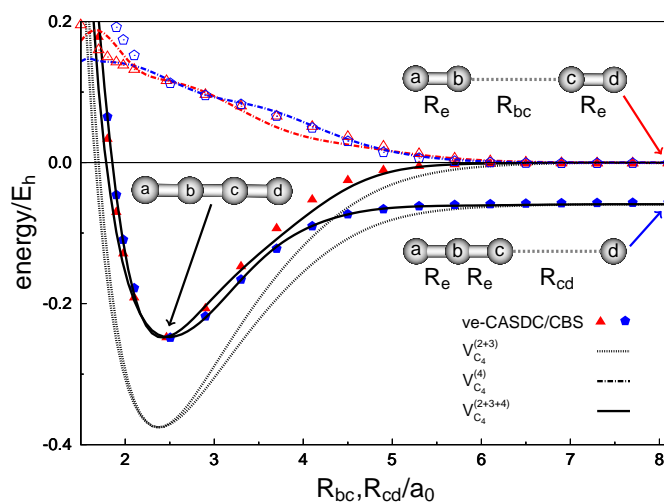


Figure 18. Relaxed 1D cuts for dissociation of $l\text{-C}_4(^3\Sigma_g^-)$ into $\text{C}_2(a^3\Pi_u)+\text{C}_2(a^3\Pi_u)$ and $l\text{-C}_3(\tilde{X}^1\Sigma_g^+)+\text{C}(^3P)$ as obtained from DMBE/ES/SS-(2+3) and DMBE/ES/SS-(2+3+4). Also shown are the approximate four-body interaction energies obtained at the ve-CASDC/CBS level and the additional term $V_{\text{C}_4}^{(4)}(\mathbf{R})$.

with respect to all fitted data set. Thus, chemical accuracy is ensured up to $\sim 334 \text{ kJ mol}^{-1}$ above the absolute linear minima with larger deviations occurring for more repulsive energy strata. The optimum numerical coefficients of Eq. (3.8) are given as electronic supplementary material.

Figures 16(b), 17(b), and 18-20 depict the most salient attributes of the full DMBE PES for triplet C_4 . As Figure 18 shows, the approximate four-body interaction energy [Eq. (3.8)] mimics well the expensive set of calculated *ab initio* points at ve-CASDC/CBS level of theory. Note that such a plot corresponds in Figure 16(b) to orthogonal cuts taken along the R_2 and R_1 directions. As clearly seen from Figure 18, the four-body term is as repulsive as $300.0 \text{ kJ mol}^{-1}$ (at ve-CASDC/CBS level) for such geometries. In fact, such a trend is further exacerbated as long as other regions of the nuclear configuration space are accessed. Yet, the simple addition of the $V_{\text{C}_4}^{(4)}(\mathbf{R})$ term makes the triplet linear structure, $l\text{-C}_4(^3\Sigma_g^-)$, to be a true minimum on the full PES with characteristic bond lengths $R_1=R_3=2.524 a_0$ and $R_2=2.435 a_0$; such a feature can best be seen from Figure 17. Moreover, the four-body term ensures that the DMBE form reproduces the correct endothermicities for dissociation into $\text{C}_2(a^3\Pi_u)+\text{C}_2(a^3\Pi_u)$ and $l\text{-C}_3(\tilde{X}^1\Sigma_g^+)+\text{C}(^3P)$, which are of about 647.8 and $504.0 \text{ kJ mol}^{-1}$, respectively. As shown in Figure 15(a), the corresponding experimental estimates are *ca.* 607.0 and $503.7 \text{ kJ mol}^{-1}$.

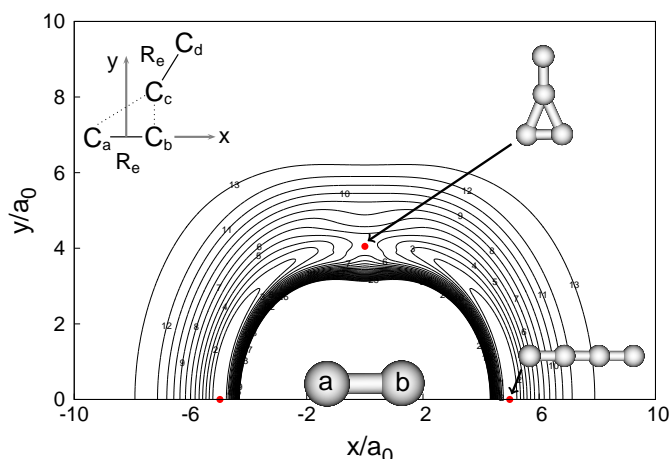


Figure 19. Partially relaxed contour plot ($2.2 \leq R_e/a_0 \leq 2.6$) of the DMBE/ES/SS-(2+3+4) PES for a C_2 fragment moving around another C_2 molecule which lies along the x axis with the origin fixed at the center of the C–C bond length. Contours are equally spaced by $0.015 E_h$, starting at $-0.7127 E_h$.

Besides accurately describing the region of the global minima, the DMBE/ES/SS-(2+3+4) form reproduces the minimum-energy interconversion pathway from $l-C_4(^3\Sigma_g^-)$ to $r-C_4(^3B_{2g})$ obtained at MRCI(Q)-8-S level, as shown in Figure 13. Yet, the triplet rhombic structure is described as a stable local minimum on the global PES (see Figure 20) with characteristic bond lengths and angles of $R_1=R_2=R_3=2.786 a_0$, $\alpha=104.8^\circ$ and $\beta=75.2^\circ$; see also Table 6. The classical barrier height predicted for such a process is $155.2 \text{ kJ mol}^{-1}$ relative to the linear minima.

Figure 17(b) illustrates the total PES for C moving around C_3 , and corresponds to plot (a) for DMBE/ES/SS-(2+3). As shown, the addition of the four-body term yields a simpler topography, in the sense of free from spurious extrema. Indeed, the T-shaped valence structure (at $x=0.000a_0$ and $y=2.686a_0$), appears in the full PES as a barrier-like feature connecting the two symmetry equivalent $l-C_4(^3\Sigma_g^-)$ structures. However, this is not a true transition state on the six-dimensional configuration space, but a saddle point of index 3, in accordance with the MRCI(Q)-8/AVTZ calculations. Note that the additional T-shaped long-range structure (at $x=0.000a_0$ and $y=4.290a_0$) form a high-symmetry D_{3h} triangle that could therefore evidence a Ci. Preliminary work at CAS(8,12)/AVTZ level using the sign-reversal property of the wave-function [167] have shown this not to be the case (at least for the ground triplet state) but revealed the presence of a high-density of close-in-energy states at this region.

The in-plane attack of C_2 to another C_2 as obtained from DMBE/ES/SS-(2+3+4) is shown in Figures 19 and 20. A notable feature from Figure 19 refers to the barrier connecting the two adjacent linear isomers, which is now a true saddle point of index 1. This feature has been confirmed by *ab initio* MRCI(Q)-8/AVTZ and CCSD(T)/AVTZ calculations. Recall that Blanksby [138] and Ngandjong *et al.* [183] using DFT predicted such a structure to be a minimum. Also seen from Figure 20 is the presence of two additional stationary points on the full PES: a slightly distorted C_{2v} capped triangle (at $x=4.582a_0$ and $y=2.642a_0$), and a *quasi*-rhombic form (at $x=5.084a_0$ and $y=0.669a_0$). Although such forms are predicted to be a minimum and transition state in 2D, this could not be confirmed here by *ab initio* calculations. Clearly, a true statement about their nature demands higher-level FVCAS/MRCI frequency calculations which are computationally unaffordable. Despite this, the chosen four-body term has been found reasonable at all investigated geometries. Of course, an enhanced fit may require an extended set of points for such geometries, and more complicated polynomial forms eventually involving all possible X_4 symmetry invariants. This is clearly a task outside the scope of the present work.

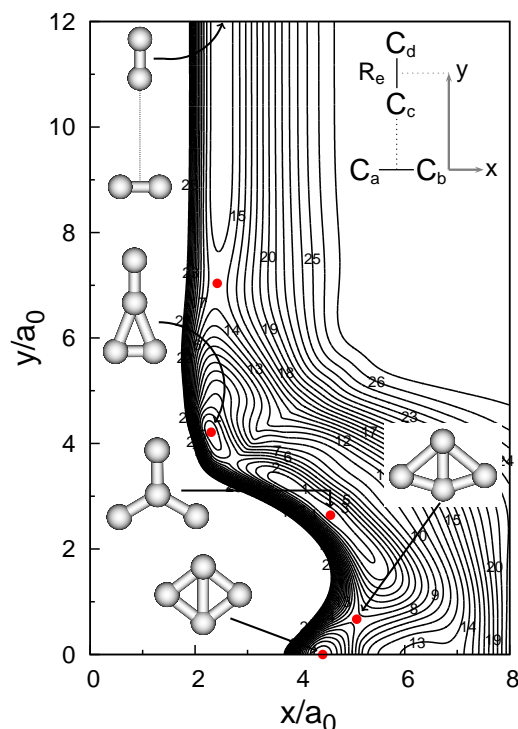


Figure 20. Partially relaxed contour plot ($2.4 \leq R_e/a_0 \leq 3.4$) for C_{2v} insertion of a C_2 fragment into another C_2 diatomic as obtained from the DMBE/ES/SS-(2+3+4) PES. Contours are equally spaced by $0.015 E_h$, starting at $-0.6770 E_h$.

4. Concluding remarks

A deep survey and analysis of the major features of C_2 , C_3 and C_4 carbon clusters has been presented. For the dimer, a summary of its current status is addressed. For C_3 , the most recent results obtained in our group were reviewed with emphasis on the modeling of its PES, which is particularly complicated due to the presence of multiple conical intersections. For the tetracarbon radical, the most stable isomeric forms of both triplet and singlet PESs and their possible interconversion pathways were examined anew by means of high-level *ab initio* calculations. Based on such results, the strategy toward a global PES for triplet C_4 has also been discussed. Starting from a truncated cluster expansion of the molecular PES that utilizes our own functions for C_3 , an approximate four-body term has been suggested using 663 accurate *ab initio* energies. The resulting full 6D DMBE form reproduces all known topographical aspects of triplet C_4 as well as its linear-rhombic isomerization path, and hence is commended for reaction dynamics studies. Clearly, the understanding of the electronic structure and properties of small precursors provides valuable information on the reactive collision processes and formation of larger C_n clusters in interstellar medium.

Glossary

ABW:	Potential energy surface of Ahmed, Balint-Kurti and Western [34].
ANO:	Atomic natural orbital basis set [37].
AVXZ:	Dunning's type augmented correlation-consistent polarized-valence basis [60,61].
CASSCF:	The complete active space self-consistent field method [175].

CAS:	Simplified notation to imply CASSCF.
CAS(<i>x,y</i>):	CASSCF specifying <i>x</i> active orbitals and <i>y</i> active electrons.
CASDC:	CASSCF energy plus dynamical correlation energy [177].
<i>c</i>-:	Cyclic molecular structure.
CBS:	The complete basis set limit [179,180].
CC:	The coupled-cluster method [59,130,133,136,137].
CCSD	CC with single and double excitations.
CCSD(T):	CCSD including triple excitations noniteratively.
CI:	The configuration interaction [56–58,131].
CISD:	CI with single and double excitations.
CISD(Q):	CISD including the Davidson correction [175].
Ci:	Conical intersection.
CSF:	The configuration state function.
<i>d</i>-:	Distorted molecular structure
dc:	Dynamical correlation.
DFT:	Density functional theory [138,183].
DMBE:	The double many-body expansion method [123–125].
DMBE-SEC:	The DMBE scaled external correlation approach [126].
EHF:	The extended Hartree-Fock energy.
ES:	The energy-switching method [173].
fc:	The frozen core approximation.
FVCAS:	The full-valence CAS method [175].
GP:	Geometric phase [164–166].
HF:	The Hartree-Fock method [175].
HOMO:	The highest occupied molecular orbital.
IR:	Abbreviation for "infrared".
IRC:	Intrinsic reaction coordinate [176,177].
irrep:	Irreducible representation.
JT:	Jahn-Teller [158].
<i>l</i>-:	Linear molecular structure.
LUMO:	The lowest unoccupied molecular orbital.
MBE:	The many-body expansion method [119,120].
MO:	Molecular orbital.
MPn:	Møller-Plesset perturbation theory [121,129].
MR:	Multi-reference electronic structure methods.
MRCI:	The MR-CI method [175].
MRCI(Q):	The MRCI method including the Davidson correction [175].
ndc:	Non-dynamical correlation.
ORC:	Optimized reaction coordinate [176,177].
PEC:	Potential energy curve.
PES:	Potential energy surface.
PJT:	Pseudo-Jahn-Teller [158].
QFF:	The quartic force field local PES.
<i>r</i>-:	Rhombic molecular structure.
rmsd:	Root mean square deviation.
RKR:	The Rydberg-Klein-Rees method [55].
RT:	Renner-Teller [158].
SCF:	The self-consistent field method [175].
SLP:	Abbreviation for "small linear parameter".
SR:	Single-reference electronic structure methods.
SS:	Potential energy surface of Schröder and Sebald [115].
VB:	The valence bond theory [18].

- ve:** valence electron approximation.
USTE: The uniform singlet- and triplet-pair extrapolation method [180].
ZPE: Zero-point energy.

Data Accessibility. The coefficients of the four-body term for the ground-state triplet PES of C_4 are available as electronic supplementary material.

Acknowledgements. This work is supported by Fundação para a Ciência e a Tecnologia and Coimbra Chemistry Centre, Portugal, through the project UI0313/QUI/2013, co-funded by FEDER/COMPETE 2020-EU. C.M. thanks also the CAPES Foundation (Ministry of Education of Brazil) for a scholarship (Process BEX 0417/13-0).

References

- Weltner W, van Zee RJ. 1989 Carbon Molecules, Ions, and Clusters. *Chem. Rev.* **89**, 1713–1747. (doi:10.1021/cr00098a005)
- van Orden A, Saykally RJ. 1998 Small Carbon Clusters: Spectroscopy, Structure, and Energetics. *Chem. Rev.* **98**, 2313–2358. (doi:10.1021/cr970086n)
- Huggins W. 1881 Preliminary Note on the Photographic Spectrum of Comet b 1881. *Proc. R. Soc. Lond.* **33**, 1–3. (doi:10.1098/rspl.1881.0060)
- Hinkle KW, Keady JJ, Bernath PF. 1988 Detection of C_3 in the Circumstellar Shell of IRC+10216. *Science* **241**, 1319–1322. (doi:10.1126/science.241.4871.1319)
- Bernath PF, Hinkle KW, Keady JJ. 1989 Detection of C_5 in the Circumstellar Shell of IRC+10216. *Science* **244**, 562–564. (doi:10.1126/science.244.4904.562)
- Lara LM, Lin ZY, Rodrigo R, Ip WH. 2011 67P/Churyumov-Gerasimenko Activity Evolution During its Last Perihelion before the Rosetta Encounter. *A&A* **525**, A36. (doi:10.1051/0004-6361/201015515)
- Cox NLJ, Patat F. 2014 Dense Molecular Clouds in the SN 2008fp Host Galaxy. *ApJ* **565**, A61–A71. (doi:10.1051/0004-6361/201219143)
- Cernicharo J, Goicoechea JR, Benilan Y. 2002 A New Infrared Band in Interstellar and Circumstellar Clouds: C_4 or C_4H ? *ApJ* **580**, L157. (doi:10.1086/345588)
- Wakelam V, Loison JC, Herbst E, Talbi D, Quan D, Caralp F. 2009 A Sensitivity Study of the Neutral-Neutral Reactions $C+C_3$ and $C+C_5$ in Cold Dense Interstellar Clouds. *A&A* **495**, 513–521. (doi:10.1051/0004-6361:200810967)
- Sakai N, Yamamoto S. 2013 Warm Carbon-Chain Chemistry. *Chem. Rev.* **113**, 8981–9015. (doi:10.1021/cr4001308)
- Koinuma H, Horiuchi T, Inomata K, Ha HK, Nakajima K, Chaudhary KA. 1996 Synthesis of Carbon Clusters and Thin Films by Low Temperature Plasma Chemical Vapor Deposition under Atmospheric Pressure. *Pure Appl. Chem.* **68**, 1151–1154. (doi:10.1351/pac199668051151)
- Su P, Wu J, Gu J, Wu W, Shaik S, Hiberty PC. 2011 Bonding Conundrums in the C_2 Molecule: A Valence Bond Study. *J. Chem. Theory Comput.* **7**, 121–130.

- (doi:10.1021/ct100577v)
13. Shaik S, Danovich D, Wu W, Su P, Rzepa HS, Hiberty PC. 2012 Quadruple bonding in C_2 and analogous eight-valence electron species. *Nat. Chem.* **4**, 195–200. (doi:10.1038/nchem.1263)
 14. Shaik S, Rzepa HS, Hoffmann R. 2013 One Molecule, Two Atoms, Three Views, Four Bonds? *Angew. Chem.* **52**, 3020–3033. (doi:10.1002/anie.201208206)
 15. Danovich D, Hiberty PC, Wu W, Rzepa HS, Shaik S. 2014 The Nature of the Fourth Bond in the Ground State of C_2 : The Quadruple Bond Conundrum. *Chem. Eur. J.* **20**, 6220–6232. (doi:10.1002/chem.201400356)
 16. Hermann M, Frenking G. 2016 The Chemical Bond in C_2 . *Chem. Eur. J.* **22**, 4100–4108. (doi:10.1002/chem.201503762)
 17. de Sousa DWO, Nascimento MAC. 2016 Is There a Quadruple Bond in C_2 ? *J. Chem. Theory Comput.* **12**, 2234–2241. (doi:10.1021/acs.jctc.6b00055)
 18. Shaik S, Danovich D, Braida B, Hiberty PC. 2016 The Quadruple Bonding in C_2 Reproduces the Properties of the Molecule. *Chem. Eur. J.* **22**, 4116–4128. (doi:10.1002/chem.201600011)
 19. Shaik S, Danovich D, Hiberty PC. 2017 To Hybridize or not to Hybridize? This is the Dilemma. *Comput. Theor. Chem.* **1116**, 242–249. (doi:10.1016/j.comptc.2017.01.017)
 20. Hirsch A. 2010 The Era of Carbon Allotropes. *Nat. Mater.* **9**, 868–871. (doi:10.1038/nmat2885)
 21. Kroto HW, Heath JR, O'Brien SC, Curl RF, Smalley RE. 1985 C_{60} : Buckminsterfullerene. *Nature* **318**, 162–163. (doi:10.1038/318162a0)
 22. Iijima S. 1991 Helical Microtubules of Graphitic Carbon. *Nature* **354**, 56–58. (doi:10.1038/354056a0)
 23. Novoselov KS, Geim AK, Morozov SV, Jiang D, Zhang Y, Dubonos SV, Grigorieva IV, Firsov AA. 2004 Electric Field Effect in Atomically Thin Carbon Films. *Science* **306**, 666–669. (doi:10.1126/science.1102896)
 24. Diederich F, Kivala M. 2010 All-Carbon Scaffolds by Rational Design. *Adv. Mat.* **22**, 803–812. (doi:10.1002/adma.200902623)
 25. Ueno Y, Saito S. 2008 Geometries, Stabilities, and Reactions of Carbon Clusters: Towards a Microscopic Theory of Fullerene Formation. *Phys. Rev. B* **77**, 085403–085413. (doi:10.1103/PhysRevB.77.085403)
 26. Kosimov DP, Dzhurakhalov AA, Peeters FM. 2008 Theoretical Study of the Stable States of Small Carbon Clusters C_n ($n=2-10$). *Phys. Rev. B* **78**, 235433–235441. (doi:10.1103/PhysRevB.78.235433)
 27. Kosimov DP, Dzhurakhalov AA, Peeters FM. 2010 Carbon Clusters: From Ring Structures to Nanographene. *Phys. Rev. B* **81**, 195414–195426. (doi:10.1103/PhysRevB.81.195414)
 28. Yen TW, Lai SK. 2015 Use of Density Functional Theory Method to Calculate Structures of Neutral Carbon Clusters C_n ($3 \leq n \leq 24$) and Study Their Variability of Structural Forms. *J. Chem. Phys.* **142**, 084313–084325. (doi:10.1063/1.4908561)

29. Lai SK, Setiyawati I, Yen TW, Tang YH. 2016 Studying Lowest Energy Structures of Carbon Clusters by Bond-order Empirical Potentials. *Theor. Chem. Acc.* **136**, 20–32. (doi:10.1007/s00214-016-2042-2)
30. Varandas AJC. 2008 Extrapolation to the Complete-Basis-Set Limit and the Implications of Avoided Crossings: The $X^1\Sigma_g^+$, $B^1\Delta_g$, and $B'^1\Sigma_g^+$ States of C_2 . *J. Chem. Phys.* **129**, 234103–234116. (doi:10.1063/1.3036115)
31. Varandas AJC. 2009 A Simple, Yet Reliable, Direct Diabatization Scheme. The $^1\Sigma_g^+$ States of C_2 . *Chem. Phys. Lett.* **471**, 315–321. (doi:10.1016/j.cplett.2009.02.028)
32. Boggio-Pasqua M, Voronin AI, Halvick P, Rayez JC. 2000 Analytical Representations of High Level *Ab Initio* Potential Energy Curves of the C_2 Molecule. *J. Mol. Struct.: THEOCHEM* **531**, 159–167. (doi:10.1016/S0166-1280(00)00442-5)
33. Terentyev A, Scholz R, Schreiber M, Seifert G. 2004 Theoretical Investigation of Excited States of C_3 . *J. Chem. Phys.* **121**, 5767–5776. (doi:10.1063/1.1786291)
34. Ahmed K, Balint-Kurti GG, Western CM. 2004 *Ab Initio* Calculations and Vibrational Energy Level Fits for the Lower Singlet Potential-Energy Surfaces of C_3 . *J. Chem. Phys.* **121**, 10041–10051. (doi:10.1063/1.1806820)
35. Rocha CMR, Varandas AJC. 2015 Accurate *Ab Initio*-Based Double Many-Body Expansion Potential Energy Surface for the Adiabatic Ground-State of the C_3 Radical Including Combined Jahn-Teller plus Pseudo-Jahn-Teller Interactions. *J. Chem. Phys.* **143**, 074302–074318. (doi:10.1063/1.4928434)
36. Rocha CMR, Varandas AJC. 2016 The Jahn-Teller plus Pseudo-Jahn-Teller Vibronic Problem in the C_3 Radical and its Topological Implications. *J. Chem. Phys.* **144**, 064309–064324. (doi:10.1063/1.4941382)
37. Parasuk V, Almlöf J. 1991 The Electronic and Molecular Structure of C_4 : Multireference Configuration-Interaction Calculations. *J. Chem. Phys.* **94**, 8172–8178. (doi:10.1063/1.460100)
38. Massó H, Senent ML, Rosmus P, Hochlaf M. 2006 Electronic structure calculations on the C_4 cluster. *J. Chem. Phys.* **124**, 234304–234311. (doi:10.1063/1.2187972)
39. Yousaf KE, Taylor PR. 2008 On the Electronic Structure of Small Cyclic Carbon Clusters. *Chem. Phys.* **349**, 58–68. (doi:10.1016/j.chemphys.2008.02.059)
40. Pitzer KS, Clementi E. 1959 Large Molecules in Carbon Vapor. *J. Am. Chem. Soc.* **81**, 4477–4485. (doi:10.1021/ja01526a010)
41. Clementi E. 1961 Electronic States in the C_4 Molecule. *J. Am. Chem. Soc.* **83**, 4501–4505. (doi:10.1021/ja01483a002)
42. Gingerich KA, Finkbeiner HC, Schmude RW. 1994 Enthalpies of Formation of Small Linear Carbon Clusters. *J. Am. Chem. Soc.* **116**, 3884–3888. (doi:10.1021/ja00088a025)
43. Sasaki K, Wakasaki T, Matsui S, Kadota K. 2002 Distributions of C_2 and C_3 Radical Densities in Laser-Ablation Carbon Plumes Measured by Laser-Induced Fluorescence Imaging Spectroscopy. *J. Appl. Phys.* **91**, 4033–4039.

- (doi:10.1063/1.1455151)
44. Belau L, Wheeler SE, Ticknor BW, Ahmed M, Leone SR, Allen WD, Schaefer HF, Duncan MA. 2007 Ionization Thresholds of Small Carbon Clusters: Tunable VUV Experiments and Theory.
J. Am. Chem. Soc. **129**, 10229–10243.
(doi:10.1021/ja072526q)
 45. Rodríguez-Fortea A, Irle S, Poblet JM. 2011 Fullerenes: Formation, Stability, and Reactivity.
WIREs Comput. Mol. Sci. **1**, 350–367.
(doi:10.1002/wcms.21)
 46. Wollaston WH. 1802 A Method of Examining Refractive and Dispersive Powers, by Prismatic Reflection.
Phil. Trans. R. Soc. A **92**, 365–380.
(doi:10.1098/rstl.1802.0014)
 47. Swan W. 1857 XXIX. On the Prismatic Spectra of the Flames of Compounds of Carbon and Hydrogen.
Trans. R. Soc. Edinburgh **21**, 411–429.
(doi:10.1017/S0080456800032233)
 48. Furtenbacher T, Szabó I, Császár AG, Bernath PF, Yurchenko SN, Tennyson J. 2016 Experimental Energy Levels and Partition Function of the $^{12}\text{C}_2$ Molecule.
ApJS **224**, 44–58.
(doi:10.3847/0067-0049/224/2/44)
 49. Swings P. 1943 Cometary Spectra (Council Report on the Progress at Astronomy).
MNRAS **103**, 86–110.
(doi:10.1093/mnras/103.2.86)
 50. Ballik EA, Ramsay DA. 1959 Ground State of the C_2 Molecule.
J. Chem. Phys. **31**, 1128–1128.
(doi:10.1063/1.1730515)
 51. Martin M. 1992 C_2 Spectroscopy and Kinetics.
J. Photochem. Photobiol. A **66**, 263–289.
(doi:10.1016/1010-6030(92)80001-C)
 52. Mulliken RS. 1939 Note on Electronic States of Diatomic Carbon, and the Carbon-Carbon Bond.
Phys. Rev. **56**, 778–781.
(doi:10.1103/PhysRev.56.778)
 53. Araki G, Watari W. 1951 Electronic States of C_2 -Molecule, II: Effect of 2s-Shells.
Progr. Theor. Phys. **6**, 945–960.
(doi:10.1143/ptp/6.6.945)
 54. Clementi E, Pitzer KS. 1960 Low Excited States in C_2 .
J. Chem. Phys. **32**, 656–662.
(doi:10.1063/1.1730776)
 55. Read SM, Vanderslice JT. 1962 Potential Energy Curves for C_2 .
J. Chem. Phys. **36**, 2366–2369.
(doi:10.1063/1.1732890)
 56. Fraga S, Ransil BJ. 1962 Studies in Molecular Structure. VII. Limited Configuration Interaction for Selected First-Row Diatomics.
J. Chem. Phys. **36**, 1127–1142.
(doi:10.1063/1.1732704)
 57. Fougere PF, Nesbet RK. 1966 Electronic Structure of C_2 .
J. Chem. Phys. **44**, 285–298.
(doi:10.1063/1.1726460)
 58. Kirby K, Liu B. 1979 The Valence States of C_2 : A Configuration Interaction Study.
J. Chem. Phys. **70**, 893–900.
(doi:10.1063/1.437480)
 59. Watts JD, Bartlett RJ. 1992 Coupled-cluster calculations on the C_2 molecule and the C_2^+ and C_2^- molecular ions.
J. Chem. Phys. **96**, 6073–6084.
(doi:10.1063/1.462649)
 60. Dunning TH. 1989 Gaussian Basis Sets for Use in Correlated Molecular Calculations. I. The Atoms Boron through Neon and Hydrogen.

- J. Chem. Phys.* **90**, 1007–1023.
(doi:10.1063/1.456153)
61. Kendall RA, Dunning TH, Harrison RJ. 1992 Electron Affinities of the First-Row Atoms Revisited. Systematic Basis Sets and Wave Functions.
J. Chem. Phys. **96**, 6796–6806.
(doi:10.1063/1.462569)
62. Bauschlicher CW, Langhoff SR. 1987 *Ab initio* calculations on C₂, Si₂, and SiC.
J. Chem. Phys. **87**, 2919–2924.
(doi:10.1063/1.453080)
63. Pradhan AD, Partridge H, Bauschlicher CW. 1994 The Dissociation Energy of CN and C₂.
J. Chem. Phys. **101**, 3857–3861.
(doi:10.1063/1.467503)
64. Peterson KA. 1995 Accurate Multireference Configuration Interaction Calculations on the Lowest ¹Σ⁺ and ³Π electronic states of C₂, CN⁺, BN, and BO⁺.
J. Chem. Phys. **102**, 262–277.
(doi:10.1063/1.469399)
65. Bruna PJ, Grein F. 2001 Spectroscopy of the C₂ Molecule: Valence and Rydberg states in the 7–10 eV region. An *Ab Initio* Study.
Can. J. Phys. **79**, 653–671.
(doi:10.1139/p01-019)
66. Müller T, Dallos M, Lischka H, Dubrovay Z, Szalay PG. 2001 A Systematic Theoretical Investigation of the Valence Excited States of the Diatomic Molecules B₂, C₂, N₂ and O₂.
Theor. Chem. Acc. **105**, 227–243.
(doi:10.1007/s002140000210)
67. Schmidt TW, Bacskay GB. 2007 Oscillator Strengths of the Mulliken, Swan, Ballik-Ramsay, Phillips, and *d*³Π_g-*c*³Σ_u⁺ Systems of C₂ Calculated by MRCI Methods Utilizing a Biorthogonal Transformation of CASSCF Orbitals.
J. Chem. Phys. **127**, 234310–234313.
(doi:10.1063/1.2806988)
68. Schmidt TW, Bacskay GB. 2011 The 1⁵Π_g state of C₂.
J. Chem. Phys. **134**, 224311–224314.
(doi:10.1063/1.3599933)
69. Krechkivska O, Bacskay GB, Troy TP, Nauta K, Kreuzer TD, Kable SH, Schmidt TW. 2015 Resonance-Enhanced 2-Photon Ionization Scheme for C₂ through a Newly Identified Band System: 4³Π_g-*a*³Π_u.
J. Phys. Chem. A **119**, 12102–12108.
(doi:10.1021/acs.jpca.5b05685)
70. Krechkivska O, Bacskay GB, Welsh BA, Nauta K, Kable SH, Stanton JF, Schmidt TW. 2016 The Ionization energy of C₂.
J. Chem. Phys. **144**, 144305–144310.
(doi:10.1063/1.4944932)
71. Krechkivska O, Welsh BA, Bacskay GB, Nauta K, Kable SH, Schmidt TW. 2017 First Observation of the 3³Π_g State of C₂: Born-Oppenheimer Breakdown.
J. Chem. Phys. **146**, 134306–134313.
(doi:10.1063/1.4979293)
72. Abrams ML, Sherrill CD. 2004 Full Configuration Interaction Potential Energy Curves for the X¹Σ_g⁺, B¹Δ_g, and B'¹Σ_g⁺ states of C₂: A challenge for Approximate Methods.
J. Chem. Phys. **121**, 9211–9219.
(doi:10.1063/1.1804498)
73. Sherrill CD, Piecuch P. 2005 The X¹Σ_g⁺, B¹Δ_g, and B'¹Σ_g⁺ states of C₂: A Comparison of Renormalized Coupled-Cluster and Multireference Methods with Full Configuration Interaction Benchmarks.
J. Chem. Phys. **122**, 124104–124120.
(doi:10.1063/1.1867379)
74. Booth GH, Cleland D, Thom AJW, Alavi A. 2011 Breaking the Carbon Dimer: The Challenges of Multiple Bond Dissociation with Full Configuration Interaction Quantum Monte Carlo Methods.
J. Chem. Phys. **135**, 084104–084117.

- (doi:10.1063/1.3624383)
75. Roskop LB, Kong L, Valeev EF, Gordon MS, Windus TL. 2014 Assessment of Perturbative Explicitly Correlated Methods for Prototypes of Multiconfiguration Electronic Structure. *J. Chem. Theory Comput.* **10**, 90–101. (doi:10.1021/ct4006773)
 76. Schleyer PvR, Maslak P, Chandrasekhar J, Grev RS. 1993 Is a C–C Quadruple Bond Possible? *Tetrahedron Lett.* **34**, 6387–6390. (doi:10.1016/0040-4039(93)85052-X)
 77. Herzberg G. 1942 Laboratory Production of the λ 4050 Group Occurring in Cometary Spectra; Future Evidence for the Presence of CH₂ Molecules in Comets. *ApJ* **96**, 314–315. (doi:10.1086/144464)
 78. Douglas AE. 1951 Laboratory Studies of the λ 4050 Group of Cometary Spectra. *ApJ* **114**, 446–449. (doi:10.1086/145486)
 79. Gausset L, Herzberg G, Lagerqvist A, Rosen B. 1963 Spectrum of the C₃ Molecule. *Discuss. Faraday Soc.* **35**, 113–117. (doi:10.1039/DF9633500113)
 80. Gausset L, Herzberg G, Lagerqvist A, Rosen B. 1965 Analysis of the 4050-Å Group of the C₃ Molecule. *ApJ* **142**, 45–82. (doi:10.1086/148262)
 81. Rohlfig EA, Goldsmith JEM. 1990 Stimulated-Emission Pumping Spectroscopy of Jet-Cooled C₃: Antisymmetric Stretch-Bend Levels. *J. Opt. Soc. Am. B* **7**, 1915–1923. (doi:10.1364/JOSAB.7.001915)
 82. Northrup FJ, Sears TJ. 1990 Stimulated-Emission Pumping Spectroscopy Study of Jet-Cooled C₃: Pure Bending Levels and Bend-Symmetric-Stretch Combination Levels of X \ddot{E} I \dot{I} 1 Σ g⁺. *J. Opt. Soc. Am. B* **7**, 1924–1934. (doi:10.1364/JOSAB.7.001924)
 83. Chen CW, Merer AJ, Chao JM, Hsu YC. 2010 Laser Excitation Spectrum of C₃ in the region 26 000–30 700 cm⁻¹. *J. Mol. Spectrosc.* **263**, 56–70. (doi:10.1016/j.jms.2010.06.010)
 84. Krieg J, Lutter V, Endres CP, Keppeler IH, Jensen P, Harding ME, Vázquez J, Schlemmer S, Giesen TF, Thorwirth S. 2013 High-Resolution Spectroscopy of C₃ Around 3 μ m. *J. Phys. Chem. A* **117**, 3332–3339. (doi:10.1021/jp3119204)
 85. Breier AA, Büchling T, Schnierer R, Lutter V, Fuchs GW, Yamada KMT, Mookerjee B, Stutzki J, Giesen TF. 2016 Lowest Bending Mode of ¹³C-Substituted C₃ and an Experimentally Derived Structure. *J. Chem. Phys.* **145**, 234302–234311. (doi:10.1063/1.4971854)
 86. Weltner W, McLeod D. 1964 Spectroscopy of Carbon Vapor Condensed in Rare-Gas Matrices at 4 and 20 K. II. *J. Chem. Phys.* **40**, 1305–1316. (doi:10.1063/1.1725313)
 87. Sasada H, Amano T, Jarman C, Bernath PF. 1991 A New Triplet Band System of C₃: The $\tilde{b}^3\Pi_g-\tilde{b}^3\Pi_u$ Transition. *J. Chem. Phys.* **94**, 2401–2407. (doi:10.1063/1.460710)
 88. Sych Y, Bornhauser P, Knopp G, Liu Y, Gerber T, Marquardt R, Radi PP. 2013 Perturbation Facilitated Two-Color Four-Wave-Mixing Spectroscopy of C₃. *J. Chem. Phys.* **139**, 154203–154209. (doi:10.1063/1.4825198)
 89. Rohlfig EA. 1995 Spectroscopic Studies of Large-Amplitude Motion in Small Clusters. In *Spectroscopy and Structure* (ed. MA Duncan), volume 3 of *Advances in Metal and Semiconductor Clusters: Spectroscopy and Structure*, chapter 2, pp. 85–111. Jai Press Inc.

90. Oka T, Thorburn JA, McCall BJ, Friedman SD, Hobbs LM, Sonnentrucker P, Welty DE, York DG. 2003 Observations of C₃ in Translucent Sight Lines.
ApJ **582**, 823–829.
(doi:10.1086/344726)
91. Ádámkóvics M, Blake GA, McCall BJ. 2003 Observations of Rotationally Resolved C₃ in Translucent Sight Lines.
ApJ **595**, 235–246.
(doi:10.1086/377305)
92. Cernicharo J, Goicoechea JR, Caux E. 2000 Far-Infrared Detection of C₃ in Sagittarius B2 and IRC+10216.
ApJ Lett. **534**, L199–L202.
(doi:10.1086/312668)
93. Mookerjea, B, Giesen, T, Stutzki, J, Cernicharo, J, Goicoechea, J R, De Luca, M, Bell, T A, Gupta, H, Gerin, M, Persson, C M, Sonnentrucker, P, Makai, Z, Black, J, Boulanger, F, Coutens, A, Dartois, E, Encrenaz, P, Falgarone, E, Geballe, T, Godard, B, Goldsmith, P F, Gry, C, Hennebelle, P, Herbst, E, Hily-Blant, P, Joblin, C, Kazmierczak, M, Kolos, R, Krelowski, J, Lis, D C, Martin-Pintado, J, Menten, K M, Monje, R, Pearson, J C, Perault, M, Phillips, T G, Plume, R, Salez, M, Schlemmer, S, Schmidt, M, Teyssier, D, Vastel, C, Yu, S, Dieleman, P, Göusten, R, Honingh, C E, Morris, P, Roelfsema, P, Schieder, R, Tielens, A G G M, Zmuidzinas, J. 2010 Excitation and Abundance of C₃ in Star Forming Cores.
A&A **521**, L13–L17.
(doi:10.1051/0004-6361/201015095)
94. Clegg RES, Lambert DL. 1982 On C₃ Molecules in Diffuse Interstellar Clouds.
Mon. Not. R. Astron. Soc. **201**, 723–733.
95. Maier JP, Lakin NM, Walker GAH, Bohlender DA. 2001 Detection of C₃ in Diffuse Interstellar Clouds.
ApJ **553**, 267–273.
(doi:10.1086/320668)
96. Roueff E, Felenbok P, Black JH, Gry C. 2002 Interstellar C₃ Toward HD 210121.
A&A **384**, 629–637.
(doi:10.1051/0004-6361:20020067)
97. Nemes L, Keszler AM, Parigger CG, Hornkohl JO, Michelsen HA, Stakhursky V. 2007 Spontaneous Emission from the C₃ Radical in Carbon Plasma.
Appl. Opt. **46**, 4032–4040.
(doi:10.1364/AO.46.004032)
98. Lopez-Quintas I, Oujja M, Sanz M, Martín M, Ganeev RA, Castillejo M. 2013 Low-Order Harmonic Generation in Nanosecond Laser Ablation Plasmas of Carbon Containing Materials.
Appl. Surf. Sci. **278**, 33–37.
(doi:10.1016/j.apsusc.2012.10.105)
99. Clementi E, McLean AD. 1962 SCF-LCAO-MO Wave Function for the $^1\Sigma_g^+$ Ground State of C₃.
J. Chem. Phys. **36**, 45–47.
(doi:10.1063/1.1732314)
100. Clementi E, Clementi H. 1962 Electron Distributions in Small Molecules.
J. Chem. Phys. **36**, 2824–2833.
(doi:10.1063/1.1732385)
101. Hoffmann R. 1966 Extended Hückel theory - V: Cumulenes, Polyenes, Polyacetylenes and C_n.
Tetrahedron **22**, 521–538.
(doi:10.1016/0040-4020(66)80020-0)
102. Liskow DH, Bender CF, Schaefer HF. 1972 Bending Frequency of the C₃ Molecule.
J. Chem. Phys. **56**, 5075–5080.
(doi:10.1063/1.1676990)
103. Perić-Radić J, Römelt J, Peyerimhoff SD, Buenker RJ. 1977 Configuration Interaction Calculation of the Potential Curves for the C₃ molecule in its Ground and Lowest-Lying Π_u States.
Chem. Phys. Lett. **50**, 344–350.

- (doi:10.1016/0009-2614(77)80197-8)
104. Römelt J, Peyerimhoff SD, Buenker RJ. 1978 *Ab Initio* MRD CI Calculations for the Electron Spectrum of the C₃ Radical.
Chem. Phys. Lett. **58**, 1–7.
(doi:10.1016/0009-2614(78)80305-4)
 105. Carter S, Mills IM, Murrell JN. 1980 Analytical Functions for the Ground State Potential Surfaces of C₃($\tilde{X}, ^1\Sigma_g^+$) and HCN($\tilde{X}, ^1\Sigma^+$).
J. Mol. Spectrosc. **81**, 110–121.
(doi:10.1016/0022-2852(80)90332-X)
 106. Carter S, Mills IM, Dixon RN. 1984 Potential Energy Surface Intersections for Triatomic Molecules.
J. Mol. Spectrosc. **106**, 411–422.
(doi:10.1016/0022-2852(84)90171-1)
 107. Murrell JN. 1990 The many-body expansion of the potential energy function for elemental clusters.
Int. J. Quant. Chem. **37**, 95–102.
(doi:10.1002/qua.560370108)
 108. Kraemer W, Bunker P, Yoshimine M. 1984 A Theoretical Study of the Rotation-Vibration Energy Levels and Dipole Moment Functions of CCN⁺, CNC⁺, and C₃.
J. Mol. Spectrosc. **107**, 191–207.
(doi:10.1016/0022-2852(84)90276-5)
 109. Jensen P. 1989 The Potential Energy Surface for the C₃ Molecule Determined from Experimental Data. Evidence for a Bent Equilibrium Structure.
Collect. Czech. Chem. Commun. **54**, 1209–1218.
(doi:10.1135/cccc19891209)
 110. Jørgensen UG, Almlöf J, Siegbahn PEM. 1989 Complete Active Space Self-Consistent Field Calculations of the Vibrational Band Strengths for C₃.
ApJ **343**, 554–561.
(doi:10.1086/167729)
 111. Jensen P, Rohlfing CM, Almlöf J. 1992 Calculation of the Complete-Active-Space-Self-Consistent-Field Potential-Energy Surface, the Dipole Moment Surfaces, the Rotation-Vibration Energies, and the Vibrational Transition Moments for C₃($\tilde{X}, ^1\Sigma_g^+$).
J. Chem. Phys. **97**, 3399–3411.
(doi:10.1063/1.462976)
 112. Špirko V, Mengel M, Jensen P. 1997 Calculation of Rotation-Vibration Energy Levels in Ground State C₃ by a Born-Oppenheimer-Type Separation of the Vibrational Motions.
J. Mol. Spectrosc. **183**, 129–138.
(doi:10.1006/jmsp.1996.7257)
 113. Mladenović M, Schmatz S, Botschwina P. 1994 Large-Scale *Ab Initio* Calculations for C₃.
J. Chem. Phys. **101**, 5891–5899.
(doi:10.1063/1.467305)
 114. Saha S, Western CM. 2006 Experimental and *Ab Initio* study of a new $\tilde{d}^1\delta_g$ state of the c₃ radical.
J. Chem. Phys. **125**, 224307–224318.
(doi:10.1063/1.2399528)
 115. Schröder B, Sebald P. 2016 High-Level Theoretical Rovibrational Spectroscopy beyond fc-CCSD(T): The C₃ molecule.
J. Chem. Phys. **144**, 044307–044318.
(doi:10.1063/1.4940780)
 116. Rocha, C. M. R. and Varandas, A. J. C.; to be submitted
 117. Rocha, C. M. R. and Varandas, A. J. C.; to be submitted
 118. Fueno H, Taniguchi Y. 1999 *Ab Initio* Molecular Orbital Study of the Isomerization Reaction Surfaces of C₃ and C₃⁻.
Chem. Phys. Lett. **312**, 65–70.
(doi:10.1016/S0009-2614(99)00861-1)
 119. Murrell JN, Carter S, Farantos SC, Huxley P, Varandas AJC. 1984 *Molecular Potential Energy Functions*.
Chichester: John Wiley & Sons.

120. Varandas AJC, Murrell JN. 1977 A Many-Body Expansion of Polyatomic Potential Energy Surfaces: Application to H_n Systems. *Faraday Discuss. Chem. Soc.* **62**, 92–109. (doi:10.1039/DC9776200092)
121. Whiteside RA, Krishnan R, Frisch MJ, Pople JA, Schleyer PVR. 1981 Cyclic C_3 Structures. *Chem. Phys. Lett.* **80**, 547–551. (doi:10.1016/0009-2614(81)85075-0)
122. Jensen P. 1988 A New Morse Oscillator-Rigid Bender Internal Dynamics (MORBID) Hamiltonian for Triatomic Molecules. *J. Mol. Spectrosc.* **128**, 478–501. (doi:10.1016/0022-2852(88)90164-6)
123. Varandas AJC. 1984 A Double Many-Body Expansion of Molecular Potential Energy Functions. *Mol. Phys.* **53**, 1303–1325. (doi:10.1080/00268978400103021)
124. Varandas AJC. 1985 A general approach to the potential energy functions of small polyatomic systems: Molecules and van der Waals molecules. *J. Mol. Struct.: THEOCHEM* **120**, 401–424. (doi:10.1016/0166-1280(85)85134-4)
125. Varandas AJC. 1988 Intermolecular and Intramolecular Potentials: Topographical Aspects, Calculation, and Functional Representation via A Double Many-Body Expansion Method. *Adv. Chem. Phys.* **74**, 255–338. (doi:10.1002/9780470141236.ch2)
126. Varandas AJC. 1989 A Semiempirical Method for Correcting Configuration Interaction Potential Energy Surfaces. *J. Chem. Phys.* **90**, 4379–4391. (doi:10.1063/1.456624)
127. Galvão BRL, Mota VC, Varandas AJC. 2015 Modeling Cusps in Adiabatic Potential Energy Surfaces. *J. Phys. Chem. A* **119**, 1415–1421. (doi:10.1021/jp512671q)
128. Galvão BRL, Mota VC, Varandas AJC. 2016 Modeling Cusps in Adiabatic Potential Energy Surfaces Using a Generalized Jahn-Teller Coordinate. *Chem. Phys. Lett.* **660**, 55–59. (doi:10.1016/j.cplett.2016.07.029)
129. Whiteside RA, Krishnan R, Defrees DJ, Pople JA, Schleyer PR. 1981 Structures of C_4 . *Chem. Phys. Lett.* **78**, 538–540. (doi:10.1016/0009-2614(81)85253-0)
130. Magers DH, Harrison RJ, Bartlett RJ. 1986 Isomers and Excitation Energies of C_4 . *J. Chem. Phys.* **84**, 3284–3290.
131. Ritchie JP, King HF, Young WS. 1986 Structures and Energies for C_4 . *J. Chem. Phys.* **85**, 5175–5182. (doi:10.1063/1.451711)
132. Pacchioni G, Koutecký J. 1988 *Ab Initio* MRD CI Investigation of the Optical Spectra of C_4 and C_5 Clusters. *J. Chem. Phys.* **88**, 1066–1073. (doi:10.1063/1.454276)
133. Bernholdt DE, Magers DH, Bartlett RJ. 1988 Stability and Properties of C_4 Isomers. *J. Chem. Phys.* **89**, 3612–3617. (doi:10.1063/1.454881)
134. Lammertsma K, Güner OF, Sudhakar PV. 1991 Rhombic C_4 . Does It Contain the Shortest Nonbonding C-C Distance? *J. Chem. Phys.* **94**, 8105–8111. (doi:10.1063/1.460093)
135. Martin JML, François JP, Gijbels R. 1991 A Critical Comparison of MINDO/3, MNDO, AM1, and PM3 for a Model Problem: Carbon Clusters C_2 – C_{10} . An *Ad Hoc* Reparametrization of MNDO Well Suited for the Accurate Prediction of their Spectroscopic Constants. *J. Comput. Chem.* **12**, 52–70.

- (doi:10.1002/jcc.540120107)
136. Martin JML, François JP, Gijbels R. 1991 *Ab Initio* Study of the Structure, Infrared Spectra, and Heat of Formation of C_4 .
J. Chem. Phys. **94**, 3753–3761.
(doi:10.1063/1.459747)
 137. Watts JD, Gauss J, Stanton JF, Bartlett RJ. 1992 Linear and Cyclic Isomers of C_4 . A Theoretical Study with Coupled-Cluster Methods and Large Basis Sets.
J. Chem. Phys. **97**, 8372–8381.
(doi:10.1063/1.463407)
 138. Blanksby SJ, Schröder D, Dua S, Bowie JH, Schwarz H. 2000 Conversion of Linear to Rhombic C_4 in the Gas Phase: A Joint Experimental and Theoretical Study.
J. Am. Chem. Soc. **122**, 7105–7113.
(doi:10.1021/ja000951c)
 139. Wang T, Buntine MA, Bowie JH. 2009 Study of the Isomers of Isoelectronic C_4 , $(C_3B)^-$, and $(C_3N)^+$: Rearrangements through Cyclic Isomers.
J. Phys. Chem. A **113**, 12952–12960.
(doi:10.1021/jp907484z)
 140. Senent ML, Massó H, Hochlaf M. 2007 Anharmonic Spectroscopic Study of the Ground Electronic State of Various C_4 Radical Isotopomers.
ApJ **670**, 1510–1517.
(doi:10.1086/522485)
 141. Wang X, Huang X, Bowman JM, Lee TJ. 2013 Anharmonic Rovibrational Calculations of Singlet Cyclic C_4 Using a New *Ab Initio* Potential and a Quartic Force Field.
J. Chem. Phys. **139**, 224302–224308.
(doi:10.1063/1.4837177)
 142. Maier JP, Walker GAH, Bohlender DA. 2002 Limits to Interstellar C_4 and C_5 toward ζ Ophiuchi.
ApJ **566**, 332–335.
(doi:10.1086/337965)
 143. Jungen M, Xu R. 2003 The Absorption Spectrum of C_4 .
Z. Phys. Chem. **217**, 105–114.
(doi:10.1524/zpch.217.2.105.22612)
 144. Weltner W, Thompson KR, DeKock RL. 1971 Spectroscopy of Carbon Molecules. IV. C_4 , C_5 , C_6 (and C_9).
J. Am. Chem. Soc. **93**, 4688–4695.
(doi:10.1021/ja00748a007)
 145. Graham WRM, Dismuke KI, Weltner J W. 1976 The C_4 Molecule.
ApJ **204**, 301–310.
(doi:10.1086/154172)
 146. Heath JR, Saykally RJ. 1991 The Structure of the C_4 Cluster Radical.
J. Chem. Phys. **94**, 3271–3273.
(doi:10.1063/1.459797)
 147. Moazzen-Ahmadi N, Thong JJ, McKellar ARW. 1994 Infrared Diode Laser Spectroscopy of the ν_3 fundamental and $\nu_3 + \nu_5 - \nu_5$ Sequence Bands of the C_4 Radical in a Hollow Cathode Discharge.
J. Chem. Phys. **100**, 4033–4038.
(doi:http://dx.doi.org/10.1063/1.466340)
 148. Xu C, Burton GR, Taylor TR, Neumark DM. 1997 Photoelectron Spectroscopy of C_4^- , C_6^- , and C_8^- .
J. Chem. Phys. **107**, 3428–3436.
(doi:10.1063/1.474715)
 149. Gakwaya S, Abusara Z, Moazzen-Ahmadi N. 2004 Vibrational Hot Bands of Linear C_4 and C_5 arising from a Bending Vibration with Two Quanta in the Lowest Bend: The $(\nu_3+2\nu_5)-2\nu_5$ Band of C_4 and the $(\nu_3+2\nu_7)-2\nu_7$ Band of C_5 .
Chem. Phys. Lett. **398**, 564–571.
(doi:10.1016/j.cplett.2004.09.130)
 150. Algranati M, Feldman H, Kella D, Malkin E, Miklazky E, Naaman R, Vager Z, Zajfman J. 1989 The Structure of C_4 as Studied by the Coulomb Explosion Method.

- J. Chem. Phys.* **90**, 4617–4618.
(doi:10.1063/1.456597)
151. Vager Z, Feldman H, Kella D, Malkin E, Miklazky E, Zajfman J, Naaman R. 1991 The Structure of Small Carbon Clusters.
Z. Phys. D **19**, 413–418.
(doi:10.1007/BF01448341)
152. Kella D, Zajfman D, Heber O, Majer D, Feldman H, Vager Z, Naaman R. 1993 Observation of Laser Excitation of Rhombic C₄ using the Coulomb Explosion Method.
Z. Phys. D **26**, 340–342.
(doi:10.1007/BF01429188)
153. Slanina Z, Zahradnik R. 1977 Calculations of Absolute Values of Equilibrium and Rate constants. 9. MINDO/2 Study of Equilibrium Carbon Vapor.
J. Phys. Chem. **81**, 2252–2257.
(doi:10.1021/j100539a011)
154. Cheung HM, Graham WRM. 1989 Electron-Spin-Resonance Characterization of Nonlinear C₄ Trapped in Solid Argon.
J. Chem. Phys. **91**, 6664–6670.
(doi:10.1063/1.457385)
155. Martin JML, Schwenke DW, Lee TJ, Taylor PR. 1996 Is There Evidence for Detection of Cyclic C₄ in IR Spectra? An Accurate *Ab Initio* Computed Quartic Force Field.
J. Chem. Phys. **104**, 4657–4663.
(doi:10.1063/1.471212)
156. Wigner E, Witmer EE. 1928 Über Die Struktur Der Zweiatomigen Molekelspektren Nach Der Quantenmechanik.
Z. Phys. **51**, 859–886.
(doi:10.1007/BF01400247)
157. Herzberg G. 1966 *Molecular Spectra and Molecular Structure III. Electronic Spectra and Electronic Structure of Polyatomic Molecules*, volume III.
New York: Van Nostrand.
158. Bersuker IB. 2006 *The Jahn-Teller Effect*.
Cambridge: Cambridge University Press.
159. Zwanziger JW, Grant ER. 1987 Topological Phase in Molecular Bound States: Application to the $E \otimes e$ System.
J. Chem. Phys. **87**, 2954–2964.
(doi:10.1063/1.453083)
160. Bersuker IB. 2013 Pseudo-Jahn-Teller Effect - A Two-State Paradigm in Formation, Deformation, and Transformation of Molecular Systems and Solids.
Chem. Rev. **113**, 1351–1390.
(doi:10.1021/cr300279n)
161. Griffith JS. 1962 *The Irreducible Tensor Method for Molecular Symmetry Groups*.
New Jersey: Prentice-Hall.
162. Garcia-Fernandez P, Bersuker IB, Boggs JE. 2006 Orbital Disproportionation and Spin Crossover as a Pseudo Jahn-Teller Effect.
J. Chem. Phys. **125**, 104102–104112.
(doi:10.1063/1.2346682)
163. Dillon JJ, Yarkony DR. 2007 Seams Near Seams: The Jahn-Teller Effect in the ${}^1E''$ State of N₃⁺.
J. Chem. Phys. **126**, 124113–124119.
(doi:10.1063/1.2710255)
164. Longuet-Higgins HC. 1975 The Intersection of Potential Energy Surfaces in Polyatomic Molecules.
Proc. R. Soc. Lond. A **344**, 147–156.
(doi:10.1098/rspa.1975.0095)
165. Herzberg G, Longuet-Higgins HC. 1963 Intersection of Potential Energy Surfaces in Polyatomic Molecules.
Discuss. Faraday Soc. **35**, 77–82.
(doi:10.1039/DF9633500077)
166. Berry MV. 1984 Quantal Phase Factors Accompanying Adiabatic Changes.
Proc. R. Soc. Lond. A **392**, 45–57.

- (doi:10.1098/rspa.1984.0023)
167. Varandas AJC, Tennyson J, Murrell JN. 1979 Chercher le Croisement. *Chem. Phys. Lett.* **61**, 431–434. (doi:10.1016/0009-2614(79)87143-2)
168. Kramida A, Ralchenko Y, Reader J, Team NA. 2015. NIST Atomic Spectra Database. <http://physics.nist.gov/asd>, National Institute of Standards and Technology, Gaithersburg, MD.
169. Varandas AJC, Murrell JN. 1981 Choosing Points in Potential Energy Surfaces for Fitting Polynomial Functions: Application of Permutational Symmetry. *Chem. Phys. Lett.* **84**, 440–445. (doi:10.1016/0009-2614(81)80381-8)
170. Porter RN, Stevens RM, Karplus M. 1968 Symmetric H_3 : A Semiempirical and Ab Initio Study of a Simple Jahn-Teller System. *J. Chem. Phys.* **49**, 5163–5178. (doi:10.1063/1.1670017)
171. Varandas AJC. 1987 A Useful Triangular Plot of Triatomic Potential Energy Surfaces. *Chem. Phys. Lett.* **138**, 455–461. (doi:10.1016/0009-2614(87)80540-7)
172. Zhang G, Chen K, Merer AJ, Hsu Y, Chen W, Shaji S, Liao Y. 2005 The 4051-Å Band of C_3 ($\tilde{A}^1\Pi_u - \tilde{X}^1\Sigma_g^+$, 000-000): Perturbed Low-J Lines and Lifetime Measurements. *J. Chem. Phys.* **122**, 244308–244315. (doi:10.1063/1.1928827)
173. Varandas AJC. 2003 A Realistic Multi-Sheeted Potential Energy Surface for $NO_2(^2A')$ from the Double Many-Body Expansion Method and a Novel Multiple Energy-Switching Scheme. *J. Chem. Phys.* **119**, 2596–2613. (doi:10.1063/1.1586911)
174. Werner HJ, Knowles PJ, Knizia G, Manby FR, Schütz M, *et al.* 2010. MOLPRO, a package of *ab initio* programs, version 2010.1. See: <http://www.molpro.net>, Cardiff, U.K., 2010
175. Szalay PG, Müller T, Gidofalvi G, Lischka H, Shepard R. 2012 Multiconfiguration Self-Consistent Field and Multireference Configuration Interaction Methods and Applications. *Chem. Rev.* **112**, 108–181. (doi:10.1021/cr200137a)
176. Varandas AJC. 2012 *Ab Initio* Treatment of Bond-Breaking Reactions: Accurate Course of HO_3 Dissociation and Revisit to Isomerization. *J. Chem. Theory Comput.* **8**, 428–441. (doi:10.1021/ct200773b)
177. Varandas AJC. 2013 Accurate Determination of the Reaction Course in $HY_2 \rightleftharpoons Y+YH$ ($Y=O,S$): Detailed Analysis of the Covalent- to Hydrogen-Bonding Transition. *J. Phys. Chem. A* **117**, 7393–7407. (doi:10.1021/jp401384d)
178. Varandas AJC. 2014 On Carbon Dioxide Capture: An Accurate *Ab Initio* Study of the Li_3N+CO_2 Insertion Reaction. *Comp. Theor. Chem.* **1036**, 61–71. (doi:10.1016/j.comptc.2014.02.022)
179. Pansini FNN, Neto AC, Varandas AJC. 2016 Extrapolation of Hartree-Fock and Multiconfiguration Self-Consistent-Field Energies to the Complete Basis Set Limit. *Theo. Chem. Acc.* **135**, 261–267. (doi:10.1007/s00214-016-2016-4)
180. Varandas AJC. 2007 Extrapolating to the One-Electron Basis-Set Limit in Electronic Structure Calculations. *J. Chem. Phys.* **126**, 244105–244119. (doi:10.1063/1.2741259)
181. Varandas AJC, Pansini FNN. 2014 Narrowing the Error in Electron Correlation Calculations by Basis Set Re-hierarchization and Use of the Unified Singlet and Triplet Electron-Pair Extrapolation Scheme: Application to a Test Set of 106 Systems. *J. Chem. Phys.* **141**, 224113–224121.

- (doi:10.1063/1.4903193)
182. Pansini FNN, Neto AC, Varandas AJC. 2015 On the Performance of Various Hierarchized Bases in Extrapolating the Correlation Energy to the Complete Basis Set Limit. *Chem. Phys. Lett.* **641**, 90–96.
(doi:http://doi.org/10.1016/j.cplett.2015.10.064)
183. Ngandjong A, Mezei J, Mougnot J, Michau A, Hassouni K, Lombardi G, Seydou M, Maurel F. 2017 Structural Stability and Growth Mechanism of Neutral and Anionic Small Carbon Clusters: Density Functional Study. *Comp. Theor. Chem.* **1102**, 105–113.
(doi:10.1016/j.comptc.2017.01.012)
184. Karton A, Tarnopolsky A, Martin JML. 2009 Atomization Energies of the Carbon Clusters C_n ($n = 2 - 10$) Revisited by Means of W4 Theory as well as Density Functional, G_n , and CBS Methods. *Mol. Phys.* **107**, 977–990.
(doi:10.1080/00268970802708959)
185. Murrell JN. 1978 Potential Energy Surfaces for Clusters of Main Group Elements. *Chem. Phys. Lett.* **55**, 1–5.
(doi:10.1016/0009-2614(78)85118-5)
186. Varandas AJC, Llanio-Trujillo JL. 2002 On Triplet Tetraoxygen: *Ab Initio* Study Along Minimum Energy Path and Global Modelling. *Chem. Phys. Lett.* **356**, 585–594.
(doi:10.1016/S0009-2614(02)00429-3)
187. Ballester MY, Varandas AJC. 2005 Double Many-Body Expansion Potential Energy Surface for Ground State HSO_2 . *Phys. Chem. Chem. Phys.* **7**, 2305–2317.
(doi:10.1039/B500990A)
188. Poveda LA, Biczysko M, Varandas AJC. 2009 Accurate *Ab Initio* based DMBE Potential Energy Surface for the Ground Electronic State of N_2H_2 . *J. Chem. Phys.* **131**, 044309.
(doi:10.1063/1.3176512)
189. Martínez-Núñez E, Varandas AJC. 2001 Single-Valued DMBE Potential Energy Surface for HSO : A Distributed n -Body Polynomial Approach. *J. Phys. Chem. A* **105**, 5923–5932.
(doi:10.1021/jp0101460)

Part III

Conclusions and Outlook

Conclusions and Outlook

This thesis provides an extensive report on the work done during the doctoral program pursued by the candidate. The main focus was to study the electronic and structural properties of elemental carbon clusters, notably C_2 , C_3 and C_4 , by exploring their potential energy surfaces (PESs). The work was divided into three main parts. Initially, a theoretical background has been given that surveys the general theory behind the methodological approaches here employed. Subsequently, the results so obtained have been gathered as manuscripts published in peer-reviewed journals. As a final topic, we hereby summarize the major achievements and scientific contributes of our research.

A global single-sheeted PES for ground-state C_3 was first reported using accurate *ab initio* energies as calibration data and the double many-body expansion (DMBE) method for the modeling. Since $C_3(1^1A')$ does not dissociate adiabatically into the ground state of its fragments [$C_2(1^1\Sigma_g^+) + C(^3P)$] but into $C_2(^3\Pi_u) + C(^3P)$, the potential energy curve of this latter diatomics has been employed as two-body terms. In that study, we have first outlined the existence of three symmetry-allowed C_{2v} conical intersections (Cis) in quite close proximity to the symmetry-required one at D_{3h} geometries, an attribute which had been previously overlooked for the carbon trimer. Because a third electronic state of $1^1A'$ symmetry ($1^1A'_1$ in D_{3h}) is close-in-energy to the pair of intersecting states ($1^1E'$ in D_{3h}) near equilateral triangular arrangements, such features have been ascribed to combined Jahn-Teller (JT) plus *pseudo*-Jahn-Teller (PJT) effects. The modeling of the adiabatic PES has then been accomplished by making use of a specially-designed functional form that warrants by built-in construction the expected cusp behavior near the minimum energy crossing point (MECP), while accurately describing asymptotic channels, long-range in-

teractions as well as all topographical attributes in the valence region. These latter include the proper description of a C_{2v} transition state responsible for the isomerization between the three symmetry-equivalent $D_{\infty h}$ global minima and other long-range extrema, some of which reported for the first time. To judge the quality of the final DMBE form, exploratory rovibrational energy calculations have also been performed, unveiling a good match of the spectrum of C_3 with a root-mean-square deviation (rmsd) of 50.4 cm^{-1} for 53 calculated levels.

The unusual topographical features so reported for C_3 have prompted us to further explore its JT plus PJT vibronic problem $[(E' + A'_1) \otimes e']$ and the results were by no means interesting. Contrary to the previous findings, the three symmetry-equivalent C_{2v} disjoint seams are not static objects with respect to the symmetry-required one but instead evolves in a non-trivial manner as the perimeter of the molecule increases. To qualitatively characterize such combined $(E' + A'_1) \otimes e'$ problem, a three-state vibronic Hamiltonian has also been proposed and the parameters least-squares fitted to accurate MRCI energies. The diabatic potential matrix so obtained was proven to accurately describe the adiabatic PESs and their inherent intricacies near the MECP. The large magnitude of the quadratic JT parameter with respect to the corresponding linear one posed serious considerations about the real nature of C_3 and led us to revisit this issue by including the title radical into a select group of species showing similar attributes, *i.e.*, the so-called small linear parameter (SLP) JT molecules, among which its congener Si_3 is also part of. The topological implications of such inherent features have also been assessed for the first time. We demonstrated that, while the adiabatic wave functions of the intersecting states change sign when transported around a loop enclosing any one of the 4 Cis, the net geometric phase effect is largely suppressed when all degeneracies are encircled at once.

In view of the intrinsic complexities of the molecule at hand and the unusual nature of the C_{2v} disjoint crossings, further attempts were made to develop a global DMBE form for C_3 that properly mimics all the aforementioned features. By finding the appropriate parametric equation that characterizes the locus of intersection, we were able to accomplish such a task and proposed the use of a specially-designed coordinate that, together with the use of the JT-type coordinate and suitably chosen polynomial forms, ensure

the expected cusp behavior of both D_{3b} and C_{2v} seams over the entire range of nuclear configuration space. Although the novel methodology has been typified here for carbon trimer, it is expected to have unprecedented applicability on modeling adiabatic PESs of SLP JT molecules.

Since its first observation in the spectra of comets in 1881, C_3 and its well-known $\tilde{A}^1\Pi_u-\tilde{X}^1\Sigma_g^+$ band system have been the subject of intense spectroscopic investigations aiming at characterizing its exceptionally large amplitude bending motion in the ground ($\tilde{X}^1\Sigma_g^+$) as well as the unusual large Renner-Teller effect in the $\tilde{A}^1\Pi_u$ excited state. Such a flurry of experimental/theoretical studies have made C_3 one of the most well-characterized non-rigid triatomics in existence and motivated several efforts toward spectroscopically accurate near-equilibrium PESs. This prompted us to propose and utilize a simplified version of the energy switching scheme (ES) in which the latest global DMBE form for C_3 was actually merged with the best currently available Taylor-series expansions for the title species: the mixed theoretical/experimental PES due to Ahmed *et al.* and the purely *ab initio* potential by Schröder and Sebald. Near spectroscopic accuracy (rmsds of $\approx 10\text{ cm}^{-1}$) has been conveyed to both ES potentials for vibrational wave numbers calculated up to about 4000 cm^{-1} above the zero point energy level, while keeping unaltered all the attributes of the original DMBE potential. As expected, by benefiting from the advantages of each separated form (and, at the same time, avoiding their most serious limitations), the final DMBE/ES PESs here obtained are suitable both for spectroscopic and reaction dynamics studies on C_3 .

The relevance of C_4 in the interstellar medium and the discrepancies concerning its ground state structure motivated us to further explore its PES by performing high-level *ab initio* calculations followed by extrapolations to the complete basis set (CBS) limit. As an inherent property of small C_n molecules (highlighted here also for C_2 and C_3), the presence of low-lying singlet/triplet electronic manifolds and/or isomeric forms are even more noticeable on C_4 . For this system, the existence of two almost isoenergetic structural isomers is widely accepted: the linear triplet chain $l\text{-}C_4(^3\Sigma_g^-)$ and the rhombic singlet $r\text{-}C_4(^1A_g)$ structure. We have investigated this issue and found that, although multi-configurational approaches predict $l\text{-}C_4(^3\Sigma_g^-)$ as the most stable form, extrapola-

tions to the CBS limit tend to favor the $r\text{-C}_4(^1A_g)$ isomer. Unfortunately, even with our best full-valence CBS protocol (for the first time applied on carbon tetramer), the energetic proximity predicted between such forms ($\approx 4.9 \text{ kJ mol}^{-1}$) is expected to be of the same order of accuracy of the *ab initio* calculations themselves, and hence any statement about the true ground-state of C_4 is very risky at present. Isomerization pathways between linear and rhombic structures on both singlet and triplet PESs have also been explored, unraveling several other stable and transient species for the title radical, some of which unreported thus far. Starting from an approximate cluster expansion constructed from two- and three-body terms only (obtained from the corresponding PES of the carbon trimer), an approximate four-body term has also been proposed and calibrated using accurate *ab initio* energies. The resulting fully six-dimensional global DMBE PES reproduces all known topographical aspects of the ground triplet state of C_4 , including its linear-rhombic isomerization pathway, as well as the correct exothermicities for the $I\text{-C}_3(\tilde{X}^1\Sigma_g^+) + \text{C}(^3P)$ and $\text{C}_2(a^3\Pi_u) + \text{C}_2(a^3\Pi_u)$ collinear reactions.

The results reported throughout this thesis provide a general overview on the most fundamental aspects regarding the smallest C_n clusters and their inherent complexities. Although such intricacies are expected to be even more pronounced on larger aggregates, the knowledge here acquired supply safe grounds on which to base the study of more involved pure carbon species. Clearly, it is believed that the potentials here obtained carry important peaces of information that could be utilized as input for the construction of PESs for larger C_n species. By employing even simpler forms for the highest order terms in the cluster expansion, this assumption is made possible, as already demonstrated here for C_4 . Suffice it to say that the current PESs for C_3 and C_4 are objects that *per se* provide valuable observables for the title systems. Among these, one can highlight the prediction of accurate reaction rate coefficients for the $\text{C} + \text{C}_2$, $\text{C}_2 + \text{C}_2$ and $\text{C} + \text{C}_3$ processes which could be extremely useful in astrochemical models (chemical reaction networks) of interstellar medium and also spectral (infrared) bands that could guide for an unambiguous assignment of these species in astrophysical sources.

Part IV

Appendices

Appendix A

Atomic units and conversion factors

Consider the Schrödinger equation for the hydrogen atom in international system of units (SI) [1]

$$\left[-\frac{\hbar^2}{2m_e} \nabla^2(\mathbf{r}) - \frac{e^2}{4\pi\epsilon_0|\mathbf{r}|} \right] \phi(\mathbf{r}) = \mathcal{E} \phi(\mathbf{r}), \quad (\text{A.1})$$

where m_e is the electron mass, e is the elementary charge and ϵ_0 is the vacuum permittivity. In turn, $\phi(\mathbf{r})$ and \mathcal{E} are the eigenfunction and associated eigenvalue, respectively, with \mathbf{r} denoting the electronic coordinates relative to the nucleus¹. Thus, \mathbf{r} is a column matrix with three Cartesian components r_α ($\alpha = x, y, z$), and therefore $|\mathbf{r}| = \sqrt{(r_x^2 + r_y^2 + r_z^2)}$. To convert the above equation into a dimensionless one, we perform the following transformation $r_x, r_y, r_z \rightarrow \xi r'_x, \xi r'_y, \xi r'_z$ and obtain

$$\left[-\frac{\hbar^2}{2m_e\xi^2} \nabla^2(\mathbf{r}') - \frac{e^2}{4\pi\epsilon_0\xi|\mathbf{r}'|} \right] \phi'(\mathbf{r}') = \mathcal{E} \phi'(\mathbf{r}'). \quad (\text{A.2})$$

The constants on the left-rand side of Eq. (A.2) can be factored, since ξ is chosen such that

$$\frac{\hbar^2}{m_e\xi^2} = \frac{e^2}{4\pi\epsilon_0\xi} = E_h, \quad (\text{A.3})$$

where E_h is the atomic unit of energy, referred to as hartree. Moreover, by solving Eq. (A.3) for ξ , we find

$$\xi = \frac{4\pi\epsilon_0\hbar^2}{m_e e^2} = a_0, \quad (\text{A.4})$$

¹It is assumed, therefore, that the center-of-mass translational motion has already been separated off.

with ξ being simply the Bohr radius a_0 which is the atomic unit of length.

By using the definition of E_h [Eq. (A.3)] in Eq. (A.2), multiplying from the left by $1/E_h$ and setting $\mathcal{E}' = \mathcal{E}/E_h$, one easily gets

$$\left[-\frac{1}{2}\nabla^2(\mathbf{r}') - \frac{1}{|\mathbf{r}'|} \right] \phi'(\mathbf{r}') = \mathcal{E}' \phi'(\mathbf{r}') \quad (\text{A.5})$$

which is the Schrödinger equation in au. The exact solution of such an equation for the ground state of the hydrogen atom yields $\mathcal{E}' = -0.5 E_h$. Table A.1 gives conversion factors between au and SI units for some usual physical quantities. Also given in Table A.2 are the energy conversion factors from E_h to non-SI units used throughout this thesis.

Table A.1: Conversion factors from au to SI for some common physical quantities [2].

Atomic unit (base units)	SI value	Name (Symbol)
Mass (m_e)	$9.109\,383\,56(11) \times 10^{-31}$ kg	Electron mass
Charge (e)	$1.602\,176\,620\,8(98) \times 10^{-19}$ C	Elementary charge
Angular momentum (\hbar)	$1.054\,571\,800(13) \times 10^{-34}$ J s ⁻¹	Planck's constant/ 2π
Energy [$m_e e^4 / (4\pi\epsilon_0 \hbar)^2$]	$4.359\,744\,650(54) \times 10^{-18}$ J	Hartree (E_h)
Length ($4\pi\epsilon_0 \hbar^2 / m_e e^2$)	$5.291\,772\,106\,7(12) \times 10^{-11}$ m	Bohr (a_0)
Time (\hbar/E_h)	$2.418\,884\,326\,509(14) \times 10^{-17}$ s	
Electric dipole moment (ea_0)	$8.478\,353\,552(52) \times 10^{-30}$ C m	

Table A.2: Energy conversion factors from au to non-SI units [2].

1 Hartree (E_h)
2625.499 638 kJ mol ⁻¹
627.509 kcal mol ⁻¹
219 474.631 370 2 cm ⁻¹
27.211 386 02 eV

Bibliography

- [1] A. Szabo and N. S. Ostlund, *Modern Quantum Chemistry: Introduction to Advanced Electronic Structure Theory*, Vol. 1 (McGraw-Hill Book Co., New York, 1989).
- [2] P. J. Mohr, B. N. Taylor, and D. B. Newell, *Rev. Mod. Phys.* **84**, 1527 (2012).

Appendix B

Derivation of the vibronic coupling constants

B.1 The linear plus quadratic $\mathbf{E} \otimes \mathbf{e}$ problem

We consider here the simplest JT problem for an X_3 -type molecule in a doubly degenerate electronic state E interacting with doubly degenerate e modes [1, 2]. The point group for such a system is D_{3h} ; however, since no out-of-plane bending of a triatomic system is possible, and since the wavefunctions for the degenerate state are assumed to be symmetric with respect to reflections in the plane of the molecule, the subgroup C_{3v} will be used instead in the present discussion. Let $|E_\theta(\mathbf{r}; \mathbf{0})\rangle$ and $|E_e(\mathbf{r}; \mathbf{0})\rangle$ be the two degenerate components of the E term which are obtained as solutions of Eq. (2.13), *i.e.*, $\{|\Gamma\gamma_i(\mathbf{r}; \mathbf{0})\rangle\} = \{|E_\theta(\mathbf{r}; \mathbf{0})\rangle, |E_e(\mathbf{r}; \mathbf{0})\rangle\}$, with associated eigenvalues $V_1(\mathbf{0}) = V_2(\mathbf{0}) = V_E^\times(\mathbf{0})$. Assume further that such terms are well separated in energy from all other electronic states and only the subspace spanned by them needs to be considered here. The corresponding components of the normal E -type displacement are denoted as Q_{e_θ} and Q_{e_e} (see Figure 2.2), while $Q_{a_{1\iota}}$ represents the totally symmetric mode which transform according the single line ι of the irrep A_1 . We define now the matrix representation of the electronic Hamiltonian $\hat{\mathcal{H}}_e(\mathbf{r}; \mathbf{Q})$ [Eq. (2.12)] in the basis $\{|E_\theta(\mathbf{r}; \mathbf{0})\rangle, |E_e(\mathbf{r}; \mathbf{0})\rangle\}$. Note that the expansion in Eq. (2.12) is here truncated at the quadratic terms (second-order

perturbation treatment). Following Eqs. (2.14)-(2.16), the associated matrix elements are then given by

$$H_{ji}(\mathbf{Q}) = V_E^\times(\mathbf{0})\delta_{ji} + \sum_{\bar{\Gamma}\bar{\gamma} \neq a_{1\nu}} F_{\bar{\Gamma}\bar{\gamma}}^{(\Gamma\gamma_j\Gamma\gamma_i)} Q_{\bar{\Gamma}\bar{\gamma}} + \sum_{\bar{\Gamma}\bar{\gamma} \neq a_{1\nu}} G_{\bar{\Gamma}\bar{\gamma}}^{(\Gamma\gamma_j\Gamma\gamma_i)} \{Q_{\bar{\Gamma}_1} \otimes Q_{\bar{\Gamma}_2}\}_{\bar{\Gamma}\bar{\gamma}} + \sum_{\bar{\Gamma}\bar{\gamma} = a_{1\nu}} \frac{1}{2} K_0^{(\Gamma)} \{Q_{\bar{\Gamma}_1} \otimes Q_{\bar{\Gamma}_2}\}_{\bar{\Gamma}\bar{\gamma}} \delta_{ji} \quad (\text{B.1})$$

where $F_{\bar{\Gamma}\bar{\gamma}}^{(\Gamma\gamma_j\Gamma\gamma_i)}$ and $G_{\bar{\Gamma}\bar{\gamma}}^{(\Gamma\gamma_j\Gamma\gamma_i)}$ are the linear and quadratic JT VCCs [see Eqs. (2.15) and (2.16)], respectively, calculated along non-totally symmetric displacements and $K_0^{(\Gamma)}$ is the primary (nonvibronic) force constant which is non-vanishing only in the totally symmetric part of the diagonal matrix elements. For convenience, we rewrite Eq. (B.1) by considering each term *per se* as a matrix element of a set of 2 by 2 sub-matrices

$$H_{ji}(\mathbf{Q}) = H_{ji}^{(0)}(\mathbf{0}) + W_{ji}^{(1)}(\mathbf{Q}) + W_{ji}^{(2)}(\mathbf{Q}) + K_{ji}(\mathbf{Q}), \quad (\text{B.2})$$

where

$$H_{ji}^{(0)}(\mathbf{0}) = V_E^\times(\mathbf{0})\delta_{ji}, \quad (\text{B.3})$$

$$W_{ji}^{(1)}(\mathbf{Q}) = \sum_{\bar{\Gamma}\bar{\gamma} \neq a_{1\nu}} F_{\bar{\Gamma}\bar{\gamma}}^{(\Gamma\gamma_j\Gamma\gamma_i)} Q_{\bar{\Gamma}\bar{\gamma}}, \quad (\text{B.4})$$

$$W_{ji}^{(2)}(\mathbf{Q}) = \sum_{\bar{\Gamma}\bar{\gamma} \neq a_{1\nu}} G_{\bar{\Gamma}\bar{\gamma}}^{(\Gamma\gamma_j\Gamma\gamma_i)} \{Q_{\bar{\Gamma}_1} \otimes Q_{\bar{\Gamma}_2}\}_{\bar{\Gamma}\bar{\gamma}}, \quad (\text{B.5})$$

and

$$K_{ji}(\mathbf{Q}) = \sum_{\bar{\Gamma}\bar{\gamma} = a_{1\nu}} \frac{1}{2} K_0^{(\Gamma)} \{Q_{\bar{\Gamma}_1} \otimes Q_{\bar{\Gamma}_2}\}_{\bar{\Gamma}\bar{\gamma}} \delta_{ji}. \quad (\text{B.6})$$

Let us start by considering the matrix elements $W_{ji}^{(1)}(\mathbf{Q})$ which contain only linear (first-order perturbation) terms of the vibronic coupling. Following Eqs. (2.14) and (2.15)

Table B.1: V coefficients for the point group C_{3v} (subgroup of D_{3h}) calculated between twofold degenerate E terms. All V that are not given are zero [3].

E	E	E	V
θ	θ	θ	$-\frac{1}{2}$
θ	ϵ	ϵ	$\frac{1}{2}$
ϵ	θ	ϵ	$\frac{1}{2}$
ϵ	ϵ	θ	$\frac{1}{2}$

as well as Table B.1, they are given by

$$\begin{aligned}
 W_{11}^{(1)}(\mathbf{Q}) &= \left\langle E_{\theta}(\mathbf{r}; \mathbf{0}) \left| \left(\frac{\partial \hat{\mathcal{U}}(\mathbf{r}; \mathbf{0})}{\partial Q_{e_{\theta}}} \right)_0 \right| E_{\theta}(\mathbf{r}; \mathbf{0}) \right\rangle Q_{e_{\theta}} \\
 &= \left\{ \bar{F}_E V \begin{pmatrix} E & E & e \\ \theta & \theta & \theta \end{pmatrix} \right\} Q_{e_{\theta}} \\
 &= - \left(\frac{1}{2} \bar{F}_E \right) Q_{e_{\theta}} \\
 &= -F_E Q_{e_{\theta}}, \tag{B.7}
 \end{aligned}$$

$$\begin{aligned}
 W_{12}^{(1)}(\mathbf{Q}) &= \left\langle E_{\theta}(\mathbf{r}; \mathbf{0}) \left| \left(\frac{\partial \hat{\mathcal{U}}(\mathbf{r}; \mathbf{0})}{\partial Q_{e_{\epsilon}}} \right)_0 \right| E_{\epsilon}(\mathbf{r}; \mathbf{0}) \right\rangle Q_{e_{\epsilon}} \\
 &= \left\{ \bar{F}_E V \begin{pmatrix} E & E & e \\ \theta & \epsilon & \epsilon \end{pmatrix} \right\} Q_{e_{\epsilon}} \\
 &= \left(\frac{1}{2} \bar{F}_E \right) Q_{e_{\epsilon}} \\
 &= F_E Q_{e_{\epsilon}}, \tag{B.8}
 \end{aligned}$$

$$\begin{aligned}
W_{21}^{(1)}(\mathbf{Q}) &= \left\langle E_\epsilon(\mathbf{r}; \mathbf{0}) \left| \left(\frac{\partial \hat{\mathcal{U}}(\mathbf{r}; \mathbf{0})}{\partial Q_{e_\epsilon}} \right)_0 \right| E_\theta(\mathbf{r}; \mathbf{0}) \right\rangle Q_{e_\epsilon} \\
&= \left\{ \bar{F}_E V \begin{pmatrix} E & E & e \\ \epsilon & \theta & \epsilon \end{pmatrix} \right\} Q_{e_\epsilon} \\
&= \left(\frac{1}{2} \bar{F}_E \right) Q_{e_\epsilon} \\
&= F_E Q_{e_\epsilon},
\end{aligned} \tag{B.9}$$

and

$$\begin{aligned}
W_{22}^{(1)}(\mathbf{Q}) &= \left\langle E_\epsilon(\mathbf{r}; \mathbf{0}) \left| \left(\frac{\partial \hat{\mathcal{U}}(\mathbf{r}; \mathbf{0})}{\partial Q_{e_\theta}} \right)_0 \right| E_\epsilon(\mathbf{r}; \mathbf{0}) \right\rangle Q_{e_\theta} \\
&= \left\{ \bar{F}_E V \begin{pmatrix} E & E & e \\ \epsilon & \epsilon & \theta \end{pmatrix} \right\} Q_{e_\theta} \\
&= \left(\frac{1}{2} \bar{F}_E \right) Q_{e_\theta} \\
&= F_E Q_{e_\theta},
\end{aligned} \tag{B.10}$$

where \bar{F}_E is the reduced matrix element and F_E the corresponding linear coupling constant. Note that no other combinations of θ and ϵ in the brackets of Eqs. (B.7)-(B.10) are here possible due to the vanishing nature of the corresponding V coefficients (see Table B.1). Before proceeding to the calculation of the matrix elements $W_{ji}^{(2)}(\mathbf{Q})$ and $K_{ji}(\mathbf{Q})$, it is convenient to provide an explicit definition of the irreducible products shown in Eqs. (2.14) and (2.16). Such quantities assume the form [3]

$$\left\{ \left(\frac{\partial \hat{\mathcal{U}}(\mathbf{r}; \mathbf{0})}{\partial Q_{\bar{\Gamma}_1}} \right)_0 \otimes \left(\frac{\partial \hat{\mathcal{U}}(\mathbf{r}; \mathbf{0})}{\partial Q_{\bar{\Gamma}_2}} \right)_0 \right\}_{\bar{\Gamma}_\bar{\gamma}} = \lambda(\bar{\Gamma})^{1/2} \sum_{\bar{\gamma}_1 \bar{\gamma}_2} V \begin{pmatrix} \bar{\Gamma}_1 & \bar{\Gamma}_2 & \bar{\Gamma} \\ \bar{\gamma}_1 & \bar{\gamma}_2 & \bar{\gamma} \end{pmatrix} \left(\frac{\partial \hat{\mathcal{U}}(\mathbf{r}; \mathbf{0})}{\partial Q_{\bar{\Gamma}_1 \bar{\gamma}_1}} \right)_0 \left(\frac{\partial \hat{\mathcal{U}}(\mathbf{r}; \mathbf{0})}{\partial Q_{\bar{\Gamma}_2 \bar{\gamma}_2}} \right)_0 \tag{B.11}$$

which means a linear combination of second derivatives with respect to the $Q_{\bar{\Gamma}_1 \bar{\gamma}_1}$ and $Q_{\bar{\Gamma}_2 \bar{\gamma}_2}$ coordinates that transform according to the line $\bar{\gamma}$ of the representation $\bar{\Gamma} \in \bar{\Gamma}_1 \otimes \bar{\Gamma}_2$. Such combinations can be found by means of group theory and the Wigner-Eckart theorem. Indeed, if $\bar{\Gamma}$ is not contained in the direct product of $\bar{\Gamma}_1$ and $\bar{\Gamma}_2$, Eq. (B.11) naturally vanishes since $V=0$. Note that $\lambda(\bar{\Gamma})$ defines the dimension of the representation

$\bar{\Gamma}$. From the above considerations and using Table B.1, the irreducible products relevant for the present formulation of the $E \otimes e$ problem are thus given by

$$\begin{aligned} \left\{ \left(\frac{\partial \hat{\mathcal{U}}(\mathbf{r}; \mathbf{0})}{\partial Q_e} \right)_0 \otimes \left(\frac{\partial \hat{\mathcal{U}}(\mathbf{r}; \mathbf{0})}{\partial Q_e} \right)_0 \right\}_{e_\theta} &= (2)^{1/2} \left\{ \text{V} \begin{pmatrix} e & e & e \\ \theta & \theta & \theta \end{pmatrix} \left(\frac{\partial^2 \hat{\mathcal{U}}(\mathbf{r}; \mathbf{0})}{\partial Q_{e_\theta}^2} \right)_0 \right. \\ &\quad \left. + \text{V} \begin{pmatrix} e & e & e \\ \epsilon & \epsilon & \theta \end{pmatrix} \left(\frac{\partial^2 \hat{\mathcal{U}}(\mathbf{r}; \mathbf{0})}{\partial Q_{e_\epsilon}^2} \right)_0 \right\} \\ &= \frac{\sqrt{2}}{2} \left\{ \left(\frac{\partial^2 \hat{\mathcal{U}}(\mathbf{r}; \mathbf{0})}{\partial Q_{e_\epsilon}^2} \right)_0 - \left(\frac{\partial^2 \hat{\mathcal{U}}(\mathbf{r}; \mathbf{0})}{\partial Q_{e_\theta}^2} \right)_0 \right\}, \end{aligned} \quad (\text{B.12})$$

$$\begin{aligned} \left\{ \left(\frac{\partial \hat{\mathcal{U}}(\mathbf{r}; \mathbf{0})}{\partial Q_e} \right)_0 \otimes \left(\frac{\partial \hat{\mathcal{U}}(\mathbf{r}; \mathbf{0})}{\partial Q_e} \right)_0 \right\}_{e_\epsilon} &= (2)^{1/2} \left\{ \text{V} \begin{pmatrix} e & e & e \\ \theta & \epsilon & \epsilon \end{pmatrix} \left(\frac{\partial^2 \hat{\mathcal{U}}(\mathbf{r}; \mathbf{0})}{\partial Q_{e_\theta} \partial Q_{e_\epsilon}} \right)_0 \right. \\ &\quad \left. + \text{V} \begin{pmatrix} e & e & e \\ \epsilon & \theta & \epsilon \end{pmatrix} \left(\frac{\partial^2 \hat{\mathcal{U}}(\mathbf{r}; \mathbf{0})}{\partial Q_{e_\epsilon} \partial Q_{e_\theta}} \right)_0 \right\} \\ &= \sqrt{2} \left\{ \frac{1}{2} \left(\frac{\partial^2 \hat{\mathcal{U}}(\mathbf{r}; \mathbf{0})}{\partial Q_{e_\theta} \partial Q_{e_\epsilon}} \right)_0 + \frac{1}{2} \left(\frac{\partial^2 \hat{\mathcal{U}}(\mathbf{r}; \mathbf{0})}{\partial Q_{e_\epsilon} \partial Q_{e_\theta}} \right)_0 \right\} \\ &= \sqrt{2} \left(\frac{\partial^2 \hat{\mathcal{U}}(\mathbf{r}; \mathbf{0})}{\partial Q_{e_\theta} \partial Q_{e_\epsilon}} \right)_0, \end{aligned} \quad (\text{B.13})$$

and, for the case of the totally symmetric combination of the second derivatives, one gets

$$\begin{aligned} \left\{ \left(\frac{\partial \hat{\mathcal{U}}(\mathbf{r}; \mathbf{0})}{\partial Q_e} \right)_0 \otimes \left(\frac{\partial \hat{\mathcal{U}}(\mathbf{r}; \mathbf{0})}{\partial Q_e} \right)_0 \right\}_{a_{1\iota}} &= (1)^{1/2} \left\{ \text{V} \begin{pmatrix} e & e & a_1 \\ \theta & \theta & \iota \end{pmatrix} \left(\frac{\partial^2 \hat{\mathcal{U}}(\mathbf{r}; \mathbf{0})}{\partial Q_{e_\theta}^2} \right)_0 \right. \\ &\quad \left. + \text{V} \begin{pmatrix} e & e & a_1 \\ \epsilon & \epsilon & \iota \end{pmatrix} \left(\frac{\partial^2 \hat{\mathcal{U}}(\mathbf{r}; \mathbf{0})}{\partial Q_{e_\epsilon}^2} \right)_0 \right\} \\ &= \frac{1}{\sqrt{2}} \left\{ \left(\frac{\partial^2 \hat{\mathcal{U}}(\mathbf{r}; \mathbf{0})}{\partial Q_{e_\theta}^2} \right)_0 + \left(\frac{\partial^2 \hat{\mathcal{U}}(\mathbf{r}; \mathbf{0})}{\partial Q_{e_\epsilon}^2} \right)_0 \right\}. \end{aligned} \quad (\text{B.14})$$

Note that the corresponding values of the V coefficients calculated between E and A_1 terms are given in Table B.2. Similarly, the corresponding tensor convolutions for the

Table B.2: V coefficients of the point group C_{3v} (subgroup of D_{3h}) calculated between twofold degenerate E and one-dimensional (totally symmetric) A_1 terms [3]. All V that are not given are zero.

E	E	A_1	V
or			
E	A_1	E	V
or			
A_1	E	E	V
θ	θ	ι	$\frac{1}{\sqrt{2}}$
ϵ	ϵ	ι	$\frac{1}{\sqrt{2}}$
θ	ι	θ	$\frac{1}{\sqrt{2}}$
ϵ	ι	ϵ	$\frac{1}{\sqrt{2}}$
ι	θ	θ	$\frac{1}{\sqrt{2}}$
ι	ϵ	ϵ	$\frac{1}{\sqrt{2}}$

symmetrized nuclear coordinates may be introduced as

$$\begin{aligned} \{Q_e \otimes Q_e\}_{e_\theta} &= (2)^{1/2} \left\{ V \begin{pmatrix} e & e & e \\ \theta & \theta & \theta \end{pmatrix} Q_{e_\theta}^2 + V \begin{pmatrix} e & e & e \\ \epsilon & \epsilon & \theta \end{pmatrix} Q_{e_\epsilon}^2 \right\} \\ &= \frac{\sqrt{2}}{2} (Q_{e_\epsilon}^2 - Q_{e_\theta}^2), \end{aligned} \quad (\text{B.15})$$

$$\begin{aligned} \{Q_e \otimes Q_e\}_{e_\epsilon} &= (2)^{1/2} \left\{ V \begin{pmatrix} e & e & e \\ \theta & \epsilon & \epsilon \end{pmatrix} Q_{e_\theta} Q_{e_\epsilon} \right\} \\ &= \frac{\sqrt{2}}{2} (Q_{e_\theta} Q_{e_\epsilon}), \end{aligned} \quad (\text{B.16})$$

and

$$\begin{aligned} \{Q_e \otimes Q_e\}_{a_1} &= (1)^{1/2} \left\{ V \begin{pmatrix} e & e & a_1 \\ \theta & \theta & \iota \end{pmatrix} Q_{e_\theta}^2 + V \begin{pmatrix} e & e & a_1 \\ \epsilon & \epsilon & \iota \end{pmatrix} Q_{e_\epsilon}^2 \right\} \\ &= \frac{1}{\sqrt{2}} (Q_{e_\theta}^2 + Q_{e_\epsilon}^2). \end{aligned} \quad (\text{B.17})$$

Once the proper analytical expressions for the irreducible products have been obtained, one can proceed further and define the matrix elements $W_{ji}^{(2)}(\mathbf{Q})$ [Eqs. (B.2) and

(B.5)] which contain quadratic (second-order perturbation) terms of the vibronic coupling. By substituting Eqs. (B.12), (B.13), (B.15) and (B.16) into the corresponding matrix elements of Eq. (B.5) and taking into account the definition of the quadratic VCC given in Eq. (2.16), one obtains

$$\begin{aligned}
& W_{11}^{(2)}(\mathbf{Q}) \\
&= \frac{1}{2} \left\langle E_{\theta}(\mathbf{r}; \mathbf{0}) \left| \left\{ \left(\frac{\partial \hat{\mathcal{U}}(\mathbf{r}; \mathbf{0})}{\partial Q_e} \right)_0 \otimes \left(\frac{\partial \hat{\mathcal{U}}(\mathbf{r}; \mathbf{0})}{\partial Q_e} \right)_0 \right\}_{e_{\theta}} \right| E_{\theta}(\mathbf{r}; \mathbf{0}) \right\rangle \{Q_e \otimes Q_e\}_{e_{\theta}} \\
&= \frac{1}{2} \left\langle E_{\theta}(\mathbf{r}; \mathbf{0}) \left| \frac{\sqrt{2}}{2} \left\{ \left(\frac{\partial^2 \hat{\mathcal{U}}(\mathbf{r}; \mathbf{0})}{\partial Q_{e_{\epsilon}}^2} \right)_0 - \left(\frac{\partial^2 \hat{\mathcal{U}}(\mathbf{r}; \mathbf{0})}{\partial Q_{e_{\theta}}^2} \right)_0 \right\} \right| E_{\theta}(\mathbf{r}; \mathbf{0}) \right\rangle \frac{\sqrt{2}}{2} (Q_{e_{\epsilon}}^2 - Q_{e_{\theta}}^2) \\
&= \left\{ \frac{1}{4} \left\langle E_{\theta}(\mathbf{r}; \mathbf{0}) \left| \left(\frac{\partial^2 \hat{\mathcal{U}}(\mathbf{r}; \mathbf{0})}{\partial Q_{e_{\epsilon}}^2} \right)_0 - \left(\frac{\partial^2 \hat{\mathcal{U}}(\mathbf{r}; \mathbf{0})}{\partial Q_{e_{\theta}}^2} \right)_0 \right| E_{\theta}(\mathbf{r}; \mathbf{0}) \right\rangle \right\} (Q_{e_{\epsilon}}^2 - Q_{e_{\theta}}^2) \\
&= \left\{ \frac{1}{4} \overline{G}_E \mathbf{V} \begin{pmatrix} E & E & e \\ \theta & \theta & \theta \end{pmatrix} \right\} (Q_{e_{\epsilon}}^2 - Q_{e_{\theta}}^2) \\
&= - \left(\frac{1}{8} \overline{G}_E \right) (Q_{e_{\epsilon}}^2 - Q_{e_{\theta}}^2) \\
&= -G_E (Q_{e_{\epsilon}}^2 - Q_{e_{\theta}}^2), \tag{B.18}
\end{aligned}$$

$$\begin{aligned}
& W_{12}^{(2)}(\mathbf{Q}) \\
&= \frac{1}{2} \left\langle E_{\theta}(\mathbf{r}; \mathbf{0}) \left| \left\{ \left(\frac{\partial \hat{\mathcal{U}}(\mathbf{r}; \mathbf{0})}{\partial Q_e} \right)_0 \otimes \left(\frac{\partial \hat{\mathcal{U}}(\mathbf{r}; \mathbf{0})}{\partial Q_e} \right)_0 \right\}_{e_{\epsilon}} \right| E_{\epsilon}(\mathbf{r}; \mathbf{0}) \right\rangle \{Q_e \otimes Q_e\}_{e_{\epsilon}} \\
&= \frac{1}{2} \left\langle E_{\theta}(\mathbf{r}; \mathbf{0}) \left| \sqrt{2} \left\{ \left(\frac{\partial^2 \hat{\mathcal{U}}(\mathbf{r}; \mathbf{0})}{\partial Q_{e_{\theta}} \partial Q_{e_{\epsilon}}} \right)_0 \right\} \right| E_{\epsilon}(\mathbf{r}; \mathbf{0}) \right\rangle \frac{\sqrt{2}}{2} (Q_{e_{\theta}} Q_{e_{\epsilon}}) \\
&= \left\{ \frac{1}{2} \left\langle E_{\theta}(\mathbf{r}; \mathbf{0}) \left| \left(\frac{\partial^2 \hat{\mathcal{U}}(\mathbf{r}; \mathbf{0})}{\partial Q_{e_{\theta}} \partial Q_{e_{\epsilon}}} \right)_0 \right| E_{\epsilon}(\mathbf{r}; \mathbf{0}) \right\rangle \right\} Q_{e_{\theta}} Q_{e_{\epsilon}} \\
&= \left\{ \frac{1}{2} \overline{G}_E \mathbf{V} \begin{pmatrix} E & E & e \\ \theta & \epsilon & \epsilon \end{pmatrix} \right\} Q_{e_{\theta}} Q_{e_{\epsilon}} \\
&= \left(\frac{1}{4} \overline{G}_E \right) Q_{e_{\theta}} Q_{e_{\epsilon}} \\
&= 2G_E Q_{e_{\theta}} Q_{e_{\epsilon}}, \tag{B.19}
\end{aligned}$$

$$\begin{aligned}
& W_{21}^{(2)}(\mathbf{Q}) \\
&= \frac{1}{2} \left\langle E_\epsilon(\mathbf{r}; \mathbf{0}) \left| \left\{ \left(\frac{\partial \hat{\mathcal{U}}(\mathbf{r}; \mathbf{0})}{\partial Q_e} \right)_0 \otimes \left(\frac{\partial \hat{\mathcal{U}}(\mathbf{r}; \mathbf{0})}{\partial Q_e} \right)_0 \right\}_{e_\epsilon} \right| E_\theta(\mathbf{r}; \mathbf{0}) \right\rangle \{Q_e \otimes Q_e\}_{e_\epsilon} \\
&= \frac{1}{2} \left\langle E_\epsilon(\mathbf{r}; \mathbf{0}) \left| \sqrt{2} \left\{ \left(\frac{\partial^2 \hat{\mathcal{U}}(\mathbf{r}; \mathbf{0})}{\partial Q_{e_\theta} \partial Q_{e_\epsilon}} \right)_0 \right\} \right| E_\theta(\mathbf{r}; \mathbf{0}) \right\rangle \frac{\sqrt{2}}{2} (Q_{e_\theta} Q_{e_\epsilon}) \\
&= \left\{ \frac{1}{2} \left\langle E_\epsilon(\mathbf{r}; \mathbf{0}) \left| \left(\frac{\partial^2 \hat{\mathcal{U}}(\mathbf{r}; \mathbf{0})}{\partial Q_{e_\theta} \partial Q_{e_\epsilon}} \right)_0 \right| E_\theta(\mathbf{r}; \mathbf{0}) \right\rangle \right\} Q_{e_\theta} Q_{e_\epsilon} \\
&= \left\{ \frac{1}{2} \bar{G}_E \mathbf{V} \begin{pmatrix} E & E & e \\ \epsilon & \theta & \epsilon \end{pmatrix} \right\} Q_{e_\theta} Q_{e_\epsilon} \\
&= \left(\frac{1}{4} \bar{G}_E \right) Q_{e_\theta} Q_{e_\epsilon} \\
&= 2G_E Q_{e_\theta} Q_{e_\epsilon}, \tag{B.20}
\end{aligned}$$

and

$$\begin{aligned}
& W_{22}^{(2)}(\mathbf{Q}) \\
&= \frac{1}{2} \left\langle E_\epsilon(\mathbf{r}; \mathbf{0}) \left| \left\{ \left(\frac{\partial \hat{\mathcal{U}}(\mathbf{r}; \mathbf{0})}{\partial Q_e} \right)_0 \otimes \left(\frac{\partial \hat{\mathcal{U}}(\mathbf{r}; \mathbf{0})}{\partial Q_e} \right)_0 \right\}_{e_\theta} \right| E_\epsilon(\mathbf{r}; \mathbf{0}) \right\rangle \{Q_e \otimes Q_e\}_{e_\theta} \\
&= \frac{1}{2} \left\langle E_\epsilon(\mathbf{r}; \mathbf{0}) \left| \frac{\sqrt{2}}{2} \left\{ \left(\frac{\partial^2 \hat{\mathcal{U}}(\mathbf{r}; \mathbf{0})}{\partial Q_{e_\epsilon}^2} \right)_0 - \left(\frac{\partial^2 \hat{\mathcal{U}}(\mathbf{r}; \mathbf{0})}{\partial Q_{e_\theta}^2} \right)_0 \right\} \right| E_\epsilon(\mathbf{r}; \mathbf{0}) \right\rangle \frac{\sqrt{2}}{2} (Q_{e_\epsilon}^2 - Q_{e_\theta}^2) \\
&= \left\{ \frac{1}{4} \left\langle E_\epsilon(\mathbf{r}; \mathbf{0}) \left| \left(\frac{\partial^2 \hat{\mathcal{U}}(\mathbf{r}; \mathbf{0})}{\partial Q_{e_\epsilon}^2} \right)_0 - \left(\frac{\partial^2 \hat{\mathcal{U}}(\mathbf{r}; \mathbf{0})}{\partial Q_{e_\theta}^2} \right)_0 \right| E_\epsilon(\mathbf{r}; \mathbf{0}) \right\rangle \right\} (Q_{e_\epsilon}^2 - Q_{e_\theta}^2) \\
&= \left\{ \frac{1}{4} \bar{G}_E \mathbf{V} \begin{pmatrix} E & E & e \\ \epsilon & \epsilon & \theta \end{pmatrix} \right\} (Q_{e_\epsilon}^2 - Q_{e_\theta}^2) \\
&= \left(\frac{1}{8} \bar{G}_E \right) (Q_{e_\epsilon}^2 - Q_{e_\theta}^2) \\
&= G_E (Q_{e_\epsilon}^2 - Q_{e_\theta}^2), \tag{B.21}
\end{aligned}$$

where \bar{G}_E is the reduced matrix element and G_E the corresponding quadratic coupling constant. Again, no other combinations of θ and ϵ in the brackets of Eqs. (B.18)-(B.21) are possible since for them $V=0$ (see Table B.1). Finally, we are now in position to calculate the diagonal matrix elements $K_{jj}(\mathbf{Q})$ (recall that off-diagonal terms are zero by symmetry)

which are the (nonvibronic) harmonic potentials around the JT reference geometry. The procedure is similar to the calculation of the $W_{ji}^{(2)}(\mathbf{Q})$ elements, with the exception that totally symmetric irreducible products [Eqs. (B.14) and (B.17)] are now employed in place of the non-totally symmetric ones. In so doing, one gets (see also Table B.2)

$$\begin{aligned}
K_{11}(\mathbf{Q}) &= \kappa_E(\mathbf{Q}) \\
&= \frac{1}{2} \left\langle E_\theta(\mathbf{r}; \mathbf{0}) \left| \left\{ \left(\frac{\partial \hat{\mathcal{U}}(\mathbf{r}; \mathbf{0})}{\partial Q_e} \right)_0 \otimes \left(\frac{\partial \hat{\mathcal{U}}(\mathbf{r}; \mathbf{0})}{\partial Q_e} \right)_0 \right\}_{a_1 \iota} \right| E_\theta(\mathbf{r}; \mathbf{0}) \right\rangle \{Q_e \otimes Q_e\}_{a_1 \iota} \\
&= \frac{1}{2} \left\langle E_\theta(\mathbf{r}; \mathbf{0}) \left| \frac{1}{\sqrt{2}} \left\{ \left(\frac{\partial^2 \hat{\mathcal{U}}(\mathbf{r}; \mathbf{0})}{\partial Q_{e_\theta}^2} \right)_0 + \left(\frac{\partial^2 \hat{\mathcal{U}}(\mathbf{r}; \mathbf{0})}{\partial Q_{e_\epsilon}^2} \right)_0 \right\} \right| E_\theta(\mathbf{r}; \mathbf{0}) \right\rangle \frac{1}{\sqrt{2}} (Q_{e_\theta}^2 + Q_{e_\epsilon}^2) \\
&= \frac{1}{2} \left\{ \frac{1}{2} \left\langle E_\theta(\mathbf{r}; \mathbf{0}) \left| \left(\frac{\partial^2 \hat{\mathcal{U}}(\mathbf{r}; \mathbf{0})}{\partial Q_{e_\theta}^2} \right)_0 + \left(\frac{\partial^2 \hat{\mathcal{U}}(\mathbf{r}; \mathbf{0})}{\partial Q_{e_\epsilon}^2} \right)_0 \right| E_\theta(\mathbf{r}; \mathbf{0}) \right\rangle \right\} (Q_{e_\theta}^2 + Q_{e_\epsilon}^2) \\
&= \frac{1}{2} \left\{ \frac{1}{2} \bar{K}_0^{(E)} \mathbb{V} \begin{pmatrix} E & E & a_1 \\ \theta & \theta & \iota \end{pmatrix} \right\} (Q_{e_\theta}^2 + Q_{e_\epsilon}^2) \\
&= \frac{1}{2} \left(\frac{1}{2\sqrt{2}} \bar{K}_0^{(E)} \right) (Q_{e_\theta}^2 + Q_{e_\epsilon}^2) \\
&= \frac{1}{2} K_0^{(E)} (Q_{e_\theta}^2 + Q_{e_\epsilon}^2), \tag{B.22}
\end{aligned}$$

and

$$\begin{aligned}
K_{22}(\mathbf{Q}) &= \kappa_E(\mathbf{Q}) \\
&= \frac{1}{2} \left\langle E_\epsilon(\mathbf{r}; \mathbf{0}) \left| \left\{ \left(\frac{\partial \hat{\mathcal{U}}(\mathbf{r}; \mathbf{0})}{\partial Q_e} \right)_0 \otimes \left(\frac{\partial \hat{\mathcal{U}}(\mathbf{r}; \mathbf{0})}{\partial Q_e} \right)_0 \right\}_{a_1 \iota} \right| E_\epsilon(\mathbf{r}; \mathbf{0}) \right\rangle \{Q_e \otimes Q_e\}_{a_1 \iota} \\
&= \frac{1}{2} \left\langle E_\epsilon(\mathbf{r}; \mathbf{0}) \left| \frac{1}{\sqrt{2}} \left\{ \left(\frac{\partial^2 \hat{\mathcal{U}}(\mathbf{r}; \mathbf{0})}{\partial Q_{e_\theta}^2} \right)_0 + \left(\frac{\partial^2 \hat{\mathcal{U}}(\mathbf{r}; \mathbf{0})}{\partial Q_{e_\epsilon}^2} \right)_0 \right\} \right| E_\epsilon(\mathbf{r}; \mathbf{0}) \right\rangle \frac{1}{\sqrt{2}} (Q_{e_\theta}^2 + Q_{e_\epsilon}^2) \\
&= \frac{1}{2} \left\{ \frac{1}{2} \left\langle E_\epsilon(\mathbf{r}; \mathbf{0}) \left| \left(\frac{\partial^2 \hat{\mathcal{U}}(\mathbf{r}; \mathbf{0})}{\partial Q_{e_\theta}^2} \right)_0 + \left(\frac{\partial^2 \hat{\mathcal{U}}(\mathbf{r}; \mathbf{0})}{\partial Q_{e_\epsilon}^2} \right)_0 \right| E_\epsilon(\mathbf{r}; \mathbf{0}) \right\rangle \right\} (Q_{e_\theta}^2 + Q_{e_\epsilon}^2) \\
&= \frac{1}{2} \left\{ \frac{1}{2} \bar{K}_0^{(E)} \mathbb{V} \begin{pmatrix} E & E & a_1 \\ \epsilon & \epsilon & \iota \end{pmatrix} \right\} (Q_{e_\theta}^2 + Q_{e_\epsilon}^2) \\
&= \frac{1}{2} \left(\frac{1}{2\sqrt{2}} \bar{K}_0^{(E)} \right) (Q_{e_\theta}^2 + Q_{e_\epsilon}^2) \\
&= \frac{1}{2} K_0^{(E)} (Q_{e_\theta}^2 + Q_{e_\epsilon}^2), \tag{B.23}
\end{aligned}$$

where $\bar{K}_0^{(E)}$ is the reduced matrix element and $K_0^{(E)}$ is the corresponding primary force constant which is equal for both $|E_\theta(\mathbf{r}; \mathbf{0})\rangle$ and $|E_e(\mathbf{r}; \mathbf{0})\rangle$ states. By considering all the set of 2 by 2 sub-matrices of Eq. (B.1) and their associated elements, the final $E \otimes e$ JT vibronic Hamiltonian is thus given by [1, 2]

$$\mathcal{H}_e = \begin{pmatrix} V_E^\times(\mathbf{0}) - F_E Q_{e\theta} - G_E(Q_{e_e}^2 - Q_{e_\theta}^2) + \kappa_E(\mathbf{Q}) & F_E Q_{e_e} + 2G_E Q_{e_e} Q_{e_\theta} \\ F_E Q_{e_e} + 2G_E Q_{e_e} Q_{e_\theta} & V_E^\times(\mathbf{0}) + F_E Q_{e_\theta} + G_E(Q_{e_e}^2 - Q_{e_\theta}^2) + \kappa_E(\mathbf{Q}) \end{pmatrix}. \quad (\text{B.24})$$

B.2 The $(\mathbf{E} + \mathbf{A}_1) \otimes \mathbf{e}$ problem

If by solving the TIESE [Eq. (2.13)] for a triangular X_3 -type molecule one obtains, besides the twofold degenerate E term with component wave functions $|E_\theta(\mathbf{r}; \mathbf{0})\rangle$ and $|E_e(\mathbf{r}; \mathbf{0})\rangle$, a non-degenerate close-in-energy A_1 state $|A_{1\iota}(\mathbf{r}; \mathbf{0})\rangle$, then all such terms get vibronically mixed along the JT-active displacements. Indeed, the vibronic problem at hand is effectively a three state one, *i.e.*, a combined JT plus PJT $[(E + A_1) \otimes e]$ [1, 4, 5]. To formulate the present case we again assume that the coupled states are well separated in energy from all other electronic terms, and hence only the subspace spanned by them needs to be considered. Let $V_1(\mathbf{0}) = V_2(\mathbf{0}) = V_E^\times(\mathbf{0})$ and $V_3(\mathbf{0}) = V_{A_1}(\mathbf{0})$ be the associated eigenvalues of the E and A_1 states, respectively. Again, the proper behavior of the adiabatic PESs in the vicinity of the high-symmetry configuration is obtained by first constructing the matrix representation of the operator $\hat{\mathcal{H}}_e(\mathbf{r}; \mathbf{Q})$ [Eq. (2.12)] in the basis $\{|E_\theta(\mathbf{r}; \mathbf{0})\rangle, |E_e(\mathbf{r}; \mathbf{0})\rangle, |A_{1\iota}(\mathbf{r}; \mathbf{0})\rangle\}$. For this, one should then determine the matrix elements of the set of sub-matrices shown in Eq. (B.2) which, for the current $(E + A_1) \otimes e$ problem, assume dimensions 3 by 3. Since the pure (2 by 2) JT problem has already been addressed in section B.1, all that remains now is to determine the corresponding PJT block which couples both E and A_1 terms. For the sake of simplicity, we assume that only first-order perturbation operators $W^{(1)}(\mathbf{r}; \mathbf{Q})$ in the expansion of Eq. (2.12) are here needed for the formulation of the PJT problem and that the corresponding $W_{ji}^{(2)}(\mathbf{Q})$ block is identically zero. Following Eqs. (2.14) and (2.15) as well as Table B.2, the remaining

$W_{ji}^{(1)}(\mathbf{Q})$ elements are thus given by

$$\begin{aligned}
 W_{13}^{(1)}(\mathbf{Q}) &= \left\langle E_\theta(\mathbf{r}; \mathbf{0}) \left| \left(\frac{\partial \hat{\mathcal{U}}(\mathbf{r}; \mathbf{0})}{\partial Q_{e_\theta}} \right)_0 \right| A_{1\iota}(\mathbf{r}; \mathbf{0}) \right\rangle Q_{e_\theta} \\
 &= \left\{ \bar{H}_{E/A_1} \mathbf{V} \begin{pmatrix} E & A_1 & e \\ \theta & \iota & \theta \end{pmatrix} \right\} Q_{e_\theta} \\
 &= \left(\frac{1}{\sqrt{2}} \bar{H}_{E/A_1} \right) Q_{e_\theta} \\
 &= H_{E/A_1} Q_{e_\theta}, \tag{B.25}
 \end{aligned}$$

$$\begin{aligned}
 W_{23}^{(1)}(\mathbf{Q}) &= \left\langle E_\epsilon(\mathbf{r}; \mathbf{0}) \left| \left(\frac{\partial \hat{\mathcal{U}}(\mathbf{r}; \mathbf{0})}{\partial Q_{e_\epsilon}} \right)_0 \right| A_{1\iota}(\mathbf{r}; \mathbf{0}) \right\rangle Q_{e_\epsilon} \\
 &= \left\{ \bar{H}_{E/A_1} \mathbf{V} \begin{pmatrix} E & A_1 & e \\ \epsilon & \iota & \epsilon \end{pmatrix} \right\} Q_{e_\epsilon} \\
 &= \left(\frac{1}{\sqrt{2}} \bar{H}_{E/A_1} \right) Q_{e_\epsilon} \\
 &= H_{E/A_1} Q_{e_\epsilon}, \tag{B.26}
 \end{aligned}$$

$$\begin{aligned}
 W_{31}^{(1)}(\mathbf{Q}) &= \left\langle A_{1\iota}(\mathbf{r}; \mathbf{0}) \left| \left(\frac{\partial \hat{\mathcal{U}}(\mathbf{r}; \mathbf{0})}{\partial Q_{e_\theta}} \right)_0 \right| E_\theta(\mathbf{r}; \mathbf{0}) \right\rangle Q_{e_\theta} \\
 &= \left\{ \bar{H}_{E/A_1} \mathbf{V} \begin{pmatrix} A_1 & E & e \\ \iota & \theta & \theta \end{pmatrix} \right\} Q_{e_\theta} \\
 &= \left(\frac{1}{\sqrt{2}} \bar{H}_{E/A_1} \right) Q_{e_\theta} \\
 &= H_{E/A_1} Q_{e_\theta}, \tag{B.27}
 \end{aligned}$$

and

$$\begin{aligned}
W_{32}^{(1)}(\mathbf{Q}) &= \left\langle A_{1\iota}(\mathbf{r}; \mathbf{0}) \left| \left(\frac{\partial \hat{\mathcal{U}}(\mathbf{r}; \mathbf{0})}{\partial Q_{e_\epsilon}} \right)_0 \right| E_\epsilon(\mathbf{r}; \mathbf{0}) \right\rangle Q_{e_\epsilon} \\
&= \left\{ \bar{H}_{E/A_1} V \begin{pmatrix} A_1 & E & e \\ \iota & \epsilon & \epsilon \end{pmatrix} \right\} Q_{e_\epsilon} \\
&= \left(\frac{1}{\sqrt{2}} \bar{H}_{E/A_1} \right) Q_{e_\epsilon} \\
&= H_{E/A_1} Q_{e_\epsilon}, \tag{B.28}
\end{aligned}$$

where, in contrast to the linear (F_E) and quadratic (G_E) JT VCCs (section B.1), H_{E/A_1} is now the linear PJT vibronic constant which effectively measures the coupling between the non-degenerate A_1 state and the pair of degenerate E terms by e vibrations. Note that, similarly to the pure $E \otimes e$ problem, any vibronic perturbation associated with the breathing normal coordinate ($Q_{a_{1\iota}}$; see Figure 2.2) is here neglected, and hence $W_{33}^{(1)}(\mathbf{Q}) = 0$. Since the linear approximation is assumed for the PJTE, *i.e.*, $W_{13}^{(2)}(\mathbf{Q}) = W_{23}^{(2)}(\mathbf{Q}) = W_{31}^{(2)}(\mathbf{Q}) = W_{32}^{(2)}(\mathbf{Q}) = 0$, we are left with the definition of the diagonal matrix element $K_{33}(\mathbf{Q})$. Following the same procedure adopted in (B.22) and (B.23), the harmonic nuclear (nonvibronic) interaction potential for the A_1 state is thus given by

$$\begin{aligned}
K_{33}(\mathbf{Q}) &= \kappa_{A_1}(\mathbf{Q}) \\
&= \frac{1}{2} \left\langle A_{1\iota}(\mathbf{r}; \mathbf{0}) \left| \left\{ \left(\frac{\partial \hat{\mathcal{U}}(\mathbf{r}; \mathbf{0})}{\partial Q_e} \right)_0 \otimes \left(\frac{\partial \hat{\mathcal{U}}(\mathbf{r}; \mathbf{0})}{\partial Q_e} \right)_0 \right\}_{a_{1\iota}} \right| A_{1\iota}(\mathbf{r}; \mathbf{0}) \right\rangle \{Q_e \otimes Q_e\}_{a_{1\iota}} \\
&= \frac{1}{2} \left\langle A_{1\iota}(\mathbf{r}; \mathbf{0}) \left| \frac{1}{\sqrt{2}} \left\{ \left(\frac{\partial^2 \hat{\mathcal{U}}(\mathbf{r}; \mathbf{0})}{\partial Q_{e_\theta}^2} \right)_0 + \left(\frac{\partial^2 \hat{\mathcal{U}}(\mathbf{r}; \mathbf{0})}{\partial Q_{e_\epsilon}^2} \right)_0 \right\} \right| A_{1\iota}(\mathbf{r}; \mathbf{0}) \right\rangle \frac{1}{\sqrt{2}} (Q_{e_\theta}^2 + Q_{e_\epsilon}^2) \\
&= \frac{1}{2} \left\{ \frac{1}{2} \left\langle A_{1\iota}(\mathbf{r}; \mathbf{0}) \left| \left(\frac{\partial^2 \hat{\mathcal{U}}(\mathbf{r}; \mathbf{0})}{\partial Q_{e_\theta}^2} \right)_0 + \left(\frac{\partial^2 \hat{\mathcal{U}}(\mathbf{r}; \mathbf{0})}{\partial Q_{e_\epsilon}^2} \right)_0 \right| A_{1\iota}(\mathbf{r}; \mathbf{0}) \right\rangle \right\} (Q_{e_\theta}^2 + Q_{e_\epsilon}^2) \\
&= \frac{1}{2} \left\{ \frac{1}{2} \bar{K}_0^{(A_1)} V \begin{pmatrix} A_1 & A_1 & a_1 \\ \iota & \iota & \iota \end{pmatrix} \right\} (Q_{e_\theta}^2 + Q_{e_\epsilon}^2) \\
&= \frac{1}{2} \left(\frac{1}{2} \bar{K}_0^{(A_1)} \right) (Q_{e_\theta}^2 + Q_{e_\epsilon}^2) \\
&= \frac{1}{2} K_0^{(A_1)} (Q_{e_\theta}^2 + Q_{e_\epsilon}^2), \tag{B.29}
\end{aligned}$$

where $\bar{K}_0^{(A_1)}$ is the reduced matrix element and $K_0^{(A_1)}$ is the corresponding primary force constant. Note that the expressions for the totally symmetric irreducible products are shown in Eqs. (B.14) and (B.17), with the V coefficient in Eq. (B.29) assuming the value of 1. By considering all the above matrix elements together with those obtained in section B.1, the final $(E + A_1) \otimes e$ (JT plus PJT) vibronic Hamiltonian thus reads [1, 4, 5]

$$\mathcal{H}_e = \begin{pmatrix} V_E^\times(\mathbf{0}) - F_E Q_{e_\theta} - G_E(Q_{e_\epsilon}^2 - Q_{e_\theta}^2) + \kappa_E(\mathbf{Q}) & F_E Q_{e_\epsilon} + 2G_E Q_{e_\epsilon} Q_{e_\theta} & H_{E/A_1} Q_{e_\theta} \\ F_E Q_{e_\epsilon} + 2G_E Q_{e_\epsilon} Q_{e_\theta} & V_E^\times(\mathbf{0}) + F_E Q_{e_\theta} + G_E(Q_{e_\epsilon}^2 - Q_{e_\theta}^2) + \kappa_E(\mathbf{Q}) & H_{E/A_1} Q_{e_\epsilon} \\ H_{E/A_1} Q_{e_\theta} & H_{E/A_1} Q_{e_\epsilon} & V_{A_1}(\mathbf{0}) + \kappa_{A_1}(\mathbf{Q}) \end{pmatrix}. \quad (\text{B.30})$$

Bibliography

- [1] I. B. Bersuker, *The Jahn-Teller Effect* (Cambridge University Press, Cambridge, 2006).
- [2] I. B. Bersuker, Chem. Rev. **101**, 1067 (2001).
- [3] J. S. Griffith, *The Irreducible Tensor Method for Molecular Symmetry Groups* (Prentice-Hall, New Jersey, 1962).
- [4] I. B. Bersuker, Chem. Rev. **113**, 1351 (2013).
- [5] P. Garcia-Fernandez, I. B. Bersuker, and J. E. Boggs, J. Chem. Phys. **125**, 104102 (2006).

Appendix C

General linear least squares method

In the process of calibrating potential energy surfaces from *ab initio* energies, one frequently faces the problem of representing sets of discrete data points (x_i, y_i) by target (continuous) functions that depends on adjustable parameters. Clearly, such a task can only be accomplished with the aid of the linear least squares method [1, 2].

Here, we assume that the set of N grid points is to be fitted to a model function of the general form

$$y(x) = \sum_{k=1}^M a_k X_k(x), \quad (\text{C.1})$$

where a_k are M disposable parameters with $X_k(x)$ defining a set of arbitrary functions of x , called the basis functions. Note that term “linear” referred throughout this section takes into account only the dependence that $y(x)$ has on its parameters a_k , regardless the order and explicit functional forms of the basis functions $X_k(x)$. Assuming that each data point has a “measurement error” (or weighting factor) σ_i , the best-fit coefficients are those that minimize the merit function

$$\chi^2 = \sum_{i=1}^N \left[\frac{y_i - \sum_{k=1}^M a_k X_k(x_i)}{\sigma_i} \right]^2. \quad (\text{C.2})$$

This can be accomplished by ensuring that χ^2 is stationary with respect to variation in

the parameters a_k , or in other words, by solving the set of M equations

$$\frac{\partial \chi^2}{\partial a_k} = \sum_{i=1}^N \frac{1}{\sigma_i^2} \left[y_i - \sum_{j=1}^M a_j X_j(x_i) \right] X_k(x_i) = 0 \quad k = 1, \dots, M. \quad (\text{C.3})$$

Interchanging the order of summations, we can write (C.3) as

$$\sum_{j=1}^M \sum_{i=1}^N \frac{X_j(x_i) X_k(x_i)}{\sigma_i^2} a_j = \sum_{i=1}^N \frac{y_i X_k(x_i)}{\sigma_i^2} \quad k = 1, \dots, M. \quad (\text{C.4})$$

The above expressions are called the normal equations of the least squares problem. In matrix form, these latter can also be defined by

$$\boldsymbol{\alpha} \cdot \mathbf{a} = \boldsymbol{\beta}, \quad (\text{C.5})$$

where

$$\alpha_{kj} = \sum_{i=1}^N \frac{X_j(x_i) X_k(x_i)}{\sigma_i^2} \quad (\text{C.6})$$

is an M by M square matrix and

$$\beta_k = \sum_{i=1}^N \frac{y_i X_k(x_i)}{\sigma_i^2} \quad (\text{C.7})$$

a column vector of length M . Note that, in Eq. (C.5), \mathbf{a} is the corresponding vector containing the M least squares parameters. The problem of determining the optimal coefficients a_k is then reduced to a matrix multiplication

$$\mathbf{a} = \boldsymbol{\alpha}^{-1} \boldsymbol{\beta}, \quad (\text{C.8})$$

or

$$a_j = \sum_{k=1}^M [\alpha]_{jk}^{-1} \beta_k = [\alpha]_{jk}^{-1} \left[\sum_{i=1}^N \frac{y_i X_k(x_i)}{\sigma_i^2} \right], \quad (\text{C.9})$$

where $[\alpha]_{jk}^{-1}$ are the corresponding elements of the inverse matrix $\boldsymbol{\alpha}^{-1}$.

Although no assumptions have been made regarding the explicit functional forms of the $X_k(x)$'s, the present discussion was restricted to those cases in which y depends on a single variable only. Clearly, there will also be situations in which y is a function of more than one variable, say a vector of variables \mathbf{x} . For such multidimensional fits, the preceding formalism is equally valid, with the exception that x is now replaced by \mathbf{x} .

Bibliography

- [1] W. H. Press, S. A. Teukolsky, W. T. Vetterling, and B. P. Flannery, *Numerical Recipes in Fortran 77: the Art of Scientific Computing*, 2nd ed., Vol. 1 (Cambridge University Press, New York, 1992).
- [2] C. L. Lawson and R. J. Hanson, *Solving Least Squares Problems*, Classics in Applied Mathematics (Prentice-Hall, Englewood Cliffs, 1974).

Appendix D

Parameters for the ground-state PESs of C_3

D.1 DMBE I PES

Table D.1: One-body term $V^{(1)}$ [Eq. (8) of chapter 6].

$V^{(1)}$	0.232 341 40
-----------	--------------

Table D.2: Coefficients for the two-body potential $V^{(2)}(\mathbf{R})$ [Eq. (8) of chapter 6].

R_e/a_0	2.479 320 12
$D/E_h a_0$	0.467 488 66
a_1/a_0^{-1}	0.850 571 03
a_2/a_0^{-2}	-1.071 149 98
a_3/a_0^{-3}	0.969 121 98
a_4/a_0^{-4}	-0.612 554 01
a_5/a_0^{-5}	0.310 832 98
a_6/a_0^{-6}	-0.094 424 41
a_7/a_0^{-7}	-0.007 369 76
a_8/a_0^{-8}	0.013 785 21
a_9/a_0^{-9}	-0.003 332 89
a_{10}/a_0^{-10}	0.000 257 90
γ_0/a_0	0.286 062 94
γ_1	15.553 200 00
γ_2/a_0	0.073 633 46
R_0/a_0	7.891 073 44
$C_5/E_h a_0^5$	14.540 400 00
$C_6/E_h a_0^6$	40.900 000 00
$C_8/E_h a_0^8$	984.720 273 07
$C_{10}/E_h a_0^{10}$	31 058.018 611 88

Table D.3: Coefficients for the three-body dynamical correlation energy term $V_{\text{dc}}^{(3)}(\mathbf{R})$ [Eq. (10) of chapter 6].

	$C_6^0(R)$	$C_6^2(R)$	$C_8^0(R)$	$C_8^2(R)$	$C_8^4(R)$	$C_{10}^0(R)$
R_M/a_0	4.500 000 00	4.500 000 00	4.471 100 00	4.482 300 00	4.487 300 00	4.452 500 00
$D_M/E_h a_0^n$	27.527 900 00	28.523 300 00	1037.637 000 00	2941.945 600 00	452.687 600 00	46 263.479 600 00
a_1/a_0^{-1}	0.994 999 99	0.763 626 10	0.931 359 73	0.798 190 39	1.235 396 71	0.896 186 14
a_2/a_0^{-2}	0.257 787 83	0.214 353 56	0.237 317 25	0.225 899 41	0.576 441 49	0.223 254 95
a_3/a_0^{-1}	0.001 395 84	-0.000 085 71	-0.000 130 49	-0.000 820 11	0.074 608 65	-0.001 827 31
b_2/a_0^{-2}	0.274 353 11	0.249 302 36	0.243 990 61	0.296 448 98	0.586 440 02	0.231 400 31
b_3/a_0^{-3}	0.025 462 46	0.006 768 50	0.024 868 58	0.021 097 93	0.073 266 21	0.026 813 74

Table D.4: Coefficients (in atomic units) for the $V'_{\text{I,EHF}}{}^{(3)}(\mathbf{R})$ term [Eq. (20) of chapter 6].

i	j	k	c_{ijk}^1	c_{ijk}^2	R'_0
0	0	0	0.909 436 33E-01	0.560 289 45E-01	3.267 966 39
1	0	0	0.978 788 59E-02	0.918 056 83E-01	
0	1	0	-0.101 623 93E+00	-0.128 719 02E+00	
2	0	0	-0.112 621 13E-01	0.437 007 07E-01	
0	0	1	-0.621 143 64E-01	0.532 406 31E-01	
1	1	0	0.449 527 02E+00	0.162 555 17E+01	
3	0	0	-0.144 289 02E-01	-0.716 502 06E-02	
0	2	0	0.503 843 79E-01	0.201 036 00E+00	
1	0	1	-0.731 913 44E-01	-0.358 721 15E-01	
2	1	0	0.292 146 38E+00	0.974 117 08E+00	
4	0	0	-0.699 694 01E-02	-0.744 909 58E-02	
0	1	1	0.287 443 03E+00	0.290 844 71E+00	
1	2	0	0.257 581 63E+01	0.199 113 59E+01	
2	0	1	-0.505 992 29E-02	0.209 507 42E-01	
3	1	0	0.776 469 05E-01	0.247 040 70E+00	
5	0	0	-0.167 250 50E-02	-0.907 673 63E-03	
0	0	2	0.941 553 11E-02	0.746 817 60E-02	
0	3	0	0.154 079 85E+00	0.506 758 04E-01	
1	1	1	0.574 792 04E-01	0.508 646 59E-01	
2	2	0	0.118 363 57E+01	0.594 069 04E+00	
3	0	1	0.152 251 68E-01	0.241 452 50E-01	
4	1	0	0.330 883 36E-01	0.611 897 60E-01	
6	0	0	-0.679 753 17E-03	0.821 591 69E-03	
0	2	1	0.118 139 43E+00	0.173 932 34E-01	
1	0	2	0.723 937 48E-02	0.287 520 74E-02	
1	3	0	0.758 982 66E+00	0.123 754 08E+00	
2	1	1	0.189 476 36E-01	0.450 854 50E-02	
3	2	0	0.201 426 09E+00	0.448 320 73E-01	

Continued on next page.

Table D.4 – *Continued from previous page.*

i	j	k	c_{ijk}^1	c_{ijk}^2	R'_0
4	0	1	0.333 739 86E-02	0.202 364 99E-02	
5	1	0	0.634 017 97E-02	0.581 278 24E-02	
7	0	0	-0.128 405 38E-04	0.124 153 54E-03	
0	1	2	0.146 265 66E-02		
0	4	0	0.609 650 11E-02		
1	2	1	0.105 448 67E-01		
2	0	2	0.158 873 87E-02		
2	3	0	0.105 115 95E+00		
3	1	1	0.712 927 62E-02		
4	2	0	0.234 226 79E-01		
5	0	1	0.519 929 18E-03		
6	1	0	0.587 778 72E-03		
8	0	0	0.485 704 60E-04		
0	0	3	-0.371 821 41E-04		
0	3	1	0.185 201 77E-03		
1	1	2	-0.256 620 12E-03		
1	4	0	0.444 814 66E-02		
2	2	1	0.247 860 35E-03		
3	0	2	0.652 337 11E-04		
3	3	0	-0.216 751 43E-02		
4	1	1	-0.530 447 49E-03		
5	2	0	-0.192 435 58E-03		
6	0	1	0.133 198 11E-03		
7	1	0	-0.213 772 74E-04		
9	0	0	0.127 624 44E-04		

Table D.5: Coefficients for the range function $T_1'(\mathbf{R})$ [Eq. (22) of chapter 6].

α/a_0^{-1}	R_0/a_0
0.620 000 00	3.267 966 39

Table D.6: Coefficients (in atomic units) for the $V_{\text{I,EHF}}^{(3)}(\mathbf{R})$ term [Eq. (24) of chapter 6].

i	j	k	c_{ijk}^3	c_{ijk}^4	R_0''
0	0	0	0.554 069 27E-04	0.121 928 09E+03	2.609 548 37
1	0	0	-0.116 158 51E+00	0.152 290 66E+05	
0	1	0	-0.105 749 02E+01	-0.848 833 46E+06	
2	0	0	-0.138 202 49E+02	0.464 923 56E+07	
0	0	1	0.323 309 44E+03		
1	1	0	-0.156 373 89E+04		
3	0	0	0.813 938 51E+04		
0	2	0	0.298 763 56E+04		
1	0	1	0.463 257 58E+06		
2	1	0	-0.125 286 57E+07		
4	0	0	0.126 022 24E+07		

Table D.7: Coefficients for the Gaussian function $T_1'(\mathbf{R})$ [Eq. (27) of chapter 6].

R_1^0/a_0	R_2^0/a_0	R_3^0/a_0	β/a_0^{-2}
2.606 660 67	2.606 660 67	2.615 323 78	1.260 000 00

D.2 DMBE II PES

Table D.8: Coefficients for the Q_3^1 equation [Eq. (17) of chapter 8].

ϱ/a_0	0.004 548 73
δ/a_0	0.025 091 03
Q_1^0/a_0	4.782 913 31
ζ_1/a_0^{-1}	1.059 386 52
ζ_2/a_0^{-2}	-0.926 173 46
ζ_3/a_0^{-3}	-0.216 477 65
ζ_4/a_0^{-4}	0.172 219 37
ζ_5/a_0^{-5}	0.682 819 12

Table D.9: Coefficients (in atomic units) for the $V_{\text{II,EHF}}^{(3)}(\mathbf{R})$ term [Eq. (22) of chapter 8].

i	j	k	c_{ijk}^1	c_{ijk}^2	R'_0
0	0	0	0.939 419 64E-01	0.552 705 80E-01	3.267 966 39
1	0	0	0.814 094 36E-02	0.867 056 28E-01	
0	1	0	-0.137 991 77E+00	-0.292 061 51E+00	
2	0	0	-0.120 752 32E-01	0.340 031 29E-01	
0	0	1	-0.526 763 00E-01	0.127 723 52E+00	
1	1	0	0.344 140 52E+00	0.126 702 81E+01	
3	0	0	-0.144 177 78E-01	-0.153 752 77E-01	
0	2	0	-0.216 556 74E+00	-0.253 399 96E-02	
1	0	1	-0.118 516 40E+00	-0.121 847 97E+00	
2	1	0	0.194 334 44E+00	0.762 417 02E+00	
4	0	0	-0.672 855 80E-02	-0.102 626 12E-01	
0	1	1	0.445 640 96E+00	0.439 870 79E+00	
1	2	0	0.210 270 11E+01	0.168 735 34E+01	
2	0	1	-0.473 015 44E-01	-0.593 511 61E-01	
3	1	0	0.424 675 61E-01	0.207 750 40E+00	
5	0	0	-0.142 313 90E-02	-0.884 966 70E-03	

Continued on next page.

Table D.9 – *Continued from previous page.*

i	j	k	c_{ijk}^1	c_{ijk}^2	R'_0
0	0	2	0.922 426 07E-02	0.722 406 87E-02	
0	3	0	0.779 262 05E-01	0.380 312 89E-01	
1	1	1	-0.430 756 62E-03	0.340 641 95E-01	
2	2	0	0.101 106 39E+01	0.535 047 68E+00	
3	0	1	0.168 777 00E-01	0.262 522 42E-01	
4	1	0	0.310 076 81E-01	0.643 720 13E-01	
6	0	0	-0.555 669 71E-03	0.101 519 27E-02	
0	2	1	0.189 073 35E+00	0.341 658 75E-01	
1	0	2	0.531 839 79E-02	0.149 953 12E-02	
1	3	0	0.659 753 28E+00	0.108 240 18E+00	
2	1	1	-0.405 365 14E-01	-0.157 367 22E-01	
3	2	0	0.187 354 02E+00	0.438 820 54E-01	
4	0	1	0.813 305 57E-02	0.583 518 01E-02	
5	1	0	0.782 028 66E-02	0.679 892 78E-02	
7	0	0	-0.102 320 71E-03	0.138 470 99E-03	
0	1	2	0.139 389 15E-02		
0	4	0	0.551 339 89E-02		
1	2	1	0.871 095 29E-02		
2	0	2	0.142 558 45E-02		
2	3	0	0.982 099 72E-01		
3	1	1	0.766 319 03E-02		
4	2	0	0.253 278 27E-01		
5	0	1	0.815 312 36E-03		
6	1	0	0.920 746 72E-03		
8	0	0	0.437 428 58E-04		
0	0	3	-0.381 045 13E-04		
0	3	1	0.175 798 20E-02		
1	1	2	-0.466 517 44E-03		
1	4	0	0.351 449 35E-02		

Continued on next page.

Table D.9 – *Continued from previous page.*

i	j	k	c_{ijk}^1	c_{ijk}^2	R'_0
2	2	1	-0.235 648 64E-02		
3	0	2	0.672 025 19E-04		
3	3	0	-0.212 710 14E-02		
4	1	1	0.215 021 73E-03		
5	2	0	0.134 146 36E-03		
6	0	1	0.641 835 27E-04		
7	1	0	-0.113 967 96E-04		
9	0	0	0.102 605 86E-04		

Table D.10: Coefficients for the range function $T'_{II}(\mathbf{R})$ [Eq. (25) of chapter 8].

α'/a_0^{-1}	R'_0/a_0
0.610 000 00	3.267 966 39

Table D.11: Coefficients (in atomic units) for the $V''_{\text{II,EHF}}{}^{(3)}(\mathbf{R})$ term [Eq. (23) of chapter 8].

i	j	k	c_{ijk}^3	c_{ijk}^4	c_{ijk}^5	R_0''
0	0	0	-0.818 307 84E-03	-0.117 434 18E+00	-0.136 264 89E-01	2.609 610 00
1	0	0	-0.763 963 41E-03	-0.157 822 96E+00	-0.160 230 67E-01	
0	1	0	-0.585 126 33E-03	-0.144 728 63E+01	0.789 401 23E-01	
2	0	0	-0.254 858 22E-02	-0.354 159 91E+00	-0.469 425 27E-01	
0	0	1	-0.507 353 54E-01	-0.278 247 47E+01	0.892 272 22E-02	
1	1	0	0.246 576 86E-01	-0.221 459 20E+01	0.354 883 89E-01	
3	0	0	-0.891 309 41E-03	-0.107 676 34E+00	-0.139 408 71E-01	
0	2	0	0.850 094 95E-01			
1	0	1	0.400 507 86E-01			
2	1	0	0.272 964 77E-01			
4	0	0	-0.901 669 22E-03			

Table D.12: Coefficients for the range function $T''_{\text{II}}(\mathbf{R})$ [Eq. (26) of chapter 8].

β''/a_0^{-1}	R_1''/a_0	$R_2'' = R_3''/a_0$
3.297 519 97	2.619 996 38	2.604 401 28

Table D.13: Coefficients (in atomic units) for the $V_{\text{II,EHF}}'''^{(3)}(\mathbf{R})$ term [Eq. (24) of chapter 8].

i	j	k	c_{ijk}^6	c_{ijk}^7	c_{ijk}^8	R_0'''
0	0	0	0.323 232 71E-05	-0.135 147 88E-01	0.512 262 98E-02	3.319 764 05
1	0	0	0.486 143 04E-04	-0.541 527 77E-01	0.117 985 61E-01	
0	1	0	-0.212 510 69E-02	0.197 689 94E+00	-0.244 890 51E-02	
2	0	0	0.213 367 05E-03	-0.851 429 17E-01	0.745 602 60E-02	
0	0	1	-0.128 324 51E-02	0.323 164 05E-01	0.641 217 47E-04	
1	1	0	-0.573 522 11E-02	0.288 432 41E+00	-0.782 019 37E-02	
3	0	0	0.357 905 16E-03	-0.478 502 57E-01	-0.534 177 23E-03	
0	2	0	0.197 085 36E-02			
1	0	1	-0.178 597 72E-02			
2	1	0	0.215 027 56E-03			
4	0	0	0.219 562 60E-03			

Table D.14: Coefficients for the range function $T_{\text{II}}'''(\mathbf{R})$ [Eq. (27) of chapter 8].

γ'''/a_0^{-1}	R_1'''/a_0	$R_2''' = R_3'''/a_0$
4.304 304 05	3.311 206 10	3.324 043 02

Table D.15: Coefficients for the non-Jahn-Teller function $\mathcal{F}_{nJT}(\mathbf{R})$ [Eq. (28) of chapter 8].

ς/a_0^{-2}	R_0^{cP}/a_0
10 000	2.885 169 41

D.3 ABW local PES

Table D.16: Coefficients (in atomic units) for the experimentally-determined ABW local PES of C₃ [Eq. (D.1)].

<i>i</i>	<i>j</i>	<i>k</i>	<i>c_{ijk}</i>	<i>i</i>	<i>j</i>	<i>k</i>	<i>c_{ijk}</i>
1	2	0	-0.752 496 8	4	0	0	0.057 189 1
1	2	2	0.018 065 6	0	2	0	0.336 895 7
1	0	2	-0.007 722 9	0	2	2	-0.006 461 4
1	0	4	0.003 213 7	0	2	4	0.027 706 7
1	0	6	-0.004 352 8	0	2	6	-0.031 560 2
1	0	8	0.001 889 5	0	2	8	0.013 800 7
1	0	10	-0.000 314 2	0	2	10	-0.002 225 3
2	0	0	0.334 939 2	0	4	0	0.117 423 1
2	2	0	0.556 112 2	0	0	2	0.000 957 0
2	0	2	-0.017 297 9	0	0	4	-0.000 361 6
2	0	4	0.005 571 6	0	0	6	0.001 217 8
3	0	0	-0.238 685 8	0	0	8	-0.000 450 0
3	0	2	0.029 711 0	0	0	10	0.000 086 3
3	0	4	-0.009 069 1				

The computed local PES for ground-state C₃ due to Ahmed, Balint-Kurti and Western (ABW) [*J. Chem. Phys.* **121**, 10041 (2004)] assumes the simple functional form

$$V_{\text{ABW}}(\mathbf{R}) = \sum_{ijk} c_{ijk} S_1^i S_2^j \theta^k, \quad (\text{D.1})$$

where

$$S_1 = \frac{1}{\sqrt{2}}(\Delta R_1 + \Delta R_2), \quad (\text{D.2})$$

and

$$S_2 = \frac{1}{\sqrt{2}}(\Delta R_1 - \Delta R_2), \quad (\text{D.3})$$

represent the symmetric and antisymmetric stretching coordinates, respectively. Note that $\Delta R_i = R_i - R_e$ ($i = 1, 2$) denote the displacements of the C-C bond lengths from the

equilibrium position $R_e = 2.46004548 a_0$, while θ in (D.1) measures the deviation from linearity. The PES terms c_{ijk} are listed in Table D.16.

D.4 SS local PES

Table D.17: Non-redundant coefficients (in atomic units) for the purely *ab initio* SS local PES of C_3 [Eq. (D.4)].

i	j	k	c_{ijk}	i	j	k	c_{ijk}	i	j	k	c_{ijk}	i	j	k	c_{ijk}
2	0	0	0.33240693	1	1	0	-0.00355710	4	0	2	0.01570702	3	0	6	0.00537182
3	0	0	-0.35060064	2	1	0	-0.00614366	3	1	2	-0.01948533	2	1	6	-0.00172969
4	0	0	0.22690209	3	1	0	-0.00075277	2	2	2	0.00576765	4	0	6	0.06314677
5	0	0	-0.11822982	2	2	0	0.00039680	1	0	4	-0.00042866	3	1	6	-0.06693212
6	0	0	0.05358855	4	1	0	0.00215995	2	0	4	0.00327471	2	2	6	0.01705080
7	0	0	-0.02849987	3	2	0	0.00544895	1	1	4	-0.00263969	1	0	8	-0.00020893
8	0	0	0.02001495	5	1	0	-0.02856759	3	0	4	-0.00321668	2	0	8	-0.00157956
0	0	2	0.00041387	4	2	0	0.00176688	2	1	4	-0.00004568	1	1	8	0.00068353
0	0	4	0.00064654	3	3	0	0.01393769	4	0	4	-0.06550030	3	0	8	-0.00220384
0	0	6	0.00016547	1	0	2	-0.00449159	3	1	4	0.06968179	2	1	8	-0.00059965
0	0	8	-0.00004851	2	0	2	-0.00103148	2	2	4	-0.05757693	4	0	8	-0.00935219
0	0	10	0.00010604	1	1	2	-0.01222084	1	0	6	0.00045529	3	1	8	0.00107021
0	0	12	-0.00004245	3	0	2	0.00155557	2	0	6	-0.00074881	2	2	8	0.04522482
0	0	14	0.00000644	2	1	2	0.01460243	1	1	6	0.00162108	1	3	8	0.00107021

The local PES reported by Schröder and Sebald (SS) [*J. Chem. Phys.* **144**, 044307 (2016)] is analytically represented as a polynomial of the form

$$V_{\text{SS}}(\mathbf{R}) = \sum_{ijk} c_{ijk} \Delta R_1^i \Delta R_2^j \theta^k, \quad (\text{D.4})$$

where, similarly to Eqs. (D.2) and (D.3), ΔR_i ($i=1, 2$) are the single C-C bond stretching coordinates defined with respect to an equilibrium position of $R_e = 2.44524892 a_0$. θ in (D.4) also denotes the instantaneous value of the bond-angle supplement. The non-redundant parameters of the SS potential are given in Table D.17. Note that, since the PES is represented in terms of displacement coordinates rather than symmetric ones as in (D.1), the coefficients with different i and j should be permutationally equivalent.

Appendix E

Rovibrational energy levels for the ground-state PESs of C₃

Table E.1: Parameters employed in the rovibrational energy calculations (see chapter 9).

Parameter	DMBE/ES/ABW ^a	DMBE/ES/SS ^a	DMBE I-II
NPNT1 ^b	26	40	34
NPNT2 ^b	56	56	56
NALF ^c	80	80	80
$r_{e,1}/a_0$ ^d	2.585	2.453	2.585
$D_{e,1}/E_h$	0.300	0.558	0.562
$w_{e,1}/E_h$	0.010	0.011	0.011
$r_{e,2}/a_0$	3.675	3.505	3.695
$D_{e,2}/E_h$	0.300	0.399	0.305
$w_{e,2}/E_h$	0.005	0.009	0.008

^a The same parameters are used for the corresponding local forms.

^b Number of DVR points in r_i ($i=1, 2$) from Gauss-(associated) Laguerre quadrature.

^c Number of DVR points in θ from Gauss-(associated) Legendre quadrature.

^d $r_{e,i}$, $D_{e,i}$ and $w_{e,i}$ are the equilibrium separation, fundamental frequency and dissociation energy of the relevant coordinate r_i ($i=1, 2$), respectively.

Table E.2: Differences (in cm⁻¹) between the observed ($G_{\text{expt.}}$) and calculated rovibrational energy levels for C₃ radical. The quantum numbers ν_1 , ν_2 and ν_3 refer to symmetric, bending and antisymmetric motions, respectively, and l_2 is the vibrational angular momentum quantum number. J is the total angular momentum quantum number.

ν_1	$\nu_2^{l_2}$	ν_3	J	$G_{\text{expt.}}^a$	Observed–calculated						Mladenović <i>et al.</i> ^g	Špirko <i>et al.</i> ^h
					DMBE/ES/ABW ^b	ABW ^c	DMBE/ES/SS ^b	SS ^d	DMBE II ^e	DMBE I ^f		
0	0 ⁰	0	0	0.0	7.9	7.6	0.0	0.0	0.0	0.0	0.0	0.0
0	1 ¹	0	1	63.4	3.1	2.9	-0.2	-0.3	2.7	1.8	-0.9	0.7
0	2 ⁰	0	0	132.8	2.7	2.5	0.1	0.0	-3.8	-8.0	-0.5	-0.2
0	3 ¹	0	1	207.3	0.3	0.1	-0.7	-0.8	-17.6	-24.6	0.8	0.3
0	4 ⁰	0	0	286.1	-0.6	-0.7	-0.7	-0.9	-29.8	-42.4	2.7	-0.3
0	6 ⁰	0	0	461.1	0.8	0.7	3.0	2.8	-31.3	-61.8	11.0	2.7
0	8 ⁰	0	0	647.6	-1.1	-1.3	3.5	3.2	8.7	-44.2	15.1	1.2
0	10 ⁰	0	0	848.4	-1.9	-2.1	5.2	4.8	50.3	-14.4	19.1	0.3
0	12 ⁰	0	0	1062.0	-2.2	-2.5	7.8	7.2	68.6	-23.3		
1	0 ⁰	0	0	1224.5	5.1	5.4	-0.3	-0.1	-9.6	63.5	5.5	1.1
0	14 ⁰	0	0	1289.3	-0.2	-0.6	13.1	12.4	71.5	71.8		
1	2 ⁰	0	0	1404.1	0.4	1.7	-1.1	-0.8	-13.3	74.1	1.0	-1.5
0	16 ⁰	0	0	1525.6	-0.4	-0.9	16.2	15.4	55.8	55.8		
1	4 ⁰	0	0	1590.1	-2.3	0.0	-2.6	-1.8	-38.0	-16.7	0.0	-1.5
0	18 ⁰	0	0	1773.4	0.2	-0.4	18.5	17.6	26.6	26.5		

Continued on next page.

Table E.2 – Continued from previous page.

v_1	$v_2^{1/2}$	v_3	J	$G_{\text{expt.}}^a$	Observed–calculated						Mladenović <i>et al.</i> ^g	Špirko <i>et al.</i> ^h
					DMBE/ES/ABW ^b	ABW ^c	DMBE/ES/SS ^b	SS ^d	DMBE II ^e	DMBE I ^f		
1	6 ⁰	0	0	1785.1	−4.9	−1.8	−3.4	−2.2	−59.6	−27.1	2.4	−3.0
1	8 ⁰	0	0	1990.5	−6.7	−3.5	−2.0	−1.0	−44.9	35.8	6.6	0.0
0	20 ⁰	0	0	2031.3	0.6	−0.1	16.2	15.3	−16.9	−18.3		
0	0 ⁰	1	0	2040.0	3.9	2.0	−0.1	0.4	−16.7	53.9	−0.6	0.1
0	1 ¹	1	1	2078.5	1.1	−0.9	0.3	−0.2	−13.7	2.8	−4.4	0.2
0	2 ⁰	1	0	2133.9	2.0	0.1	−0.3	−0.5	−25.6	6.9	−4.7	0.1
0	3 ¹	1	1	2191.1	−1.2	−3.0	−2.6	−3.1	−36.3	−88.8	−5.7	0.2
1	10 ⁰	0	0	2210.5	−3.7	−0.9	5.8	6.3	5.3	40.8	15.3	3.3
0	22 ⁰	0	0	2299.4	1.1	0.1	7.0	5.9	−61.3	−61.6		
0	5 ¹	1	1	2330.0	−1.7	−3.7	−2.4	−3.6	−22.8	−97.3	−2.1	0.0
2	0 ⁰	0	0	2435.2	−2.2	2.4	−2.1	−0.6	−16.0	−15.5	10.5	−10.4
1	12 ⁰	0	0	2439.9	−1.0	1.3	15.2	15.1	30.4	41.3		
0	7 ¹	1	1	2489.7	−0.7	−3.0	0.7	−1.6	28.9	−81.9	3.3	0.2
0	24 ⁰	0	0	2575.9	−0.3	−1.5	−11.7	−13.6	43.6	35.2		
2	2 ⁰	0	0	2656.3	−10.1	0.3	−5.5	−1.6	−25.6	−30.3	3.9	−2.0
0	9 ¹	1	1	2665.7	0.3	−2.6	5.4	1.9	49.0	40.3	8.1	−0.1
1	14 ⁰	0	0	2669.7	−7.6	−5.9	17.3	16.6	45.0	43.9		

Continued on next page.

Table E.2 – *Continued from previous page.*

v_1	$v_2^{1/2}$	v_3	J	$G_{\text{expt.}}^a$	Observed–calculated						Mladenović <i>et al.</i> ^g	Špirko <i>et al.</i> ^h
					DMBE/ES/ABW ^b	ABW ^c	DMBE/ES/SS ^b	SS ^d	DMBE II ^e	DMBE I ^f		
0	11 ¹	1	1	2856.8	1.6	−1.8	12.4	7.6	57.0	48.9		
2	4 ⁰	0	0	2876.9	−13.9	1.7	−7.9	−1.2	−45.4	−53.2	0.4	−5.4
1	16 ⁰	0	0	2919.7	−3.5	−2.4	33.0	31.6	45.8	42.1		
0	13 ¹	1	1	3060.7	2.4	−1.6	21.0	15.1	64.8	58.9		
2	6 ⁰	0	0	3099.9	−16.8	3.2	−9.3	0.1	−69.7	−79.2	1.6	−3.4
1	18 ⁰	0	0	3170.5	−7.9	−7.4	35.7	34.7	−25.7	−29.8		
1	0 ⁰	1	0	3259.9	−1.3	1.1	−3.7	0.1	−29.9	−31.4		
0	15 ¹	1	1	3278.1	4.4	−0.4	28.3	22.5	54.9	51.6		
1	1 ¹	1	1	3327.5	−7.6	−3.2	−6.6	−3.1	−32.0	−37.8		−21.1
1	3 ¹	1	1	3475.9	−11.1	−4.5	−9.1	−5.4	−44.0	−54.9		−21.5
0	17 ¹	1	1	3506.8	6.0	0.4	29.0	23.5	−9.2	−16.3		
3	0 ⁰	0	0	3636.1	−20.0	−0.1	−7.1	−1.0	−20.9	−20.5		−13.5
1	5 ¹	1	1	3641.3	−11.2	−3.0	−8.7	−4.7	−57.0	−72.7		−17.4
0	19 ¹	1	1	3743.3	4.3	−2.2	34.1	23.6	−77.7	−83.3		
1	7 ¹	1	1	3820.9	−9.2	−1.4	−3.8	−1.7	−30.2	−44.1		−14.5
3	2 ⁰	0	0	3894.3	−37.6	−0.4	−17.0	−1.9	−37.2	−42.1		−20.2
0	21 ¹	1	1	3995.0	6.3	−1.0	8.9	3.9	−28.0	−31.7		

Continued on next page.

Table E.2 – Continued from previous page.

v_1	$v_2^{1/2}$	v_3	J	$G_{\text{expt.}}^a$	Observed–calculated						Mladenović <i>et al.</i> ^g	Špirko <i>et al.</i> ^h
					DMBE/ES/ABW ^b	ABW ^c	DMBE/ES/SS ^b	SS ^d	DMBE II ^e	DMBE I ^f		
1	9 ¹	1	1	4012.3	−7.0	−1.1	4.8	3.4	17.2	7.5	−13.5	
0	0 ⁰	2	0	4035.4	10.1	0.3	5.8	3.1	−19.8	−37.0	−7.2	
0	2 ⁰	2	0	4110.9	10.8	2.4	1.3	1.9	−21.1	−41.7	−5.3	
3	4 ⁰	0	0	4146.3	5.2	2.2	−25.2	−1.5	−54.4	−62.9	−21.1	
0	4 ⁰	2	0	4211.3	13.3	3.8	6.4	0.9	24.8	13.4	−4.9	
1	11 ¹	1	1	4216.4	−3.9	−0.4	18.1	13.2	26.9	16.4		
0	23 ¹	1	1	4252.9	5.2	−3.6	−29.4	−33.5	−60.8	−65.4		
0	6 ⁰	2	0	4339.4	15.4	5.0	13.3	1.3	42.2	28.1	−4.8	
3	6 ⁰	0	0	4392.8	−61.9	2.1	−35.6	−3.3	−82.5	−92.8	−20.9	
1	13 ¹	1	1	4432.6	−0.2	0.8	35.1	27.8	27.5	20.4		
2	0 ⁰	1	0	4459.3	−18.7	−1.0	−11.0	0.0	−36.3	−37.0		
0	8 ⁰	2	0	4489.2	22.1	6.6	23.0	4.8	54.6	38.8	−4.5	
2	1 ¹	1	1	4557.1	−25.4	0.3	−13.2	1.2	−40.4	−44.9	−39.8	
3	8 ⁰	0	0	4641.0	−68.9	2.6	−39.7	−2.2	−100.1	−110.5	−18.1	
0	10 ⁰	2	0	4651.6	21.2	3.2	30.0	6.5	27.8	17.3	−9.7	
1	15 ¹	1	1	4659.1	2.9	1.4	7.7	33.1	32.4	21.3		
2	3 ¹	1	1	4745.7	−34.1	0.8	−18.2	0.2	−44.8	−55.1	−42.0	

Continued on next page.

Table E.2 – *Continued from previous page.*

v_1	$v_2^{1/2}$	v_3	J	$G_{\text{expt.}}^a$	Observed–calculated						Mladenović <i>et al.</i> ^g	Špirko <i>et al.</i> ^h
					DMBE/ES/ABW ^b	ABW ^c	DMBE/ES/SS ^b	SS ^d	DMBE II ^e	DMBE I ^f		
4	0 ⁰	0	0	4828.7	−52.0	−1.6	−17.0	−1.3	−25.0	−25.0		
0	12 ⁰	2	0	4832.5	24.4	3.2	33.2	9.7	−9.8	−18.3		
1	17 ¹	1	1	4895.7	5.8	1.8	54.6	58.7	−73.9	−85.5		
2	5 ¹	1	1	4938.8	−40.4	2.1	−23.3	−0.8	−64.8	−79.2		−38.3
0	14 ⁰	2	0	5029.0	28.2	4.1	50.3	21.5	13.1	1.5		
2	7 ¹	1	1	5139.1	−42.0	3.1	−22.1	0.1	−66.7	−83.5		−34.6
0	16 ⁰	2	0	5236.6	30.4	3.6	47.3	36.5	37.8	33.1		
1	0 ⁰	2	0	5265.4	−16.5	−7.7	−17.9	−2.7	−47.6	−53.2		
2	9 ¹	1	1	5347.1	6.6	2.9	−11.4	4.0	−7.3	−40.5		−32.7
1	2 ⁰	2	0	5367.2	−16.4	−7.2	−14.6	−4.2	−45.1	−58.7		
1	4 ⁰	2	0	5495.4	−16.6	−5.7	−14.1	−7.2	−46.8	−70.2		
2	11 ¹	1	1	5564.7	−31.6	2.8	8.4	14.0	30.5	25.2		
1	6 ⁰	2	0	5643.5	−11.4	−4.2	−3.0	−7.8	−0.7	−17.2		
3	1 ¹	1	1	5766.3	−9.0	−0.4	−32.2	1.6	−49.5	−53.5		
1	8 ⁰	2	0	5809.1	−4.0	−2.5	13.6	−3.1	32.3	14.5		
1	10 ⁰	2	0	5989.2	10.3	−1.5	35.5	3.6	29.4	8.4		
3	3 ¹	1	1	5991.9	−22.7	1.2	−43.9	1.3	−52.7	−63.4		

Continued on next page.

Table E.2 – Continued from previous page.

v_1	$v_2^{1/2}$	v_3	J	$G_{\text{expt.}}^a$	Observed–calculated						Mladenović <i>et al.</i> ^g	Špirko <i>et al.</i> ^h
					DMBE/ES/ABW ^b	ABW ^c	DMBE/ES/SS ^b	SS ^d	DMBE II ^e	DMBE I ^f		
5	0 ⁰	0	0	6013.6	−86.5	−2.1	−29.2	−1.5	−28.6	−29.0		
3	5 ¹	1	1	6214.0	−99.6	2.6	−55.7	−0.4	−71.0	−86.0		
3	7 ¹	1	1	6437.7	9.7	4.2	−61.4	−0.9	−86.5	−103.6		
3	9 ¹	1	1	6663.1	−104.8	2.8	−53.6	−0.3	0.0	−85.1		
3	11 ¹	1	1	6896.6	−0.9	3.2	−26.5	8.6	−11.5	−20.9		
4	1 ¹	1	1	6962.2	−4.1	−1.9	−54.3	1.3	−57.6	−1.1		
3	13 ¹	1	1	7134.9	−3.9	1.4	5.2	23.4	10.3	−0.6		
6	0 ⁰	0	0	7191.3	−97.9	−1.5	−36.4	−1.6	−32.6	−33.3		
4	3 ¹	1	1	7220.2	13.3	−0.6	−72.2	0.7	−60.7	−71.9		
4	5 ¹	1	1	7470.6	14.2	1.0	−87.9	−1.4	−81.3	−95.3		
4	9 ¹	1	1	7962.9	0.0	1.1	−97.7	−5.1	−99.7	−117.9		
5	1 ¹	1	1	8146.4	12.0	−4.4	−68.1	−0.3	−65.6	−69.6		
4	11 ¹	1	1	8214.1	−5.1	2.8	−69.7	1.9	−58.4	−70.8		
7	0 ⁰	0	0	8361.5	−77.1	−0.3	−37.5	−2.1	−37.2	−38.2		
5	3 ¹	1	1	8435.8	3.3	−2.1	−59.6	0.6	−72.0	−82.3		
4	13 ¹	1	1	8467.5	−0.4	2.1	−27.9	1.4	−19.2	15.3		
5	5 ¹	1	1	8712.8	−25.9	−1.3	−101.8	−2.5	−89.3	−103.9		

Continued on next page.

Table E.2 – *Continued from previous page.*

v_1	$v_2^{1/2}$	v_3	J	$G_{\text{expt.}}^a$	Observed–calculated							
					DMBE/ES/ABW ^b	ABW ^c	DMBE/ES/SS ^b	SS ^d	DMBE II ^e	DMBE I ^f	Mladenović <i>et al.</i> ^g	Špirko <i>et al.</i> ^h
rmsd					26.9	2.9	31.0	12.5	45.7	53.4	7.3	15.4

^a Ref. 1.^b This work [2].^c Ref. 1. Reported values are from the present work [2].^d Ref. 3. Reported values are from the present work [2].^e Ref. 4.^f Ref. 5.^g Ref. 6.^h Ref. 7.

Bibliography

- [1] K. Ahmed, G. G. Balint-Kurti, and C. M. Western, *J. Chem. Phys.* **121**, 10041 (2004).
- [2] C. M. R. Rocha and A. J. C. Varandas, submitted (2017).
- [3] B. Schröder and P. Sebald, *J. Chem. Phys.* **144**, 044307 (2016).
- [4] C. M. R. Rocha and A. J. C. Varandas, submitted (2017).
- [5] C. M. R. Rocha and A. J. C. Varandas, *J. Chem. Phys.* **143**, 074302 (2015).
- [6] M. Mladenović, S. Schmatz, and P. Botschwina, *J. Chem. Phys.* **101**, 5891 (1994).
- [7] V. Špirko, M. Mengel, and P. Jensen, *J. Mol. Spectrosc.* **183**, 129 (1997).

Appendix F

Parameters for the ground-state triplet PES of C_4

Table F.1: Coefficients (in atomic units) for the $V^{(4)}(\mathbf{R})$ term [Eq. (3.8) of chapter 10].

Coeff.	$P_1^{(4)}$	$P_2^{(4)}$	$P_3^{(4)}$	$P_4^{(4)}$
c_0	-0.478 167 76E+04	-0.237 711 77E+01	-0.811 573 50E+02	0.615 133 80E+04
c_1	-0.271 472 12E+04	0.709 260 49E+01	-0.207 888 33E+02	-0.102 657 22E+04
c_2	-0.525 205 53E+03	-0.219 888 93E+01	0.106 814 06E+02	0.210 207 69E+03
c_3	0.169 299 51E+01	0.000 000 00E+00	0.555 662 02E+01	0.000 000 00E+00
c_4	0.545 580 51E+01	0.000 000 00E+00	0.276 525 65E+01	0.000 000 00E+00
c_5	0.368 088 65E+02	0.191 584 55E+00	0.000 000 00E+00	0.000 000 00E+00
c_6	-0.635 472 28E+01	0.000 000 00E+00	0.000 000 00E+00	0.000 000 00E+00
c_7	-0.542 893 47E+01	0.000 000 00E+00	0.000 000 00E+00	0.000 000 00E+00
c_8	-0.795 888 36E+01	-0.669 460 77E-01	-0.518 205 18E+01	0.873 630 69E+01
c_9	-0.172 935 81E+01	0.247 421 20E-01	0.161 920 20E+01	-0.754 415 45E+00
c_{10}	-0.123 823 45E+01	0.333 573 10E-01	-0.188 633 58E+01	0.222 863 66E+01
R_0	2.081 905 27	2.730 220 79	2.385 206 86	2.567 589 96

Table F.2: Coefficients (in atomic units) for the $V^{(4)}(\mathbf{R})$ term [Eq. (3.8) of chapter 10].

Coeff.	$P_5^{(4)}$	$P_6^{(4)}$	$P_7^{(4)}$
c_0	0.294 312 41E+00	0.426 956 33E+01	-0.204 080 25E+01
c_1	0.665 881 76E+00	0.302 731 99E+00	0.119 338 45E+01
c_2	-0.423 009 05E+00	-0.197 031 03E+01	-0.629 823 09E+00
c_3	-0.189 612 64E+00	0.460 204 35E+00	-0.550 706 57E-01
c_4	-0.272 134 74E+00	0.555 094 15E+00	-0.399 972 30E-01
c_5	-0.455 491 75E-01	0.000 000 00E+00	0.000 000 00E+00
c_6	0.229 975 15E+00	0.000 000 00E+00	0.367 447 80E-01
c_7	0.236 455 58E+00	0.000 000 00E+00	-0.640 015 36E-02
c_8	0.282 137 11E+00	-0.136 311 14E+01	0.398 203 61E-01
c_9	0.211 564 54E-01	-0.801 353 03E-01	-0.393 972 10E-01
c_{10}	0.529 894 86E-01	-0.257 833 33E+00	0.415 407 85E-02
R_0	3.135 912 28	3.000 000 00	3.629 201 37

Table F.3: Coefficients for the Gaussian functions $G_i(\mathbf{T})$ [Eq. (3.8) of chapter 10].

Gaussian	γ_i/a_0^{-2}
G_1	0.254 469 99
G_2	0.100 000 00
G_3	0.237 106 61
G_4	0.327 077 57
G_5	0.500 000 00
G_6	0.600 000 00
G_7	0.450 000 00

